Investigations of Formaldehyde Oxime, its Polymers and Coordination Compounds. I

K. A. JENSEN and ARNE HOLM

On the Nature of the So-Called "Triformoxime" and Isolation of the Authentic Trimer, 1,3,5-Trihydroxyhexahydro–1,3,5-triazine

Det Kongelige Danske Videnskabernes Selskab
Matematisk-fysiske Meddelelser **40**: 1

Kommissionær: Munksgaard
1978

Contents

Synopsis

Evidence obtained from chemical properties and infrared spectra shows that the so-called triformoxime or trimeric formaldehyde oxime is actually a chain-polymer. The known acetyl and benzoyl derivatives of formaldehyde oxime are, however, derivatives of a cyclic trimer, 1,3,5-trihydroxyhexahydro-1,3,5-triazine, and are derived neither from the polymer, nor from monomeric formaldehyde oxime. Similarly, the known hydrochloride, $(CH_2NOH)_3HCl$, and also other salts, contain the cyclic trimer, but on neutralization they depolymerize to formaldehyde oxime.

The cyclic trimer was isolated from partially polymerized formaldehyde oxime in the form of a molecular complex containing dioxane and in a pure state from a neutralized solution of the hydrochloride in ethanol. Both products are rapidly transformed into the insoluble polymer.

An analysis of the ^{1}H NMR spectra of neutralized solutions of $(CH_2NOH)_3HCl$ in deuterium oxide has shown that, in aqueous solution, an equilibrium exists between monomeric and trimeric formaldehyde oxime which, at higher pH values, is shifted towards the monomeric form. The compound, which can be extracted with ether from aqueous solutions at pH *ca.* 8, is the monomer but, with HCl, CH_3I, $(CH_3CO)_2O$, etc., it gives derivatives of the trimer.

K. A. Jensen *and* Arne Holm
Chemical Laboratory 2
The H. C. Ørsted Institute
University of Copenhagen

Printed in Denmark by Bianco Lunos Bogtrykkeri A/S. ISBN 87-7304-096-7

I. Introduction

While investigating the composition of the ligand in the coordination compounds[1] prepared from "triformoxime hydrochloride", $(H_2CNOH)_3 \cdot HCl$ (*1*), we became interested in the nature of the polymer of formaldehyde oxime which is usually described as a trimer (*e.g.* in Beilstein's handbook and Rodd's Chemistry of Carbon Compounds). Its properties, however, are much more like those of a chain polymer. It is an amorphous solid, insoluble in most solvents, and in fact looks much like paraformaldehyde. Like the latter, it is depolymerized on heating and gives vapour of monomeric formaldehyde oxime. The spectroscopic properties of gaseous, monomeric formaldehyde oxime are well known; both its infrared (IR) spectrum[2,3] and its microwave spectrum[4,5] have been investigated. Condensation of the vapour yields either the white solid polymer (*2*) or the liquid monomer (*3*). The latter is rapidly transformed into the same white solid. Decomposition of *2* and *3* sometimes takes place explosively on heating, with the formation of water and hydrogen cyanide.

Monomeric formaldehyde oxime (*3*) was obtained by Dunstan and Bossi[7] by distillation of the ether extract of an aqueous solution of formaldehyde oxime. A liquid distils at 83 °C/760 mmHg leaving a residue (*2*b) which is insoluble in ether. It is difficult to eliminate ether completely from the distillate but we have otherwise confirmed the results of Dunstan and Bossi. The ^1H NMR spectrum of the liquid in $CDCl_3$ shows only signals for monomeric formaldehyde oxime (see Section IV) and none which may be ascribed to a polymer.

II. Properties of the Polymeric Products

The following polymeric products were shown to give almost identical infrared spectra.

2a. The white amorphous solid obtained according to Scholl,[6] by mixing concentrated solutions of hydroxylamine and formaldehyde.

2b. The white solid obtained according to Dunstan and Bossi,[7] by evaporation of the ether extract of a neutralized aqueous solution of hydroxylammonium chloride and formaldehyde.

2c. The white solid which is formed from *2a* or *2b* on sublimation.

2d. The white solid which is formed as a residue, and in various parts of the distillation apparatus, during distillation of the monomer.

2e. The white solid which is formed from the liquid monomer (*3*) at room temperature (or slowly even at −80 °C) or which separates rapidly from a solution of monomeric formaldehyde oxime in carbon tetrachloride.

The polymeric formaldehyde oxime is a white solid which depolymerizes at 132-134 °C. Condensation of the vapour usually yields the polymer again. The mass spectrum of the vapour shows the presence of the molecular ion of the monomer with no indication of the formation of oligomers. The polymer is insoluble in common solvents, but on prolonged heating dissolves both in water and in some organic solvents; it does not separate again when the solutions are cooled. Ebulliometric measurements in acetone indicate the solute to be monomeric formaldehyde oxime (found M = 50, calc. 45).

Although all the above mentioned products (*2a-e*) exhibit identical infrared spectra and show no significant differences in their C, H, N analyses, the reaction with nickel(II) chloride[1] reveals a very remarkable difference between freshly prepared products formed by polymerization of the monomer (*2b-e*) and the products formed directly from aqueous formaldehyde and hydroxylamine (*2a*): the former immediately gives a very intense colour while *2a* gives no reaction (or slowly develops a very faint colour); however, if *2a* is first dissolved in hydrochloric acid, the same intense colour is obtained as with the other products on addition of $NiCl_2$ and NaOH. This difference is explained as being due to the presence of the genuine trimer (see section V) in freshly prepared polymerization products; the latter lose the ability to give a positive nickel reaction after some time because the trimer is transformed into the polymer.

Polymerization of formaldehyde oxime apparently does not take place in dilute aqueous solution. When an aqueous solution of hydroxylammonium chloride is reacted with formaldehyde and the solution is then neutralized no separation of the polymer occurs; according to our NMR spectroscopic investigation (section IV) the initially formed "triformoxime hydrochloride" (*1*) on neutralization is converted almost quantitatively into monomeric formaldehyde oxime. On the other hand, if the hydroxylammonium chloride is neutralized before the addition of formaldehyde, separation of the polymer begins in a few minutes. Clearly the

polymer is not formed in aqueous solution by polymerization but by polycondensation:

$$n\ HO{-}CH_2OH + n\ H{-}\underset{\underset{OH}{|}}{N}{-}H \rightarrow HO{-}CH_2{-}\underset{\underset{OH}{|}}{N}{-}CH_2{-}\underset{\underset{OH}{|}}{N}{-}\cdots$$

In this case there is the possibility that the second terminal group is also an $HO{-}CH_2$ group. This circumstance, together with differences in degree of polymerization, may account for some observed variation in the properties of the polymeric products.

The polymeric products dissolve rapidly in hydrochloric acid, but it takes hours or even days to dissolve them in boiling water (product *2a* dissolves more slowly that products *2b-e*). Dissolution is much accelerated by the addition of NaCl and occurs with depolymerization; monomeric formaldehyde oxime distils over with the steam and polymerizes again in the condenser. Some hydrolysis also takes place. After prolonged boiling, the aqueous solution contains formaldehyde and hydroxylamine but (according to the nickel reaction) no monomeric or trimeric formaldehyde oxime. When a neutralized solution of hydroxylammonium chloride and formaldehyde is evaporated *in vacuo* a solid is formed in the condenser. This solid exhibits the same infrared spectrum as the other polymer samples.

The infrared spectra of the polymers are rather simple and apparently do not differ much from the spectrum of gaseous formaldehyde oxime, investigated by Califano and Lüttke.[3] However, most of the bands should be re-assigned (see the detailed discussion of the infrared spectra of the polymers in the following publication)[8]. Only the following results from the investigation will be mentioned here: We succeeded in recording the infrared spectrum of monomeric formaldehyde oxime as a liquid film although the liquid solidified in less than 5 min. The spectrum exhibited the $\nu(C{=}N)$ band clearly at 1630 cm^{-1}, the CH_2 twisting band at 780 cm^{-1} and the $\nu(N{-}O)$ band (vs) at 900 cm^{-1} (assignments according to Ref. 3). The solidification of the film resulted in the disappearance of the two first mentioned bands and a shift of the 900 cm^{-1} band to 840 cm^{-1}.

The infrared spectra of the polymeric products support the conclusion that the latter are chain polymers analogous to paraformaldehyde; the spectra are not compatible with the assumption that the polymer is "triformoxime", *i.e.* 1,3,5-trihydroxyhexahydro-1,3,5-triazine. The possibility[9] that the polymer might be a dimer or trimer analogous to glycolaldehyde, glyceraldehyde or dihydroxyacetone is also ruled out by the infrared spectra. Furthermore, from the chemical properties of the polymers, structures of the latter type seem improbable. The infrared

spectra exhibit no bands attributable to ether linkages, so that the possibility of the chain containing CH_2–O–CH_2 groups seems to be ruled out.

A polymer analogous to paraformaldehyde would have the formula:

$$HO\text{–}(CH_2\text{–}\underset{\displaystyle OH}{\underset{|}{N}}\text{–})_nH \quad \text{or} \quad (CH_3NO)_n + H_2O$$

One of the terminal groups could, however, be an oxime group:

$$HO\text{–}(CH_2\text{–}\underset{\displaystyle OH}{\underset{|}{N}}\text{–})_{n-1}CH{=}NOH \quad \text{or} \quad (CH_3NO)_n + O$$

A structure of the latter type could conceivably result from an oxygen catalysed polymerization of monomeric formaldehyde oxime.

When the polymer is formed in solution from hydroxylamine and formaldehyde it may contain two $-CH_2OH$ terminal groups:

$$HO\text{–}(CH_2\text{–}\underset{\displaystyle OH}{\underset{|}{N}}\text{–})_{n-1}CH_2OH \quad \text{or} \quad (CH_3NO)_n - N + HO$$

It is not possible to distinguish between the three formulae by elemental analysis when $n > ca.\ 10$.

The carbon and nitrogen analyses are often slightly lower, and the oxygen analyses slightly higher, than those corresponding to the formula $(CH_3NO)_n$, indicating that the degree of polymerization may be no greater than corresponding to $n = 20\text{-}30$. Since the polymer is insoluble and reacts chemically only under concomitant depolymerization it has not been possible to determine its molecular weight.

III. Derivatives of Trimeric Formaldehyde Oxime

The assumption that the polymer should be trimeric has been based mainly on the isolation of a hydrochloride with the composition $(CH_3NO)_3 \cdot HCl$ (*1*) and on the observed molecular weight of the acetyl derivative (*4*), which may be prepared by the addition of acetic anhydride to the above mentioned ether extract

of formaldehyde oxime.[7] These compounds cannot, however, be prepared directly from the solid polymer. Although the latter dissolves in dilute hydrochloric acid it is not re-precipitated when the solution is neutralized, indicating that the reaction with hydrochloric acid is accompanied by depolymerization. When the polymer is dissolved in methanol containing HCl, the hydrochloride (*1*) (identity proved by its infrared spectrum) can be precipitated by the addition of ether. Acid anhydrides and acid chlorides react only slowly with the solid polymer forming triacyl derivatives of the trimer. No partially acylated derivatives of the solid polymer could be prepared.

A hydrochloride with the formula $(CH_2NOH \cdot HCl)_n$ has been isolated as the initial product from the reaction of hydrogen chloride with an ether solution of formaldehyde oxime.[10] However, it can only be obtained with this high HCl content when it is dried in a stream of gaseous HCl. Otherwise it rapidly loses HCl and is transformed into *1*. These crude samples of *1* usually contain more than 1, and less than 3, mol HCl (quite often we have obtained a product analysing as a dihydrochloride), but when the crude hydrochloride is dissolved in methanol and precipitated with ether the hydrochloride with the composition $(CH_3NO)_3 \cdot HCl$ * is always obtained as a well-defined and quite stable product.

The infrared spectra of the hydrochlorides with higher HCl content do not differ very much from that of *1*. However, this is not significant because the products lose HCl so easily. Sluiter[10] determined the base constants of the bases present in $H_2NOH \cdot HCl$ and *1* by measurements of the catalytic effect of the hydrochlorides on ester hydrolysis and sugar inversion and obtained the values 2.4×10^{-12} and 3.0×10^{-13}, respectively. Although these values may not be very exact by modern standards, the qualitative result seems quite unambiguous: when present in an equivalent amount, $CH_2NOH \cdot HCl$ exerts a smaller catalytic effect than *1*, although it contains three times as much HCl per nitrogen atom and accordingly must be the hydrochloride of a stronger base. This latter species must either be trimeric, and therefore an isomer of the base contained in *1*, or it must be monomeric formaldehyde oxime. Sluiter favoured the first possibility and advanced the hypothesis that the loss of HCl was the result of a rearrangement of 1,3,5-trihydroxyhexahydro-1,3,5-triazine into the 2,4,6-trihydroxy isomer. This conclusion is now quite untenable and so we must conclude that the primary product is the hydrochloride of monomeric formaldehyde oxime. This is consistent with our NMR measurements on ether solutions, which reveal only signals attributable to formaldehyde oxime monomer.

* This is also the composition of commercial products sold under the name "formaldoxime hydrochloride".

The fact that a pure product with a lower HCl content than *1* is never obtained shows that we are not dealing with hydrochlorides of the chain polymer. However, over a period of time the composition of the product (*1*) sometimes changes, either because of the formation of the solid polymer (decreasing HCl content) or because of hydrolysis with the formation of hydroxylammonium chloride (increasing HCl content). A hydrobromide,[7] hydroiodide,[7] hydrogen nitrate,[11] and methiodide[12] with corresponding compositions are also known.

The infrared spectrum of the hydrochloride (*1*) is rather complex and quite different from that of the polymers. A comparison with the infrared spectrum of the free trimer leaves no doubt that it is a hydrochloride of the latter.

Both the acetyl derivative (*4*) and the hydrochloride (*1*) give an instantaneous colour reaction with nickel chloride on addition of base. Since it had been shown that the ligand present in the resulting complexes is the anion of monomeric formaldehyde oxime[1] we gave serious consideration to the possibility that the hydrochloride and the acetyl derivative might be derived from monomeric formaldehyde oxime. This appeared to be supported by the fact that the infrared bands corresponding to CH_2 deformation in the acetyl and benzoyl derivatives occur at the unusually frequency of 1415 cm^{-1}, *i.e.* almost as low as for monomeric formaldehyde oxime (1410 cm^{-1}) and much lower than for the polymers (1460 cm^{-1}). However, a similar lowering of the CH_2 deformation frequency has been observed for certain heterocyclic systems[14] and furthermore the infrared spectra of the acetyl and benzoyl derivatives in chloroform solution provide no indication of the presence of a double bond, even at high concentrations. That these compounds are in fact trimeric was confirmed by MS and by determination of their molecular weight in solution by various methods (cryoscopic, ebulliometric, thermoelectric).

The electric dipole moment of the acetyl derivative was found to be 3.25 debye in dioxane. This rules out the possibility that this compound might be (associated) formaldehyde *N*-acetyloxime.

Finally, the ^1H NMR spectra of the acetyl and benzoyl derivatives indicate the expected ratios of 3:2 and 5:2, respectively, for the two types hydrogen atoms in each compound. This rules out the possibility of these compounds being derivatives of a trimer analogous to glyceraldehyde or dihydroxyacetone. Accordingly it seems almost certain that these compounds are derivatives of 1,3,5-trihydroxyhexahydro-1,3,5-triazine. To substantiate this conclusion an X-ray diffraction study of the acetyl derivative has been carried out.[13] This shows that the acetyl derivative contains a six-membered hexahydrotriazine ring in the chair conformation with three axial *N*-acetoxy groups.

It was found that the acetyl derivative is rapidly hydrolysed by NaOH; thus to

explain the formation of metal complexes with monomeric formaldehyde oxime from *1* or *4*, one has only to assume that the hexahydrotriazine ring is rapidly depolymerized in solution.

Several years ago we demonstrated (unpublished) the presence of monomeric formaldehyde oxime in aqueous solutions of *1* by IR spectroscopy (sharp band at 1620 cm^{-1} for a solution of *1* in D_2O). NMR studies have now provided evidence that in fact a reversible equilibrium is easily established between 1,3,5-trihydroxy-hexahydro-1,3,5-triazine and formaldehyde oxime. Surprisingly, however, these investigations also showed that although the complexes are derived from the monomer, they are not formed directly from this but *via* the trimer.

IV. ^1H NMR Spectra

The ^1H NMR spectrum of a solution of $(H_2CNOD)_3 \cdot DCl$ in D_2O (pH = 1.1) shows two doublets at δ 7.11 and 6.11, and two singlets at δ 4.82 and 4.65 (the δ values are pH-dependent, cf. Table 1). The first singlet is due to water. Assuming the presence of a cyclic hexahydro-1,3,5-triazine system, the other singlet at δ 4.65 can be ascribed to the methylene protons. The corresponding signal for 1,3,5-trimethoxyhexahydro-1,3,5-triazine[15] occurs at δ 4.15 and that for the acetyl derivative (*4*) at δ 4.53. For none of these hexahydrotriazines is splitting of the signal of the methylene protons observed; this phenomenon is most likely a consequence of rapid interconversion between axial and equatorial protons at room temperature. Likewise the signal due to the methylene protons of other hexahydrotriazines,[16–18] with the exception of 1,3,5-trinitrosohexahydro-1,3,5-triazine,[16] appears only as a singlet.

The doubles at δ 7.11 and 6.61 are assigned to monomeric formaldehyde oxime. These doublets occur at δ 7.07 and 6.49 for a solution of pure, liquid formaldehyde oxime in $CDCl_3$, the singlet due to the trimer being totally absent. Solutions of formaldehyde oxime in CCl_4 or ether also contain only the monomeric form (Table 1). Similar δ-values for the doublets have been found in previous studies of the ^1H NMR spectra of solutions of monomeric formaldehyde oxime prepared by extraction of aqueous solutions with various solvents and without isolation of the pure compound.[19–21] The existence of the trimer was not noted in these investigations.

When distilled monomeric formaldehyde oxime is dissolved in D_2O and immediately examined by ^1H NMR, signals from both the monomeric and trimeric forms are observed in the spectrum. The integrals of these signals correspond

Table 1. Chemical shifts (δ) for methylene protons for $H_2C{=}NOH$ and $(CH_2NOH)_3$.

solvent	trimer	monomer		
		trans	cis	J (Hz)
CCl_4 *		6.98	6.38	8.0
$CDCl_3$		7.07	6.49	8.5
$(C_2H_5)_2O$		7.00	6.38	9.0
$(CD_3)_2CO$	4.00	6.94	6.34	9.0
$(CD_3)_2SO$	3.84**	6.92	6.38	9.0
D_2O pH 1.1	4.65	7.11	6.61	7.5
2.5	4.64	7.10	6.60	8.0
4.2	4.22	7.10	6.60	8.0
7.3	4.17	7.10	6.60	8.0
10.4	4.08	6.97	6.42	8.0
11.9	3.97	6.97	6.42	10.0

* The solution of $H_2C{=}NOH$ in CCl_4 is rapidly transformed into a gel of the polymer.
** δ for OH proton 8.25.

Table 2. Percentages of monomeric formaldehyde oxime[a], present in solutions of $(CH_2NOD)_3DCl$ in D_2O as a function of pH, temperature and initial concentration of $(CH_2NOD)_3DCl$ (C_0).

Temperature 39 °C. C_0 = 0.347 mol l^{-1}

pH:	1.3	1.7	1.9	2.2	3.0	4.2
% monomer:	80	84	87	93	94	97

C_0 = 0.759 mol l^{-1}. pH = 1.05

Temperature, °C:	25	30	35	40
% monomer:	44	56	62	65

Temperature 25 °C

C_0:	0.334	0.436	0.573	0.759	2.5
pH:	1.26	1.18	1.12	1.05	
% monomer:	68	63	56	44	~0

a) Calculated from the ^1H NMR spectra:
% monomer = 100(M)/[(M)+1/3(T)], where (M) and (T) are the integrated intensities of the signals due to the monomer and the trimer.

initially to 60-70 % of the monomer and 40-30 % of the trimer (c = *ca.* 1 mol/l). This must be considered a kinetically controlled ratio. At pH *ca.* 7 an equilibrium is slowly established but after several hours the mixture contains *ca.* 95 % of the monomer, in agreement with the results obtained starting with the hydrochloride of the trimer or the pure trimer (see later).

The AB system arises because of the difference in shielding of the methylene protons in *cis* (c) and *trans* (t) positions:

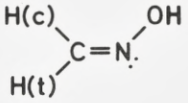

The equilibrium concentrations of the monomer and the trimer in aqueous solution can be calculated from the initial concentrations of the hydrochloride and the integrated intensities of the signals due to the methylene protons. As shown in Table 2 the ratio of monomer to trimer is dependent on the total concentration, the pH of the medium, and the temperature. The depolymerization of the trimer is favoured by diminishing concentration, increasing temperature, and increasing pH. At pH values higher than 3 only a few percent of the trimer is present in equilibrium with the monomer.

The existence of an "inactive" form of *1* has been postulated[22–26] to explain the observation that a dilute solution of *1* does not give the usual colour reaction with metal ions (Ni^{2+}, Mn^{2+}, Fe^{2+}). As can be seen from Table 2, the degree of depolymerization of *1* increases with decreasing concentration and in very dilute solutions only monomeric formaldehyde oxime is present. Thus it must be concluded that the "inactive form" is monomeric formaldehyde oxime and that the coloured complexes are formed only at concentrations where a significant proportion of the trimer is present.

Our measurements indicate that at low pH values an equilibrium between monomeric and trimeric formaldehyde oxime is established immediately. ^1H NMR provides no indication of the formation of a hydrate of the oxime, $HOCH_2$–NHOH, and the trimerization of *3* therefore undoubtedly proceeds *via* the protonated oxime (Scheme 1).

In accordance with Scheme 1 the quantity [trimer] × [monomer]$^{-3}$ is found to be approximately constant for a variety of initial concentrations and constant pH. At constant initial concentration, and for pH values varying between 1 and 2, the quantity [trimer] × [monomer]$^{-3}$ × [H^+]$^{-1}$ is approximately constant. At pH values higher than 4 the depolymerization reaction is slow (cf. Table 3). A limiting

Scheme 1

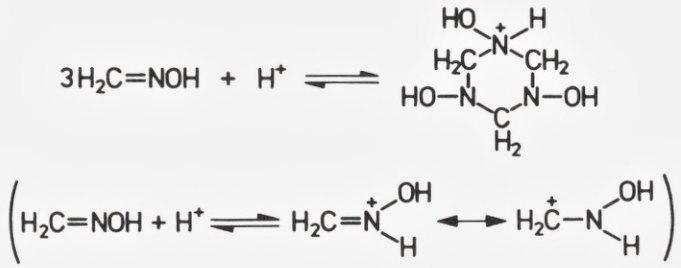

value of the ratio trimer/monomer is reached only after several hours and is largely independent of pH. It is quite possible that the depolymerization process is in fact irreversible under these conditions. Although a small amount of the trimer is also formed from the monomer in alkaline solution this might occur via a reaction analogous to the polymerization of liquid or gaseous formaldehyde oxime, a process which is apparently an oxygen-catalyzed radical reaction.

The chemical shifts and the coupling constants for the ^{1}H NMR resonances of formaldehyde oxime in alkaline solution are close to the values observed for solutions in non-aqueous solvents. This indicates that *3* is not transformed into its anion to any appreciable extent even at pH 12 (pk_a values near 13 have been given for various oximes[27]). Below pH 2 the peaks broaden. This is indicative of the protonation of a base whose strength is of the order of magnitude 10^{-13}, as found by Sluiter.[10] The protonation of formaldehyde oxime in strongly acid solution is also evident from polarographic measurements on *1*.[22] Likewise the δ-value for the trimer at pH 1 applies to the cation. That the hexahydrotriazinium ion gives rise to only one singlet is explicable on the basis of rapid exchange of the proton between the three nitrogen atoms.

The ^{1}H NMR spectrum of the methiodide (6) in D_2O provides no indication of the presence of a six-membered ring. In addition to the methylene signals of formaldehyde oxime, the spectrum shows signals due to formaldehyde and the N-methylhydroxylammonium ion, together with a signal at δ 3.52 which is

Table 3. Percentages of monomeric formaldehyde oxime present in solutions of the trimer, 1,3,5-trihydroxyhexahydro-1,3,5-triazine, in D_2O (35 °C; c = 0.75 mol l^{-1}).

pH	Time after dissolution			
	15 min	1 h	4 h	24 h
4.2	90	91	94	94
7-9	12	35	62	83
11	33	61		96

Scheme 2

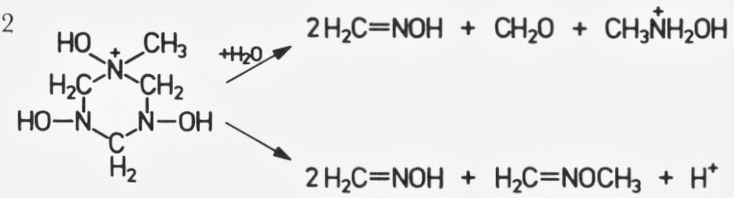

assigned to the methyl group of *O*-methylformaldehyde oxime[15] (the possibility that it might originate from the methylene protons of a compound $CH_3N(OH)CH_2OH$ is probably ruled out; see Experimental). The formation of *N*-methylhydroxylamine by hydrolysis proves that compound *6* is *N*-methylated. The simultaneous formation of an *O*-methyl compound must then be due to a nitrogen → oxygen transfer of the methyl group during the decomposition (Scheme 2).

From the integrated intensities of the *N*- and *O*-methyl signals it can be seen that the two compounds are formed in approximately equal amounts. There is overlap between the methylene signals of formaldehyde oxime and its *O*-methyl derivative but the presence of the latter is confirmed by the integrated intensity of the methylene signals being higher than calculated for 2 mol of formaldehyde oxime.

The ^1H NMR spectrum of the methiodide (*6*) in DMSO-d_6 indicates that the compound decomposes immediately in this medium with the formation of formaldehyde oxime and its *O*-methyl derivative[15] but without the formation of *N*-methylhydroxylamine. The hydrochloride (*1*) is also immediately and completely transformed into the oxime on dissolution in DMSO-d_6.

At higher concentrations of $(H_2CNOD)_3 \cdot DCl$ in D_2O, and at higher temperatures, abnormal results are sometimes obtained: For example, in some experiments the concentration of the monomer was found to decrease with increasing temperature. This indicates that in addition to trimerization a chain polymerization may set in, as is also evident from the precipitation of the solid polymer in more concentrated solutions. As a result of this complication, and because the instrument used in this investigation does not give data of sufficient precision for the calculation of thermodynamic constants, we did not carry out a great number of measurements. However, we feel that we have demonstrated that formaldehyde oxime may polymerize to a cyclic trimer and that the trimer is nearly completely depolymerized on neutralisation.

NMR spectroscopy also sheds light on the following rather puzzling observations made during various preparations of formaldehyde oxime:

a) When formaldehyde is added to an aqueous solution of hydroxylammonium

chloride and the solution is neutralized, extraction with a few portions of ether usually gives lower yields of formaldehyde oxime than when the hydroxylammonium chloride solution solution is made alkaline before the addition of formaldehyde. However, continuous extraction with ether furnished a good yield of the oxime.

b) When the solution of hydroxylammonium chloride and formaldehyde is made alkaline (pH 10-11) before extraction with ether, the yields of the oxime diminish markedly. When the ether extracts no longer give a positive reaction with nickel(II) the aqueous phase still gives a positive reaction.

These observations are explicable on the basis of the following results obtained by ^{1}H NMR spectroscopy of solutions with concentrations similar to those employed in preparative procedures (2.5 M):

Formaldehyde and hydroxylammonium chloride react in aqueous solution rapidly and quantitatively with the formation of *1*, and at sufficiently high concentrations no monomeric oxime is formed. A solution obtained by adding formaldehyde to a neutralized solution of hydroxylammonium chloride shows signals for both the oxime and the trimer, but the latter signal disappears slowly. Immediate extraction with ether may therefore give a low yield of the oxime whereas continuous extraction extended over several hours gives a good yield.

If the hydroxylammonium chloride solution is made alkaline before the addition of formaldehyde the resulting solution displays only the signals of the oxime; this procedure might therefore seem to be the more convenient for the preparation of the oxime (and was used in the original paper by Dunstan and Bossi[7]). However, at high concentrations the oxime may polymerize to the insoluble polymer which separates as a gel-like precipitate before the oxime has been extracted.

The ^{1}H NMR spectrum of a solution of *1* which is suddenly made alkaline reveals the presence of a considerable amount of the trimer. This is simply because the equilibrium corresponding to pH ca. 1 is "frozen", the depolymerization of the trimer occurring only slowly in alkaline solution. Because of its great hydrophilicity the trimer cannot be extracted with ether. When the pH of the solution is adjusted to 3-4 the trimer depolymerizes and the monomer can then be obtained by extraction of the neutralized solution.

The ^{1}H NMR spectra show no new signals when an excess of hydroxylammonium chloride or formaldehyde is employed (with or without addition of NaOH), *i.e.* there is no indication of the formation of the species $CH_2(NHOH)_2$ or $HON(CH_2OH)_2$.

V. Isolation of free 1,3,5-Trihydroxyhexahydro-1,3,5-Triazine

The above mentioned measurements indicate that the free base is present in an alkaline solution of *1*, but attempts to extract it with ethyl acetate or pentyl alcohol (after extraction of the monomer with ether) were unsuccessful because it polymerized during evaporation of the solvents. The authentic trimer was successfully isolated as a dioxane adduct in the following manner: Formaldehyde oxime remaining after evaporation of an ether solution immediately polymerizes exothermically when the temperature is around 0 °C. If the product is extracted with dioxane before it has completely solidified some of it goes into solution, and on removal of the solvent in vacuum a white solid is obtained whose composition corresponds approximately to $(CH_2NOH)_3 \cdot {}^1/_2C_4H_8O_2$. This substance is soluble in water and gives a positive nickel reaction. An aqueous solution shows initially only the ^1H NMR signals of the trimer and of dioxane, but weak signals for the monomer soon appear. After some hours the signals of the monomer become very strong while that of the trimer diminishes. At room temperature the solid substance rapidly loses dioxane and is transformed into the insoluble polymer.

We finally succeeded in preparing a solvent-free product in the manner described in the Experimental. After recrystallization from ethyl acetate, analyses and MS proved it to have the formula $C_3H_9N_3O_3$ and ^1H NMR showed it to be the desired free base, *7*. It is a colourless substance which is readily soluble in water and alcohols but is insoluble in ether, chloroform, benzene, etc. At room temperature it is rapidly transformed into the insoluble polymer. A prerequisite for this transformation is ring-opening, which is catalyzed by acids and bases (see below) and probably also by oxygen and certain metal ions. When the compound has been purified meticulously it can be kept unchanged for months in a refrigerator at −20 °C. The presence of small amounts of the polymer in the trimer is revealed by its IR spectrum and gives rise to turbidity of aqueous solutions.

At pH *ca.* 7 the trimer is only slowly transformed into formaldehyde oxime (Table 3 and Fig. 1) but at pH values lower than 4 equilibrium is established almost instantaneously (Scheme 2 and Fig. 1). The transformation is also (irreversibly) base-promoted but is only reasonably rapid at pH values higher than 10. Depolymerization in this case probably proceeds *via* the anion (Scheme 3).

Scheme 3

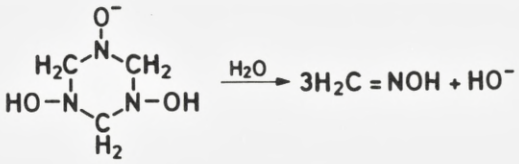

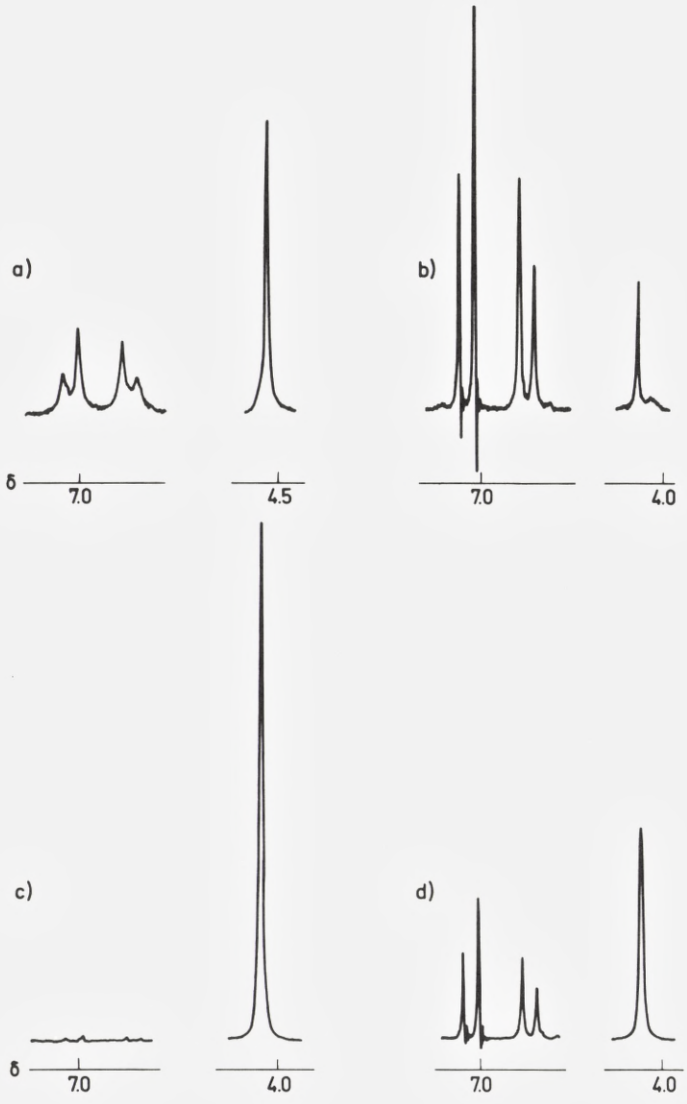

Fig. 1.
^{1}H NMR spectra of solutions of 1,3,5-trihydroxyhexahydro-1,3,5-triazine in D_2O with or without addition of DCl.
a) pH 2.5;
b) 4.2;
c) pH 7, recorded 10 min after dissolution;
d) pH 7 after 24 h.

Potentiometric titrations indicate *7* to be a very weak acid with a pK_a value near 11. Since it is a trivalent acid and is transformed into formaldehyde oxime, which is also an acid, it would be very difficult to determine a more precise value.

In alcohols the transformation of *7* into the monomer *3* is much slower than in water. In methanol only traces of *3* are formed after 24 h. Compound *7* is also soluble in DMSO and (in contrast to the hydrochloride or methiodide) is not detectably transformed into the monomer in this solvent.

On addition of peroxodisulfate to an alkaline solution of *7* a red colour develops. It was shown by ESR spectroscopy that this colour reaction is due to the formation of free radicals. These are probably derived from the anion of the trimer but their exact nature has not been established. The free radical derived from the monomer[28] is not formed under these conditions. A pink colour also develops when a concentrated solution of *1* is neutralized, probably due to oxidation of *7* by atmospheric oxygen.

Compound *7* is easily acylated by acetic anhydride or benzoyl chloride to give derivatives *4* and *5* which are identical with those prepared from the monomer. On heating, the benzoyl derivative forms benzoic acid and HCN. 1,3,5-Triazine could neither be detected in this reaction nor when *7* was heated with dehydrating agents (*cf.* the formation of 1,3,5-triazine from formamide[29]). In the latter case *7* was transformed into the polymer.

VI. Experimental

The 60 MHz ^1H NMR spectra were measured using a Varian A-60 A instrument. Sodium 3-(trimethylsilyl)propanesulfonate (DSS) was used as internal standard for D_2O solutions, and TMS for the measurements in $CDCl_3$ and CCl_4. The temperature at which the spectra were recorded was determined from the position of the signals of ethylene glycol. Infrared spectra were recorded on a Perkin Elmer Model 337 grating spectrophotometer. Mass spectra were obtained with an AEI-902 mass spectrometer at 70 eV using the direct sample-insertion system.

For the determination of the dipole moment of the acetyl derivative *4* a Dipolmeter DM 01 instrument from Wissenschaftlich-Technische Werkstätten, Weilheim, was used.

For pH measurements, a pH meter 22 from Radiometer, Copenhagen, was used. Melting points (corrected) were determined with a Kofler hot-stage microscope.

Oxygen analyses were carried out by the Unterzaucher method. We thank Mr.

R. Amsler of the NOVO Microanalytical Laboratory for performing these analyses.

Elemental analyses agree within ± 0.4 % units with the calculated values, unless the values found have been given.

1,3,5-Trihydroxyhexahydro-1,3,5-triazinium chloride, "triformoxime hydrochloride" (1). a) Hydroxylammonium chloride (40 g) was added with stirring to aqueous formaldehyde (40 %; 44 ml); it rapidly dissolved and the temperature rose to *ca.* 35 °C. The solution was then evaporated almost to dryness *in vacuo*. Benzene (200 ml) was added and most of it removed by distillation *in vacuo*. This treatment was repeated and ethanol (150 ml) was added to the residue. The mixture was cooled overnight in a refrigerator and the crystalline precipitate was collected, washed with a little cold ethanol and dried *in vacuo* over KOH. Yield: 29,5 g (90 %) of coulourless crystals with m.p. 132-133 °C (closed tube; decomp.). This procedure furnishes a pure product directly.

The solution of *1* can also be prepared by stirring a suspension of paraformaldehyde in an aqueous solution of hydroxylammonium chloride at 60 °C until dissolution is complete. This method was used for the preparation of $(D_2CNOH)_3 \cdot HCl$ from paraformaldehyde-d_2.

b) Compound *1* has also been prepared several times by the original procedure[7], *i.e.* by bubbling dry HCl through a cooled ether solution of formaldehyde oxime prepared as for compound *3*. In this case the crude product contains excess of HCl and must be recrystallized, preferably by dissolving it in warm ethanol, adding ether until precipitation begins and then cooling at ≤ 0 °C. Recrystallization results in considerable loss of material (30-40 %), and it was shown that this is due to extensive solvolysis to formaldehyde and hydroxylamine taking place in the hot alcoholic solution. Anal. $C_3H_{10}ClN_3O_3$: C, H, N, Cl.

The chloride *1* is very soluble in ethylene glycol, cellosolve, DMF and similar solvents but only slightly soluble in cold methanol or ethanol and insoluble in most other organic solvents.

Main IR bands (KBr): 3220 vs, 3040 m, 2840 s, 2620 s, 2520 m, 1538 m, 1436 m, 1405 s, 1345 m, 1300 vw, 1252 w, 1202 s, 1178 s, 1130 m, 1040 m, 970 m, 948 s, 798 s, 710 w, 620 m, br, 560 s, 548 s, 500 w, 433 s.

Poly(formaldehyde oxime) (2). The various forms of *2* were prepared wither from aqueous solution (*2a*) according to Scholl[6] or by spontaneous polymerization of gaseous or liquid formaldehyde oxime (*2b-e*). Some 20 different samples have yielded practically identical infrared spectra. Their analytical composition is somewhat variable (C 24.6-27.3; H 6.51-6.88; N 28.4-31.7; O 34.8-38.6) but shows

no apparent correlation with the method of preparation. (Representative analyses: Found (C, H, N, O): *2a* 25.7; 6.88; 31.7; 34.8. *2d* 26.3; 6.70; 30.5; 35.7. *2e* 25.8; 6.51; 30.0; 37.5. Calc. for $(CH_3NO)_n$: C 26.65; H 6.66; N 31.1; O 35.5.)

The polymer may be prepared in good yield by heating a mixture of *1* and CaO in a sublimation apparatus. In this process the trimer is depolymerized and the monomer condenses on the cool surface where it rapidly becomes transformed into the polymer. This method was also used to prepare $(D_2CNOH)_n$ for the infrared spectroscopic investigation.[8]

The products *2b-e* may give a positive nickel reaction due to traces of the trimer. The latter may be removed simply by washing with hot water or ethanol.

The mass spectra of the polymers were identical to that of the monomer. There was no indication of the formation of ions heavier than those formed from the monomer.

The white, amorphous (according to X-ray powder diagrams) solids are insoluble in all solvents except those in which depolymerization can take place. Krässig and Ringsdorf[30] found the molecular weight of *2* to be *ca.* 150 in caprolactam, but this result is due to depolymerization to the trimer *7*. When *2* was dissolved in molten caprolactam the presence of *7* could be proved by the colour reaction with nickel(II) chloride.

The polymers are easily dissolved in strong acids. Solutions in 1 M DCl/D_2O show only the NMR signal of the hexahydrotriazinium ion. The polymers are also soluble in warm NaOH. Solutions in 1 M $NaOD/D_2O$ show only the signals of formaldehyde oxime. These solutions give a negative reaction with nickel(II) chloride, showing that the coloured complexes are not formed directly from the monomer. When the alkaline solutions are acidified and again made alkaline there is a strong, positive nickel(II) reaction.

On boiling a suspension of *2* in benzene with acetic anhydride or benzoyl chloride the derivatives of the trimer (*4* and *5*) are formed.

Formaldehyde oxime (3). A solution of *1*, prepared according to *1a*, was diluted with 100 ml of water, cooled in ice and adjusted to pH 8 with 10 M NaOH. When the solution became neutral a faint red colour developed. The solution was extracted continuously with 300 ml of ether for 24 h. After that time the pH of the solution was 9 and the aqueous phase gave a negative nickel(II) reaction while the ether phase gave a strongly positive reaction. After drying the ether phase ($MgSO_4$) the bulk of the solvent was removed *in vacuo*. The remaining liquid was distilled at normal pressure, the receiver being cooled in dry-ice/acetone. Gas chromatography and ^1H NMR indicated that the liquid still contained some ether. It was therefore redistilled, removing practically all the remaining ether; b.p. 82-83 °C

(759 mmHg), m.p. −5° C. At room temperature the oxime polymerizes completely in a few minutes. It can be kept at −80° C for some time but not without the formation of some of the polymer.

^{1}H NMR spectrum, see Table 1.

MS [m/e (% rel.int.)]: 46 (2), 45 (100, [M]), 44 (9), 43 (6), 32 (2), 30 (5), 29 (2), 28 (32, [M–OH]), 27 (25, [M–H_2O]), 26 (2).

1,3,5-Triacetoxyhexahydro-1,3,5-triazine (4). Acetic anhydride (4 ml) was added to the carefully dried ether solution (40 ml) of formaldehyde oxime prepared as above and the solution was kept for several days in a refrigerator until colourless crystals of the acetyl derivative had formed. Yields are very variable. M.p. 132-133 °C (TLC-pure; lit.[7] 133). Anal. $C_8H_{15}N_3O_6$: C, H, N. The compound is readily soluble in water, ethanol and chloroform, slightly soluble in CCl_4, and insoluble in ether. It can be recrystallized from ethyl acetate. It is easily hydrolysed in alkaline solution (when 0,1 M NaOH was added to an aqueous solution at such a rate as to maintain a pH value of 10.5 hydrolysis was complete in *ca.* 2 h).

This compound could be prepared in higher yield from the trimer (*7*): 400 mg of *7* was dissolved in 1 ml of acetic anhydride and the solution was kept for one day at room temperature. Excess acetic anhydride was removed *in vacuo*. The residue was dissolved in chloroform and the solution was washed with water, dried with $MgSO_4$ and concentrated *in vacuo*. On addition of ether 450 mg of *4* were obtained.

The same compound has also been obtained from the polymer (see under *2*) or by passing ketene through a solution of formaldehyde oxime in ether. In the latter case the resulting solution was distilled *in vacuo* and the fraction passing over at 34-60 °C (12 mmHg) was recrystallized from abs. ethanol.

Dipole moment (dioxane, 20 °C): 3.25 D.

Mol.wt. (thermoelectric meth., $CHCl_3$): 260 ± 2, calc. 261. ^{1}H NMR ($CDCl_3$): δ 4.53 (s, 2H), 2.08 (s, 3H).

IR (KBr): 3020 w, 2940 w, 1750 vs, 1415 m, 1363 s, 1240 vs, 1200 vs, 1142 s, 1040 m, 1002 m, 972 m, 943 m, 895 s, 880 s, 802 s, 648 m. Most of these bands can be assigned to the groups CH_2, CH_3, and O–$COCH_3$. The strong doublet at 880 + 895 cm^{-1} (in $CHCl_3$ a singlet at 887 cm^{-1}) is assigned to ν(N–O) and the 1040 cm^{-1} band to ν(C–N).

MS [*m/e* (% rel.int.)]: 261 (1, [M]), 201 (1, [M–CH_3CO_2H]), 174 (9, [M–$CH_2NOCOCH_3$]), 132 (6, [174 – CH_2CO]), 88 (25, [$CH_2NHOCOCH_3^+$]), 60 (21, [$CH_3CO_2H^+$]), 45 (27), 44 (14), 43 (100, [CH_3CO^+]), 42 (29), 32 (14), 27 (12).

1,3,5-Tribenzoyloxyhexahydro-1,3,5-triazine (5). An aqueous solution of hydroxylammonium chloride (20 g) and formaldehyde (40 %, 22 g) was neutralized and shaken with benzoyl chloride (40 g), keeping the solution neutral by addition of sodium carbonate. The white precipitate (30 g) which separated was collected and extracted with boiling ethanol-water (1:1) acidified with HCl, and the insoluble material was recrystallized from chloroform-ethanol. Yield 14 g (33 %) with m.p. 176-177 °C (TLC-pure; lit.[7] 159). Anal. $C_{24}H_{21}N_3O_6$: C, H, N. Mol.wt. 447 (MS). ^{1}H NMR ($CDCl_3$): δ 5.00 (s, 2H); 7.0-8.0 (m, 5H). The IR spectrum is dominated by the strong bands due to the benzoyl groups. The following bands can with reasonable certainty be assigned to the triazine system: 1415 (δ CH_2), 950, 830, and 780 cm^{-1}.

The acidic ethanolic solution remaining after treatment of the crude product yielded on addition of water a solid which on recrystallization from ethanol-water gave 8 g of *O,N*-dibenzoylhydroxylamine (dibenzohydroxamic acid); m.p. 166-167°C (lit.[31] 165).

Compound *5* has also been prepared from the polymer (*2*; *q.v.*), and from the trimer (*7*): compound *7* (270 mg) was dissolved in pyridine (5 ml) and benzoyl chloride (840 mg) was added dropwise to the solution while cooling in ice. The final solution was diluted with water and extracted with chloroform. Work-up of the solution yielded 300 mg of *5*.

Compound *5* decomposes on melting with the formation of HCN together with a white sublimate, identified as benzoic acid, and a dark brown residue (polymer of HCN). 1,3,5-Triazine could not be detected.

N-Methyl-1,3,5-trihydroxyhexahydro-1,3,5-triazinium iodide (6).

An excess of methyl iodide (10 g) was added to an extract (cf. *3*) containing *ca.* 2 g of formaldehyde oxime in 50 ml of ether.[12] Slightly yellow crystals (4.9 g) separated from the solution when this was kept for some days in a refrigerator at 0-5 °C. They could not be recrystallized but were washed with ether. The compound melted with decomposition near 100 °C. Anal. $C_4H_{12}IN_3O_3$: C, H, N. It is readily soluble in water, methanol or dimethyl sulfoxide but is simultaneously decomposed with the formation of formaldehyde oxime. In aqeous solution the other products formed are formaldehyde, *N*-methylhydroxylammonium ion and formaldehyde *O*-methyloxime.

^{1}H NMR (D_2O): δ 6,57 (d), 7.06 (d), 4.79 (s, CH_2O), 3.00 (s, $CH_3NH_2OH^+$), 3.52 (s, $-OCH_3$).

The compound $CH_3N(OH)–CH_2–N(OH)CH_3$, prepared according to Ulrich and Sayigh[32], shows two peaks in $CDCl_3$ at δ 3.43 (2H) and 2.60 (6H); in D_2O it shows 4 peaks at δ 3.72, 3.52, 2.68 and 2.64, probably because of partial hydro-

lysis to $CH_3N(OH)CH_2OH$. On acidification of the D_2O solution there are only two signals at δ 3.00 and 3.51. However, the latter is a broad peak which is quite different from the 3.52 peak seen for the solution of the methiodide.

The IR spectrum of the methiodide is similar to that of the hydrochloride (*1*).

1,3,5-Trihydroxyhexahydro-1,3,5-triazine (7). The hydrochloride *1* (17 g) was suspended in water (15 ml). The suspension was cooled in ice, and a solution of KOH (5.6 g) in water (10 ml) was added gradually until pH was *ca.* 7. Ethanol (250 ml) was added and the precipitated KCl was collected and discarded. The solution was concentrated *in vacuo* and the remaining water was removed by repeated evaporation with addition of ethanol and benzene. Finally, the solution was evaporated to dryness and the residue was extracted with 400 ml of boiling ethyl acetate. Only part of the material dissolved but on cooling the solution and decanting it from the crystalline residue renewed treatment of the latter with a further portion of the solvent caused most of it to dissolve. Ether (400 ml) was added to the combined ethyl acetate solution and the crystals were collected after cooling overnight. Yield 5.7-6.9 g (42-51 %). For analytical purposes 1 g of product was recrystallized from 60 ml of ethyl acetate (yield 0.5 g). Traces of ethyl acetate were removed by drying under high vacuum until the IR spectrum showed no absorption in the 1700 cm^{-1} range.

Anal. $C_3H_9N_3O_3$: C, H, N. Slow evaporation of the ethyl acetate solution yields compound *7* as large, colourless crystals.

Compound *7* sublimes perceptibly even at 50 °C, the vapoxr being the monomer. It melts essentially unchanged (IR spectrum) at 114-115 °C but the melt is fairly rapidly transformed (*via* the monomer) into the polymer. On heating *7* with dehydrating agents such as CaO or CaC_2 it is similarly transformed into the polymer (no 1,3,5-triazine could be detected). ^1H NMR spectra, see Tables 1 and 3 and Figure 1. Main IR bands (KBr): 3420 vs, 3200 sh, 3110 vs, 2950 w, 2880 vs, 1490 sh, 1470 s, 1430 m, 1380 s, 1365 sh, 1305 w, 1292 m, 1245 w, 1168 s, 1005 m, 970 sh, 955 s, 918 s, 815 m, 795 s, 730 s, 710 sh, 585 m, 572 s, 560 sh, 505 m, 440 sh, 430 m.

Compound *7* forms a dioxane adduct (m.p. *ca.* 90 °C) which according to elemental analyses has the composition $C_3H_9N_3O_3 \cdot {}^1/_2C_4H_8O_2$. Its ^1H NMR spectrum in D_2O shows the proton signals of *7* and of dioxane (δ 3.72) in the expected ratio (3:2). Its infrared spectrum exhibits only the absorption bands of *7* and dioxane. At room temperature it loses dioxane and is transformed into the polymer.

References

1. Jensen, K. A. *To be Published.*
2. Zumwaldt, L. R. and Badger, R. M. *J. Chem. Phys. 7* (1939) 235.
3. Califano, S. and Lüttke, W. *Z. Phys. Chem.* (Frankfurt am Main) *6* (1956) 83.
4. Levine, L. N. *J. Mol. Spectrosc. 8* (1962) 276.
5. Krishna Pillai, M. G. *J. Phys. Chem. 66* (1962) 179.
6. Scholl, R. *Ber. Deut. Chem. Ges. 24* (1891) 573.
7. Dunstan, W. R. and Bossi, A. L. *J. Chem. Soc. 73* (1898) 353.
8. Andersen, F. A. and Jen ·n, K. A. *K. Dan. Vidensk. Selsk., Mat.-Fys. Medd. 40:12* (1978).
9. Bartušek, M. and Okáč, A. *Collect. Czech. Chem. Commun. 26* (1961) 2174; *Z. Anal Chem. 178* (1960) 198.
10. Sluiter, C. H. *Rec. Trav. Chim. Pays-Bas 36* (1917) 1.
11. Bamberger, E. and Mùller, J. *Ber. Deut. Chem. Ges. 32* (1899) 3546, p. 3554.
12. Dunstan, W. R. and Goulding, E. *J. Chem. Soc. 71* (1897) 573, p. 575.
13. Jerslev, B., Brehm, L., and Gabrielsen, M. V. *Acta Chem. Scand.* In press.
14. Tarte, P. and Laurent, P. A. *Bull. Soc. Chim. Belg. 70* (1961) 43.
15. Jensen, K. A., Buus, L., and Holm, A. Acta Chem. Scand. *B31* (1977) 28.
16. Stefaniak, L., Urbanski, T. Witanowski, M., and Januszewski, H. *Rocz. Chem. 44* (1969) 1687.
17. Jones, R. A. Y., Katritzky, A. R., and Snarey, M. *J. Chem. Soc. (B) 1970*, 135.
18. Duke, R. P., Jones, R. A. Y., Katritzky, A. R., Scattergood, R., and Riddell, F. G. *J. Chem. Soc. Perkin Trans. II. 1973*, 2109.
19. Shapiro, B. L., Ebersole, S. J., and Kopchik, R. M. *J. Mol. Spectrosc. 11* (1963) 326.
20. Shapiro, B. L., Ebersole, S. J., Karabatsos, G. J., Vane, F. M., and Manatt, S. L. *J. Amer. Chem. Soc. 85* (1963) 4041.
21. Crépaux, D. and Lehn, J. M. *Mol. Phys. 14* (1968) 547.
22. Bartušek, M. and Okáč, A. *Collect. Czech. Chem. Commun. 26* (1961) 52.
23. Marczenko, Z. and Minczewski, J. *Chem. Anal.* (Warsaw) *5* (1960) 747,903.
24. Marczenko, Z. and Minczewski, J. *Rocz. Chem. 35* (1961) 1223.
25. Marczenko, Z. and Kasiura, K. *Chem. Anal.* (Warsaw) *6* (1961) 37.
26. Marczenko, Z. *Bull. Soc. Chim. Fr.* 1964, 939.
27. King, C. V. and Marion, A. P. *J. Amer. Chem. Soc. 66* (1944) 977.
28. Adams, J. Q. *J. Amer. Chem. Soc. 89* (1967) 6022.
29. Sloan, C. L. and Barber, W. A. *J. Org. Chem. 27* (1962) 1073.
30. Krässig, H. and Ringsdorf, H. *Makromol. Chem. 22* (1957) 163, p. 180.
31. de Paolini, I. *Gazz. Chim. Ital. 62* (1932) 1098.
32. Ulrich, H. and Sayigh, A. A. R. *J. Chem. Soc. 1963*, 1098.

Investigations of Formaldehyde Oxime, itsPolymers and Coordination Compounds. II

FLEMMING A. ANDERSEN and K. A. JENSEN

The Infrared Spectrum of Poly(formaldehyde oxime)

Det Kongelige Danske Videnskabernes Selskab
Matematisk-fysiske Meddelelser **40**:2

Kommissionær: Munksgaard
1978

Contents

Synopsis

The infrared spectra of solid poly(formaldehyde oxime) and three deuterated species: poly(formaldehyde-d_2 oxime), poly(formaldehyde oxime-d) and poly(formaldehyde-d_2 oxime-d) have been measured in the region 4000-300 cm^{-1}. Vibrational assignments have been made for all the fundamentals on the basis of the observed isotopic frequency shifts and by comparing the spectrum of poly (formaldehyde oxime) with the spectra of related polymers. The assumption that the backbone of poly(formaldehyde oxime) is a planar zig-zag chain is consistent with the results obtained.

Flemming A. Andersen
Institute for Chemistry
Faculty of Medicine
University of Copenhagen

K. A. Jensen
Chemical Laboratory 2
The H. C. Ørsted Institute
University of Copenhagen

Printed in Denmark by Bianco Lunos Bogtrykkeri A/S. ISBN 87-7304-098-3

I. Introduction

In the preceding paper[1] evidence was presented supporting the view that the so-called "triformoxime" is not a trimer of formaldehyde oxime but a chain polymer. The present investigation was undertaken to substantiate this conclusion.

The infrared spectra of poly(formaldehyde oxime), $(CH_2NOH)_n$, as well as of its deuterated species, poly(formaldehyde-d_2 oxime), $CD_2NOH)_n$, poly(formaldehyde oxime-d), $(CH_2NOD)_n$, and poly(formaldehyde-d_2 oxime-d), $(CD_2NOD)_n$, have been measured. Both $(CH_2NOH)_n$ and $(CD_2NOH)_n$ were prepared in two different ways, *viz* by a polymerisation and by a polycondensation (see II.1). The products from the two types of reaction are referred to as A and B, respectively, in the present paper. The other two species, $(CH_2NOD)_n$ and $(CD_2NOD)_n$, were, however, prepared only by polycondensation.

The two compounds A and B have been shown not to be crystalline by the X-ray powder diffraction. The assignments of the infrared spectra have therefore been based on the assumption that poly(formaldehyde oxime) is an amorphous chain polymer, the backbone of which is a planar zig-zag chain, of repeating $-CH_2NOH-$ units as indicated in Fig. 1.

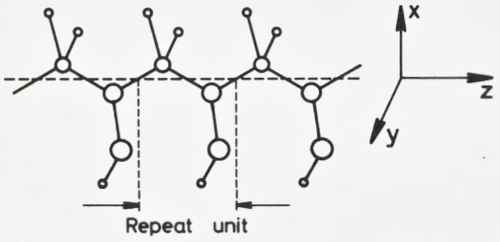

○ OXYGEN
○ NITROGEN
○ CARBON
○ HYDROGEN

Fig. 1. Poly(formaldehyde oxime) chain. The carbon and nitrogen atoms lie in the *xz*-plane (cp. Fig. 2), the CH, NO, and OH bonds in the *xy*-plane.

II. Experimental

1. Preparations

As discussed in the preceding paper[1] a polymer of formaldehyde oxime can be obtained either by spontaneous polymerisation of the (gaseous or liquid) monomer (products A) or by polycondensation of formaldehyde with hydroxylamine in aqueous solution (products B).

It was not possible to achieve a satisfactory degree of exchange of OD groups for OH groups simply by treatment of the polymeric products with D_2O, possibly because of the existence of strong hydrogen bonds in these compounds. The deuterated species were therefore prepared by condensation of CH_2O or CD_2O with deuterated hydroxylamine in D_2O. Even then complete deuteration could not be achieved (cf. IV.1).

The CD_2-compounds were prepared from paraformaldehyde-d_2, which was either depolymerised to CD_2O or transformed into $(CD_2NOH)_3HCl$, the latter two of which furnished the polycondensate (B) or the polymer (A), respectively (see Ref. 1, p. 17).

2. Spectroscopic Procedure

The infrared spectra of the compounds in KCl, KBr, CsCl and CsBr discs (1-3 mg sample in 300 mg matrix) were measured in the region 4000-300 cm^{-1} using a Perkin-Elmer Model 225 spectrometer. The resolution was 1-2.5 cm^{-1} throughout the entire frequency region. The absolute accuracy of wavenumber readings on the spectrometer itself is better than ± 0.02 % and on the recorded spectra it is about $\pm$ 0.5-1 cm^{-1}. However, the accuracy of the frequencies given is believed to be no better than $\pm$ 1-2 cm^{-1} for narrow bands and $\pm$ 3-5 cm^{-1} for broad bands and shoulders. This is mainly due to the fact that the positions of most of the bands are somewhat dependent on the matrix material used. This is especially true for the $(CH_2NOH)_n$ bands at 430 cm^{-1} and 3300 cm^{-1} for which variations in band frequency of about 5 and 10 cm^{-1}, respectively, have been observed. The accuracy of $\pm$ 0.5-1 cm^{-1} in measurement of the band frequencies was obtained by expanding the spectra adequately. The following abscissa expansions were used:

spectral region	cm^{-1} per cm on the chart paper
3500-2000 cm^{-1}	50 cm^{-1}/cm and 10 cm^{-1}/cm
2500-1000 cm^{-1}	25 cm^{-1}/cm and 5 cm^{-1}/cm
1000- 400 cm^{-1}	10 cm^{-1}/cm
460- 300 cm^{-1}	5 cm^{-1}/cm

III. Theory

Symmetry and Normal Vibrations

The general theory of the internal vibrations of chain molecules has been thoroughly treated by several authors.[2] However, for the convenience of the reader a brief survey of the general features of the theory will be given.

For a non-linear molecule containing N atoms the number of nonzero normal vibrational modes is $3N$-6. The infrared spectrum of a polymer might therefore be expected to be very complicated, showing a large number of absorption bands. However, it may be shown that for an infinite polymer chain which is regularly arranged in a series of repeating units of identical conformation only those vibrational modes can be infrared (or Raman) active for which all such units are vibrating in phase. These are the socalled factor group vibrations. If there are r atoms in the repeating units the number of modes of non-zero frequency will be $3r$-4, since there are 4 modes of zero frequency (three translations of the whole chain and one rotation around the chain axis).

For real polymer chains containing a finite number N of repeating units a splitting of each vibrational mode into N vibrations is to be expected due to the interaction between the N adjacent repeating units. However, it turns out that of the N vibration frequencies the factor group vibration frequency is by far the most intense. All the others are either of zero intensity or quite weak.

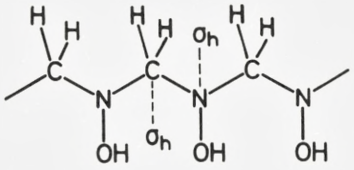

Fig. 2. Symmetry elements in an extended, infinite poly(formaldehyde oxime) chain.

From considerations of the symmetry elements of the repeating unit the symmetry species can be predicted. Fig. 2 shows the symmetry elements for the repeating unit of an infinite extended poly(formaldehyde oxime) chain. Here σ_h is a mirror plane in the xy-plane. The symmetry elements of the infinite extended poly(formaldehyde oxime) chain is the unit translation (which is equivalent to the identity E for the repeating unit) in addition to an infinite number of mirror planes σ_h. These elements form a line group and the elements of the repeating unit together with the unit translation form a sub-group of the line group, a socalled factor group. This group is not, however, a point group, but it can be shown that there is a point group which is isomorphous with the factor group. For the poly-

(formaldehyde oxime) chain with the symmetry elements E and σ_h this point group is C_s. In Table 1 are given the symmetry species and the number of vibration modes including zero modes.

Table 1. Symmetry species for the point group C_s and for the isomorphous line group of the poly-(formaldehyde oxime) chain. Number of vibration modes.

Point group C_s	E	σ_h		
Line group	E	σ_h	Zero modes	Number of vibration modes *
A'	+1	+1	T_x, T_y, R_z	12
A''	+1	−1	T_z	6

* Number of vibration modes for an isolated, extended, infinite poly(formaldehyde oxime) chain (including zero modes).

The characterization of chain molecules by line groups is, however, only correct if interaction between neighbouring chains can be neglected. Although there is a vibrational interaction between adjacent chains it is usually small compared with the interaction between adjacent repeating units within the same chain. For crystalline polymers this inter-chain interaction is regular and well-defined and is expected to cause a splitting of the absorption bands into a number of peaks, depending on the number of chains passing through a unit cell and on the selection rules. For amorphous polymers the interaction is of a random nature and for most compounds will give rise to a broadening of absorption bands. The line group analysis can therefore be considered to be a reasonable satisfactory approximation for amorphous polymers.

It follows from Table 1 that vibrations of species A' must be symmetrical with respect to both types of symmetry operation and that vibrations of species A'' are antisymmetric with respect to the mirror plane. The normal vibrations of a single poly(formaldehyde oxime) chain are shown in Figures 3, 4 and 5. The symmetry coordinates have been chosen in such a way that each of them – besides having the correct symmetry – also represents a rough approximation to the real mode of vibration for the chain.

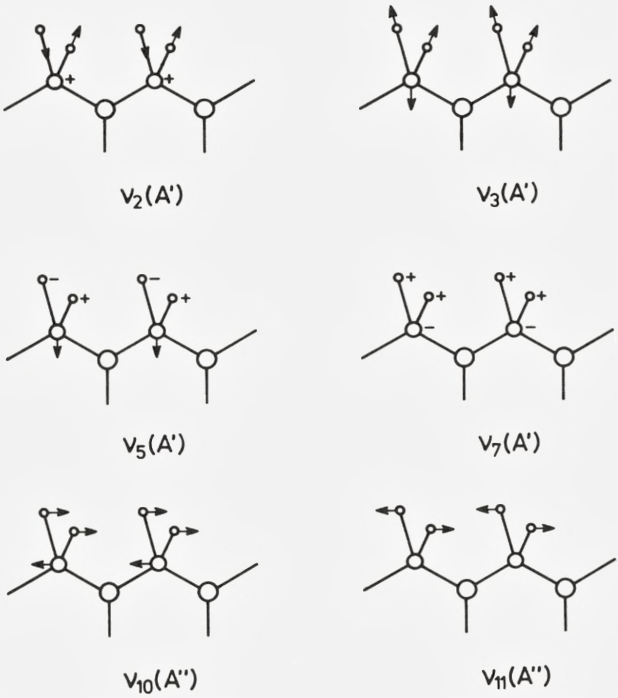

Fig. 3. Normal vibrations of the CH_2 groups of poly(formaldehyde oxime). The CH_2 groups are shown slightly twisted with respect to the *xy*-plane.

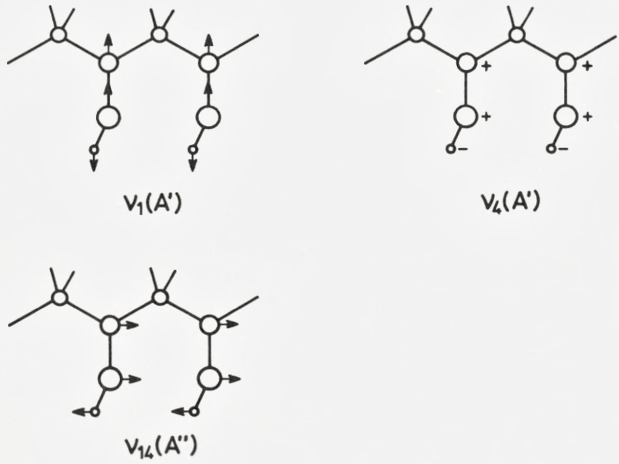

Fig. 4. Normal vibrations of the OH groups of poly(formaldehyde oxime). The OH groups lie in the *xy*-plane but are shown slightly twisted.

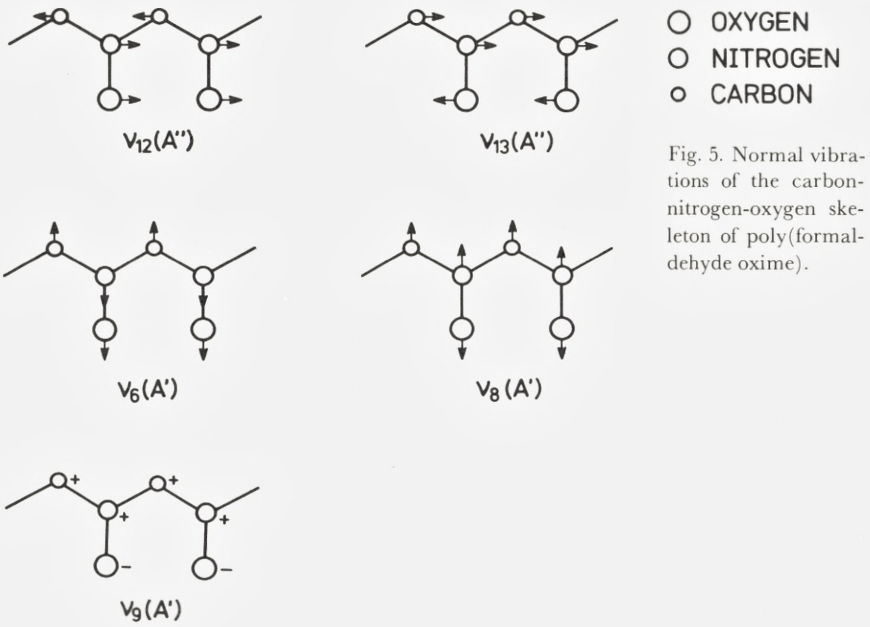

Fig. 5. Normal vibrations of the carbon-nitrogen-oxygen skeleton of poly(formaldehyde oxime).

In the high frequency range (above 2000 cm^{-1}) the true normal coordinates are in general well approximated by group symmetry coordinates, *i.e.* the $CH_2(CD_2)$ and OH(OD) stretching vibrations may be considered to be "pure" vibrations. However, at lower frequencies coupling between vibrations may occur if the groups are vibrating with nearly the same frequency, if they are situated near to each other and if the vibrations have the same symmetry. In such cases the fundamental vibrations will be rather "impure" because the valence coordinates mix in forming the normal coordinates, *i.e.* the group symmetry coordinates will be poor approximations to the true normal coordinates.

IV. Discussion of the Spectra

1. Results

The infrared spectra of poly(formaldehyde oxime), $(CH_2NOH)_n$, and its deuterated species $(CD_2NOH)_n$, $(CH_2NOD)_n$ and $(CD_2NOD)_n$ were measured in the solid state as described above. The spectra are shown in Figures 6, 7, 8, 9, 10, 11 and

12. It can be seen that apart from being rather simple the spectra of $(CH_2NOH)_n$ formed by polymerisation (A) and by polycondensation (B) look very much the same; this is also true for $(CD_2NOH)_n$. The indication is thus that the structures of A and B are very similar.

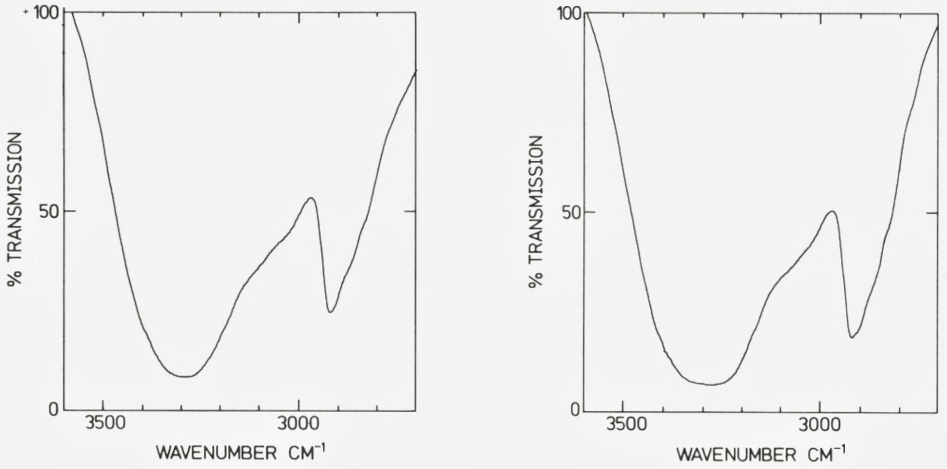

Fig. 6. Infrared absorption bands of $(CH_2NOH)_n$ in the region 3600-2700 cm^{-1}. Left: compound A. Right: compound B.

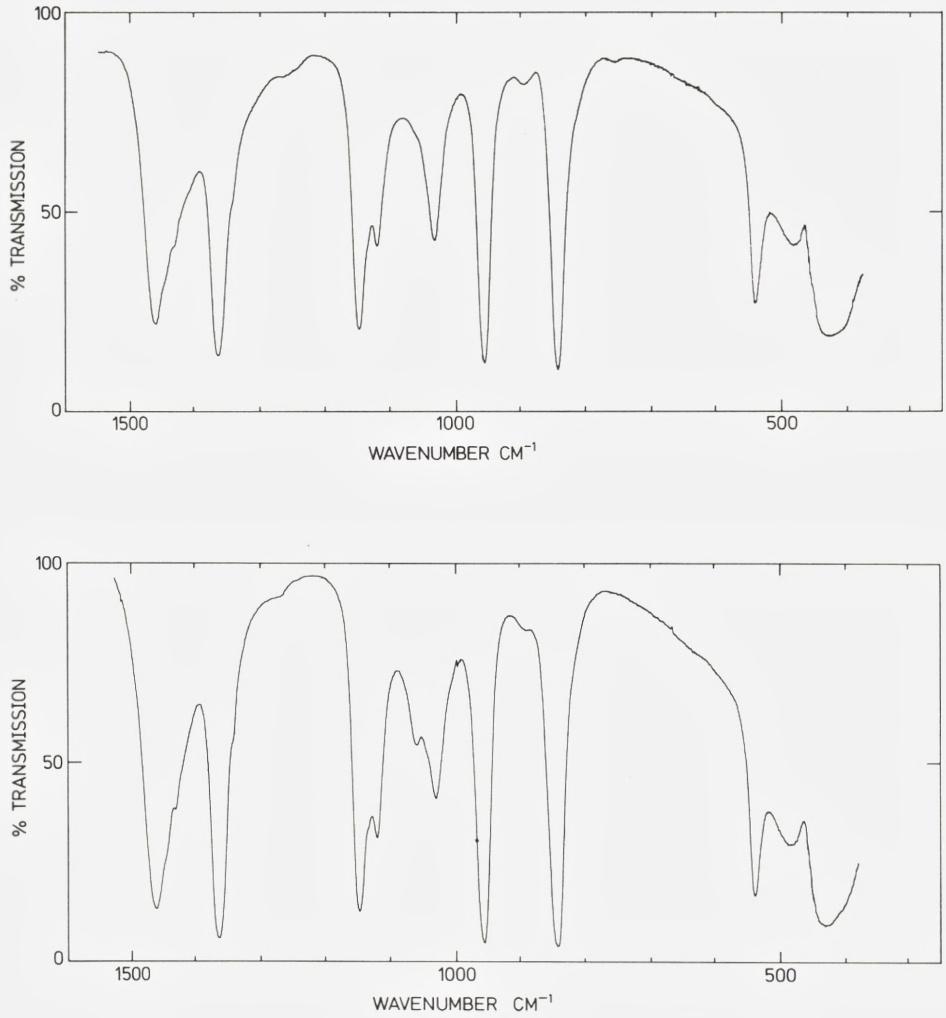

Fig. 7. Infrared spectrum of $(CH_2NOH)_n$ in the region 1550-400 cm^{-1}. Upper spectrum: compound A. Lower spectrum: compound B.

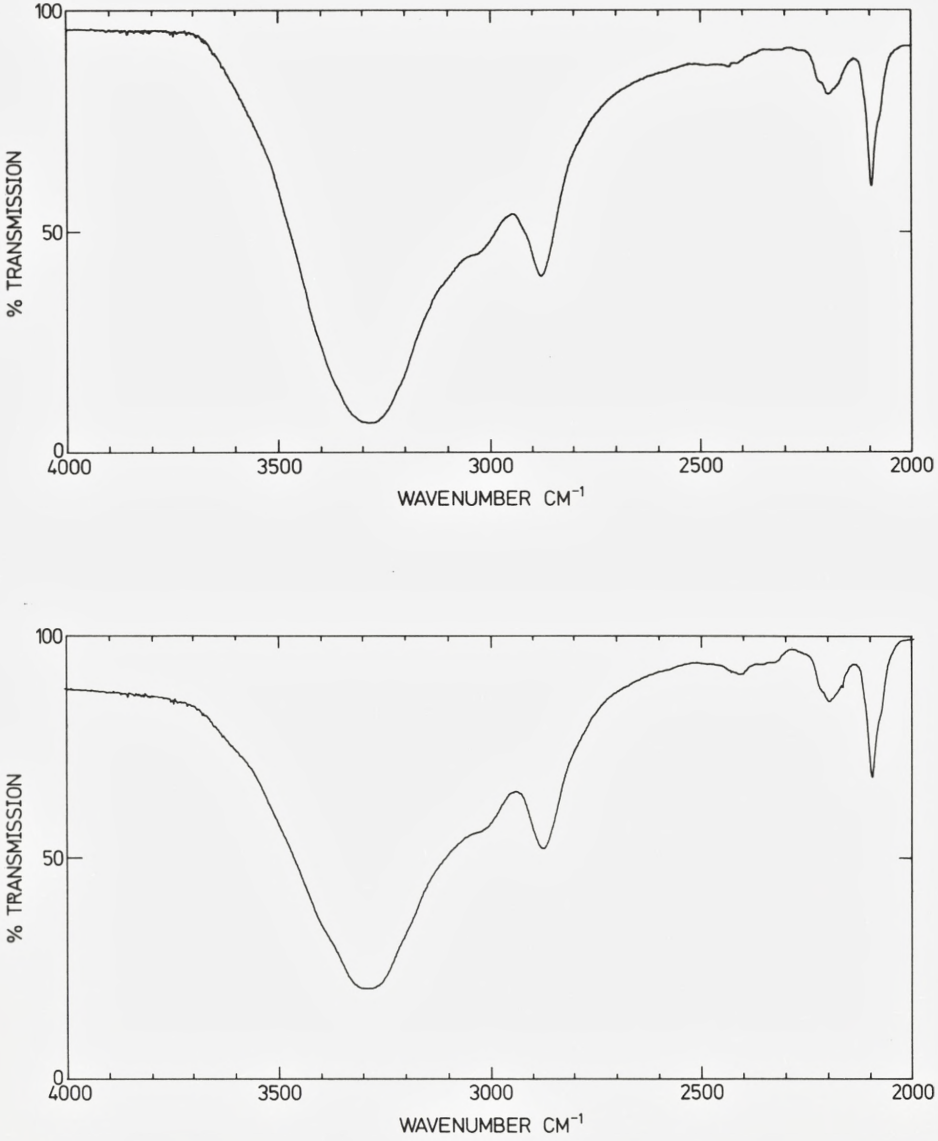

Fig. 8. Infrared absorption bands of $(CD_2NOH)_n$ in the region 4000-2000 cm^{-1}. Upper spectrum: compound A. Lower spectrum: compound B.

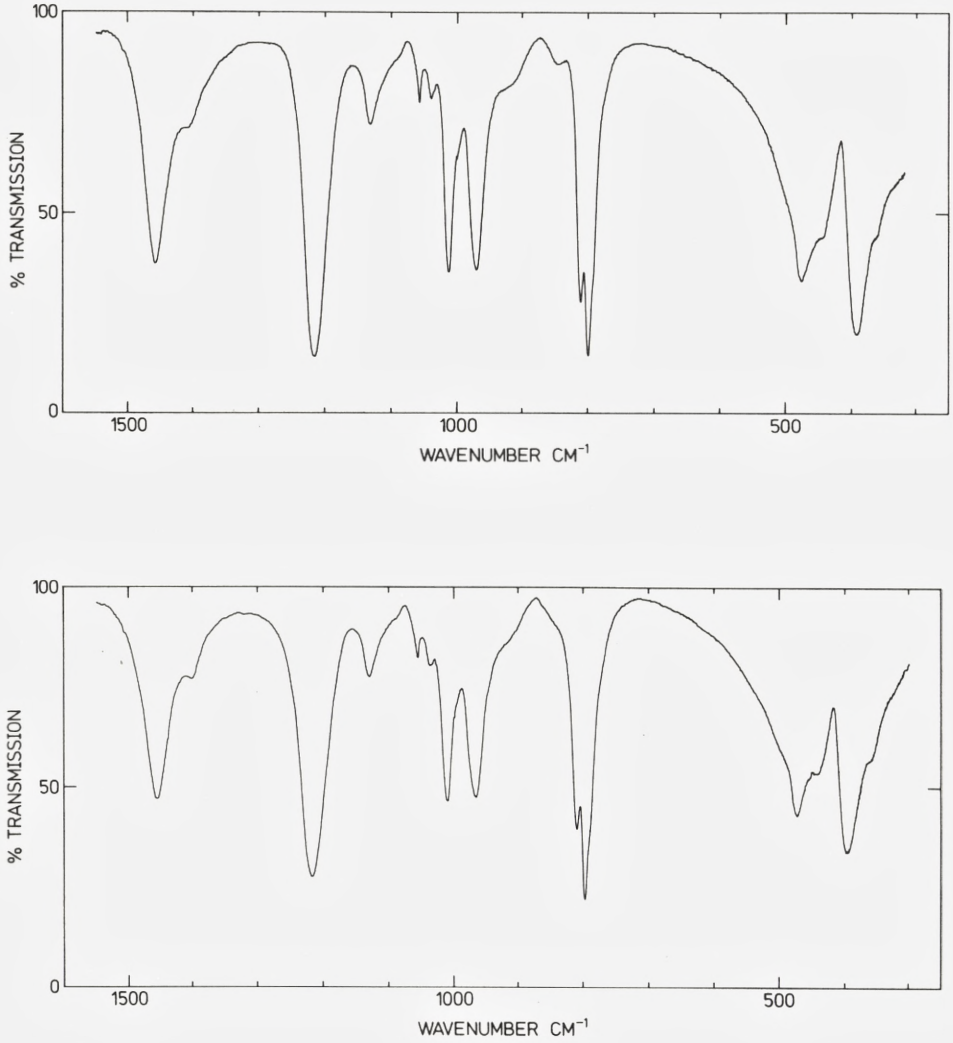

Fig. 9. Infrared spectrum of $(CD_2NOH)_n$ in the region 1550-300 cm^{-1}. Upper spectrum: compound A. Lower spectrum: compound B.

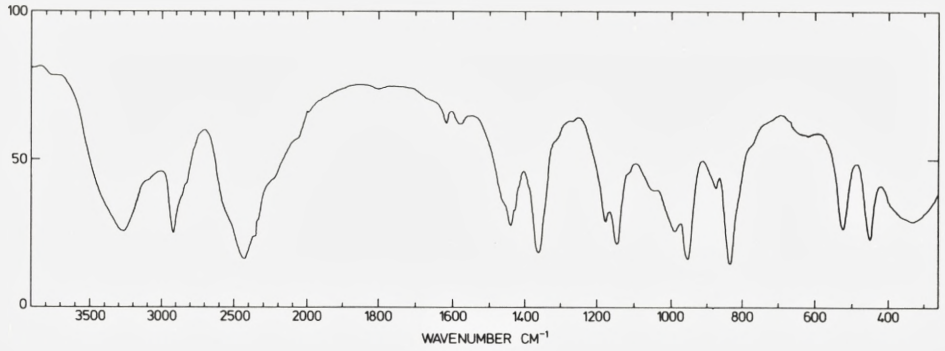

Fig. 10. Infrared spectrum of $(CH_2NOD)_n$ in the region 4000-350 cm^{-1}.

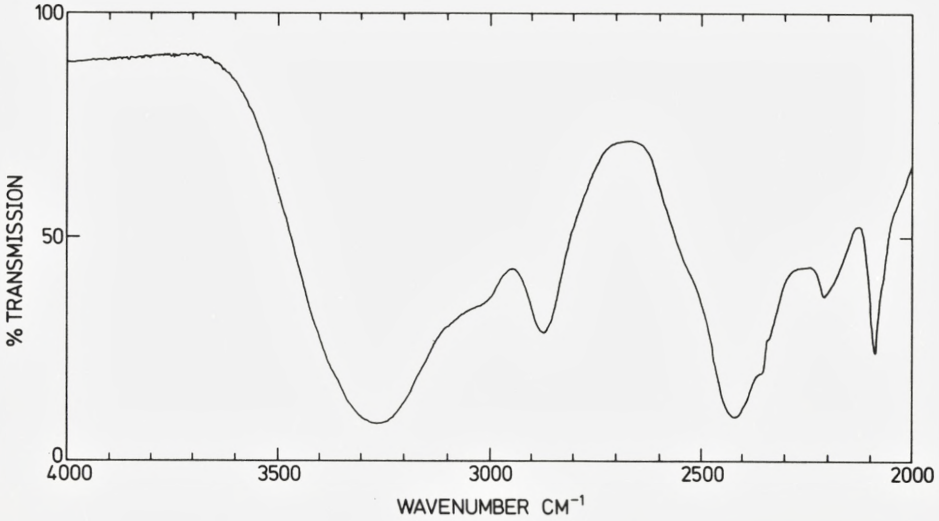

Fig. 11. Infrared spectrum of $(CD_2NOD)_n$ in the region 4000-2000 cm^{-1}.

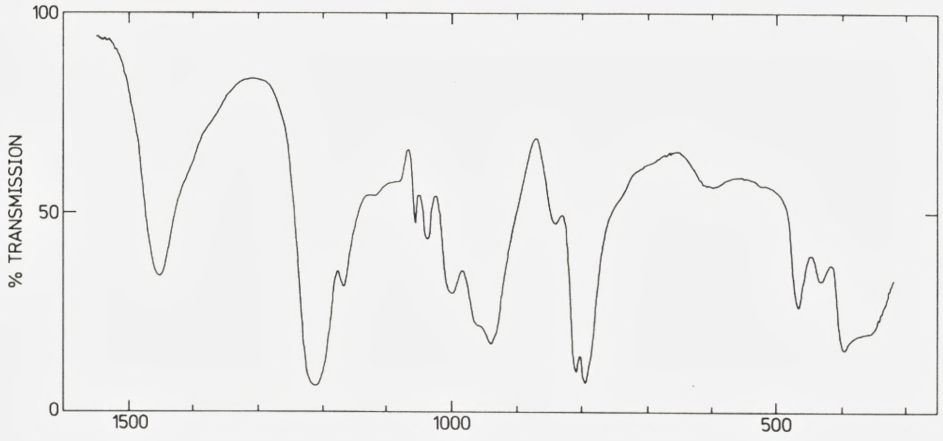

Fig. 12. Infrared spectrum of $(CD_2NOD)_n$ in the region 1550-300 cm^{-1}.

In the spectra of $(CH_2NOD)_n$ and $(CD_2NOD)_n$ two strong absorption bands are found at 2400 cm^{-1} and 3300 cm^{-1}. The former originates from the OD stretching vibration while the band at 3300 cm^{-1} is the OH stretching band also observed in the spectra of (CH_2NOH) and $(CD_2NOH)_n$. This shows that both of the two OD deuterated samples still contain OH groups. Now, the change in dipole moment with respect to the vibrational coordinate $\left(\frac{\partial \mu}{\partial Q}\right)$, which determines the integrated absorption intensity of a fundamental band, is expected to be considerably smaller for the OD vibration than for the OH vibration, thereby giving rise to a lower intensity of the OD band as compared with the OH band. This makes it difficult to estimate the relative content of OD groups in the samples of $(CH_2NOD)_n$ and $(CD_2NOD)_n$ merely by comparing the observed intensities of the OD and OH stretching bands in the two spectra. However, since the observed intensity of the OD band in the spectra of $(CH_2NOD)_n$ and $(CD_2NOD)_n$ is greater than, and about equal to the intensity of the OH band, respectively, one may conclude that the degree of deuteration for both samles is considerably higher than 50 %. By comparing the intensity ratios for other bands in the spectra of the two samples the content of OD groups has been estimated to about 80-90 % for the $(CH_2NOD)_n$ sample and 70-80 % for the $(CD_2NOD)_n$ sample. Although deuteration is thus far from complete it has proved possible to unambigously assign the fundamental bands of $(CH_2NOD)_n$ and $(CD_2NOD)_n$ and to obtain reliable values of the band frequencies.

As discussed above the interaction between adjacent chains in amorphous polymers is expected to produce a broadening of the infrared absorption bands. This is in good agreement with the experimental results of the present investigation. No sharp bands are observed in the spectra, the half-band widths of most of the bands being 20-40 cm^{-1}. However, a few bands show greater half-band widths. The band at 3300 cm^{-1} (O–H stretching) seen in the spectra of $(CH_2NOH)_n$ and $(CD_2NOH)_n$, and the band at 2415 cm^{-1} (O–D stretching) observed in the spectra of $(CH_2NOD)_n$ and $(CD_2NOD)_n$ display half-band widths of ca. 400 cm^{-1}. The exceptional broadening of these two bands almost certainly arises from inter-chain and perhaps intra-chain hydrogen bonding. Likewise, the bands at 430 cm^{-1} and 335 cm^{-1} in the spectra of $(CH_2NOH)_n$ and $(CH_2NOD)_n$, respectively, which originate from the OH and OD out-of-plane deformation modes, are rather broad with half-band widths of 100-150 cm^{-1}. For the 1460 cm^{-1} band (OH bending), however, the broadening is less pronounced, the half-band width being only 50-60 cm^{-1}.

2. Procedure of Assignment

It follows from the above discussion, that the number of fundamental bands which one will expect to find in the infrared spectrum of poly(formaldehyde oxime) is $3r - 4 = 14$, since there are six atoms in the repeating unit (cp. Fig. 1) and all the normal vibrations are infrared active according to the selection rules.

For the assignment of the observed bands to fundamental frequencies the following procedure was adopted:

(1) Bands which shifted appreciably on deuteration of OH groups were assigned as OH vibrations.

(2) Bands which showed appreciable shifts on deuteration of CH_2 groups were assigned as vibrations involving CH_2 motions.

(3) Bands which were only slightly affected on deuteration of OH groups and CH_2 groups must correspond to skeletal vibrations.

(4) The assignments of the fundamental frequencies of poly(formaldehyde oxime) should compare reasonable well with the results obtained by other workers for related polymers such as polymethylene, polyoxymethylene and polyvinyl alcohol (see Table 3).

As far as points (1), (2) and (3) are concerned it must be kept in mind, however, that coupling between OH(OD) or $CH_2(CD_2)$ deformation vibrations and skeletal vibrations may decrease the isotopic frequency shifts for the OH and CH_2 deformation bands considerably, while on the other hand appreciable shifts of the skeletal bands will be observed as a result of the coupling.

In general one may conclude that whenever the ratio ν^H/ν^D of an OH or a CH_2 group vibration frequency to the new frequency arising on deuterium substitution

has a value in the range 1.3-1.4, the OH (and OD) or CH_2 (and CD_2) vibration in question may be considered a "pure" group vibration. For "pure" skeletal vibrations ν^H/ν^D will be close to 1.0, while ratios of 1.1-1.2 for hydrogen vibrations as well as skeletal vibrations are indicative of strong coupling and therefore of "impure" or "mixed" vibrations.

V. Fundamental Frequencies

As already mentioned there are 14 fundamentals, *viz* nine of species *A'* and five of species *A"* (cf. Table 1), whose assignments will be discussed in the present section. Using the approximation of group vibrations six of the fundamentals correspond to CH_2 vibrations and three to OH vibrations, the remaining five being skeletal vibrations (cf. Figures 3, 4 and 5). The resulting assignments are shown in Table 2. It can bee seen that the fundamental frequencies of poly(formaldehyde oxime) formed by polymerisation (A) and by polycondensation (B), respectively, are almost identical, so that it is reasonable to conclude that the structures of the compounds A and B must also be very similar. For this reason and for the sake of simplicity the frequency values mentioned in the discussion below refer to the spectra of the compound B unless otherwise stated.

Table 2. Assignments and wavenumbers of fundamental bands for poly(formaldehyde oxime) and its deuterated species *.

Assignments	Species	$(CH_2NOH)_n$ A	$(CH_2NOH)_n$ B	$(CD_2NOH)_n$ A	$(CD_2NOH)_n$ B	$(CH_2NOD)_n$ B	$(CD_2NOD)_n$ B
ν_1	*A'*	3300[a] vs br	3290[a] vs br	3290[a] vs br	3300[a] vs br	2435[a] s br	2425[a] s br
ν_2	*A'*	2923 s	2924 s	2195 w	2202 w	2924 s	2195 sh
ν_3	*A'*	2904 sh	2905 sh	2098 m	2101 m	2905 sh	2098 m
ν_4	*A'*	1460 s	1460 s	1455 s	1455 s	1177 m	1168 m
ν_5	*A'*	1444 sh	1444 sh	1130 w	1130 w	1442 m	1120 sh
ν_{10}	*A"*	1364 s	1364 s	1216 s	1217 s	1363 s	1214 s
ν_{11}	*A"*	1280 sh	1270 sh	915? w	916? w	1270 sh	—
ν_{12}	*A"*	1148 s	1148 s	1012 m	1011 m	1147 s	1001 m
ν_6	*A'*	1035 m	1031 m	968 m	968 m	994 m	940 m
ν_7	*A'*	957 s	958 s	811 m	810 m	957 s	809 m
ν_8	*A'*	841 s	841 s	799 s	799 s	837 s	795 s
ν_9	*A'*	540 m	539 m	474 m	474 m	527 m	468 m
ν_{13}	*A"*	457 sh	458 sh	442 sh	442 sh	452 m	435 m
ν_{14}	*A"*	430[a] s br	437[a] s br	395 s	397[a] s	~335[a] m br	359 m

* Abbreviations used: s, m, w, v, sh, br indicate strong, medium, weak, very, shoulder and broad, respectively. A and B denote two different ways of preparing the compounds (see text).

[a] Band position dependent on the concentration of the sample in the disc and on the alkalimetal halide used as matrix (see text).

1. CH_2 Vibrations

In the C–H stretching region a strong absorption band is observed at about 2900 cm^{-1} in the spectrum of $(CH_2NOH)_n$, the frequency at intensity maximum being 2924 cm^{-1}. Shoulders are seen on the low frequency side of the band at 2905, 2875 and 2855 cm^{-1}. The bands at 2924 and 2905 cm^{-1} are assigned to asymmetric and symmetric CH_2 stretching vibrations, ν_2 and ν_3, in good agreement with the values 2937 and 2908 cm^{-1} obtained for polyvinyl alcohol (cf. Table 3). The remaining two bands are assigned as the first overtones of the OH bending vibration ν_4 and the CH_2 bending vibration ν_5, the calculated values being $2\nu_4 = 2920$ cm^{-1} and $2\nu_5 = 2888$ cm^{-1}. The observed anharmonicities, $\nu_{obs.}-\nu_{calc.}$, of –45 cm^{-1} and –33 cm^{-1}, respectively, are, however, somewhat larger than expected for OH and CH_2 deformations, probably because of Fermi resonance with ν_3 and with the OH stretching vibration ν_1 at 3290 cm^{-1}. In the spectrum of $(CD_2NOH)_n$ the only band observed around 2900 cm^{-1} is a band of medium intensity at 2877 cm^{-1} which must therefore be $2\nu_4$ (observed at 2875 cm^{-1} in the spectrum of $(CH_2NOH)_n$). The ν_2 and ν_3 bands are found in the expected region at ca. 2200 and ca. 2100 cm^{-1}, the isotopic frequency shifts being of the magnitude expected for "pure" group vibrations.

Of the four CH_2 deformations the CH_2 bending vibration ν_5 is assigned to a shoulder of medium intensity at 1444 cm^{-1} on the low frequency side of the strong band at 1460 cm^{-1} which corresponds to the OH bending vibration ν_4 (see below). On C-deuteration the 1444 cm^{-1} band shifts to 1130 cm^{-1}, the ratio ν^H/ν^D being close to 1.3, while the 1460 cm^{-1} band is barely affected. On deuteration of the OH groups ν_4 is weakened considerably so that ν_5 appears cleanly at 1442 cm^{-1}. The strong absorption at 1364 cm^{-1} undoubtedly corresponds to the CH_2 wagging vibration ν_{10} which is found in the same region in the spectra of $(CH_2)_n$, $(CH_2O)_n$ and $(CH_2CHOH)_n$ (cf. Table 3). The isotopic frequency shift on C-deuteration is, however, only about 150 cm^{-1}, which yields a frequency ratio ν^H/ν^D of only 1.12, indicating that the vibration is very "impure". As discussed at greater length below this is due to strong coupling between ν_{10} and the skeletal vibration ν_{12} in either $(CH_2NOH)_n$ or $(CD_2NOH)_n$.

Table 3. Compilation of fundamental vibration frequencies for poly(formaldehyde oxime) (compound B) and some related polymers.

Approximate type of vibration	$(CH_2)_n$[3,4] cm^{-1}	$(CH_2O)_n$[5] cm^{-1}	$(CH_2CHOH)_n$[6,7] cm^{-1}	$(CH_2NOH)_n$ cm^{-1}
OH stretch.	—	—	~3340	~3290
CH_2 asym.stretch.	2919	2979	2937	2924
		2978		
CH_2 sym.stretch.	2851	2919	2908	2905
OH bend.	—	—	ca. 1430[c]	1460
CH_2 bend.	1473	1471	1428[e]	1444
	1463			
CH_2 wag.	1367[a]	1434	1383[e]	1364
	1352[a]	1381		
CH_2 twist.	1306[a]	1286	?	1270
CC,CO or CN asym.stretch.	1131[b]	1097	1141	1148
		1091		
CC,CO or CN sym.stretch.	1061[b]	932	913	1031
CH_2 rock.	731	1235[d]	849[f]	958
	720	903		
CO or NO stretch.	—	—	1093	841
CO or NO bend.	—	—	480	539
CO or NO wag.	—	—	410	458
OH wag.	—	—	610	437

[a] Observed for amorphous polymer.[3]
[b] From the Raman spectrum.
[c] Coupling band: coupling of OH bending and CH_2 (or CH) wagging modes.
[d] Coupling band: CH_2 rocking mode coupled with COC bending and CO sym. stretching modes.
[e] From the infrared spectrum of $(CH_2CHOD)_n$.
[f] Observed for amorphous polymer.[6]

The CH_2 twisting vibration is found at 1306 and 1286 cm^{-1} for $(CH_2)_n$ and $(CH_2O)_n$, the bands being of very low intensity as a result of the small change in dipole moment during the vibration. For this reason the weak shoulder observed at about 1270 cm^{-1} for $(CH_2NOH)_n$ is assigned to the twisting vibration ν_{11}. On C-deuteration the band disappears and a weak band is then seen at 916 cm^{-1}. The latter is believed to correspond to the CD_2 twisting vibration (which is found at 909 cm^{-1} for $(CH_2)_n$) possibly overlapped by the combination band $\nu_9 + \nu_{13} =$ 916 cm^{-1}. Just as for polyoxymethylene the ratio ν^H/ν^D is close to 1.4 indicating that the CH_2 twisting mode is a "pure" vibration.

The CH_2 rocking vibration in $(CH_2O)_n$ has been assigned to a very strong band at 903 cm^{-1}, and for $(CH_2CHOH)_n$ to a band of medium intensity at 849 cm^{-1}. In $(CH_2NOH)_n$ two strong absorptions occur in this region, one at 958 cm^{-1} and the other at 841 cm^{-1}. For $(CD_2NOH)_n$ these bands are shifted to 810 cm^{-1} and 799 cm^{-1}, respectively. Because of the larger isotopic shift of about 150 cm^{-1} the band at 958 cm^{-1} must be due to the CH_2 rocking mode ν_7, whereas the 841 cm^{-1} band is due to a skeletal vibration, the N–O stretching vibration ν_8 (see below). The 810 cm^{-1} band of medium intensity is assigned to CD_2 rocking since the integrated absorption intensity of a CH_2 band in general decreases upon deuterium substitution; the strong band at 799 cm^{-1} must therefore arise from N–O stretching in $(CD_2NOH)_n$. The low frequency ratio ν^H/ν^D of 1.18 for the rocking vibration shows that it is considerably "mixed" like the CH_2 (or CD_2) wagging, the rocking vibration and the skeletal vibration ν_9 being strongly coupled (see below).

2. OH Vibrations

The O–H stretching vibration ν_1 of $(CH_2NOH)_n$ occurs in the spectrum as a very strong and extremely broad band at about 3300 cm^{-1} which shifts to 2435 cm^{-1} on deuteration of the OH groups. Shoulders are observed in the spectrum of the $(CH_2NOD)_n$ sample on the high frequency side of both bands, at approximately 3420 and 2560 cm^{-1}. These additional bands probably correspond to the asymmetric O–H and O–D stretching vibrations of HDO and D_2O, respectively, and arise from a small residue of D_2O and HDO in the sample.

The two OH deformations, *viz* the in-plane deformation (or bending) ν_4 and the out-of-plane deformation (or wagging) ν_{14}, are observed as strong, broad absorptions at 1460 and ca. 435 cm^{-1}. For $(CH_2NOD)_n$ they are shifted to 1177 and ca. 335 cm^{-1}, respectively, the two bands being of medium intensity. The assignment of the OH bending vibration is in good agreement with the values of ca. 1430 and 1477 cm^{-1} which have been obtained for $(CH_2CHOH)_n$ and solid acetone oxime $(CH_3)_2C{=}NOH$,[8] respectively, while the OH wagging frequencies of 610 and 790 cm^{-1} for these compounds are considerably higher than that found for $(CH_2NOH)_n$. However, the frequency ratio $\nu^H/\nu^D = 1.30$ shows that the 435 and 335 cm^{-1} bands are due to hydrogen and deuterium vibrations, respectively, and for this reason must be assigned to ν_{14}.

3. Skeletal Vibrations

The bands due to the five skeletal vibrations are found in the region 1200-400 cm^{-1}. The asymmetric C–N stretching mode ν_{12} is assigned to the strong band at 1148 cm^{-1} in good agreement with the assignments for the corresponding skeletal vibrations of $(CH_2)_n$, $(CH_2O)_n$ and $(CH_2CHOH)_n$ (cf. Table 3). On C-deutera-

tion the band shifts to 1011 cm^{-1}. However, this vibration is not appreciably affected by deuteration of OH groups, the band being observed at 1147 cm^{-1} for $(CH_2NOD)_n$. The large isotopic shift is an indication of strong coupling between the asymmetric C–N stretching vibration and a hydrogen (or deuterium) vibration, the observed frequency ratio ν^H/ν^D being as high as 1.14. On the other hand, as mentioned above, the frequency ratio for the CH_2 wagging ν_{10} is unexpectedly low (1.12). Since coupling can occur only between vibrations of the same symmetry species it follows that it must be the asymmetric C–N stretching- and the CH_2 (or CD_2) wagging mode which couple strongly. It is therefore not really valid to ascribe the observed bands to "asymmetric C–N stretching" and "CH_2 (or CD_2) wagging" since the actual mode of vibration in this case is a combination of both.

The symmetric C–N stretching (or CON bending) mode ν_6 gives rise to a band of medium intensity at 1031 cm^{-1} which shifts to 968 cm^{-1} on C-deuteration. The isotopic shifts indicates coupling, probably with the CH_2 (or CD_2) rocking vibration, both vibrations being of symmetry species A'. On deuteration of the OH groups the band appears at 994 cm^{-1}, the ratio $\nu^H/\nu^D = 1.04$ indicating weak coupling probably to the OH (or OD) bending vibration for which $\nu^H/\nu^D = 1.24$. As already mentioned, the strong band at 841 cm^{-1} is assigned to the N–O stretching mode ν_8 which like the ν_6 band is affected by C-deuteration, showing that the N–O stretching vibration is also a "mixed" vibration.

The remaining two skeletal bands, due to the NO bending mode ν_9 and the NO wagging mode ν_{13}, are expected to be found in the region below 800 cm^{-1}. In polyvinyl alcohol the CO bending frequency is situated at 480 cm^{-1} and the CO wagging at 410 cm^{-1} (cf. Table 3). The band of medium intensity at 539 cm^{-1} in the spectrum of $(CH_2NOH)_n$ is therefore assigned to ν_9 whereas the shoulder which is just observable at ca. 458 cm^{-1} on the high frequency side of the strong band ν_{14} is presumed to correspond to ν_{13}.

The assignments are supported by the results obtained for the deuterated compounds. For $(CH_2NOD)_n$ the bands are observed as separate bands of medium intensity at 527 and 452 cm^{-1}, respectively, while the 458 cm^{-1} band shifts on C-deuteration to 442 cm^{-1}. The 539 cm^{-1} band, however, shifts to 474 cm^{-1} for $(CD_2NOH)_n$, the high frequency ratio ν^H/ν^D of 1.14 revealing strong coupling between the NO bending- and probably the CH_2 (or CD_2) rocking vibrations.

4. Poly(formaldehyde-d_2 oxime-d)

The spectrum of $(CD_2NOD)_n$ supports the assignments given above. All the fundamental CD_2 bands and bands due to skeletal vibrations coupled to CH_2 (or CD_2) vibrations are observed at frequencies close to but slightly lower than

those observed for $(CD_2NOH)_n$. Similarly, the OD bands are found at slightly lower frequencies than for $(CH_2NOD)_n$, except for the OD wagging which appears at 359 cm^{-1}, *i.e.* at a higher frequency than in $(CH_2NOD)_n$. The origin of this effect may be differences in hydrogen bonding in $(CD_2NOD)_n$ and $(CH_2NOD)_n$.

VI. Other Bands

1. Terminal Groups

Since the poly(formaldehyde oxime) chains contain a finite number of repeating units, bands due to the terminal groups of the chains are expected to appear in the infrared spectra provided that the number of units is not too high, that the integrated intensities of the terminal group absorption bands are not too low, and that the bands are not obscured by other bands of the polymer.

When poly(formaldehyde oxime) is formed by polymerisation the composition of the polymer may be as in I or II below,

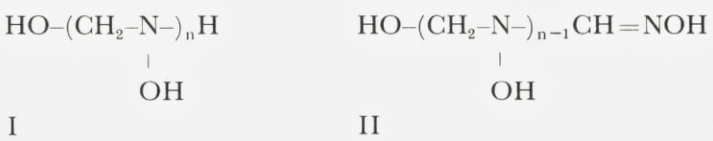

I II

one of the terminal groups in formula II being an oxime group. When the polymer is formed in solution by polycondensation it may contain one $-CH_2OH$ terminal group (formula I) but it is also possible that it contains an $-NHOH$ terminal group (formula III) or that both of the terminal groups are $-CH_2OH$ groups (formula IV):

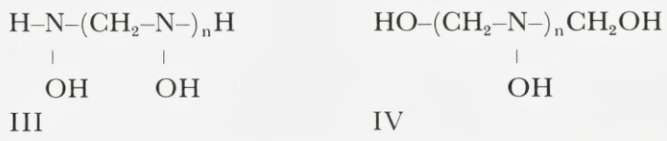

III IV

The $-CH_2OH$ group should give rise to a band near 1050 cm^{-1} due to the C–O stretching vibration. In the spectrum of $(CH_2NOH)_n$ formed by polymerisation (A) a weak shoulder is observed at 1062 cm^{-1}. However, in $(CH_2NOH)_n$ formed by polycondensation (B) a band of somewhat higher intensity appears at 1061

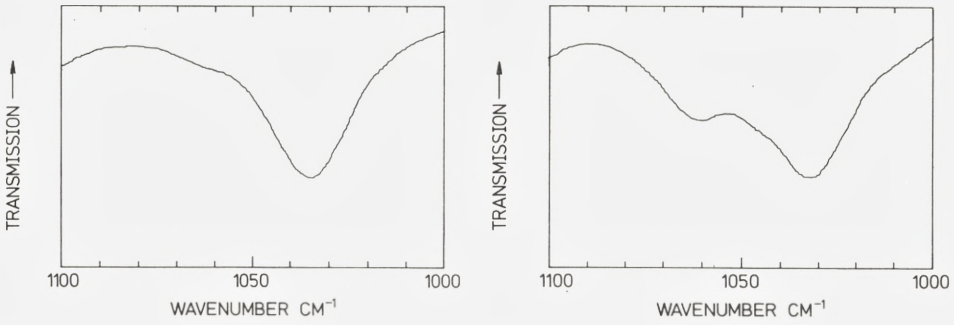

Fig. 13. Infrared absorptions of $(CH_2NOH)_n$ in the region 1100-1000 cm^{-1}. Left: compound A. Right: compound B.

cm^{-1}, separated from the 1031 cm^{-1} band (ν_6) (cf. Fig. 13). Both bands are believed to be due to the C–O stretching of the $-CH_2OH$ group, the difference in intensity indicating that the concentration of $-CH_2OH$ groups is higher in compound B than in compound A. This may be explained partly by assigning formula IV for B and formula I for A, and partly by assuming the occurrence of fewer repeating units in the chains of B. For the deuterated analogues of compound B the C–O stretching band is found at 1034 cm^{-1} for $(CD_2NOH)_n$ and at 1050 cm^{-1} for $(CH_2NOD)_n$, the isotopic shifts being of the expected magnitude; this band is not observed in the spectrum of $(CD_2NOD)_n$ since it overlaps with other bands.

In the spectrum of $(CH_2NOH)_n$ (both A and B) the weak band observed at 893 cm^{-1} is somewhat more intense for A than for B. This band is ascribed to the –NHOH terminal group or the combination $\nu_{13} + \nu_{14}$ which in the spectrum of A is presumed to coincide with the N–O stretching mode of the $-CH=NOH$ terminal group. This is in good agreement with the infrared results for formaldehyde oxime $CH_2=NOH$, obtained by Califano and Lüttke,[8] who found the N–O stretching mode at 888 cm^{-1}. For $(CD_2NOH)_n$ this band appears as a weak shoulder at 896 cm^{-1}. The weak band at 878 cm^{-1} in the spectrum of $(CH_2NOD)_n$ (compound B) is probably associated with the N–O stretching mode of the –NDOD terminal group, the frequency for ND_2OD being 874 cm^{-1}. However, it may also be interpreted as being the combination band $(\nu_7 + \nu_{13}) - \nu_9 = 882$ cm^{-1}. The weak, broad absorption at 842 cm^{-1} in the spectrum of the fully deuterated compound B is probably a superimposition of several combination bands lying in the region 827-855 cm^{-1}.

Finally a weak, broad band at ca. 485 cm^{-1} in the spectrum of $(CH_2NOH)_n$, which is somewhat more intense for B than for A, is assigned to the OH wagging

vibration of the $-CH_2OH$ terminal group since it disappears on the deuteration of the OH groups. However, the OH(OD) wagging is not observed in the spectra of the deuterated species because of overlapping with strong fundamental bands.

2. Overtones and Combinations

In addition to the fundamental bands a considerable number of weak bands have been measured and interpreted as being overtone and combination bands, many of the bands appearing in the spectra as shoulders. A striking feature is that it has been necessary to explain most of the bands as difference bands. This is due to the considerable population of the low lying levels for the modes ν_9, ν_{13} and ν_{14}.

The remaining bands have been interpreted as binary summation bands, except for a few bands which have been explained as ternary summation bands. The assignments of all the combination bands of $(CH_2NOH)_n$ and its deuterated species will be given in a separate paper.[9]

Although the combination bands are generally much weaker than the fundamentals, two such bands of medium intensity have been observed in the spectrum of $(CH_2NOH)_n$. As already mentioned above the band at 2875 cm^{-1} is assigned to the first overtone of the OH bending mode ν_4, the exceptionally high intensity of the band being due to Fermi resonance, probably with the symmetric CH_2 stretching vibration ν_3 and the OH stretching vibration ν_1. The band observed at 1121 cm^{-1} which is not seen for $(CD_2NOH)_n$ and $(CH_2NOD)_n$, is interpreted as $(\nu_{12} + \nu_{14}) - \nu_{13} = 1127$ cm^{-1}, in agreement with the deuteration experiments.

VII. Conclusion

The vibrational analysis of the infrared spectra of poly(formaldehyde oxime) and its deuterated analogues presented above lends strong support to the conclusion that poly(formaldehyde oxime) is a chain polymer, the carbon-nitrogen skeleton of which is a planar zig-zag chain. It has been established that the repeating unit of the extended polymer chain is $-CH_2NOH-$.

References

1. Jensen, K. A. and Holm, A. *K. Dan. Vidensk. Selsk., Mat.-Fys. Medd. 40:2* (1978).
2. See R. Zbinden, *Infrared Spectroscopy of High Polymers.* (Academic Press, New York and London, 1964).
3. Zbinden, R. *loc. cit.* p. 88.
4. Tasumi, M. and Shimanouchi, T. *J. Mol. Spectrosc. 9* (1962) 261.
5. Tadokoro, H., Kobayashi, M., Kawaguchi, Y., Kobayachi, A., and Murahashi, S. *J. Chem. Phys. 38* (1963) 703.
6. Krimm, S. *Fortschr. Hochpolymer. Forsch. 2* (1960) 51.
7. Tadokoro, H., Nagai, H., Seki, S., and Isamu, N. *Bull Chem. Soc. Japan 34* (1961) 1504.
8. Califano, S. and Lüttke, W. *Z. Phys. Chem.* (Frankfurt am Main) *6* (1956) 83.
9. Andersen, F. A. To be published.

Stopping Power of Swift Hydrogen and Helium Ions in Gases

By F. BESENBACHER, H. H. ANDERSEN,
P. HVELPLUND, *and* H. KNUDSEN

Det Kongelige Danske Videnskabernes Selskab
Matematisk-fysiske Meddelelser **40**:3

Kommissionær: Munksgaard
1979

DET KONGELIGE DANSKE VIDENSKABERNES SELSKAB
udgiver følgende publikationsrækker:

THE ROYAL DANISH ACADEMY OF SCIENCES AND LETTERS
issues the following series of publications:

	Bibliographical Abbreviation
Oversigt over Selskabets Virksomhed (8°) *(Annual in Danish)*	Overs. Dan. Vid. Selsk.
Historisk-filosofiske Meddelelser (8°)	Hist. Filos. Medd. Dan. Vid. Selsk.
Historisk-filosofiske Skrifter (4°) *(History, Philology, Philosophy, Archaeology, Art History)*	Hist. Filos. Skr. Dan. Vid. Selsk.
Matematisk-fysiske Meddelelser (8°) *(Mathematics, Physics, Chemistry, Astronomy, Geology)*	Mat. Fys. Medd. Dan. Vid. Selsk.
Biologiske Skrifter (4°) *(Botany, Zoology, General Biology)*	Biol. Skr. Dan. Vid. Selsk.

Selskabets sekretariat og postadresse
The address of the Academy is:

Det Kongelige Danske Videnselskabernes Selskab,
Dantes Plads 5,
DK-1556 Copenhagen V.
Denmark.

Selskabets kommissionær
The publications are sold by the agent of the Academy:

MUNKSGAARDS BOGHANDEL,
6, Nørregade,
DK-1165 Copenhagen K.
Denmark.

Stopping Power of Swift Hydrogen and Helium Ions in Gases

By F. BESENBACHER, H. H. ANDERSEN,
P. HVELPLUND, *and* H. KNUDSEN

Det Kongelige Danske Videnskabernes Selskab
Matematisk-fysiske Meddelelser **40**: 3

Kommissionær: Munksgaard
1979

Contents

Synopsis

Stopping powers of H_2, He, N_2, O_2, CO_2, Ne, Ar, Kr, and Xe for 40-keV to 1-MeV hydrogen ions and 100-keV to 2.4-MeV helium ions have been measured to an accuracy of $\pm 2.5\%$ (2σ). The stopping powers for hydrogen show good agreement with most other published results and with the Andersen and Ziegler tabulations, while those for helium ions are up to 6% lower than the helium data of Chu and Powers. With higher-order Z_1 correction terms included in the theoretical description, Bonderup's calculated shell-corrections based on the Lindhard-Scharff model, are in good agreement with the experimental proton data for $E_p \geq 100$ keV, and experimental I values may be deduced. Within the velocity region $4.4 \lesssim v/v_0 \lesssim 4.9$ and for target materials with $1 \leq Z_2 \leq 54$, the experimental findings support Lindhard's and Esbensen's value for the Barkas correction. The stopping-power ratios S_{He}/S_H depend strongly on Z_2 and deviate significantly from the mean-square charge state obtained from experimental equilibrium charge state distributions.

Institute of Physics, University of Aarhus
DK-8000 Aarhus C, Denmark

Printed in Denmark by Bianco Lunos Bogtrykkeri A/S. ISSN 0023-3323. ISBN 87-7304-097-5

§1. Introduction

The energy loss of an ion beam traversing matter is a phenomenon of basic interest to atomic physics and has been the subject of much theoretical and experimental work. However, there is still a great need for a better understanding of the details of the stopping processes.

It is the purpose of the present work, through accurate measurements to test the Lindhard-Scharff model (Lindhard and Scharff 1953, 1960) and its refinements for the average energy-loss (Bonderup 1967) and energy straggling (Bonderup and Hvelplund 1971). Especially it is of interest to examine the so-called shell corrections at the present rather low energies, and to investigate Sigmund's molecular correlation effect in energy straggling (Sigmund 1976).

A detailed understanding of the underlying mechanisms is imperative for obtaining the kind of comprehensive and accurate energy loss and straggling information necessary in, for example, a composition analysis of thin films via Rutherford-backscattering or nuclear reaction techniques.

We have carried out a systematic investigation of the stopping power and energy straggling for hydrogen and helium ions in H_2, He, N_2, O_2, CO_2, Ne, Ar, Kr, and Xe at ion energies 40 keV $\lesssim E_H \lesssim$ 1 MeV and 100 keV $\lesssim E_{He} \lesssim$ 2.4 MeV. Gaseous targets were chosen so as to avoid specific solid-state effects that might obscure especially the straggling results.

The present paper deals with the stopping-power results only. A forthcoming publication (Besenbacher et al. 1980) will deal with the straggling results, some of which have already been published (Besenbacher et al. 1977).

After a brief review of the energy-loss theory in §2, the experimental procedure and data treatment will be discussed in §3. In §4, the experimental results will be presented and compared with empirical stopping-power tabulations and other published results and, finally, in §5, the experimental data will be discussed and compared with theory.

§2. Theory

As discussed by Bohr (1948), two distinctly different mechanisms are responsible for the slowing-down of nonrelativistic charged particles: (*i*) Electronic stopping, i.e., energy loss to excitation and ionization, and (*ii*) Nuclear stopping, i.e., energy transfer leading to translatory motion of the struck atom as a whole. In the present velocity range $v \gtrsim v_o$ (v_o is the Bohr velocity $e^2/\hbar$), and with our experimental geometrical arrangement, the nuclear energy loss is almost negligible (see below).

At high velocities, where

$$\varkappa_B = \frac{2\mathcal{Z}_1 v_o}{v} < 1\,, \tag{1}$$

a quantal perturbation treatment is applicable and gives the wellknown Bethe formula (Bethe 1930). According to this formula, the specific electronic energy loss suffered by a heavy incoming particle with charge $\mathcal{Z}_1 e$ and velocity v penetrating a target of atomic number $\mathcal{Z}_2$ and density N (atoms per unit volume) is given by

$$\left(-\frac{dE}{dR}\right)_e = \frac{4\pi \mathcal{Z}_1^2 e^4}{mv^2} N \mathcal{Z}_2 L(v, \mathcal{Z}_2) \tag{2}$$

where

$$L(v, \mathcal{Z}_2) = L_o = \log\left(\frac{2mv^2}{I}\right) - \log\left(1 - \left(\frac{v}{c}\right)^2\right) - \left(\frac{v}{c}\right)^2 - \frac{C(v, \mathcal{Z}_2)}{\mathcal{Z}_2} \tag{3}$$

Here, m and $-e$ are the electron mass and charge, respectively, and c the velocity of light. The main parameters of the Bethe formula are the mean ionization potential I and the shell corrections $C/\mathcal{Z}_2$. The former is defined by

$$\log I = \frac{1}{\mathcal{Z}_2} \sum_i f_{oi} \log \hbar\, \omega_{oi} \tag{4}$$

where f_{oi} are the dipole oscillator strengths corresponding to the transition frequencies ω_{oi} for the atomic system. A direct calculation of I from this formula has until recently been impeded due to the lack of knowledge about the distribution of oscillator strength in the relevant energy region, i.e., from 10-1000 eV. In a Thomas-Fermi model the calculation of I is very much simplified since f_{oi} is a function of $\omega/\mathcal{Z}_2$ only and Bloch (1933) showed within this model that

$$I/\mathcal{Z}_2 = I_o = \text{constant}. \tag{5}$$

This result is in qualitative agreement with the experimental results for heavier atoms and empirically I_o is of the order of 10 eV. For lighter atoms the cut-off in $f(\omega, \mathcal{Z}_2)$ close to the Rydberg frequency leads to a somewhat higher value of $I/\mathcal{Z}_2$ (Lindhard 1964).

To calculate $L(v, \mathcal{Z}_2)$ in formula (2) and thereby to determine the mean ionization potential and the shell corrections, Lindhard and Scharff (1953, 1960) considered the target as a collection of free electron gases. The function $L(v, \mathcal{Z}_2)$ pertaining to an atom was obtained as an average over the electron

cloud of the quantity $L(\varrho, v)$ for a gas of density ϱ (Lindhard 1954). As a first approximation, they introduced the expression

$$L(v, Z_2) = \frac{1}{Z_2} \int 4\pi r^2 \varrho(r) \cdot L(r, v) dr$$

$$= \frac{1}{Z_2} \int_{r_{min}}^{\infty} 4\pi r^2 \varrho(r) \cdot \log \frac{2mv^2}{\gamma \hbar \omega_o(r)} dr \; ; \; \frac{2mv^2}{\gamma \hbar \omega_o(r_{min})} = 1 \qquad (6)$$

Here $\varrho(r)$ is the electron density of the target atom, $\omega_o(r)$ is the local plasma frequency $(4\pi e^2 \varrho(r)/m)^{1/2}$; and γ is a constant of the order of $\sqrt{2}$ by means of which they took into account the binding of the electrons. In the Lindhard-Scharff model the mean ionization potential can be calculated from

$$\log I = \frac{1}{Z_2} \int 4\pi r^2 \varrho(r) \log [\gamma \hbar \omega_o(r)] \, dr \qquad (7)$$

Bonderup and Lindhard (1967) and Chu and Powers (1972) calculated I from this formula using Hartree-Fock charge distributions and found significant oscillations superimposed on a slow decrease of I/Z_2 with increasing Z_2. Even though formula (7) was based on qualitative arguments, the results of the calculations agree fairly well with experiments. It deserves attention that very recently Inokuti et al. (1978) calculated I values by directly using formula (4) in a form appropriate for a continuous distribution of oscillator strengths. They started with the Hartree-Slater central potential model and carried through explicit calculations of df/dE for the entire spectrum from the dipole matrix elements between initial and final electron states. The variation of their I/Z_2 values with Z_2 is similar to that based on the Lindhard-Scharff model which, however, generally gives approximately 30% higher results. This ratio is close to the number $\gamma \sim \sqrt{2}$ which appears as a factor in the I value obtained from formula (7). This result lends strong support to formula (7).

The results based on the Lindhard-Scharff model were so promising even down to velocities of the order of a few times v_o that it was natural to repeat the averaging procedure in formula (6) with a more accurate expression for the electron gas function $L(\varrho, v)$. This was done by Lindhard and Winther (1964), and Bonderup (1967) applied their electron gas results to compute the shell corrections C/Z_2 in formula (3). The first-order Lenz-Jensen distribution was used for the function $\varrho(r)$. The function C/Z_2 is useful in a comparison between theory and experiment since, in contrast to the I value, this quantity is rather insensitive to the details in the distribution of the outermost electrons.

Since the Bethe treatment is based on a first-order perturbation calculation,

the resulting stopping power is proportional to $\mathcal{Z}_1^2$. However, both range measurements by Barkas (for a survey, see Heckman 1970) and accurate p and α stopping power measurements by Andersen et al. (1969) provided convincing evidence for the existence of higher-order $\mathcal{Z}_1$ correction terms to the stopping formula. Expanding $L(v, \mathcal{Z}_2)$ in powers of $\mathcal{Z}_1$ we have the expression

$$L = L_o + \mathcal{Z}_1 \cdot L_1 + \mathcal{Z}_1^2 \cdot L_2 \tag{8}$$

where L_0 is given by Eq. (3) whereas L_1 corresponds to a $\mathcal{Z}_1^3$-correction and L_2 to a $\mathcal{Z}_1^4$-correction in the Bethe stopping-power formula. Terms of still higher order are neglected.

The $\mathcal{Z}_1^3$-term, often called the Barkas correction, stems from adiabtic screening effects and receives contributions from both close and distant projectile-electron collisions. An electron gas calculation by Lindhard (1976) and Esbensen (1977) gave the following correction factor

$$\mathcal{Z}_1 \cdot L_1 = \frac{3\pi}{2} \cdot \frac{\mathcal{Z}_1 e^2 \omega_o}{m \cdot v^3} \cdot L_o \tag{9}$$

This result is approximately twice that of previous calculations by Ashley et al. (1972, 1973) and by Jackson and McCarthy (1972), both of which neglect the contribution from close collisions.

Bloch's (1933) universal stopping formula which is valid for all values of $\varkappa_B$ describe the transition between Bethe's quantal and Bohr's (1948) classical stopping formula and contains these in the limits of small and large $\varkappa_B$, respectively. Thus, Bloch's formula contains a correction to the Bethe formula. The correction derives from close collisions only and to first order in $\varkappa_B$ it is given by

$$\mathcal{Z}_1^2 L_2 = -1.202 \left(\frac{\varkappa_B}{2}\right)^2 = -1.202 \cdot \frac{\mathcal{Z}_1^2 v_0^2}{v^2} \tag{10}$$

As pointed out by Lindhard (1976), the Bloch correction is important when comparing p and α measurements.

At low velocities, $v \lesssim v_o \mathcal{Z}_1^{2/3}$, the nuclear as well as the electronic collisions contribute to the slowing-down. The total stopping cross section $S = \mathcal{N}^{-1}\left(-\frac{dE}{dR}\right)$ may be written as

$$S = S_e + S_n \,. \tag{11}$$

Simple theoretical considerations lead to velocity-proportional electronic stopping, and a Thomas-Fermi calculation by Lindhard and Scharff (1961) gives

$$S_e = \xi_e 8\pi e^2 a_o \frac{Z_1 Z_2}{(Z_1^{2/3} + Z_2^{2/3})^{3/2}} v/v_o \,, \; v < v_o Z_1^{2/3} \tag{12}$$

where $\xi_e \sim Z_1^{1/6}$.

In our experimental setup, collisions contributing heavily to the nuclear stopping cause the particles to be scattered out of the angularly narrow forward directed analyzed beam. Hence, only the restricted nuclear-stopping power, denoted by S_n^*, contributes to the measured stopping power. The quantity S_n^* was calculated by Fastrup et al. (1966), and their result may be written as

$$S_n^* = 2.61 \times 10^{-16} \frac{Z_1^2 Z_2^2}{E[\mathrm{keV}]} [M_1/M_2] \, \Phi(\tau) \left[\frac{\mathrm{eV\ cm^2}}{\mathrm{atom}} \right]. \tag{13}$$

Here, the dimensionless quantity $\Phi(\tau)$ is a function of $\tau = N\Delta R \pi a^2$ only, where a is the TF screening radius, $a = 0.8853\, a_o (Z_1^{2/3} + Z_2^{2/3})^{-1/2}$ and $N\Delta R$ the target thickness. Based on the Lenz-Jensen differential-scattering cross section, the function $\Phi(\tau)$ has been calculated numerically and the result is shown in Fig. 1.

Fig. 1: Function used for calculation of the restricted nuclear stopping power S_n^*. For explanation, cf. text.

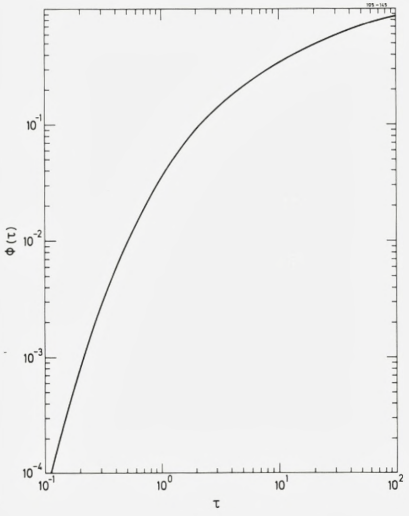

§3. Experimental Procedure and Data Treatment

To perform a systematic investigation of energy loss for light ions in gases, we have measured the stopping powers of nine stopping gases (H_2, He, N_2, O_2,

CO_2, Ne, Ar, Kr, and Xe) for 40-keV to 1-MeV hydrogen and 100-keV to 2.4-MeV helium ions. To cover a large energy region, the measurements were carried out at three different accelerators, an HVEC 2-MV Van de Graaff with magnetic analysis of the energy-degraded beam and a 400-kV Van de Graff and a 100-kV electromagnetic isotope separator both with electrostatic energy analysis. In Table I are shown the energies used at the different accelerators.

Table I

	E_H	E_{He}
2-MV V.d.G.	$0.2 \lesssim E_H \lesssim 1$ MeV	$0.2 \lesssim E_{He} \lesssim 2.4$ MeV
400-kV V.d.G.	$50 \lesssim E_H \lesssim 300$ keV	$100 \lesssim E_{He} \lesssim 300$ keV
100-kV sep.	$35 \lesssim E_H \lesssim 70$ keV	

The overlap of ion energies investigated with the different machines and analyzing techniques is important since it gives a valuable check on the reproducibility of the experimental data.

The experimental setups are shown in Figs. 2 and 3. After acceleration and momentum analysis in a double-focusing sector magnet, the beam is passed through the differentially pumped target region, energy-analyzed by means of an analyzing magnet or an electrostatic analyzer and detected by a solid-state detector.

A. Stopping cell, gas equipment, and pressure measurement.

The stopping cell is a 504 ± 2 mm long, stainless-steel cylinder of 40-mm diameter. Each end of the gas cell is sealed with brass discs with circular, 0.2-mm diameter apertures. By means of a vacuum feed-through, which allows positional adjustments under vacuum, the gas cell is mounted in a 600-mm long cylinder with 2-mm diameter circular entrance and exit apertures. The pressure in the second differential pumping section and the beam lines is typically around $1\text{-}3 \times 10^{-6}$ torr, while the pressure in the first differential pumping region is $P_1 \simeq 10^{-4} P_G$, P_G being the pressure in the gas cell. The purity of the gases was stated by the commercial supplier (Norsk Hydro) to be better than 99.9%.

It is crucial for obtaining reproducible results that the pressure in the gas cell is kept constant. The stability of the target pressure was maintained via a motor-driven, servo-controlled needle valve (Granville-Phillips Company, Series 216). The gas-cell pressure, $0.1 \lesssim P_G \lesssim 2$ torr, was measured with a membrane manometer (C.G.S. Datametrics, type 1083) equipped with a Barocel Pressure Sensor, type 523 H-15. The stated hysteresis was 0.003% and the instrument ranged from zero to two torr with a calibration uncertainty of

0.5%. Owing to the automatic digital readout of the manometer, it was possible to keep a running check of the pressure stability, which was better than 1%.

A mercury thermometer was placed in thermal contact with the vacuum feed-through and thus in contact with the gas cell. The measured temperature was $T = (24.5 \pm 2.5)$°C which, to within the stated accuracy, is identical to the target-gas temperature since the localized heating effects caused by the energy dissipation of the passage of the beam through the gas cell can be shown to give rise to a temperature increase of the target gas of less than 0.7°C. This estimate is based on a steady state. In a previous calculation of the localized heating effect by Bourland et al. (1971) the heat conductivity is neglected. Hence a steady state is not established, and their calculation gave too high an increase of the target temperature.

The target thickness $N\Delta R$ (molecules/cm^2) is found by integrating the local number density $\mu(x)$ along the beam-path length, i.e.

$$N\Delta R = \int_{-\infty}^{\infty} \mu(x)\,dx\,. \tag{14}$$

According to Heinemeier et al. (1975), $\mu(x)$ can be estimated in the following way (*i*) The pressure is constant within the target cell. (*ii*) Outside the target cell the density is found as a sum of two terms (*a*) A constant corresponding to the pressure in the differentially pumped region. (*b*) A varying term which is equal to the target pressure out to a distance equal to the target aperture and then falls off as the inverse square of the distance. Based on this and assuming the ideal gas law we obtain for the target thickness

$$N\Delta R(\text{mol/cm}^2) = A\,\frac{273.15}{273.15+T(^\circ C)}\,\frac{P_G(\text{torr})}{760}\,\ell_{eff}(\text{cm}) \tag{15}$$

where

$$\ell_{eff} = \ell + 2(r_1+r_2) + (\ell_1-\ell)\,P_1/P_G\,. \tag{16}$$

$A = 2.6871\times10^{19}$ (molecules/cm^3) is Loschmidt's number, (ℓ, P_G) and (ℓ_1, P_1) are the length of and the pressure in the gas cell and the first differentially pumped cylinder, respectively, and r_1 and r_2 are the radii of the entrance and exit apertures, respectively. In the present work, the effective length is approximately 0.2% larger than the length of the cell.

B. Energy-analyzing system, detectors, and beam contamination.

The energy-degraded beam was energy-analyzed by a 120-mm radius, 66° cylindrical analyzer (Fig. 2) at the 400-kV Van de Graaff and the 100-kV sepa-

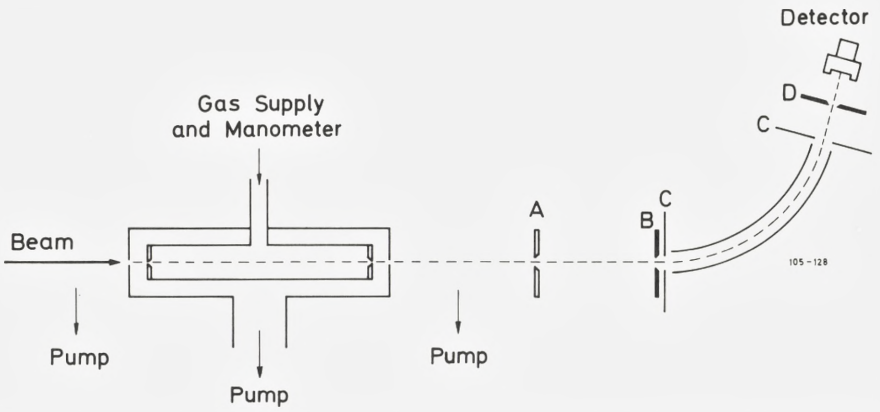

Fig. 2: Experimental setup used at the 400-kV Van de Graaff and at the 100-kV isotope separator.

rator. The analyzer electrodes are 4.9 mm apart and connected to a ~ 12.5 kV symmetric high-voltage supply, which corresponds to the deflection of 0.3 MeV singly charged particles. Apparatures A and B, two 1-mm-wide slits, and aperture D, a 0.42-mm-wide slit, are beam-defining, while the apertures C are used to scrape off scattered halos from the beam.

By extrapolation of the FWHM of the measured energy-loss distributions to zero pressure, we found an energy-independent relative energy resolution (FWHM/E_i) of 0.74%.

The energy calibration was carried out at the 400-kV Van de Graaff accelerator by means of the $^{19}F(p,\alpha)^{16}O$ reaction ($E_{res} = 340.46 \pm 0.04$ keV; $\Gamma = 2.4 \pm 0.2$ keV) as the primary standard. The calibration was checked at the 100-kV isotope separator, at which the accelerator voltage was measured directly by a high-voltage probe to within ± 150 V. The measured beam energies and acceleration voltages agreed within the stated accuracy. The analyzer linearity was investigated in connection with measurements of lithium stopping powers (Andersen et al. 1978). Li^+ and Li^{++} beams emerging from krypton and xenon targets much thicker than the mean-free path for charge-exchange processes were analyzed and requiring a difference of a factor of two in the reference voltages, it was found that the measured energies for Li^+ and Li^{++} agreed within ± 0.2%. The uncertainty in the absolute calibration of the electrostatic analyzer is estimated to be 0.4%.

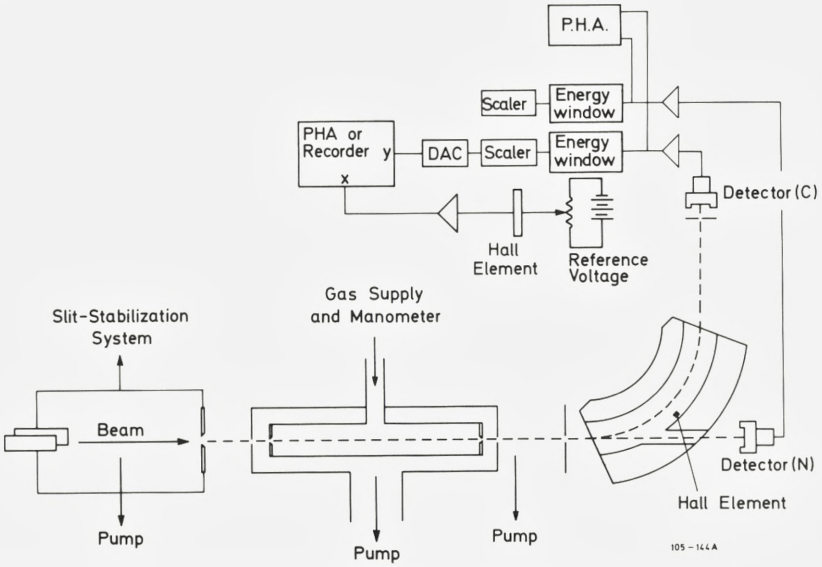

Fig. 3: Experimental setup used at the 2-MV Van de Graaff accelerator.

At the 2-MV Van de Graaff, the energy-loss distributions were analyzed by a 40-cm radius, 90° double-focusing sector magnet (Fig. 3). The magnetic field was measured with a Hall probe, the integral linearity of which was found to be better than 0.5%. The differential linearity of the Hall probe checked by a NMR fluxmeter was better than 0.1%. Tantalum slits with openings of 0.45 mm were placed immediately in front of detector C, and we found a relative energy resolution (FWHM/E_1) of 0.10%. The incoming beam was momentum-analyzed in a 72° double-focusing sector magnet with an energy dispersion of $\Delta E/E \sim 7 \times 10^{-5}$. Hence, in order to obtain a position-stable beam at the target, we used a slit-stabilization system (shown in Fig. 3), which is a feed-back system consisting of two vertical stainless-steel "knives" in front of the target chamber and a set of vertical deflection plates at the exit of the bending magnet.

For the present stopping-power and straggling measurements, the use of solid-state surface-barrier detectors is important. From the detector energy spectrum, it was possible (*i*) to reveal the presence of low-energy, slit-edge-

scattered particles and (*ii*) to identify a possible oxygen-beam contaminant with the same kinetic energy as a primary helium beam. The contaminant is formed by electron loss between the base plate and the bending magnet from a $^{16}O^{+}$ beam accelerated together with He^{+}. Due to the higher pulse-height defect (Steinberg et al. 1972) of the oxygen than that of the helium beam, it is possible to separate the oxygen and helium beams in the pulse-height spectrum. Actually, only once, just after reloading the ion source and under bad vacuum conditions, we did observe any substantial contamination.

C. Electronic equipment.

At the 400-keV Van de Graaff and the separator, use of the electrostatic analyzer for the energy analysis enabled us to apply the multiscaling-sweep technique previously employed for lateral spread measurements (Knudsen et al. 1976). A single-channel window was positioned around the main peak in the energy spectrum from the solid-state detector, and the selected signal was fed to the multichannel analyzer, running in multiscaling mode. After adequate biasing and amplification, the horizontal sweep voltage of the multichannel scope was used as an external reference signal for the analyzer high-voltage power supply. The energy window of the analyzer was thus swept over the energy distribution of the beam synchronously with the multiscaler. Through a simultaneous measurement of the reference voltage for the electrostatic analyzer with a digital voltmeter, the energies corresponding to the upper and lower ends of each sweep were determined, and the energy distribution appeared directly as a spectrum in the multichannel analyzer without transformation. Using this sweep technique we did not need any beam normalization, while the experimental equipment used at the 2-MV Van de Graaff and shown in Fig. 3 utilized detector N as a normalizing device.

D. Data treatment.

With a few exceptions, the pressure in the stopping cell was chosen to make the target thickness satisfy the following criterion,

$$\varkappa_V = (\Omega/T_m)^2 = N\Delta R \frac{\pi Z_1^2 Z_2 e^4}{4E^2} (M_1/m)^2 > 10 . \tag{17}$$

According to Bohr (1948) and Vavilov (1957), Gaussian energy-loss distributions are obtained when inequality (17) is fulfilled. This was confirmed by the measured energy spectra. In the inequality (17), Ω is the standard deviation of the

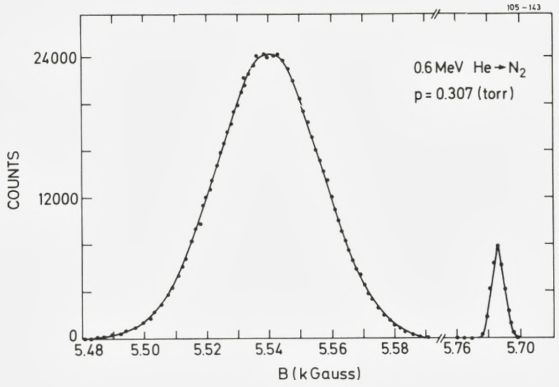

Fig. 4: Momentum distribution of an incident 600-keV beam and the same beam emerging from an N_2 target.

energy-loss distribution, approximated by the Bohr formula (Bohr 1948), $\Omega_B^2 = 4\pi Z_1^2 Z_2 e^4 N \Delta R$, and T_m is the maximum energy transfer in a single collision with an electron.

With the analyzing magnet, momentum spectra were obtained at each beam energy with and without gas in the stopping cell. A typical momentum distribution is shown in Fig. 4. From the energy-versus-field relation, the energy loss is given by

$$\Delta E = E_i \cdot \frac{\Delta B}{B_i}\left(2 - \frac{\Delta B}{B_i}\right), \tag{18}$$

where $\Delta B/B_i$ is the relative reduction in magnetic field. This shows that for small changes ($\Delta B/B_i \ll 1$), the B axis can be considered as an energy axis. Alternatively, the mean energy loss and the standard deviation are determined from

$$<\Delta E> = E_i - (E_1 + E_2)/2 \tag{19}$$

and

$$\Omega_E = \frac{E_2 - E_1}{2\sqrt{2 \log 2}} \tag{20}$$

where E_1 and E_2 are the energies corresponding to the half-maximum positions for the momentum distribution. Formula (19) is preferable to formula (18) in a calculation of $<\Delta E>$ due to the larger uncertainty in the determination of the peak position compared to the HWHM positions of the distribution.

With the electrostatic analyzer, determination of the primary-beam energy was more problematic as transmission of the beam without gas in the cell would damage the detector. Hence, the following procedure was adopted: At each

selected beam energy, energy-loss spectra for all gases were measured without changing any of the accelerator settings which may influence the energy, and, at least for one particular gas, energy distributions were measured at three different pressures, corresponding to an energy loss of approximately 5, 9, and 13%. A straight line was fitted to the three measured average energies versus target pressure, and the extrapolation to zero pressure gave a preliminary value of the unattenuated beam energy. Provided the stopping power in question was energy-independent, this value was correct. This not being the case, the preliminary primary energies were used to calculate preliminary stopping powers, and primary energies were obtained through iteration. The uncertainty in the determination of $<\Delta E>$ from formula (19) was 1.5% (2σ). Finally, experimental stopping cross sections are obtained as

$$S_o = \frac{<\Delta E>}{N\Delta R} . \tag{21}$$

E. Stopping cross sections and corrections.

The electronic-stopping cross section S_e is derived from the observed stopping cross section S_o through subtraction of the restricted nuclear-stopping cross section S_n^* given by formula (13), i.e.,

$$S_e = S_o - S_n^* . \tag{22}$$

For all combinations of target, projectile, and energy, the correction for nuclear collisions is less than 0.5%. However, the correction has been taken into account whenever it exceeds 0.1%.

The energy attributed to the measured stopping cross section is to first order in $<\Delta E>/E$ given by

$$E_{av} = E_i - <\Delta E>/2 . \tag{23}$$

An expansion by Andersen et al. (1966) of $S(E_{av})$ in powers of $<\Delta E>/E$ gives a quadratic correction term to the stopping cross section. As the relative energy loss was always less than 15%, this correction was less than 0.1% and hence omitted.

F. Experimental accuracy.

First, we summarize the quoted systematic errors stemming from uncertainties in the incident-energy E_i(0.3-0.5%), the differential (0.1%), and the integral

(0.5%) linearity of the Hall element, the linearity (0.2%) and the absolute calibration (0.4%) of the electrostatic analyzer, the effective target length (0.4-0.6%) and, finally, the calibration of the membrane manometer (0.5%).

The non-systematic errors originate from uncertainties in the absolute gas temperature (<1%), the pressure in the gas cell (<1%), the HWHM for the degraded energy-loss distribution due to counting statistics (1.5%), and the determination of the length of the sweeping interval (0.3%).

From the uncertainties, all of which correspond to two standard deviations (2σ), it is concluded that the stopping powers are measured to within an uncertainty of 2.5% (2σ).

§4. Experimental Results and Comparison with other Data

The experimental electronic-stopping powers S_e for hydrogen and helium ions in H_2, He, N_2, O_2, Ne, Ar, Kr, Xe, and CO_2 are plotted in Figs. 5-18 as functions of E_{av}. In the figures, the present results have been compared with most other published hydrogen and helium energy-loss data. The scatter of our data points is consistent with the estimate of the measuring accuracy given above.

A. Hydrogen stopping powers.

Recently Andersen and Ziegler (1977) published tabulations of hydrogen stopping powers for all elements in the energy range 10 keV $<(E/\text{amu})<$ 20 MeV. These semi-empirical stopping-power fits are plotted in Figs. 5-13. From the figures we first note that for most of the targets used, good agreement exists between the Andersen and Ziegler semi-empirical stopping-power fits and the present experimental results for energies $E \gtrsim 100$ keV. However, the semi-empirical fits have a tendency of being slightly low around the stopping-power maximum, and for Xe targets, the fit to our data as well as to those previously published is rather poor over a broad energy range. The present results agree within the stated accuracy with the averaged S_H-values found by Reynolds et al. (1953), the accuracy of which is 2-4% (2σ), while the data obtained by Phillips (1953) are systematically $\sim 15\%$ lower. Since Phillip's results are included in the data on which the tabulations by Andersen and Ziegler are based, their curve appears to be too low for energies $E \lesssim 100$ keV.

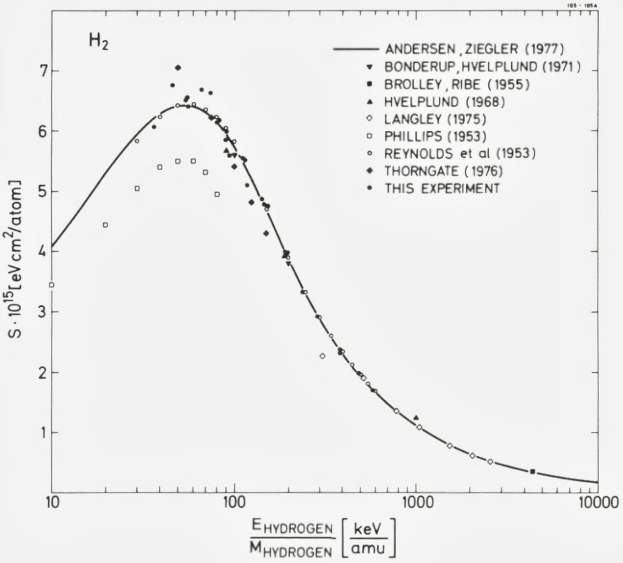

Fig. 5: Stopping-power results for hydrogen in H_2.

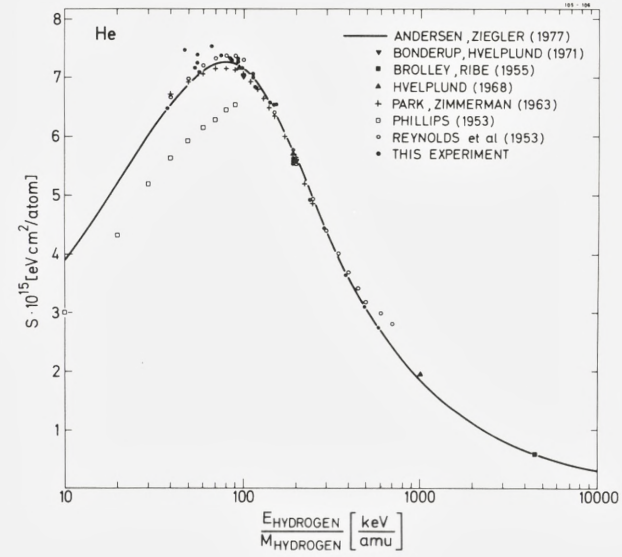

Fig. 6: Stopping-power results for hydrogen in helium.

Fig. 7: Stopping-power results for hydrogen in N_2.

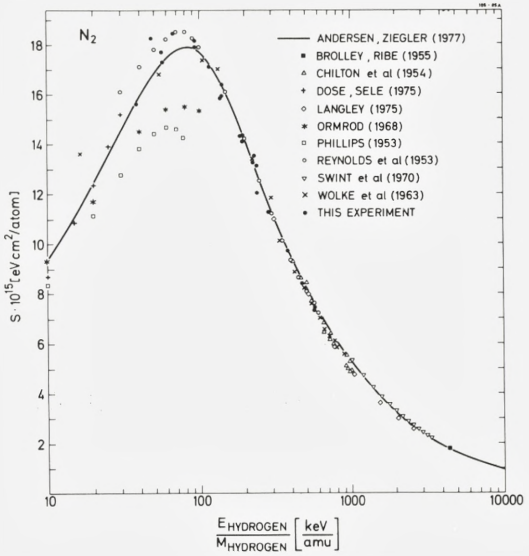

Fig. 8: Stopping-power results for hydrogen in O_2.

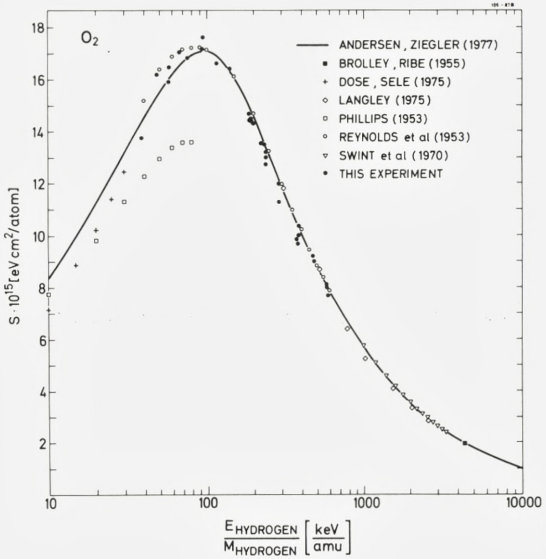

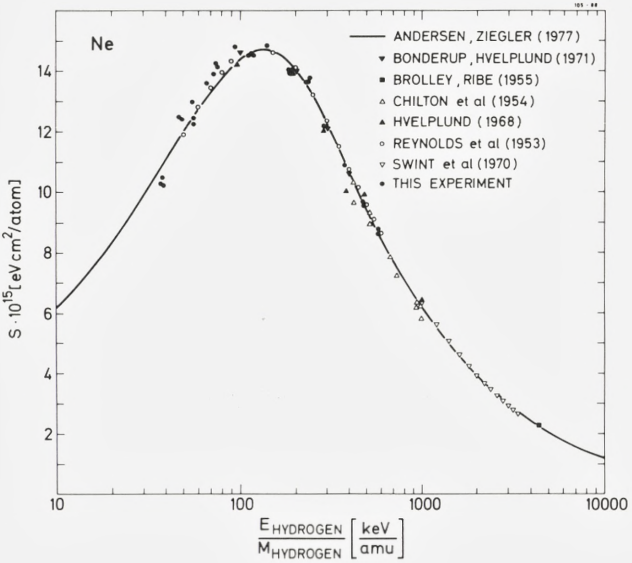

Fig. 9: Stopping-power results for hydrogen in neon.

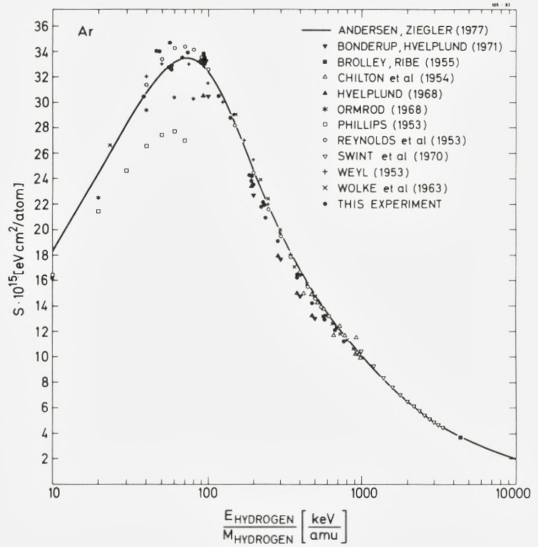

Fig. 10: Stopping-power results for hydrogen in argon.

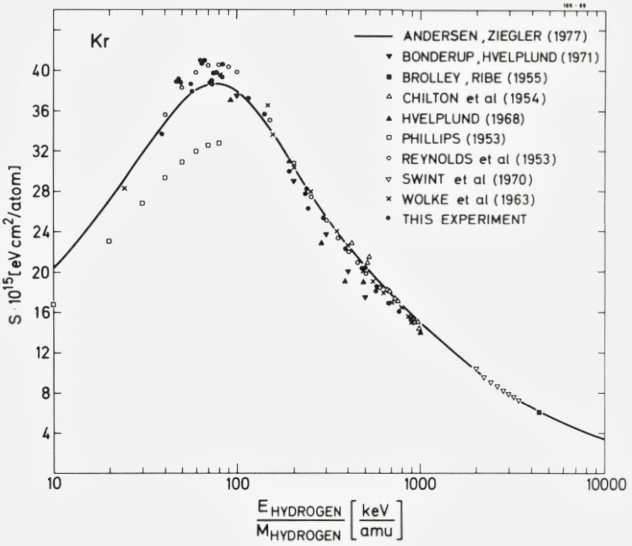

Fig. 11: Stopping-power results for hydrogen in krypton.

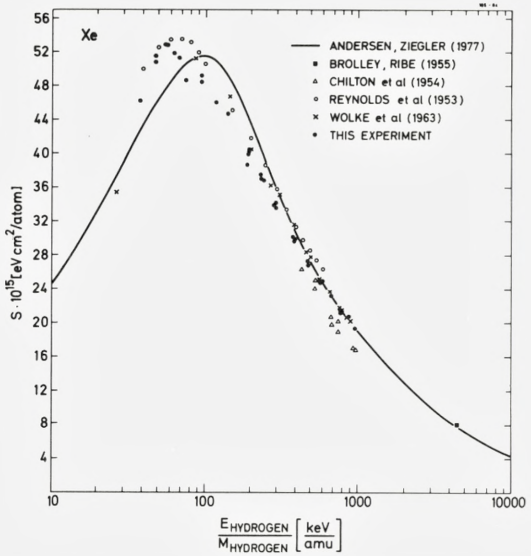

Fig. 12: Stopping-power results for hydrogen in xenon.

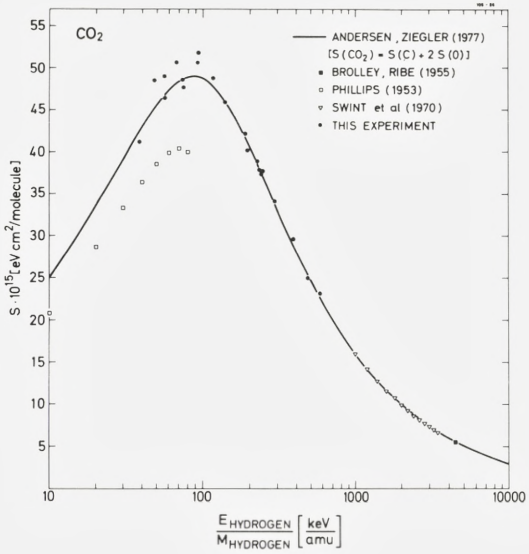

Fig. 13: Stopping-power results for hydrogen in CO_2.

B. Helium stopping powers.

Very recently, Ziegler (1978) published helium stopping-power tabulations similar to those of Andersen and Ziegler (1977) mentioned above. As the present experimental results are included in Ziegler's helium-data base, they constitute no independent check of these tables. Hence the tabulations are not included in Figs. 14-18. Nor are the polynomial fits made by Ziegler and Chu (1974) since for the present gases, these fits are identical to the averaged S_{He} values of the Baylor group (see below) as plotted in Figs. 14-18.

With a setup more or less equivalent to the present one, the Baylor group, Bourland, Chu, and Powers (1971) and Chu and Powers (1971) have made a systematic investigation of α-particle stopping cross sections in gases. The stated accuracy of their measurements ranges from 1.5% to 3% (2σ). As can be seen from the figures, the measurements performed by the Baylor group are higher by 1-6% than the present S_{He} results. This difference is not understood at present. However, it should be pointed out that the Baylor group employed a non-energy dispersive detector (a Faraday cup), and hence could not reveal the presence of slit-edge-scattered particles and/or a possible oxygen contamination of the helium beam. As they have not published the straggling results, it is not possible to disclose whether beam contamination and/or pressure fluctuations were significant. Finally, as a McLeod gauge was used, the pressure could not

be checked continuously. However, it should be noted that the Baylor group performed independent measurements in a sealed gas cell, using a solid-state detector. These measurements ($\pm 5.4\%$ to $\pm 6.7\%$ (2σ)) were not as accurate as the differentially pumped gas-cell measurements but they did agree with the latter to within the stated accuracy.

In this connection, it should be noted that the reliability of the present measurements is enhanced due to the fact that the stopping cross sections for both hydrogen and helium ions were measured in the same gases, and the present S_H data agree with most other S_H data.

The stopping cross sections by Hvelplund (1968, 1971) for helium in H_2, He, O_2, and Ne are systematically 10-15% below the present data. This discrepancy is difficult to understand since Hvelplund's equipment was similar to that used here. However, it is fair to mention that the data by Fastrup et al. (1968), and the lithium stopping power results by Andersen et al. (1978) lie 10-16% and 20% above Hvelplund's results, respectively. Hvelplund's proton stopping-power and straggling data (Bonderup and Hvelplund 1971) are in much better agreement with our present data.

Using a natural α-emitter source and a solid-state detector, Hanke and Bichsel (1970), Palmer (1966), and Rotondi (1968) measured range-energy relations for α particles in Ar, H_2, CO_2, N_2, and O_2. Hanke and Bichsel made a thorough data evaluation, taking into account corrections for multiple scattering, discrete energy loss (Lewis correction), undetected energy losses in the detector gold-surface layer, and adjoining dead layer and energy loss due to self-absorption in the source head. Thus, by differentiating the range-energy curve, they determined the stopping cross section for helium in argon with a claimed accuracy of 0.2% for $E_{He} > 2$ MeV, decreasing to 1.5% for $E_{He} \sim 1$ MeV. Palmer and Rotondi did not correct their range-energy results, and this may explain why their stopping-power results, especially around the maximum, deviate significantly from the present data.

By using an ^{241}Am α source and a solid-state detector, Kerr et al. (1966) and Wenger et al. (1973) have measured S_{He} at energies $0.3 \lesssim E_{He} \lesssim 5$ MeV by either varying the pressure in the absorber chamber between 0 and 720 mm Hg (Kerr et al. 1966) or by changing the distance between source and detector with the gas held between them kept at a pressure of 2.54 torr above atmospheric pressure (Wenger et al. 1973). Since there is a large uncertainty in the energy, which they attribute to the measured stopping power due to the large energy loss and as the above corrections to the stopping power are not taken into account, it is evident that these measurements are vitiated by large uncertainties. This is also the case for the data by Ramirez et al. (1969) for similar reasons.

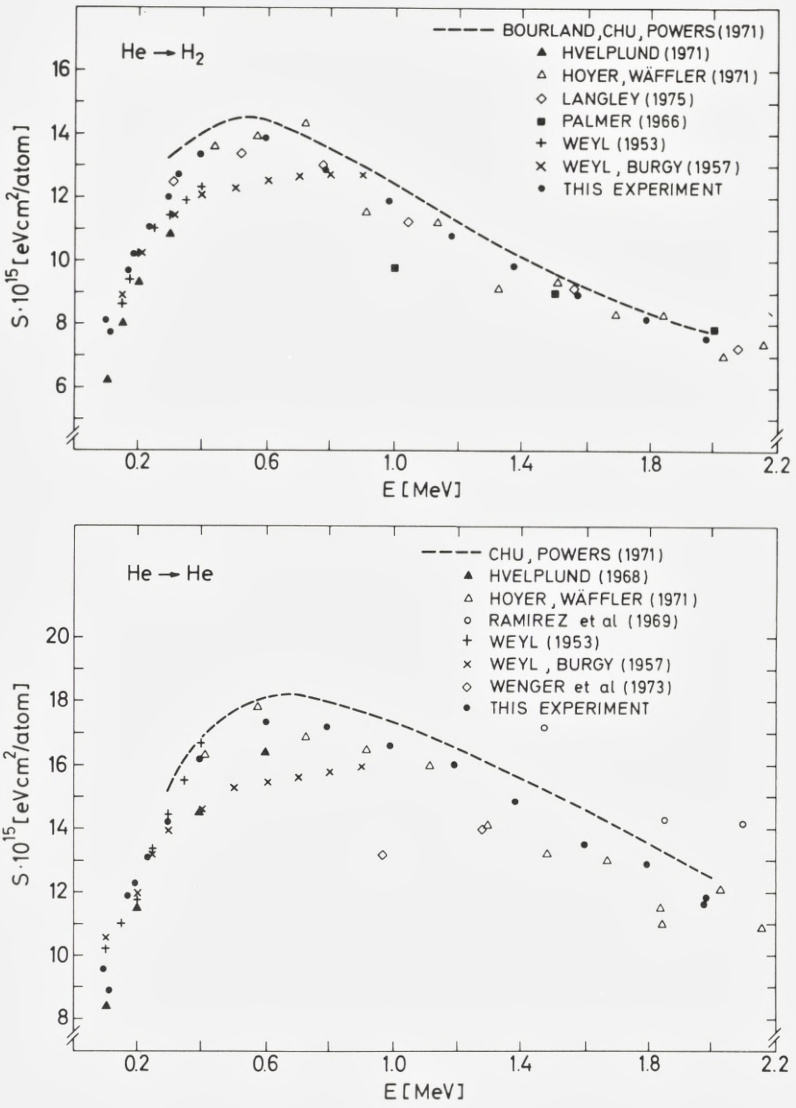

Fig. 14: Stopping-power results for helium in H_2 and He.

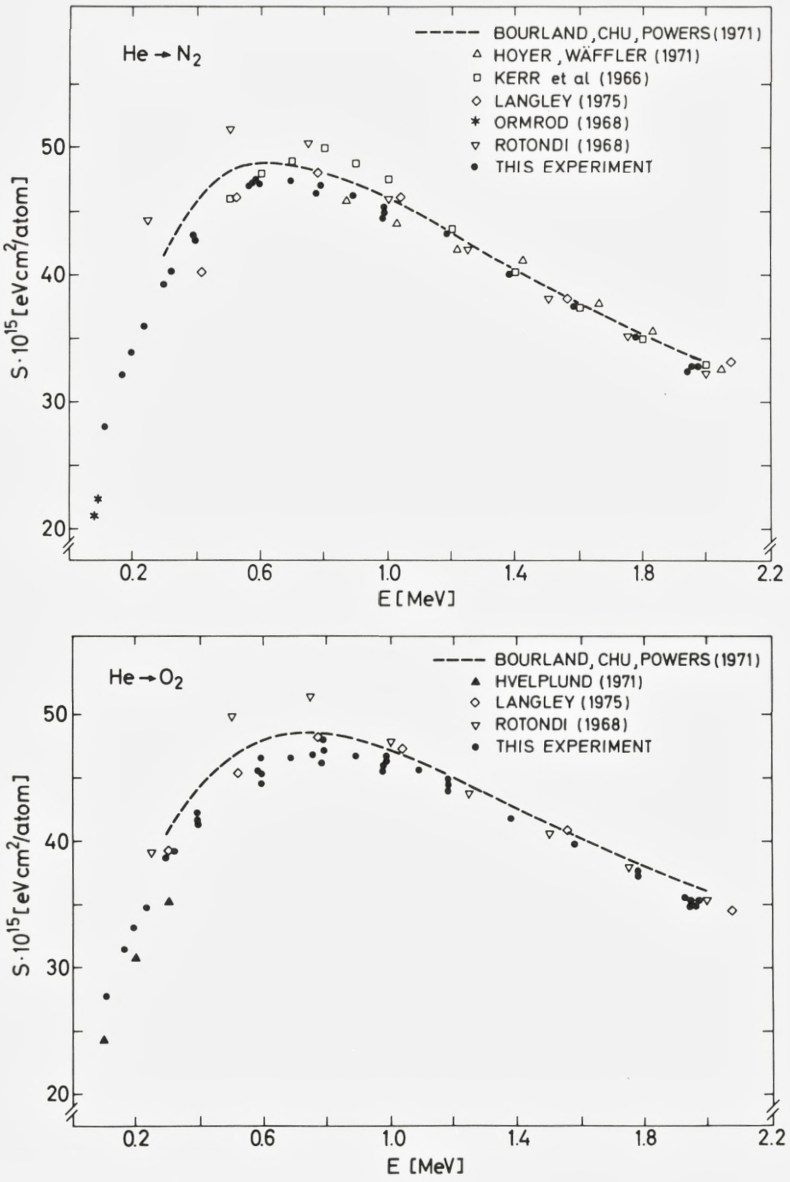

Fig. 15: Stopping-power results for helium in N_2 and O_2.

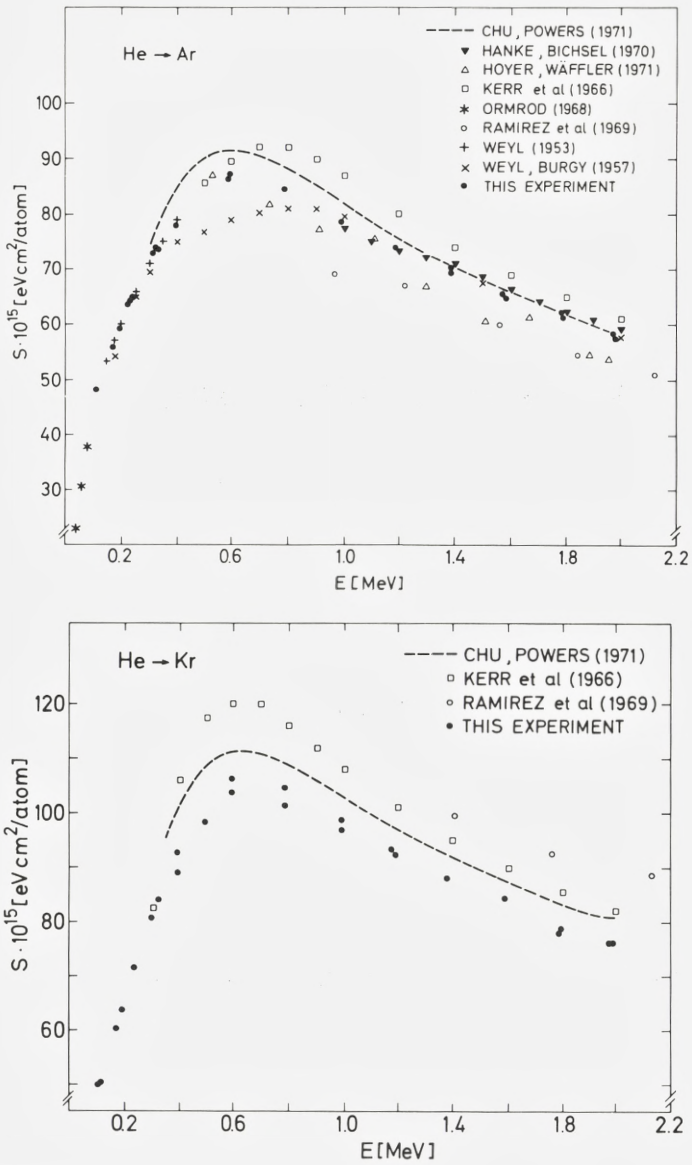

Fig. 16: Stopping-power results for helium in argon and krypton.

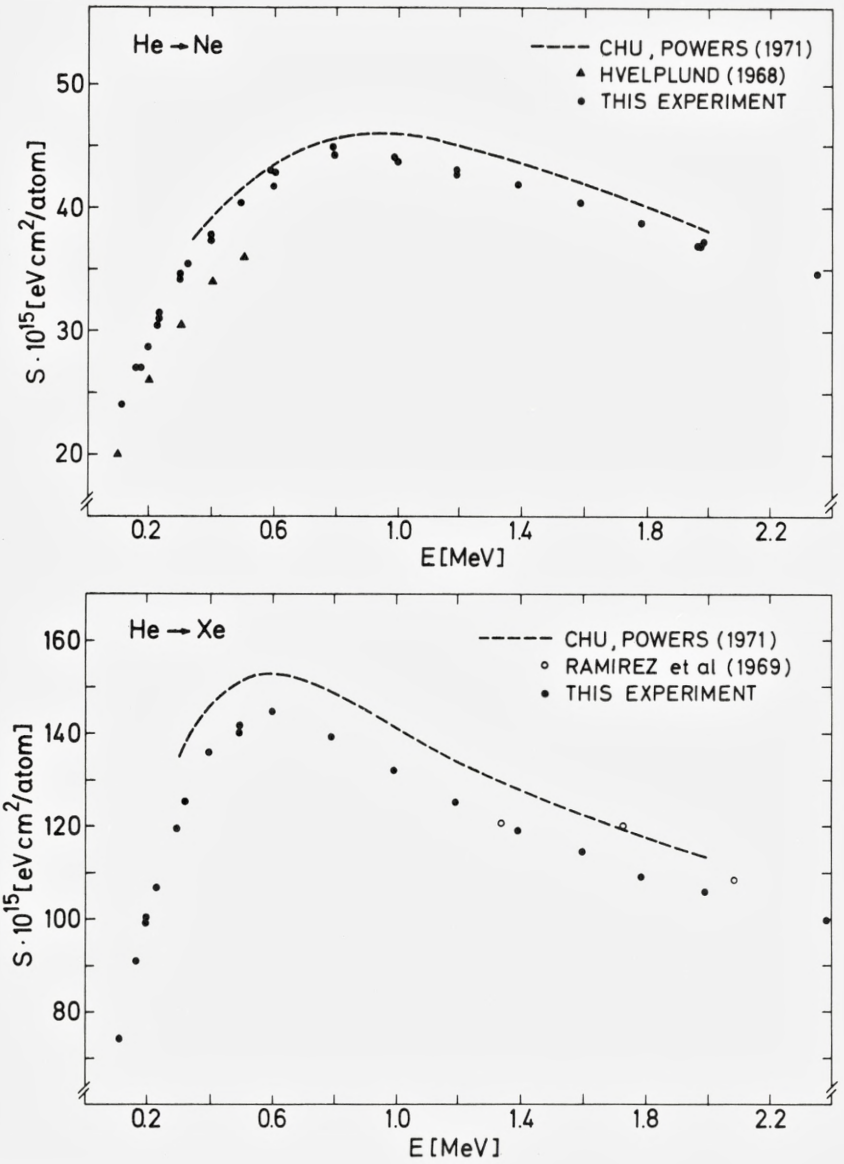

Fig. 17: Stopping-power results for helium in neon and xenon.

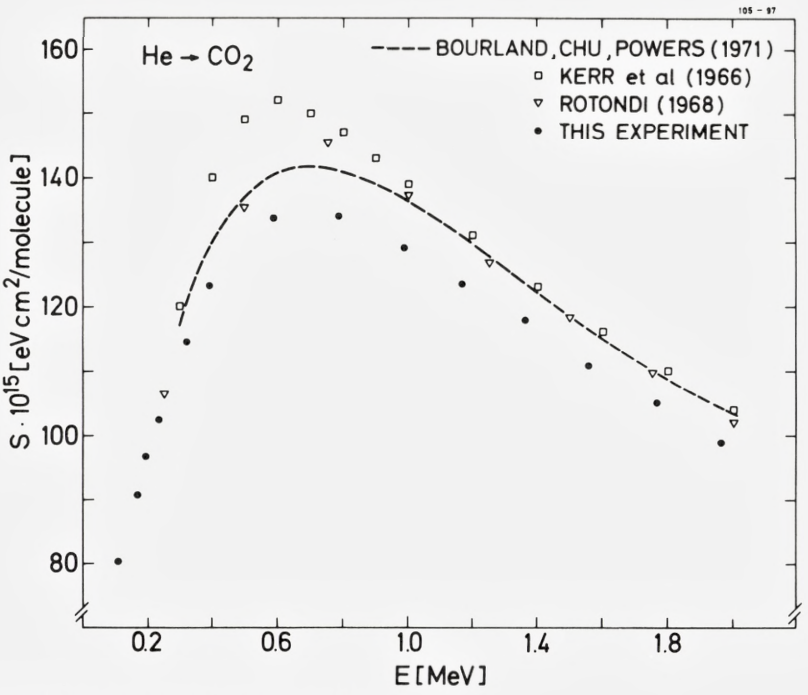

Fig. 18: Stopping-power results for helium in CO_2.

§5. Comparison with Theory

A. Shell corrections and I values.

Before making any comparison of the experimental results with the calculations based on the Lindhard-Scharff model and its refinements, we should emphasize that the region of validity of a perturbation treatment for a free electron gas is restricted to $\varkappa_B < 1$ or $v > 2v_o Z_1$ (Bonderup 1967), i.e., to hydrogen and helium energies higher than ~ 100 keV and ~ 1600 keV, respectively. Therefore any comparison between the present helium stopping powers and existing calculations should be taken with some reservation.

As argued in §2, it is advantageous to apply the so-called shell corrections C/Z_2 rather than $L(v, Z_2)$ in a detailed comparison between theory and experiment. Introducing Bichsel's (1964) reduced stopping-power variable,

$$X = \log\left(\frac{2mv^2}{1-(v/c)^2}\right) - \left(\frac{v}{c}\right)^2 - 1/\mathcal{Z}_2 \frac{mv^2}{4\pi e^4 \mathcal{Z}_1^2} S_{\text{exp}} \ , \tag{24}$$

we may deduce empirical shell corrections from the experimental hydrogen stopping powers using formulas (2) and (3) as

$$(C/\mathcal{Z}_2)^*_{\text{exp}} = X^H_{\text{exp}} - \log I \, . \tag{25}$$

As will be discussed later the shell corrections deduced from this formula are not genuine shell corrections and are therefore labelled with an asterix.

In Figs. 19 and 20, experimental shell corrections $(C/\mathcal{Z}_2)^*$ obtained from formula (25) are presented as a function of energy. The I values used are those extracted by Andersen and Ziegler (1977) from their fits to previously published data. Comparison is made to Bonderup's (1967) theoretical calculations $(C/\mathcal{Z}_2)_B$ and to the empirical shell corrections by Andersen and Ziegler. As an indication of the sensitivity of $(C/\mathcal{Z}_2)^*$ to uncertainties in the S_H data, the distance between the dashed line "3% effect on stopping" and the zero line gives the change in $(C/\mathcal{Z}_2)^*$ due to a 3% change in stopping power. An increase in stopping power gives a lower X value and hence a lower $(C/\mathcal{Z}_2)^*$ value.

From Figs. 19 and 20 it is observed that the experimental $(C/\mathcal{Z}_2)^*$ data deviate significantly from Bonderup's shell corrections $(C/\mathcal{Z}_2)_B$ both in size and shape (see, e.g., H $\rightarrow$ Ne). Until recently, it was believed that this discrepancy was due to a defiency in the theoretical model in the energy region discussed here. However, all possible deviations from formulas (2) and (3) such as higher-order $\mathcal{Z}_1$ corrections are automatically included in the empirical $(C/\mathcal{Z}_2)^*$ values. According to formula (8), the correct shell correction is determined from

$$(C/\mathcal{Z}_2) = X^H_{\text{exp}} - \log I + \mathcal{Z}_1 L_1 + \mathcal{Z}_1^2 L_2 \, . \tag{26}$$

Therefore the experimental $(C/\mathcal{Z}_2)^*$ proton values in Figs. 19 and 20 should be compared to the following "apparent" theoretical shell-corrections

$$(C/\mathcal{Z}_2)^*_{th} = (C/\mathcal{Z}_2)_B - (L_1 + L_2) \, . \tag{27}$$

In calculating $(C/\mathcal{Z}_2)_{th}{}^*$, we have used the Bloch expression, formula (10), for L_2. According to the discussion in connection with formula (9), the Barkas correction L_1 has been set equal to twice the quantity given by Jackson and McCarthy (1972)

$$L_1 = 2L_1{}^{JM} = 2\frac{F\left(\frac{v}{v_o}\frac{1}{\mathcal{Z}_2^{1/2}}\right)}{\mathcal{Z}_2{}^{1/2}} L_o \, . \tag{28}$$

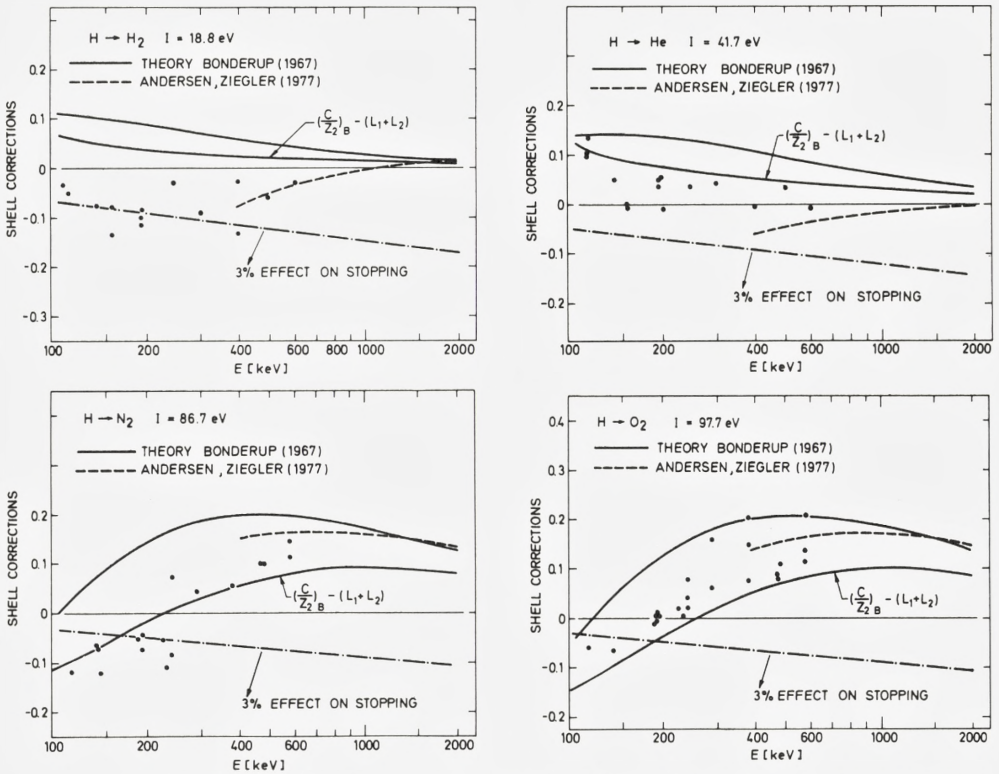

Fig. 19: Experimental shell corrections for H_2, He, N_2, and O_2 obtained from Eq. (25) (points), compared with Andersen and Ziegler's semiempirical fit (dashed), Bonderup's theoretical values and those values corrected for higher-order Z_1 effects, according to Eq. (27). The I values are those given by Andersen and Ziegler (1977).

In calculating L_1 for the heavier elements, we have extrapolated $L_1{}^{JM}$ slightly outside the stated region of validity given by $\frac{1}{Z_2^{1/2}} \frac{v}{v_o} \gtrsim 0.8$. Theoretical shell corrections obtained from formula (27) are also plotted in Figs. 19 and 20.

In the cases of N_2, Ne, Ar, and Xe, the corrected values $(C/Z_2)_{th}^* = (C/Z_2)_B - (L_1 + L_2)$ show perfect agreement with the experimental values $(C/Z_2)^*$. For H_2, He, O_2, and Kr, the energy dependence of the experimental data $(C/Z_2)^*$ agrees much better with the energy dependence of the corrected values

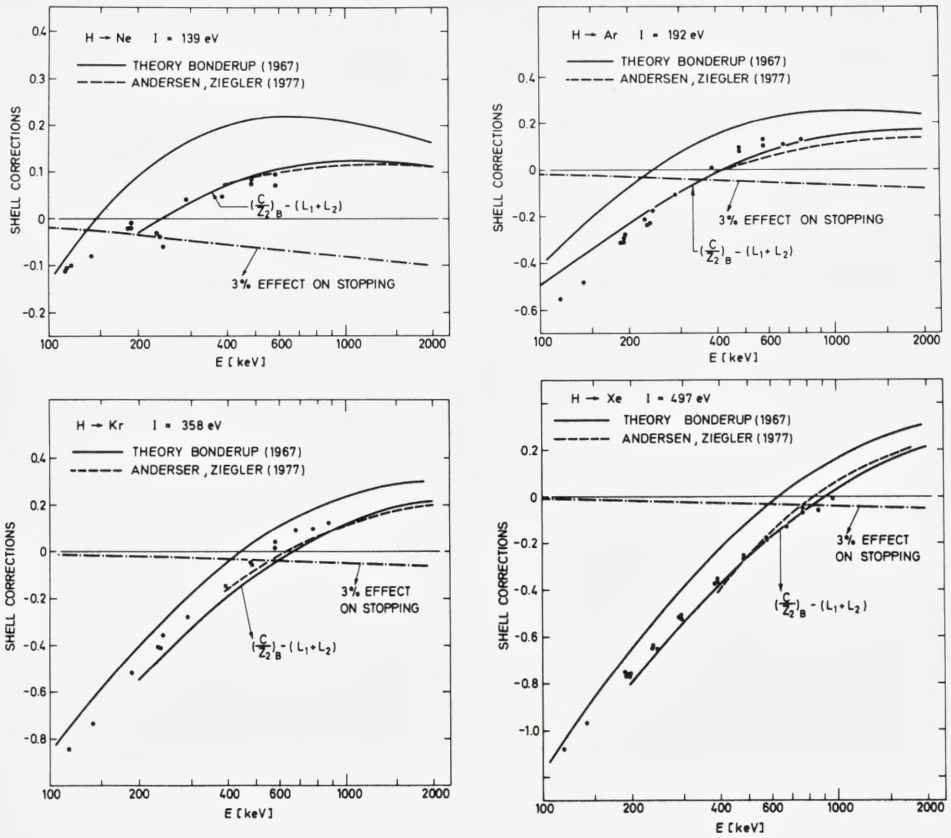

Fig. 20: Experimental shell corrections for Ne, Ar, Kr, and Xe. See caption to Fig. 19 for further explanation.

$(C/Z_2)^*_{th} = (C/Z_2)_B - (L_1 + L_2)$ than with that of $(C/Z_2)_B$. However, there is a systematic shift in the absolute value between $(C/Z_2)^*$ and $(C/Z_2)^*_{th}$, which may originate in the choice of I value. A change of I to $I - \Delta I$ changes the experimental $(C/Z_2)^*$ data by the additive amount $\Delta I/I$. In this way, experimental I values are determined from the present data. In Table II, the resulting experimental ionization potentials are compared with those given by Andersen and Ziegler (1977) and Chu and Powers (1972).

Table II

I(eV)	H_2	He	N_2	O_2	Ne	Ar	Kr	Xe
Present results	17.6	40.7	86.7	102.1	139	194	376	497
Andersen-Ziegler	18.8	41.7	86.7	97.7	139	194	358	497
Chu-Powers			92.4	110	160	207	403	529

It is concluded that the present I values, which constitute an independent check of the Andersen and Ziegler I values, are in good agreement with these, while the theoretical I values by Chu and Powers are systematically too high.

Above, we used the experimental shell corrections $(C/\mathcal{Z}_2)^*$ as a standard and corrected Bonderup's theoretical calculations $(C/\mathcal{Z}_2)_B$ for comparison. Andersen et al. (1977) employed $(C/\mathcal{Z}_2)_B$ as a standard and corrected $(C/\mathcal{Z}_2)^*$ by adding (L_1+L_2) for comparison. The reason for our approach is that in the present energy region, we are not able to determine L_1 and L_2 experimentally as was done by Andersen and coworkers and hence we could not obtain experimentally determined genuine shell corrections with which to compare the theoretical $(C/\mathcal{Z}_2)_B$ results.

A different approach is to use the empirical fits for L_1 and L_2 extracted from the measurements by Andersen et al. (1977) and denoted by L_1^A and L_2^A, respectively. For $\mathcal{Z}_2 > 10$, good agreement is found between $(C/\mathcal{Z}_2)_B - (L_1+L_2)^A$ and formula (27) shown in Figs. 19 and 20, while the agreement becomes increasingly unsatisfactory for $\mathcal{Z}_2 < 10$. As Andersen and coworkers measured stopping powers of Al, Cu, Ag, and Au, their empirical fits for L_1 and L_2 should be employed only for $13 \lesssim \mathcal{Z}_2 \lesssim 79$, in which case they give results which are consistent with the present data.

Concerning Andersen and Ziegler's (1977) "fitted shell corrections", $(C/\mathcal{Z}_2)^{AZ}$, all higher-order $\mathcal{Z}_1$ contributions are piled onto these, and $(C/\mathcal{Z}_2)^{AZ}$ should therefore be compared with the present results $(C/\mathcal{Z}_2)^*$ or with $(C/\mathcal{Z}_2)_B - (L_1+L_2)$. In the cases of Xe, Kr, Ar, Ne, and O_2, there is good agreement between $(C/\mathcal{Z}_2)^{AZ}$ and the present data $(C/\mathcal{Z}_2)^*$. For N_2, the curve for $(C/\mathcal{Z}_2)^{AZ}$ is somewhat higher than $(C/\mathcal{Z}_2)^*$, while for H_2 and He, the fit $(C/\mathcal{Z}_2)^{AZ}$ deviates both in magnitude and energy dependence from the present results. If Andersen and Ziegler had based their fit for H_2 and He not on the scarse and scattered available experimental data points but had extrapolated the shell-correction fit obtained for other elements with $\mathcal{Z}_2 \geq 3$ to the cases of H_2 and He, the present H_2 and He results would have agreed with the general trend on the $(C/\mathcal{Z}_2)^{AZ}$ curves.

B. Experimental determination of the Z_1^3 correction.

We assumed above that the Barkas and the Bloch corrections were given by the formulas (28) and (10), respectively. Andersen et al. (1977) have demonstrated that this is approximately correct for $7 \lesssim v/v_o \lesssim 12$. In our case we can extract information on the higher order Z_1 terms only when the helium ions are known not to carry electrons in a bound state. Equilibrium charge-state measurements show that this is the case for $E_{He} \gtrsim 1.6\text{-}2$ MeV. Furthermore, from measurements with hydrogen and helium ions only, it is not possible to distinguish between Z_1^3 and Z_1^4 corrections. However, based on the results by Andersen et al. (1977), it seems reasonable to assume that L_2 is given approximately by the Bloch expression, formula (10). As follows from Eqs. (8) and (24), experimental L_1 values may then be extracted from the formula

$$L_1^{exp} = X_H^{exp} - X_{He}^{exp} - 3L_2 \,. \tag{29}$$

The uncertainties in L_1^{exp} are calculated under the assumption that the uncertainty in L_2 is $\sim 20\%$.

In Fig. 21, experimental L_1 values for H_2, N_2, O_2, Ne, Ar, and Xe are compared with the theoretical estimate for L_1 given by Eq. (28), which is a good

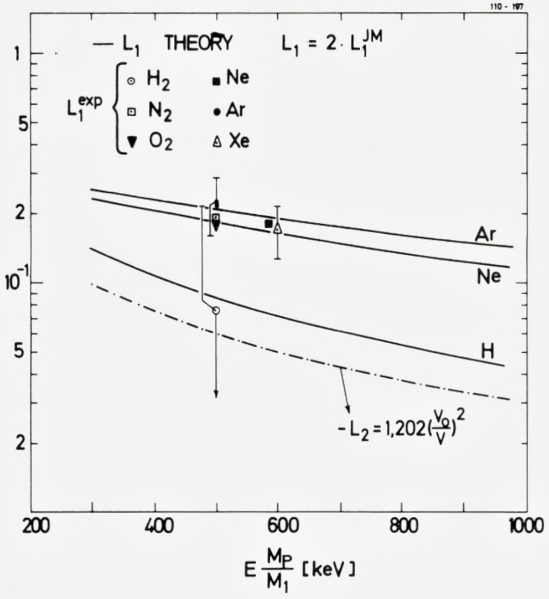

Fig. 21: Experimental results for the Z_1^3 factor L_1 obtained from Eq. (29). Theoretical curves for L_1 (solid) and L_2 (dot-and-dash) are Eqs. (28) and (10) respectively.

approximation to the results of Lindhard (1976) and Esbensen (1977). From Fig. 21, it is concluded that the experimental L_1 values are in good agreement with the expression $L_1 = 2L_1^{JM}$. This supports Lindhard's and Esbensen's value for the Z_1^3 correction and thereby the L_1 expression used in the preceding section in connection with the discussion of shell corrections. It should be noted that the deviation of L_1^{exp} from L_1^{JM} cannot be explained as a charge-state effect since the introduction of an effective charge state $Z_{HE}^* < 2$ would increase the L_1^{exp} values in Fig. 21.

Ranges of Σ^+ and Σ^- in emulsion for $v \sim 20v_0$ were found to differ by an amount corresponding to the value given by Lindhard (1976), while the range differences in hydrogen were a factor of five larger than Lindhard's prediction (for a review of the experimental range data, see Heckman (1970)). On this background it is important that the present experimental L_1 for hydrogen agrees with Lindhard's findings. The large uncertainty in $L_1(H_2)$ is due to the high $L(v, Z_2)$ value.

Only Ward et al. (1976) have previously analyzed their data for Z_1^3 effects for $v/v_0 < 5$. They measured stopping cross sections for hydrogen and helium in aluminum and found that, within the experimental uncertainty, the quantity $(S_{He} - 4S_H)/S_{He}$ was equal to zero for $v/v_0 \sim 4.5$. From this they concluded that no Z_1^3 effect was present. However, taking into account the Z_1^4 correction, we find

$$\frac{S_{He} - 4S_H}{S_{He}} = \frac{L_1 + 3L_2}{L + 2L_1 + 4L_2} = 0.84\% \quad \text{for} \quad v/v_0 = 4.5.$$

This is in perfect agreement with the results in Fig. 12 of the paper by Ward et al., and their data hence confirm the magnitude of the higher-order Z_1 effects found in this work.

C. Helium stopping powers.

As mentioned above, it is not possible to make any detailed comparison between S_{He} data and perturbation calculations for a free electron gas at the present energies. In spite of this, Rousseau et al. (1971) have used the Lindhard-Winther expressions for an electron gas with the charge-densities obtained from Hartree-Fock-Slater wave functions to calculate the stopping cross section for 0.4-2 MeV α particles. The calculations, with which Chu and Powers (1971) compare their noble-gas results, are wrong due to problems with the joining of the asymptotic expressions by Lindhard and Winther. Comparing the present S_{He} results with later and corrected calculations by Ziegler and Chu (1974), we find surpris-

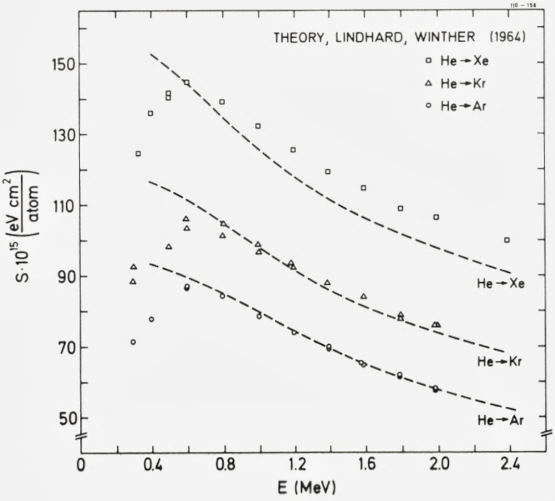

Fig. 22: Stopping cross sections for He penetrating Ar, Kr, and Xe compared with calculations by Ziegler and Chu (1974) based on Lindhard-Winther theory.

ingly good agreement (to within $\pm 7\%$ even at energies as low as $E_{He} \sim 600$ keV). Figure 22 shows the situation for Xe, Kr, and Ar.

D. The ratio S_{He}/S_H as a function of velocity.

As mentioned above, a quantal perturbation calculation of the stopping cross section is restricted to velocities $v > 2v_0 Z_1$. At lower velocities, it has, nevertheless, been suggested that the usual stopping formula (2) be applied with the charge number Z_1 replaced by an effective charge number, i.e.

$$S = \frac{4\pi e^4 Z_2}{mv^2} (Z_1^*)^2 L(v, Z_2) . \tag{30}$$

Many authors have used this approach to analyze experimental stopping-power data in terms of charge states, comparing heavy-ion stopping powers with corresponding proton-stopping powers at the same velocity. It should, however, be emphasized that no theoretical basis exists for this charge-state scaling procedure.

In Fig. 23, the ratio between the present hydrogen and helium stopping powers measured at the same velocity are shown as smooth curves. These data lead to the following conclusions:

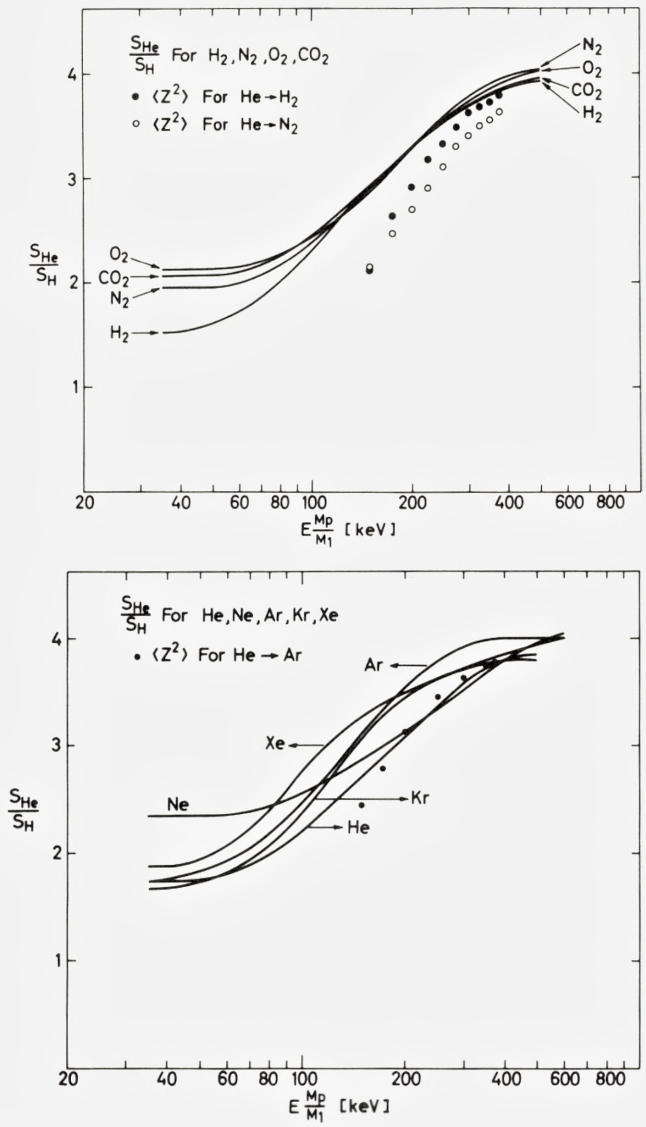

Fig. 23: Experimental stopping-power ratios (solid curves) of He ions to hydrogen ions evaluated at the same velocity, compared with Pivovar's (1961) measured mean-square charge state for He ions in H_2, N_2, and Ar.

(1) The ratios S_{He}/S_H are not independent of Z_2, as was also found by Sautter and Zimmermann (1965). Thus it is not possible, at least not for gases, in a simple way to scale $S_{He}(v, Z_2)$ to $S_H(v, Z_2)$ or vice versa.

(2) From being a constant nearly equal to four for E/amu > 500 keV, S_{He}/S_H decreases with decreasing velocity and approaches another constant value for E/amu $\lesssim$ 50 keV, and this value depends strongly on Z_2. If the stopping power in the low energy region is written in power form as $S = kE^p$, k and p being constants, the exponents p are approximately equal for hydrogen and helium ions in a given target material. According to the wellknown Lindhard-Scharff (1961) velocity-proportional stopping formula (12), the constant ratio is given by

$$(S_{He}/S_H)^{LS} = 2^{7/6} \frac{(1+Z_2^{2/3})^{3/2}}{(2^{2/3}+Z_2^{2/3})^{3/2}} . \tag{31}$$

In Table III, the experimental ratios are compared with the L-S values for E/amu $\lesssim$ 50 keV. Rather good agreement is found for the lighter target elements.

Table III

	H_2	He	N_2	O_2	Ne	Ar	Kr	Xe
exp.	1.53	1.75	1.95	2.15	2.35	1.75	1.65	1.88
L-S	1.53	1.65	1.88	1.90	1.93	2.02	2.09	2.12

It might be noted that our lithium stopping-power results for the same gases (Andersen et al. 1978) at energies 25 keV $\lesssim$ E/amu $\lesssim$ 75 keV, give exponents p which are systematically higher than 0.5 while those for helium are lower than 0.5 (see Table IV in the next section). Thus the S_{Li}/S_{He} ratios are energy-dependent.

(3) From formula (30), the ratio S_{He}/S_H is given by

$$S_{He}/S_H = (Z^*_{He})^2/(Z^*_H)^2 \times L_{He}/L_H . \tag{32}$$

Since $L_{He}/L_H \simeq 1$ and $(Z^*_H)^2 \simeq 1$ for $E_H \gtrsim 150$ keV, one would expect that $S_{He}/S_H \simeq (Z^*_{He})^2$ down to $E(M_p/M) \gtrsim 150$ keV. In Fig. 23, the (S_{He}/S_H) ratios in H_2, N_2, and Ar are compared with the mean-square charge states

$$<Z^2> = \sum_i i^2 \times F_{i\infty} \tag{33}$$

for helium in H_2, N_2, and Ar obtained from equilibrium charge-state measurements by Pivovar et al. (1961). $F_{i\infty}$ denotes the equilibrium charge-state fraction

of the beam in charge state i. A discrepancy of the order of 10% is revealed for E/amu $\lesssim$ 375 keV.

It is concluded that at the one percent level the helium stopping powers, at least for gases, are inconsistent with Eq. (30) with $(Z_1^*)^2$ equal to the mean-square charge state measured directly, and the present results support the theoretical reservation against Eq. (30). The parameter $(Z_1^*)^2$ is no more than a scaling parameter which, on the other hand, appears to be useful for a prediction of unmeasured heavy-ion stopping powers with a required accuracy in the 15 percent range.

Concerning the ratios S_{He}/S_H, it should be emphasized that the S_{He} and S_H results were measured with the same setup. Therefore most of the systematic errors cancel, and this results in rather accurate ratios with $2\sigma \sim 2.8\%$. Many authors have extracted S_{He}/S_H ratios by comparing S_{He} and S_H measured by different groups. In this case, two sets of systematic errors are superimposed.

E. Velocity-proportional region.

For $v < v_0 Z_1^{2/3}$, it has been demonstrated experimentally (see, e.g., Hvelplund and Fastrup (1968) and Hvelplund (1971)) that as a function of Z_1 and Z_2, the electronic stopping exhibits oscillations around the smooth curve given by Eq. (12). These oscillations may be understood in terms of the Lindhard-Scharff picture. The stopping power is proportional to the transport cross section for electrons scattered by a screened $L\mathcal{J}$ potential around the ion, and this cross section exhibits oscillations similar to the one responsible for the Ramsauer-Townsend effect encountered in the scattering of low energy electrons by atoms (Lindhard and Finnemann (1968)). Since the Z oscillations damp out at increasing energies, deviations from the $E^{1/2}$ dependence of S_e are expected, and experimental electronic-stopping cross sections are usually fitted to the convenient form $S_e = k \times E^p$, where k and p are constants. In Table IV, the present S_{He} results for the energy interval of 100-350 keV are presented in this form. (With E expressed in keV, the resulting stopping cross sections are obtained in units of 10^{-15} eV cm^2/atom.)

Table IV

$S_e = kE^p$	H_2	He	N_2	O_2	Ne	Ar	Kr	Xe
k	1.45	1.86	5.46	5.59	3.72	6.85	5.12	7.28
p	0.37	0.36	0.35	0.34	0.39	0.41	0.48	0.49

From Fig. 16, the argon data of Weyl (1953) for $150 \lesssim E_{He} \lesssim 300$ keV are observed to be in perfect agreement with the present results. The energy dependence of the argon and N_2 data of Ormrod (1968) for $10 \lesssim E_{He} \lesssim 100$ keV deviates from that of the present data. It has, however, also been observed in previous experiments that the exponent p may depend rather strongly on the energy interval.

§6. Conclusion

Stopping powers for hydrogen ions in the energy region 40 keV to 1 MeV and helium ions of 100 keV to 2.4 MeV have been measured in H_2, He, N_2, O_2, CO_2, Ne, Ar, Kr, and Xe with an accuracy of $\pm 2.5\%$ (2σ). While the hydrogen-stopping powers show good agreement with most other published data and with Andersen and Ziegler's empirical stopping-power tabulations, the helium-stopping powers are systematically lower than those of the Baylor group by 1-6%. Higher-order Z_1 effects greatly influence the evaluation of shell corrections. With these effects taken into account, the empirical shell corrections, extracted from the experimental proton stopping-power data, are in good agreement with Bonderup's theoretical calculations, based on the Lindhard-Scharff model, at energies as low as $0.1 \lesssim E_H \lesssim 1$ MeV. Experimental I values are extracted and are in satisfactory agreement with those given by Andersen and Ziegler. Z_1^3 correction terms to the Bethe formula have been deduced from the experimental data, and within the accuracy of the experiment, they agree with Lindhard's and Esbensen's value. From a comparison of the stopping powers for helium and hydrogen ions at the same velocity, it has been shown that S_{He}/S_H for $1.25 \lesssim v/v_0 \lesssim 5$ depends strongly on Z_2 and deviates significantly from the mean-square charge states $<Z^2>_{He \to Z_2}$ obtained directly in equilibrium charge-state measurements.

Acknowledgements

We are much indebted to E. Bonderup and J. Lindhard for their continuous interest in the present work and for the help and guidance received from them. The assistance extended to us from the technical staff, especially V. Toft, is gratefully acknowledged. Finally, we wish to thank A. Grandjean and I. Schmidt for their competent assistance in the preparation of the present article.

References

H. H. Andersen, J. F. Bak, H. Knudsen, and B. R. Nielsen, Phys. Rev. *A 16*, 1929 (1977).

H. H. Andersen, F. Besenbacher, and H. Knudsen, Nucl. Instrum. Methods *149*, 121 (1978).

H. H. Andersen, A. F. Garfinkel, C. C. Hanke, and H. Sørensen, Kgl. Dan. Vidensk. Selsk. Mat. Fys. Medd. *35*, No 4 (1966).

H. H. Andersen, H. Simonsen, and H. Sørensen, Nucl. Phys. *A 125*, 171 (1969).

H. H. Andersen and J. F. Ziegler, *Hydrogen Stopping Powers and Ranges in All Elements* (Pergamon, N.Y., 1977).

J. C. Ashley, R. H. Ritchie, and W. Brandt, Phys. Rev. B *5*, 2393 (1972) ibid A *8*, 2402 (1973).

F. Besenbacher, H. H. Andersen, P. Hvelplund, and H. Knudsen (to be published) (1980).

F. Besenbacher, J. Heinemeier, P. Hvelplund, and H. Knudsen, Phys. Lett. *61A*, 75 (1977).

H. A. Bethe, Ann. Phys. *5*, 325 (1930).

H. Bichsel, in: *Studies in Penetration of Charged Particles in Matter*, NAS-NRC Publ. 1133 (1964) p. 17.

F. Bloch, Ann. Phys. *16*, 285 (1933).

F. Bloch, Z. Phys. *81*, 363 (1933).

N. Bohr, Kgl. Danske Vidensk. Selskab, Mat. Fys. Medd. 18, No. 8 (1948).

E. Bonderup, Kgl. Danske Vidensk. Selsk. Mat. Fys. Medd. *35*, No 17 (1967).

E. Bonderup and P. Hvelplund, Phys. Rev. A *4*, 562 (1971).

E. Bonderup and J. Lindhard (1967) (private communication).

P. D. Bourland, W. K. Chu, and D. Powers, Phys. Rev. B *3*, 3625 (1971).

J. E. Brolley and F. L. Ribe, Phys. Rev. *98*, 1112 (1955).

A. B. Chilton, J. N. Cooper, and J. C. Harris, Phys. Rev. *93*, 413 (1954).

W. K. Chu and D. Powers, Phys. Rev. B *4*, 10 (1971).

W. K. Chu and D. Powers, Phys. Lett. *40A*, 23 (1972).

V. Dose and G. Sele, Z. Phys. *A 272*, 237 (1975).

H. Esbensen, Thesis, University of Aarhus (unpublished) (1977).

B. Fastrup, A. Borup, and P. Hvelplund, Can. J. Phys. *46*, 489 (1968).

B. Fastrup, P. Hvelplund, and C. A. Sautter, Kgl. Dan. Vidensk. Selsk. Mat. Fys. Medd. *35*, No 10 (1966).

C. C. Hanke and H. Bichsel, Kgl. Dan. Videnskab. Selsk. Mat.-Fys. Medd. *38*, No 3 (1970).

H. H. Heckman, in: *Penetration of Charged Particles in Matter:* A Symposium: NAS-NRC Publication, Washington, D.C. (1970).

J. Heinemeier, P. Hvelplund, and F. R. Simpson, J. Phys. B *8*, 1880 (1975).

U. Hoyer and H. Wäffler, Z. Naturforsch. *26a*, 592 (1971).

P. Hvelplund, Thesis, University of Aarhus (unpublished) (1968).

P. Hvelplund, Kgl. Dan. Vidensk. Selsk. Mat.-Fys. Medd. *38*, No 4 (1971).

P. Hvelplund and B. Fastrup, Phys. Rev. *165*, 408 (1968).

M. Inokuti, T. Baer, and J. L. Dehmer, Phys. Rev. A *17*, 1229 (1978).

J. D. Jackson and R. L. McCarthy, Phys. Rev. B *6*, 4131 (1972).

G D. Kerr, L. M. Hairr, N. Underwood, and A. W. Walker, Health Phys. *12* 1475 (1966).

H. Knudsen, F. Besenbacher, J. Heinemeier, and P. Hvelplund, Phys. Rev. A *13*, 2095 (1976).

R. A. Langley, Phys. Rev. B *12*, 3575 (1975).

J. Lindhard, Kgl. Dan. Vidensk. Selsk. Mat.-Fys. Medd. *28*, No 8 (1954).

J. Lindhard, in: *Studies in Penetration of Charged Particles in Matter*, NAS-NRC Publ. 1133 (1964) p. 1.

J. Lindhard, Nucl. Instr. Methods *132*, 1 (1976).

J. Lindhard and J. Finnemann, private communication and J. Finnemann, Thesis, University of Aarhus (unpublished) (1968).
J. Lindhard and M. Scharff, Kgl. Dan. Vidensk. Selsk. Mat.-Fys. Medd. *27*, No 15 (1953).
J. Lindhard and M. Scharff, in: *Report on Conference on Penetration of Atomic Particles*. Gatlinburg, 1958, NAS-NRC Publ. 752, (1960) p. 49.
J. Lindhard and M. Scharff, Phys. Rev. *124*, 128 (1961).
J. Lindhard and Aa. Winther, Kgl. Danske Vidensk. Selsk. Mat.-Fys. Medd. *34*, No 4 (1964).
J. H. Ormrod, Can. J. Phys. *46*, 497 (1968).
R. B. J. Palmer, Proc. Phys. Soc. Lond. *87*, 681 (1966).
J. T. Park and E. J. Zimmermann, Phys. Rev. *131*, 1611 (1963).
J. A. Phillips, Phys. Rev. 90, 532 (1953).
L. I. Pivovar, V. W. Tubaev, and M. T. Noikov, Zh. Eksp. Teor. Fiz. *41*, 26 (1961) [Sov. Phys.-JETP *14*, 20 (1962)].
J. J. Ramirez, R. M. Prior, J B. Swint, A. R. Quinton, and R. A. Blue, Phys. Rev. *179*, 310 (1969).
H. K. Reynolds, D. N. F. Dunbar, W. A. Wenzel, and W. Whaling, Phys. Rev. *92*, 742 (1953).
C. C. Rousseau, W. K. Chu, and D. Powers, Phys. Rev. A *4*, 1066 (1971).
E. Rotondi, Radiat. Res. *33*, 1 (1968).
C. A. Sautter and E. J. Zimmermann, Phys. Rev. *A140*, 490 (1965).
P. Sigmund, Phys. Rev. A *14*, 996 (1976).
E. P. Steinberg, S. B. Kaufman, B. D. Wilkins, C. E. Gross, and M. J. Fluss, Nucl. Instr. Methods *99*, 309 (1972).
J. B. Swint, R. M. Prior, and J. J. Ramirez, Nucl. Instr. Methods *80*, 134 (1970).
J. H. Thorngate, ORNL-TM-5165 (1976).
P. V. Vavilov, Zh. Eksp. Teor. Fiz. *32*, 920 (1957) [Sov. Phys.-JETP *5*, 749 (1957)].
D. Ward, J. S. Foster, H. R. Andrews, I. V. Mitchell, G. C. Ball, W. G. Davies, and G. J. Costa, AECL-5313 (1976).
F. Wenger, R. P. Gardner, and K. Verghese, Health Phys. *25*, 67 (1973).
P. K. Weyl, Phys. Rev. *91*, 289 (1953).
P. K. Weyl and M. T. Burgy (1957) (unpublished); their results are quoted by D. I. Porat and K. Ramavataram, Proc. Phys. Soc. Lond. *A252*, 394 (1960).
R. L. Wolke, W. N. Bishop, E. Eichler, N. R. Johnson, and G. D. O'Kelley, Phys. Rev. *129*, 2591 (1963).
J. F. Ziegler, *Helium Stopping Powers and Ranges in All Elements* (Pergamon, N.Y., 1978).
J. F. Ziegler and W. K. Chu, Atomic Data and Nuclear Data Tables *13*, 463 (1974).

Indleveret til Selskabet november 1978.
Færdig fra trykkeriet august 1979.

Det Kongelige Danske Videnskabernes Selskab

Matematisk-fysiske Meddelelser

Mat. Fys. Medd. Dan. Vid. Selsk.

Priser excl. moms

Vol. 39 (*uafsluttet/unfinished*)

1. LINDHARD, J.: On the Theory of Measurement and its Consequences in Statistical Dynamics. 1974 ..... 50.–
2. KLEIN, OSKAR: Le principe d'équivalence d'Einstein utilisé pour une alternative de la cosmologie relativiste en regardant le système des galaxies comme limité et non comme l'univers. 1974 ..... 40.–
3. ANDERSEN, NILS, and SIGMUND, PETER: Energy Dissipation by Heavy Ions in Compound Targets. 1974 ..... 50.–
4. SIDENIUS, G.: Systematic Stopping Cross Section Measurement with Low Energy Ions in Gases. 1974 ..... 40.–
5. PEDERSEN, GERT KJÆRGÅRD: Borel Structure in Operator Algebras. 1974 40.–
6. KALCKAR, JØRGEN, and ULFBECK, OLE: On the Problem of Gravitational Radiation. 1974 ..... 40.–
7. MØLLER, C.: A Study in Gravitational Collapse. 1975 ..... 40.–
8. HYNNE, F.: A Class of Molecular Correlation Functions Related to Ursell Functions. 1975 ..... 40.–
9. KALCKAR, JØRGEN, and ULFBECK, OLE: Studies in Classical Electron Theory. I. 1976 ..... 50.–
10. ANDERSEN, J. U.; ANDERSEN, S. KJÆR, and AUGUSTYNIAK, W. M.: Channeling of Electrons and Positrons, Correspondence between Classical and Quantal Descriptions. 1977 ..... 60.–
11. SIGMUND, PETER: Classical Scattering of Charged Particles by Molecules: Single and Multiple Collisions at Small Angles. 1977 ..... 40.–
12. DAHL, JENS PEDER: The Spinning Electron. 1977 ..... 50.–
13. MØLLER, C.: On the Crisis in the Theory of Gravitation and a Possible Solution. 1978 ..... 40.–
14. CRAWFORD, D. L.; OLSEN, E. H., and STRÖMGREN, BENGT: Analysis Based on Determinations of Colour Excesses, Distances, Ages and Masses for Early Group B and A Stars Brighter than $V = 6.^{m}_{5}$ .....

Vol. 40 (*uafsluttet/unfinished*)

1–2. Investigations of Formaldehyde Oxime, its Polymers and Coordination Compounds.

1. JENSEN, K. A., and HOLM, ARNE: On the Nature of the So-Called "Triformoxime" and Isolation of the Authentic Trimer, 1,3,5-Trihydroxyhexahydro–1,3,5-triazine. 1978 ..... 40.–
2. ANDERSEN, FLEMMING A., and JENSEN, K. A.: The Infrared Spectrum of Poly(formaldehyde oxime). 1978 ..... 40.–
3. BESENBACHER, F., ANDERSEN, H. H., HVELPLUND, P., and KNUDSEN, H.: Stopping Power of Swift Hydrogen and Helium Ions in Gases. 1979 ... 50.–
4. RASMUSEN, HANS QVADE: Three Revolutions of the Comets Halley and Olbers 1759–2024. 1979 ..... 60.–
5. SIGMUND, PETER: Statistics of Particle Penetration. 1978 ..... 50.–
6. AABOE, ASGER, and HAMILTON, N.T.: Contributions to the Study of Babylonian Lunar Theory. 1979 ..... 50.–

Printed in Denmark by Bianco Lunos Bogtrykkeri A/S. ISSN 0023-3323. ISBN 87-7304-097-5

Three Revolutions of the Comets Halley and Olbers 1759–2024

By HANS QVADE RASMUSEN

Det Kongelige Danske Videnskabernes Selskab
Matematisk-fysiske Meddelelser **40**:4

Kommissionær: Munksgaard
1979

Synopsis

The basis elements and the perturbed motion of the periodic comets Halley and Olbers during their two preceding revolutions and the present one have been computed; ephemerides for their coming return are derived. A non-gravitational effect has been taken into account, and it is shown that in addition to this the comets have been perturbed by other, unknown forces.

HANS QVADE RASMUSEN
Værslevgaard
DK-400 Kalundborg
Denmark

Contents

Printed in Denmark by Bianco Lunos Bogtrykkeri A/S. ISSN 0023-3323. ISBN 87-7304-083-5

I. Introduction

The problem of the origin of non-gravitational forces and their influence on the motion of comets might be solved by orbits computed in strict accordance with the law of gravitation for periodic comets with longer periods, 60 to 76 years, because these comets remain near the Sun only for a short time compared with the length of their revolution, so that a non-gravitational effect near the Sun can be estamated after a long period of accumulation.

On the other hand, if there is an effect originating in an unknown mass far from the Sun, this might be recognized as a slowly perturbation in the varying elements of long periodic comets, which coulrd hardly be realized in the case of short periodic comets moving nearer to the Sun.

Among the 67 periodic comets known for more than one revolution, only 5 have orbits of this dimension, and only 3 of them, comet Hallay and the periodic comets Pons-Brooks and Olbers, have been observed sufficiently for accurate orbit determination.

The orbit of comet Halley has been investigated by several independant computers, while for comet Pons-Brooks there is no definitive computation. The orbit of periodic comet Olbers has been investigated by Bessel[1] and Ginzel[2] but only for the first revolution. A repetition of Ginzel's computation including the second revolution has been carried out by myself and published in two papers[3]. The second of these investigations reproduces the time of perihelion 1818, 1887 and 1956 fairly well, provided the mass of Jupiter is given a correction og -0.34 per cent. It is also shown that just the same correction to the Jupiter mass will bring the orbit of comet Halley computed by Cowell and Crommelin[4] into accordance with the recognized time of perihelion in 1759, 1835 and 1910.

However, this correction to the mass of Jupiter can not be accepted. But then the elements drived for comet Olbers, and the semi-major axis in particular, are not correct and must be improved using the usual mass of Jupiter. This will be done in the present paper, which also includes the predicted ephemeris for the next return in 2023–2024.

The salient point of the investigation is the fact, that residuals in positions at the apparitions before and after those returns, which are used to fix the orbit orientation, might indicate that forces not originating in the Sun and the 9 planets must perturb the orbit, provided the residuals can not be eliminated by changing the comet's length in the orbit. This is because a Solar pressure would push in the direction of the radius vector and could not change the inclination of the comet's orbit.

II. Comet Halley

The present orbit computation for comet Halley is based on Bobone's alements and his normal places for the 1910 return[5] and on the normal places for the preceding return in 1835 given by Westphalen[6]. Both sets are reduced to the equinox of 1950.0 and are given in Tables 1 and 2 together with the geocentric distances T of the comet and the corresponding Solar coordinates interpolated from Herget's table[7].

The improvement of the elements for 1910 is done by runs of integrations back to 1835 where the integrated time of perihelion for 1835 was compared with Westphalen's T. The improvement of the semi-major axis in 1910 has been done provisionally by the integral:

$$da = \frac{k}{3\pi\sqrt{a}}(T \text{ integrated} - T \text{ Westphalen})$$

da has been multiplied with each of the coefficients for this element in the equations of condition for 1910, and the products subtracted from the residuals on the right hand side. Then a least square solution repeated twice leads to the preliminar elements IV (Table 5).

Among several repeated integrations and solutions by least squares using the equations of condition for both apparitions the elements Va were chosen as basis for further computations. In this solution the inapplicable coefficients to dT for 1910 in the equations for 1835 have been ignored. A correction of the elements Va by least squares using the residuals from the 1910 return only but without any further correction of the semi-major axis gives the elements Vb. Both sets of elements are shown in Table 5.

Both orbits were integrated back to 1759 and forwards to 1986. The resulting elements, coordinates, velocities and perturbations are shown in Tables 5, 9, 10 and are almost identical for the two orbits. The residuals to the normal places are given in Tables 8. The residuals 14 to 20 in 1835 apparently are somewhat large, but only because here the comet's geocentric distances, shown in Table 2 are less than 0.25 A.U. As a further check the elements for J.E.D. 2391500.5 in 1835, derived from integration Vb were improved by the residuals and equations of condition only for 1835. But here the value of the semi-major axis of integration Vb in 1835 was adopted. The resulting elements Vc are shown in Table 5 and the final residuals for 1835 are seen in Table 8. The latter are smaller than those of Va and Vb, and much like Westphalen's residuals, which in his paper are given with opposite sign as c-o. However, the integration back to 1759 for these elements gives practically the same result as Va and Vb, and is not published.

A few words should be said about the equations of condition given in Tables 3 and 4. The method described by Stracke[8] has been chosen even if it requires the use of the equatorial values of the elements ω, Ω, i. The method, however, has certain advantages. When a comet moves fast near its perihelion in an extremely eccentric orbit, the differential coefficients expressed in the polar coordinate system are less sensitive for second order errors than the vector coefficients in the Cartesian system. Moreover, if arranged in Cracowian matrixes, Stracke's method is quite as simple as those described by Banachiewicz and Herget. In the least squares solution the weights given by Bobone have been slightly altered. So the numbers 16 to 19 have got their weights reduced to half the value, because at this time the distance of the comet from the Earth is less than half a unit. This fact, together with the elongation distance from the Sun, produces phase angles, which give some systematic errors in the observations.

The perturbed motion of the comet has been computed by Cowell's method, arranged in a suitable programme for simultaneous electronic integration of the coordinates of the comet orbits Va and Vb and 9 major planets, done by Ole Møller at the Aarhus University. The basis coordinates and velocities for the comet and planets are given in Table 12. The latter are derived by integration in the barycentre S_1 from the values given by Schubarth and Stumpff[9]. The coordinates and velocities for Mercury are derived from Duncombe's table[10]. The planetary masses are those given by Clemence[11].

As comet Halley approaches Mercury in 1835 and 1910, the perturbation from this planet has been accurately taken into account in the region of perihelion by using half a day step integration. But the long run through the outer orbit has been calculated by neglecting the direct integration of Mercury's motion and attraction on the comet, the Sun and the planets. Instead the mass of Mercury has been added to that of the Sun. This requires that, on the dates of change over, the coordinates and velocities of all the bodies get a reduction from the heliocentric origo S_0 to the barycentric S_1 and vice versa[12] by:

$$d\boldsymbol{r} = -m_1\boldsymbol{r}_1 : (1+m_1) \qquad \frac{d\boldsymbol{r}}{dt} = -\frac{d\boldsymbol{r}_1}{dt} : (1+m_1)$$

Then the integration step can be increased to 4 days, and the total number of integrations for each of the 11 bodies is reduced to about 22000.

III. The Effect of Non-Gravitational Forces on Comet Halley

In Table 9 are given the osculating elements at different epochs within the integrated periods, and here the elements Va and Vb in columns 1 and 2 show that the integrated time of perihelion in 1759 is $T = $ J.D. 2363588.25. However, the elements derived by Rosenberger from observations of that apparition give the perihelion time $T = $ J.D. 2363592.55 which is $4^{d}.30$ later than the integration shows. This means that the elements of 1835 must have their osculating period diminished by $4^{d}.30$ in order to reproduce the observations of 1759. But in that case a further forward integration from 1835 with the same reduced period and the corresponding semi-major axis will show an integrated T in 1910 to be the same $4^{d}.30$ too early, i.e. the increase of the period has been confirmed.

If this phenomenon should be a result of the Solar effect on the comet, it will not be correct to consider it a constant daily increase in the semi-major axis; this action must have reached its climax in the days near the time of perihelion. Now the basis elements of the 1910 return osculate 193 days before the perihelion date. Then the radius vector was 3.1 unit or 5.3 times the perihelion distance of the comet orbit. Therefore a Solar effect on the comet was reduced to 1:28. We may take it that a Solar effect on the comet has insignificant influence before that day, and that the integrated motion back to 1835 is almost in accordance with the law of gravitation. At the perihelion in 1835, of course, the Sun will also push the comet and give the non-gravitational delay of $4^{d}.30$ in 1759. It is important to keep in mind that by the backwards integration the effect acts with opposite sign.

During the perihelion passage in 1910 comet Halley gets a similar push by the Solar effect which will increase the period and delay the time of perihelion at the next return in 1986. This effect I have tried to take into account in the following way. At J.D. 2418980.5, which is 199 days after T in 1910, the radius vector reaches 3.2 and presumably the Solar effect again has terminated. On this day the osculating elements Va and Vb shown in Table 6 have been derived from the integrated coordinates and velocities. By means of the residuals from Table 8 and the correction d period $= 4^{d} \rightarrow da = 0.001721500$ the equations of condition for the 1910 return have been solved again. The resulting corrections lead to the elements VIa and VIb. These elements, too, are shown in Table 6, and they are used as basis for a further integration forwards to 1986.

On the days around the expected day of perihelion in 1986 the elements are derived from the integrations of all 4 orbits. They are arranged in Table 10, where 4 columns give the different systems of osculating elements. The differences VIa minus Va are given as the variation corresponding to the resulting $3^{d}.9585$

delay in arriving to the perihelion in 1986. The differences of the variations in e and a show how sensitive the perturbation on these elements are. In Table 11 is given the predicted ephemeris for the coming return computed from the integrated coordinates of orbit Va, while the orbit VIa has been used to compute the variation in the positions due to $3^{d}.95852$ delay in the period. Also the star aberration is given in the ephemeris; it must be added to the geocentric observation before this is compared with the epehemeris position interpolated to $t - 0.00577\ \varrho$.

By means of the variation given in Tables 10 and 11 we can correct the elements and the ephemeris as soon as the comet has been observed.

$$\text{Delay} = 3.95852 \cdot \text{residual} : \text{variation}$$
$$\text{Correction} = \text{variation} \cdot \text{delay} : 3.95852$$

The existence of perturbations not originating in a radial pressure from the Sun can be proved if the corrected elements can not reproduce the new observations.

No attempt has been made to compute the residuals between the integrated orbits and the observations of 1759. But there is an easier way to show the missing perturbations in the integrated orbits.

The elements derived by Rosenberger from the 1759 observations, when reduced to the equinox 1950.0 and supplied with perturbations from 2363592.5 to 2363680.5 are compared with the integrated elements Vb Table 9 column 2, which originate in the 1910 apparition. The differences show the missing perturbations especially in Ω and i.

	Rosenberger 1759	Vb 1759	Correction to Integration
Epoch	2363680.5	2363680.5	
T	2363592.55055	2363588.24892	$4^{d}.30163$
ω	$110^{\circ}.7390$	$110^{\circ}.6878$	$0^{\circ}.0512$
Ω	56.5739	56.5280	0.0459
i	162.3980	162.3705	0.0275
q	0.5845238	0.5844825	0.0000413
e	0.9676585	0.9676633	−0.0000048

IV. Periodic Comet Olbers

In my previous investigation the elements for the 1887 return were in accordance with the time of perihelion in 1815, 1887 and 1956 provided the mass of Jupiter, used in the integration, gets the correction −0.34 per cent. But the residuals were not confirmed by means of continuous integration. The elements for 1956 were corrected assuming that the variation of the integrated period and the osculating semi-major axis in 1956 are both linear functions of the correction to the Jupiter mass. But only the first conclusion is true, therefore the elements for 1956 need a further correction based on the unchanged value for the mass of Jupiter. This correction has been made by means of least squares improvement with the residuals from the 1956 apparition combined with runs of integration from 1956 to 1887. The resulting elements of the final improvement are shown in Table 13 which also includes the integration back to 1815 and forwards to the next return in 2024.

In Table 14 are shown the normal places for all three apparitions and the perturbations from the epoch of osculation for the elements together with the residuals of the comparison with the normal places. These residuals are quite satisfactory in 1956 but a bit systematic in 1887 corresponding to a variation of p.004 in the denominator of the reciprocal mass of Jupiter used in the integration, which is due to the close approach of the comet to this planet in 1889.

For 1815 the time of perihelion has been corrected by $5^{d}.49562$ in the comparison with the normal places.

The predicted ephemeris for the next return in 2023–2024 is given in Table 15 together with the variation in the positions corresponding to an arrival 5 days later.

As in the case of comet Halley we can deduce the remaining perturbation by comparing the integrated elements 1815 VIIa in Table 13 with the elements computed by Ginzel[12] from the 1815 observations, when these last elements are integrated forwards to the same epoch as VIIa.

	Ginzel 1815	VIIa 1815	Correction to Integration
Epoch	2384250.5	2384250.5	
T	2384089.98880	2384084.48910	$5^{d}.49970$
ω	$65^{\circ}.57832$	$65^{\circ}.57331$	$0^{\circ}.00501$
Ω	85.34303	85.33798	0.00505
i	44.49993	44.49916	0.00077
q	1.2127846	1.2128258	−0.0000412
e	0.9310991	0.9316803	−0.0005812

V. Conclusion

The comparison of elements integrated from the basis apparitions with elements for the apparitions 1759 and 1815 discloses perturbations not originating in a Solar effect, because this can not alter the elements Ω and i. Most likely these unidentified perturbations originate in attractions from unknown masses far from the Sun or in pressure produced by streams of captured interstellar dust near the Sun. In the last case no constant effect in Ω and i could be expected.

An investigation by Yeomans[14], which includes a non-gravitational term in the direction of the radius vector of comet Halley represents the perihelion date back to the apparition in 1607, and also shows that no transverse non-gravitational reduction is required, unless the 1909–1911 observations are included in the solution, and prior to the 1910 return there does not appear to be a time dependence in the transverse non-gravitational accelerations for nearly a millennium.

The computers who in the future adjust the elements of these comets by means of the coming observations, will find out whether a similar discrepancy will appear between their improved elements and the elements predicted in this paper.

In this connection it is emphasized that after the 1986 apparition of comet Halley the comet will have been very well observed during three consecutive apparitions.

VI. Acknowledgement

The many runs of numerical integration have been done electronically at the Aarhus University by Mr. Ole Møller, mag. scient. by use of his own programme, and he has kindly helped by doing several control computations of different reductions. I am deeply indebted to Mr. Møller, for without his careful help, I would not have been able to carry out the investigation at all.

I also thank the authorities of the Aarhus University for having placed at my disposal the electronic computers belonging to the institution.

References on the last page.

Table 1.

	Jul. Ephem. Day 2410000 +	Comet Halley: Normal Places 1909–1911 α 1950.0	δ 1950.0	ϱ	Solar Coordinates X	Y	Z
1	8568.000107	95°20'36.84	17° 7'41.44	3.366	1.0013710	0.0724983	0.0314418
2	8596.000108	93 16 36.28	31 16 40.27	2.536	0.9169238	-0.3580033	-0.1553089
3	8628.000109	79 42 45.30	16 40 34.41	1.704	0.5657185	-0.7435594	-0.3225623
4	8648.000110	61 18 4.43	15 25 25.78	1.405	0.2493935	-0.8741928	-0.3792215
5	8660.000110	48 4 28.72	13 48 12.81	1.355	0.0421861	-0.9016866	-0.3911535
6	8676.000111	32 29 46.62	11 16 28.73	1.427	0.2352531	-0.8758700	-0.3799465
7	8688.000112	23 56 44.33	9 45 39.17	1.542	0.4323787	-0.8106762	-0.3516687
8	8704.000112	16 20 34.19	8 34 18.66	1.712	0.6637094	-0.6683246	-0.2899086
9	8712.000113	13 42 30.73	8 16 53.75	1.787	0.7608592	-0.5765350	-0.2500957
10	8720.000113	11 35 20.77	8 8 31.31	1.846	0.8429829	-0.4733570	-0.2053339
11	8732.000114	9 0 5.18	8 7 23.19	1.895	0.9348099	-0.3020114	-0.1310029
12	8740.000114	7 27 43.50	8 10 54.10	1.894	0.9736083	-0.1799297	-0.0780481
13	8780.000115	358 47 0.53	8 1 5.99	1.264	0.8857137	0.4344799	0.1884846
14	8788.000115	358 5 51.50	8 4 21.44	0.984	0.8150226	0.5418352	0.2350511
15	8796.000117	0 0 21.37	8 49 56.55	0.675	0.7292565	0.6392035	0.2772852
16	8804.000117	9 57 49.78	11 53 52.89	0.363	0.6299710	0.7248116	0.3144256
17	8815.000117	116 28 59.64	12 36 40.04	0.194	0.4750438	0.8204694	0.3559186
18	8818.000117	135 11 27.31	6 50 58.76	0.286	0.4297361	0.8417809	0.3651610
19	8822.000117	145 56 51.44	3 5 43.75	0.430	0.3676337	0.8668547	0.3760359
20	8826.000117	151 10 54.72	1 12 32.96	0.582	0.3038421	0.8880051	0.3852115

21	8831.000117	154	54	21.38	- 0	8	44.49	0.771	0.2221672	0.9087608	0.3942181
22	8840.000119	158	43	20.69	- 1	33	20.95	1.108	0.0716138	0.9298014	0.4033445
23	8848.000119	160	57	9.77	- 2	24	34.75	1.397	-0.0636193	0.9307304	0.4037418
24	8864.000119	164	22	36.36	- 3	48	42.77	1.941	-0.3283791	0.8826578	0.3828919
25	8888.000121	168	44	55.19	- 5	50	7.29	2.652	-0.6757444	0.6941598	0.3011195
26	8984.000125	181	24	23.02	-14	46	20.02	3.909	-0.6909160	-0.6511153	-0.2824575
27	9012.000128	181	36	34.21	-17	3	50.34	3.811	-0.2705334	-0.8690534	-0.3769947
28	9040.000128	178	29	0.55	-18	30	38.26	3.611	0.2139143	-0.8804776	-0.3819464
29	9068.000128	171	24	5.13	-18	14	30.70	3.450	0.6472706	-0.6815754	-0.2956603
30	9096.000128	161	52	2.96	-15	37	13.81	3.494	0.9271020	-0.3206944	-0.1391101
31	9124.000132	153	29	49.20	-11	32	22.30	3.834	0.9904010	0.1154625	0.0500922
32	9152.000132	148	41	33.48	- 7	49	57.12	4.421	0.8271983	0.5256160	0.2280126
33	9180.000132	147	20	43.64	- 5	27	5.22	5.129	0.4788910	0.8185809	0.3550959

The normal places in A.J. Vol. 71 p. 23 show the printing errors:
No. 9: for $13^{\circ}20'20.''21$ read $13^{\circ}11'20.''21$. No. 17 for $11^{\circ}42'34.''08$ read $12^{\circ}42'34.''08$

Table 2.

	Jul. Ephm. Day 2390000 +	Comet Halley: Normal Places 1835–1836 α 1950.0	δ 1950.0	ϱ	Solar Coordinates X	Y	Z
1	1514.310053	87°33'39".37	23°49'44".92	1.878	-0.8881820	0.4424851	0.1920154
2	1519.698829	88 43 4.53	24 28 12.97	1.696	-0.9271459	0.3662686	0.1589349
3	1525.297568	89 58 26.92	25 17 24.34	1.502	-0.9593915	0.2838830	0.1231752
4	1533.757370	92 5 32.80	27 1 18.12	1.199	-0.9916144	0.1548226	0.0671641
5	1539.622060	93 54 2.08	28 50 18.21	0.984	-1.0019341	0.0632780	0.0274370
6	1545.250472	96 15 12.32	31 30 44.20	0.775	-1.0023586	-0.0252302	-0.0109756
7	1548.827006	98 25 57.23	34 5 13.50	0.643	-0.9977623	-0.0813946	-0.0353504
8	1551.648106	100 56 16.80	36 58 18.96	0.539	-0.9914797	-0.1254775	-0.0544866
9	1553.411838	103 9 8.91	39 22 25.11	0.475	-0.9863705	-0.1528935	-0.0663857
10	1555.473105	106 53 50.80	43 3 17.84	0.401	-0.9792525	-0.1847402	-0.0802071
11	1557.427082	112 37 48.42	47 46 58.91	0.335	-0.9713744	-0.2147179	-0.0932167
12	1558.398526	116 57 24.40	50 42 26.60	0.304	-0.9670502	-0.2295335	-0.0996460
13	1559.448580	123 35 0.43	54 18 47.50	0.272	-0.9620729	-0.2454759	-0.1065643
14	1560.371394	132 5 42.77	57 43 32.27	0.247	-0.9574396	-0.2594209	-0.1126157
15	1561.436441	146 53 57.11	61 21 12.99	0.222	-0.9517920	-0.2754343	-0.1195646
16	1562.473270	167 54 7.94	63 5 8.71	0.202	-0.9459861	-0.2909354	-0.1262912
17	1564.343354	209 19 1.00	56 9 4.98	0.187	-0.9347509	-0.3186583	-0.1383213
18	1564.443778	211 4 45.37	55 25 10.97	0.187	-0.9341200	-0.3201381	-0.1389635
19	1564.514582	212 16 55.31	54 53 21.21	0.187	-0.9336735	-0.3211808	-0.1394160
20	1567.198866	239 39 53.36	32 16 2.43	0.216	-0.9157175	-0.3603474	-0.1564124

21	1572.904294	255	11	8.33	5	13	13.76	0.385	-0.8710198	-0.4409321	-0.1913857
22	1579.832918	259	45	54.96	- 5	54	1.05	0.639	-0.8052803	-0.5328950	-0.2312998
23	1588.164978	260	38	1.30	-11	36	43.73	0.946	-0.7109075	-0.6330807	-0.2747756
24	1671.418608	236	29	34.09	-29	46	54.67	1.574	0.6155771	-0.7053652	-0.3061087
25	1680.237729	231	0	36.29	-31	17	37.06	1.475	0.7286028	-0.6098164	-0.2646352
26	1686.547303	225	59	5.76	-32	12	43.44	1.407	0.7989580	-0.5323567	-0.2310199
27	1692.560907	220	11	58.31	-32	49	19.96	1.347	0.8569465	-0.4524127	-0.1963245
28	1701.213297	210	11	6.85	-32	54	28.97	1.282	0.9235376	-0.3288460	-0.1426906
29	1709.802007	198	51	5.79	-31	38	58.52	1.255	0.9688778	-0.1988580	-0.0862753
30	1719.813510	185	37	13.19	-28	19	44.95	1.285	0.9945594	-0.0419014	-0.0181602
31	1727.435225	176	47	43.80	-24	53	31.29	1.358	0.9940483	0.0787208	0.0341936
32	1729.364869	174	48	37.50	-23	58	1.16	1.382	0.9911753	0.1091162	0.0473860
33	1744.806535	162	47	43.09	-16	56	33.40	1.661	0.9294479	0.3451996	0.1498383
34	1765.596426	155	3	48.91	-10	21	0.40	2.188	0.7457046	0.6225451	0.2702038

A.N. 575 pag. 373: Westphalen's 4 normal places of 1835 Oct. 8 are united to No. 14

Table 3.
Comet Halley: Equations of Condition for Declination 1909–1911

	$\frac{d\alpha \cos\delta}{d\Omega}$	$\frac{d\alpha \cos\delta}{di}$	$\frac{d\alpha \cos\delta}{d\omega}$	$\frac{d\alpha \cos\delta}{de}$	$\frac{d\alpha \cos\delta}{dT}$	$\frac{d\alpha \cos\delta}{da}$		$d\alpha \cos\delta$	w
1	0.906	-0.230	-0.909	12.91	0.00050	-0.0253	=	-0.20	36
2	1.077	-0.277	-1.086	16.56	0.00074	-0.0321	=	-0.90	31
3	1.446	-0.294	-1.487	26.12	0.00278	-0.0495	=	0.64	31
4	1.595	-0.180	-1.671	33.32	0.00628	-0.0622	=	1.02	31
5	1.487	-0.059	-1.576	34.12	0.00851	-0.0631	=	-0.14	41
6	1.174	0.073	-1.257	30.17	0.01008	-0.0553	=	0.60	29
7	0.948	0.121	-1.015	26.07	0.01030	-0.0475	=	0.64	33
8	0.727	0.136	-0.781	21.65	0.01022	-0.0394	=	0.20	28
9	0.652	0.133	-0.699	20.04	0.01022	-0.0364	=	-0.59	20
10	0.594	0.127	-0.633	18.75	0.01032	-0.0341	=	-0.10	23
11	0.530	0.113	-0.558	17.35	0.01067	-0.0315	=	-0.15	18
12	0.492	0.103	-0.515	16.45	0.01116	-0.0299	=	-0.03	19
13	0.297	-0.007	-0.276	12.04	0.01389	-0.0219	=	-0.02	29
14	0.180	-0.068	-0.145	14.11	0.01218	-0.0257	=	-0.29	20
15	-0.092	-0.171	0.153	23.69	0.00787	-0.0433	=	0.96	24
16	-1.073	-0.346	1.200	60.95	-0.01001	-0.1113	=	0.25	12
17	-1.721	1.562	1.761	37.74	-0.10549	-0.0663	=	-2.22	14
18	-0.016	1.156	-0.010	-12.81	-0.04946	0.0252	=	1.55	19
19	0.578	0.794	-0.612	-25.23	-0.02098	0.0473	=	-0.33	13
20	0.721	0.604	-0.751	-25.94	-0.01083	0.0482	=	-0.30	29

21	0.761	0.472	-0.784	-24.29	-0.00508	0.0453	=	-0.98	36
22	0.755	0.348	-0.770	-21.22	-0.00109	0.0395	=	0.24	31
23	0.739	0.289	-0.749	-19.22	0.00029	0.0358	=	-0.10	10
24	0.712	0.222	-0.718	-16.64	0.00134	0.0311	=	0.44	14
25	0.694	0.172	-0.696	-14.53	0.00177	0.0272	=	0.31	9
26	0.786	0.118	-0.786	-13.03	0.00199	0.0246	=	-1.31	2
27	0.874	0.125	-0.871	-13.77	0.00201	0.0260	=	-0.19	2
28	1.014	0.145	-1.005	-14.86	0.00193	0.0282	=	1.40	12
29	1.165	0.175	-1.143	-15.71	0.00165	0.0302	=	0.64	5
30	1.244	0.198	-1.207	-15.30	0.00115	0.0302	=	1.81	9
31	1.198	0.198	-1.151	-13.54	0.00067	0.0271	=	3.35	4
32	1.089	0.180	-1.041	-11.58	0.00040	0.0235	=	2.52	3
33	0.988	0.158	-0.942	-10.11	0.00031	0.0207	=	-0.18	3

Table 3. (continued).
Comet Halley: Equations of Condition for Declination 1909–1911

	$\frac{d\delta}{d\Omega}$	$\frac{d\delta}{di}$	$\frac{d\delta}{d\omega}$	$\frac{d\delta}{de}$	$\frac{d\delta}{dT}$	$\frac{d\delta}{da}$		$d\delta$	w
1	-0.087	-0.789	0.289	-4.43	-0.00046	0.0085	=	0".51	33
2	-0.108	-0.980	0.332	-5.41	-0.00058	0.0103	=	0.88	75
3	-0.071	-1.349	0.328	-5.80	-0.00067	0.0110	=	-0.07	52
4	0.038	-1.536	0.205	-3.65	-0.00016	0.0070	=	-0.56	62
5	0.100	-1.514	0.107	-1.58	0.00055	0.0032	=	0.28	62
6	0.118	-1.318	0.024	0.35	0.00146	-0.0004	=	-0.20	57
7	0.101	-1.127	-0.006	1.01	0.00185	-0.0016	=	-0.16	38
8	0.072	-0.897	-0.031	1.46	0.00216	-0.0025	=	-0.42	48
9	0.060	-0.799	-0.042	1.64	0.00228	-0.0028	=	-0.75	38
10	0.049	-0.710	-0.052	1.81	0.00241	-0.0032	=	-1.31	18
11	0.033	-0.590	-0.067	2.09	0.00269	-0.0037	=	-1.67	31
12	0.023	-0.514	-0.076	2.24	0.00294	-0.0040	=	-1.44	29
13	-0.050	0.027	-0.112	2.01	0.00586	-0.0037	=	-1.42	62
14	-0.081	0.274	-0.107	1.88	0.00645	-0.0034	=	0.38	57
15	-0.145	0.719	-0.075	2.85	0.00678	-0.0053	=	-0.15	41
16	-0.343	1.864	0.058	7.33	0.00542	-0.0135	=	-0.54	20
17	0.891	4.757	-1.173	-32.51	0.04786	0.0584	=	0.18	24
18	0.376	3.110	-0.473	-11.29	0.02761	0.0198	=	-1.82	13
19	0.114	2.208	-0.112	- 1.63	0.01477	0.0024	=	0.66	22
20	0.034	1.733	-0.015	1.26	0.00916	-0.0027	=	0.19	48

21	-0.003	1.400	0.078	2.45	0.00549	-0.0048	=	0.20	44
22	-0.022	1.064	0.129	3.20	0.00298	-0.0062	=	-0.07	62
23	-0.026	0.904	0.147	3.33	0.00186	-0.0064	=	-0.34	14
24	-0.026	0.723	0.163	3.34	0.00081	-0.0064	=	-0.08	26
25	-0.021	0.594	0.173	3.24	0.00020	-0.0062	=	0.89	9
26	0.041	0.515	0.183	2.98	-0.00041	-0.0056	=	-2.39	6
27	0.067	0.542	0.196	3.13	-0.00051	-0.0059	=	0.06	5
28	0.077	0.594	0.229	3.61	-0.00062	-0.0067	=	-1.40	12
29	0.052	0.631	0.299	4.45	-0.00069	-0.0083	=	-1.79	21
30	0.001	0.653	0.375	5.12	-0.00061	-0.0098	=	-1.75	7
31	-0.028	0.582	0.399	4.95	-0.00040	-0.0097	=	-1.72	5
32	-0.027	0.512	0.371	4.23	-0.00020	-0.0085	=	-1.81	6
33	-0.018	0.448	0.332	3.54	-0.00010	-0.0073	=	-1.84	1

Table 4.
Comet Halley: Equations of Condition for Right Ascension 1835–1836

	$\frac{d\alpha\cos\delta}{d\Omega}$	$\frac{d\alpha\cos\delta}{di}$	$\frac{d\alpha\cos\delta}{d\omega}$	$\frac{d\alpha\cos\delta}{de}$	$\frac{d\alpha\cos\delta}{dT}$	$\frac{d\alpha\cos\delta}{da}$ T 1835	$\frac{d\alpha\cos\delta}{da}$ T 1910		$d\alpha\cos\delta$	w
1	0.700	-0.217	-0.729	16.37	0.0005	-0.0305	- 1.2	=	0".92	21
2	0.601	-0.235	-0.738	17.07	0.0002	-0.0318	- 0.4	=	1.36	23
3	0.715	-0.258	-0.751	18.06	-0.0003	-0.0336	0.6	=	2.08	23
4	0.732	-0.308	-0.774	19.70	-0.0016	-0.0337	3.7	=	1.67	18
5	0.743	-0.360	-0.793	21.31	-0.0033	-0.0397	7.5	=	2.19	28
6	0.744	-0.438	-0.805	23.18	-0.0063	-0.0432	14.4	=	1.56	28
7	0.730	-0.516	-0.801	24.44	-0.0097	-0.0456	22.0	=	2.32	23
8	0.678	-0.605	-0.760	24.69	-0.0144	-0.0462	32.6	=	1.79	23
9	0.614	-0.681	-0.702	24.16	-0.0188	-0.0453	40.6	=	-0.43	18
10	0.462	-0.802	-0.560	20.91	-0.0200	-0.0450	45.2	=	3.78	14
11	0.148	-0.964	-0.252	13.58	-0.0390	-0.0274	88.3	=	1.66	14
12	-0.078	-1.068	-0.028	8.28	-0.0472	-0.0182	106.9	=	4.99	5
13	-0.618	-1.192	0.525	- 6.93	-0.0619	0.0125	139.5	=	5.19	5
14	-1.284	-1.301	1.211	- 29.41	-0.0777	0.0508	176.1	=	9.34	24
15	-2.438	-1.318	2.420	- 66.52	-0.1116	0.1179	252.9	=	10.97	5
16	-3.815	-1.220	3.893	-121.45	-0.1155	0.2184	261.8	=	17.69	5
17	-4.647	-0.333	4.893	-170.08	-0.0890	0.3083	200.4	=	15.91	5
18	-4.607	-0.285	4.857	-169.69	-0.0855	0.3077	193.9	=	17.05	5
19	-4.576	-0.252	4.828	-169.28	-0.0835	0.3070	189.3	=	16.74	5
20	-2.729	0.391	2.973	-118.76	-0.0227	0.2124	51.7	=	9.14	9

21	-0.688	0.326	0.814	- 46.27	0.0095	0.0845	- 21.5	=	-0.48	14
22	-0.050	0.160	0.117	- 20.91	0.0142	0.0382	- 37.5	=	-0.10	32
23	0.196	0.056	-0.161	- 11.64	0.0130	0.0212	- 35.1	=	-1.68	18
24	0.710	-0.078	-0.767	- 22.12	0.0119	0.0399	- 26.9	=	1.36	1
25	0.844	-0.056	-0.908	- 25.10	0.0120	0.0453	- 27.1	=	4.79	1
26	0.969	-0.029	-1.036	- 27.64	0.0120	0.0500	- 27.1	=	7.84	2
27	1.093	0.009	-1.178	- 30.26	0.0118	0.0549	- 26.6	=	2.49	2
28	1.333	0.085	-1.338	- 33.78	0.0110	0.0616	- 24.9	=	2.16	9
29	1.531	0.176	-1.582	- 35.82	0.0095	0.0657	- 21.5	=	2.72	4
30	1.647	0.270	-1.676	- 35.11	0.0064	0.0650	- 15.9	=	0.31	14
31	1.627	0.314	-1.637	- 32.59	0.0052	0.0607	- 11.6	=	10.35	9
32	1.621	0.321	-1.627	- 31.79	0.0047	0.0593	- 10.6	=	1.75	3
33	1.430	0.326	-1.412	- 25.05	0.0022	0.0473	- 5.0	=	5.03	3
34	1.172	0.278	-1.143	- 18.46	0.0009	0.0353	- 2.1	=	15.07	1

Table 4.
Comet Halley: Equations of Condition for Declination 1835–1836

	$\frac{d\delta}{d\Omega}$	$\frac{d\delta}{di}$	$\frac{d\delta}{d\omega}$	$\frac{d\delta}{de}$	$\frac{d\delta}{dT}$	$\frac{d\delta}{da}$ T 1835	$\frac{d\delta}{da}$ T 1910		$d\delta$	w
									"	
1	-0.195	-0.847	0.266	- 6.60	-0.0018	0.0121	4.0	=	- 2.78	21
2	-0.228	-0.895	0.292	- 7.48	-0.0021	0.0137	4.7	=	0.75	23
3	-0.272	-0.959	0.329	- 8.67	-0.0025	0.0159	5.7	=	- 0.95	23
4	-0.373	-1.094	0.412	- 11.45	-0.0036	0.0209	8.2	=	0.17	18
5	-0.488	-1.233	0.510	- 14.63	-0.0050	0.0269	11.4	=	0.60	28
6	-0.674	-1.425	0.672	- 20.24	-0.0074	0.0368	16.8	=	1.35	28
7	-0.870	-1.596	0.871	- 28.35	-0.0110	0.0516	25.0	=	0.90	23
8	-1.114	-1.764	1.073	- 33.93	-0.0135	0.0617	30.6	=	3.73	23
9	-1.330	-1.885	1.278	- 40.96	-0.0166	0.0745	44.3	=	1.80	18
10	-1.684	-2.031	1.619	- 52.81	-0.0214	0.0960	48.7	=	4.84	14
11	-2.163	-2.134	2.092	- 65.45	-0.0274	0.1265	62.1	=	6.27	14
12	-2.475	-2.168	2.407	- 79.18	-0.0306	0.1457	69.4	=	5.50	5
13	-2.794	-2.072	2.740	- 87.74	-0.0316	0.1709	72.0	=	7.70	5
14	-3.026	-1.907	2.992	-104.90	-0.0287	0.1911	65.2	=	6.98	24
15	-2.971	-1.545	2.964	-108.81	-0.0135	0.1988	30.8	=	7.70	5
16	-2.127	-1.092	2.115	- 86.91	0.0221	0.1598	- 50.0	=	0.18	5
17	0.800	-1.140	-1.023	12.22	0.0951	-0.0194	-222.4	=	-10.69	5
18	0.918	-1.187	-1.156	16.85	0.1001	-0.0276	-226.8	=	-11.56	5
19	0.995	-1.221	-1.245	19.81	0.1015	-0.0331	-229.9	=	-11.27	5
20	1.501	-2.295	-2.007	52.84	0.0885	-0.0976	-200.6	=	-11.62	9

21	0.172	-1.571	-0.577	13.23	0.0275	-0.0236	- 62.2	=	- 4.68	14
22	-0.112	-0.733	-0.169	1.37	0.0103	-0.0024	- 15.4	=	- 1.72	28
23	-0.124	-0.256	-0.081	- 1.21	0.0064	0.0022	- 12.2	=	- 1.39	18
24	0.285	0.869	-0.171	- 4.31	0.0005	0.0080	- 1.1	=	4.92	6
25	0.334	0.976	-0.180	- 4.04	-0.0001	0.0076	- 0.2	=	- 2.04	8
26	0.358	1.057	-0.170	- 3.41	-0.0007	0.0065	1.5	=	- 1.04	4
27	0.362	1.134	-0.140	- 2.29	-0.0013	0.0045	3.0	=	0.68	3
28	0.317	1.231	-0.044	0.42	-0.0024	-0.0003	5.4	=	5.02	4
29	0.210	1.292	0.112	4.08	-0.0033	-0.0070	7.4	=	- 3.68	4
30	0.051	1.295	0.311	7.95	-0.0035	-0.0142	7.9	=	- 2.94	15
31	-0.042	1.249	0.418	8.38	-0.0031	-0.0173	6.9	=	-12.68	9
32	-0.058	1.233	0.436	9.70	-0.0029	-0.0177	6.6	=	- 6.80	6
33	-0.106	1.065	0.469	9.01	-0.0016	-0.0167	3.6	=	- 2.83	1
34	-0.138	0.844	0.392	6.52	-0.0005	-0.0124	1.2	=	- 9.72	1

TABLE 4 concluded

Table 5.
Comet Halley: Basis Elements

Elements Observations		Preliminary *IV* 1910	Improved *Va* 1910–1835	Improved *Vb* 1910	Improved *Vc* 1835
Epoch		2418588.5	2418588.5	2418588.5	2391500.5
T (J.E.D.)		2418781.679713	2418781.679695	2418781.679726	2391598.938822
T (E.T.)		1910 4 20.179713	1910 4 20.179696	1910 4 20.179726	1835 11 16.438822
ω	Ecliptic 1950.0	111° 43' 25".120	111° 43' 25".386	111° 43' 25".213	110° 40' 51".946
Ω		57 50 43.903	57 50 44.869	57 50 44.075	56 48 3.133
i		162 12 53.108	162 12 52.744	162 12 53.126	162 15 20.794
ω	Equator 1950.0	188° 35' 23".470	188° 35' 23".038	188° 35' 23".478	188° 27' 36".983
Ω		131 36 58.218	131 36 57.389	131 36 58.302	131 31 44.379
i		159 45 47.556	159 45 47.186	159 45 47.509	160 4 59.425
q		0.58713829528	0.58714240530	0.58713893730	0.58659293060
e		0.96727918590	0.96727895732	0.96727915059	0.96741424985
a		17.9438779700	17.9438782258	17.9438782258	18.0015168550
n		46".6801361445	46".6801351462	46".6801351462	46".4561187966
Period		27763d.415170	27763d.415764	27763d.415764	27897d.293910

Px	0.5519170735	0.55191930163	0.55191739046	0.55223221660
Py	-0.8322970589	-0.83229571320	-0.83229684593	-0.83218250107
Pz	-0.0516638141	-0.05166169099	-0.05166385932	-0.05011849809
Qx	-0.7927887852	-0.79278652243	-0.79278854290	-0.79372758686
Qy	-0.5044876308	-0.50448981523	-0.50448786954	-0.50642086493
Qz	-0.3420207193	-0.34202274224	-0.34202092880	-0.33694869845
x	0.7583468030	0.75834712957	0.75834713832	0.95301407948
y	2.8753737992	2.87537003181	2.87537316472	1.51213998044
z	0.9130140045	0.91301577960	0.91301482991	0.62175081673
dx/dt	0.002686871124	0.0026868887679	0.0026868730491	0.0009220855059
dy/dt	-0.012686525728	-0.0126865303200	-0.0126865254493	-0.0167680480718
dz/dt	-0.002365624262	-0.0023656169012	-0.0023656270162	-0.0037779512674

Table 6.
Comet Halley

Elements Observations	Integrated *Va* 1910–1835	Integrated *Vb* 1910	Corrected *VIa* 1910–1835	Corrected *VIb* 1910
Osculation	2418980.5	2418980.5	2418980.5	2418980.5
T (J.E.D.)	2418781.690756	2418781.690537	2418781.690789	2318781.690570
T (E.T.)	1910 4 20.190756	1910 4 20.190537	1910 4 20.190789	1910 4 20.190570
ω Ecliptic	111° 43' 18".726	111° 43' 18".552	111° 43' 17".766	111° 43' 18".303
Ω 1950.0	57 51 39.418	57 51 38.623	57 51 39.352	57 51 38.557
i	162 13 8.706	162 13 9.087	162 13 8.646	162 13 9.027
ω Equator	188° 35' 15".863	188° 35' 17".302	188° 35' 15".507	188° 35' 16".946
Ω 1950.0	131 37 53.266	131 37 54.178	131 37 53.085	131 37 53.997
i	159 45 34.589	159 45 34.912	159 45 34.595	159 45 34.918
q	0.58698393730	0.58698047000	0.58698256970	0.58697910209
e	0.96736228924	0.96736248090	0.96736548904	0.96736568070
a	17.9848378942	17.9848372706	17.9865593942	17.9865587706
n	46".5207580785	46".5207604981	46".5140794608	46".5140818800
Period	27858^{d}.531407	27858^{d}.529958	27862^{d}.531410	27862^{d}.529961

Px	0.55217083702	0.55216892731	0.55217147390	0.55216956295
Py	-0.83212896251	-0.83213009519	-0.83212857681	-0.83212971031
Pz	-0.05166000859	-0.05166217565	-0.05165941370	-0.05166158084
Qx	-0.79261768354	-0.79261970389	-0.79261718082	-0.79261920184
Qy	-0.50471559572	-0.50471365194	-0.50471634345	-0.50471439847
Qz	-0.34208094828	-0.34207913493	-0.34208100982	-0.34207919665
x	-3.05045067345	-3.05045233942	-3.05045956967	-3.05046387414
y	0.53198107798	0.53199763824	0.53197638204	0.53199482496
z	-0.71039107602	-0.71038009769	-0.71039539777	-0.71038468711
dx/dt	-0.0105815098186	-0.0105814834441	-0.0105815772982	-0.0105815438913
dy/dt	0.0075311468662	0.0075311823625	0.0075311184444	0.0075311527318
dz/dt	-0.0010714364970	-0.0010713947194	-0.0010714660567	-0.0010714226440

Table 7.

	Perturbation at 1835 Return from 2391500.5 to Date of Normal Places					Perturbation at 1910 Return from 2418588.5 to Date of Normal Places				
	10^8	$10^8\,\eta$	$10^8\,\eta$	P.α	P.δ	$10^8\,\zeta$	$10^8\,\xi$	$10^8\,\zeta$	P.α	P.δ
				s	s				s	s
1	- 16	18	6	0.01	0.00	- 56	65	29	0.07	0.00
2	6	- 7	- 2	- 0.01	- 0.00	- 105	119	50	0.15	0.00
3	181	- 232	- 80	- 0.28	- 0.02	- 165	191	79	0.25	-0.01
4	419	- 551	- 195	- 0.96	- 0.16	- 281	321	130	0.52	-0.06
5	608	- 817	- 294	- 1.56	- 0.36	- 372	424	211	0.82	-0.07
6	911	- 1268	- 464	- 2.30	- 0.68	- 464	529	207	1.26	-0.33
7	1173	- 1680	- 624	- 2.73	- 0.91	- 531	594	230	1.70	-0.59
8	1566	- 2321	- 882	- 3.25	- 1.20	- 580	647	247	2.14	-0.96
9	1782	- 2668	- 1027	- 3.52	- 1.36	- 611	679	257	2.48	-1.34
10	2007	- 3023	- 1179	- 3.80	- 1.52	- 649	716	268	2.90	-2.06
11	2347	- 3546	- 1413	- 4.26	- 1.79	- 684	749	275	3.14	-3.21
12	2564	- 3857	- 1560	- 4.57	- 1.99	- 702	765	279	2.99	-4.05
13	5718	- 4198	- 840	- 6.72	- 2.67	- 722	779	281	2.13	-5.21
14	7837	- 5424	- 285	-10.93	- 2.95	- 738	792	282	0.26	-6.38
15	9774	- 7906	- 24	-24.45	- 4.66	- 757	821	282	- 6.32	-7.58
16	11036	- 11106	- 174	-74.53	-11.44	- 786	817	276	-14.27	-7.27
17	11536	- 15804	- 762	-35.74	36.90	- 804	844	270	-22.42	-0.98
18	11481	- 17092	- 976	29.31	10.38	- 806	845	269	-22.21	-0.62
19	11322	- 18777	- 1277	44.23	- 0.96	- 808	847	268	-22.06	-0.38
20	11074	- 20412	- 1588	44.50	- 4.17	- 837	879	241	-13.25	0.01

21	10657	- 23380	- 1986	44.52	- 5.44	- 919	977	147	- 6.12	1.13
22	9662	- 25716	- 2709	38.09	- 5.97	-1192	1449	64	- 4.65	0.20
23	8563	- 28479	- 3347	35.64	- 6.01	-1333	1195	-193	- 3.36	-0.83
24	5888	- 33545	- 4591	32.72	- 5.91	-2625	11463	646	- 8.29	-4.54
25	918	- 40387	- 6372	30.83	- 5.62	-2073	12385	940	-15.38	-4.92
26	-27621	- 67255	-12863	36.34	- 2.64	-1659	12994	1146	-17.72	-4.98
27	-37542	- 76493	-14666	42.70	- 1.29	-1241	13539	1344	-20.30	-4.74
28	-47666	- 86519	-16418	52.86	- 0.67	- 600	14271	1628	-24.22	-3.62
29	-57753	- 97282	-18134	65.98	- 2.33	82	14937	1908	-25.18	-1.56
30	-67579	-108658	-19809	76.18	- 6.43	940	15655	2279	-28.41	1.34
31	-76985	-120522	-21439	78.09	- 9.67	1637	16156	2494	-27.17	2.97
32	-85813	-132756	-23027	74.42	-10.37	1823	16282	2561	-26.75	3.28
33	-93905	-145172	-24538	69.85	- 9.80	3388	17201	3096	-22.63	4.35
34						5790	18298	3874	-18.24	4.01

Table 8.
Comet Halley: Final Residuals

	Va 1910		*Vb* 1910		*Va* 1835		*Vb* 1835		*Vc* 1835	
	$d\alpha \cos\delta$	$d\delta$	$d\alpha \cos\delta$	$d\delta$	$d\alpha \cos\delta$	$d\delta$	$d\alpha \cos\delta$	$d\delta$	$d\alpha \cos\delta$	$d\delta$
1	-0".20	0".34	-0".18	0".45	1".20	-3".37	1".03	-3".04	0".82	-3".25
2	-0.90	0.65	-0.88	0.80	1.64	0.04	1.45	0.43	1.29	0.20
3	0.85	-0.44	0.70	-0.16	2.32	-1.75	2.12	-1.30	1.96	-1.56
4	1.47	-0.96	1.11	-0.64	1.79	-0.96	1.56	-0.32	1.47	-0.67
5	0.47	-0.11	0.02	0.19	1.85	-0.79	1.97	-0.07	1.89	-0.51
6	1.25	-0.53	0.71	-0.27	1.28	-0.55	1.00	0.38	0.96	-0.24
7	1.29	-0.45	0.74	-0.22	1.71	-1.54	1.41	-0.37	1.39	-1.31
8	0.79	-0.66	0.29	-0.48	0.70	0.66	0.40	2.06	0.38	1.02
9	-0.01	-0.97	-0.50	-0.79	-2.05	-1.88	-2.31	-0.23	2.37	-1.49
10	0.46	-1.51	-0.03	-1.35	1.14	0.23	0.96	2.24	1.23	0.64
11	0.37	-1.86	-0.09	-1.70	-2.46	-0.16	2.28	3.16	-2.73	1.24
12	0.50	-1.60	0.02	-1.45	-0.31	-1.16	0.28	2.37	-0.32	0.05
13	0.45	-1.49	0.00	-1.41	-1.98	0.77	-1.38	3.83	-2.46	1.35
14	0.33	0.37	-0.24	0.40	-0.15	0.02	0.98	3.32	-0.76	0.36
15	2.18	0.04	1.11	-0.10	-0.54	2.23	1.65	5.60	-1.94	2.70
16	3.79	0.30	0.79	-0.39	1.19	-0.75	4.85	1.90	0.59	-0.15
17	0.85	-0.47	-1.45	-0.04	1.46	-0.77	5.66	-0.25	0.37	0.50
18	1.16	-1.47	1.64	-1.86	3.01	-1.50	7.19	-1.07	1.97	0.02
19	-1.71	1.40	-0.45	0.70	2.89	-1.03	7.07	-0.66	1.86	0.53
20	-1.81	0.99	-0.48	0.26	3.22	-2.18	4.70	-2.13	2.21	-0.36

21	-2.46	0.97	-1.18	0.26	-0.90	-2.46	0.29	-1.82	-1.35	-1.46
22	-1.11	0.65	0.06	-0.01	0.62	-1.15	1.25	-0.62	-0.24	-0.63
23	-1.36	0.36	-0.28	-0.27	-0.63	-1.20	-0.15	-0.85	-1.15	-0.86
24	-0.71	0.55	0.27	-0.03	1.04	5.08	2.39	4.95	-0.43	4.43
25	-0.73	1.48	0.15	0.94	4.26	-1.85	5.79	-2.06	2.50	-2.59
26	-2.35	-1.76	-1.47	-2.34	7.12	-0.81	8.82	-1.11	5.09	-1.59
27	-1.32	0.75	-0.36	0.12	1.55	0.98	3.41	0.56	-0.77	0.21
28	0.17	-0.62	1.22	-1.35	0.90	6.08	2.98	5.41	-1.81	5.44
29	-0.70	-0.87	0.45	-1.72	1.08	-3.02	3.36	-3.96	-2.04	-3.42
30	0.47	-0.74	1.61	-1.68	-1.52	-1.93	0.69	-3.17	-4.94	-1.99
31	2.13	-0.74	3.19	-1.67	8.48	-11.57	10.55	-12.87	5.20	-11.42
32	1.46	-0.90	2.37	-1.76	-0.63	-5.59	1.90	-6.98	-3.39	-5.43
33	-1.10	-1.04	-0.31	-1.79	3.38	-1.57	4.97	-2.86	0.54	-1.29
34					13.73	-8.63	14.95	-9.67	11.46	-8.42
ϵ	5".37		4".10		8".18		10".18		7".61	

Table 9.
Coment Halley: Integrated Elements, Coordinates, Velocities and Perturbations

Basis	*Va*	*Vb*	*Va*	*Vb*
Osculation	2363680.5	2363680.5	2391500.5	2391500.5
T (J.E.D.)	2363588.251964	2363588.248917	2391598.938921	2391598.938927
T (E.T.)	1759 3 8.751964	1759 3 8.748917	1835 11 16.438921	1835 11 16.438927
ω	110° 41' 16".508	110° 41' 16".138	110° 40' 53".396	110° 40' 53".173
Ω Ecliptic	56 31 41.722	56 31 40.840	56 48 3.287	56 48 2.444
i 1950.0	162 22 13.256	162 22 13.634	162 15 20.315	162 15 20.693
q	0.5844864725	0.5844825439	0.5865899834	0.5865865086
e	0.9676630898	0.9676632839	0.9674144119	0.9674146066
a	18.074901680	18.074888682	18.001515931	18.001516855
n	46".173485487	46".173535294	46".456122257	46".456118681
Period	28068d.056512	28068d.026235	27897d.291832	27897d.293980
Px	0.5488777146	0.5488762241	0.5522266539	0.5522247522
Py	-0.8342232729	-0.8342241299	-0.8321861823	-0.8321873152
Pz	-0.0529602235	-0.0529621723	-0.0501186659	-0.0501208090
Qx	-0.7968114374	-0.7968131537	-0.7937308231	-0.7937328333
Qy	-0.5030097058	-0.5030082313	-0.5064153594	-0.5064134341
Qz	-0.3347727126	-0.3347708431	-0.3369493498	-0.3369475072

x	-1.7047886078	-1.7048418891	0.9530188598	0.9530175653
y	-0.2770784638	-0.2770433340	1.5121343353	1.5121377682
z	-0.5243313767	-0.5243330316	0.6217509568	0.6217491305
dx/dt	-0.015737387976	-0.015737097276	0.000921995806	0.000921986016
dy/dt	0.007622852440	0.007622958884	-0.016768061997	-0.016768054467
dz/dt	-0.002395227770	-0.002395085389	-0.003777956236	-0.003777959548
Perturbation	1835 to 1759	1835 to 1759	1910 to 1835	1910 to 1835
In T	$-113^{d}.39513$	$-113^{d}.39603$	$580^{d}.67438$	$580^{d}.67497$
In ω	$23''.112$	$22''.965$	$-3751''.990$	$-3752''.040$
In Ω	$-981''.565$	$-981''.604$	$-3761''.582$	$-3761''.631$
In i	$412''.941$	$412''.941$	$147''.571$	$147''.567$
In e	0.0002486779	0.0002486773	0.0001354546	0.0001354560
In a	0.073385749	0.073371827	0.057637705	0.057638627

Table 10.
Comet Halley: Integrated Elements Near Perihelion 1986 at J. E. D. 2446400.0 + *t*

t		*Va*	Variation	*VIa*	*Vb*	*VIb*
64.5	T=	66.963692	3.958522	70.922214	66.963519	70.921812
66.5	T=	66.963687	3.958519	70.922206	66.963514	70.921804
68.5	T=	66.963183	3.958518	70.922201	66.963510	70.921800
70.5	T=	66.963680	3.958519	70.922199	66.963507	70.921797
72.5	T=	66.963677	3.958519	70.922196	66.963503	70.921794
64.5	ω=	111.855507	-0.000281	111.855226	111.855459	111.855179
66.5	ω=	111.855578	-0.000256	111.855322	111.855530	111.855275
68.5	ω=	111.855620	-0.000215	111.855405	111.855573	111.855358
70.5	ω=	111.855644	-0.000185	111.855459	111.855597	111.855412
72.5	ω=	111.855657	-0.000167	111.855490	111.855610	111.855443
64.5	Ω=	58.152710	-0.000379	58.152331	58.152490	58.152111
66.5	Ω=	58.152801	-0.000340	58.152461	58.152581	58.152241
68.5	Ω=	58.152857	-0.000292	58.152565	58.152637	58.152344
70.5	Ω=	58.152891	-0.000260	58.152631	58.152671	58.152411
72.5	Ω=	58.152912	-0.000241	58.152671	58.152692	58.152451
64.5	i=	162.238504	-0.000065	162.238439	162.238609	162.238544
66.5	i=	162.238495	-0.000060	162.238435	162.238600	162.238541
68.5	i=	162.238488	-0.000059	162.238429	162.238593	162.238534
70.5	i=	162.238481	-0.000058	162.238423	162.238587	162.238528
72.5	i=	162.238477	-0.000060	162.238417	162.238583	162.238523

64.5	e=	0.9672795251	0.0000022460	0.9672817711	0.9672797171	0.9672819633
65.5	e=	0.9672789890	0.0000028105	0.9672817995	0.9672791810	0.9672819916
66.5	e=	0.9672783710	0.0000032024	0.9672815734	0.9672785630	0.9672817654
67.5	e=	0.9672777403	0.0000033986	0.9672811389	0.9672779323	0.9672813309
68.5	e=	0.9672771371	0.0000034438	0.9672805809	0.9672773291	0.9672807729
69.5	e=	0.9672765793	0.0000034002	0.9672799795	0.9672767713	0.9672801715
70.5	e=	0.9672760716	0.0000033161	0.9672793877	0.9672762637	0.9672795796
71.5	e=	0.9672756128	0.0000032197	0.9672788325	0.9672758049	0.9672790245
72.5	e=	0.9672751990	0.0000031250	0.9672783240	0.9672753911	0.9672785160
64.5	a=	17.943116098	0.001505260	17.944621358	17.943115725	17.944621082
65.5	a=	17.942822288	0.001815394	17.944637682	17.942821904	17.944637366
66.5	a=	17.942483472	0.002030732	17.944514204	17.942483081	17.944513849
67.5	a=	17.942137629	0.002138596	17.944276225	17.942137238	17.944275841
68.5	a=	17.941806851	0.002163577	17.943970428	17.941806460	17.943970029
69.5	a=	17.941500942	0.002139749	17.943640691	17.941500555	17.943640287
70.5	a=	17.941222565	0.002093598	17.943316163	17.941222180	17.943315760
71.5	a=	17.940970949	0.002040777	17.943011726	17.940970567	17.943011326
72.5	a=	17.940744001	0.001988885	17.942732886	17.940743623	17.942732492

Table 11.
Comet Halley: Predicted Ephemeris

0^h E.T.		α 1950.0	Var. α	Aber.	δ 1950.0	Var. δ	Aberr.	ϱ	Var. ϱ
1981 Oct.	23	$7^h17^m36^s.23$	$3^s.99$	$0^s.26$	8°43' 3".9	-24".4	4".2	12.807	0.021
	27	7 17 13.88	4.06	0.36	8 39 49.3	-24.2	4.0	12.720	0.021
	31	7 16 46.16	4.13	0.45	8 36 46.4	-24.0	3.7	12.634	0.021
Nov.	4	7 16 13.09	4.21	0.54	8 33 56.6	-23.9	3.4	12.550	0.021
	8	7 15 34.71	4.30	0.63	8 31 21.2	-23.8	3.1	12.467	0.021
	12	7 14 51.10	4.40	0.72	8 29 1.1	-23.7	2.8	12.387	0.021
	16	7 14 2.36	4.51	0.81	8 26 57.6	-23.6	2.5	12.309	0.021
	20	7 13 8.62	4.63	0.88	8 25 11.7	-23.5	2.2	12.233	0.021
	24	7 12 10.02	4.76	0.96	8 23 44.3	-23.4	1.8	12.161	0.021
	28	7 11 6.77	4.89	1.03	8 22 36.4	-23.4	1.5	12.093	0.021
Dec.	2	7 9 59.14	5.04	1.10	8 21 49.0	-23.4	1.1	12.028	0.021
	6	7 8 47.44	5.19	1.16	8 21 22.5	-23.4	0.7	11.966	0.021
	10	7 7 32.03	5.35	1.21	8 21 17.5	-23.4	0.3	11.910	0.021
	14	7 6 13.27	5.52	1.25	8 21 34.2	-23.4	0.0	11.857	0.021
	18	7 4 51.53	5.69	1.29	8 22 12.9	-23.5	-0.4	11.809	0.021
	22	7 3 27.23	5.85	1.32	8 23 13.7	-23.6	-0.8	11.767	0.021
	26	7 2 0.81	6.04	1.35	8 24 36.6	-23.7	-1.1	11.729	0.021
	30	7 0 32.80	6.21	1.36	8 26 21.5	-23.9	-1.5	11.696	0.021
1982 Jan.	3	6 59 3.70	6.38	1.37	8 28 27.8	-24.1	-1.9	11.668	0.021
	7	6 57 34.05	6.57	1.37	8 30 55.0	-24.3	-2.2	11.645	0.021
	11	6 56 4.36	6.74	1.36	8 33 42.4	-24.5	-2.5	11.628	0.021
	15	6 54 35.14	6.91	1.35	8 36 49.0	-24.8	-2.8	11.616	0.021
	19	6 53 6.87	7.08	1.32	8 40 13.9	-25.1	-3.1	11.609	0.021

	23	6 51 40.08	7.25	1.29	8 43 56.2	-25.4	-3.4	11.607	0.021
	27	6 50 15.29	7.39	1.25	8 47 54.8	-25.7	-3.6	11.610	0.021
	31	6 48 53.01	7.55	1.20	8 52 8.2	-26.1	-3.9	11.617	0.021
Oct.	22	7 10 28.18	5.36	0.28	9 28 26.3	-33.6	4.0	10.777	0.024
	26	7 10 0.20	5.47	0.37	9 24 49.6	-33.3	3.8	10.687	0.024
	30	7 9 25.76	5.59	0.46	9 21 25.2	-33.1	3.6	10.598	0.024
Nov.	3	7 8 44.85	5.72	0.56	9 18 14.7	-32.9	3.3	10.511	0.024
	7	7 7 57.47	5.87	0.65	9 15 19.3	-32.7	3.0	10.426	0.024
	11	7 7 3.65	6.04	0.74	9 12 40.5	-32.6	2.8	10.343	0.024
	15	7 6 3.46	6.22	0.82	9 10 19.6	-32.5	2.5	10.263	0.024
	19	7 4 57.04	6.43	0.90	9 8 18.2	-32.3	2.1	10.185	0.024
	23	7 3 44.62	6.64	0.98	9 6 37.2	-32.1	1.8	10.111	0.024
	27	7 2 26.48	6.87	1.05	9 5 18.0	-32.1	1.5	10.040	0.024
Dec.	1	7 1 2.93	7.12	1.11	9 4 21.2	-32.1	1.2	9.973	0.024
	5	6 59 34.30	7.37	1.17	9 3 47.7	-32.0	0.8	9.910	0.024
	9	6 58 0.99	7.65	1.22	9 3 38.0	-32.0	0.5	9.851	0.024
	13	6 56 23.41	7.93	1.27	9 3 52.9	-32.1	0.1	9.797	0.024
	17	6 54 42.08	8.22	1.31	9 4 32.7	-32.2	-0.2	9.748	0.024
	21	6 52 57.57	8.52	1.34	9 5 37.6	-32.4	-0.6	9.704	0.024
	25	6 51 10.49	8.82	1.36	9 7 7.6	-32.6	-0.9	9.664	0.024
	29	6 49 21.47	9.13	1.37	9 9 2.3	-32.8	-1.3	9.630	0.024
1883 Jan.	2	6 47 31.14	9.43	1.38	9 11 21.3	-33.0	-1.6	9.602	0.024
	6	6 45 40.11	9.74	1.37	9 14 4.0	-33.3	-2.0	9.578	0.024
	10	6 43 49.05	10.04	1.36	9 17 9.7	-33.6	-2.3	9.560	0.024
	14	6 41 58.64	10.34	1.34	9 20 37.7	-34.0	-2.5	9.548	0.024
	18	6 40 9.59	10.62	1.31	9 24 27.0	-34.4	-2.8	9.540	0.024

Table 11.
Comet Halley: Predicted Ephemeris

0^h E.T.		α 1950.0	Var. α	Aberr.	δ 1950.0	Var. δ	Aberr.	ϱ	Var. ϱ
1983 Jan.	22	$6^h38^m22^s.56$	$10^s.90$	$1^s.27$	9°28'36".3	-34".8	-3".1	9.538	0.024
	26	6 36 38.21	11.17	1.23	9 33 4.0	-35.2	-3.3	9.540	0.024
	30	6 34 57.11	11.44	1.18	9 37 48.8	-35.6	-3.5	9.547	0.024
Feb.	3	6 33 19.80	11.70	1.12	9 42 49.0	-36.2	-3.7	9.559	0.024
	7	6 31 46.80	11.91	1.06	9 48 3.4	-36.6	-3.9	9.575	0.024
	11	6 30 18.60	12.08	0.99	9 53 30.1	-37.2	-4.0	9.596	0.024
	15	6 28 55.69	12.26	0.92	9 59 7.7	-37.7	-4.2	9.620	0.024
	19	6 27 38.46	12.44	0.83	10 04 54.2	-38.3	-4.3	9.647	0.024
Nov.	22	6 51 07.22	10.71	1.02	10. 9 8.7	-50.5	1.8	7.738	0.029
	26	6 49 19.97	11.20	1.09	10 7 32.9	-50.4	1.5	7.665	0.029
	30	6 47 25.13	11.72	1.15	10 6 22.4	-50.3	1.2	7.596	0.029
Dec.	4	6 45 23.17	12.28	1.21	10 5 38.6	-50.2	0.9	7.530	0.029
	8	6 43 14.65	12.86	1.25	10 5 22.3	-50.2	0.5	7.470	0.029
	12	6 41 0.25	13.47	1.30	10 5 34.4	-50.2	0.2	7.414	0.029
	16	6 38 40.72	14.10	1.33	10 6 15.3	-50.3	-0.1	7.364	0.029
	20	6 36 16.85	14.74	1.36	10 7 25.2	-50.4	-0.4	7.319	0.029
	24	6 33 49.45	15.39	1.37	10 9 3.9	-51.6	-0.7	7.279	0.029
	28	6 31 19.38	16.06	1.38	10 11 11.5	-50.8	-1.0	7.244	0.029
1984 Jan.	1	6 28 47.59	16.73	1.38	10 13 47.6	-51.2	-1.3	7.215	0.029
	5	6 26 15.08	17.39	1.37	10 16 51.9	-51.5	-1.5	7.192	0.029
	9	6 23 42.86	18.04	1.35	10 20 23.5	-51.9	-1.8	7.174	0.029
	13	6 21 11.98	18.68	1.32	10 24 21.4	-52.3	-2.0	7.162	0.029
	17	6 18 43.38	19.30	1.28	10 28 44.4	-52.8	-2.3	7.155	0.029

	21	6	16	18.00	19.89	1.24	10	33	30.8	-53.3	-2.5	7.155	0.028
	25	6	13	56.68	20.45	1.19	10	38	39.5	-53.9	-2.7	7.156	0.028
	29	6	11	40.30	20.98	1.13	10	44	8.9	-54.5	-3.0	7.164	0.028
Feb.	2	6	9	29.67	21.48	1.06	10	49	57.5	-55.2	-3.1	7.177	0.028
	6	6	7	25.56	21.93	0.99	10	56	3.6	-55.9	-3.3	7.193	0.028
	10	6	5	28.63	22.35	0.91	11	2	25.2	-56.6	-3.5	7.214	0.028
	14	6	3	39.41	22.73	0.82	11	9	0.4	-57.4	-3.6	7.238	0.028
	18	6	1	58.37	23.06	0.73	11	15	47.1	-58.3	-3.7	7.266	0.028
	22	6	0	25.86	23.34	0.64	11	22	43.7	-59.2	-3.8	7.296	0.028
	26	5	59	2.17	23.59	0.55	11	29	48.4	-60.1	-3.9	7.328	0.028
Mar.	1	5	57	47.60	23.79	0.45	11	36	59.4	-61.0	-4.0	7.363	0.028
	5	5	56	42.32	23.95	0.36	11	44	15.0	-62.0	-4.0	7.399	0.028
	9	5	55	46.43	24.07	0.27	11	51	33.2	-63.0	-4.0	7.437	0.028
	13	5	54	59.94	24.16	0.15	11	58	52.1	-64.1	-4.0	7.476	0.028
	17	5	54	22.76	24.20	0.06	12	6	10.1	-65.1	-4.0	7.515	0.028
	21	5	53	54.73	24.21	-0.03	12	13	25.3	-66.3	-4.0	7.554	0.028
Oct.	31	6	39	14.57	17.75	0.66	12	18	44.0	-110.4	2.7	5.277	0.036
Nov.	4	6	37	19.01	18.82	0.75	12	14	48.3	-110.2	2.6	5.182	0.036
	8	6	35	8.22	20.03	0.84	12	11	10.7	-109.9	2.4	5.090	0.036
	12	6	32	42.07	21.39	0.93	12	7	53.0	-109.6	2.2	5.001	0.036
	16	6	30	0.58	22.90	1.01	12	4	56.8	-109.2	2.0	4.916	0.036
	20	6	27	3.88	24.56	1.09	12	2	24.0	-108.7	1.8	4.834	0.036
	24	6	23	52.34	26.38	1.16	12	0	16.2	-108.3	1.6	4.757	0.036
	28	6	20	26.60	28.34	1.22	11	58	35.2	-107.7	1.4	4.685	0.036
Dec.	2	6	16	47.53	30.44	1.27	11	57	21.9	-107.0	1.1	4.618	0.036
	6	6	12	56.19	32.66	1.32	11	56	37.4	-106.3	0.9	4.556	0.036

Table 11.
Comet Halley: Predicted Ephemeris

0^h E.T.		α 1950.0	Var. α	Aberr.	δ 1950.0	Var. δ	Aberr.		Var. ϱ
1984 Dec.	10	$6^h\ 8^m53^s.81$	$35^s.00$	$1^s.35$	$11^\circ56'22''.5$	$-105''.4$	$0''.7$	4.500	0.036
	14	6 4 41.80	37.43	1.37	11 56 37.5	-104.5	0.5	4.449	0.036
	18	6 0 21.74	39.95	1.39	11 57 22.9	-103.4	0.3	4.405	0.036
	22	5 55 55.48	42.50	1.39	11 58 39.4	-102.2	0.1	4.366	0.036
	26	5 51 25.06	45.07	1.39	12 0 27.2	-101.0	-0.1	4.334	0.036
	30	5 46 52.63	47.63	1.36	12 2 46.5	- 99.6	-0.3	4.309	0.036
1985 Jan.	3	5 42 20.34	50.16	1.34	12 5 37.0	- 98.2	-0.5	4.289	0.036
	7	5 37 50.31	52.62	1.30	12 8 58.4	- 96.8	-0.7	4.275	0.036
	11	5 33 24.58	54.99	1.25	12 12 49.8	- 95.4	-0.9	4.268	0.036
	15	5 29 5.12	57.24	1.19	12 17 11.3	- 94.0	-1.1	4.265	0.035
	19	5 24 53.83	59.36	1.12	12 22 2.4	- 92.8	-1.3	4.269	0.035
	23	5 20 52.54	61.32	1.04	12 27 23.0	- 91.5	-1.5	4.277	0.035
	27	5 17 2.82	63.12	0.96	12 33 12.2	- 90.6	-1.7	4.289	0.035
	31	5 13 26.03	64.75	0.87	12 39 29.1	- 89.9	-1.9	4.306	0.035
Feb.	4	5 10 3.20	66.20	0.78	12 46 12.3	- 89.1	-2.1	4.327	0.035
	8	5 6 55.19	67.48	0.68	12 53 20.8	- 88.8	-2.2	4.351	0.035
	12	5 4 2.59	68.59	0.58	13 0 53.6	- 88.8	-2.4	4.377	0.035
	16	5 1 25.95	69.52	0.47	13 8 49.7	- 89.0	-2.5	4.406	0.035
	20	4 59 5.62	70.30	0.36	13 17 7.7	- 89.6	-2.7	4.437	0.035
	24	4 57 1.75	70.92	0.26	13 25 46.2	- 90.4	-2.8	4.469	0.035
	28	4 55 14.28	71.41	0.15	13 34 43.5	- 91.8	-3.0	4.503	0.035
Mar.	4	4 53 42.99	71.77	0.04	13 43 57.5	- 93.5	-3.1	4.536	0.035
	8	4 52 27.54	72.01	-0.06	13 53 26.5	- 95.4	-3.3	4.570	0.035

	12	4	51	27.54	72.14	-0.16	14	3	8.8	- 97.7	-2.3	4.603	0.035
	16	4	50	42.61	72.17	-0.26	14	13	3.0	-100.5	-3.4	4.636	0.036
	20	4	50	12.31	72.07	-0.36	14	23	7.3	-103.1	-3.4	4.667	0.036
	24	4	49	56.12	71.98	-0.46	14	33	20.0	-106.9	-3.5	4.697	0.036
	28	4	49	53.45	71.77	-0.54	14	43	39.1	-110.7	-3.5	4.725	0.036
Apr.	1	4	50	3.66	71.50	-0.63	14	54	2.3	-114.8	-3.5	4.751	0.036
	5	4	50	26.09	71.18	-0.71	15	4	28.0	-119.2	-3.5	4.775	0.036
	9	4	51	0.13	70.81	-0.80	15	14	54.8	-123.9	-3.5	4.796	0.037
	13	4	51	45.23	70.39	-0.87	15	25	21.2	-128.9	-3.5	4.814	0.037
	17	4	52	40.86	69.94	-0.94	15	35	45.6	-134.3	-3.4	4.829	0.037
	21	4	53	46.44	69.45	-1.00	15	46	6.5	-140.0	-3.3	4.841	0.037
Aug.	23	6	3	54.48	40.43	-0.75	19	21	44.2	-503.8	1.3	3.181	0.055
	25	6	4	52.61	39.70	-0.72	19	23	41.3	-515.7	1.3	3.124	0.055
	27	6	5	48.39	38.97	-0.68	19	25	39.6	-528.3	1.4	3.067	0.055
	29	6	6	41.64	38.24	-0.64	19	27	39.6	-541.2	1.4	3.009	0.056
	31	6	7	32.17	37.50	-0.60	19	29	42.0	-554.8	1.4	2.950	0.056
Sep.	2	6	8	19.77	36.78	-0.56	19	31	47.2	-569.0	1.4	2.891	0.056
	4	6	9	4.21	36.08	-0.52	19	33	56.0	-584.0	1.4	2.831	0.057
	6	6	9	45.22	35.39	-0.48	19	36	8.9	-599.6	1.4	2.770	0.057
	8	6	10	22.53	34.74	-0.44	19	38	26.6	-616.1	1.4	2.709	0.057
	10	6	10	55.82	34.11	-0.39	19	40	49.9	-633.4	1.4	2.648	0.058
	12	6	11	24.76	33.53	-0.35	19	43	19.7	-651.8	1.4	2.586	0.058
	14	6	11	48.95	32.99	-0.30	19	45	57.0	-671.2	1.4	2.523	0.058
	16	6	12	8.01	32.53	-0.26	19	48	42.5	-691.8	1.4	2.460	0.059
	18	6	12	21.46	32.17	-0.21	19	51	37.7	-713.7	1.3	2.397	0.059
	20	6	12	28.85	31.90	-0.16	19	54	43.4	-737.1	1.3	2.334	0.059

TABLE 11 continued

Table 11.
Comet Halley: Predicted Ephemeris

0^h E.T.	α 1950.0	Var. α	Aberr.	δ 1950.0	Var. δ	Aberr.	ϱ	Var. ϱ
1985 Sep. 22	$6^h12^m29^s.65$	31.76	-0.11	19°58′ 1.″2	-762.″0	1.″3	2.270	0.060
24	6 12 23.29	31.77	-0.06	20 1 32.2	-788.7	1.2	2.206	0.060
26	6 12 9.13	31.97	-0.01	20 5 17.9	-817.3	1.2	2.141	0.060
28	6 11 46.45	32.42	0.04	20 9 19.8	-848.0	1.2	2.077	0.061
30	6 11 14.44	33.12	0.09	20 13 39.3	-881.2	1.1	2.012	0.061
Oct. 2	6 10 32.18	34.17	0.15	20 18 18.4	-917.0	1.1	1.947	0.061
4	6 9 38.60	35.63	0.20	20 23 18.5	-955.8	1.0	1.882	0.062
6	6 8 32.53	37.59	0.26	20 28 41.7	-997.8	1.0	1.817	0.062
8	6 7 12.60	40.14	0.32	20 34 29.7	-1043.5	0.9	1.753	0.063
10	6 5 37.28	43.45	0.37	20 40 44.6	-1093.2	0.9	1.688	0.063
12	6 3 44.77	47.63	0.43	20 47 28.0	-1147.4	0.9	1.623	0.064
14	6 1 33.09	52.92	0.49	20 54 42.0	-1206.7	0.8	1.559	0.064
16	5 58 59.89	59.54	0.56	21 2 28.1	-1271.5	0.8	1.495	0.064
18	5 56 2.57	67.79	0.62	21 10 47.7	-1342.2	0.8	1.431	0.064
20	5 52 38.06	78.05	0.68	21 19 41.2	-1419.3	0.8	1.368	0.065
22	5 48 42.88	90.77	0.75	21 29 8.6	-1503.1	0.8	1.305	0.065
24	5 44 12.93	106.51	0.81	21 39 7.9	-1593.8	0.9	1.244	0.066
26	5 39 3.46	125.99	0.88	21 49 35.6	-1691.6	0.9	1.183	0.066
28	5 33 8.96	150.07	0.95	22 0 24.7	-1795.2	1.0	1.123	0.066
30	5 26 23.03	179.79	1.02	22 11 24.3	-1903.5	1.1	1.064	0.066
Nov. 1	5 18 38.35	216.42	1.08	22 22 17.2	-2013.4	1.3	1.007	0.067
2	5 14 21.38	239.64	1.11	22 27 33.8	-2074.4	1.4	0.976	0.067
3	5 9 46.50	261.55	1.15	22 32 38.2	-2120.0	1.5	0.952	0.067

4	5	4	52.54	239.62	1.19	22	37	25.5	-2169.8	1.7	0.925	0.066
5	4	59	38.24	316.86	1.22	22	41	50.4	-2215.5	1.8	0.898	0.066
6	4	54	2.32	349.00	1.25	22	45	45.4	-2255.4	2.0	0.873	0.066
7	4	48	3.47	384.44	1.28	22	49	2.1	-2287.5	2.1	0.847	0.066
8	4	41	40.40	423.42	1.31	22	51	31.3	-2309.6	2.3	0.822	0.066
9	4	34	51.82	466.14	1.34	22	53	2.0	-2318.8	2.6	0.799	0.066
10	4	27	36.62	512.80	1.36	22	53	21.7	-2311.9	2.8	0.776	0.065
11	4	19	53.51	563.69	1.38	22	52	16.2	-2285.1	3.1	0.754	0.065
12	4	11	41.76	618.77	1.40	22	49	29.9	-2234.5	3.4	0.733	0.064
13	4	3	0.64	678.08	1.42	22	44	45.5	-2155.3	3.7	0.712	0.064
14	3	53	49.82	741.51	1.43	22	37	44.7	-2043.1	4.1	0.693	0.063
15	3	44	9.34	808.80	1.43	22	28	8.4	-1893.2	4.4	0.676	0.062
16	3	33	59.74	879.52	1.42	22	15	36.9	-1700.9	4.8	0.659	0.061
17	3	23	22.13	953.04	1.42	21	59	51.6	-1462.6	5.2	0.644	0.059
18	3	12	18.20	1028.57	1.41	21	40	34.9	-1175.4	5.5	0.630	0.058
19	3	0	50.39	1105.03	1.39	21	17	32.0	- 838.1	5.9	0.618	0.056
20	2	49	1.75	1181.28	1.36	20	50	32.0	- 451.1	6.2	0.608	0.055
21	2	36	55.96	1255.96	1.33	20	19	28.9	- 17.5	6.5	0.599	0.052
22	2	24	37.37	1327.66	1.28	19	44	22.9	457.7	6.8	0.592	0.050
23	2	12	10.66	1394.98	1.24	19	5	20.7	965.9	7.0	0.586	0.048
24	1	59	40.90	1456.61	1.18	18	22	36.3	1496.9	7.2	0.583	0.045
25	1	47	13.13	1511.39	1.12	17	36	29.9	2039.2	7.3	0.581	0.043
26	1	34	52.44	1558.39	1.05	16	47	28.5	2580.3	7.3	0.581	0.040
27	1	22	43.51	1597.03	0.98	15	56	2.9	3107.3	7.3	0.583	0.037
28	1	10	50.61	1627.00	0.91	15	2	47.8	3608.1	7.3	0.586	0.034
29	0	59	17.46	1648.35	0.83	14	8	18.5	4072.8	7.1	0.591	0.031

Table 11.
Comet Halley: Predicted Ephemeris.

0^h E.T.	α 1950.0	Var. α	Aberr.	δ 1950.0	Var. δ	Aberr.	ϱ	Var. ϱ
1985 Nov. 30	$0^h48^m\ 7^s.08$	$1661^s.37$	$0^s.76$	$13^\circ13'10''.3$	$4493''.0$	$6''.9$	0.598	0.028
Dec. 1	0 37 21.84	1666.60	0.68	12 17 56.7	4863.6	6.7	0.606	0.025
2	0 27 3.44	1664.79	0.60	11 23 7.7	5181.4	6.4	0.616	0.022
3	0 17 12.96	1656.74	0.53	10 29 9.9	5446.0	6.1	0.627	0.019
4	0 7 50.90	1643.36	0.45	9 36 25.3	5658.9	5.8	0.639	0.016
5	23 58 57.30	1625.55	0.38	8 45 11.5	5823.0	5.4	0.653	0.013
6	23 50 31.78	1603.49	0.31	7 55 42.3	5942.6	5.0	0.668	0.010
7	23 42 33.69	1580.01	0.24	7 8 6.9	6022.4	4.7	0.683	0.007
8	23 35 2.08	1558.18	0.17	6 22 31.8	6067.7	4.3	0.699	0.006
9	23 27 55.90	1526.22	0.11	5 38 59.9	6083.7	3.9	0.716	0.004
10	23 21 13.90	1497.75	0.05	4 57 32.3	6075.2	3.6	0.734	0.002
11	23 14 54.84	1468.88	-0.01	4 18 7.7	6046.4	3.2	0.752	-0.001
12	23 8 57.39	1439.98	-0.07	3 40 43.4	6002.2	2.8	0.771	-0.004
13	23 3 20.24	1411.36	-0.13	3 5 15.7	5945.7	2.4	0.791	-0.006
14	23 58 2.11	1383.27	-0.18	2 31 40.0	5880.2	2.1	0.810	-0.007
15	22 53 1.71	1355.91	-0.23	1 59 51.1	5808.3	1.8	0.830	-0.008
16	22 48 17.85	1329.41	-0.28	1 29 43.4	5732.2	1.5	0.850	-0.010
17	22 43 49.36	1303.87	-0.33	1 1 11.4	5653.9	1.1	0.871	-0.011
18	22 39 35.15	1279.37	-0.38	0 34 9.4	5574.9	0.8	0.892	-0.012
19	22 35 34.19	1255.97	-0.42	0 8 31.6	5496.5	0.5	0.913	-0.014
20	22 31 45.50	1233.68	-0.46	-0 15 47.5	5419.6	0.3	0.934	-0.015
21	22 28 8.16	1212.53	-0.50	-0 38 53.0	5345.0	0.0	0.955	-0.016
22	22 24 41.33	1192.52	-0.54	-1 0 50.2	5273.3	-0.2	0.981	-0.017

	23	22	21	24.19	1173.61	-0.58	-1	21	43.9	5205.0	-0.5	0.997	-0.018
	25	22	15	16.13	1139.08	-0.65	- 2	0	39.1	5079.9	-1.0	1.040	-0.020
	27	22	9	38.61	1108.77	-0.72	- 2	36	12.6	4971.5	-1.4	1.081	-0.022
	29	22	4	26.96	1082.48	-0.78	- 3	8	54.7	4880.4	-1.9	1.123	-0.023
	31	21	59	37.14	1059.84	-0.84	- 3	39	12.3	4807.0	-2.3	1.163	-0.023
1986 Jan.	2	21	55	5.60	1040.79	-0.90	- 4	7	29.4	4751.3	-2.6	1.203	-0.024
	4	21	50	49.22	1024.89	-0.95	- 4	34	7.2	4712.8	-3.0	1.241	-0.024
	6	21	46	45.25	1012.09	-1.00	- 4	59	24.8	4691.3	-3.3	1.278	-0.024
	8	21	42	51.23	1002.15	-1.04	- 5	23	39.6	4686.4	-3.6	1.314	-0.024
	10	21	39	4.97	994.86	-1.08	- 5	47	7.5	4697.8	-3.9	1.348	-0.024
	12	21	35	24.49	990.07	-1.12	- 6	10	3.2	4725.1	-4.1	1.380	-0.023
	14	21	31	48.03	987.56	-1.16	- 6	32	40.4	4767.8	-4.4	1.410	-0.022
	16	21	28	14.03	987.17	-1.19	- 6	55	12.0	4825.8	-4.6	1.439	-0.021
	18	21	24	41.16	988.66	-1.22	- 7	17	49.6	4898.3	-4.8	1.464	-0.019
	20	21	21	8.28	991.81	-1.24	- 7	40	44.3	4985.0	-5.0	1.487	-0.017
	22	21	17	34.51	996.32	-1.26	- 8	4	5.9	5084.8	-5.2	1.508	-0.016
	24	21	13	59.19	1001.88	-1.28	- 8	28	3.2	5196.7	-5.3	1.525	-0.013
	26	21	10	21.91	1008.13	-1.30	- 8	52	43.9	5319.0	-5.4	1.539	-0.010
	28	21	6	42.55	1014.64	-1.32	- 9	18	14.1	5449.7	-5.5	1.550	-0.007
	30	21	3	1.26	1020.96	-1.32	- 9	44	38.7	5586.8	-5.6	1.557	-0.004
Feb.	1	20	59	18.41	1026.69	-1.32	-10	12	0.7	5727.2	-5.6	1.560	-0.000
	3	20	55	34.63	1031.38	-1.33	-10	40	22.0	5868.5	-5.7	1.559	0.004
	5	20	51	50.64	1034.75	-1.33	-11	9	42.7	6007.7	-5.7	1.554	0.009
	7	20	48	7.28	1036.60	-1.33	-11	40	2.5	6142.8	-5.7	1.545	0.013
	9	20	44	25.30	1036.91	-1.32	-12	11	20.6	6272.4	-5.6	1.532	0.017
	11	20	40	45.38	1035.84	-1.31	-12	43	36.0	6395.7	-5.6	1.515	0.022

TABLE 11 concluded

Table 12.
Comet Halley: Basis Coordinates for Start of Integration

J.E.D. 2418588.5	x (S_1)	y (S_1)	z (S_1)
Venus	.3720827394320E+00	-.5615673140927E+00	-.2764641955338E+00
Earth + Moon	.9617121702447E+00	.2467671567426E+00	.1070555007404E+00
Mars	.1380402591052E+01	.2417910855197E+00	.7373661631856E-01
Jupiter	-.5434331995464E+01	.2043834768717E+00	.2206889954132E+00
Saturn	.8767959378869E+01	.3114463977633E+01	.9088856991986E+00
Uranus	.6921089069977E+01	-.1677881951750E+02	-.7450068957807E+01
Neptune	-.9232165223838E+01	.2628860026057E+02	.1100115593703E+02
Pluto	.2966449724886E+01	.4350623239824E+02	.1284122615541E+02
Comet Halley Va	.7583470709200E+00	.2875370029060E+01	.9130157841600E+00
Comet Halley Vb	.7583470796600E+00	.2875373161970E+01	.9130148344700E+00
Reduct. S_0 to S_1	-.5866000000000E-07	-.2750000000000E-08	.4560000000000E-08
J.E.D. 2418588.5	**x (S_0)**	**y (S_0)**	**z (S_0)**
Mercury	.3518821000000E+00	.1649250000000E-01	-.2737860000000E-01
Venus	.3720827980920E+00	-.5615673113427E+00	-.2764642000938E+00
Earth + Moon	.9617122289047E+00	.2467671594926E+00	.1070554961804E+00
Mars	.1380402649712E+01	.2417910882697E+00	.7373661175856E-01
Jupiter	-.5434331936804E+01	.2043834796217E+00	.2206889908532E+00
Saturn	.8767959437529E+01	.3114463980383E+01	.9088856946386E+00
Uranus	.6921089128637E+01	-.1677881951475E+02	-.7450068962367E+01
Neptune	-.9232165165177E+01	.2628860026332E+02	.1100115593247E+02
Pluto	.2966449783546E+01	.4350623240099E+02	.1284122615085E+02
Comet Halley Va	.7583471295700E+00	.2875370031810E+01	.9130157796000E+00
Comet Halley Vb	.7583471383200E+00	.2875373164720E+01	.9130148299100E+00

J.E.D. 2418980.5	x (S_1)	y (S_1)	z (S_1)
Venus	-.6279916783481E+00	-.3386502288602E+00	-.1128455365510E+00
Earth + Moon	.7337482620950E+00	.6115560461179E+00	.2652942813447E+00
Mars	-.1498983843619E+01	-.5573847068530E+00	-.2153935320705E+00
Jupiter	-.4861866114242E+01	-.2295881286949E+01	-.8660702134156E+00
Saturn	.7657333358135E+01	.4887470769569E+01	.1689679116348E+01
Uranus	.8329200959851E+01	-.1629049662946E+02	-.7256003880795E+01
Neptune	-.1040146026495E+02	.2591015470812E+02	.1087552406722E+02
Pluto	.2088319642487E+01	.4330097430078E+02	.1304238809606E+02
Comet Halley Va	-.3050450609914E+01	.5319811085182E+00	-.7103910662029E+00
Comet Halley Vb	-.3050452275879E+01	.5319976687797E+00	-.7103800878715E+00
Comet Halley VIa	-.3050459506130E+01	.5319764125800E+00	-.7103953879600E+00
Comet Halley VIb	-.3050463810600E+01	.5319948555000E+00	-.7103846773000E+00
Reduct. S_0 to S_1	.6354000000000E-07	.3054000000000E-07	.9814000000000E-08

Final Coordinates

J.E.D. 2444240.5	x (S_0)	y (S_0)	z (S_0)
Comet Halley Va	-.4996041993945E+01	.1516167456123E+02	.2359277198460E+01
Comet Halley Vb	-.4996017063671E+01	.1516168218334E+02	.2359298416028E+01
Comet Halley VIa	-.5005461545914E+01	.1517690737548E+02	.2360420022175E+01
Comet Halley VIb	-.5005435999270E+01	.1517691415756E+02	.2360441220376E+01
Reduct. S_0 to S_1	.3307290000000E-07	.6299690000000E-07	.3034100000000E-07

Table 12.
Comet Halley: Basis Velocities for Start of Integrations.

J.E.D. 2418588.5	dx/dt (S_0)	dy/dt (S_0)	dz/dt (S_0)
Venus	.172438908899 12E-01	.976503252979 27E-02	.330844902024 90E-02
Earth + Moon	-.491604319803 10E-02	.151459264706 11E-01	.657023004694 79E-02
Mars	-.194495201989 08E-02	.135741592778 65E-01	.628299620023 94E-02
Jupiter	-.464789391798 72E-03	-.661173887319 25E-02	-.282542359702 46E-02
Saturn	-.222865984247 43E-02	.479077841443 39E-02	.207638286506 21E-02
Uranus	.364716086125 47E-02	.111826552519 65E-02	.438448351108 96E-03
Neptune	-.300529947789 44E-02	-.908984962895 62E-03	-.296815095294 35E-03
Pluto	-.224008860417 03E-02	-.496726235485 39E-03	.521182099695 40E-03
Comet Halley Va	.268688972654 00E-02	-.126865346307 00E-01	-.236561930790 00E-02
Comet Halley Vb	.268687400770 00E-02	-.126865297600 00E-01	-.236562942290 00E-02
Reduct. S_0 to S_1	.958600000000 00E-09	-.431070000000 00E-08	-.240670000000 00E-08

J.E.D. 2418588.5	dx/dt (S_0)	dy/dt (S_0)	dx/dt (S_0)
Mercury	-.575154000000 00E-02	.258641200000 00E-01	.144402500000 00E-01
Venus	.172438899313 12E-01	.976503684049 27E-02	.330845142694 90E-02
Earth + Moon	-.491604415663 10E-02	.151459307813 11E-01	.657023245364 79E-02
Mars	-.194495297849 08E-02	.135741635885 65E-01	.628299860693 94E-02
Jupiter	-.464790350398 72E-03	-.661173456249 25E-02	-.282542119032 46E-02
Saturn	-.222866080107 43E-02	.479078272513 39E-02	.207638527176 21E-02
Uranus	.364715990265 47E-02	.111826983589 65E-02	.438450757808 96E-03
Neptune	-.300530043649 44E-02	-.908980652195 62E-03	-.296812688594 35E-03
Pluto	-.224008956277 03E-02	-.496721924785 39E-03	.521184506395 40E-03
Comet Halley Va	.268688876794 00E-02	-.126865303200 00E-01	-.236561690120 00E-02
Comet Halley Vb	.268687304910 00E-02	-.126865254493 00E-01	-.236562701620 00E-02

J.E.D. 2418980.5	dx/dt (S_1)	dy/dt (S_1)	dz/dt (S_1)
Venus	-.98223830155442E-02	-.15908991893113E-01	-.77867842475649E-02
Earth + Moon	-.11850520872740E-01	.11627646964681E-01	.50438986855709E-02
Mars	.57241254296914E-02	-.10686066562883E-01	-.50593230880308E-02
Jupiter	.33155783725653E-02	-.58442615729121E-02	-.25886479008709E-02
Saturn	-.34180266707703E-02	.42093324393680E-02	.18874557074356E-02
Uranus	.35336484791820E-02	.13718640678921E-02	.55114572467727E-03
Neptune	-.29596789219142E-02	-.10212369338571E-02	-.34392680946788E-03
Pluto	-.22400148053003E-02	-.55024430495935E-03	.50521888527470E-03
Comet Halley Va	-.10581510960364E-01	.75311503375451E-02	-.10714345208538E-02
Comet Halley Vb	-.10581484585989E-01	.75311858337442E-02	-.10713927433074E-02
Comet Halley VIa	-.10581578440000E-01	.75311219156600E-02	-.10714640806300E-02
Comet Halley VIb	-.10581545033100E-01	.75311562031000E-02	-.10714206679000E-02
Reduct. S_0 to S_1	-.11418000000000E-08	.34713000000000E-08	.19761000000000E-08

Final Velocities

J.E.D. 2444240.5	dx/dt (S_0)	dy/dt (S_0)	dz/dt (S_0)
Comet Halley Va	.23871124047642E-02	.38026852618534E-02	-.27662379619593E-03
Comet Halley Vb	.23871036447878E-02	-.38026893320326E-02	-.27663309506129E-03
Comet Halley VIa	.23857225384082E-02	-.37985982811474E-02	-.27600003707802E-03
Comet Halley VIb	.23857138584609E-02	-.37986026010257E-02	-.27600936959510E-03
Reduct. S_0 to S_1	-.32976340000000E-08	.14420700000000E-08	.11109600000000E-08

Table 13.
Integrated Elements of Comet Olbers Based on Improved Elements 1955 (VII C)

Elements	1815 (VII a)	1887 (VII b)	1955 (VII C)	2023 (VII d)
Osculation	2384250.5	2410550.5	2435320.5	2460000.5
x	-0.793907136	-0.708888372	2.566460980	3.766649922
y	-2.404254313	0.270538186	2.966922831	3.271100821
z	-0.401071969	0.929620751	1.273466768	-2.437346339
dx/dt	0.00339630757	-0.008436445507	-0.007988662498	-0.006604721062
dy/dt	-0.01066512733	-0.020080955946	-0.002857598905	-0.001404039502
dz/dt	-0.00942952765	-0.001323531605	0.007348293310	0.006589805078
T (J.E.D.)	2384084.48910	2410553.47168	2435643.65225	2460487.28282
T (E.T.)	1815 4 20.98910	1887 10 8.97293	1956 6 19.15225	2024 6 25.78282
ω Ecliptic	65°.573314	65°.344061	64°.627618	64°.377599
Ω 1950.0	85.337983	85.366492	85.416008	85.235710
i	44.499160	44.569836	44.607568	44.619470
q	1.212825768	1.19911627	1.17866090	1.17503019
e	0.931680321	0.930979122	0.930255960	0.930227660
a	17.75221701	17.37323983	16.89980827	16.84091696
n	0°.013177262957	0°.01361077603	0°.01418670192	0°.01426118154
Px	-0.613658317	-0.611630368	-0.606958096	-0.603658298
Py	0.172643763	0.175691275	0.186569629	0.192280591
Pz	0.770465834	0.771388922	0.772524202	0.773708494

Q_x	-0.367980569	-0.369634506	-0.376298791	-0.381629857
Q_y	-0.925883210	-0.925526736	-0.923650841	-0.921760197
Q_z	-0.085618820	-0.082283676	-0.072583361	-0.068678882

All figures in this table are in barycentre S_1 and $k(\sqrt{1 + m_1})$ = 0.01720210038 is used to derive the elements.

Table 14.

Comet Olbers: J.E.D.	Normal Places α 1950.0	Normal Places δ 1950.0	Perturbation dα	Perturbation dδ	Residuals dα cos δ	Residuals dδ	Weight
2384049.96285	54°52' 2".1	37°50'16".6	13".6	3".2	2".8	12".9	2
4063.96285	61 56 46.7	44 50 7.3	12.6	1.0	8.6	15.5	7
4073.96285	69 2 35.8	49 44 6.0	11.8	- 0.7	9.3	12.6	9
4085.96285	80 46 45.4	55 11 2.7	10.2	- 3.1	5.5	6.9	5
4098.96285	98 56 10.8	59 41 17.5	7.7	- 5.8	2.5	- 3.4	8
4109.96285	118 55 58.3	61 10 30.0	4.7	- 6.7	0.3	9.0	6
4122.96285	144 5 16.3	58 50 17.2	0.7	- 7.8	- 5.3	1.3	5
4134.96285	163 38 40.2	52 56 17.1	- 1.3	- 5.9	-12.7	5.6	5
4148.96285	180 21 2.7	43 23 33.5	- 2.7	- 3.3	- 1.9	8.8	3
4160.96285	190 49 6.0	34 31 55.9	- 2.8	- 2.0	- 2.6	10.6	6
4184.96285	206 1 52.7	18 22 20.1	- 1.6	- 0.4	8.4	-15.5	1
4210.96285	218 32 35.7	5 7 57.2	- 0.6	0.0	13.5	- 1.0	0
2410516.0	136 28 13.5	29 41 9.8	0.0	- 0.1	- 1.3	0.6	24
532.0	155 12 29.0	29 37 6.0	0.0	0.0	- 1.5	0.1	36
543.0	168 46 47.0	28 9 25.1	0.0	0.0	- 0.5	- 0.5	13
566.0	195 51 4.0	21 38 55.7	0.0	0.0	2.9	- 0.5	13
589.0	218 9 16.1	13 9 1.6	0.1	- 0.2	4.7	- 1.2	7
609.0	233 30 6.4	6 30 42.8	0.1	- 0.6	4.4	- 2.2	4
629.0	245 54 44.0	1 21 11.4	0.1	- 1.0	4.8	- 3.1	7
653.0	257 46 21.8	- 2 59 30.8	- 0.1	- 1.6	5.7	- 5.5	4
684.0	268 49 50.8	- 6 31 42.2	- 1.0	- 2.7	4.7	- 3.5	2
719.0	275 12 50.1	- 9 20 47.7	- 3.2	- 4.7	7.1	- 3.6	2
734.0	275 37 44.1	-10 37 20.9	- 4.6	- 5.7	3.7	- 5.6	1

2435423.82352	61 38 43.5	-19 54 46.1	- 2.0	- 0.8	3.5	- 0.2	4
487.00169	44 18 21.6	- 9 34 48.0	- 6.3	- 0.9	- 0.4	- 1.4	10
510.16260	43 31 19.8	- 1 40 23.9	- 7.7	- 0.3	0.3	0.1	24
542.84532	48 47 26.4	10 28 0.1	- 9.1	1.6	- 1.1	1.2	22
569.66930	58 18 48.8	20 56 57.2	- 9.3	4.9	1.8	- 1.8	6
583.96790	65 4 34.9	26 19 51.8	- 8.5	7.5	0.9	- 0.6	6
600.10550	75 24 18.3	32 43 7.0	- 5.3	11.4	- 2.2	0.1	4
612.68104	85 25 21.3	37 19 10.9	0.1	14.6	0.0	1.5	6
630.61402	103 48 4.5	42 36 57.7	15.1	17.4	0.4	- 0.8	4
653.11957	123 37 53.0	44 26 12.9	44.3	10.0	- 0.7	1.7	4
675.11800	163 42 24.8	38 26 7.1	59.1	11.7	- 0.3	- 3.7	4
700.58413	190 39 9.8	25 8 0.8	51.7	34.2	- 1.3	- 1.5	11
719.06780	205 6 47.8	15 7 3.9	42.9	41.0	1.7	1.5	4
728.54636	211 24 54.4	10 28 59.2	38.9	42.0	0.6	1.5	4

The values of the original weights for 1815 and 1887 have been reduced in order to obtain homogeneity between the old systems and the new one used for the 1956 apparition.

Table 15.
Predicted Ephemeris for Comet Olbers.

0^h E.T.	α 2000.0	δ 2000.0	ϱ	r	Var. α	Var. δ	Var. ϱ	Var. r
2023 Aug. 14	$4^h 16^m 20^s$	$-13^\circ 59'.8$	4.060	4.066	$-101^s.6$	$-23'.6$	0.078	0.046
24	4 21 46	-14 31.5	3.843	3.972	-110.9	- 24.8	0.079	0.047
Sep. 3	4 26 5	-15 12.1	3.626	3.877	-120.9	- 26.0	0.080	0.047
13	4 29 0	-16 0.7	3.413	3.782	-131.5	- 27.1	0.082	0.048
23	4 30 15	-16 55.8	3.205	3.685	-142.4	- 28.2	0.085	0.048
Oct. 3	4 29 34	-17 54.8	3.007	3.588	-153.1	- 29.0	0.088	0.048
13	4 26 39	-18 54.2	2.822	3.490	-162.8	- 29.6	0.092	0.049
23	4 21 19	-19 48.5	2.652	3.391	-170.5	- 30.0	0.096	0.049
Nov. 2	4 13 31	-20 31.1	2.503	3.292	-174.8	- 30.1	0.101	0.050
12	4 3 25	-20 54.3	2.376	3.191	-174.2	- 30.2	0.107	0.050
22	3 51 33	-20 50.0	2.274	3.090	-167.7	- 30.4	0.112	0.050
Dec. 2	3 38 43	-20 11.9	2.197	2.987	-155.6	- 31.0	0.118	0.051
12	3 25 58	-18 57.2	2.146	2.885	-138.9	- 32.5	0.122	0.051
22	3 14 21	-17 6.3	2.118	2.780	-120.0	- 34.9	0.126	0.052
2024 Jan. 1	3 4 47	-14 43.8	2.111	2.676	-101.3	- 38.1	0.129	0.052
11	2 57 50	-11 56.0	2.119	2.571	- 84.9	- 42.1	0.131	0.052
21	2 53 47	- 8 49.2	2.139	2.465	- 72.1	- 46.5	0.133	0.053
31	2 52 41	- 5 30.1	2.165	2.359	- 63.3	- 51.3	0.134	0.053
Feb. 10	2 54 26	- 2 2.2	2.193	2.253	- 58.7	- 56.2	0.135	0.053
20	2 58 52	1 31.2	2.220	2.147	- 58.4	- 61.3	0.135	0.053

Mar. 1	3	5	50	5	8.4	2.242	2.041	- 62.1	- 66.4	0.135	0.053
11	3	15	13	8	48.5	2.257	1.936	- 70.3	- 71.8	0.134	0.053
21	3	26	56	12	31.1	2.264	1.832	- 83.2	- 77.3	0.134	0.052
31	3	41	3	16	16.0	2.261	1.730	-102.0	- 83.0	0.133	0.051
Apr.10	3	57	40	20	3.0	2.247	1.632	-127.8	- 88.9	0.132	0.049
20	4	17	4	23	51.3	2.224	1.538	-163.0	- 94.7	0.131	0.047
30	4	39	37	27	39.3	2.191	1.450	-210.2	-100.2	0.130	0.044
Maj 10	5	5	54	31	23.6	2.149	1.370	-273.9	-104.6	0.128	0.040
20	5	36	38	34	58.5	2.100	1.300	-358.4	-107.3	0.125	0.035
30	6	12	41	38	14.0	2.047	1.244	-467.9	-106.4	0.120	0.028
Jun. 9	6	54	45	40	55.4	1.993	1.203	-602.5	-100.0	0.115	0.020
19	7	42	59	42	42.6	1.942	1.180	-751.4	- 85.7	0.107	0.012
29	8	36	14	43	13.3	1.901	1.177	-887.4	- 62.1	0.095	0.001
Jul. 9	9	31	47	42	10.7	1.875	1.193	-972.6	- 30.5	0.081	-0.008
19	10	26	4	39	31.6	1.869	1.228	-980.9	4.4	0.063	-0.018
29	11	16	10	35	31.0	1.888	1.279	-919.0	36.1	0.042	-0.026
Aug. 8	12	0	39	30	34.5	1.935	1.345	-815.8	60.1	0.020	-0.033
18	12	39	33	25	11.3	2.009	1.422	-701.4	74.6	-0.003	-0.038
28	13	13	34	19	45.8	2.109	1.507	-594.1	80.8	-0.023	-0.042
Sep. 7	13	43	39	14	35.0	2.229	1.600	-501.1	80.2	-0.042	-0.046
17	14	10	37	9	48.7	2.365	1.697	-423.5	77.0	-0.058	-0.049
27	14	35	11	5	30.9	2.513	1.797	-359.7	71.4	-0.071	-0.050
Oct. 7	14	57	51	1	42.3	2.666	1.900	-307.4	65.0	-0.082	-0.051
17	15	19	2	-1	38.4	2.822	2.005	-264.4	58.8	-0.090	-0.052
27	15	38	58	-4	15.9	2.975	2.110	-228.8	53.0	-0.097	-0.053

References

1. F. W. Bessel. Abhandl. der Königl. Akademie der Wissens. Berlin 1812–1813 p. 119.
2. F. W. Ginzel. Veröff. Rechen-Inst. Berlin Nr. 3 1893.
3. H. Q. Rasmusen 1. Kgl. Danske Vidensk. Selsk. Mat.-Fys. Medd. 24 Nr. 18 1948 and 2. Publ. og Mindre Medd. fra Københavns Observatorium Nr. 194 1967.
4. P. H. Cowell and A. C. D. Crommelin. Publ. der Astron. Gesells. XXIII. 1910.
5. P. E. Zadunaisky. The Astronom. Journal Vol. 71 Nr. 1 1966.
6. H. Westphalen. Astronom. Nachrichten No. 573, 574, 575. 1846.
7. P. Herget. Astronomical Papers Vol. XIV. 1953.
8. G. Stracke. Bahnbestimmung der Planeten und Kometen. p. 321. 1929.
9. J. Schubart and P. Stumpff. Veröff. Astron. Rechen-Inst. Heidelberg Nr. 18. 1966.
10. Duncombe, Tufekcioglu and Larson. United States Naval Observ. Circ. Nr. 106. 1965.
11. G. M. Clemence. Astronomical Papers Vol. XIII Part UV. 1953.
12. H. Q. Rasmusen and O. K. Hesselberg. Kgl. Danske Vidensk. Selsk. Mat.-Fys. Medd. 28-10 195
13. Rosenberger. Astronm. Nachr. XII. 190. 1835.
14. D. K. Yeomans. Astronomical Journal Vol. 82 Nr. 6. 1977.

Errata.

Page 22 column 2 line 7 for $188^{\circ}35'23\overset{''}{.}038$ read $188^{\circ}35'22\overset{''}{.}038$
column 4 line 13 for $46\overset{''}{.}4561187966$ read $46\overset{''}{.}456118681$
column 4 line 14 for $27897\overset{d}{.}293910$ read $27897\overset{d}{.}293980$
Page 28 column 9 line 9 for 2.37 read -2.37

Indleveret til Selskabet oktober 1978.
Færdig fra trykkeriet september 1979.

Statistics of Particle Penetration

By PETER SIGMUND

Det Kongelige Danske Videnskabernes Selskab
Matematisk-fysiske Meddelelser **40**:5

Kommissionær: Munksgaard
1978

Contents

Synopsis

An attempt is made to formulate a statistical theory of particle penetration phenomena in real, i.e. nonrandom stopping media. The treatment concentrates on individual collision events that are well localized in space, but correlated via the trajectory of the penetrating particle. Since Poisson statistics does not govern a sequence of collision events in an ordered structure, the mean-free-path concept fails, and penetration theory has to be developed from the bottom. As it turns out, the cross section keeps to be the leading concept when defined as an atomic parameter without recourse to the mean free path. However, a sequence of competing correlation terms occurs which do not influence the average behavior of the beam but enter fluctuations and higher-order averages. These correlation terms depend on the structure of the stopping medium. The leading one contains the pair correlation function of the structure, and can be expressed in terms of the structure factor as measured in x-ray or neutron diffraction.

As a main result, one obtains an extension of Bothe's formula—which governs the statistics of particle penetration through thin layers—to ordered matter. The more specific discussion refers to energy loss and multiple scattering of heavy charged particles, as well as inner-shell processes, in ideal molecular gases, real gases, and amorphous solids or liquids. Previous results derived for the energy loss and multiple scattering of ions in molecular gases are contained in the present description. In that work it has already been documented that correlation effects may become pronounced when the cross sections are large. The present work shows that correlations may be positive or negative, dependent on whether the attractive or repulsive interaction between target particles dominates in the range of impact parameters governing the collision events in question.

PETER SIGMUND
Physical Laboratory II
H. C. Ørsted Institute
DK-2100 Copenhagen Ø

present address:
Physics Institute
Odense University
DK-5230 Odense

Printed in Denmark by Bianco Lunos Bogtrykkeri A-S. ISSN 0023-3323. ISBN 87-7304-067-3

1. Introduction

In studies of the interaction of particles with matter, it is convenient to distinguish between collision and penetration phenomena. Collisions are distinct events on a microscopic level, such as the excitation of an electron by an alpha particle or the dissociation of a molecule by a photon. Penetration phenomena may be observed on a larger scale, under conditions where the chance for one particle to undergo several collisions is appreciable. Typical examples of penetration phenomena are the stopping and multiple scattering of charged particles in dense matter, and various ionization phenomena.

From an experimental point of view, the transition between collision and penetration phenomena is gradual. Collision phenomena are investigated by means of thin targets to ensure single events. The requirements to be imposed on a target in order to be called "thin" depend on the desired accuracy of experimental results. Even in a dilute gas target, there is a non-zero probability for more than one collision in an individual passage.

From a theoretical point of view, one may consider collision events to be governed by the appropriate equations of motion, such as Schrödinger's equation, while statistical considerations are essential in the treatment of penetration phenomena.

The statistical theory of particle penetration was developed early in this century[1-4]. This theory is generally based on the assumption of statistical independence of different collision events. Therefore, quantitative predictions originate in Poisson's distribution, Boltzmann's equation, or equivalent first principles.

According to standard penetration theory[5], the probability P for a projectile to initiate a certain event while penetrating a small path length Δx is

$$P = \mathcal{N}\Delta x\sigma\,, \tag{1}$$

where $\mathcal{N}$ is the number of target particles (atoms, molecules, electrons, etc) per volume, and σ the cross section for the event in question. A necessary condition for sucessive events to be statistically independent is the possibility to make Δx small enough so that $P \ll 1$. A lower limit of Δx is set by the duration of a collision. For an order-of-magnitude estimate, take an interaction radius a, and set $\Delta x \gtrsim 2a$, $\sigma \sim \pi a^2$, and $\mathcal{N} \sim (3/4\pi)(2/d)^3$, where d is a mean interparticle spacing in the target. Then, successive collisions can be statistically independent only if

$$P \sim 12(a/d)^3 \ll 1\,; \tag{2}$$

For processes on an atomic scale, this condition is easily fulfilled when the target is a gas. In solid or other dense media, eq. (2) is obeyed for processes on a nuclear scale, while for atomic processes, it is more or less violated except for very rare events.

Once eq. (2) is not fulfilled, the concept of a free flight path becomes meaningless, and hence Poisson statistics does not readily apply. Conversely, the very fact of an appreciable probability for a projectile to interact with every target particle along its path suggests an influence of target structure on the statistics of collision processes. Another important consequence is the possibility of collective processes that has been pointed out long ago[6,7].

The present paper deals with the statistics of penetration phenomena in situations where the basic collision events are well-localized but not statistically independent. There is a wide range of penetration phenomena—in particular in solid targets—where correlations between individual collision events are nonnegligible but not dominating. In the opposite case of strong correlation, a redefinition of the basic collision event may be possible such as to make correlations weak. An attempt is made in this work to provide a description that is flexible enough to allow for both spatial and other types of correlations.

The relation between such a treatment and conventional penetration theory is similar in several ways to that between the kinetic theory of real and ideal gases, and some of the statistical methods applied here are indeed common in gas theory.

Despite the desired flexibility, the guiding principles have been chosen to aim at a treatment of heavy-charged-particle penetration phenomena, where the importance of correlation effects has been documented recently[8–12].

At present, the treatment has been limited to the case of negligible feedback of collisions on the motion of the projectile particle. This implies small energy loss and deflection and, more important, neglect of possible changes of projectile state during penetration. A more general treatment incorporating the latter class of phenomena is in preparation[13].

In sects. 2 & 3, general expressions are derived for the frequency spectrum of individual collision events and the cumulative effect of collisions in the presence of correlations. The main result of this treatment is a generalization of Bothe's formula[2] to correlated systems. In sections 4 and 5, spatial correlations are considered by means of an impact-parameter treatment of individual collisions. In section 6, comments will be made on how to select suitable statistical variables, and in section 7, various methods of evaluating cumulative effects are extended to correlated systems. Finally, section 8 contains more explicit results for energy loss and multiple scattering. In particular, this section provides the link between the general considerations made in the present work and the more special situations treated earlier[9,10,12].

2. Statics of a Single Type of Event

Take a target with a number of independent degrees of freedom, or modes of excitation, and consider a specific event, called A in the following. As an example, take a solid target, and denote by A the process of K-shell excitation in any of the constituent atoms of the solid which may be assumed monoatomic for the moment.

Let a projectile interact with the target, but disregard all action of the target on the projectile. Within the above example, take an energetic ion moving on a straight line through the solid with negligible energy loss, and disregard electron capture and loss as well as excitation and deexcitation of the ion.

In the following, it will be convenient to speak of an "ion" and "target atoms" as well as the "passage" of an ion, even though the projectile need not be an ion and the target particles might be electrons, nucleons, molecules, plasmons, phonons, etc. It will, however, be assumed that the target has macroscopic dimensions, i.e., that the number of target atoms is large.

Even though we deal with independent modes of excitation in the target, there may exist a more or less pronounced correlation of events A in any individual passage. Within the above example, only those atoms have nonzero probability for K-shell excitation that are located within some microscopically small distance from the trajectory of the ion. Thus, excitation processes in different target atoms are correlated via the trajectory of the ion.

Suppose there are z different ways of initiating event A, i.e. z different target atoms. Let P_i $(i = 1, \ldots z)$ be the probability for initiating A in the i-th atom in a particular passage. Then, the probability F_n for n events A in that passage is given by

$$F_n = \sum_{1 \le i_1 < \ldots < i_n \le z} P_{i_1} \ldots P_{i_n} \cdot \prod_{j(\neq i_1, \ldots i_n)} (1 - P_j) \; ; \; n = 0, 1, \ldots z \; ; \tag{3}$$

each term in the sum representing the probability for event A to occur in a given selection of n atoms, and not to occur in the remaining $(z\text{-}n)$ atoms. The sum includes all $\binom{z}{n}$ different selections of n atoms.

The F_n are readily seen to be the coefficients of a power series expansion of the generating function (or partition function)

$$f(s) = \prod_{i=1}^{z} (1 - P_i + sP_i) \equiv \sum_{n=0}^{z} F_n s^n \tag{4}$$

where s is a dimensionless variable with no physical significance at this point.

From (4) one obtains

$$f(1) = 1 = \sum_{n=0}^{z} F_n \, , \tag{5a}$$

i.e., the individual probabilities add up to 1. Moreover, taking derivatives one obtains average values,

$$f'(1) = \sum_n nF_n = \sum_i P_i \; ; \tag{5b}$$

$$f''(1) = \sum_n n(n-1)F_n = \sum_{i \neq j} P_i P_j \; ; \tag{5c}$$

etc. This results in the Taylor series

$$f(s) = 1 + (s-1) \sum_i P_i + \tfrac{1}{2}(s-1)^2 \sum_{i \neq j} P_i P_j \ldots \tag{6}$$

Consider now the average $\overline{F_n}$ over many different passages, i.e. the frequency spectrum for event A when a macroscopic beam of projectiles interacts with the target.

Let us make the important assumption at this stage that the beam is homogeneous, i.e. equal *a priori* probability P per beam particle to undergo event A for all target atoms,

$$\overline{P_i} = P \quad \text{for } i = 1, \ldots z \tag{7}$$

Eq. (7) requires that no target atoms are "shadowed" systematically by others. The relation is readily fulfilled in case of an ion beam spread uniformly over a macroscopic target area, since it has already been assumed that individual trajectories are not governed by target structure, and that energy loss and scattering are inappreciable. An example of a situation where (7) is not generally fulfilled is that of an internal source of projectiles, e.g. from radioactive decay[12], and, especially, channeling phenomena in crystals[14].

In case of a homogeneous beam, (5b) and (7) yield[14]

$$\bar{n} = \sum_n n\overline{F_n} = \sum_i \overline{P_i} = zP \; ; \tag{8}$$

Similarly, from (5c),

$$\overline{n^2} - \bar{n}^2 = zP(1-P) + \sum_{i \neq j} Q_{ij} \tag{9}$$

where

$$Q_{ij} = \overline{(P_i - P)(P_j - P)} \tag{9a}$$

Obviously, Q_{ij} is a measure of the correlation between the events initiated in two given atoms i and j.

Let us now make use of the assumption that z is a large number, i.e., that we deal with a macroscopic target. With target thickness x and target (or beam) area S, we have

$$z = NSx\,, \tag{10}$$

so z can be made as large as desired by a mere increase of S. So long as the projectiles interact over a microscopic distance, this does not affect the essential physical properties of the system. (We keep in mind that bounds exist on the target thickness x because of the requirement of negligible beam attenuation).

By definition of P, we must have

$$P = \frac{\sigma}{S}, \tag{11}$$

where σ is the cross section for event A. Obviously, P is a very small quantity, unlike the statistical variables P_i which may take on values between 0 and 1.

From (8), (10), and (11), one obtains the standard prescription for determining cross sections[5],

$$\bar{n} = Nx\sigma\,; \tag{12}$$

Note, however, that $\bar{n}$ need not be small in order that (12) be valid, nor has it been assumed that collision events be statistically independent.

Consider now the fluctuation, eq. (9), in case of a macroscopic target. We have $zP(1-P) \cong zP$, since $P \ll 1$. The correlation coefficients Q_{ij} differ from zero only if atoms i and j lie within some welldefined microscopic volume. Hence, if the target area S is made very large, only one summation in the double sum extends over all atoms while the other is limited. In other words, the double sum increases as $\propto z$ rather than $\propto z^2$, so we can write

$$\overline{n^2} - \bar{n}^2 = z(P + \Delta P_2) \tag{13}$$

with

$$\Delta P_2 = \tfrac{1}{z} \sum_{i \neq j} Q_{ij}\quad, \tag{13a}$$

and ΔP_2 being finite for $z \to \infty$.

Consider now the beam average over the partition function (6),

$$\bar{f}(s) = 1 + (s-1)\bar{n} + \tfrac{1}{2}(s-1)^2(\overline{n^2} - \bar{n}) + \ldots \equiv \sum_n \overline{F}_n s^n \; ; \tag{14}$$

After insertion of (12) and (13) one finds

$$\bar{f}(s) = 1 + (s-1)zP + \tfrac{1}{2}(s-1)^2[(zP)^2 + z\Delta P_2] + \ldots \tag{14'}$$

or, rearranging according to powers of z,

$$\bar{f}(s) = 1 + z[(s-1)P + \tfrac{1}{2}(s-1)^2 \Delta P_2 + \ldots] + \tfrac{1}{2}z^2[(s-1)^2 P^2 + \ldots] + \ldots \tag{14''}$$

where the dots indicate terms containing correlations.

It is evident (and well-known[15]) that in the absence of correlations, $\bar{f}(s)$ becomes exponential,

$$\bar{f}(s) = e^{(s-1)zP}; \tag{15}$$

This results in Poisson's distribution[1,5]

$$\overline{F}_n = e^{-Nx\sigma} \; \frac{(Nx\sigma)^n}{n!} \tag{16}$$

for the frequency spectrum of an individual event A governed by a cross section σ.

It is tempting to generalize eq. (15) in accordance with (14''), i.e. to write

$$\bar{f}(s) = e^{z[(s-1)P + \frac{1}{2}(s-1)^2 \Delta P_2 + \ldots]}; \tag{17}$$

The proof is central. It is carried out, therefore, in some detail.

Write the beam average of eq. (6) in the form

$$\bar{f}(s) = \sum_{n=0}^{z} \frac{a_n}{n!}(s-1)^n \, , \tag{18}$$

where

$$a_n = \sum_{i_1 \neq \ldots \neq i_n} \overline{P_{i_1} \ldots P_{i_n}} \qquad \text{for} \qquad n \geqslant 1$$

$$1 \qquad\qquad\qquad\qquad n = 0$$

Introducing correlation coefficients

$$b_n = \sum_{i_1 \neq \ldots \neq i_n} Q_{i_1 \ldots i_n}; \qquad n \geqslant 1 \tag{19}$$

with

$$Q_{i_1 \ldots i_n} = \overline{(P_{i_1} - P) \ldots (P_{i_n} - P)} \tag{20}$$

we find the following identities,

$$a_n = b_n - \sum_{m=1}^{n} (-)^m \binom{n}{m} (z-n+m) \ldots (z-n+1) P^m a_{n-m}$$

$$\cong b_n - \sum_{m=1}^{n} (-)^m \binom{n}{m} (zP)^m a_{n-m} \quad \text{for} \quad 1 \leqslant n \ll z ;$$

From this follows

$$a_n = \sum_{m=0}^{n} \binom{n}{m} b_{n-m} (zP)^m \tag{21}$$

with $b_0 = 1$. Insertion of (21) into (18), and rearrangement of summations yields

$$\bar{f}(s) \cong e^{(s-1)zP} \sum_{n \geqslant 0} \frac{b_n}{n!} (s-1)^n ; \tag{22}$$

Errors in (22) arise from those terms where n becomes comparable with z. (Note that $z \propto S$ while $z \cdot P$ is independent of S).

Consider first the case where all P_i are uncorrelated. Then, $b_n = 0$ for $n \geqslant 1$, and (22) becomes identical with eq. (15).

Consider next the case of pair correlations only, which may be realized by a diatomic molecular gas. Then, higher-order correlations are nonzero only to the extent that they can be decomposed into pair correlations. By means of simple combinatorics, (19) yields

$$b_{2m} = (2m-1)(2m-3) \ldots 3 \cdot 1 \, (b_2)^m$$

$$b_{2m-1} = 0$$

for $m = 1, 2 \ldots$. Therefore,

$$\sum_0 \frac{b_n}{n!}(s-1)^n = e^{\frac{1}{2}(s-1)^2 b_2};$$

With this, and (13a) and (19), (22) becomes identical with (17).

In case where both second and third order correlations are present, while higher correlations decompose, one finds

$b_4 = 3(b_2)^2$;
$b_5 = 10 b_2 b_3$;
$b_6 = 15(b_2)^3 + 20(b_3)^2$;
$b_7 = 105(b_2)^2 b_3$;
etc.

so

$$\sum_0 \frac{b_n}{n!}(s-1)^n = e^{\frac{1}{2}(s-1)^2 b_2 + \frac{1}{6}(s-1)^3 b_3};$$

Similarly, in case of higher correlations, one may write

$$\bar{f}(s) = e^{z\{(s-1)P + \sum_{n \geqslant 2} \frac{\Delta P_n}{n!}(s-1)^n\}} \tag{23}$$

where

$$\Delta P_n = \frac{1}{z} \sum_{i_1 \neq \ldots \neq i_n}^{(i)} Q_{i_1 \ldots i_n}, \tag{24}$$

and the index (i) indicates that only irreducible n-th order correlations are to be included in the sum.

In the above treatment, z was essentially considered infinite. This requires the functional behavior of $\bar{f}(s)$ to be determined by a number n_0 of terms in the Taylor series (18) with $n_0 \ll z$. If s is restricted to the range $|s| \leqslant 1$, and the ΔP_n bounded according to $|\Delta P_n| \lesssim P$, one must require that the relation

$$\frac{(zP)^n}{n!} \ll 1$$

be obeyed for all $n \geqslant n_0$ with some value $n_0 \ll z$. By means of Stirling's formula and eq. (12), this becomes equivalent with

$$\frac{\mathcal{N}x\sigma}{\log \frac{n_0}{e}} < 1, \tag{25}$$

where $e = 2.718$. By comparison with eqs. (1) and (2) one finds that (25) is a rather weak requirement.

In most applications of the present treatment, only pair correlations are important, i.e. all ΔP_n for $n \geqslant 3$ can be ignored. In that case, $\bar{f}(s)$ according to (23) reduces to a generating function for Hermite polynomials[16]. By term-by-term comparison with (14) one finds

$$\overline{F}_n = e^{-z(P-\Delta P_2/2)} \cdot \sum_{m=0}^{[n/2]} \frac{(z\Delta P_2/2)^m \, [z(P-\Delta P_2/2)]^{n-2m}}{m!\,(n-2m)!}; \tag{26}$$

This is a generalization of Poisson's formula (16) to systems with pair correlation.

In subsequent applications, the partition function $\bar{f}(s)$ itself will actually become more useful than the frequency spectrum $\overline{F}_n$.

3. Cumulative Effect of a Multitude of Events

Consider now two mutually exclusive events A_1 and A_2 such that one ion can initiate A_1 or A_2 in a given target atom, or none but not both. Let P_{i1} and P_{i2} be the respective probabilities ($i = 1, \ldots z$), and let $F_{n_1 n_2}$ be the joint frequency spectrum for n_1 events A_1 and n_2 events A_2 in an individual passage. This quantity follows readily from the partition function

$$f(s_1, s_2) = \prod_{i=1}^{z} ((1 - P_{i1} - P_{i2}) + s_1 P_{i1} + s_2 P_{i2}) = \sum_{0 \leqslant n_1 + n_2 \leqslant z} F_{n_1 n_2} s_1^{n_1} s_2^{n_2}, \tag{27}$$

where s_1 and s_2 are independent dimensionless variables. Eq. (27) is a straight generalization of eq. (4).

Taylor expansion of (27) similar to (6) yields

$$f(s_1, s_2) = 1 + \sum_{\alpha} (s_\alpha - 1) \sum_i P_{i\alpha} + \tfrac{1}{2} \sum_{\alpha\beta} (s_\alpha - 1)(s_\beta - 1) \sum_{i \neq j} P_{i\alpha} P_{j\beta} + \ldots \tag{28}$$

or, by analogy with (17) or (23),

$$\bar{f}(s_1, s_2) = \exp z\{\sum_{\alpha}(s_\alpha - 1)P_\alpha + \tfrac{1}{2}\sum_{\alpha\beta}(s_\alpha - 1)(s_\beta - 1)\Delta P_{2,\alpha\beta} + \ldots\} \tag{29}$$

where

$$P_\alpha = \overline{P_{i\alpha}} \tag{29a}$$

$$\Delta P_{2,\alpha\beta} = \frac{1}{z}\sum_{i \neq j}\overline{(P_{i\alpha} - P_\alpha)(P_{j\beta} - P_\beta)} \tag{29b}$$

etc., and $\alpha, \beta = 1, 2$.

Consider now some cumulative effect U,

$$U = n_1 u_1 + n_2 u_2 = \sum_{\alpha} n_\alpha u_\alpha ,$$

where u_α is the contribution of an individual event of type A_α to U. Then, the probability density $G(U)$ is given by

$$G(U) = \sum_{n_1, n_2}\overline{F_{n_1 n_2}}\ \delta(U - \sum_{\alpha} n_\alpha u_\alpha)$$

or, after Fourier transformation,

$$G(U) = \frac{1}{2\pi}\int_{-\infty}^{\infty} dt\, e^{itU}\cdot\sum_{n_1 n_2}\overline{F}_{n_1 n_2}\cdot(e^{-itu_1})^{n_1}\cdot(e^{-itu_2})^{n_2}; \tag{30}$$

Comparison with (27) shows that the integrand can be expressed by means of the partition function $\bar{f}(s_1, s_2)$. Hence,

$$G(U) = \frac{1}{2\pi}\int dt e^{itU}\cdot\bar{f}(e^{-itu_1}, e^{-itu_2})$$

or, after insertion of (28),

$$G(U) = \frac{1}{2\pi}\int_{-\infty}^{\infty} dt e^{itu - z\Delta} \tag{31}$$

with

$$\Delta = \sum_{\alpha}(1 - e^{-itu_\alpha})P_\alpha - \tfrac{1}{2}\sum_{\alpha\beta}(1 - e^{-itu_\alpha})(1 - e^{-itu_\beta})\Delta P_{2,\alpha\beta} + \ldots \tag{32}$$

The notation has been chosen so that eq. (32) remains true for any number of events A_α, $\alpha = 1,2,3,\ldots$ Moreover, if α is a continuous variable, the quantities $P_\alpha, \Delta P_{2,\alpha\beta}$ go over into corresponding probability densities and correlation functions. Finally, if u_α (and U) is a vectorial rather than a scalar quantity, eqs. (31) and (32) have to be read correspondingly, with t being a vector variable, too.

In the absence of correlations, (31) reduces to Bothe's formula[2]

$$G(U) = \frac{1}{2\pi}\int_{-\infty}^{\infty} dt e^{itU - Nx\sum_\alpha (1-e^{-itu_\alpha})\sigma_\alpha} \tag{33}$$

which is the conventional starting point for the theory of small-angle multiple scattering[2,12] and energy-loss spectra[4], when specified suitably. Standard derivations[4,17] of eq. (33) are based on Boltzmann's equation.

For completeness one may wish to generalize eq. (32) to the case of a polyatomic target. Let there be $z_{(I)}$ atoms of species I $(= 1, 2, \ldots)$, and allow each species to undergo a set of events $A_{(I)\alpha}$ with $\alpha = 1, 2, \ldots$ Then, eq. (32) amplifies to

$$\Delta = \sum_I c_{(I)} \sum_\alpha (1 - e^{-itu_{(I)\alpha}}) P_{(I)\alpha} -$$

$$-\tfrac{1}{2}\sum_{I,J} c_{(I)} c_{(J)} \sum_{\alpha,\beta} (1 - e^{-itu_{(I)\alpha}}) \cdot (1 - e^{-itu_{(J)\beta}}) \Delta P_{2(IJ)\alpha\beta} + - \ldots, \tag{34}$$

where $P_{(I)\alpha}$ is the probability per beam particle to initiate an event $A_{(I)\alpha}$ in a given target atom of type I, i.e.

$$P_{(I)\alpha} = \frac{\sigma_{(I)\alpha}}{S}, \tag{35}$$

and $\sigma_{(I)\alpha}$ the respective cross section. $c_{(I)}$ is the concentration of species I,

$$c_{(I)} = z_{(I)}/z, \tag{36}$$

and $u_{(I)\alpha}$ the contribution of one event $A_{(I)\alpha}$ to the cumulative effect U. Finally,

$$\Delta P_{2(IJ)\alpha\beta} = \frac{z}{z_{(I)} z_{(J)}} {\sum\sum}' \overline{(P_{i\alpha} - P_{(I)\alpha})(P_{j\beta} - P_{(J)\beta})} \tag{37}$$

where the prime indicates omission of the term $i \neq j$ (for $I = J$).

4. Spatial Correlation. Impact Parameter Treatment

In this section, correlations will be evaluated for the case where the target particles (preferably atoms or molecules) can be taken as well localized in space for a certain amount of time, and where the essential parameter determining the collision events is the initial location of a target particle relative to the trajectory of a beam particle.

Let $\boldsymbol{p}$ be the vectorial impact parameter with respect to some specified point 0 within the target particle, e.g. the nucleus of an atom or the center-of-mass of a molecule. If the probability to initiate an event A in a given target particle depends on $\boldsymbol{p}$ only, we have

$$\sigma = \int P(\boldsymbol{p})\, d^2p \tag{38}$$

according to (11). If $P(\boldsymbol{p})$ is essentially different from zero only for $\boldsymbol{p}$ covering some microscopic area $\ll S$, the integration in (38) can in practice be extended over the entire $\boldsymbol{p}$-plane.

Consider now the correlation coefficient Q_{ij}, eq. (9a) for two target particles i and j, located in $\boldsymbol{r}_i = (x_i, \varrho_i)$ and $\boldsymbol{r}_j = (x_j, \varrho_j)$, respectively. Here, the x-axis is parallel to the trajectory, and ϱ_i and ϱ_j are two-dimensional vectors specifying lateral positions. Let the trajectory have the lateral coordinate ϱ.

Introducing Fourier transforms

$$\sigma(\boldsymbol{k}) = \int_S d^2p P(\boldsymbol{p}) e^{i\boldsymbol{k}\cdot\boldsymbol{p}}; \tag{38a}$$

$$P(\boldsymbol{p}) = \frac{1}{S}\sum_{\boldsymbol{k}} \sigma(\boldsymbol{k}) e^{-i\boldsymbol{k}\cdot\boldsymbol{p}}; \tag{38b}$$

we can write

$$P_i - P = P(\varrho - \varrho_i) - P = \frac{1}{S}{\sum_{\boldsymbol{k}}}' \sigma(\boldsymbol{k}) e^{-i\boldsymbol{k}\cdot(\varrho - \varrho_i)}, \tag{39}$$

where the prime indicates ommission of the term $\boldsymbol{k} = 0$. Then, averaging over the beam yields

$$Q_{ij} = \frac{1}{S}\int d^2\varrho (P_i - P)(P_j - P) = \frac{1}{S^2}{\sum_{\boldsymbol{k}}}' |\sigma(\boldsymbol{k})|^2 e^{i\boldsymbol{k}\cdot(\varrho_i - \varrho_j)}; \tag{40}$$

Similarly, the higher correlation coefficients, eq. (20), read

$$Q_{i_1 \ldots i_n} = \sum_{\boldsymbol{k}_1}' \cdots \sum_{\boldsymbol{k}_n}' \delta_{\boldsymbol{k}_1 + \ldots + \boldsymbol{k}_n, 0} \cdot \prod_{m=1}^{n} \left(\frac{\sigma(\boldsymbol{k}_m)}{S} e^{i \boldsymbol{k}_m \cdot \varrho_{i_m}} \right)$$

where $\delta_{\boldsymbol{k},\boldsymbol{k}'}$ is Kronecker's symbol.

From (13a) and (40) we obtain the leading correlation term in eq. (17),

$$z \Delta P_2 = \frac{1}{S^2} \sum_{\boldsymbol{k}}' |\sigma(\boldsymbol{k})|^2 < \sum_{i \neq j} e^{i \boldsymbol{k} \cdot (\varrho_i - \varrho_j)} > ; \tag{41}$$

Here, the sum over individual target particles has been put into brackets that symbolize their distribution. Indeed, in an experiment, projectiles hit the target at different times. Therefore, a time average is taken over the set of instantaneous positions $\{\boldsymbol{r}_1, \ldots \boldsymbol{r}_z\}$.

As it stands, eq. (41) implies that all motion of target atoms during the time interval of an individual passage can be ignored. In practice, target motion is required only to be inappreciable for the amount of time needed by the projectile to penetrate the correlation volume, i.e., the volume within which atomic positions are strongly correlated. In the absence of long-range order, this does not mean a severe restriction even for only moderately fast projectiles. (Otherwise time-dependent correlations have to be introduced[18]). Systems with long-range order such as crystals need special care for a different reason (cf. below).

The quantity in brackets in eq. (41) is quite closely related to the structure factor that is measured in conventional diffraction experiments. Indeed, take a situation where the target thickness x is much larger than the range of the correlation of the structure in question, i.e., disregard surface effects. By means of the pair distribution[19] $g_2(\boldsymbol{r})$ --- $\mathcal{N} \cdot g_2(\boldsymbol{r}) d^3 r$ is the probability to find a target particle in $(\boldsymbol{r}, d^3 r)$ if there is one in $\boldsymbol{r} = 0$ --- we have

$$< \sum_{i \; j} e^{i \boldsymbol{K} \cdot (\boldsymbol{r}_i - \boldsymbol{r}_j)} > = z \; < \sum_{i}' e^{i \boldsymbol{K} \cdot \boldsymbol{r}_i} > = z \cdot \mathcal{N} \int d^3 r g_2(\boldsymbol{r}) e^{i \boldsymbol{K} \cdot \boldsymbol{r}} = \tag{42}$$

$$= z \cdot \mathcal{N} \cdot \int d^3 r (g_2(\boldsymbol{r}) - 1) e^{i \boldsymbol{K} \cdot \boldsymbol{r}} \text{ for } \boldsymbol{K} \neq 0$$

where $\boldsymbol{K} = (0, \boldsymbol{k})$. With the common definition [20] of the structure factor

$$\hat{S}(\boldsymbol{K}) - 1 = \mathcal{N} \int d^3 r (g_2(\boldsymbol{r}) - 1) e^{i \boldsymbol{K} \cdot \boldsymbol{r}}, \tag{43}$$

(41) reads

$$z\Delta P_2 = \mathcal{N}x\frac{1}{S}\sum_{\boldsymbol{k}}{}'|\sigma(\boldsymbol{k})|^2(\hat{S}(\boldsymbol{k})-1) = \mathcal{N}x\frac{1}{(2\pi)^2}\int d^2k\,|\sigma(\boldsymbol{k})|^2(\hat{S}(\boldsymbol{k})-1)\,, \quad (44)$$

where $\hat{S}(\boldsymbol{k})$ stands for $\hat{S}((0,\boldsymbol{k}))$.

For third-order correlations, eqs. (24) and (41) yield

$$z\Delta P_3 = \mathcal{N}x\frac{1}{(2\pi)^4}\int d^2k\int d^2k'\cdot\sigma(\boldsymbol{k})\sigma(\boldsymbol{k}')\sigma^*(\boldsymbol{k}+\boldsymbol{k}')\cdot(\hat{S}(\boldsymbol{k},\boldsymbol{k}')-1)\,, \quad (45)$$

where

$$\hat{S}(\boldsymbol{K},\boldsymbol{K}')-1 = \mathcal{N}^2\int d^3r\,e^{i\boldsymbol{K}\cdot\boldsymbol{r}}\cdot\int d^3r'e^{i\boldsymbol{K}'\cdot\boldsymbol{r}'}\cdot[g_3(\boldsymbol{r};\boldsymbol{r}')-1]\,, \quad (45a)$$

and $\mathcal{N}^2g_3(\boldsymbol{r};\boldsymbol{r}')d^3rd^3r'$ is probability to find atoms in $(\boldsymbol{r},d^3r)$ and $(\boldsymbol{r}',d^3r')$ if there is one in $\boldsymbol{r}=0$. Higher-order correlations form correspondingly.

These results are readily generalized to the multitude of events discussed in the foregoing section. By comparison with (9a) and (13a) we find instead of (44)

$$z\Delta P_{2(IJ)\alpha\beta} = \mathcal{N}x\frac{1}{(2\pi)^2}\int d^2k\sigma_{(I)\alpha}(\boldsymbol{k})\cdot\sigma^*_{(J)\beta}(\boldsymbol{k})\,(\hat{S}_{(IJ)}(\boldsymbol{k})-1)\,, \quad (46)$$

where

$$\hat{S}_{(IJ)}(\boldsymbol{K})-1 = \mathcal{N}\int d^3r(g_{2(IJ)}-1)\cdot e^{i\boldsymbol{K}\cdot\boldsymbol{r}} \quad (46a)$$

and $\mathcal{N}c_{(J)}g_{2(IJ)}(\boldsymbol{r})d^3r$ is the probability to find an atom of type J in $(\boldsymbol{r},d^3r)$ if there is an atom of type I in $\boldsymbol{r}=0$.

Formal evaluation of eq. (42) for an ideal crystal yields

$$\sum_{i\neq j}e^{i\boldsymbol{K}\cdot(\boldsymbol{r}_i-\boldsymbol{r}_j)} = z^2\sum_{\boldsymbol{Q}}\delta_{\boldsymbol{K},\boldsymbol{Q}}\,, \quad (47)$$

where $\boldsymbol{Q}$ runs over the reciprocal lattice[21] of the structure in question. Consequently, one would find from (41)

$$z\Delta P_2 = \mathcal{N}^2x^2\sum_{\boldsymbol{q}}{}'|\sigma(\boldsymbol{q})|^2 \quad (47')$$

where $\boldsymbol{Q} = (0, \boldsymbol{q})$. Thus, long-range order causes an x^2-dependence of $z \cdot \Delta P_2$ on target thickness which is essentially different from what was found in eq. (45). At the same time, the validity of the various assumptions entering (47′) is by no means proven. Indeed, ignoring governed motion in crystals in the discussion of the effects of long-range order is hardly justified. Therefore, the following discussion will concern systems with short-range order only.

For very thin targets, surface effects become important in the structural correlations, so eq. (44) is no longer obvious. As an extreme example, take a planar layer characterized by a correlation $\hat{g}_2(\varrho) - 1$. Then, (41) yields

$$z\Delta P_2 = n\frac{1}{(2\pi)^2}\int d^2k\,|\sigma(\boldsymbol{k})|^2 \cdot n\int d^2\varrho\,(\hat{g}_2(\varrho) - 1)\,e^{i\boldsymbol{k}\cdot\varrho}, \tag{48}$$

where $n = z/S$. The only noticeable difference between (48) and (44) lies in the quantitative behavior of the two pair distribution functions.

It may be worthwhile to stress that the description put forward in this section is based on the assumption that individual events are correlated *only* through the trajectory of the projectile. In particular, the characterization of the elementary event by a probability $P(\boldsymbol{p})$, as expressed by eqs. (38) and (40), rather than a quantal transition amplitude ignores quantal interference between different events. Thus, the treatment excludes coherent scattering processes (in the language of diffraction theory[18]). Also, it is implied that the basic event is defined in a manner so that individual interaction regions do not overlap substantially.

5. Examples: Molecular Gas, Hard-Sphere Gas, and Amorphous Solid

A very simple case of a medium with short-range order is an ideal gas consisting of randomly oriented diatomic molecules. When viewed as an assembly of atoms, such a system has pair correlations only, and the correlation function can be approximated by

$$g_2(\boldsymbol{r}) - 1 = \frac{\delta(r-d)}{4\pi\mathcal{N}d^2} \tag{49}$$

in the simplest case of a homonuclear molecule with individual atoms assumed spherically symmetric, and vibrational motion around the equilibrium distance d ignored. ($\mathcal{N}$ is the number of *atoms* per volume). Then, (43) and (44) yield

$$\hat{S}(\boldsymbol{K}) - 1 = \frac{\sin Kd}{Kd} \tag{49a}$$

and

$$z\Delta P_2 = \mathcal{N}x \frac{1}{2\pi d} \int_0^\infty dk |\sigma(k)|^2 \sin kd \,; \tag{50}$$

Expressions of this type have been investigated previously[9,10]. A very important limiting case is that of short-range interaction, where the cross section (38) is made up predominantly from contributions within the range $p \ll d$. Setting

$$P(\boldsymbol{p}) \sim \sigma \cdot \delta(\boldsymbol{p}) \tag{51}$$

in (38a), one obtains from (50)

$$z\Delta P_2 \sim \mathcal{N}x \cdot \frac{\sigma^2}{2\pi d^2} \tag{52}$$

It is easily shown[9,10] that (52) is the leading term in an asymptotic expansion of (50) in terms of $\sigma/2\pi d^2$. Thus, the short-range approximation applies for $\sigma \ll 2\pi d^2$; this means that correlation effects are supposed not to be dominating.

It may be worthwhile to stress that correlations in the ideal molecular gas originate in the (deliberately taken) view of the system as an assembly of atoms. If, instead, the description is based on projectile-molecule collisions as the basic event, Poisson statistics applies. Indeed, previous derivations[9,10] of the present results were found along that line which is, in fact, more direct in case of the molecular gas, but much less general. Thus, with regard to the present description, the molecular gas constitutes mainly a useful test case.

As another illustrative example, consider a real gas, e.g. a noble gas with a hard-sphere-like repulsive interaction, so that

$$g_2(\boldsymbol{r}) \cong \begin{cases} 0 & \text{for } r < b \\ 1 & \text{for } r > b \end{cases} \tag{53}$$

where b is twice the hard-sphere radius. Then, (43) and (44) yield

$$\hat{S}(\boldsymbol{k}) - 1 = -\frac{4\pi\mathcal{N}}{k^3}(\sin kb - kb \cos kb) \tag{53a}$$

and

$$z\Delta P_2 = -\mathcal{N}x \cdot 2\mathcal{N}\int_0^b r\,dr \int_0^\infty dk\,|\sigma(k)|^2 \sin kr\,; \tag{54}$$

In the short-range limit, (54) reads

$$z\Delta P_2 \sim -\mathcal{N}x\sigma^2 \cdot 2\mathcal{N}b\,, \tag{55}$$

i.e., ΔP_2 becomes negative. Unlike (52), (55) is a density-dependent correction to $z \cdot P$, as is obvious from the underlying physical model.

For a more general system, eq. (44) reads in the short-range limit

$$z\Delta P_2 \sim \mathcal{N}x \frac{\sigma^2}{(2\pi)^2} \int d^2k\,(\hat{S}(\boldsymbol{k}) - 1)\,;$$

Let the medium be isotropic, i.e., $g_2(\boldsymbol{r}) \equiv g_2(\boldsymbol{r})$. Then, (43) reads

$$\hat{S}(\boldsymbol{K}) - 1 = \mathcal{N} \int_0^\infty 4\pi r^2 dr (g_2(r) - 1) \frac{\sin Kr}{Kr}, \tag{56}$$

so

$$z\Delta P_2 \sim \mathcal{N}x\sigma^2 \cdot 2\mathcal{N} \int_0^\infty dr (g_2(r) - 1)\,; \tag{57}$$

Also this result has been derived previously for a special case[12]. It shows that in the case of short-range interaction, the sign of the correlation term ΔP_2 is determined by the sign of the structural pair correlation function $g_2(r) - 1$. In case of a positive correlation, like (49), ΔP_2 becomes positive, cf. (52), and vice versa for eqs. (53) and (55).

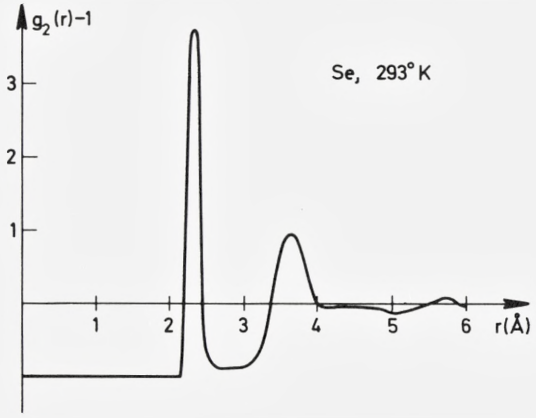

Fig. 1. Pair Correlation for amorphous selenium at room temperature, measured by means of neutron diffraction[22]. In the region $r \lesssim 2\text{Å}$, $g_2(r)$ has been set equal to zero, while the function tabulated in ref. 22 oscillates, and takes on negative values in certain intervals. (In the evaluation of eq. (57), however, the tabulated function has been employed).

In a liquid or amorphous solid, the pair correlation function looks generally like in Fig. 1, i.e., both positive and negative values are represented. The most predominant effects are the repulsive interaction at small r, giving rise to a contribution of the type of eq. (54) or (55), and a nearest-neighbor correlation of the type of eq. (50) or (52). However, while in a real gas, N is so small that (55) is a minute correction, the high density of amorphous matter makes the repulsive region dominate, as is evident from the figure. For amorphous selenium, integration of a measured correlation function[22] yields

$$4\pi N\int_0^\infty dr(g_2(r)-1) = -C\text{Å}^{-2}\ ;$$

with* $C \simeq 1.3$.
Thus, the resulting correlation term in the short-range limit

$$z\Delta P_2 = -Nx\frac{\sigma^2}{2\pi}\cdot\frac{C}{\text{Å}^2}$$

is very similar in magnitude but opposite in sign to the one for the diatomic gas, eq. (52).

It is instructive to study the behavior of eqs. (50) and (54) in case the interaction is not of extreme short-range nature like (51). For analytic convenience, take the following model,

$$\sigma(k) = \sigma\cdot e^{-ka} \tag{58}$$

corresponding to

$$P(\boldsymbol{p}) = \frac{\sigma a}{2\pi}(p^2+a^2)^{-3/2} \tag{58a}$$

according to eq. (38b). Here, a is an arbitrary interaction radius. When (58) is inserted into (50) and (54) one obtains

$$z\Delta P_2 = \frac{Nx\sigma^2}{2\pi(d^2+4a^2)} \tag{59a}$$

---

* The numerical value of the constant C has been determined by straight summation of the tabulated values of structure factor and pair correlation in ref. 22. Both procedures lead to the same value $C \simeq 1.3$ within their apparent accuracy of ± 20 pct. The actual error in C may be greater: Because of experimental limitations on the range of k-values covered, the pair distribution $g_2(r)$ as deduced in ref. 22 takes on negative values in certain intervals. This unphysical behavior has not been corrected for in the present evaluation of C.

for the diatomic gas, and

$$z\Delta P_2 = -\mathcal{N}x\sigma^2 \cdot 2\mathcal{N}\left[b - 2a\,\mathrm{arctg}\frac{b}{2a}\right] \tag{59b}$$

for the hard-sphere gas.

Eqs. (52) and (55) are limiting cases of (59a) and (59b) for small values of a, as expected. In the opposite limit of $a \gg b, d$, one obtains, instead,

$$z\Delta P_2 \sim \frac{\mathcal{N}x\sigma^2}{8\pi a^2} \tag{60a}$$

for the molecular gas, and

$$z\Delta P_2 \sim -\mathcal{N}x\sigma^2 \cdot \frac{\mathcal{N}b^3}{6a^2} \tag{60b}$$

for the hard-sphere gas.

One may recognize that ΔP_2 *decreases* monotonically when a increases from zero to infinity, i.e., correlations are seemingly most pronounced in the limit of short-range interaction. In interpreting this result, the reader ought to keep in mind that it only holds to the extent that the cross section is kept constant. Most often, σ itself will increase approximately as $\propto a^2$.

It is also obvious that (59b) decreases more rapidly with increasing a than does (59a). Therefore, one may anticipate that in case of an amorphous medium, the relative significance of repulsive and attractive correlations is shifted in the direction of increased importance of positive correlations for long-range interaction. Whether or not this leads to positive values of ΔP_2 depends on the details of the interaction and the structure.

The results derived so far—when suitably extended to more general situations as prescribed in sect. 3—are of immediate significance when fluctuations are to be determined, cf. eq. (13). Higher than pair correlations do not enter here. When interest ist directed toward a frequency spectrum like (26) or the probability density of some cumulative effect, like (31), the significance of higher-order correlations, ΔP_n for $n \geqslant 3$ needs to be discussed.

Let us consider the limit of short-range interaction. Insert (45a) into (45), and apply (51). Then,

$$z\Delta P_3 \sim \mathcal{N}x\sigma^3 \cdot \mathcal{N}^2 \int d^3r \int d^3r' \cdot (g_3(\boldsymbol{r}\,;\boldsymbol{r}') - 1)\,\delta(\varrho)\,\delta(\varrho') \tag{61}$$

where $\boldsymbol{r} = (x, \varrho)$ and $\boldsymbol{r}' = (x', \varrho')$.

If the medium is isotropic, the correlation function $g_3(\boldsymbol{r};\boldsymbol{r}')-1$ is invariant toward rotation of the coordinate system, i.e. it can only depend on $\boldsymbol{r}, \boldsymbol{r}'$, and $|\boldsymbol{r}-\boldsymbol{r}'|$. Therefore, the angular integrations can be carried out, and

$$z\Delta P_3 \sim Nx\sigma^3 \cdot (2N)^2 \int_0^\infty dr \int_0^\infty dr' [\hat{g}_3(r;r')-1], \tag{62}$$

where

$$\hat{g}_3(r;r') = \frac{1}{2}[g_3(r,r',|r-r'|)+g_3(r,r',r+r')]\ ; \tag{62a}$$

Thus, we obtain the important result that in the short-range limit, ΔP_3 picks up only correlations between *collinear* atomic positions.

This means that in a polyatomic molecular gas, triple (and higher) correlations are significant only provided that are collinear atoms. The magnitude of these correlations has been investigated in considerable detail in the special case of multiple scattering off triatomic molecules[10]. These estimates will not be repeated here. However, comparison of eq. (62) with eq. (57) shows that the ratio of $\Delta P_3/\Delta P_2$ is of higher order small in terms of $\sigma/2\pi d^2$, in addition to the fact that its numerical value must be small in the absence of any correlation that forces three or more atoms on straight lines.

Thus, it appears that within the range of validity of the short-range approximation, i.e., so long as correlation effects are moderate, pair correlations are responsible for the dominant correction to Poisson statistics, and higher correlations can be ignored in the extended Bothe formula.

In the opposite limit of long-range interaction, such a simple picture can hardly be expected to be true. Indeed, collective effects, and hence higher correlations tend to be important in such situations. It is, therefore, advisable to redefine the basic event and thus to create a description where correlations are moderate or even weak. Such a procedure will be sketched in the following section.

6. Selection of Statistical Variables

In the two previous sections, attention was restricted to collisions between well-localized particles, e.g. projectile ions and target atoms. The (more or less pronounced) deviations from Poisson statistics are in this case directly related with spatial correlations between target atoms. It is worth noting that such spatial correlations only exist when the target atoms interact. Indeed, Poisson statistics does apply in case of an ideal gas, while deviations were found in case of molecular binding, the real gas, and the amorphous solid.

This is a rather general result. Indeed, it appears that at least in case of large cross sections, correlation effects are the rule rather than the exception in particle penetration through non-

random media. However, one has the option of selecting generalized coordinates describing the initiated events in a way so correlations are minimized. Rather than trying to establish general criteria for a wide variety of phenomena, let us consider two simple examples that illustrate this point.

First, take the process of K-shell excitation by an ion beam in an amorphous solid, and ask for the probability G_ν for ν target-K-shell vacancies per ion.

Consider two types of correlation. First, every target atom has two K-electrons, and the respective excitation probabilities may be strongly correlated. Only in the limit of very-high-speed ions would it be feasible to treat this type of correlation within the short-range approximation. Second, consider the spatial correlation between different target atoms. Since, for ions with moderate velocities (comparable with the velocities of K- or L-shell electrons) cross sections for K-excitation can become appreciable on an atomic scale[23], the latter class of correlation may well be sizable. It is, however, weak enough to be well described by the short-range approximation. A third (and often important[23]) correlation effect associated with the projectile state is outside the scope of this paper and therefore ignored.

From the point of view of simplicity of the general statistical description, one might initially attempt to describe the system in terms of one type of target particle (K-electron) and one type of event (K-excitation). Although the two K-electrons are strongly correlated, such a description may be feasible for high-speed ions where Poisson's law is almost fulfilled since spatial correlations are negligible and binding effects small. However, at moderate velocities, in the presence of both types of correlation, one would have to cope with correlations of both third and fourth order. Instead, it is more attractive to apply the (conventional) description in terms of the *atom* as the basic target particle and two types of event, A_1 and A_2, representing single and double K-excitation, respectively. Then, eq. (31) yields

$$G_\nu = \frac{1}{2\pi}\int_0^{2\pi} dt e^{it\nu - z\Delta} \tag{63}$$

with

$$\Delta = \frac{1}{S}\left\{\sigma(t) - \sigma^2(t)\cdot N\int_0^\infty dr(g_2(r)-1)\right\} \tag{64}$$

and

$$\sigma(t) = (1-e^{-it})\sigma_1 + (1-e^{-2it})\sigma_2 \; ; \tag{65}$$

Here, σ_1 and σ_2 are the cross sections for single and double excitation of the K-shell of an individual atom, and $g_2(r)-1$ is the pair correlation characterizing the structure of the amorphous target. The short-range approximation has been applied to correlations between different target atoms, and the integration over t in (63) has been restricted to an interval size 2π, unlike in (31), in order to produce a probability G_ν instead of a density $G(\nu)d\nu$.

Further evaluation of eq. (63) in case where σ_1 and σ_2 are well-known parameters could be done by way of the procedure discussed in the subsequent section.

Determination of the atomic parameters σ_1 and σ_2 is a problem of atomic physics that has been investigated in specific cases[23–25]. The description of correlations in terms of impact parameters appears too qualitative to be applied in cases where proper quantal calculations are available, but may well be helpful in situations where only empirical cross sections exist. Since the present discussion serves to illustrate a rather specific point, this line is not followed presently.

The second example concerns the energy loss of an ion penetrating a molecular gas target. This problem has been treated previously as a rather simple case where correlations play a role, both from a particle-penetration[9] and a molecular-collisions[26] point of view. The present discussion concentrates on the question of finding the most suitable variables to minimize correlation effects in energy-loss straggling.

It is convenient, for that purpose, to switch to the notation used in previous work[9,26]. We consider the fluctuation in *nuclear* energy loss,

$$\overline{(\Delta E - \overline{\Delta E})^2} = \mathcal{N}' x W = \mathcal{N}' x \; < \; d^2 p (T(p_1) + T(p_2))^2 \; > \tag{66}$$

of an ion to an ideal gas of homonuclear diatomic molecules. Here, p_1 and p_2 are impact parameters relative to target nuclei, $T(p)$ is the energy transferred to an atom in an individual ion-atom collision at impact parameter p (calculated from classical scattering theory), and $\mathcal{N}'$ the number of molecules per volume. W is called the straggling parameter of a molecule. It is readily seen to have the form

$$W = W_1 + W_2 + 2\Delta W_{12}\,, \tag{67}$$

where

$$W_1 = W_2 = \int d^2 p (T(p))^2 \tag{67a}$$

is the straggling parameter of an individual atom, and

$$\Delta W_{12} = \; < \int d^2 p \, T(p_1) \, T(p_2) \; > \tag{68}$$

a correlation term.

It has been shown[9] that ΔW_{12} becomes

$$\Delta W_{12} \; \sim \frac{S_1 S_2}{2\pi d^2} \tag{69}$$

in the short-range limit, i.e., for large internuclear distance d. Here,

$$S_1 = S_2 = \int d^2 p \, T(p) \tag{69a}$$

is the atomic stopping cross section. Conversely, in the long-range limit, i.e., for small d, one finds[9]

$$\Delta W_{12} \sim W_1 - \frac{d^2}{6}\int d^2p\left(\frac{dT}{dp}\right)^2 ; \tag{70}$$

Eq. (69) shows that in the short-range limit, the correlation term ΔW_{12} is small, while according to (70), it is large in the long-range limit. In other words, the statistical variables $T_1(=T(p_1))$ and T_2 are appropriate to describe the interaction in the short-range limit, but are inconvenient in the opposite case. In a triatomic molecule, or a dense medium, higher correlations would enter essentially.

It is more attractive, for long-range interaction, to split the energy loss according to

$$T_1 + T_2 \equiv T_e + T_i \tag{71}$$

into an elastic and an inelastic part T_e and T_i, respectively, where

$$T_e = \frac{1}{4M}(\boldsymbol{P}_1 + \boldsymbol{P}_2)^2 , \quad T_i = \frac{1}{4M}(\boldsymbol{P}_1 - \boldsymbol{P}_2)^2 , \tag{71a}$$

and $\boldsymbol{P}_1 = \boldsymbol{P}\boldsymbol{p}_1)$ and $\boldsymbol{P}_2 = \boldsymbol{P}(\boldsymbol{p}_2)$ are momentum transfers to individual atoms. $\boldsymbol{p}_1$ and $\boldsymbol{p}_2$ are vectorial impact parameters, and M is the atomic mass.

The straggling parameter splits correspondingly into

$$W = W_e + W_i + 2\Delta W_{ei} , \tag{72}$$

where W_e and W_i represent the fluctuation in elastic and inelastic energy loss, respectively, and ΔW_{ei} a correlation term.

In appendix A, the following expressions are derived for the three terms,

$$W_e = < \int d^2p\, T_e^2 > \sim 4W_1 - \frac{d^2}{6}\int d^2p\left(\frac{dT}{dp}\right)^2 , \tag{73a}$$

$$W_i = < \int d^2p\, T_i^2 > \sim \frac{d^2}{6}\int d^2p\left(\frac{dT}{dp}\right)^2 , \tag{73b}$$

$$\Delta W_{ei} = < \int d^2p\, T_e\, T_i > \sim 0 \tag{73c}$$

in the long-range approximation, and

$$W_e \sim W_i \sim \tfrac{1}{2} W_1 + \frac{S_1 S_2}{2\pi d^2} \tag{74a}$$

$$\Delta W_{ei} \sim \tfrac{1}{2} W_1 \tag{74b}$$

in the short-range approximation.

Thus, the correlation is weak in the long-range limit but strong in the opposite case. In other words, the statistical variables T_e and T_i are complementary to T_1 and T_2.

As is indicated in appendix A, the evaluation hinges on the simplifying assumption of small-angle scattering. The present results should, therefore, not be utilized uncritically in molecular-collision physics. The example does, however, illustrate in a very simple way the usefulness of introducing "collective" modes to reduce correlation effects in the long-range approximation.

There is another, essentially independent reason to favor collective coordinates T_e and T_i in case of long-range interaction.The use of the energy-loss functions $T(p_1)$ and $T(p_2)$ in eq. (66) implies that the constituent atoms in the molecule act as free atoms with regard to scattering of the projectile. This approximation, while justified for close collisions, must in general break down for distant collisons because of the distortion of the projectile-atom interaction by valence effects. This does not affect the conclusion that T_e and T_i are appropriate variables for collisions at large impact parameters, but the relation with atomic scattering parameters becomes more complex than indicated in eq. (71a).

7. Evaluation of Cumulative Effects

Before going into applications, let us look at various ways of how to evaluate some cumulative effect U on the basis of eqs. (31) and (32), or (34).

Quite often, one will be satisfied with the average value $\bar{U}$ and the fluctuation $\overline{\Delta U^2} = \overline{(U-\bar{U})^2}$. According to (31) we have

$$\overline{U^n} = \int dU U^n G(U) = i^n \frac{\partial^n}{\partial t^n} e^{-z\Delta(t)} \Big|_{t=0}, \tag{75}$$

i.e.,

$$\int dU G(U) = 1 ; \tag{76a}$$

$$\bar{U} = z \sum_\alpha u_\alpha P_\alpha ; \tag{76b}$$

$$\overline{\Delta U^2} = z \left(\sum_\alpha u_\alpha^2 P_\alpha + \sum_{\alpha\beta} u_\alpha u_\beta \Delta P_{2,\alpha\beta} \right) ; \tag{76c}$$

These relationships could also have been derived directly from eqs. (8) and (13). Eq. (76b) and the first part of (76c) are the usual relations for mean value and fluctuation[5]. The rest of (76c) is not present in standard penetration theory for random media.

In particular, in case of short-range interaction, eqs. (57) and (76c) yield

$$\overline{\Delta U^2} \cong \mathcal{N}x\left\{\sum_\alpha u_\alpha^2\sigma_\alpha + \left(\sum_\alpha u_\alpha\sigma_\alpha\right)^2 \cdot 2\mathcal{N}\int_0^\infty dr(g_2(r)-1)\right\} \tag{77}$$

for an isotropic medium.

In case of a polyatomic target, we have

$$\overline{U} = z\sum_I c_{(I)}\sum_\alpha u_{(I)\alpha}P_{(I)\alpha}\,; \tag{76b'}$$

$$\overline{\Delta U^2} = z\left\{\sum_I c_{(I)}\sum_\alpha u_{(I)\alpha}^2 P_{(I)\alpha} + \sum_{IJ} c_{(I)}c_{(J)}\sum_{\alpha\beta} u_{(I)\alpha}u_{(J)\beta}\Delta P_{2(IJ)\alpha\beta}\right\} \tag{76c'}$$

according to (34), and

$$\overline{\Delta U^2} \cong \mathcal{N}x\left\{\sum_I c_{(I)}\sum_\alpha u_{(I)\alpha}^2\sigma_\alpha + \right. \tag{77'}$$

$$\left. + \sum_{IJ} c_{(I)}c_{(J)}\left(\sum_\alpha u_{(I)\alpha}\sigma_\alpha\right)\cdot\left(\sum_\beta u_{(J)\beta}\sigma_\beta\right)\cdot 2\mathcal{N}\int_0^\infty dr(g_{2(IJ)}(r)-1)\right\}$$

by means of (46) and (46a) if the short-range approximation is valid. (77') approaches a similar form as (77) only if the medium is disordered, i.e., when $g_{2(IJ)}(r)-1$ is independent of I and J.

Extension of these relationships to vectorial quantities and to the continuum case is straightforward.

Consider next the case of a discrete probability distribution, as discussed briefly in the foregoing section. For simplicity, let u_α be given by

$$u_\alpha = \nu\,;\ \nu = 0, \pm 1, +2, \ldots \tag{78}$$

so

$$U = \sum n_\nu \nu$$

and

$$G_U = \frac{1}{2\pi}\int_0^{2\pi} dt e^{itU - z\Delta(t)} \tag{79}$$

or

$$G_U = \frac{1}{2\pi i}\oint d\zeta\,\zeta^{-1-U}e^{-z\Delta(\zeta)}$$

with

$$\Delta(\zeta) = \sum_{\nu} (1-\zeta^{\nu}) P_{\nu} - \tfrac{1}{2} \sum_{\nu\mu} (1-\zeta^{\nu})(1-\zeta^{\mu}) \Delta P_{2,\nu\mu} \; ; \tag{80}$$

The integration over ζ goes along a closed path including the point $\zeta = 0$. Hence,

$$G_U = \frac{1}{U!} \frac{\partial^U}{\partial \zeta^U} e^{-z\Delta(\zeta)} \Big|_{\zeta=0} \; ; \tag{81}$$

Thus, exact evaluation of the generalized Bothe formula is possible in this case.

Eq. (81) may become useful in the analysis of ionization phenomena.

Let us return to the more general case of a probability density (31), but apply the diffusion approximation[27], i.e., assume that the bits u_{α} are "small". Then, (32) reads

$$\Delta \cong it \sum_{\alpha} u_{\alpha} P_{\alpha} + \tfrac{1}{2} t^2 \left(\sum_{\alpha} u_{\alpha}^2 P_{\alpha} + \sum_{\alpha\beta} u_{\alpha} u_{\beta} \Delta P_{2,\alpha\beta} \right) \tag{82}$$

up to second order in u_{α}, and (31) yields

$$G(U) = \frac{1}{\sqrt{2\pi \overline{\Delta U^2}}} e^{\frac{-(U-\bar{U})^2}{2\overline{\Delta U^2}}} \tag{83}$$

with $\bar{U}$ and $\overline{\Delta U^2}$ given by (76b) and (76c). The limitations of the gaussian approximation have been discussed extensively[2,5,17,27].

Finally, let us write eq. (32) in the case of short-range interaction,

$$z\Delta \cong \mathcal{N}x \left\{ \sum_{\alpha} (1-e^{-itu_{\alpha}}) \sigma_{\alpha} - \tfrac{1}{2} \left(\sum_{\alpha} (1-e^{-itu_{\alpha}}) \sigma_{\alpha} \right)^2 \cdot 2\mathcal{N} \int_0^{\infty} dr (g_2(r) - 1) \right\} ; \tag{84}$$

Eq. (84) offers itself for a perturbation treatment[8,10] in case of weak correlation. Indeed, take some representative value of t in the Bothe integral (33), such as the median value $t_m(U)$ defined by

$$\int_{-\infty}^{\infty} dt e^{itU - \mathcal{N}x\sigma(t)} = 2 \cdot \int_{t_m}^{\infty} dt e^{itU - \mathcal{N}x\sigma(t)}, \tag{85}$$

and write (84) in the form

$$z\Delta \cong \mathcal{N}x \cdot \sigma(t) \left\{ 1 - \frac{\sigma(t_m)}{2} \cdot \frac{1}{2\pi d_{eff}^2} \right\} = \mathcal{N}x_{eff} \sigma(t) \tag{86}$$

with

$$\sigma(t) = \sum_{\alpha} (1-e^{-itu_{\alpha}}) \sigma_{\alpha} \tag{87a}$$

$$\frac{1}{2\pi d_{eff}} = 2N\int_0^\infty dr(g_2(r)-1) \tag{87b}$$

and

$$x_{eff} = x\left\{1-\tfrac{1}{2}\frac{\sigma(t_m)}{2\pi d_{eff}^2}\right\}; \tag{87c}$$

In this manner, for weak correlation, results derived on the basis of Poisson statistics can be modified such as to incorporate correlations.

8. Applications

Stopping of Charged Particles.

Let us consider a standard problem of the theory of particle penetration, the energy-loss spectrum of a charged particle after penetration of a path length x in a stopping medium. According to common notation[1,5,28,29], the individual event is characterized by a spectrum σ_α of energy loss T_α or, in continuum notation, $d\sigma(T)$, so the mean energy loss $\overline{\Delta E}$ and fluctuation $\Omega^2 = (\Delta E - \overline{\Delta E})^2$ are given by (76b) and (76c),

$$\overline{\Delta E} = NxS; \tag{88}$$

$$\Omega^2 = Nx(W+\Delta W); \tag{89}$$

where

$$S = \sum_\alpha T_\alpha\sigma_\alpha = \int T d\sigma(T); \tag{88a}$$

$$W = \sum_\alpha T_\alpha^2\sigma_\alpha = \int T^2 d\sigma(T); \tag{89a}$$

$$\Delta W = \frac{1}{(2\pi)^2}\int d^2k|S(\boldsymbol{k})|^2(\hat{S}(\boldsymbol{k})-1); \tag{89b}$$

and

$$S(\boldsymbol{k}) = \sum_\alpha T_\alpha\sigma_\alpha(\boldsymbol{k}) \tag{90}$$

according to eq. (44). The quantity $S(\boldsymbol{k})$ can also be written in the form

$$S(\boldsymbol{k}) = \int d^2p e^{i\boldsymbol{k}\cdot\boldsymbol{p}}\overline{T}(\boldsymbol{p}) \tag{90'}$$

by means of (38a), where

$$\overline{T}(\boldsymbol{p}) = \sum_{\alpha} T_{\alpha} P_{\alpha}(\boldsymbol{p}) = \int dT\, T P(\boldsymbol{p}, T)\,, \tag{90a}$$

and $P(\boldsymbol{p}, T)\,dT$ is the probability for energy loss (T, dT) in a collision at impact parameter $\boldsymbol{p}$. By comparison of (90) with (88a), as well as (38a) with (38), it is evident that

$$S(\boldsymbol{k} = 0) = S\,, \tag{91}$$

and therefore, in the short-range limit,

$$\Delta W \cong \frac{S^2}{(2\pi)^2} \int d^2k\, (\hat{S}(\boldsymbol{k}) - 1) = S^2 \cdot 2\mathcal{N} \int_0^{\infty} dr (g_2(r) - 1)\,, \tag{92}$$

where the second identity assumes the medium to be isotropic. The latter result has been mentioned in ref. 12.

Specifically, for a diatomic gas, insertion of (49a) into (89b) yields

$$\Delta W = \frac{1}{2\pi d} \int_0^{\infty} dk\, |S(k)|^2 \sin kd\,, \tag{93}$$

a result that has been derived previously by a rather different procedure[9]. The consequences of eq. (93) have been discussed in considerable detail[9,12]. It is, however, worthwhile to repeat that in the short-range approximation, ΔW becomes positive for the molecular gas. Experimental checks[11] have confirmed both the sign and the magnitude of the predicted values of ΔW.

According to the discussion following eq. (57), the value of ΔW in case of an amorphous stopping medium is roughly equal in magnitude, but opposite in sign, to the one for the diatomic gas. For example, for amorphous selenium (cf. footnote on p. 20),

$$\Delta W \cong -\frac{S^2}{2\pi} \cdot \frac{1.3}{\mathring{A}^2}\,;$$

For the full energy-loss spectrum $G(\Delta E)\,d(\Delta E)$, eq. (32) yields

$$G(\Delta E) = \frac{1}{2\pi} \int_{-\infty}^{\infty} dt e^{it\Delta E - z\Delta(t)} \equiv \frac{1}{2\pi i} \int_{c-i\infty}^{c+i\infty} ds e^{s\Delta E - z\Delta(-is)} \tag{94}$$

where

$$z\Delta(t) = \mathcal{N}x \left\{ \sigma_{tr}(t) - \tfrac{1}{2} \cdot \frac{1}{(2\pi)^2} \cdot \int d^2k\, |\sigma_{tr}(t, \boldsymbol{k})|^2 (\hat{S}(\boldsymbol{k}) - 1) \right\} \tag{95}$$

and

$$\sigma_{tr}(t,\boldsymbol{k}) = \sum_{\alpha}(1-e^{-itT_\alpha})\sigma_\alpha(\boldsymbol{k}) \; ; \tag{95a}$$

$$\sigma_{tr}(t) \equiv \sigma_{tr}(t,\boldsymbol{k}=0) \; ; \tag{95b}$$

The second version of eq. (94) is a generalization of Landau's formula[4] to a nonrandom stopping medium. In the short-range limit, for an isotropic medium, eq. (95) simplifies to

$$z\Delta(t) = \mathcal{N}x\left\{\sigma_{tr}(t) - [\sigma_{tr}(t)]^2 \cdot \mathcal{N}\int_0^\infty dr(g_2(r)-1)\right\} ; \tag{96}$$

When (95) is evaluated in the diffusion approximation, eq. (82), (94) takes the form of a gaussian with the width Ω^2, eq. (89), centered around $\overline{\Delta E}$, eq. (88). Expansion up to third order in t yields an extension of Vavilov's formula[30],

$$z\Delta(t) \cong \mathcal{N}x\{itS + \tfrac{1}{2}t^2(W+\Delta W) - \tfrac{1}{6}it^3(Q+\Delta Q)\} \tag{97}$$

where

$$Q = \sum T_\alpha^3\sigma_\alpha = \int T^3 d\sigma(T) \; ; \tag{98}$$

and

$$\Delta Q = 3\cdot\frac{1}{(2\pi)^2}\int d^2k(\hat{S}(\boldsymbol{k})-1)\cdot \mathrm{Re}\,S(\boldsymbol{k})\,W^*(\boldsymbol{k}) \; ; \tag{99}$$

In particular, in the short-range approximation, we have

$$\Delta Q \cong 3SW\cdot 2\mathcal{N}\int_0^\infty dr(g_2(r)-1) \tag{99'}$$

and therefore

$$\frac{\Delta Q/Q}{\Delta W/W} \cong 3\frac{W^2}{QS}, \tag{100}$$

independent of the actual correlation function. The dimensionless ratio (100) is of the order of ~ 1, cf. eqs. (88a), (89a), and (98). Therefore, the skewness correction $\Delta Q/Q$ must normally be suspected to be of the same order of magnitude as the straggling correction $\Delta W/W$.

After insertion of (97) into (94) one obtains

$$G(\Delta E) \cong \frac{1}{2\pi}\int_{-\infty}^{\infty} dt e^{-\frac{t^2}{2}\mathcal{N}x(W+\Delta W)}\cdot\cos\{t(\Delta E - \mathcal{N}xS) + \tfrac{1}{6}t^3\mathcal{N}x(Q+\Delta Q)\} \tag{101}$$

or, in terms of Airy functions[16], the usual expression[29,30] with W replaced by $W+\Delta W$ and Q by $Q+\Delta Q$.

With regard to experimental checks of correlation effects on energy loss, straggling measurements on amorphous solids are desirable, preferably in targets where the pair correlation or the structure factor are known with sufficient accuracy, so that at least one of the two integrals in eq. (92) can be evaluated. As was the case in molecular targets, one might first wish to trace the energy region where $|\Delta W/W|$ is largest, i.e., where the stopping power has its maximum. In this region, the significant contributions to the stopping power originate from collisions at impact parameters $\lesssim a_0 v/v_0$ with $v \sim v_0$ for light ions,[5] where a_0 and v_0 are the Bohr radius and Bohr velocity. Therefore, the short-range approximation appears acceptable.

As a word of caution, one may add that the straggling and skewness parameters occurring in this discussion are to be understood strictly as defined through the second and third moment over an energy-loss distribution integrated over all scattering angles at a well-defined penetration depth. They are not necessarily related in a simple manner with the half-width of an energy-loss distribution integrated over a limited range of scattering angles. However, the problem of finding such a relationship[5] is only loosely connected with the effect of correlations on straggling, and therefore not discussed in more detail in this context.

Multiple Scattering

The problem of small-angle multiple scattering is a two-dimensional analog of the problem of energy loss, except for the fact that energy loss is a one-way process[31]. For a recent summary, the reader is referred to ref. 12.

In accordance with the notation applied in ref. 12, consider a series of scattering processes at small angles $\vec{\varphi}$, and take $\vec{\varphi}$ as a vector in a plane perpendicular to the beam. Then, the angular distribution after path length x reads, according to (31),

$$G(\boldsymbol{\alpha})d^2\alpha = \frac{d^2\alpha}{(2\pi)^2}\int d^2\varkappa e^{i\boldsymbol{\varkappa}\cdot\boldsymbol{\alpha}-z\Delta(\boldsymbol{\varkappa})}, \tag{102}$$

where, by means of (32) and (44)

$$z\Delta(\boldsymbol{\varkappa}) = Nx\left\{\sigma_0(\boldsymbol{\varkappa}) - \tfrac{1}{2}\cdot\frac{1}{(2\pi)^2}\cdot\int d^2k(\hat{S}(\boldsymbol{k})-1)\sigma(\boldsymbol{\varkappa},\boldsymbol{k})\sigma(\boldsymbol{\varkappa},-\boldsymbol{k})\right\}, \tag{103}$$

and

$$\sigma(\boldsymbol{\varkappa},\boldsymbol{k}) = \sum_{\vec{\varphi}} (1 - e^{-\boldsymbol{\varkappa}\cdot\vec{\varphi}}) \sigma_{\vec{\varphi}}(\boldsymbol{k}) \equiv \sum_{\vec{\varphi}} \int d^2p P_{\vec{\varphi}}(\boldsymbol{p}) e^{i\boldsymbol{k}\cdot\boldsymbol{p}} (1 - e^{-i\boldsymbol{\varkappa}\cdot\vec{\varphi}}) \; ; \tag{104a}$$

$$\sigma_0(\boldsymbol{\varkappa}) \equiv \sigma(\boldsymbol{\varkappa}, 0) \; ; \tag{104b}$$

Multiple scattering is normally dominated by nuclear collisions[5]. Therefore, application of the short-range approximation appears well justified[10], and

$$z\Delta(\varkappa) \cong \mathcal{N}x \left\{ \sigma_0(\boldsymbol{\varkappa}) - [\sigma_0(\boldsymbol{\varkappa})]^2 \cdot \mathcal{N} \int_0^\infty dr (g_2(r) - 1) \right\} ; \tag{105}$$

The transport cross section $\sigma_0(\boldsymbol{\varkappa})$ simplifies to

$$\sigma_0(\boldsymbol{\varkappa}) = \int d\sigma(\varphi) (1 - \mathcal{J}_0(\varkappa\varphi)) \equiv \sigma_0(\varkappa) \tag{104b'}$$

in case of azimuthally symmetric scattering. Similarly, (102) reads

$$G(\boldsymbol{\alpha}) \equiv G(\alpha) = \frac{1}{2\pi} \int_0^\infty \varkappa d\varkappa \mathcal{J}_0(\varkappa\alpha) e^{-z\Delta(\varkappa)} ; \tag{106}$$

Eq. (106) is Bothe's formula in the standard form applying to small-angle scattering. $\mathcal{J}_0$ is the zero-order Bessel function of the first kind.

Eq. (105) can be discussed along the same lines as eq. (96). In the particular case of a diatomic molecule, (105), (106), and (49) yield

$$G(\alpha) \cong \frac{1}{2\pi} \int_0^\infty \varkappa \mathrm{d}\varkappa \mathcal{J}_0(\varkappa\alpha) \cdot e^{-\mathcal{N}x\{\sigma_0(\varkappa) - \frac{1}{2}(\sigma_0(\varkappa))^2/2\pi d^2\}} , \tag{107}$$

a result that has been derived previously by a different procedure; it has also been evaluated explicitly, and confirmed experimentally[8,10].

It is an interesting feature of eq. (107) that it predicts a *smaller* half-width of the multiple-scattering profile for a diatomic gas, in comparison with the equivalent random medium. Since, in the short-range limit, the sign of the correction depends on the factor $2\mathcal{N}\int_0^\infty dr(g_2(r) - 1)$, cf. eq. (57), it may readily be concluded that for an amorphous target, the multiple scattering profile is *broader* than the profile for an otherwise equivalent random medium.

However, correlation effects on the multiple-scattering half-width in molecular gases have been found to be pronounced only at extremely small target thicknesses which are hard to achieve experimentally in solids. Therefore, these effects are important only in case of very thin amorphous layers ($\ll 100\,\text{Å}$).

Appendix A. Derivation of eqs. (73) and (74)

According to (71a) we have

$$T_{\{\epsilon\}\atop\{i\}} = \tfrac{1}{2}(T_1 + T_2) \pm \frac{\boldsymbol{P}_1 \cdot \boldsymbol{P}_2}{2M} \tag{A1}$$

and hence

$$W_{\{\epsilon\}\atop\{i\}} = <\int d^2p\, T_{\{\epsilon\}\atop\{i\}}{}^2 > = \tfrac{1}{4} <\int d^2p (T_1 + T_2)^2 > + X_1 \pm X_2 \tag{A2}$$

$$\Delta W_{ei} = <\int d^2p\, T_e T_i > = \tfrac{1}{4} <\int d^2p (T_1 + T_2)^2 - X_1 \tag{A3}$$

where

$$X_1 = \frac{1}{4M^2} <\int d^2p (\boldsymbol{P}_1 \cdot \boldsymbol{P}_2)^2 > \tag{A4}$$

and

$$X_2 = \frac{1}{4M^2} <\int d^2p (P_1{}^2 + P_2{}^2)(\boldsymbol{P}_1 \cdot \boldsymbol{P}_2) > ; \tag{A5}$$

Let us assume small-angle scattering to be dominating. Then, the momentum transfer is approximately perpendicular to the ion trajectory, or

$$\boldsymbol{P}_1 \equiv \boldsymbol{P}(\boldsymbol{p}_1) \cong \frac{\boldsymbol{p}_1}{p_1} P(p_1), \tag{A6}$$

and correspondingly for $\boldsymbol{P}_2$.

Intergrals are evaluated within the following scheme[9,10],

$$<\int d^2p f(\boldsymbol{p}_1, \boldsymbol{p}_2) > = \int d^2p_1 \int d^2p_2 f(\boldsymbol{p}_1, \boldsymbol{p}_2) < \delta(\boldsymbol{p}_1 - \boldsymbol{p}_2 - \boldsymbol{b}) >,$$

where $\boldsymbol{b}$ is the projection of the molecular axis on a plane perpendicular to the ionic trajectory. Moreover,

$$< \delta(\boldsymbol{p}_1 - \boldsymbol{p}_2 - \boldsymbol{b}) > \sim \frac{1}{2\pi d^2} + \mathrm{O}\left\{\frac{1}{d^4}\right\} \tag{A7a}$$

for short-range interaction, and

$$< \delta(\boldsymbol{p}_1 - \boldsymbol{p}_2 - \boldsymbol{b}) > \sim \delta(\boldsymbol{p}_1 - \boldsymbol{p}_2) + \frac{d^2}{6} \vec{\nabla}^2_{\boldsymbol{p}_1} \delta(\boldsymbol{p}_1 - \boldsymbol{p}_2) + \mathrm{O}\{d^4\} \tag{A7b}$$

for long-range interaction. After carrying out the integrations one finds

$$X_1 \sim \begin{cases} \dfrac{S_1^{\,2}}{4\pi d^2} & \text{(short-range)} \\ W_1 - \dfrac{d^2}{12}\int d^2p\left(\dfrac{dT}{dp}\right)^2 & \text{(long-range)} \end{cases} \tag{A8}$$

and

$$X_2 \sim \begin{cases} 0 & \text{(short-range)} \\ 2W_1 & \text{(long-range)} \end{cases} \tag{A9}$$

apart from terms that are small of order d^{-4} or d^4, respectively. After inserting X_1 and X_2 into (A2) and (A3), and applying (69) and (70), one finds (73) and (74).

Acknowledgements

My thanks are due to Nils Andersen, Harry Bernas, Kim Carneiro, Camille Cohen, Arnold Russek, Georg Sidenius, and Stig Steenstrup for valuable comments and suggestions, to George Amsel for constructive criticism, Jens Lindhard for useful suggestions concerning the manuscript, and professor C. Møller for his kind encouragement. Especially, I should like to thank the participants of four symposia on multiple scattering and related energy loss problems for providing much of the stimulation for the work described in this article.

References

1. N. Bohr, Phil. Mag. (VI) *30*, 581 (1915).
2. W. Bothe, Z. Physik *4*, 300 (1921), ibid. *5*, 63 (1921).
3. G. Wentzel, Ann. Physik *4*, *69*, 335 (1922).
4. L. Landau, J. Phys. USSR *8*, 201 (1944).
5. N. Bohr, Mat. Fys. Medd. Dan. Vid. Selsk. *18*, no. 8 (1948).
6. E. Fermi, Phys. Rev. *57*, 485 (1950).
7. Aa. Bohr, Mat. Fys. Medd. Dan. Vid. Selsk. *24*, no. 19 (1948).
8. G. Sidenius, N. Andersen, P. Sigmund, F. Besenbacher, J. Heinemeier, P. Hvelplund, & H. Knudsen, Nucl. Inst. Meth. *134*, 597 (1976).
9. P. Sigmund, Phys. Rev. A *14*, 996 (1976).
10. P. Sigmund, Mat. Fys. Medd. Dan. Vid. Selsk. *39*, no. 11 (1977).
11. F. Besenbacher, J. Heinemeier, P. Hvelplund, & H. Knudsen, Phys. Lett. *61 A*, 75 (1977).
12. P. Sigmund, Ann. Israel Phys. Soc. *1*, 69 (1977).
13. P. Sigmund, in preparation. Two preprints by the author (FL II Monographs 77-23 and 77-25) are partially in error and have been withdrawn from publication.
14. J. Lindhard, Mat. Fys. Medd. Dan. Vid. Selsk. *34*, no. 14 (1965).
15. W. Feller, An Introduction to Probability Theory and its Applications, Vol. I, Third Edition, Wiley (1968).
16. M. Abramowitz & I. A. Stegun, Handbook of Mathematical Functions, Dover (1965).
H. A. Bethe, Phys. Rev. *89*, 1256 (1953).
18. L. van Hove, Phys. Rev. *95*, 249 (1954).
19. J. O. Hirschfelder, C. F. Curtiss, & R. B. Bird, Molecular Theory of Gases and Liquids, Wiley (1954).
20. P. A. Egelstaff, An Introduction to the Liquid State, Academic Press (1967).
21. C. Kittel, Introduction to Solid State Physics, 4th edition, Wiley & Sons (1971).
22. F. Yssing Hansen, T. Steen Knudsen, & K. Carneiro, J. Chem. Phys. *62*, 1556 (1975).
23. W. E. Meyerhof & K. Taulbjerg, Ann. Rev. Nucl. Sci. *27*, 279 (1977).
24. D. H. Madison & E. Merzbacher, *in* Atomic Inner-Shell Processes, B. Craseman, editor, Academic Press. Vol. I (1975).
25. J. H. McGuire & P. Richard, Phys. Rev. A *8*, 1374 (1973).
26. P. Sigmund, J. Phys. B *11*, L 145 (1978), P. Sigmund & A. Russek, in preparation.
27. S. Chandrasekhar, Rev. Mod. Phys. *15*,1 (1943).
28. H. A. Bethe, Ann. Phys. (5) *5*, 325 (1930).
29. U. Fano, Ann. Rev. Nucl. Sci. *13*, 1 (1963).
30. P. V. Vavilov, Zh. Eksp. Teor. Fiz. *32*, 920 (1957) (Engl. Transl. Sov. Phys.-JETP *5*, 749 (1957)).
31. J. Lindhard & V. Nielsen, Mat. Fys. Medd. Dan. Vid. Selsk. *38*, no. 9 (1971).

Contributions to the Study of Babylonian Lunar Theory

By ASGER AABOE *and* NORMAN T. HAMILTON

Det Kongelige Danske Videnskabernes Selskab
Matematisk-fysiske Meddelelser **40**:6

Kommissionær: Munksgaard
1979

Synopsis

The principal part of the present contributions to the study of Babylonian lunar theory is a reconstruction of a scheme for computing the length of time intervals consisting of six consecutive synodic months. The authors give direct textual evidence for this scheme and employ it to bring under control several texts – most of them concerned with eclipses – in which six-month intervals play a role, and which hitherto have defied complete numerical analysis. Further, they take this opportunity to publish some results of their concern with the corpus of lunar texts of System A, most of them edited in ACT: new datings, interpretations, and joins of fragmentary texts.

ASGER AABOE
Yale University
New Haven, Connecticut
U.S.A.

NORMAN T. HAMILTON
Computer Center
University of Illinois at Chicago Circle
Chicago, Illinois
U.S.A.

Printed in Denmark by Bianco Lunos Bogtrykkeri A/S. ISSN 0023-3323 – ISBN 87-7304-071-1

To Otto Neugebauer
on the occasion of his eightieth birthday, 26 May 1979,
with admiration, gratitude, and affection.

In the present paper our chief concern is with the precise manner of computing certain time-intervals between like syzygies – conjunctions or oppositions of Sun and Moon – within Babylonian lunar theory according to System A. These intervals are the lengths of five or of six consecutive lunations, both important for the construction of eclipse tables, and they are affected by the variation in apparent lunar and solar velocities. The Babylonian numerical techniques for introducing the latter influence have long been reproducible and understood, and it is the ancient accounting for the effects of lunar anomaly that we are here bringing under exact control for the first time.

Our access to the electronic computers of our institutions, particularly the one at the Computer Center of the University of Illinois at Chicago Circle, is in large measure responsible for our success in reconstructiong the ancient scheme for deriving V and W, as we call the functions of relevance for 5-month and 6-month intervals, respectively.

In what follows, we first outline the background of our problem and present its solution. Next, we draw attention to direct textual support for our reconstructed scheme, and to texts that employ it. Finally, we take this opportunity to publish some new results on the corpus of lunar texts of System A in ACT,[1] though they have nothing directly to do with the functions V and W. In three instances we have joined new fragments to those published in ACT. In the rest we have used the extensive tables generated by our computers to date texts that remained undated in ACT, or to learn more about them in other respects.

All the cuneiform tablets we have occasion to mention happen to derive from the astronomical archive in Babylon – none is from Uruk – and they all came to the British Museum through acquisition from dealers during the last decades of last century. The hitherto unpublished texts, and the photographs, are published here through the courtesy of the Trustees of the British Museum.

A. Aaboe had the opportunity to collate several of the relevant texts in the British Museum in August 1977, enjoying once more the hospitality of the Department of Western Asiatic Antiquities[2] and of their Keeper, Dr. *Edmond Sollberger*.

1. For this and other abbreviations see the Bibliography.

2. *A. Aaboe's* previous visits to the British Museum, during which some of the fragments published below were rejoined, were supported by various grants from the National Science Foundation and by a Guggenheim Fellowship. The photographs are published through the courtesy of the Trustees of the British Museum.

1° Introduction of W and V

Otto Neugebauer's Astronomical Cuneiform Texts – ACT for short – appeared in 1955 and contained editions of the then known cuneiform texts that deal with mathematical astronomy, some 300 in number and almost all of the Seleucid period. Since then particular interest has been centred on a group of new texts, published by *Neugebauer* and by *Aaboe*, that threw light on a certain problem raised and left unsolved in ACT. It concerns the manner in which time intervals between like syzygies – either conjunctions or oppositions of Sun and Moon – were computed in the lunar theory according to System A.

The length of the true synodic month, say, from one conjunction to the next, is affected by the variation in both lunar and solar velocity. Babylonian lunar theory of both System A and System B separate these effects into two independent additive terms and consider the synodic month to be

$$1 \text{ month} = 29^{d} + G^{H} + J^{H} \text{ (see footnote 3)}$$

where G depends on lunar anomaly, and J on solar anomaly or rather on the Sun's longitude, for no distinction is drawn between sidereal and anomalistic year. System A has J depend directly on solar longitude in a manner that was under complete arithmetical control in ACT, and that makes astronomical sense as well. However, the derivation of G in this system raised difficulties, not of arithmetical, but of astronomical character.

Column G is derived from Column Φ, a zig-zag function of extrema

$M = 2;17,4,48,53,20^{H}$ and $m = 1;57,47,57,46,40^{H}$

and monthly difference

$$d = 0;2,45,55,33,20^{H/m}.$$

The period of Φ is the anomalistic month and Φ is, in fact, in precise phase with lunar velocity F. Column Φ is the second column of a standard lunar ephemeris according to System A, just following the one giving year and month. The sole purpose of Φ seemed to be to serve as a basis for the computation of G. The transformation of Φ into G is the subject of several procedure texts, a new variant of which we publish below as "ACT No. 207cc augmented." The scheme is summarised in Table 1 which in essence is a copy of the table given in ACT, p.60. It presents a selection of values of Φ – it matters whether such a value belongs to an ascending or descending branch of the zig-zag function, and this is indicated by the

3. $1^{d} = 6^{H} = 6{,}0$ (time) degrees. The large hour (H) is introduced for convenience in modern text editions; the Babylonian unit is the time degree (uš).

Table 1.

Φ		G	Interpol.
2;13,20↓	2;15,48,8,53,20↑	2;40	0
2;13,2,13,20↓	2;15,30,22,13,20↑	2;40,17,46,40	1
2;12,44,26,40↓	2;15,12,35,33,20↑	2;40,53,20	2
2;12,26,40↓	2;14,54,48,53,20↑	2;41,46,40	3
2;12,8,53,20↓	2;14,37,2,13,20↑	2;42,57,46,40	4
2;11,51,6,40↓	2;14,19,15,33,20↑	2;44,26,40	5
2;11,33,20↓	2;14,1,28,53,20↑	2;46,13,20	6
2;11,15,33,20↓	2;13,43,42,13,20↑	2;48,17,46,40	7
2;10,57,46,40↓	2;13,25,55,33,20↑	2;50,40	8
2;10,40↓	2;13,8,8,53,20↑	2;53,20	9
2;10,22,13,20↓	2;12,50,22,13,20↑	2;56,5,55,33,20	9;20
⋮	⋮	⋮	⋮
1;58,31,6,40↓	2;0,59,15,33,20↑	4,46,42,57,46,40	9;20
1;58,13,20↓	2;0,41,28,53,20↑	4,49,11,6,40	8;20
1;57,55,33,20↓	2;0,23,42,13,20↑	4,51,21,28,53,20	7;20
1;57,58,8,53,20↑	2;0,5,55,33,20↑	4,53,14,4,26,40	6;20
1;58,15,55,33,20↑	1;59,48,8,53,20↑	4,54,48,53,20	5;20
1;58,33,42,13,20↑	1;59,30,22,13,20↑	4,56	4
	1;59,12,35,33,20↑	4,56,35,33,20	2
	1;58,54,48,53,20↑	4,56,35,33,20	0
	1;58,37,2,13,20↑	4,56	2

Interpolation coefficients belong to the preceding intervals

small arrows – and the corresponding values of G. If a value of Φ is not in the table, the corresponding G-value is found by linear interpolation in Table 1. Thus the arithmetical structure of the Φ-G scheme was completely under control in ACT, but it was otherwise with its astronomical signifiance. It was not even known in what units Φ was measured – as indicated above, they turned out to be large hours.

The text that established this, and which brought Φ in connexion with the length of a Saros (an interval of 223 months) – we call it the Saros Text – was published by *Neugebauer* in 1957. The text is difficult and still not fully understood, but it enabled *Neugebauer* to perceive astronomical relations between Φ and G, and recognise that the difference between the length of 223 consecutive months and Φ should be constant. *B. L. van der Waerden* [1966] suggested that this constant should be a whole number of days (6585) and put forward the conjecture that the Φ-function when in actual use, and not just employed as an indicator of lunar anomaly, should be truncated above and below.

Beginning in 1968, *Aaboe* published a series of texts that were concerned with Column Φ in relation to other functions, measuring the length of various numbers of consecutive lunations. It was particularly Text E in *Aaboe* [1968] that offered an insight into a consistent methodology underlying the derivation of such inter-

vals as G from Φ. Text E dealt in tabular form with Φ and a function Λ, attested and named already in ACT though then of unknown significance, but in such a manner that it enabled *Aaboe* to identify Φ beyond doubt, as well as Λ, and to give an astronomical justification of the table's structure.

It appeared that Λ played a role equivalent to that of G, but for intervals of twelve months. Thus the twelve-month interval, or "year", is

$$12 \text{ months} = 354^{d} + \Lambda^{H} + Y^{H}$$

where Λ depends on Φ, i. e. on lunar anomaly, and Y on longitude (this component was found later, see *Aaboe* [1969]; we may add that though Y is closely related to J, it is not precisely equal to the sum of the relevant twelve J-values but incorporates an additive constant so that it vanishes on most of the fast arc, like J; this constant is absorbed in the mean value of Λ). With the method underlying Text E, *Aaboe* could justify the Φ-G scheme (see *Aaboe* [1968] and, most recently, HAMA).

Prompted by various ephemerides, mostly eclipse texts, *Aaboe* [1971] proposed the existence of an analogous function W concerned with six-month intervals and restored a small fragment of an auxiliary table according to the methods for generating G and Λ from Φ, but failed to reach perfect agreement with the ephemerides. He took the total length of the six lunations preceding syzygy number n to be

$$6 \text{ months} \equiv W(n) + Z(n),$$

modulo an integral number of days, where $W(n)$ depends on lunar anomaly, and $Z(n)$ on solar anomaly (the integral number of days is either 176, 177, or 178). The term $Z(n)$ offers no difficulties, for it is simply the sum of $J(n)$ and its five monthly predecessors (see, e. g. *Aaboe* [1971]); but it is not so with $W(n)$. Disregarding for the moment the five-month intervals, it is this function we find in the eclipse text ACT No. 60, Column VIII, and *Neugebauer* assumed, very naturally, that is should be the sum of the six relevant G-values, but this assumption led to perfect agreement with the preserved values of the text only in very few instances. To be sure, the deviations were in general small – small enough to allow a secure identification of the astronomical meaning of this column – but they seemed to be of a systematic character. Thus it was clear to *Neugebauer* that his assumption could not offer a consistent explanation of the arithmetical structure of Column VIII of No. 60.

It turns out that all but a few of the entries in this column – still excepting the five month intervals – can be exactly derived by linear interpolation in a Φ-W table (Table 2) which is gathered in the following simple arithmetical fashion (most of the few exceptions appear to be consequences of very natural arithmetical mistakes).

Table 2.

	Φ	W	Interpol.
1.	2, 13, 20 ↓	15, 5, 11, 6, 40	
	2, 13, 2, 13, 20 ↓	6, 34, 48, 53, 20	28; 42, 30
	2, 12, 44, 26, 40 ↓	5, 58, 40	26, 42, 30
	2, 12, 26, 40 ↓	5, 51, 21, 14, 4, 26, 40	24, 40, 50
5.	2, 12, 8, 53, 20 ↓	5, 44, 37, 31, 51, 6, 40	22; 42, 30
	2, 11, 51, 6, 40 ↓	5, 38, 29, 22, 57, 46, 40	20, 42, 30
	2, 11, 33, 20 ↓	5, 32, 56, 47, 24, 26, 40	18, 42, 30
	2, 11, 15, 33, 20 ↓	5, 27, 59, 45, 11, 6, 40	16, 42, 30
	2, 10, 57, 46, 40 ↓	5, 23, 38, 16, 17, 46, 40	14, 42, 30
10.	2, 10, 40 ↓	5, 19, 52, 20, 44, 26, 40	12; 42, 30
	2, 10, 22, 13, 20 ↓	5, 16, 41, 58, 31, 6, 40	10, 42, 30
	2, 10, 4, 26, 40 ↓	5, 14, 7, 9, 37, 46, 40	8, 42, 30
	2, 9, 46, 40 ↓	5, 12, 11, 36, 17, 46, 40	6, 30
	2, 9, 28, 53, 20 ↓	5, 10, 47, 54, 4, 26, 40	4, 42, 30
15.	2, 9, 11, 6, 40 ↓	5, 9, 59, 45, 11, 6, 40	2; 42, 30
	2, 8, 53, 20 ↓	5, 9, 47, 9, 37, 46, 40	0, 42, 30
	2, 8, 35, 33, 20 ↓	5, 10, 10, 7, 24, 26, 40	1; 17, 30
	2, 8, 17, 46, 40 ↓	5, 11, 8, 38, 31, 6, 40	3; 17, 30
	2, 8 ↓	5, 12, 42, 42, 57, 46, 40	5; 17, 30
20.	2, 7, 42, 13, 20 ↓	5, 14, 50, 22, 13, 20	7; 10, 50
	2, 7, 24, 26, 40 ↓	5, 17, 35, 33, 20	9; 17, 30
	2, 7, 6, 40 ↓	5, 20, 58, 1, 28, 53, 20	11; 23, 20
	2, 6, 48, 53, 20 ↓	5, 24, 54, 19, 15, 33, 20	13; 17, 30
	2, 6, 31, 6, 40 ↓	5, 29, 26, 10, 22, 13, 20	15; 17, 30
25.	2, 6, 13, 20 ↓	5, 34, 33, 34, 48, 53, 20	17; 17, 30
	2, 5, 55, 33, 20 ↓	5, 40, 16, 32, 35, 33, 20	19; 17, 30
	2, 5, 37, 46, 40 ↓	5, 46, 35, 3, 42, 13, 20	21; 17, 30
	2, 5, 20 ↓	5, 53, 29, 8, 8, 53, 20	23; 17, 30
	2, 5, 2, 13, 20 ↓	54, 48, 53, 20	25; 4, 10
30.	2, 4, 44, 26, 40 ↓	9	27; 17, 30
	2, 4, 26, 40 ↓	17, 40, 44, 26, 40	29, 17, 30
	2, 4, 8, 53, 20 ↓	26, 51, 51, 6, 40	31
	2, 3, 51, 6, 40 ↓	36, 20, 44, 26, 40	32
	2, 3, 33, 20 ↓	46, 7, 24, 26, 40	33
35.	2, 3, 15, 33, 20 ↓	56, 11, 51, 6, 40	34
	2, 2, 57, 46, 40 ↓	1, 6, 34, 4, 26, 40	35
	2, 2, 40 ↓	1, 17, 14, 4, 26, 40	36
	2, 2, 22, 13, 20 ↓	1, 28, 11, 51, 6, 40	37
	2, 2, 4, 26, 40 ↓	1, 39, 27, 24, 26, 40	38
40.	2, 1, 46, 40 ↓	1, 51, 0, 44, 26, 40	39
	2, 1, 28, 53, 20 ↓	2, 2, 51, 51, 6, 40	40
	2, 1, 11, 6, 40 ↓	2, 15, 0, 44, 26, 40	41
	2, 0, 53, 20 ↓	2, 27, 27, 24, 26, 40	42
	2, 0, 35, 33, 20 ↓	2, 40, 11, 51, 6, 40	43
45.	2, 0, 17, 46, 40 ↓	2, 53, 14, 4, 26, 40	44
	2 ↓	3, 6, 34, 4, 26, 40	45
	1, 59, 42, 13, 20 ↓	3, 20, 11, 51, 6, 40	46
	1, 59, 24, 26, 40 ↓	3, 34, 5, 25, 55, 33, 20	46; 53, 20
	1, 59, 6, 40 ↓	3, 48, 18, 45, 55, 33, 20	48
50.	1, 58, 48, 53, 20 ↓	4, 2, 49, 52, 35, 33, 20	49
	1, 58, 31, 6, 40 ↓	4, 17, 38, 45, 55, 33, 20	50
	1, 58, 13, 20 ↓	4, 32, 27, 39, 15, 33, 20	50
	1, 57, 55, 33, 20 ↓	4, 47, 16, 32, 35, 33, 20	50
	1, 57, 58, 8, 53, 20 ↑	5, 2, 5, 25, 55, 33, 20	50
55.	1, 58, 15, 55, 33, 20 ↑	5, 16, 54, 19, 15, 33, 20	50
	1, 58, 33, 42, 13, 20 ↑	5, 31, 37, 17, 2, 13, 20	49, 40
	1, 58, 51, 28, 53, 20 ↑	5, 45, 51, 51, 6, 40	48; 4, 10
	1, 59, 9, 15, 33, 20 ↑	5, 59, 48, 8, 53, 20	47; 2, 30
	1, 59, 27, 2, 13, 20 ↑	13, 8, 53, 20	45; 2, 30
60.	1, 59, 44, 48, 53, 20 ↑	25, 54, 4, 26, 40	43; 2, 30
	2, 0, 2, 35, 33, 20 ↑	38, 1, 28, 53, 20	40, 55
	2, 0, 20, 22, 13, 20 ↑	49, 32, 13, 20	38, 51, 15
	2, 0, 38, 8, 53, 20 ↑	1, 0, 27, 24, 26, 40	36, 51, 15
	2, 0, 55, 55, 33, 20 ↑	1, 10, 47, 2, 13, 20	34, 51, 15
65.	2, 1, 13, 42, 13, 20 ↑	1, 20, 27, 9, 37, 46, 40	32; 37, 55
	2, 1, 31, 28, 53, 20 ↑	1, 29, 25, 40, 44, 26, 40	30; 17, 30

	Φ	W	Interpol.
66.	2, 1, 31, 28, 53, 20 ↑	1, 29, 25, 40, 44, 26, 40	
	2, 1, 49, 15, 33, 20 ↑	1, 38, 1, 58, 31, 6, 40	29; 2, 30
	2, 2, 7, 2, 13, 20 ↑	1, 46, 2, 42, 57, 46, 40	27; 2, 30
	2, 2, 24, 48, 53, 20 ↑	1, 53, 27, 54, 4, 26, 40	25; 2, 30
70.	2, 2, 42, 35, 33, 20 ↑	2, 0, 17, 17, 2, 13, 20	23; 1, 40
	2, 3, 0, 22, 13, 20 ↑	2, 6, 28, 1, 28, 53, 20	20, 51, 15
	2, 3, 18, 8, 53, 20 ↑	2, 12, 3, 12, 35, 33, 20	18, 51, 15
	2, 3, 35, 55, 33, 20 ↑	2, 17, 2, 50, 22, 13, 20	16, 51, 15
	2, 3, 53, 42, 13, 20 ↑	2, 21, 24, 56, 17, 46, 40	14, 44, 35
75.	2, 4, 11, 28, 53, 20 ↑	2, 25, 3, 27, 24, 26, 40	12; 17, 30
	2, 4, 29, 15, 33, 20 ↑	2, 28, 19, 45, 11, 6, 40	11; 2, 30
	2, 4, 47, 2, 13, 20 ↑	2, 31, 0, 29, 37, 46, 40	9; 2, 30
	2, 5, 4, 48, 53, 20 ↑	2, 33, 5, 40, 44, 26, 40	7; 2, 30
	2, 6, 22, 35, 33, 20 ↑	2, 34, 37, 2, 13, 20	5; 8, 20
80.	2, 5, 40, 22, 13, 20 ↑	2, 35, 27, 46, 40	2, 51, 15
	2, 5, 58, 8, 53, 20 ↑	2, 35, 42, 57, 46, 40	0; 51, 15
	2, 6, 15, 55, 33, 20 ↑	2, 35, 22, 35, 33, 20	1; 8, 45
	2, 6, 33, 42, 13, 20 ↑	2, 34, 26, 40	3; 8, 45
	2, 6, 51, 28, 53, 20 ↑	2, 32, 51, 51, 6, 40	5; 20
85.	2, 7, 9, 15, 33, 20 ↑	2, 30, 34, 48, 53, 20	7; 42, 30
	2, 7, 27, 2, 13, 20 ↑	2, 27, 55, 33, 20	8; 57, 30
	2, 7, 44, 48, 53, 20 ↑	2, 24, 40, 44, 26, 40	10; 57, 30
	2, 8, 2, 35, 33, 20 ↑	2, 20, 50, 22, 13, 20	12; 57, 30
	2, 8, 20, 22, 13, 20 ↑	2, 16, 22, 13, 20	15; 5
90.	2, 8, 38, 8, 53, 20 ↑	2, 11, 17, 24, 26, 40	17; 8, 45
	2, 8, 55, 55, 33, 20 ↑	2, 5, 37, 2, 13, 20	19; 8, 45
	2, 9, 13, 42, 13, 20 ↑	1, 59, 21, 6, 40	21; 8, 45
	2, 9, 31, 28, 53, 20 ↑	1, 52, 25, 40, 44, 26, 40	23, 22, 5
	2, 9, 49, 15, 33, 20 ↑	1, 44, 48, 38, 31, 6, 40	25; 42, 30
95.	2, 10, 7, 2, 13, 20 ↑	1, 36, 49, 22, 57, 46, 40	26, 57, 30
	2, 10, 24, 48, 53, 20 ↑	1, 28, 14, 34, 4, 26, 40	28, 57, 30
	2, 10, 42, 35, 33, 20 ↑	1, 19, 4, 11, 51, 6, 40	30, 57, 30
	2, 11, 0, 22, 13, 20 ↑	1, 9, 18, 1, 28, 53, 20	32; 58, 20
	2, 11, 18, 8, 53, 20 ↑	58, 53, 12, 35, 33, 20	35; 8, 45
100.	2, 11, 35, 55, 33, 20 ↑	47, 52, 50, 22, 13, 20	37; 8, 45
	2, 11, 53, 42, 13, 20 ↑	36, 16, 54, 48, 53, 20	39; 8, 45
	2, 12, 11, 28, 53, 20 ↑	24, 3, 27, 24, 26, 40	41; 15, 25
	2, 12, 29, 15, 33, 20 ↑	11, 6, 25, 11, 6, 40	43; 42, 30
	2, 12, 47, 2, 13, 20 ↑	5, 57, 47, 9, 37, 46, 40	44; 57, 30
105.	2, 13, 4, 48, 53, 20 ↑	5, 43, 52, 20, 44, 26, 40	46, 57, 30
	2, 13, 22, 35, 33, 20 ↑	5, 29, 26, 47, 24, 26, 40	48; 41, 15
	2, 13, 40, 22, 13, 20 ↑	5, 14, 42, 57, 46, 40	49; 42, 55
	2, 13, 58, 8, 53, 20 ↑	4, 59, 54, 4, 26, 40	50
	2, 14, 15, 55, 33, 20 ↑	4, 45, 5, 11, 6, 40	50
110.	2, 14, 33, 42, 13, 20 ↑	4, 30, 16, 17, 46, 40	50
	2, 14, 51, 28, 53, 20 ↑	4, 15, 27, 24, 26, 40	50
	2, 15, 9, 15, 33, 20 ↑	4, 0, 41, 6, 40	49, 51, 15
	2, 15, 27, 2, 13, 20 ↑	3, 46, 12, 35, 33, 20	48, 51, 15
	2, 15, 44, 48, 53, 20 ↑	3, 32, 1, 51, 6, 40	47; 51, 15
115.	2, 16, 2, 35, 33, 20 ↑	3, 18, 11, 43, 42, 13, 20	46, 41, 40
	2, 16, 20, 22, 13, 20 ↑	3, 4, 36, 32, 35, 33, 20	45; 51, 15
	2, 16, 38, 8, 53, 20 ↑	2, 51, 19, 8, 8, 53, 20	44; 51, 15
	2, 16, 55, 55, 33, 20 ↑	2, 38, 19, 30, 22, 13, 20	43; 51, 15
	2, 16, 55, 55, 33, 20 ↓	2, 25, 37, 39, 15, 33, 20	42; 51, 15
120.	2, 16, 38, 8, 53, 20 ↓	2, 13, 13, 34, 48, 53, 20	41, 51, 15
	2, 16, 20, 22, 13, 20 ↓	2, 1, 7, 17, 2, 13, 20	40; 51, 15
	2, 16, 2, 35, 33, 20 ↓	1, 49, 18, 45, 55, 33, 20	39; 51, 15
	2, 15, 44, 48, 53, 20 ↓	1, 37, 48, 1, 28, 53, 20	38; 51, 15
	2, 15, 27, 2, 13, 20 ↓	1, 26, 35, 55, 33, 20	37; 48, 20
125.	2, 15, 9, 15, 33, 20 ↓	1, 15, 40, 44, 26, 40	36; 51, 15
	2, 14, 51, 28, 53, 20 ↓	1, 5, 3, 20	35; 51, 15
	2, 14, 33, 42, 13, 20 ↓	54, 43, 42, 13, 20	34; 51, 15
	2, 14, 15, 55, 33, 20 ↓	44, 41, 51, 6, 40	33; 51, 15
	2, 13, 58, 8, 53, 20 ↓	34, 57, 46, 40	32; 51, 15
130.	2, 13, 40, 22, 13, 20 ↓	25, 31, 28, 53, 20	31; 51, 15
	2, 13, 22, 35, 33, 20 ↓	16, 22, 57, 46, 40	30; 51, 15
	2, 13, 20 ↓	15, 5, 11, 6, 40	30

ACT No. 1005

First we take a sequence of Φ-values covering one wave of the Φ-function fairly densely. More specifically, we begin with the value 2,13,20↓ and proceed in steps of 17,46,40, reflecting as usual in Φ's extrema (see Table 2). The difference 17,46,40 has astronomical significance: it is the effective change in Φ over one Saros, or 223 months. This fact is of absolute essence in other tables involving Φ, but here any other small regular number might in principle have served as well. This particular choice of spacing between the Φ-values offers, however, the convenience that the first 56 entries in the Φ-column of Table 2 are also found in the Φ-G scheme (Table 1), and various other advantages as well. After 131 steps we are very nearly back to the initial value of Φ.

Next we associate with each of these 131 Φ-values a value of W which is the sum of six successive monthly G-values, the last of which corresponds to the relevant Φ-value.

As an example, consider the first entry in the table. The Φ-value is 2,13,20↓, and it and its five monthly prececessors have associated with them, according to Table 1, the following G-values:

$\Phi_0 = 2;13,20\downarrow \quad \sim \quad G_0 = 2;40^{H}$
$\Phi_{-1} = 2;16,5,55,33,20\downarrow \quad \sim \quad G_{-1} = 2;40$
$\Phi_{-2} = 2;15,17,46,40\uparrow \quad \sim \quad G_{-2} = 2;40,42,57,46,40$
$\Phi_{-3} = 2;12,31,51,6,40\uparrow \quad \sim \quad G_{-3} = 2;58,58,45,55,33,20$
$\Phi_{-4} = 2;9,45,55,33,20\uparrow \quad \sim \quad G_{-4} = 3;24,47,24,26,40$
$\Phi_{-5} = 2;7\uparrow \quad \sim \quad G_{-5} = \underline{3;50,36,\ 2,57,46,40}$
whose sum is: $\sum G = 18;15,\ 5,11,\ 6,40^{H}$

or, reduced modulo 6 in the first place, 15,5,11,6,40 which is the value of W entered opposite 2,13,20↓ in the table.

Thus the Φ-W table is constructed, and if we wish to find a value of W corresponding to a Φ-value that does not occur in the first column, we simply interpolate linearly. The relevant interpolation coefficients are given in the last column of Tables 2a and b (such a coefficient belongs to the interval preceding the line in which it is entered).

This scheme, motivated only by a desire for arithmetical convenience, serves to explain precisely several hitherto puzzling lunar texts where intervals of six months are of concern, as we shall see.

Intervals of six months are, of course, primarily of interest when one is dealing with eclipses, but here an occasional five-month interval will occur. It is a natural assumption that there was a table, similar to that for W, for five-month intervals, and *Aaboe* [1971] constructed such a function – he called it V – according to the same general principles that underlie the Φ-G and Φ-Λ schemes. In fact, it turns

out that the length of a five month interval was derived by combined use of the tables for W and G. More precisely, to compute the length of the five months previous to syzygy number n one found first the six-month interval belonging to the *next* syzygy and then subtracted the length of the last month or, if we retain the notation V for the five month interval,

$$V(n) = W(n+1) - G(n+1).$$

2° Textual Evidence for **Φ**-W Scheme

There is direct textual evidence that the Babylonian astronomers possessed a scheme much like Table 2. First there is the small fragment BM 45930 (Text D in *Aaboe* [1971]) whose preserved surface corresponds to the outlined area between lines 36 and 47 of Table 2, except for isolated digits. *Aaboe* recognised that he was dealing with a function concerning the length of six-month intervals, named it W, and reconstructed the scheme according to the general methodology of functions related to Φ. His reconstruction fits the fragment perfectly, but it failed to reproduce exactly the entries in texts like No. 60. As fate would have it, his Text D is broken just so that it can equally well be accounted for by *Aaboe's* scheme as by Table 2, for it covers almost precisely the intersection of the two schemes. A few more preserved lines would surely have deviated from the values reconstructed by *Aaboe*, for not only is there close agreement between Table 2 and the ephemerides, but ACT No. 207 gives the endings of lines 15-26 of the scheme's W-values, and ACT No. 1005 actually preserves eight lines of the interpolation column of Table 2.

ACT No. 207 (BM 33593)
Transcription: Table 3.
The text is a fragment with only one side preserved. *Neugebauer* restored lines 8' to 14' as though they belonged to the Φ-G scheme, but could not make sense of the first seven lines. In fact, the text agrees perfectly with the endings of the W-values in lines 15 to 26 of Table 2. We think it unlikely that this fragment derives from the same tablet as Text D in *Aaboe* [1971]. The phrase *šá alla* [. . .] (whatever is beyond/below) indicates that an interpolation is called for. Thus we find, for example, in ACT No. 200b, Section 2 the formular "*šá alla x* dirig gam *y* DU-*ma* . . ." which means "whatever exceeds *x* multiply by *y* . . ." where interpolation is described. For the rest of the phrase see ACT No. 1005 below.

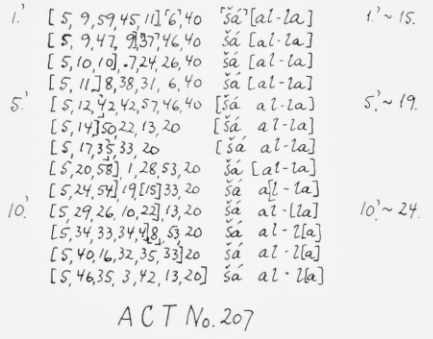

ACT No. 1005 (BM 34497)

This small fragment is published in transcription among the unidentified texts at the end of ACT, and in *Pinches's* copy as LBAT No. 156. It contains the outlined interpolation coefficients from line 121 to 128 of Table 2. What raises our identification of the text beyond any doubt is the presence of the peculiar value 37;48,20 in line 124, for it breaks an otherwise simple and natural pattern. In *Neugebauer's* transcription the numbers from Table 2 are preceded by initial 10's. However, an inspection of *Pinches's* copy shows that what *Neugebauer* read as 10 is almost certainly the sign GAM of two diagonal wedges and this is confirmed by collation. The second and third preserved lines end with remnants of signs that *Neugebauer* read as DU (rá) on which basis he surmised that the text gave a list of coefficients. The phrase "gam *x* DU" means "multiply by *x*" (cf. glossary of ACT and commentary to No. 207 above). In the fourth line is preserved what may be part of the last digit of a W-value.

Where Pinches read 32 in the last line, *Neugebauer* read 33 in agreement with Table 2. *Neugebauer's* reading is confirmed by collation.

3° Texts Employing W and V

We shall now turn to ephemerides containing the W-function. In our discussion we shall limit ourselves to the relevant columns; for the full extent of these texts we refer the reader to the original publications.

ACT No. 60 (BM 45688)
This large, well-preserved tablet from Babylon concerns lunar eclipse possibilities from S. E. 137 to 160 (=–174/3 to –151/0). It gives information about those members of a sequence of consecutive oppositions of the Moon where lunar latitude at a change of sign is smaller in absolute value. Curvature suggests that the right third of the tablet is broken off, so that it very likely contained all necessary columns up to and including at least Column M, the moment of syzygy, here opposition.

In Table 4 we have extracted Columns I, II, and VIII from this text, the column giving year and month, Column Φ, and a column with W and V. The lines are mostly six months apart. A dotted line indicates an occasional five-month interval and in the following line a value of V is in order in Column VIII.

Where the preserved numbers in Column VIII agree with the scheme in Table 2 – or with the rule for computing a five-month interval – we have simply supplied the missing digits of the recomputed values in square brackets. Where they disagree, we have added the correctly computed number in the last column of Table 4. For an explanation of most of these divergencies, see the critical apparatus below.

We have a particular affection for this text: from its Column B *Kugler* (BMR p. 55f) managed to discover for the first time the rules for computing lunar longitudes according to System A, a remarkable achievement since it contains longitudes, not month by month, but 5 or 6 months apart. *Strassmaier's* copy is published in BMR, Tafel XIII, and *Pinches's* as LBAT No. 50.

Critical Apparatus
With but three exceptions, each of the errors in Column VIII can be explained as the result of a simple misuse of Table 2. We include a discussion of these, for such errors – rare in the astronomical literature as whole – afford us an insight into the computational routines of the Babylonian astronomers. Thus we learn that when they entered their version of Table 2 with a given value of Φ, they invariably related it to the Φ-value in the *first* line of the interval to which it belongs. In three instances they erred by taking the interpolation coefficient from the line just before that of the correct one. In four cases the error consists in a shift of the interpolated part one sexagesimal place to the right or left of the correct position.

Obv. 1. 1: We cannot derive this value from Table 2. A recent collation shows clearly 20,52,5[0. . .], with 4[0] possible in the last place, but not 20,32,5[0. . .] as in ACT.

Obv. 1. 2:

We have for

$2{,}17\ \text{VIII}:\Phi = 1;58,40,44,26,40\uparrow$

Table 2, 1. 56: $1;58,33,42,13,20\uparrow \sim 5;31,37,17,\ 2,13,20$

$0;\ 0,\ 7,\ 2,13,20 \times 49;40 = 0;\ 5,49,30,22,13,20$

$W = 5;37,26,47,24,26,40$

which agrees with the text's 5,37,26,47 [. . .]. However, 49;40 is the interpolation coefficient for the interval preceding 1. 56. The correct coefficient, 48;4,10, is found in 1. 57.

Obv. 1. 3:

If we use the interpolation coefficient 49;51,15 (1. 112) we obtain in a like manner

$$W = 3;54,50,17,7,46,40^{H}$$

(text: 3,54,50,17,$\overline{6}$[. .]). The correct coefficient is 48;51,15 (1. 113).

Obv. 1. 4:

If we use the interpolation coefficient 37 (1. 38) we get

$$W = 1;30,56,17,46,40^{H}$$

(text: 1,30,56,17,4[0. . .]). The correct coefficient is 38 (1. 39).

Obv. 1. 11:

We obtain the text's $0;13,20,22,13,20^{H}$ if we enter Table 2 with

$$\Phi = 2;4,35,33,20\downarrow$$

instead of the correct

$$\Phi = 2;4,35,55,33,20\downarrow.$$

Obv. 1. 21:

At 2,26 VII we expect a value of V for the five-month interval. If we go one month ahead to month VIII we find the value of Φ to be

$$\Phi = 1;59,54,48,53,20\uparrow$$

to which Table 2 assigns $W = 0;32,43,14,26,40^{H}$. This is precisely the entry of the text, so the scribe forgot to subtract the appropriate value of G, namely

$$G = 4;54,13,20^{H}.$$

Four of the next five errors arise from a misalignment of the interpolated part. We shall only deal with the first of them in detail since the rest follow the same pattern.

Table 4.

	I	II	VIII	
Obv. 1.	2,17 V	2,13,30,44,26,40↓	20,52,50[////////]	20,34,22,2,13,20
	VIII	1,58,40,44,26,40↑	5,37,26,47[////////]	5,37,15,33,1,28,53,20
	2,18 I	2,15,16,17,46,40↑	3,54,50,17,6[////////]	3,54,57,19,21,6,40
	VII	2,2,17,46,40↓	1,30,56,17,40[////////]	1,31,0,44,26,40
5.	XII	2,7,7,46,40↑	4,19,14,.,44,26,40]	
	2,19 VI	2,10,26,17,46,40↓	5,17,25,36,6,40]	
	XII	2,1,45,11,6,40↑	1,36,3,39,26,[40]	
	2,20 VI	2,15,48,53,20↓	1,40,26,19,10	
	XII	1,59,13,20↓	3,42,58,45,55,3[3,20]	
10.	2,21 V	2,12,58,8,53,20↑	5,49,5,24,4,26[40]	
	XI	2,4,35,55,33,20↓	13,20,22,10[////////]	13,9,31,17,46,40
	2,22 V	2,7,35,33,20↑	2,26,22,12,24[26,40]	
	X	2,12,44,26,40↓	2,13,41,28,53,20]	
	2,23 III	1,59,27,2,13,20↑	13,8,53,20]	
15.	IX	2,16,2,35,33,20↑	3,18,11,43,42,13[20]	
	2,24 III	2,1,31,28,53,20↓	2,1,8,8,53,20	
	IX	2,10,40↑	1,20,24,27,35,33,[20]	
	2,25 III	2,6,54,4,26,40↓	5,23,45,24,4,26,40	
	IX	2,5,17,24,26,40↑	2,34,10,23,27,24,26,40	
20.	2,26 II	2,12,16,40↓	5,47,34,9,4,26,40	
	VIII	1,58,27,2,13,20↓	32,43,14,26,40	1,38,29,54,26,40
	2,27 I	2,13,44,26,40↑	5,14,39,34,4,26,40	5,11,19,15,33,20
	VII	2,3,49,37,46,40↓	37,9,37,46,40	
	2,28 I	2,8,21,51,6,40↑	2,15,56,49,15,33,20	
25	VII	2,9,12,13,20↓	5,10,.2,45,44,26,40]	
	XII$_2$	2,2,59,15,33,20↑	2,.23,4,36[////]	2,6,4,51,12,13,20
	2,29 VI	2,14,34,48,53,20↓	55,22,25,50]	
	XI	2,.45,11,6,40↓	5[53,17,2,13,20]	
Rev. 1.	2,30 V	2,11,26,17,46,40↑	5[3,]5[0,32,24,26,40]	
	XI	2,6,7,46,40↓	5,36,20,4[5,22,13,20]	
	2,31 V	2,6,3,42,13,20↑	2,3[0].4,2[0////////]	2,35,36,35,50
	X	2,11,30,22,13,20↓	5,32[7,17,2,13,20]	
5.	2,32 IV	2,.41,6,40↑	1,2,1[0,40,44,26,40]	
	X	2,16,52,57,46,40↓	2,25,35,1[0////////]	2,23,33,38,31,6,40
	2,33 IV	2,.17,24,26,40↓	2,53,30,44[26,40]	
	IX	2,9,8,8,53,20↑	3,31,10,16,3[0,44,26,40]	
	2,34 II	2,8,25,55,33,20↓	5,41,51,58,2[0////////]	5,10,41,49,15,33,20
10.	VIII	2,3,45,33,20↑	2,19,24,48,[34,46,53,20]	
	2,35 II	2,13,48,31,6,40↓	29,51,2,2,13,[20]	
	VIII	1,58,22,57,46,40↑	5,22,43,49,37,46,[40]	
	2,36 II	2,14,58,31,6,40↑	4,9,37,34,54[26,40]	4,9,36,34,54,26,40
	VII	2,2,35,33,20↓	1,19,58,31[6,40]	
15.	XII$_2$	2,6,50↑	3,24,10,46////]	4,24,10,40,44,26,40
	2,37 VI	2,10,44,4,26,40↓	5,20,44,[7,13,20]	
	XII	2,1,27,24,26,40↑	1,27,22[16,6,40]	
	2,38 VI	2,16,6,40↓	2,34[////////////]	1,52,1,8,3,20
	XII	1,59,31,6,40↓	[////////////////]	
20.	2,39 VI	2,12,40,22,13,20↑	[////////////////]	
	XII	2,4,53,42,13,20↓	[////////////////]	
	2,40 V	2,7,17,46,40↑	[////////////////]	

From ACT No. 60

Obv. l. 22:

The computation should have proceeded thus:

2,27 I: $\Phi = 2;13,44,26,40\uparrow$

Table 2, l. 107: $\underline{2;13,40,22,13,20\uparrow} \quad \sim 5;14,42,57,46,40$

$\underline{0;\ 0,\ 4,\ 4,26,40 \times 50} \quad = 0;\ 3,23,42,13,20$

which yields $\overline{W = 5;11,19,15,33,20^{H}}.$

If, however, the interpolated part by mistake is moved one place to the right we obtain

$$\begin{array}{r} 5;14,42,57,46,40 \\ \underline{-0;\ 0,\ 3,23,42,13,20} \\ 5;14,39,34,\ 4,26,40. \end{array}$$

which is precisely the value in the text.

Obv. l. 26:

If the interpolated part is shifted one place to the right we get

$$W = 2;0,23,4,36,23,20^{H}$$

(text: 2,.,23,4,36[. . .]).

Rev. l. 3:

The reading given in Table 4 is not at all secure. However, we are fairly certain that neither the correct value, nor the results of natural mistakes can be brought in agreement with the preserved traces.

Rev. l. 6:

Shifting the interpolated part one place to the right we get

$$W = 2;25,35,35,14,48,53,20^{H}$$

(text: 2,25,35,1[0 . . .] ending with one corner wedge).

Rev. l. 9:

If we move the interpolated part one place to the left we get

$$W = 5;41,51,58,31,6,40^{H}$$

(text: 5,41,51,58,2[0 . . .] ending with two corner wedges).

Rev. l. 13:

The text has 37 for 36 in the third place.

Rev. l. 15:

The text has 3 for 4 in the first place.

Rev. l. 18:

Only traces of the first two digits remain. The best reading is 2,34 [. . .], but it is not very secure. However, they clearly do not agree with the correct value of

$$W = 1;52,1,8,3,20^{H}.$$

ACT No. 61a (BM 77238)

This fragmentary text, also from Babylon, concerns solar eclipse possibilities, but it is in other respects quite like No. 60. However, it contains further columns with corrections for solar anomaly and variable length of daylight while such columns were broken away from No. 60. In Table 5, the V-W column of No. 61a is presented in the manner of Table 4. The first line contains a V-value, computed as described above, though proper consideration of latitude would have placed the five-month interval one line earlier. Except for the remnants of line 2 the preserved parts are in agreement with the W-scheme in Table 2.

Critical Apparatus

l. 2: If we enter Table 2 with

$$\Phi = 2;15,40,17,46,40\uparrow$$

instead of the correct value

$$\Phi = 2;15,41,17,46,40\uparrow$$

we obtain $W = 3;35,38,4,54,26,40^{H}$

(text: [. . .] 5,38,4,54,26,40).

Table 5.

	[T]	[Φ]	I	
1.	3,11* II	1,59,5,44,26,40↑	[3,0,33,14,54,26,40	(5 mo.)
	VIII	2,15,41,17,46,40↑	[////35,38,4,54,26,40	3,34,50,13,39,26,40
	3,12 I	2,1,52,46,40↓	[1,47,2,24,26,40	
	VII	2,10,18,42,13,20↑	[1,31,11,32,7,46,40	
5.	3,13 I	2,7,15,22,13,20↓	[1,19]18,53,57,2,13,20	
	VII	2,4,56,6,40↑	[2,32]4,23[25,33,20]	

From ACT No. 61a

ACT No. 55 (BM 46015)

This text was first published in ACT. *Neugebauer* realised that an advance of one line in the text very likely corresponded to a 12-month interval, at least in most cases. However, he recognised the entry in Obv. Col. II, l.4 as the G-value belonging to the conjunction at the end of S.E. 3,2 III. With his newly gained knowledge of the family of functions related to Φ, *Aaboe* [1971] identified most of the entries of the text's second column as Λ-values, confirmed *Neugebauer's* dating, and restored the text. He further identified the entry in Obv. II, 1.3 as a W-value,

but could not reproduce it precisely. He realised that the text broke an interval of one Saros (223 months) into 18 twelve-month intervals, one six-month, and one one-month interval, or

$$223 \text{ months} = (18 \cdot 12 + 1 \cdot 6 + 1 \cdot 1) \text{ months}.$$

The later columns contain corrections for solar anomaly, and for seasonal change in length of daylight, and finally the corrected values of Λ, W, and G.

For the W-value in Obv. II, l.3 *Aaboe* read with *Neugebauer*

$$W = 1,.,6,55,48,20 \text{ tab.}$$

The Φ-value given by *Aaboe* for this line (S.E. 3,2 II) is

$$\Phi = 2;0,37,35,33,20\uparrow$$

to which Table 2 assigns

$$W = 1;0,6,55,58,20^{H}.$$

Thus the last bit of ACT No. 55 is explained, for the next to last digit is poorly preserved and can be read 58 equally well as 48 (confirmed by recent collation).

ACT No. 54 (BM 35231+ 35355)

This text, composed of two small rejoined fragments, is published in transcription as ACT No. 54 and, in *Pinches's* copy, as LBAT Nos. 47 and 48. *Neugebauer* recognised that it is part of an eclipse text, and identified the character of the columns. The text, it now turns out, does indeed deal with eclipse possibilities – solar eclipses – from S.E. 235 to 241, as far as it is preserved. In Table 6 (p. 19) we have reconstructed the relevant columns of the text, numbering them so that Column I is the first of which any trace is preserved (this is little enough: merely traces of a final 1a1).

Critical Apparatus

II,8': only traces of tops of signs remain.
III,8': the last two digits are nearly destroyed.
III,10': 3,1*9,9* should be 3,1*8,47*; this error affects the rest of Column M.
III,14': [ ],39,21 – reading uncertain, but traces are not consistent with the correct value of 3,51,37.
IV,14': leading digit – all preserved – could also be 5.

Comments

We have included in Table 6 only those columns that are relevant for the restoration of the fragment. We shall here merely identify them briefly and refer to ACT and later publications for further explanations:

Columns T_1 and Φ_1 we have already met. The subscript$_1$ means, in the conven-

tion of ACT, that we are dealing with conjunctions rather than oppositions of Sun and Moon.

Column B_1 gives the common longitude of Sun and Moon at conjunction. It is computed on the basis of a step-function which, in modern terms, can be looked upon as giving solar velocity in degrees per month, thus:

from Virgo 13° to Pisces 27°: $w_1 = 30°/m$

from Pisces 27° to Virgo 13°: $w_2 = 28;7,30°/m$.

Column C_1 gives length of daylight in large hours as a function of solar longitude. For the scheme for converting B_1 into C_1 see ACT.

Column E_1 gives lunar latitude at conjunction in še (barley corn) where

$$1 \text{ še} = 0;0,50°.$$

These values are designated

lal lal (positive, increasing)	u u (negative, decreasing)
lal u (positive, decreasing)	u lal (negative, increasing)

with a terminology peculiar to Column E (elsewhere lal means negative, as in Columns I and II, or decreasing, while tab means positive or increasing). For the structure of Column E see ACT, HAMA, and *Aaboe-Henderson* [1975]. It is Column E that guides the selection of the conjunctions included in the text: they are the ones at which E at a sign change has smaller absolute value, as already mentioned.

Column [0] contains the values of V or W, whichever is appropriate, computed from Table 2. V is found in lines 7' and 14', just after 5-month intervals.

Column I contains corrections due to solar anomaly. It is based on Column J which complements G to form the time interval, less 29 days, from one to the next like syzygy. Column J vanishes on most of the fast arc and has the value

$$J = -0;57,3,45^H$$

on most of the slow, with occasional transitional, always negative, values (see ACT p. 61). We find here in Column I the sum of the five or six appropriate J-values; where it is six the entry is the function called Z above and in *Aaboe* [1971]. We might point out that the last line should be blank, for the longitude and its four predecessors all belong to the fast arc (we are dealing with a five-month interval).

In Column II, the first where numbers are preserved, we find corrections C' for variation of length of daylight. We have simply, and with sign,

$$C'(n) = \tfrac{1}{2}(C(n-1) - C(n)).$$

The next column is the equivalent of Column K in the ephemerides and gives the sum of the entries in the preceding three columns so that for a six-month interval we have

$$\tilde{K}(n) = W(n) + Z(n) + C'(n),$$

reduced modulo 6^H to the smallest positive value. The entries are abbreviated to three digits.

The last preserved column, Column M, gives the moment of conjunctions, measured in large hours before sunset (šú). It is derived by continued subtraction from an initial value of the entries in Column $\tilde{K}$. A comparison with modern tables shows that though the exlipse possibilities are correctly identified, the moment of conjunction given in Column M is consistently 10 hours wrong.

To the right of Column M in Table 6 we have added values of $\tilde{K}$ computed to four places for comparison with the text's Column III. The deviations form no recognizable pattern.

4° Other Lunar Texts of System A

ACT No. 207cc augmented.

Contents: Procedure text for converting Φ into G.

Photograph and Transcription: pp. 20-23.

Description of Text:

BM 36438 (= ACT No. 207cc) is joined by B.M. 37012, 37026, 37274, and 37319 to form the lower part of a tablet with right, left, and bottom edges preserved.

Translation:

With but two exceptions the text adheres to a formular – the text employs two close variants – which freely translated says:

opposite a put b; whatever exceeds a, until c, multiply by 3,22,30; multiply the result by d and add (subtract) the result to (from) b and put the result down.

Here *a* stands for a Φ-value in the standard table for converting Φ into G, *b* is the corresponding G-value, *c* is the neighbouring Φ-value to *a*, and *d* is the change in G over the interval from *a* to *b*.

The two exceptions (Obv. lines 6' and 7', and lines 12' and 13') both concern intervals in which G stays constant. Here the statement is:

Opposite a put b; until c add or subtract nothing.

Critical Apparatus:

Reverse line 9': the text has as the second factor 1,34,48,*8*,53,20 for 1,34,48, 53,20.

Table 6.
(pp. 16-18).
(ACT No. 54).

	[-V(T,)]	[-IV(Φ,)]	[-III(B,)]	[-II(C,)]	[-I(E,)]	[0(V,W,)]	I(ΣJ,)	II(C,)	III($\tilde{K}$,)	IV(M,)	
1.	235 ♈ X	2,12,27,13,20 ↓	23,12 ♐	2,25,45,36	51,17,18 ω lal	5,51,39,56,45,53,20	[1,34,43,25,30 lal]	[34]1,57 tab	4,50,54		4,50,53,28
	236 ♉ XI	1,59,44,15,33,20 ↑	15,52,15 ♑	3,35,12,30	34,14,54 lal ω	25,30,9,43,20	[3,41,1,19,30 lal]	[3]14,43,27 lal	2,9,46		2,9,45,23
	237 ♊ XII	2,6,19,48,53,20 ↑	12,8 ♐	2,24,17,4	10,27,30 lal lal	3,5,2,1,3,53,20	[1,55,46,24,30 lal]	35,27,43 tab	1,44,44		1,44,43,20
	237 ♊ I	2,1,14,15,33,20 ↓	5,33,15 ♑	3,35,24,30	33,1,54 ω ω	2,12,51,40	[3,19,58,20,30 lal]	35,33,43 lal	4,17,20		4,17,19,37
	238 ♋ II	2,10,57,13,20 ↑	1,4 ♐	2,25,11,28	1,12,12,18 lal lal	1,11,1,49,34,4,26,40	[2,14,49,13,30 lal]	35,6,31 tab	5,29,19		5,29,18,57
	♌ III	2,6,36,51,6,40 ↓	25,11,15 ♊	3,34,1,30	1,40,18,42 ω ω	5,27,38,23,14,26,40	[2,58,55,21,30 lal]	34,25,1 lal	1,55,38		1,54,38,1
	♍ IV	2,2,48,42,13,20 ↑	20 ♋	2,36	1,58,34,18 ω lal	4,31,18,33,11,40 (V)	[2,37,52,22,30 lal]	29,•,45 tab	2,22,26		2,22,24,56
	239 ♎ V	2,14,45,22,13,20 ↓	16,41,15 ♉	3,22,40,30	1,9,55,54 lal ω	1,1,30,20,8,20	[1,40,48,37,30 lal]	[23,20,15 lal]	4,57,22		4,57,21,28
	♏ VI	1,58,9,48,53,20 ↓	8,56 ♏	2,40,42,40	56,49,30 ω lal	4,35,23,34,48,53,20	[3,55,59,6,30 lal]	[20,58,55 tab]	1,•,•,22		1,0,23,23
	240 ♐ VII	2,14,1,40 ↑	6,18,45 ♉	3,17,32,30	2,39,6 lal ω	4,56,58,8,53,20	[1,9,45,38,30 lal]	[18,24,55 lal]	3,19,9		3,18,47,35 !
	♑ VIII	2,3,32,24,26,40 ↓	27,52 ♎	2,48,5,20	4,55,18 lal lal	46,38,53,20	[4,17,2,5,30 lal]	[14,43,35 tab]	[2]4,41,19		2,44,20,23
	♑ IX	2,8,39,4,26,40 ↑	25,56,15 ♈	3,10,37,30	1,4,37,42 ω ω	2,10,59,40,47,13,20	[58,42,39,30 lal]	[11,16,5 lal]	1,1,1		1,1,0,56
	241 ♒ X	2,8,55 ↓	16,48 ♎	2,55,28	1,6,40,6 lal lal	5,9,48,20,27,46,40	[4,38,5,7,30 lal]	[7,34,45 tab]	3,39,18		39,18,1
	XI	2,0,30,33,20 ↑	16,48 ♓	2,44,32	1,50,42,54 lal ω	3,46,9,33,50,33,20 (V)	[ ]	[5,28 tab]	[ ]39,21	4L	3,51,37,34 !

ACT No. 207 c+ . . .
Obv.

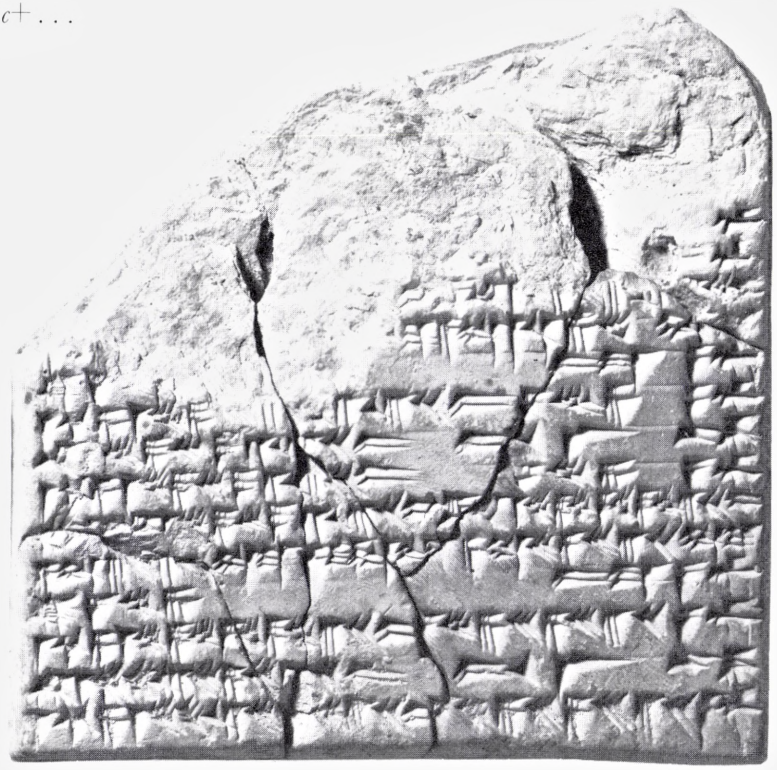

Commentary:

This text confirms the standard rules for converting Φ into G by linear interpolation in the Φ-G table (Table 1). The only feature of interest is the manner in which the interpolation is handled. Each interpolation involves a multiplication of the relevant increment of Φ, not by the usual single interpolation coefficient, but by two factors. The first is always

$$\frac{1}{17,46,40} = 3,22,30,$$

where 17,46,40 is the difference $\Delta\Phi$ between two consecutive listed values of Φ, and the other factor, varying from instance to instance, is ΔG, the difference between the two relevant tabulated values of G. Trivially,

$$3,22,30 \cdot \Delta G$$

Transcription:

Obverse

–2' [*ana tar-ṣa* 1,57,58,8,53,20 tab 4,53,14,4,26,40 gar-*an*]
–1' [*mim-ma šá al* 1,57,58,8,53,20 tab dir en 1,58,15,55,33,20 tab]
0 [a-rá 3,22,30 DU-*ma šá* DUL+ DU-*ka* a-rá 1,34,48,53,20 DU-*ma*]
1' [ki 4,53,14,4,26,40 tab-*ma* gar-]*an*
2' [*ana tar-ṣa* 1,58,15,55,33,20 tab 4,54,48,53,20] gar-*an*
3' [*mim-ma šá al* 1,58,15,55,33,20] tab dir en 1,58,33,42,13,20 tab
4' a-rá[3,22,30 DU-*ma šá* DUL+ DU-]*ka* a-rá 1,11,6,40 DU-*ma*
5' ki 4,[54,48,53,20] tab-*ma* gar-*an*
6' *ana tar-ṣa* 1,58,33,42,13,20 tab 4,56 gar-*an*
7' en 1,58,37,2,13,20 tab tab *u* lal nu tuk
8' *ana tar-ṣa* 1,58,37,2,13,20 tab 4,56 gar-*an*
9' *mim-ma šá al* 1,58,37,2,13,20 tab dir en 1,58,54,48,53,20 tab
10' a-rá 3,22,[30] DU-*ma šá* DUL+ DU-*ka* a-rá 35,33,20 DU-*ma*
11' ki 4,56 tab-*ma* gar-*an*
12' *ana tar-ṣa* 1,58,54,48,53,20 tab 4,56,35,33,20 gar-*an*
13' en 1,59,12,35,33,20 tab tab *u* lal nu tuk
14' *ana tar-ṣa* 1,59,12,3[5],33,20 tab 4,56,35,33,20 gar-*an*

---

is the standard interpolation coefficient. For the linear stretch of G we are told (Rev. lines 20-21) to apply the two factors

$$3,22,30 \cdot 2,45,55,33,20$$

which product, indeed, comes out to be 9,20 as it should. The second factor is readily recognized as $d(\Phi)$, the monthly difference in Φ, but it is also, as we have learnt, the Sarosly difference in G, and so corresponds to 17,46,40, the Sarosly difference in Φ.

The preserved part of the text happens to begin with the smallest Φ-value on an ascending branch, takes us through the maximum of G, and ends with one of the two linear stretches of G. It is our guess that about half of the original tablet is lost so that only the middle of the text is preserved.

ACT No. 207 c+ . . .
Rev.

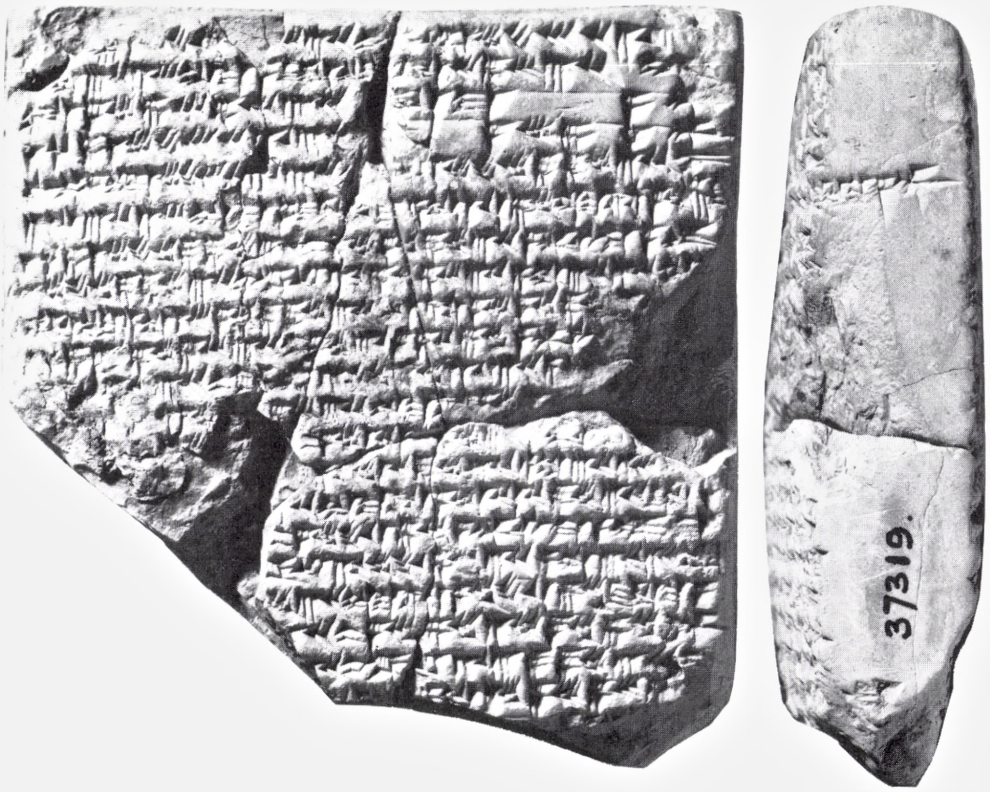

As an illustration of the perverse situations that may arise – and often do – when one is forced to use fragmentary material we can point to *Neugebauer's* reconstruction of the text on the basis of BM 36438 only. This fragment is the one at the lower right corner of the obverse and the upper right corner of the reverse (see the photograph), and whenever an interpolation coefficient is expected, either 3,22,30 or $\triangle G$ is preserved, but not both. *Neugebauer* identified 3,22,30 as the reciprocal of $\triangle\Phi$, recognized the values of $\triangle G$, and drew the conclusion, entirely reasonable in view of the evidence, that the interpolation scheme was wrong.

Reverse

1. *mim*-[*ma šá*] *al* 1,59,12,[35,]33,20 tab dir en 1,59,30,22,13,[20 tab]
2. a-rá 3,22,30 DU-*ma šá* DUL+ DU-*ka* a-rá 35, 33, 20 DU-[*ma*]
3. ta 4,56,35,33,20 [DU]L+ DU-*ma* gar-*an*
4. *ana tar-ṣa* 1,59,30,22,13,20 [ta]b 4,56 gar-*an*
5. *mim-ma šá al* 1,59,30,22,13,20 t[ab dir] en 1,59,48,8,53,20 tab
6. a-rá 3,22,30 DU-*ma šá* DUL+ DU–*ka* a-rá 1,11,6,40 DU-*ma* ta 4,56 DUL+ DU-*ma* gar-*an*]
7. *ana tar-ṣa* 1,59,48,8,53,20 tab 4,54,48,53,20 gar-*an mim-ma šá al*
8. 1,59,48,8,53,20 tab dir en 2,.,5,55,33,20 a-rá 3,22,30 DU-*ma*
9. *šá* DUL+ DU-*ka* a-rá 1,34,48,{8,}53,20 DU- <*ma*> ta 4,54,48,53,20 [DUL+ DU-*ma* gar-*an*]
10. *ana tar-ṣa* 2,.,5,55,33,20 tab 4,53,14,4,26,40 gar-*an mim*-[*ma šá al*]
11. [2,0,5,55]33,20 tab dir en 2,.,23,42,13,20 a-rá [3,22,30 DU-*ma šá*]
12. [DUL+ DU-*ka* a-rá 1,52,35,]33,20 DU-*ma* ta [4,53,14,4,26,40 DUL+ DU-*ma* gar-*an*]
13. [*ana tar-ṣa* 2,0,23,42,13,20] tab 4,51,21,28,53,20 gar-*an mim-ma* [*šá al*]
14. [2,0,23,42,13,20 tab dir en] 2,.,41,28,53,20 a-rá 3,22,30 DU [-*ma*]
15. [*šá* DUL+ DU-*ka* a-rá 2,10,22,13,]20 DU-*ma* ta 4,51,21,28,53,20 DUL+ DU- <*ma*> gar-*an*
16. [*ana tar-ṣa* 2,0,41,28,53,20] tab 4,49,11,6,40 gar-*an mim-ma šá al-la*
17. [2,0,41,28,53,20 tab] dir en 2,.,59,15,33,20 a-rá 3,22,30 DU-*ma*
18. [*šá* DUL+ DU-*ka* a-rá 2,28,8,]53,20 DU-*ma* ta 4,49,11,6,40 DUL+ DU-*ma* gar <-an>
19. [*ana tar-ṣa* 2,0,59,15,33,] 20 tab 4,46,42,57,46,40 gar-*an*
20. [*mim-ma šá al* 2,0,59,15,33,] 20 tab dir en 2,13,8,8,53,20 tab
21. [a-rá 3,22,30 DU-*ma šá* DUL+ DU-*ka*] a-rá 2,45,55,33,20
22. [DU-*ma* ta 4,46,42,57,46,40 DUL+ DU-*ma* gar-*an*]

BM 40094, Reverse,+ ACT No. 128
Contents:]K_1, M_1, Λ_1, Y_1, C_1', $\tilde{K}_1$, M_1, P_3 for Philip Arrhidaeus 6,VI to 7,XII (= S.E. –6,VI to –5,XII).
Transcription: Table 7, p. 27.
Photograph: p. 25.

Description of Text

The text ACT No. 128 (BM 45662) is a fragment with only one side, and part of lower and right edge preserved. It now joins the reverse of BM 40094 so that the mended break runs through Columns V and VI of the transcription. Part of Column VIII (P_3) is on the right edge (not shown in the photograph). Upper and lower edges of BM 40094 are preserved, but parts of its surface, particularly the first five lines of Reverse, Column III, are rather badly eroded. We believe that the present text is a copy of an ill-preserved exemplar, for it contains an unusual number of isolated errors without consequence readily committed when one copies a poor text (e.g., 8 for 5, and 5 for 8).

We have not reproduced a copy of the obverse of BM 40094, for the join adds nothing to this side, yet we have retained and extended the numbering of columns from *Aaboe* [1969] though Column I (K) is not preserved on the reverse of this fragment. For the contents of the obverse we refer to *Aaboe's* publication with corrections given below.

The scribe's ductus is such that it is often difficult to distinguish between his "tab," "20," and "." where "." denotes the separation mark of two diagonal wedges used for zero.

Critical Apparatus (in part excerpted from *Aaboe* [1969]).

Rev. II,7': [2,1,] 1 is also possible.

Rev. II,8: [4],57,*44* (or *45*) should be 4,57,46 (cf. VIII,8).

Rev. II,14: 1,*49*,*5* should be 1,*39*,*35* (cf. VII,14), isolated error.

Rev. III,7: 1,33,25,53,*58*, . . . should be 1,33,25,53,*56*,6,40, an error without consequence.

Rev. III,8: *1*,23,36,45,47,13,20 should be *2*,23,36,45,47,13,20, isolated error.

Rev. III,13: 3,29,11,*6*,40 should be 3,29,11,40, error without consequence.

Rev. III,18: the Λ-value should be denoted lal, isolated error.

Col.IV: Except in the first six lines of the obverse, the values are denoted lal instead of tab, perhaps in imitation of Col.J.

Rev. line 5: Col. IV,5 is empty; the Y-value should be 8,14,32,30 tab. In Col. V,5 the text has 8,12,35,30 tab; this should be 3,35,55 tab. In Col. VI,5 we read 3,36,45 with the final 5 damaged; this should be 0;7,29 tab. It is likely that the scribe copied from a text which, like his copy, occasionally ran the columns together, and in which line 5 of the reverse was damaged; and that he copied what he saw in

BM 40094, Rev.+ACT No. 128

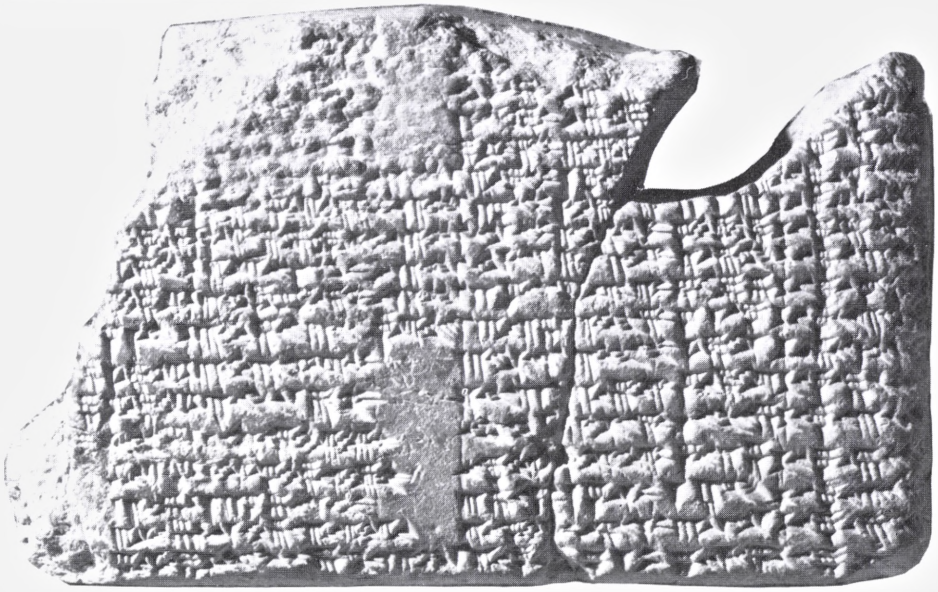

the correct line, but shifted one column to the right. The join adds no new information about this line.

Rev. V,5: see note to Rev. line 5.

Rev. V,16: *3*,6,24 should be *2*,6,24, isolated error.

Rev. VI,3: reading uncertain.

Rev. VI,5: see note to Rev. line 5.

Rev. VI,10: the best, but far from secure reading is 4,12,23; the correct value 4,6,13 is not consistent with the traces.

The following errors in *Aaboe's* transcription and restoration of the obverse should be noted:

Obv. IV,5,6: these two lines should not be blank, but should both give 21,2,59 tab.

Obv. V,5: 1,[19,30 lal] should be 1,[16 lal].

Obv. V,9: 1,53,4[0 lal] should be 1,53,3[6 lal].

Obv. VI,5: [3,31,49 tab] should be [3,52,56 tab].

Obv. VI,6: [2,45,38 tab] should be [3,6,41 tab].

Commentary

When BM 40094 was first published it presented several singular features: it was the oldest datable lunar ephemeris, and it was the only lunar ephemeris that month by month gave the function Λ and its corrections, Y and c̃', for solar anomaly and change of length of daylight. Only here was found the column κ̃, the sum of Λ, Y, and c̃', which represents the length of a normal year, except for an integral number of days, and adjusted to a variable sunset epoch. To these unique traits we now add one more: our text is the only lunar ephemeris that contains two nearly identical, but differently computed columns M (giving the moment of conjunction in large hours before sunset).

ACT No. 128 complements Column K̃ of BM 40094 and adds the second Column M and a Column P_3 which gives date of the last visibility of the Moon and the time interval from moonrise to sunrise on that morning. The inclusion of Column P_3 and the absence of a Column P_1 (first visibility) raise a problem we shall return to briefly below.

We are convinced that Column VII, the second Column M, is computed from Column VI (K̃) and an initial value in 12-line steps thus:

$$M(n) = M(n\text{-}12) - \tilde{K}(n).$$

The text provides only one instance where this can be checked:

$$\begin{array}{rl} \text{VII,6} & : \text{M(6)} = [5,26,3]6\ \check{\text{s}}\acute{\text{u}} \\ -\text{VI,18}: & -\tilde{\text{K}}(18) = \quad 5,\ \ 1 \\ \hline \text{VII,18}: & \text{M(18)} = 5,21,35\ \check{\text{s}}\acute{\text{u}} \end{array}$$

where, alas, only the last digit of VII,6 is preserved.

Aaboe surmised in 1969 that a main purpose of Λ and its corrections is to provide a much needed control for Column M – a conglomerate of quite unrelated parts which is difficult to check with rules of the common kind – and this appears confirmed by the join.

Finally, to find the dates in Column VIII (P_3) and, for that matter, in Column II (M) – dates are omitted in the second Column M – we must know the character, full or hollow, of the relevant month, and this we learn from Column P_1, which is not in our text. Thus our text is not self-contained, and this information must have been drawn from elsewhere. It is at first sight welcome to have our evidence of the poorly understod visibility columns increased by the entries in Column P_3. This much seems clear, however, that it was very poorly computed – in lines 12, 15, and 16 even the date is wrong – so it looks at present as if this join offers little hope of advancing our understanding of how the visibility columns were constructed, and we shall here refrain from any further analysis of Column VIII.

	[T,]	[Φ,]	[B,]	[C,]	[F,]	[G,]	[J,]	[C',]	[I(K,)]	
Rev. 1.	S.E. -6 VII	2, 9, 31, 40	20;16 ♑	2,35,53,36	14, 2,12, 11, 15	3, 3,57,46,40		+ 8,37,52	3,12,36	1.
	VIII	2, 6,45,44,26,40	20;16 ♐	2,26,37,52	13,20,12, 11, 15	3,29,46,25, 11, 6,40		+ 4,37,52	3,34,24	
	IX	2, 3,59,48,53,20	20;16 ♉	2,25,22, 8	12,38,12, 11, 15	3,55,35, 3,42,13,20		+ 37,52	3,56,13	
	X	2, 1,13,53,20	20;16 ♒	2,32, 6,24	11,56,12, 11, 15	4,21,23,42,13,20		- 3,22, 8	4,18,2	
5.	XI	1,58,27,57,46,40	20;16 ♓	2,46,50,40	11,14,12, 11, 15	4,47, 9, 11,51, 6,40		- 7,22, 8	4,39,47	5.
	XII	1,59,53,53,20	18;48,45 ♈	3, 5,52,30	11,35,57, 11, 15	4,54,18,16,17,46,40	- 44,15,18,30	- 9,30,55	4, 0,32	
	-5 I	2, 2,39,48,53,20	16;56,15 ♉	3,22,46,30	12,17,57, 11, 15	4,31, 4,26,40	- 57, 3,45	- 8,27	3,25,34	
	II	2, 5,25,44,26,40	15; 3,45 ♊	3,32,40,30	12,59,57, 11, 15	4, 5,15,48, 8,53,20	- 57, 3,45	- 4,57	3, 3,15	
	III	2, 8, 11, 40	13, 11,15 ♋	3,35,34,30	13,41,57, 11, 15	3,39,27, 9,37,46,40	- 57, 3,45	- 1,27	2,40,56	
10.	IV	2,10,57,35,33,20	11;18,45 ♌	3,31,28,30	14,23,57, 11, 15	3,13,38,31, 6,40	- 57, 3,45	+ 2,3	2,18,38	10.
	V	2,13,43,31, 6,40	9,26,15 ♍	3,20,13,30	15, 5,57, 11, 15	2,48,19,15,33,20	- 57, 3,45	+ 5,37,30	1,56,53	
	VI	2,16,29,26,40	9,12 ♎	3, 0,32	15,47,57, 11, 15	2,40	- 7,13,40,30	+ 9,50,45	2,42,37	
	VII	2,14,54,15,33,20	9;12 ♑	2,40,32	15,23,57,33,45	2,40		+ 10	2,50	
	VIII	2,12, 8,20	9;12 ♐	2,28,19,12	14,41,51,33,45	2,43, 0,33,20		+ 6, 6,24	2,49, 7	
15.	IX	2, 9,22,27,26,40	9;12 ♉	2,24, 6,24	13,59,51,33,45	3, 5,24,11,51, 6,40		+ 2, 6,24	3, 7,31	15.
	X	2, 6,36,28,53,20	9;12 ♒	2,27,53,36	13,17,51,33,45	3,31,12,50,22,13,20		- 1,53,36	3,29,19	
	XI	2, 3,50,33,20	9;12 ♓	2,39,40,48	12,35,51,33,45	3,57, 1,28,53,20		- 5,53,36	3,51, 8	
	XII	2, 1, 4,37,46,40	8,26,15 ♈	2,58,57,30	11,53,51,33,45	4,22,50, 7,24,26,40	- 23,12,19,30	- 9,38,21	3,49,59	

	II(M,)	III(Λ,)	IV(Y,)	V(C̃')	VI(K̃,)	VII(M,)	VIII(P̃3)				
Rev. 1.	[1,55,33 šú]	[1,55, 2,59,23,53,20		[2,12,48 lal]	[1,52,50 tab]	[1,55,35 šú]	[.. .. ..]				
	[4,21, 9 šú]	1, 4,52, 7,32,46,40		44,16 lal	[1, 4, 8 tab]	[4,21,10 šú]	[.. .. ..]				
	[24,56 šú]	14,41,15,41,40 tab		44,16 tab	15,26 [tab]	[24,58 šú]	[..]2,3[0 kur]				
	[2, 6,54 šú]	19, 1,17,46,40 lal		2,12,48 tab	16,48 [a ŋ]	[2, 7 šú]	[27] 27,50 kur	28	2[0	kur]	
5.	[3,27, 7 šú]	4,21, . 52,46,40 lal	<8,14,32,30>	8,12,35,30 tab	3,36,55, [ ]	[3,27,12 šú]	27 15,20 kur				
	[5,26,35 šú	43,15, 2, 5 tab	21, 2,59 lal	3,27,30 tab	1, 7,46 tab]	[5,26,36 šú	28 14,30 kur				
	[2, 1] 2 šú	1,33,25,53,58, ...	21, 2,59 lal	2, 4,30 tab	1,56,33 tab	2, 1, 3 šú	27 20,40 kur	28	2[0	kur]	
	[4]7,57,44 šú	1,23,36,45,47,13,20 tab	21, 2,59 lal	41,30 tab	2,45,21 tab	4,57,48 šú	27 16,40 kur				
	[ ]2,16,50 šú	3,13,31,40 tab	21, 2,59 lal	41,30 lal	3,33,52 tab	2,16,49 šú	27 23 kur				
10.	[ ] 5,58,12 šú	3,47,14, 4,26,40 tab	21, 2,59 lal	2, 4,30 lal	4,12,23 tab	5,58, 6 šú	27 14,30 kur				
	[2]8 4, 1,19 šú	3,55,33,20 tab	7,13,40,30 lal	3,32, 5 lal	3,59,15 tab	4, 1,17 šú	27 23,40 kur				
	[2]8 1,18,42 šú	3,53,10,22,13,20 tab		3,41,20 lal	3,49,29 tab	1,18,41 šú	26 31,40 kur	27	12,1[0	kur]	
	[2]8 4,28,42 šú	3,29,11, 6,40 tab		2,19,12 lal	3,26,52 tab	4,28,43 šú	27 18,10 kur				
	[2]8 1,49, 5 šú	2,42,25,50,13,53,20 tab		50,40 lal	2,41,35 tab	1,39,35 šú	27 23,10 kur				
15.	[2]8 4,32, 4 šú	1,52,14,58,22,46,40 tab		37,52 tab	1,52,53 tab	4,32, 5 šú	27 16,30 kur				
	[ ] 1, 2,46 šú	1, 2, 4, 6,31,40 tab		3, 6,24 tab	1, 4,11 tab	1, 2,49 šú	27 22,20 kur	28	12,1[0	kur]	
	[2]9 3,11,36 šú	11,56,23,33,53,20		3,34,56 tab	15,31 tab	3,11,41 šú	27 16,50 kur				
	[2]9 5,21,38 šú	19,29,26,40 <lal>	21, 2,59 lal	3,27,30 tab	5, 1 tab	5,21,35 šú	28 1[.,]0 kur				

Table 7.

BM 40094, Rev.+ ACT No. 128

Neugebauer assigned tentatively ACT No. 128 to System B, in error, it now appears. The absence of dates in its Column M, and of the usual difference column (K), were indeed puzzling out of the context provided by the join with BM 40094.

ACT No. 3b and BM 37375 (80-6-17,1132)
Contents:
Obverse: Cols. C_1,K_1,M_1,P_1,P_3; Reverse: Cols. $P_{2,1}$,$P_{2,2}$,$P_{2,3}$,$P_{2,4}$ for part of S.E. 2,22.
Transcription: Table 8.
Description of Text:

Though too much clay is missing for a physical join, there can be no doubt that these two fragments derive from the same tablet. Clay, hand, size of writing, and shape and dimensions of the lower edge all agree. Further, both fragments have an intercalary month XII_2 in the last line of the obverse, and the moments of last visibility in BM 37375 all precede very nicely the corresponding moments of conjunction in No. 3b. The missing sliver contained most of the column of first visibility on its obverse, and the middle section of the me-column on its reverse.

It is very fortunate that No. 3b could be dated, for without a date BM 37375 would be quite uninteresting. As it is now, it adds new evidence about the difficult and imperfectly understood visibility columns. For a restoration of most of the missing columns we refer to the partial duplicate ACT No. 3a.
Critical Apparatus.
Obv. line 1': illegible traces of a second choice remain on the edge; the traces following the 11 in Col. V are conformal with 27 11,33 kur[as well as 27 11 kur 26[.
Rev. IV,4: 20 gar could be read 24.

ACT No. 53 (BM 34083 (Sp. 181))
Contents: Columns T_1,B_1, and Ψ_1 for solar eclipse possibilities for at least 216 years, including S.E. 137 to 343.
Arrangement: The text turns from obv. to rev. about the right edge, like a page of a book, which is unusual for Babylon.
Copy: LBAT No. 49.
Transcription: Table 9 (one side).
Description of Text:

Neugebauer restored the text in ACT under the assumption that it dealt with solar eclipses on its "obverse" and lunar eclipses on its "reverse" which is badly

Table 8.

		I	II	III	IV	V	Edge
Obv. 1.' 2,22	VIII	[7, . ,48 tab]	[5 . ,20]	[apin ////, 2,17,11 šú]	[	] [apin 27 11 kur 2 e	[////////] 1.'
	IX	[3, . ,48 tab]	[4,51,38]	[gan ////, 3,25,33 šú	[	] [gan 26 19,20 kur	
	X	[59,12 lal]	[4,22, Y ab 29	5, 3,29 šú	[	] [ab 27 17,20 kur	
	XI	[4,59,]12 lal	3,52,16 zíz 28	1, 11,13 šú	[	] [zíz 27 13,40 kur	
5.'	XII	[8,52,27 lal	3,12,18 še 29	3,58,54 šú	[	]50 še 28 11,20 kur	27 20,20 kur 5.'
	XII$_2$	[9,22,30 lal	1,59,12 dirig 28	1,59,42 šú	[	] dirig 27 16,30 kur	
Rev. 1. 2,22	I	[ ]4 1,50 šú	15 4,50 na	1[4	clay missing	]50 me 15 12,20 ge$_6$	
	II	[14] 6,40 šú	15 2 na	1[4		] me 15 3,20 ge$_6$	
	III	[šú	15 9 na	1[4		]4 me 16 7,30 ge$_6$	
	IV	[šú]	[2,]0 na	[		]50 me 15 20 gar ge$_6$	
5.	V	[šú]	[na	[		3,40 me 15 2,10 ge$_6$	
	VI	[šú]	[na]	[		] me 16 4,20 ge$_6$	

ACT No. 31b ⟵ ⟶ B.M. 37375

Table 9.

	[-I (T_1)]	[O(B_1)]	I(Ψ_1)	II (T_1)	III(B_1)	[IV(Ψ_1)]	
1.'	2,18 XII	15,26,15 ♈	[20, 5,49] ḫab	dir	[25,33,45 ♈]	19, 2,51	1.'
	2,19 VI	5,36 ♎	[19,30,]13 ḫab	2,37 [kin]	[16,24 ♎]	19,21,15	
	XII	5, 3,45	[31,]8,37 ḫab	še	[5,[11,15 ♈]	30,15,39	
	2,20 VI	24,32 ♍	[29,47,41 ḫab	2,38 kin	5,[20 ♎]	29,38,43	
5.'	XI 5 áb	24,32 ♒	[13]51 ḫab	zíz 7 áb	5,[20 ♓]	4,53	5.'
	2,21 IV	15,18,45 ♌	[2]7,35 ḫab	2,39 kin	24,[16 ♍]	39,56,11	
	X	13,28 ♒	[10,13,]9 ḫab	ab	24,[16 ♒]	10,22,21	
	2,22 IV	4,56,15 ♌	[11,40],23 ḫab	2,40 sig	1,5,[3,45 ♌]	10,37,25	
	X	2,24 ♒	[20,48,47] ḫab	gan	13,[12 ♒]	20,39,49	
10.'	2,23 III	24,33,45 ♋	[22,53,11, ḫab	2,41 sig	4,[41,15 ♌]	21,50,13	10.'
	IX	21,20 ♉	[31],6,15 ḫab	gan	[2, 8 ♒]	30,57,17	
	2,24 III	14,11,15 ♋	[34,5,]9 ḫab	2,42 gu$_4$	[24,18,45 ♋]	33, 3, 1	
	IX	10,16 ♉	[41,23,43] ḫab	apin	[21, 4 ♉]	41,14,45	
	2,25 II 5 áb	5,41,15 ♊	[5,43,33 ḫab]	2,43 [bar 5 áb]	[15,48,45 ♊]	4,40,35	

ACT No. 53 "Rev."

preserved. We shall suggest that the identification of obverse and reverse is wrong and that Side A, as we rename what *Neugebauer* called "reverse," presents solar eclipses preceding in time those given on Side B (ACT's "obverse"); *Neugebauer's* assumption that Side A concerned lunar eclipses led to severe difficulties. Incidentally, *Pinches's* original copy sheet agrees with our identification of obverse and reverse.[4]

We have nothing to change in *Neugebauer's* treatment of Side B; in fact, we shall use the peculiar rules he extracted from this side in our proposed restoration of Side A. Further, we shall rely heavily on *Pinches's* hand copy (LBAT No. 49) of this side.

The text was first noticed by *Strassmaier* (in June 1891, according to his notebook) and he says about the "reverse," as he also called our Side A: "*Rückseite sind nur Spuren von 3 Kolumnen so:* [copy of three lines follow] *u.s.w.; es ist nichts sicher, zu sehr beschädigt.*" In Col. II, 5' he read "zíz 5 áb," a reading *Neugebauer* followed, though *Pinches* here read "zíz 7 áb." For the year numbers in lines 2' and 4' *Strassmaier* and *Pinches* both give 2,37 and 2,38, while *Neugebauer* has 5,37 and 5,38. The photograph used by *Neugebauer*, and taken about 1950, supports the alternate readings equally well or ill and shows a text so damaged that we doubt that a collation would be of much help – in fact, we had not yet grown interested in the problems raised by this text when *Aaboe* collated some of the other tablets discussed here.

We mention these things to point to the fragility of the evidence. On the other hand, we have good reasons to trust the acuity of the remarkable *T. G. Pinches* when he had a difficult text in hand.

Critical Apparatus

The numbers given in Columns I and III of Table 9 are computed by us; any deviation from *Pinches's* copy is noted below.

I, 3': [31,1]8,37: *Pinches* read 33 in the last place.
II, 5': 7áb: so *Pinches; Strassmaier* and *Neugebauer* read 5 áb (see above).
II, 6': kin: *Pinches* gives a damaged dir; *Neugebauer* read šu.
II, 7': ab should be zíz. This error affects all subsequent dates in the text, including those of Side B; henceforth each month name is one too early.
III, 3': 15,[11,15]: *Pinches* read 13 in the first place, with bottom of the 3 damaged.

4. We are indebted to Professor *Neugebauer* for having placed at our disposal his photographs of the relevant ACT texts as well as copies of parts of *Strassmaier's* notebooks, with his transcription of *Strassmaier's* German shorthand, and of *Pinches's* original copy sheets.

III, 5': 5,[20]: *Pinches* read a damaged 8 in the first place.
III, 6: 24,[16]: *Pinches* read 26 in the first place with the top of the 6 damaged.
III, 7': 24,[16]: *Pinches* read 25 with damaged 5.

Commentary

We shall first briefly introduce the "eclipse magnitude" Ψ which plays an essential role in this text. It is a simple transform of lunar latitude, E, usually defined only at syzygies where exlipse possibilities are announced, and computed according to the rule

$$\Psi = 17;24 \begin{cases} +\frac{E}{6} \text{ near the ascending node} \\ -\frac{E}{6} \text{ near the descending node.} \end{cases}$$

Ψ is measured in fingers (šu-si) while E's units are barley corn (še) – in a four-digit value of E the first two indicate the integral number of še. Closely related to Ψ is Ψ" which is defined for *all* syzygies. Ψ" is a zig-zag function of extrema

$$M = -m = 2{,}0 \ ,$$

but of differences that depend on longitude (for details see ACT, *Aaboe-Henderson* [1975], or HAMA). Near the nodes Ψ and Ψ" agree but for sign:

$$\Psi = \begin{cases} \Psi'' \text{ near ascending node} \\ \\ -\Psi'' \text{ near descending node.} \end{cases}$$

We can now state the results of *Neugebauer's* analysis of Side B. He proposed that it gave year and month, longitude, and Ψ for solar eclipse possibilities, arranged in columns of 38 lines (corresponding to one Saros) each, selected according to an unusual principle, but with an error of one month in the dates.

Normally we find, as mentioned, eclipse possibilities selected on the basis of Column E, lunar latitude: they are the syzygies at which lunar latitude, when listed monthly, near a sign change has smaller absolute value. Here, however, the rule is that one selects the syzygy at which Ψ for the first time becomes positive or, what is the same thing, the syzygy just after Ψ" has changed sign. The E-rule and the Ψ-rule, as we call them, agree often, but not always.

We have reconstructed Side A on the basis of the Ψ-rule. This rule implies an occasional, but very rare interval of 7 months, flanked by two 5-month intervals, between consecutive "eclipse possibilities" (which the more correct E-rule also does, but at different syzygies). The last time this happens during the historically relevant period is at the conjunctions S.E. 138 VI, 138 XI, 139 VI, and 139 XI. These are covered in our text, and *Pinches* read 7 áb (7 months)

where we would normally expect 5 áb. It also appears that it is in this part of the text that the error in month names begins. The month names še (XII), kin (VI), zíz (XI) in lines 3', 4', and 5' are clear and correct. On line 6' *Pinches* copies a damaged dir (XII_2) which makes no sense, but here one should probably read kin (VI) and thus obtain the 7-month interval. In line 7' we expect zíz (XI), but find ab (X), and from there onward all months are one too early. If *Neugebauer's* reading of šu (IV) in line 6' is followed we would have two consecutive 5-month intervals followed by 6-month intervals, which is also a possible reconstruction.

That the Ψ-rule is employed is shown by line 6' where we find 2,39 kin (VI) and line 13' where we find apin (VIII). In both cases the E-rule would select the previous conjunction (we are allowing for the systematic error in the latter instance).

The Ψ-rule makes little astronomical sense as a guide for choosing eclipse possibilities. It has in practice the effect of advancing the nodes by 2;17° on the average, which is gross compared with the error in Column E (about $\frac{1}{2}$° in S.E. 200; see *Aaboe-Henderson* [1975]). It may, however, be we who are wrong when we identify our tablet as an eclipse text, for it could equally well be an auxiliary table simply presenting a rational selection of corresponding values of T, B, and Ψ for a purpose we cannot quite see. Indeed, the term ḫab can mean "eclipse magnitude" or "positive value of Ψ" as well as "eclipse warning" (see Excursus: The Term ḫab-rat, ACT p. 197).

ACT No. 207f (BM 42685)
Contents: Column Φ_1 tabulated at 12-month intervals, very likely beginning S.E. 200, III.
Transcription: Table 10.
Photograph: ACT Plate 243.

Critical Apparatus

line 3': the 5 is fairly clear, and 0 is certainly excluded, so the numbers are values of Φ_1, not Φ_2.

line 11': *Neugebauer* read 42,14. The 42 could be 52 in which case all dates are advanced 265 months.

Commentary

The preserved endings agree with the endings in Column Φ_1 in ACT No. 55, Reverse, lines 8'-18' (restored until line 10' in *Aaboe* [1971]). Dating is unique if 42 in line 11' is taken seriously, otherwise see Critical Apparatus.

Table 10.

	[T,]	Φ_1	
1'	3,20 III	[2, 3, 5]44,26[40	tab]
	3,21 III	[1,57,5]2,46,40	[lal]
	3,22* III	[2, 3, 1]5,22,13,20	lal
	3,23 II	[2, 8, 37]57,46,40	lal
5'	3,24 II	[2,14, 0]33,20	lal
	3,25* II	[2,14,46]28,53,20	tab
	3,26 I	[2, 9, 23]53,20	tab
	3,27 I	[2, 4, 1]17,46,40	tab
	3,28** I	[1,58,38]42,13,20	tab
10'	XII	[2, 2, 19]48,53,20	lal]
	3,29 XII	[2, 7],42,24,26,40	lal]

ACT No. 207f

ACT Nos. 22 and 23

We finally present in Tables 11 and 12 reconstructions of ACT Nos. 22 and 23 which were dated from preserved or reconstructed sections of Column K. Incidentally, ACT No. 20 was similarly dated and reconstructed, and published in *Aaboe* [1974].[5] Our dating of No. 22 – unique within the relevant period like the other datings – confirms *Neugebauer's* remark (ACT p. 104) that its Column K_2 is a close parallel to that in No. 15.

Appendix

BM 37021 (80-6-17,765)

Just after our manuscript was submitted we managed to date the text BM 37021. Since it presents two points of particular interest, we shall briefly describe it and its contents here, while the text will be published fully later in another context.

BM 37021 is from the Babylon archive and is a fragment measuring 7.5 cm by 14 cm. Upper and lower, but no other edges are preserved. When the tablet was first seen by Aaboe in 1963 it was quite illegible, but after it was baked and cleaned a few signs could be made out, though its surface remains in a wretched state. The upper edge carries a colophon stating that the text was copied from a wax tablet.

The text has 10 lines to a side and presents in pairs of columns, that continue

5. Nos. 20 and 23 were first dated in 1972 with the kind help of Mr. *C. Anagnostakis*.

from the Obverse across the lower edge to the Reverse, corresponding values of K_1 and M_1 for a long sequence of unidentified months. Indeed, of Column M_1 only the *hours* are given, denoted šú (before sunset). The term BAL indicates when an extra day has been included as 6^H in Column M_1, a useful warning when one computes the dates of Column M_1 (for which Column P_1 is needed). BAL occurs in the lines immediately after the borrowing of a whole day.

Of Column I remain only the endings of M_1, mostly šú and šú BAL, but we could date the three values of K_1 preserved in Column II, lines 2, 3, and 4 uniquely to S.E. 46, months X, XI, and XII with our computer-generated tables. The remaining traces of K_1-values are, with one exception, consistent with our recomputation, and the dating is secure.

Column I, line 1, would then correspond to S.E. 45* month II, and we believe this to be the beginning of the text. There is evidence of entries for 60 months, and the tablet's curvature suggests that when unbroken it covered 100 months, or some 8 years.

Two features of the text are noteworthy: its early date and the fact that it is an auxiliary table of System A giving selected columns of monthly values, very likely for the purpose of constructing ephemerides. Such auxiliary tables of System B from Uruk abound, but so far the only text of this sort of System A was ACT No. 70. This text from Babylon is also the oldest dated lunar text in ACT (S.E. 49 to 60), but otherwise the lunar texts of System A are on the whole younger than those of System B. We do not know how much of this apparent trend is due to accidents of the spade, scientific and otherwise, but the early dates of the contents of BM 40094+ ACT No. 128 (see above) and of the present text will surely have to be taken into account in attempts at reconstructing the relationship between the lunar Systems A and B.

Table 11.

		[T_1]	[B_1]	[C_1]	[E_1]	[F_1]	[G_1]	[J_1]	[C_1']	[K_1]	I (M_1)	II and Edge (P_1 & P_3)	
Obv.	1.	209 XII	10, 3, 45 ♈	3, 0, 2, 30	- 5, 47, 39, 57	13, 34, 32, 48, 45	3, 20, 57, 31, 51, 6, 40	- 26, 30, 8, 30	- 9, 42, 35	2, 44, 44	[ ] šú]	[bar]13 kur	1.
		210 I	8, 11, 15 ♉	3, 18, 47, 30	- 3, 48, 54, 15	12, 52, 32, 48, 45	3, 46, 46, 10, 22, 13, 20	- 57, 3, 45	- 9, 22, 30	2, 40, 20	[ ] šú]	[gu$_4$]be 27 17,1[0 kuš]r	
		II	6, 18, 45 ♊	3, 30, 31, 30	- 1, 16, 17, 6	12, 10, 32, 48, 45	4, 12, 34, 48, 53, 20	- 57, 3, 45	- 5, 52	3, 9, 39	[ ] šú]	[sig] 16,16 26 19,30 be	
		III	4, 26, 15 ♋	3, 35, 15, 30	+ 2, 32, 37, 9	11, 28, 32, 48, 45	4, 38, 23, 27, 24, 26, 40	- 57, 3, 45	- 2, 22	3, 38, 57	[ ] šú]	[šu]be 27 16,40 kur	
	5.	IV	2, 33, 45 ♌	3, 32, 59, 30	+ 4, 31, 22, 51	11, 21, 36, 33, 45	4, 56, 35, 33, 20	- 57, 3, 45	+ 1, 8	4, 0, 39	[ ] šú	i[zi] 1 13[ ] 28 12 [k]ur 9 be 27 24	5.
		V	41, 15 ♍	3, 23, 43, 30	+ 6, 30, 8, 33	12, 3, 36, 33, 45	4, 39, 53, 20	- 57, 3, 45	+ 4, 38	3, 47, 27	[ ] šú	kin 1 17 28 22 kur 7 be 20 be	
		VI	29, 52 ♍	3, 6, 45, 20	+ 5, 50, 52, 45	12, 45, 36, 33, 45	4, 14, 4, 41, 28, 53, 20	- 24, 58, 50, 30	+ 8, 29, 5	3, 57, 34	[ ] šú	[du$_6$ 1] 16,40 tab ina 30-šú 10 uš 9 be 27 15	
		VII	29, 52 ♎	2, 46, 45, 20	+ 3, 44, 37, 3	13, 27, 36, 33, 45	3, 48, 16, 2, 57, 46, 40		+ 10	3, 58, 16	[ ]6, 9 šú	[apin 3]0 1[ ] 27 26 kur [6]e	
		VIII	29, 52 ♏	2, 32, 3, 12	+ 52, 42, 42	14, 9, 36, 33, 45	3, 22, 27, 24, 26, 40		+ 7, 21, 4	3, 29, 48	[ ]6, 21 šú	gan 1 17 [	
	10.	IX	29, 52 ♐	2, 25, 21, 4	- 2, 51, 54, 21	14, 51, 36, 33, 45	2, 56, 38, 45, 55, 33, 20		+ 3, 21, 4	2, 59, 59	[,32 šú	ab 30 12[	10.
		X	29, 52 ♑	2, 26, 38, 56	- 4, 58, 10, 3	15, 33, 36, 33, 45	2, 40, 15, 22, 13, 20		- 38, 56	2, 39, 36	[šú]	[zíz 1	

		[T_2]	[B_2]	[C_2]	[E_2]	[F_2]	[G_2]	[J_2]	[C_2]	I(K_2)	II (M_2)		
Rev.	0.	210 IV	18,30 ♑	3, 34, 52	- 3, 32	15, 53, 26, 15	2, 40	- 57, 3, 45	- 44, 30	[1, 42, 11]	[šu ... 4, 42, 19 du]		0.
		V	16, 37, 30 ♒	3, 29, 21	- 5, 30, 45, 42	15, 18, 22, 30	2, 40	- 57, 3, 45	+ 2, 45, 30	[1, 45, 41]	[izi 1 28, 0 du]		
		VI	14, 52 ♓	3, 16, 45, 20	- 6, 54, 0, 36	14, 36, 22, 30	2, 44, 53, 20	- 53, 30, 43	+ 6, 17, 50	[1, 57, 40]	[kin 1 2, 25, 40 du]		
		VII	14, 52 ♈	2, 56, 45, 20	- 4, 47, 44, 54	13, 54, 22, 30	3, 8, 46, 25, 11, 6, 40		+ 10	[3, 18, 46]	[du$_6$ 1 5, 44, 26 du]		
		VIII	14, 52 ♉	2, 38, 3, 12	- 2, 41, 29, 12	13, 12, 22, 30	3, 34, 35, 3, 42, 13, 20		+ 9, 21, 4	[3, 43, 56]	[apin 30 14 3, 28, 22 du]		
	5'.	IX	14, 52 ♊	2, 27, 21, 4	+ 1, 13, 33	12, 30, 22, 30	4, 0, 23, 42, 13, 20		+ 5, 21, 4	[4, 5, 44]	[gan 1 14 1, 34, 6 du]		5'.
		X	14, 52 ♋	2, 24, 38, 56	+ 3, 55, 2, 12	11, 48, 22, 30	4, 26, 12, 20, 44, 26, 40		+ 1, 21, 4	[4, 27, 33]	[a]b 30 15 ., 1, 39 du		
		XI	14, 52 ♌	2, 29, 56, 48	+ 6, 1, 17, 54	11, 6, 22, 30	4, 51, 10, 37, 2, 13, 20		- 2, 38, 56	[4, 48, 32]	zíz 1 14 4, 50, 11 du		
		XII	14, 52 ♍	2, 43, 14, 40	+ 6, 16, 26, 24	11, 43, 46, 52, 30	4, 51, 13, 20		- 6, 38, 56	[4, 44, 35]	še 30 15 3, 34, 46 du		
	10'.	XII$_2$	13, 45 ♎	3, 2, 30	+ 4, 14, 38, 42	12, 25, 46, 52, 30	4, 26, 15, 48, 8, 53, 20	- 33, 59, 2	- 9, 37, 40	[3, 42, 39]	dirig 30 16 1, 17, 25 du		10'.
		211 I	11, 52, 30 ♍	3, 20, 45	+ 2, 7, 46	13, 7, 46, 52, 30	4, 0, 27, 9, 37, 46, 40	- 57, 3, 45	- 9, 7, 30	[2, 54, 16]	bar 1 15 4, 11, 41 du		

ACT No. 22

Table 12.

		[T_1]	[B_1]	[C_1]	[E_1]	[F_1]	[G_1]	[J_1]	I (C_1')	II (K_1)	III (M_1)	IV (P_1)	
	0.	152 III	15, 33, 45 ♋	3, 35, 15, 30	- 1, 28, 59, 30	15, 34, 4, 41, 15	2, 40	- 57, 3, 45	1, 8 lal]	[1, 41, 48]	[sig ... 2, 56, 28 šú]	[šu ...]	0.
		IV	13, 41, 15 ♌	3, 30, 31, 30	+ 2, 26, 15, 57	14, 52, 4, 41, 15	2, 40, 44, 48, 53, 20	- 57, 3, 45	2, 22 tab]	[1, 46, 3]	[šu ... 1, 10, 25 šú]	iz[i] 10, 1[0 ...]	
		V	11, 48, 45 ♍	3, 18, 47, 30	+ 4, 25, 1, 39	14, 10, 4, 41, 15	2, 59, 7, 24, 26, 40	- 57, 3, 45	5, 52 tab]	[2, 7, 55	izi 29 5, 2, 30 šú	kin [1] 10, 2[0 ...]	
		VI	11, 44 ♎	2, 58, 50, 40	+ 6, 30, 58, 21	13, 28, 4, 41, 15	3, 24, 56, 2, 57, 46, 40	- 2, 24, 33, 30	9, 58, 25 tab]	[3] 32, 30	kin 28 1, 30 šú	du$_6$ [30] 13[	
		VII	11, 44 ♍	2, 39, 18, 24	+ 5, 46, 45, 57	12, 46, 4, 41, 15	3, 50, 44, 41, 28, 53, 20		9, 46, 8 tab]	4, ., 30	du$_6$ 29 3, 29, 30 šú	apin 1 16[	
	5'.	VIII	11, 44 ♏	2, 27, 46, 8	+ 3, 40, 30, 15	12, 4, 4, 41, 15	4, 16, 33, 20		5, 46, 8 tab]	4, 22, 19	apin 29 5, 7, 11 šú	gi[an] 1 18..[	5'.
		IX	11, 44 ♑	2, 24, 13, 52	+ 44, 29, 6	11, 22, 4, 41, 15	4, 42, 21, 58, 31, 6, 40		1, 46, 8] tab	4, 44, 7	gan 28 ., 23, 4 šú	[ab 1] 29, 1[0	
		X	11, 44 ♒	2, 28, 41, 36	- 2, 56, 1, 9	11, 28, 4, 41, 15	4, 56, 15, 11, 6, 40		2, 13, 52 [al	4, 54, 1	ab 28 1, 29, 3 šú	[zíz]z 1 22[	
		XI	11, 44 ♓	2, 41, 9, 20	- 5, 2, 16, 51	12, 10, 4, 41, 15	4, 35, 54, 48, 53, 20		6, 13, 52 [al]	[4, 29, 41]	zíz .. 2, 59, 22 šú]	[še	
		XII	10, 48, 45 ♈	3, 0, 32, 30	- 7, 4, 51, 33	12, 52, 4, 41, 15	4, 10, 6, 10, 22, 13, 20	- 28, 1, 26, 30	9, 41, 35 lal]	[3, 32, 23]	[še .. 5, 26, 59 šú]	[	

ACT No. 23

Bibliography

Aaboe [1968]: *Asger Aaboe, Some Lunar Auxiliary Tables and Related Texts from the Late Babylonian Period.* Mat. Fys. Medd. Dan. Vid. Selsk. *36*, no. 12 (1968).

Aaboe [1969]: *Asger Aaboe, A Computed List of New Moons for 319 B.C. to 316 B.C. from Babylon: B.M. 40094.* Mat. Fys. Medd. Dan. Vid. Selsk. *37*, no. 3 (1969).

Aaboe [1971]: *Asger Aaboe, Lunar and Solar Velocities and the Length of Lunation Intervals in Babylonian Astronomy.* Mat. Fys. Medd. Dan. Vid. Selsk. *38*, no. 6 (1971).

Aaboe [1974]: *Asger Aaboe, Scientific Astronomy in Antiquity.* Phil. Trans. R. Soc. Lond. A. *276* (1974), pp. 21-42.

Aaboe-Henderson [1975]: *Asger Aaboe* and *Janice A. Henderson, The Babylonian Theory of Lunar Latitude and Eclipses According to System A.* Archives internationales d'histoire des sciences, vol. 25 (1975), pp. 181-222.

ACT: *O. Neugebauer, Astronomical Cuneiform Texts.* 3 vols. London (Lund-Humphries) 1955.

BMR: *F. X. Kugler, Die babylonische Mondrechnung.* Freiburg, 1900.

HAMA: *O. Neugebauer, A History of Ancient Mathematical Astronomy.* Studies in the History of Mathematics and Physical Sciences, vol. 1 (in 3 parts). New York-Heidelberg-Berlin (Springer) 1975.

LBAT: *A. Sachs* (ed.), *Late Babylonian Astronomical and Related Texts Copied by T.G. Pinches and J.N. Strassmaier.* Providence, Rhode Island (Brown University Press) 1955.

Neugebauer [1975]: *O. Neugebauer, "Saros" and Lunar Velocity in Babylonian Astronomy.* Mat. Fys. Medd. Dan. Vid. Selsk. *31*, no. 4 (1957).

v.d. Waerden [1966]: *B.L. van der Waerden, Anfänge der Astronomie.* Groningen (Noordhoff), 1966.

Indleveret til Selskabet august 1978.
Færdig fra trykkeriet februar 1979.

Lifetime Measurements for Heavy-Ion-Induced Fission by the Crystal-Blocking Technique

By J. U. ANDERSEN, A. S. JENSEN, K. JØRGENSEN,
E. LÆGSGAARD, K. O. NIELSEN,
J. S. FORSTER, I. V. MITCHELL, D. WARD,
W. M. GIBSON, *and* J. J. CUOMO

Det Kongelige Danske Videnskabernes Selskab
Matematisk-fysiske Meddelelser **40**:7

Kommissionær: Munksgaard
København 1980

Synopsis:

The crystal-blocking technique has been applied to study the time development of fission induced by heavy-ion (^{12}C, ^{16}O, ^{19}F) bombardment of tungsten (and gold). Thin single crystals have been used as targets and the blocking patterns have been recorded with 2-dimensional position-sensitive detectors, which are thin enough ($\sim 20\mu$m) to separate fission fragments from scattered projectiles with the same energy. The blocking dips are analyzed as superpositions of two components, corresponding to short and long lifetimes, and the information extracted is the relative amount of fission with lifetimes $\tau \gtrsim 10^{-16}$ sec. In this analysis, the short-lifetime component is represented by a blocking dip for elastic scattering at lower bombarding energy, which is scaled to the average energy and nuclear charge of fission fragments. The long-lifetime component is represented by a calculated dip. The dependence on bombarding energy of the fraction of fission with long-lifetime has been studied systematically for ^{12}C and ^{16}O bombardment of tungsten in the energy range 80 MeV to 115 MeV. In agreement with expectations based on qualitative considerations, the long-lifetime component initially increases with energy, reaching a maximum of $\sim 20\%$, and then decreases to $\sim 5\%$ at the highest energy. For ^{16}O on W supplementary measurements have been made of the fission cross section for the different W isotopes and of the angular distribution of fission fragments. The results are used together with the lifetime data to determine parameters in a statistical-model calculation of the fission process, which follows the distribution in spin and energy of the fissioning nuclei through the neutron-evaporation cascade. All the experimental results are reproduced with a consistent set of parameter values, and the combination of experimental data turns out to be very effective in constraining the variation of these parameters. In particular, the information obtained from the lifetime measurements on the distribution of fission over stages in the neutron evaporation cascade is important for the interpretation of the measurement of fission-fragment anisotropy, which depends sensitively on the temperature of the fissioning nucleus.

J. U. Andersen, A. S. Jensen, K. Jørgensen, E. Lægsgaard, and *K. O. Nielsen*
Institute of Physics, University of Aarhus, DK-8000 Aarhus C, Denmark.

J. S. Forster, I. V. Mitchell, and *D. Ward*
AECL, Chalk River Nuclear Laboratories, Chalk River, Ontario, Canada.

W. M. Gibson
Department of Physics, State University of New York at Albany, Albany, N.Y. 12222, U.S.A.

J. J. Cuomo
Watson IBM Research Laboratory, Yorktown Heights, NY. 10568, U.S.A.

Printed in Denmark by Bianco Lunos Bogtrykkeri A/S. ISSN 0023-3323. ISBN 87-7304-107-6.

Contents

1. Introduction

The blocking lifetime technique for measurement of nuclear lifetimes in the range ($< 10^{-15}$ s), where nucleon emission dominates the decay of excited nuclei, has been applied to study a variety of processes [1,2]. It is basically a time-of-flight technique which utilizes the fact that displacements of target atoms from lattice sites by more than ~ 0.1 Å can be distinguished by a filling-in of the blocking dip in yield of emitted, charged particles. The method was first established about ten years ago, and from the beginning, investigations of nuclear fission played an important role [3-5]. Systematic studies of neutron-induced fission of uranium isotopes [6-9] have shown that for low excitation energies E*, the lifetime decreases with excitation energy to $\tau \sim 10^{-16}$ s for E* ~ 10 MeV. For higher energies, the lifetime becomes too short to be measured with the technique, and only an upper limit can be established (e.g., $\tau < 10^{-17}$ s for helium-induced fission of ^{238}U at E* = 20 MeV[5]).

An important exception to this behaviour occurs at projectile energies close to threshold for higher-chance fission. It has been observed for both proton bombardment[4] and neutron bombardment[9] of ^{238}U that just above threshold for fission after emission of one neutron (second-chance fission), the blocking dips for fission fragments are filled-in by a slow fission component. Similarly, at higher energies, the fission lifetime would be expected to depend strongly on the average number of neutrons evaporated prior to fission. In fact, only if this number is small ($\lesssim 1$) can the process be usefully characterized by a single lifetime. This problem is crucial for the interpretation of blocking measurements of fission induced by heavy-ion bombardement. Since the heavy ion must have sufficient energy to overcome the Coulomb barrier, the excitation energy will always be high enough to allow evaporation of several neutrons from the compound nucleus.

The pioneering measurements of lifetimes for heavy-ion induced fission were made by Karamyan and co-workers [10,11]. They measured blocking patterns for fission induced by bombardment of tantalum and tungsten crystals with heavy ions (boron, carbon, oxygen, neon, and phosphorus) and identified significant lifetime effects for excitation energies as high as 120 MeV. By assuming that the number of neutrons emitted prior to fission was small, they interpreted these

effects as evidence for a surprisingly long lifetime, $10^{-17} - 10^{-18}$ s, of the initially formed nucleus as compared to expected lifetimes of $10^{-19} - 10^{-20}$ sec. This implies that the nuclear temperature is much lower at high excitation energy than that calculated from a Fermi-gas model with the usual parameter values and, correspondingly, that the level density is much higher than that estimated from such a calculation (see, for example, the discussion by Karamyan et al.[2]).

The present study was stimulated by and is an extension of the work of Karamyan and co-workers. By the use of thin crystal targets, improved angular resolution and statistics, and two-dimensional, position-sensitive semiconductor systems which allow detection of both fission fragments and elastically scattered projectiles, it was felt that additional information on the time evolution of the decay could be obtained. In a preliminary report[12], it was shown that the new results were inconsistent with an interpretation involving delayed decay of the initial compound nucleus. A comparison of blocking dips for fission fragments with blocking dips for elastically scattered ions revealed large effects of compound-nucleus recoil, but a detailed analysis of the shape of these dips showed that the filling-in must be due to a fission component with very long lifetime, $\tau \gtrsim 10^{-16}$ s (with most of the fission occurring within a time too short to be measured, $\tau < 10^{-17}$ s). The long lifetime was interpreted as fission after evaporation of several neutrons, and this interpretation was substantiated by the calculations of Hagelund and Jensen[13], which were prompted by these measurements. Since then, the calculations have been improved[14] mainly by a modification of the analytical level-density expression[15]. We shall present some of the new results and compare them with our data.

The importance of higher-chance fission is also indicated by other types of measurements, e.g., of the angular distribution of fission fragments[16]. It is a simple consequence of the fact that for the systems studied, the neutron-binding energy B_n and the fission barrier B_f are comparable in magnitude. In fig. 1, taken from Huizenga and Vandenbosch[17], the ratio Γ_n/Γ_f, calculated from a Fermi-gas model, is shown as a function of excitation energy for different relative magnitudes of B_n and B_f. The energy dependence is governed mainly by the ratio of Boltzmann factors, $\exp((B_f - B_n)/T)$, where T is the nuclear temperature ($T \propto E^{1/2}$). For $B_n \simeq B_f$, this ratio is almost constant, and fission after evaporation of one or more neutrons will then be as important as first-chance fission.

On the other hand, the fission yield is dominated by first-chance fission in both the limits $B_f \gg B_n$ and $B_f \ll B_n$; in the former limit, the fission probability decreases rapidly with decreasing excitation energy, and in the latter limit, very few compound nuclei survive first-chance fission. Since the fission barrier depends strongly on the fissionability parameter Z^2/A, the variation between these limits can be investigated by a variation of the target-projectile combination.

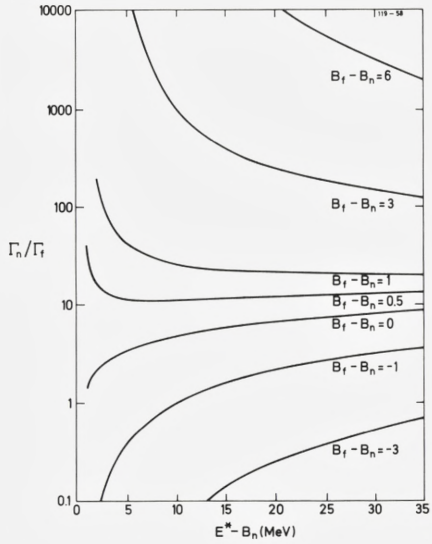

Fig. 1: The dependence of Γ_n/Γ_f on excitation energy for different values of $(B_f - B_n)$. Level-density parameters a_f and a_n were assumed equal to 25 MeV^{-1} and B_n equal to 6 MeV. The figure is taken from ref. 17, with a small correction of notation $(E_f \rightarrow B_f)$.

For a fixed value of Z^2/A, the effective fission barrier may be varied by changing the bombarding energy and thereby the average angular momentum of the compound nuclei. For the very large values of angular momentum attained in heavy-ion reactions, the rotational energy of the compound nucleus may be comparable to the fission barrier. At the saddle point for fission, the moment of inertia is increased by the deformation, and the fission barrier is effectively reduced by the corresponding change in rotational energy, $B_f^{eff} = B_f - \Delta E_{rot}$. The different curves in fig. 1 may therefore also represent different values of angular momentum.

If $B_f > B_n$ for $I = 0$, we may then expect the following variation with bombarding energy: Close to the fission threshold, the yield is dominated by first-chance fission. At somewhat higher energies, the effective fission barrier B_f^{eff}, corresponding to a larger average angular momentum, is reduced to $B_f^{eff} \simeq B_n$ and the contribution from late-stage fission is large. For even higher bombarding energies, $B_f^{eff} < B_n$, and the fission yield is again dominated by the contribution from the first stages of the evaporation chain.

This picture is, of course, greatly simplified. The change in Γ_n/Γ_f with neutron evaporation is not caused by the decrease in temperature alone; other effects such as changes in shell corrections and in the neutron binding energy are also important, but they do not change the qualitative conclusion concerning the energy dependence of the contribution from late-stage fission.

In the present report, we give a detailed account of the experimental investigation. Both from a technical and analytical point of view, it represents a new

development of the crystal-blocking technique. The interpretation of the results in terms of a multi-component time distribution has been established by a large number of measurements with different target thickness, target temperature, crystal orientation, and varying projectile energy. The variation of the magnitude of the long-lifetime component with projectile energy has been measured for oxygen on tungsten in the energy range from 90 to 115 MeV and for carbon on tungsten from 80 to 87 MeV. The results are in qualitative agreement with the simple predictions discussed above.

Detailed numerical calculations of the type introduced by Hagelund and Jensen[13] have been performed. In order to determine some of the parameters in the calculations, we have made systematic measurements of fission cross sections and also of the angular distribution of fission fragments for all four tungsten isotopes (^{182,183,184,186}W) bombarded by ^{16}O in the energy range 90-108 MeV. The combination of such different types of information is found to reduce considerably the ambiguity in selection of parameters for the calculations; in particular, the calculations illustrate the value of the new type of information obtained from blocking measurements.

2. Experimental Details

2.1 *Equipment*

A plan view of the experimental apparatus is shown in fig. 2. Ion beams from the Chalk River MP tandem accelerator entered the target chamber through collimators to produce a beam spot on the target of $\lesssim 0.5$-mm diameter. For the target-detector distances used ($\gtrsim 105$ mm), this resulted in sufficient spatial resolution in the blocking patterns for all target tilt angles and detector angles.

Single-crystal targets (see sec. 2.2) were mounted in a two-axis goniometer which allowed translation of the target in its own x and y frame while preserving the crystal orientation, beam-spot size, and beam-spot position with respect to the detectors. The target-crystal assembly was surrounded by a metal shroud, which was liquid nitrogen cooled to inhibit contamination of the crystal surface. The crystals could also be cooled by heat transfer through a copper braid attached to the rear of the sample holder.

The target chamber and shroud design allowed the detector assemblies to be located in the horizontal plane at any of four predetermined angular settings, viz. $-100°$, $+130°$, and 160-170° on either side of the beam (see fig. 2). Hence, detector pairs could be set to subtend angles of 70° or 90° at the target when we wished to record, simultaneously, two blocking patterns along axial directions of the same symmetry, viz. $<111>$ or $<100>$.

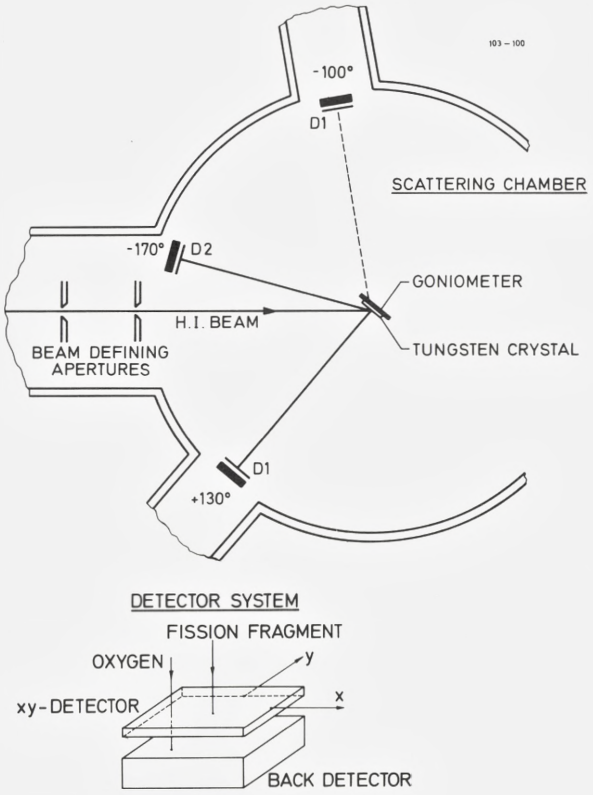

Fig. 2: Plane view of the experimental apparatus. The detectors were placed ~105 mm from the crystal. A detector system, consisting of a position-sensitive front detector and a back detector, is shown separately. The orientation of the crystal corresponds to a blocking angular-distribution measurement around a < 111 > axial direction at 130° to the beam.

2.2 *Crystals*

In contrast to other fission-lifetime measurements based on the blocking technique, thin crystals ($\lesssim 4000$ Å) were used in the present experiments, alleviating uncertainties that arise from depth-dependent cross sections and dechanneling effects. The tungsten crystals were grown epitaxially on Al_2O_3 or MgO, and the gold crystals on NaCl. The use of low-Z-material substrates ensured that there were no troublesome background radiations during heavy-ion bombardment and, consequently, there was no need to remove the crystals from their backings.

Crystal thicknesses were measured by backscattering of 2-MeV He^+ or H^+ beams, and the crystal quality was determined by measuring the minimum yield χ_{min} for 2-MeV He^+ ions incident along a low-index axis. Results for the four tungsten crystals used are shown in table 1. Also shown are the χ_{min} values obtained from 40-MeV ^{16}O-ion blocking dips. The He^+-beam analyses made use of a surface-barrier detector of 15 keV resolution, the χ_{min} values being obtained

Table 1. Properties of the W crystals used in the blocking lifetime measurements. The thickness t, the axis normal to the crystal surface, and the minium yields χ are given. The χ_{He} values were determined as near-surface for channeling of 2.0 MeV ^{4}He particles while the χ_0 values were determined from blocking measurements of 40 MeV elastically scattered ^{16}O ions and are averaged over the crystal thickness.

No.	t[Å]	Axis	χ_{He}	χ_0	Comment
W1	1130	< 110 >	~ 5%	12%	~ 15° off < 110 >
W2	3800	< 111 >	1%	5%	twinned
W3	3350	< 111 >	2%	9%	
W4	570	< 111 >	2%	9%	

from near-surface scattering (see fig. 3). With the oxygen beam, the χ_{min} values were determined from spectra recorded with the modest energy resolution of the detector D1 (see sec. 2.4) and therefore represent averages over the entire crystal thickness. Since depth discrimination was not possible in the fission measurement, these depth-averaged χ_{min} values are the more relevant ones for comparison with blocking of fission fragments.

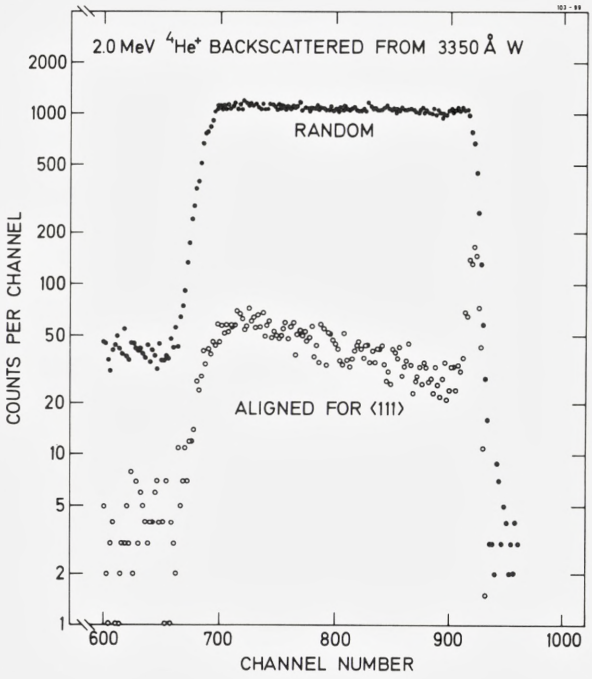

Fig. 3: Spectrum of back-scattered $^4He^+$ ions from the W crystal W3. The closed circles correspond to the case where the beam was incident in a non-channeling direction in the crystal, and the open circles correspond to alignment of a < 111 > axis with the beam direction. The two spectra were recorded for the same number of incident beam particles.

The crystals described in table 1 represent a large variation in thickness, orientation, and quality. The use of such different targets provided an important test of the reproducibility of the observed lifetime effects.

2.3 *Crystal Temperature and Radiation Damage*

At room temperature, the blocking patterns for ^{16}O ions elastically scattered from gold crystals were rather poor, but when the crystals were cooled to ~ 100 K, the elastic blocking patters had much lower minimum yields. Consequently, all fission-fragment blocking measurements with gold were made with the crystals cooled to 100 K. For the tungsten crystals, the χ_{min} values for elastically scattered ^{16}O ions were very good ($\sim$8-10%) at room temperature. Since radiation damage is expected to be worse at lower temperatures, all tungsten measurements except one were made at room temperature.

Radiation-damage effects on the blocking measurement were avoided by translating the crystal at regular intervals. After each 50 μC of accumulated heavy-ion charge, the crystal was translated 0.5 mm, the diameter of the beam as defined by the collimators. This amount of charge was chosen on the basis of measurement with 40-MeV oxygen-ion bombardment, which showed radiation-damage effects in cold gold crystals after 200 μC of accumulated charge. (No distinction is made here between primary radiation damage in the metal film and crystal damage or distortion resulting from radiation damage in the substrate.) For each target position, data accumulation was separated with appropriate markers on the magnetic tape used for data acquisition so that each segment could be evaluated separately for crystal degradation. No evidence of radiation damage was observed.

2.4 *Detectors*

The measurements were made using two specially fabricated silicon-detector systems[18], denoted D1 and D2 in fig. 2. As shown in the lower part of the figure each system consisted of two planar diodes; the front counter had an active area of 14×14 mm^2 and was $\sim 20\mu$m thick. This thickness was sufficient to stop fission fragments but small enough to allow light energetic particles, e.g. elastically scattered ^{16}O, to pass through and be detected in the large-area detector at the back, thus allowing discrimination between fission fragments and the light particles. The front counter was position sensitive in both the x and the y directions[18]. Three signals were obtained from this detector, consisting of the products $E \cdot x$, $E \cdot y$, and $E \cdot (1-x)$. Electronic processing of these three pulses gave signals proportional to energy, x position, and y position. Each signal was encoded by an ADC with

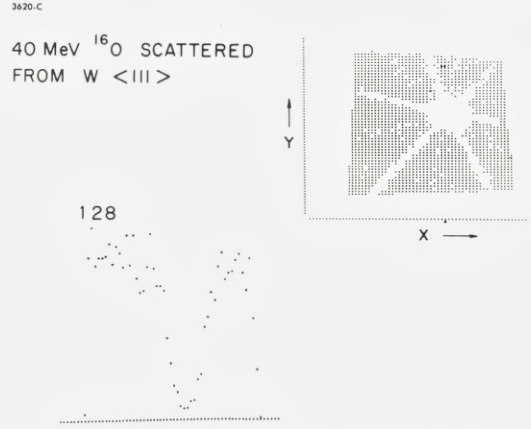

Fig. 4: Photograph of the on-line computer display for 40-MeV ^{16}O bombardment of a W< 111 > crystal. The black dots in the upper right 2-d spectrum correspond to (x, y) channels with a number of counts greater than a preselected minimum value. In the lower left corner, a y scan through the centre of the axial blocking dip is shown; the x value is indicated by a black dot on the x axis.

a conversion range of 256 channels, and the data were written event by event on magnetic tape by the Chalk River PDP-1 computer. A preliminary analysis, in the form of an energy spectrum and a 64 × 64 two-dimensional position spectrum, was made on-line for each detector system. Fig. 4 shows a typical two-dimensional blocking pattern for 40-MeV ^{16}O elastically scattered from a tungsten crystal. The axial and planar minima for this < 111 > direction are clearly visible in the two-dimensional display in the upper right portion of the figure. In the lower left corner is a plot of intensity in the y direction, through the center of the axial dip, for the x position indicated by the dot on the x axis.

The main requirements on the detection system are that it should be able to discriminate fission fragments from all background radiation and to record two-dimensional blocking patterns with high angular resolution. It is possible to satisfy these requirements with the plastic or glass-plate track detectors used in previous blocking-technique measurements of fission lifetimes [10,11], but the experiment control provided by the on-line display and the accessibility of the data for analysis are very important advantages of the present technique.

3. Measurements and Data Reduction

3.1 *Method of Measurement*

Blocking patterns of fission fragments were measured with gold crystals for ^{16}O-ion bombarding energies of 86 and 90 MeV and with tungsten crystals for ^{12}C-ion bombarding energies of 80, 82.5, 85, and 87 MeV, for ^{16}O-ion bombarding energies of 90, 94, 96, 97, 102, 108, and 115 MeV, and for ^{19}F-ion bombarding energies of 95 and 108 MeV. Measurements were also made for elastic scattering of 25-MeV ^{12}C and 25- and 40-MeV ^{16}O-ions.

The tungsten crystal used in the initial measurements (W1) was grown epitaxially with a $< 110 >$ axis nearly perpendicular to its surface. With this axis at 45° to the incident beam, blocking patterns were simultaneously measured for fission-fragment emission along the $< 111 >$ axes at $+170°$ and at $+100°$ to the incident-beam direction. In this geometry, the incident-beam direction, and therefore the compound-nucleus recoil direction, was parallel to a {110} plane. In order to avoid the reduction of yield resulting from channeling of the incident ions, the crystal was tilted slightly (one degree) from the planar direction. Measurements were also made using the same crystal for simultaneous blocking along two $<100>$ axial directions. In this case, one detector was located at $+100°$ and the other at $-170°$ to the incident beam, and the recoil was nearly parallel to a {100} planar direction. As mentioned earlier, the other tungsten crystals used were oriented with a $<111>$ axis normal to the surface. For these crystals, blocking measurements were made sequentially for recoil at 15° and 50° to the $<111>$ axis by orienting the crystal so that the $<111>$ surface normal was directed first at one and then at the other detector, located at the appropriate scattering angles. This method precludes simultaneous measurements of blocking in two directions, but it was found that the results were reproducible. The method has the advantage that while a blocking measurements is being made with one detector, fission fragments striking the other detector emerge from the crystal in a random or non-blocking direction and provide a test of detector response to a uniform exposure. It also allows a free choice of the direction of the recoil relative to the major crystal planes.

3.2 *Data Analysis*

Data analysis was carried out on the Chalk River PDP-10 computer by setting windows on the fission energy spectra and accumulating two-dimensional (64×64) position spectra from the event-mode recorded data. Typical fission energy spectra for 102-MeV ^{16}O and 85-MeV ^{12}C bombardment of tungsten are shown in fig. 5 for detectors located at $-165°$ and $+130°$ to the beam. The energy windows used in the analysis are indicated by horizontal lines with downward pointing arrows at either end. Windows were chosen that were symmetric about the fission peak in the energy spectrum so that a symmetric average over fission-fragment charge and mass, about the mean value, would be taken. This is necessary for comparison of the experimental and calculated blocking patterns since the calculations are made with the average charge and mass for the emitted fragment (see sec. 4). A test of the importance of the spread around the average value was made for the case of 102-MeV ^{16}O bombardment of tungsten, where good statistical accuracy was obtained; analysis of the data with wide and narrow fission

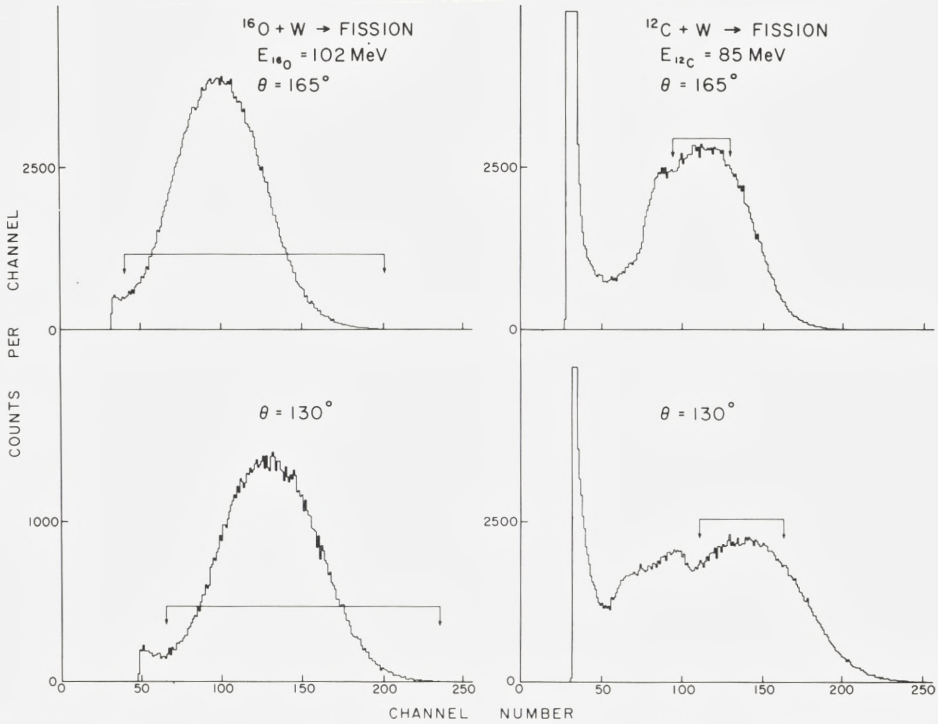

Fig. 5: Fission energy spectra from the position-sensitive front detector for 102-MeV ^{16}O and 85-MeV ^{12}C bombardement of W, for two angles of observation. The horizontal lines with downward pointing arrows indicate the windows used in the analysis to generate the two-dimensional patterns.

energy windows gave blocking patterns which were identical, within statistical errors.

3.3 *Detector Non-Linearities*

With the very thin position-sensitive detectors used in these measurements, there is a problem with non-linearities in the position spectra. These arise from non-uniformities in sheet resistance over the implantation region of the detector and from the compromises required in electronic-shaping time constants[18].

In order to correct the data for non-linearity effects the following correction procedure was applied: Masks, consisting of a thin piece of brass with a square array of holes, 0.5-mm diameter, accurately positioned with 1.5-mm spacing between centres, were placed over each detector. An amorphous tungsten target was bombarded with 40-MeV ^{16}O ions, and two-dimensional position spectra

were recorded for each detector. The centroid, in x and y, for each peak in the two-dimensional spectra corresponding to the holes in the masks was determined by a computer program.

Due to the detector non-linearities, the (x, y) values were not uniformly spaced. The distortion was least-squares fitted by a polynomial which connected the experimental set of (x, y) values with an ideal, uniformly spaced set of (x′, y′) values. The polynomial had the form

$$x = a_0 + a_1 x' + a_2 x'^2 + a_3 y' + a_4 y'^2 + a_5 x' y' + a_6 x' y'^2 + a_7 x'^2 y'$$

and similarly for y with coefficients b_0 to b_7. The number of experimental (x, y) values used in the fitting was usually ~ 80.

The polynomial was used to calculate the position in the distorted spectrum from which to take counts to be put in the corrected two-dimensional spectrum. In general, the position calculated in the distorted spectrum did not have integer (x, y) values, and contributions to the counts transferred to the new spectrum were taken from the four surrounding points with integer coordinate values, weighted according to the distance of the point from the calculated position (x, y). In this way, the integral linearity distortion has been corrected for, and the variation in differential linearity was corrected for separately through multiplication with the local Jacobian of the coordinate transformation.

3.4 *Fission Cross Sections*

In order to aid the interpretation of lifetime distributions, we measured fission cross sections for ^{16}O bombardment of the four tungsten isotopes, $^{182,183,184,186}W$, in a separate experiment. Thin targets ($\sim$100-250 $\mu g/cm^2$) of tungsten oxide, enriched to greater than 98% isotopic purity, on 30-$\mu g/cm^2$ aluminium backings were used. Three thin silicon surface-barrier detectors were placed in a scattering chamber at angles of 100°, 130°, and 170° to the beam direction, and the yield of fission fragments was measured as a function of ^{16}O bombarding energy over the range 90 to 108 MeV. The relative solid angles were determined with a 40-MeV ^{16}O beam using the Rutherford scattering cross section.

The beam current was monitored with a detector at 40°, measuring the elastic-scattering yield. An absolute calibration of the cross sections was obtained by measuring the 40° fission and elastic yield for 97-MeV ^{16}O in one of the fission counters, moved to 40°. The angular distribution of fission fragments was measured in detail for one isotope and one energy (see sec. 3.5) and was assumed to be the same for all energies and isotopes. In fact, the energy dependence of the anisotropy, discussed below, has only a small influence ($< 5\%$) on the evaluation of the total cross sections.

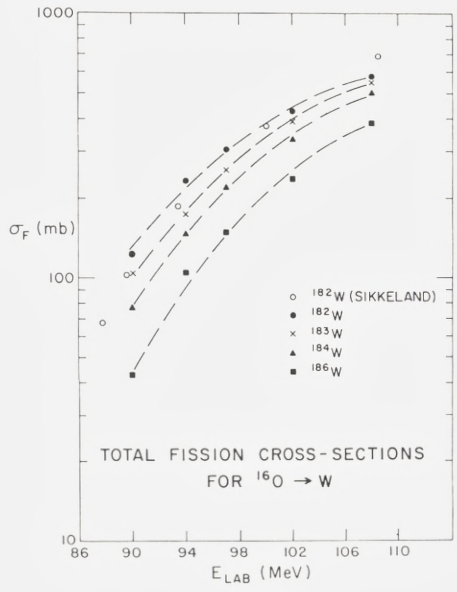

Fig. 6: Measured fission cross sections for ^{16}O-induced fission of the W isotopes, ^{182,3,4,6}W, as functions of ^{16}O bombarding energy. The data of Sikkeland [19] for ^{16}O-induced fission of ^{182}W are also shown.

The measured cross sections are shown in fig. 6 for each isotope as a function of ^{16}O bombarding energy. The results of Sikkeland[19] for ^{182}W, also shown in fig. 6, are consistent with the present data.

3.5 *Fission-Fragment Angular Distributions*

The angular distribution contains important information about the angular momentum and excitation energy of fissioning nuclei, which may be used in the comparison with calculations (see sec. 6). A measurement of the angular distribution of fission fragments, from 40° to 170° in steps of 10°, was made for 97-MeV ^{16}O on ^{183}W, and the results are shown in fig. 7, where angles and solid angles have been converted into the center-of-mass system. As described in the previous section, this measurement allows determination of the total cross section from the yield measured at one angle (if symmetry around 90° is assumed). The limited information for other isotopes and energies obtained in connection with the measurements of cross sections (cf. sec. 3.4) is given in table A4 in the appendix. As a check, a few measurements with a movable counter were made for the isotope ^{182}W. The results are shown in fig. 21 and discussed in sec. 6.4.

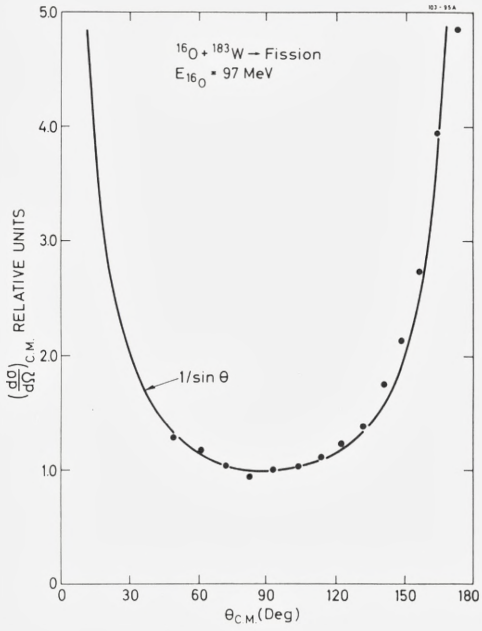

Fig. 7: Fission-fragment angular distribution in the centre-of-mass system for ^{16}O-induced fission of ^{183}W. The experimental angular distribution is compared with a $(\sin \theta)^{-1}$ distribution.

4. Analysis

4.1 *Circular Integration*

As shown in fig. 4, the blocking patterns exhibit strong planar blocking effects in addition to the axial blocking dip. Our analysis is based on the axial dip alone, and in order to eliminate the influence of planar effects, the dip is constructed from circular averages around the minimum. Compared to taking a simple one-dimensional cut through the minimum, this procedure has the advantages of improving statistical accuracy and eliminating planar effects since the planar dips are compensated for by an enhanced yield between planes. On the other hand, by averaging one loses information about asymmetries in the dip associated with lifetime effects.

The first step in the averaging procedure is the determination of the dip centre. We have tried two methods: (i) To search for a minimum number of counts within a small area, and (ii) to determine the centre from the symmetry of the counts at the edges of the dip. The latter procedure is normally more accurate, but it is also more sensitive to detector non-linearities. We have therefore mainly used the first method. A simple measure of the accuracy of the search is the variation of the centre coordinates with the size (radius) of the small area

used in the search. For blocking patterns with reasonable statistics, the accuracy is better than 10% of the half-width at half minimum of the dip. For most purposes, this is sufficient, but if the dip contains structure in the centre (e.g., a flux peak, cf. below), the detailed shape of the circular-averaged dip may depend critically on the centre coordinates. Such structure may be seen more clearly from linear scans through the blocking pattern, as shown in fig. 8.

Normally, the yield as a function of the distance from the centre of the dip is determined from averages over circular rings. For large radii, the rings will intersect the edges of the detector where the yield may be distorted, and these regions are therefore not included in the circular averages. In order to minimize effects of detector non-linearity, the region used for constructing the blocking

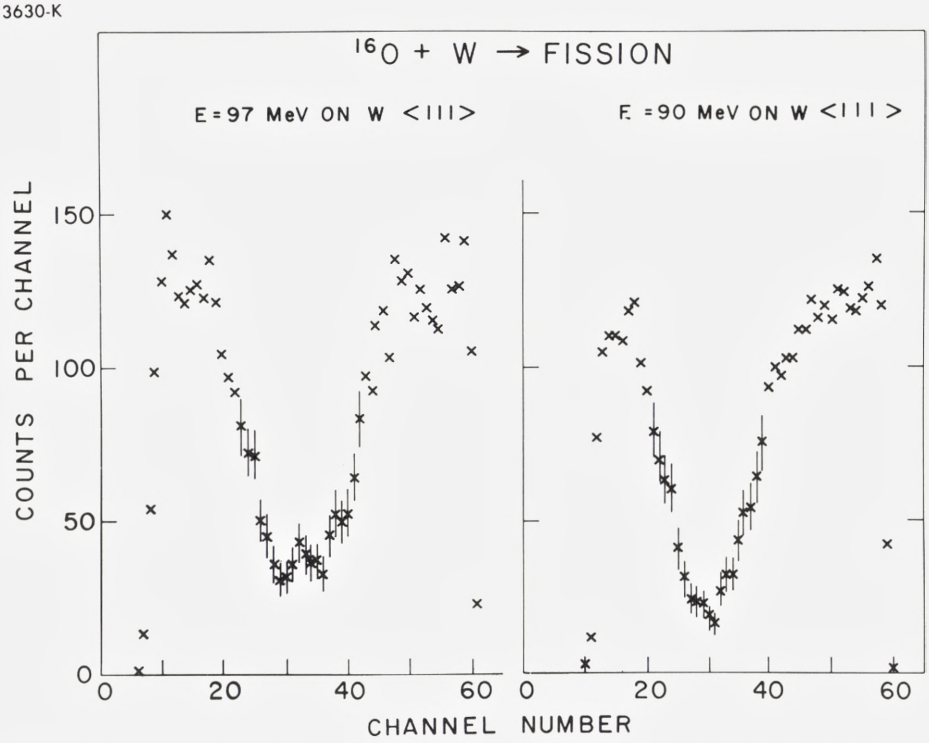

Fig. 8: Linear scans across the 2-d blocking patterns in the < 111 > direction for 90- and 97-MeV ^{16}O-induced fission of W. The 90-MeV data correspond to a recoil direction of the compound nucleus toward the nearest-neighbour < 111 > row of atoms. The 97-MeV data correspond to a recoil directed toward the centre of a < 111 > channel, which results in a "flux peak" in the centre of the blocking dip, as described in the text (cf. figs. 10 and 11).

dip was chosen to be nearly symmetric around the dip centre. A check of distortion due to edge effects or non-linearity is obtained from analysis of 'random' patterns, i.e., two-dimensional spectra containing no strong axial or planar blocking features. In most cases, the circular integration for these spectra gave a yield as a function of distance from the centre coordinates, which was constant within a few percent. In a few cases, we have made a small correction based on the shape of the 'random' spectrum (cf. table 3).

4.2 *Identification of Lifetime Effects*

In order to identify possible effects of a nuclear recoil on the blocking dips, one must compare with a dip obtained in a situation where such effects are known to be absent ('zero-lifetime normalization'). A common method[1] consists of measuring the blocking dips for axes at different angles θ to the incident beam, i.e., to the recoil direction. For small recoil distances, the minimum yield χ of the dip is proportional to the mean-square displacement $<r^2>$,

$$\chi = CNd\pi < r^2 > , \tag{1}$$

where N is the atomic density, d is the spacing of atoms along the axis in question, and C is a constant ($C \simeq 2$-3), which was originally introduced by Barrett[20] to account for deviations from the simple continuum approximation [21] where $C = 1$. For the difference in minimum yield, $\Delta\chi = \chi_1 - \chi_2$, between blocking dips at two different angles θ_1 and θ_2 to the recoil direction, one obtains

$$\Delta\chi = 2CNd\pi v^2\tau^2(\sin^2\theta_1 - \sin^2\theta_2) . \tag{2}$$

Here, v denotes the recoil velocity, τ the lifetime, and we have assumed the decay to be exponential. In this way, the contribution to $<r^2>$ from thermal vibrations is eliminated. Also, other contributions to the minimum yield from, e.g., dechannelling or crystal imperfections, are strongly reduced.

This type of analysis has been applied to the lifetime investigation of heavy-ion-induced fission by the Dubna group[10,11], and substantial lifetime effects have been observed. However, our measurements do not show any significant dependence of the minimum yield on the angle θ between the recoil direction and the axis [12]. This is illustrated by the results for 96-MeV ^{16}O on tungsten shown in the upper part of fig. 9. A substantial influence on the dip of a nuclear recoil is revealed only by a comparison to the blocking dips obtained for elastic scattering of 40-MeV oxygen. In the figure, these dips have been scaled in angle by a factor $(Z_{ff}/Z_O)^{1/2} \cdot (E_O/E_{ff})^{1/2}$, where Z and E denote nuclear charge and energy of fission fragments and of scattered oxygen. The average fission-fragment energy E_{ff} is calculated from published values of the energy release in fission[22].

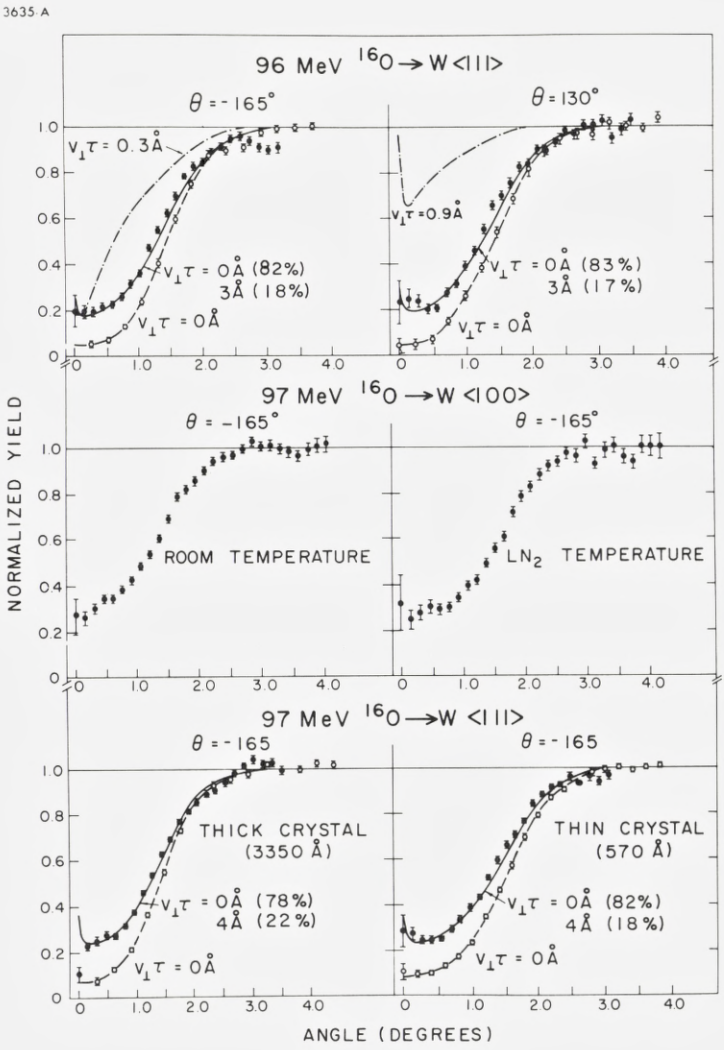

Fig. 9: Fission-fragment blocking dips (closed circles) for 96- and 97-MeV ^{16}O bombardment of W. Results are shown for different angles θ between the incident beam and the axis, different crystal temperatures, and different crystal thicknesses. Also shown, as open circles, are blocking dips for 40-MeV ^{16}O elastic scattering, scaled in angle by $(Z_{ff}/Z_o)^{1/2} \times (E_o/E_{ff})^{1/2}$ (see text). Included in the 96-MeV plots are predicted blocking dips for $v_\perp\tau = 0.3$ Å and 0.9 Å. Solid lines through the data points are fits with the indicated amounts of short- and long-lived fission components.

The elastic minimum yields are seen to be lower by ~ 0.15. The middle and lower pairs of measurements in fig. 9 demonstrate that this difference is not caused by a difference in multiple scattering for fission fragments and oxygen. A decrease in crystal temperature to liquid-nitrogen temperature strongly reduces scattering due to thermal vibrations, and as shown in the middle part of fig. 9, the $<100>$ dip for fission fragments becomes wider, but the minimum yield is nearly unaffected. Neither does the variation of the crystal thickness by a factor of 6 change the difference between minimum yields for fission fragments and elastically scattered oxygen, as shown in the lower pair of blocking dips in fig. 9. We interpret this difference in the minimum yield as being due to a fission component with a lifetime so long that the corresponding average recoil distance perpendicular to the blocking axis is large, even for $\theta = -165°$. It can be seen from fig. 9 that the dips are consistent with this interpretation. The solid line through the data points has been obtained by a superposition of dips corresponding to a short lifetime ($v_\perp \tau = 0$) and a long lifetime ($v_\perp \tau = 2$ or 3 Å). The short-lifetime dip is obtained from elastic scattering of oxygen, scaled as indicated above, and the long-lifetime dip from the calculation described below. This interpretation is consistent with all our data.

4.3 *Calculation of Dips*

The dependence of the blocking dip on the average recoil distance has been calculated in the "statistical-equilibrium multistring" approximation[1]. We shall first describe the model and present some results and then discuss briefly the accuracy and limitations of such a calculation.

The first assumption is that the trajectories of the emitted fission fragments may be described as motion in a transverse potential obtained by averaging the crystal potential along the axial direction. This is normally denoted the continuum approximation [21,23]. With sufficient accuracy, we may represent the potential from a string of atoms by the standard potential of Lindhard[21],

$$U(r) = \frac{Z_1 Z_2 e^2}{d} \log((Ca/r)^2 + 1) . \qquad (3)$$

Here, Z_1 and Z_2 are the nuclear charges of the particle and the crystal atoms, respectively, d is the atomic spacing in the string, r is the perpendicular distance from the string, and a is the Thomas-Fermi screening distance, $a = a_0 0.885 (Z_1^{2/3} + Z_2^{2/3})^{-1/2}$, where a_0 is the Bohr radius. The constant C is a potential parameter, which is normally taken to be $C = \sqrt{3}$. It is convenient to introduce a characteristic angle ψ_1, by

$$\psi_1 = \left(\frac{2Z_1 Z_2 e^2}{Ed}\right)^{1/2}, \tag{4}$$

where E is the particle energy. Combining eqs. (3) and (4) gives

$$U(r) = \tfrac{1}{2} E\psi_1^2 \log\left((Ca/r)^2 + 1\right). \tag{5}$$

The total crystal potential is taken to be the sum of single string potentials. In the following, this sum i denoted by U. Since the potential decreases rapidly at large distances, only a few strings need be included. Fig. 10 shows contour plots of the multistring potential for a < 111 > direction in tungsten.

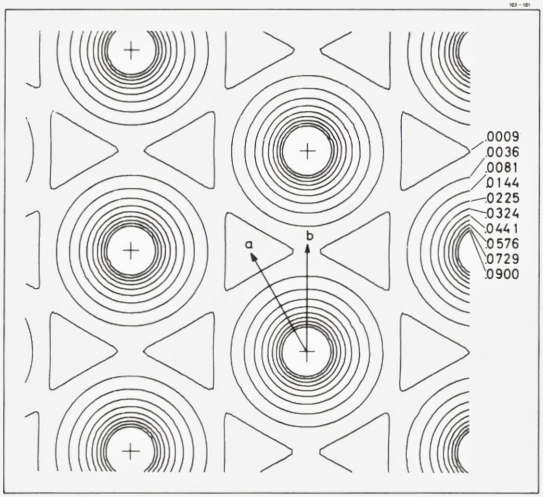

Fig. 10: Continuum potential-energy contours for fission fragments (Z = 41, A = 100) channeled along the < 111 > direction in W. The contours correspond to constant steps in ψ, and the numerical values shown express $E\psi^2$ in units of $E\psi_1^2$ The two recoil directions indicated by arrows a and b correspond to the two linear scans in fig. 8. The centers of atomic strings are marked by crosses. The distance between centers is 2.58 Å.

For a particle moving in this potential, the transverse energy $E_\perp = E\varphi^2 + U(\bar{r})$ will be conserved. Here φ is the instantaneous angle of motion with respect to the string direction and $\bar{r}$ is the position in the transverse plane. The motion of a particle with a given transverse energy $E_\perp$ is restricted to the area in the transverse plane $U(\bar{r}) < E_\perp$, i. e., bounded by the contour corresponding to $U(\bar{r}) = E_\perp$. In statistical equilibrium, the particle is found with equal probability anywhere in this area[21],

$$P(\bar{r}) = \begin{cases} 1/A(E_\perp) & \text{for } U(\bar{r}) < E_\perp \\ 0 & \text{for } U(\bar{r}) > E_\perp \end{cases}, \tag{6}$$

where $A(E_\perp)$ is the allowed area (per unit cell).

Assuming statistical equilibrium, we may write an expression for the probability for particles emitted inside the crystal (isotropically) at position $\bar{r}$ in the transverse plane to emerge from the crystal at an angle ψ to the axis,

$$\Pi(\bar{r},\psi) = \int_{U(\bar{r})}^{\infty} dE_\perp \frac{1}{A(E_\perp)} \int d^2\bar{r}' \delta(E\psi^2 + U(\bar{r}') - E_\perp) . \quad (7)$$

This probability or yield is normalized to unity in the random case, i.e., for $U(\bar{r}) \equiv 0$.

Performing the integration over $E_\perp$, we obtain

$$\Pi(\bar{r},\psi) = \int d^2\bar{r}' \frac{1}{A(E\psi^2 + U(\bar{r}'))} \Big|_{E\psi^2 + U(\bar{r}') > U(\bar{r})} \quad (8)$$

If the emitting nucleus is recoiling, with a transverse direction specified by a unit vector $\bar{e} = (e_x, e_y)$, expression (8) must be averaged over the one-dimensional distribution $f(r)$ of points $\bar{r} = r\bar{e}$, and the total yield at angle ψ becomes

$$P(\psi) = \int_0^{\infty} dr f(r) \Pi(r\bar{e},\psi) . \quad (9)$$

For exponential decay with lifetime τ and recoil velocity $v_\perp$ perpendicular to the axis, we have

$$f(r) = \frac{1}{v_\perp \tau} e^{-r/v_\perp \tau} . \quad (10)$$

We have neglected the thermal vibrations, which is reasonable if $v_\perp \tau \gg u_1$, where u_1 is the one-dimensional RMS vibrational amplitude. For $v_\perp \tau \gtrsim u_1$, a simple correction to eq. (9) consists in replacing $\bar{r} = r(e_x, e_y)$ by $(((re_x)^2 + u_1^2)^{1/2}, ((re_y)^2 + u_1^2)^{1/2})$. This correction has been included in the numerical calculations presented below (fig. 11).

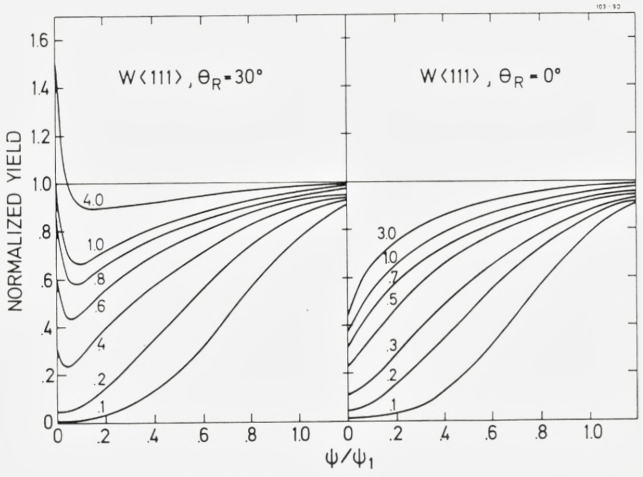

Fig. 11: Calculated blocking dips for fission fragments along a <111> axis in W, using the continuum potentials shown in fig. 10. Blocking dips are shown for recoil angles, θ_R, of 0° and 30° between the transverse component $\bar{v}_\perp$ of the recoil velocity and the direction to the nearest-neighbour string (directions b and a in fig. 10), and the values of $v_\perp \tau$ (in Å) are indicated.

The formulae (8)-(10) lend themselves readily to numerical evaluation. The main job is the construction of tables for the functions U and A. By using symmetry arguments, the evaluation may be restricted to a small fraction of the unit cell. The contour plots of the potentials shown in fig. 10 were calculated by the computer program used to evaluate the blocking dips shown in fig. 11. For comparison, it should be noted that the width of an elastic dip ($v_\perp \tau = 0$) is $(\psi_{1/2}/\psi_1) \sim 1$. For small average displacements, the main effect on the dip is a narrowing, while for larger displacements, the increase in minimum yield is the dominant feature. For $v_\perp \tau \gtrsim 2$ Å, there is virtually no dependence on the magnitude of $v_\perp \tau$.

The recoil directions for the two sets of curves shown in Fig. 11 are specified by the values of θ_R, which is the angle between the projection of the recoil direction on the transverse plane and the direction to the nearest neighbouring string (cf. fig. 10). The values of θ_R have been chosen to correspond to the measurements presented in the following section. For $\theta_R = 30°$, the recoil is towards the centre of the channel where the potential has a minimum. Fission fragments emitted there give rise to a sharp peak at very small angles. This phenomenon was first observed in measurements of the location of interstitial impurities by the channeling technique[24]. It may be noted also that calculations very similar to those presented above have been used to interpret other such measurements[25]. The importance of the recoil direction for nuclear-lifetime measurements was first pointed out by Hashimoto et al.[26].

Finally, a brief comment on the accuracy expected from these calculations. The two basic approximations applied are conservation of transverse energy and statistical equilibrium in the transverse phase space for fixed transverse energy. For thin targets, the first approximation is violated mainly by fluctuations in scattering by a string, due to thermal vibrations of the string atoms. This effect will be strong only for large transverse energies when the particle can penetrate close to the centre of strings, i.e., to distances comparable to the vibrational amplitude[27]. The elastic blocking dip ($v_\perp \tau = 0$) will be very sensitive to this thermal multiple scattering, but for values of $v_\perp \tau$ where the predicted blocking dip is significantly narrower than the elastic one, the sensitivity is much smaller [1,28]. The second approximation of statistical equilibrium is not expected to be strictly fulfilled, and indeed it is a very interesting possibility that one may be able to derive information about the magnitude of the nuclear recoil from asymmetries of the blocking dip. By performing the circular averaging, however, one eliminates such asymmetries and effectively imposes an equilibrium in momentum space. It is expected, therefore, that even for relatively thin crystals, the assumption of statistical equilibrium is a good approximation for calculations of the azimuthally averaged blocking dips.

4.4 *Fitting Procedure*

As illustrated in fig. 9, the measured blocking dips have been fitted by a superposition of two components, a long-lifetime component represented by a calculated curve and a short-lifetime component ($v_\perp \tau = 0$) represented by the scaled blocking dip for elastic scattering. The advantage of using the elastic dip for zero-lifetime normalization is that the influence of crystal imperfections, including thermal vibrations, is taken into account. The question is, however, how accurate the simple scaling is. Consider first the scaling of the halfwidth of the dip. For a perfect crystal without thermal multiple scattering, this scaling should be accurate for high projectile energies. More precisely, the condition[23,29] is that

$$\varrho/(\psi_1 d) > 1\,, \tag{11}$$

where we have used the symbol ϱ for the two-dimensional vibrational amplitude, $\varrho = \sqrt{2}u_1$. This condition is only marginally fulfilled for the fission fragments, but the deviation from scaling should be small[28]. Because of thermal multiple scattering, the width of a blocking dip varies fairly rapidly with crystal thickness for small thicknesses[30]. This effect is not identical for elastic scattering of 40-MeV oxygen and for fission fragments since the characteristic depth z_n for thermal scattering depends[21] on the magnitude of the characteristic scattering angle ψ_1 given by eq. (4), $z_n \propto \psi_1^{-2}$. However, the effect should be small. The halfwidths for the blocking dips for elastically scattered oxygen are all very close to ψ_1 (within $\sim 5\%$), and the halfwidth estimated from the standard potential is, in the absence of multiple scattering[21],

$$\psi_{1/2} = \psi_1 [\tfrac{1}{2} \log ((Ca/\varrho)^2/\log 2 + 1)]^{1/2} = 1.08\psi_1 \tag{12}$$

at room temperature, where $\varrho \sim 0.07$ Å[31]. Thus the reduction caused by thermal scattering is $\lesssim 10\%$. We may also note that the dependence of the half-width, eq. (12), on the screening length a is weak, and therefore the variation of the scaling factor in eq. (12) with Z_1 is very small.

Other factors affecting the accuracy of the scaling are the large energy spread for fission fragments (cf. fig. 5) and the influence of angular resolution, which will depend on the width of the blocking dip. Such effects only become important if a very detailed interpretation of the shape of the blocking dip is attempted. Our analysis is based on simple two-component fits and the accuracy of the scaling of the width of the elastic dip seems sufficient for this purpose. In particular, the lower pair of measurements in fig. 9 shows that the angular scaling is not much affected by multiple-scattering effects.

Scaling of the minimum yield is also supported by the measurements for very different crystal thickness. Multiple-scattering effects are expected to be somewhat stronger for fission fragments than for backscattered 40-MeV oxygen, and

the observation of fission dips with a minimum yield almost identical to that of the corresponding elastic dip (see sec. 5) is therefore another strong indication that the scaling of the minimum yield is reasonably accurate. The magnitude of the minimum yield depends on the quality of the thin single crystals used as targets (cf. table 1), and one of the advantages of using the elastic dips for zero-lifetime determination is that effects due to crystal imperfection are largely cancelled. It is necessary also to correct the calculated dips for these effects, and in the fits we have replaced the calculated yield function Y_c by $Y_c(1-\chi_{el})+\chi_{el}$, where χ_{el} is the measured minimum yield for the elastic blocking dip. This correction becomes important when an intermediate-lifetime component ($0.1\,\text{Å} < v_\perp\tau < 1\,\text{Å}$) is included in the analysis.

Some comments about the selection of parameters for the fits are also in order. First, normalization of the fission dip was treated as an adjustable parameter. In some cases, the random level is not very well established, and the normalization may appear to be wrong (cf. upper left corner in fig. 9). However, at large angles, the circular average includes regions close to the detector edge, and spurious structure due to detector non-linearity may appear. For these cases, we found similar structure in an analysis of the corresponding blocking pattern taken for a random direction, using the same dip centre. Second, the average recoil distance $v_\perp\tau$ for the long-lifetime component was chosen; detailed arguments for the specific choices will be given later. Third, an upper limit on the angular range for fitting was specified. For the simple two-component fits, the first six points in the bottom region of the dip were selected, thus emphasizing agreement in minimum yield. The computer program determined the relative magnitudes of the two components, which gave the lowest value of χ^2 over that angular region. For most cases, the uncertainty in the determination of the magnitude of the long component was ~1-2%. Thus, the two upper dips in fig. 9 correspond to the same magnitude of the long component, and the difference between the long-lifetime components for the two lower dips is barely significant.

5. Data Presentation

5.1 *Data for* $^{16}O \rightarrow Au$

In the first series of measurements, fission induced by oxygen bombardment of gold crystals was investigated. At that time, we were still looking for a dependence of the minimum yield on the angle θ between the recoil direction and the blocking axis (cf. sec. 4.2). The blocking dips for fission fragments were measured along two <110> directions at approximately $+170°$ and $-100°$ to the beam direction, respectively. Results for four different runs are shown in table 2. For each dip,

Table 2. Minimum yields of fission-fragment blocking dips for ^{16}O induced fission of ^{197}Au at observation angles of $-100°$ and $170°$ to the beam. The minimum yields χ are determined by the counts contained within the circle with the specified radius, normalized to the random level of the blocking dip. The radius and the half angle $\psi_{1/2}$ of the blocking dips are given in units of channels in the 2-d spectrum. $\Delta\chi$ is the difference in minimum yield between the forward and backward counters.

Energy (MeV)	Angle (deg)	Radius	χ(%)	$\psi_{1/2}$	Angle (deg)	Radius	χ(%)	$\psi_{1/2}$	$\Delta\chi$(%)
90	170	2.5	14.0 ± 2.2	9.0	-100	2.0	13.5 ± 3.0	7.3	-0.5 ± 3.5
		5.0	20.0 ± 1.3			4.0	19.5 ± 2.0		-0.5 ± 2.4
90	170	2.5	17.5 ± 1.4	9.7	-100	2.0	18.3 ± 2.0	7.3	0.8 ± 1.8
		5.0	22.5 ± 0.8			4.0	23.0 ± 1.1		0.3 ± 1.4
86	170	2.5	13.4 ± 1.9	9.0	-100	2.0	16.7 ± 3.1	7.5	3.3 ± 3.6
		5.0	16.9 ± 1.0			4.0	20.6 ± 1.5		3.7 ± 1.8
86	170	2.5	14.7 ± 2.3	9.5	-100	2.0	14.2 ± 3.1	7.9	-0.7 ± 3.9
		5.0	19.8 ± 1.3			4.0	19.3 ± 1.7		-0.5 ± 2.2

two values of the minimum yield χ are given. They have been obtained by averaging the counts in the centre of the dip within a circle with a diameter equal to 25% and 50% of the full width at half maximum of the dip. The uncertainties are based on counting statistics only. For both bombarding energies, the difference $\Delta\chi$ is zero within an error of two percent.

Unfortunately, we did not at that time use a zero-lifetime calibration based on elastic scattering of oxygen, but from a comparison with the minimum yield for backscattering of 2-MeV helium ($\chi \simeq 7\%$ averaged over the crystal thickness), we may conclude that a possible long-lifetime component must contribute less than 10% to the fission yield. A difference between the shapes of the blocking dips for the two bombarding energies does suggest the presence of a long-lifetime component, at least for E = 90 MeV.

5.2 *Data for* $^{16}O \rightarrow W$

The experiments with tungsten targets have all been analyzed as discussed in secs. 3 and 4, and the results are given in table 3. The quality of the two-component fits may be judged from figs. 12 and 13, which show results from two different runs with different target crystals. The data in fig. 12 were obtained with the two $<111>$ axes in the directions of the two detectors simultaneously, while the blocking dips shown in fig. 13 were obtained separately for different crystal tilts.

In most cases, the two components chosen for the fit correspond to very short and very long recoils. Only for E = 90 MeV does the dip at $\theta = -165°$ indicate the presence of a significant component with an intermediate lifetime. The three

3635 C

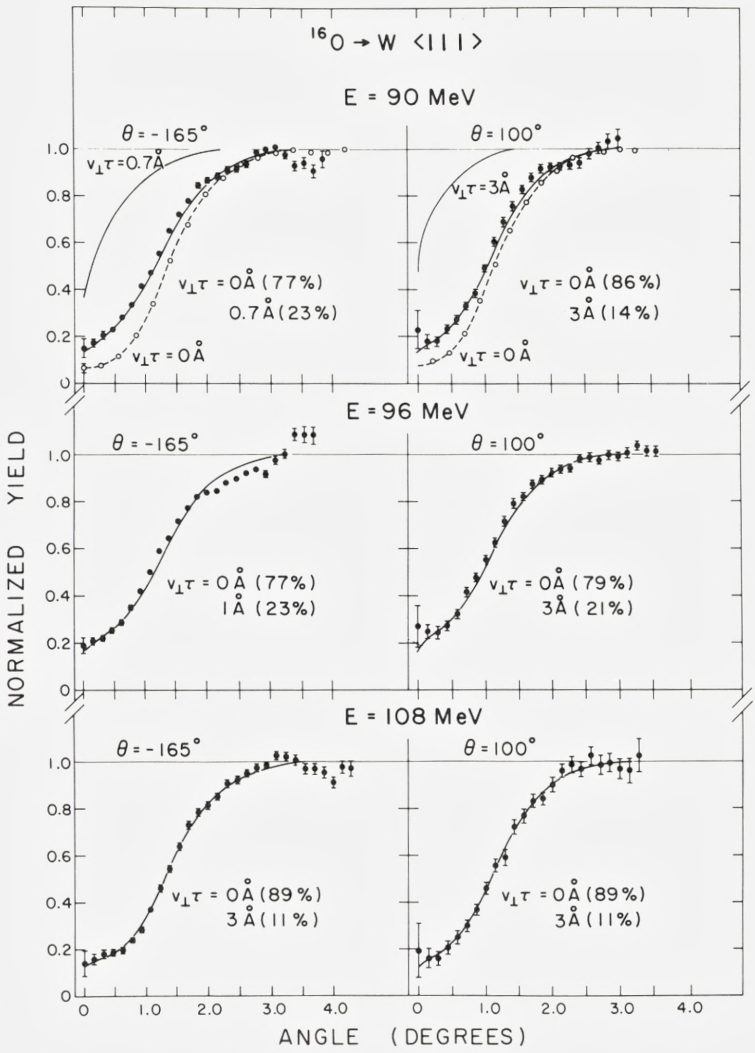

Fig. 12: Fission-fragment blocking dips (closed circles) for 90-, 96-, and 108-MeV ^{16}O bombardment of W. The recoil angle is $\theta_R = 0°$ (direction b in fig. 10). The solid curves are fits by a superposition of two components with different average recoil distances $v_\perp\tau$ (see text). For 90-MeV are shown the blocking dips for 40-MeV ^{16}O elastic scattering (open circles) scaled in angle and the calculated dips for a long average recoil (upper solid curve), which represent the two components in the fit.

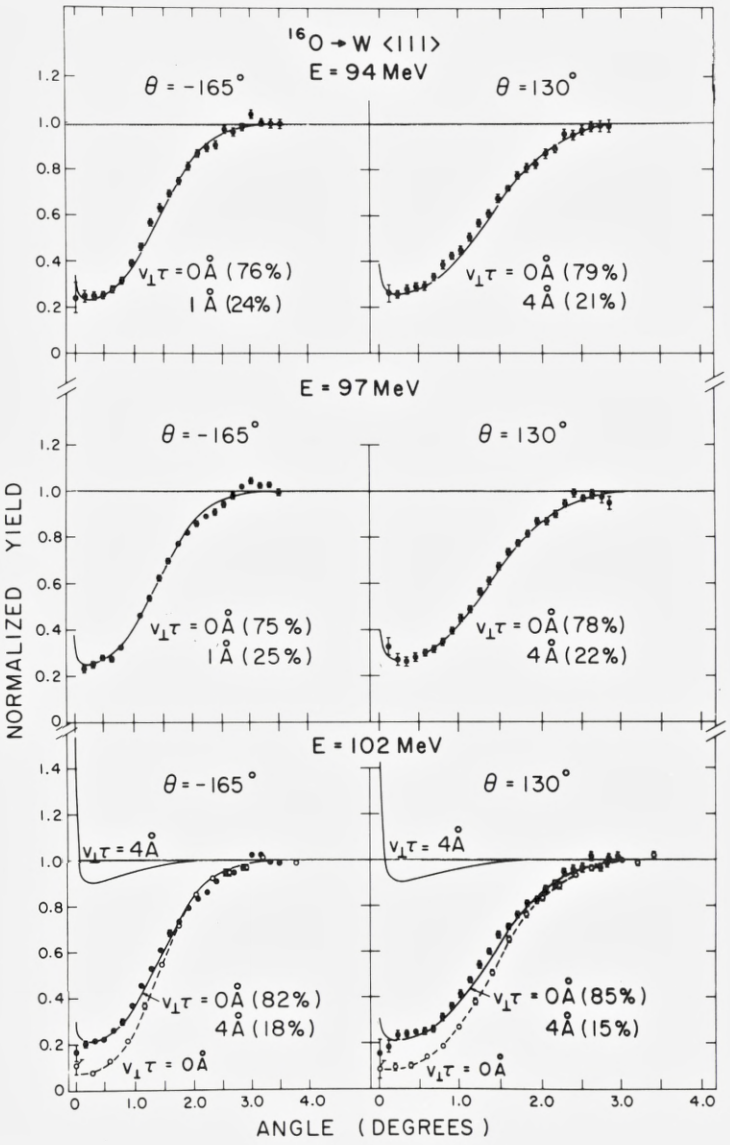

Fig. 13: Fission-fragment blocking dips for 94-, 97-, and 102-MeV bombardment of W for $\theta_R = 30°$ (direction a in fig. 10). The solid lines through the data are two-component fits, and the two components are shown for 102 MeV (cf. caption to fig. 12).

Energy (MeV)	Crystal	Det. Angles	$v_\perp\tau$(Å)	Amount χ_L(%)
90	W1	−165	0.7	20.6 ± 1.4
			0.5	23.5 ± 1.7
90	W1	−165	0.7	22.9 ± 0.5
			0.5	26.0 ± 0.7
		−100	2.0	14.9 ± 1.2
			3.0	15.0 ± 1.2
94	W3	−165	1.0	23.5 ± 0.6*
			4.0	20.3 ± 0.6*
		130	4.0	21.4 ± 0.9
96	W1	−165	1.0	25.8 ± 1.0
			3.0	23.2 ± 0.8
		−100	3.0	17.0 ± 3.1
96	W1	−165	1.0	23.1 ± 0.2
		−100	3.0	22.3 ± 1.4
96	W1	−165	1.0	19.7 ± 1.2
		−100	3.0	22.1 ± 4.6
96	W2	−165	1.0	21.5 ± 0.8
			3.0	18.4 ± 0.8
		130	3.0	16.8 ± 1.0
97	W3	−165	1.0	24.4 ± 0.4*
			4.0	21.5 ± 0.3*
		130	4.0	21.9 ± 0.8
97	W3	−168	1.0	23.3 ± 0.9
			4.0	19.8 ± 0.6
		160	1.0	21.3 ± 0.9
			4.0	18.2 ± 0.7
97	W4	−165	2.0	18.3 ± 0.5
			4.0	17.4 ± 0.5
102	W3	−165	4.0	17.9 ± 0.2*
		130	4.0	15.4 ± 0.6
108	W1	−165	3.0	10.9 ± 0.6
		−100	3.0	10.9 ± 2.4
108	W3	−165	4.0	13.7 ± 1.2
		130	4.0	10.7 ± 0.6
115	W3	−165	4.0	5.8 ± 0.5
		130	4.0	4.1 ± 1.8

Table 3. Results of two-component fits to W(^{16}O, f) data. The beam energy and crystal identification are given in the first two columns (cf. table 1 for characterization of crystals), and in the third column

the angle of the detector to the beam direction is specified. The blocking dips are fitted with a superposition of two components, one with a short lifetime, $v_\perp\tau = 0$, and one with the average perpendicular recoil distance given in the fourth column. The magnitude of this long-lifetime component χ_L is given in the last column, with an error corresponding to an increase of unity in χ^2 for the fit. For some cases, two equally good fits are given. Note that different choices of $v_\perp\tau \gtrsim 2$ Å are equivalent, i.e., a blocking dip corresponding to very long lifetimes may be represented by any value $v_\perp\tau \gtrsim 2$ Å. For the cases marked with an asterisk, the magnitude of χ_L obtained from the fit was increased by 2% as a correction for nonlinearity. Also the corresponding numbers in figs. 9 and 13 have been corrected.

measurements at 90 MeV are all fitted well with a long component with recoil $v_\perp\tau = 0.7$ Å for the backward detector (table 3, one result given in ref. 12). The corresponding recoil for the forward counter is larger by a factor of ~ 4, i.e., close to 3 Å.

For the intermediate energies, 94-97 MeV, a recoil of $v\tau \simeq 4$ Å, corresponding to $v_\perp\tau \simeq 1$ Å for the backward detector, has been chosen for the fits shown in the figures. The arguments for this choice are not very strong, and the dips can be fitted equally well with $v_\perp\tau = 4$ Å for the backward counter. As seen in the table, this changes the magnitude of the long component by $\sim 2\%$. The choice of the value of $v\tau \sim 4$ Å is based on analysis of fine structure in the dips, which for these energies shows evidence of asymmetries correlated with the recoil direction.

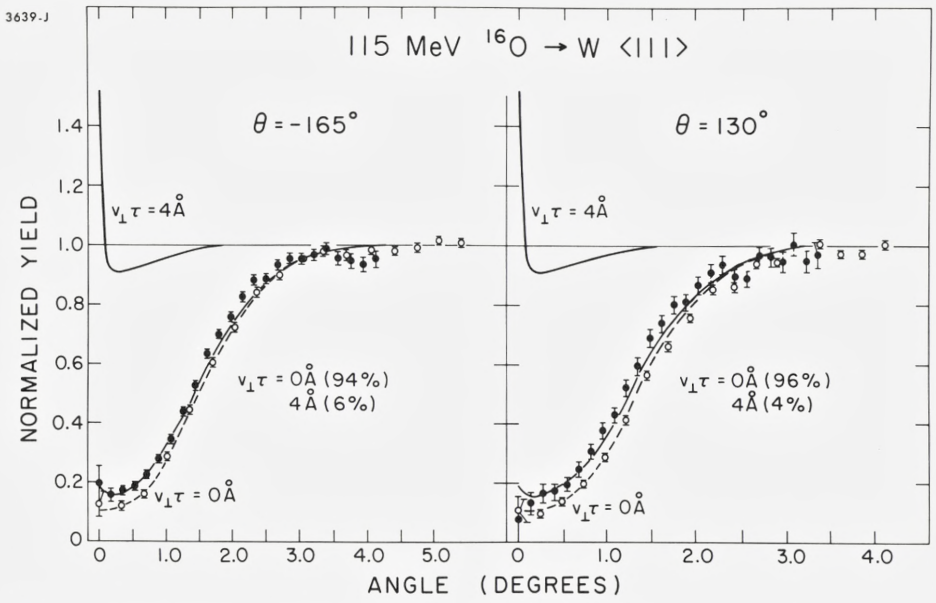

Fig. 14: Fission-fragment blocking dips for 115-MeV ^{16}O bombardment of W for $\theta_R = 30°$. Also shown are the short- and long-recoil dips used in the fit.

From table 3 it can be seen that the magnitude of the long component varies systematically with energy, and different measurements at the same energy are reasonably consistent. The errors given in the table are based on the χ^2 analysis and do not include uncertainties associated with the determination of a random level (normalization) or of the elastic dip. At the high bombarding energies, the magnitude of the long component approaches zero. The results and analysis of the measurements at 115 MeV are shown in fig. 14. The fact that the fission dips for some cases are close to the scaled elastic dip is a crucial check of the method of analysis, as discussed in sec. 4.4.

5.3 *Dependence on Recoil Direction*

The measurements shown in figs. 12 and 13 correspond to two different recoil directions. As discussed in sec. 4.3, the central structure of the blocking dips will, for long recoil distances, depend on whether the recoil is directed towards the centre of the channel (fig. 13) or is parallel to the side of the channel (fig. 12), and the calculated dips for these two situations are shown in fig. 11. The data in the two figures are not in all cases consistent with the predicted structure. This may at least partly be due to the difficulty of locating the centre of the dip. A change in centre coordinates by one channel, which is about the uncertainty of the determination, may in some cases lead to a significant change in the central structure of the circular averaged dip. A better check of the predicted dependence on recoil direction is obtained from linear scans through the dip centre. Such scans, corresponding to the two different recoil directions, are shown in fig. 8. The peak due to flux peaking in the centre of the scan for 97 MeV is clearly indicated, while for the 90-MeV scan, there is a narrow dip in the centre. For the measurements shown in fig. 12, the recoil is parallel to a side of the channel, but the data do not confirm the predicted narrow dip at the centre for the forward counter ($\theta = 100°$). A possible explanation for this discrepancy may be that the recoil direction for compound nuclei fissioning after evaporation of several neutrons is affected by the neutron emission, and the angular distribution will have a width of a few degrees. This may influence the central structure if the recoil is very long. It is then important also to consider whether the recoiling atoms may be deflected by neighbouring atoms, but this appears not to be the case for the geometry of the present measurements.

5.4 *Data for* $^{12}C \rightarrow W$ *and* $^{19}F \rightarrow W$

The measurements presented in table 3 demonstrate the disappearance of the long-lifetime component at high bombarding energies, as predicted from the

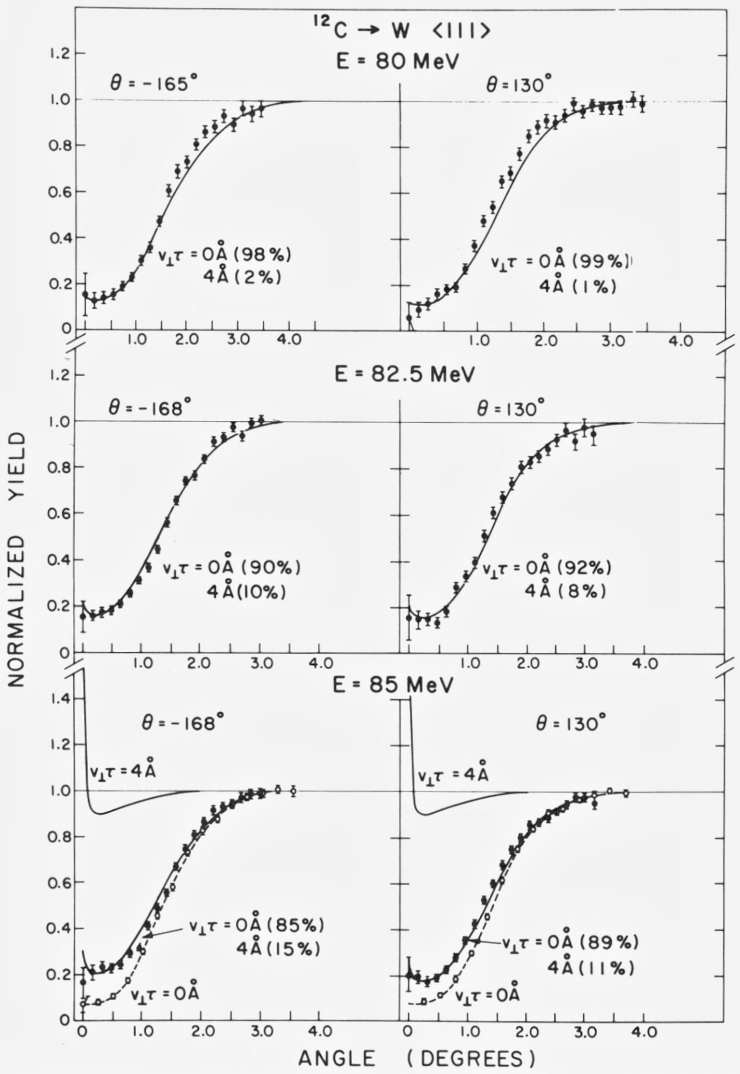

Fig. 15: Fission-fragment blocking dips for 80-, 82.5-, and 85-MeV ^{12}C bombardment of W for $\theta_R = 30°$. For 85-MeV, the short- and long-recoil dips used in the fits are also shown.

qualitative discussion in the introduction. Unfortunately, it was not possible to check the low-energy limit for ^{16}O projectiles. Close to the Coulomb barrier, the elastic, or quasi-elastic, large-angle scattering becomes very strong compared to the fission yield, and the fission fragments could not be separated from back-scattered oxygen. This separation is possible for ^{12}C projectiles (cf. fig. 5) because

Table 4. Results of two-component fits to W(^{12}C,f) data (see table 3).

E(MeV)	Det. Angle	$v_\perp\tau$(Å)	Amount χ_L(%)
80	−165°	4.0	1.8 ± 1.2
	130°	4.0	1.8 ± 2.0
82.5	−168°	4.0	9.1 ± 0.6
	130°	4.0	6.6 ± 1.2
85	−168°	4.0	15.0 ± 0.8
	130°	4.0	11.2 ± 0.6
87	−165°	4.0	14.5 ± 0.5

of the lower stopping power and the consequent lower value of the maximum energy deposited in the thin counters. The results of a series of measurements between 80 and 85 MeV are shown in fig. 15. The dips are again fitted by two components and the resulting magnitudes are given in table 4, which also includes one measurement at 87 MeV. It is seen that the long component increases with energy, being virtually zero at 80 MeV. Like the result for 115-MeV ^{16}O on tungsten, this is an important check of the validity of the analysis based on a comparison with scaled elastic dips. The energy dependence of the long component is consistent with the qualitative discussion in the introduction since in this energy region, the fission probability is small and increases rapidly with energy[32,34].

Only two short runs were made for ^{19}F bombardment of tungsten, one at 95 MeV and one at 108 MeV. Least-squares fits to the backward-counter ($\theta = -165°$) data gave long-lifetime components of 16 ± 8% ($v_\perp\tau = 1$ Å for 96 MeV and 10 ± 0.5% ($v_\perp\tau = 4$ Å) for 108 MeV. The statistical error for the 95-MeV point is large, but the results are in qualitative agreement with the energy dependence of the ^{16}O + W data (cf. fig. 16).

6. Discussion and Comparison with Calculations

6.1 *Qualitative Remarks*

Before making a comparison with detailed calculations, we examine the results on the basis of the simple qualitative picture described in the introduction. For this purpose, the magnitude of the long-lifetime component χ_L for fission induced by oxygen bombardment of tungsten is shown in fig. 16 as a function of bombarding energy. The decrease of χ_L at the highest bombarding energies was, as discussed in the introduction, expected because of the increase in fissionability at high angular momentum. Also, the increase in initial excitation energy of the com-

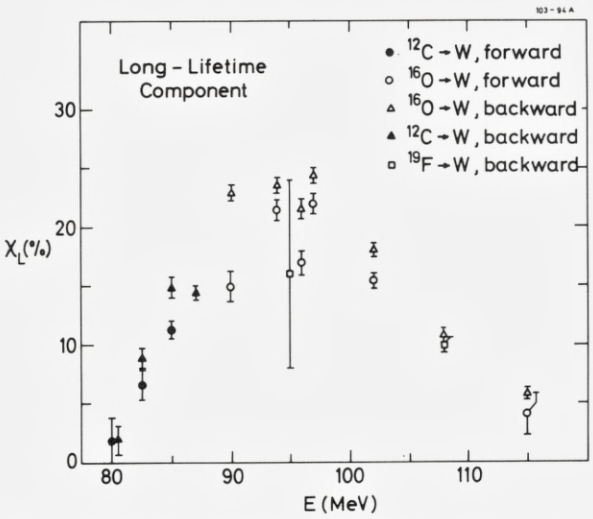

Fig. 16: The percentage of a long-lived component in the ^{12}C, ^{16}O, and ^{19}F-induced fission of W, as a function of projectile bombarding energy. The results have been obtained from two-component fits to the blocking dips measured at different detector angles (backward $\sim 165°$, forward 100° or 130°, cf. tables 3 and 4).

pound nucleus will in itself tend to reduce the importance of fission at low excitation energy, since the number of neutrons to be evaporated before fission increases.

The behaviour at low bombarding energy could not, for technical reasons, be studied for oxygen projectiles (cf. sec. 5.4). However, the measurements with carbon as projectile have been included in the figure, and these data confirm the predicted increase of χ_L, from an initally low value, with bombarding energy. Plotting the data against projectile bombarding energy is somewhat arbitrary. For a given bombarding energy, both the excitation energies (cf. table 5) and the angular-momentum distributions are rather different for the different compound nuclei, but for the present qualitative discussion, this is not so important.

Fig. 16 shows values of χ_L for both detector systems; there appears to be a systematic difference with the backward detector ($\theta \sim 165°$) having the larger value of χ_L. This effect will be discussed later together with the anisotropy of the fission-fragment angular distributions.

Table 5. Relative abundance of W isotopes and Q values for fusion with ^{12}C and ^{16}O.

Isotope of tungsten	Abundance (%)	Fusion Q Value	
		^{12}C	^{16}O
182	26.2	−16.0	−27.1
183	14.3	−15.3	−25.8
184	30.7	−13.8	−24.3
186	28.7	−11.5	−21.3

6.2 *Calculations*

It is only through a comparison with realistic calculations, such as those of Hagelund and Jensen[13], that the full information contained in the measurements is brought out. Considerable improvements have been made in the calculations, and details are given in the Appendix. Fig. 17 shows results for the fission and neutron-evaporation process for two ^{16}O bombarding energies. In the initially formed compound nucleus, ^{198}Pb, the excitation energy is well defined, and the top curve for both cases shows the contributions from different spin values to the total first-chance fission yield. These curves deviate from the triangular shape of the spin distribution due to the spin dependence of the fission probability, which is quite strong for the largest angular-momentum values.

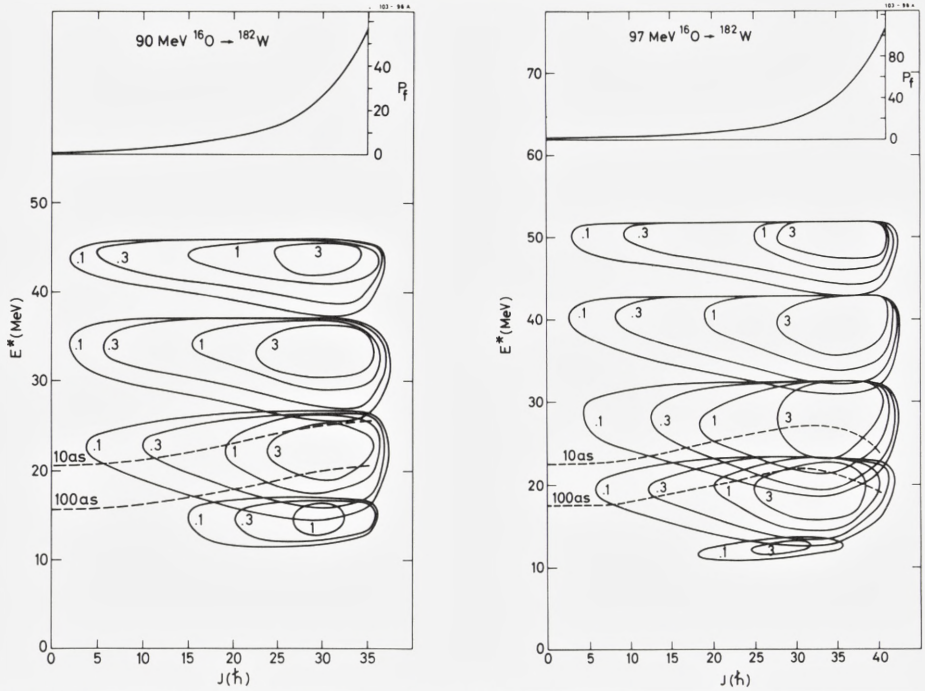

Fig. 17: Calculated contour diagrams of the population distribution, weighted with the fission probability, in excitation energy E* and spin J for 90- and 97-MeV ^{16}O-induced fission of ^{182}W. The curves centred at different excitation energy correspond to successive nuclei resulting from the nucleus after emission of one to five neutrons, i.e., with A = 197, 196, 195, 194, 193. The dashed lines are for constant lifetimes of 10 and 100 as for the isotopes A = 195 (90 MeV) and A = 194 (97 MeV). For the compund nucleus ^{198}Pb itself, the excitation energy is well defined, 55 MeV and 62 MeV for ^{16}O energy 90 MeV and 97 MeV, respectively, and the top curves show the fission probability as a function of spin, weighted by the triangular spin distribution. Values are in units of 10^{-4} $\hbar^{-1}$, and the numbers on the contours are in units of 10^{-4} $\hbar^{-1}$ MeV^{-1}.

For higher-chance fission, the distribution in excitation energy becomes increasingly broad owing to the spread in energy of evaporated neutrons. The fission contributions are indicated by contours of constant yield. The different stages contribute almost equally and fission at high spin values dominates.

The lifetime is determined mainly by the excitation energy. The dashed lines indicate contours of constant lifetime for the compound nucleus after evaporation of three and four neutrons, respectively, for 90- and 97-MeV bombarding energy. For the lowest spin values, neutron evaporation dominates, and the excitation energy for constant lifetime increases with increasing spin. For high-spin values, the fission width increases rapidly for fixed excitation energy, and therefore the dashed curves bend down as seen for the 97-MeV case. The two dashed curves divide the (E*,J) plane into three regions, corresponding approximately to short, intermediate, and long lifetimes ($v\tau \simeq 3$ Å for $\tau = 10^{-16}$ s). The calculations presented in fig. 17 indicate that for 90-MeV bombarding energy, the lifetime distribution will have a large component in the intermediate-lifetime region, while for 97 MeV, long-lifetime values will be strongly populated.

The choice of parameters used in the calculations is dicussed in detail in the Appendix. Here, we comment briefly on the constraints imposed by the three types of data.

(i) Total fission cross sections

If the cross section for complete fusion is known, a measured fission cross section may be converted into an effective fission probability P_f summed over all stages of fission, and this quantity depends sensitively on the magnitude of the fission barriers. The requirement that the calculations reproduce the measured fission cross sections for all ^{16}O bombarding energies for all tungsten isotopes is the main constraint on the absolute magnitude of the fission barrier and its variation with mass number. With the parameters given in the Appendix, all measured fission cross sections are reproduced within 10% (cf. tables A2 and A3).

(ii) Lifetime distributions

The importance of fission at the different stages of the evaporation chain depends on the relative magnitude of the corresponding fission barriers, and the long-lifetime component will thus be very sensitive to the A dependence of the fission barrier. This dependence is already constrained by the total cross sections, but when the mass is reduced by neutron evaporation, the excitation energy is also reduced, and the effective fission barrier may change due to the temperature dependence of shell corrections. The magnitude of such corrections and the manner in which they are included in the level density are therefore of special importance for the calculated lifetime distributions.

(iii) Fission-fragment angular distributions

The anisotropy of the fission-fragment angular distributions depends on the angular-momentum distribution, the effective moment of inertia at the barrier deformation, and the average temperature of the fissioning nuclei. The temperature is constrained by the lifetime measurements, the moments of inertia may be calculated as rigid-body values if the deformation at the barrier is known, and the measured anisotropy then sets narrow limits for the spin distribution of the fissioning nuclei. As mentioned above, this distribution is important for the analysis of the total cross-section measurements. In the interpretation of the lifetime measurements, it is necessary to take into account the large anisotropy in the angular distributions. This is discussed later in connection with the comparison of measured and calculated angular distributions of fission fragments.

6.3 *Lifetime Distributions*

Some calculated lifetime distributions are shown in figs. 18-20. In fig. 18 the variation of the lifetime distribution with bombarding energy is shown for the most important isotope, ^{182}W. In qualitative agreement with the measurements shown in fig. 16, the long-lifetime component ($\tau > 10^{-16}$ s) initially increases with increasing bombarding energy to a maximum $\chi_L \simeq 20\%$ between 90 and 100 MeV.

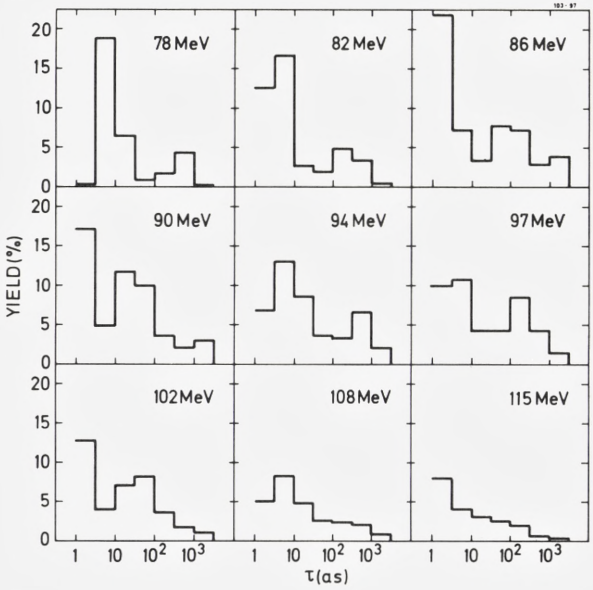

Fig. 18: The calculated percentage yield for ^{16}O-induced fission of ^{182}W as a function of lifetime τ for nine bombarding energies. The total yield for each bombarding energy is 100%, but only those components with $\tau > 1$ as are shown.

It is important to note that although the absolute magnitude of χ_L in the intermediate-energy region has been fitted by parameter adjustment to agree with experiment, this is not the case for the energy dependence of χ_L.

The distributions shown in fig. 18 have structure corresponding to the separation into the different stages of fission in the evaporation chain (cf. fig. 17). With increasing bombarding energy, the average lifetime for a particular stage decreases by about one order of magnitude per 10 MeV. The contribution from fission for A = 195 (fourth chance) moves from $\tau \sim 10^{-16} - 10^{-15}$ s at 78-82 MeV to $\tau \sim 10^{-17} - 10^{-16}$ s at 90 MeV and finally to short lifetimes, $\tau < 10^{-17}$ s, for 97 MeV and above. At the highest bombarding energies, there is little structure in the lifetime distributions since the energy distributions for the last stages of fission overlap strongly.

The lifetime measurements were made with tungsten targets of natural composition, and the results must be compared to a weighted sum of lifetime distri-

Fig. 19: Calculated yield as a function of lifetime for ^{16}O-induced fission of natural-composition W at 90-MeV bombarding energy. The weights assigned to the different isotopes have been obtained from the measured cross sections combined with the natural abundances.

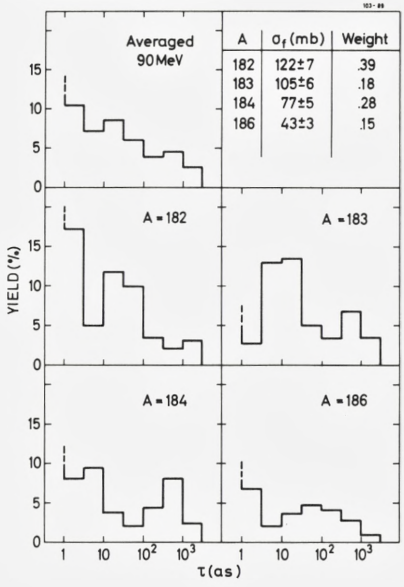

Fig. 20: Calculated yield, as a function of lifetime, for ^{16}O-induced fission of natural-composition W at 97-MeV bombarding energy (cf. caption to fig. 19).

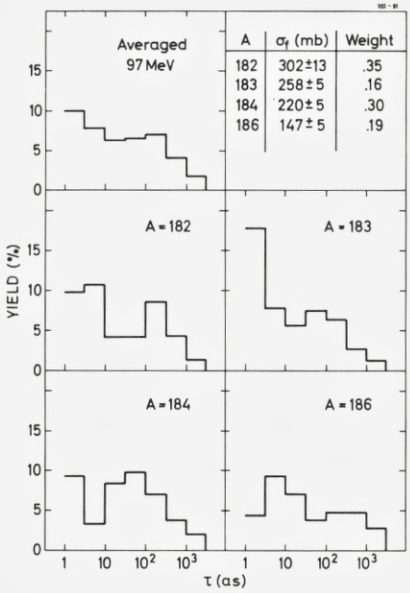

butions for the individual isotopes. The relative abundances and Q values for the different isotopes are given in table 5. Since the Q values are different for the different isotopes, the averaging smears most of the structure in the individual lifetime distributions. The results for 90- and 97-MeV bombarding energy are shown in figs. 19 and 20. There is little difference between these two lifetime distributions, but in qualitative agreement with experiment, the number of fissioning nuclei having lifetimes $\tau \simeq 10^{-17} - 10^{-16}$ s is slightly larger at 90 MeV.

Fission from long-lived, $\tau > 10^{-16}$ s, compound nuclei will contribute a long-recoil component for both the backward and the forward detectors. The projection factors ($\sin\theta$) for the two directions of observation differ by a factor 3-4, corresponding approximately to one interval in lifetime in figs. 18-20. The long-recoil components in the two directions should therefore differ by an amount approximately equal to the population of the interval $\tau = 3 \times 10^{-17} - 10^{-16}$ s, i.e., the long component χ_L should be larger by about 5% in the forward detector for the cases illustrated in figs. 19 and 20. As seen in table 3 and fig. 16, this is not the case. However, the apparent inconsistency may be explained by the large anisotropy of the fission-fragment angular distributions, as discussed below.

6.4 *Fission-Fragment Angular Distributions*

In the fission of high-spin compound nuclei created by heavy-ion bombardment, the fragment angular distribution is strongly anisotropic[33]. The reason for this is that, due to the large nuclear deformation at the fission barrier, the moment of inertia will be very different for rotations with angular momentum parallel and perpendicular to the axis of deformation; therefore, the rotational energy will depend on the relative orientation of the spin and the deformation axis. For an axially symmetric deformation, one may denote the two moments of inertia by $\mathfrak{I}_{\parallel}$ and $\mathfrak{I}_{\perp}$ and introduce an effective moment of inertia by $1/\mathfrak{I}_e = 1/\mathfrak{I}_{\parallel} - 1/\mathfrak{I}_{\perp}$. The decisive parameter is the ratio of the difference in rotational energy to the nuclear temperature [33], $2p = \hbar^2 I(I+1)/(2T\mathfrak{I}_e)$ where $I\hbar$ is the angular momentum. When p is large, the fragments will be emitted preferentially in the plane perpendicular to the angular-momentum vector. For a compound nucleus created by ion bombardment, the spin is perpendicular to the beam direction, and confinement of the fission fragments to the plane perpendicular to the spin direction corresponds to an angular distribution proportional to $1/\sin\theta$, where θ is the angle relative to the beam direction. For finite values of p, the angular distribution will deviate from $1/\sin\theta$ at angles close to 0° and 180° and reach a maximum depending on the parameter p. A measurement of the anisotropy therefore determines the effective value of p.

The main problem in the analysis is usually that all three quantities in the

expression for p, i.e., I, $\mathfrak{J}_e$, and T, are uncertain. In the present case, there is independent information on the effective temperature from the lifetime measurements since the main uncertainty is associated with the fission distribution over several stages in the evaporation cascade. The effective moment of inertia may be calculated from rigid-body values if the nuclear deformation at the barrier is known. In the present calculations, we have chosen the value corresponding to the liquid-drop barrier. It is shown in the Appendix that it is possible to reproduce the measured anisotropies as well as the total fission cross sections with values of the maximum compound-nucleus spin which are consistent with the theoretical estimates of Bass[35]. A comparison of measured anisotropies and predictions for

Fig. 21: Angular distributions of fission fragments for 90-, 94-, and 97-MeV ^{16}O bombardment of ^{182}W, normalized to a $(\sin\theta)^{-1}$ distribution at 140° in the centre-of-mass system. The solid lines are calculated angular distributions, summed over all stages of fission.

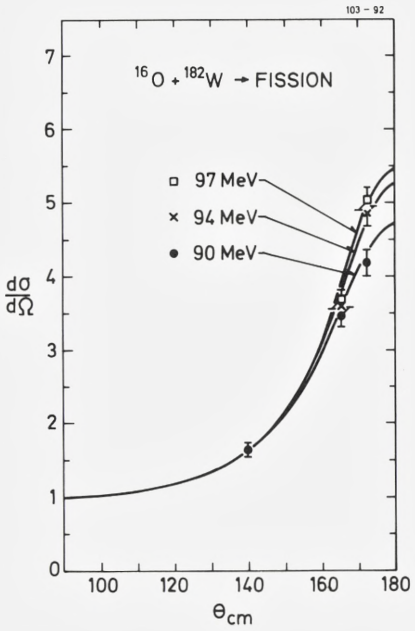

Fig. 22: Calculated fission-fragment angular distributions for 90-MeV ^{16}O bombardment of ^{182}W. The fission yield has been divided into three lifetime regions corresponding approximately to the short-, intermediate-, and long-lifetime regions of sensitivity in the blocking lifetime measurements. The dashed curve is the average angular distribution obtained by adding the contributions from all lifetimes.

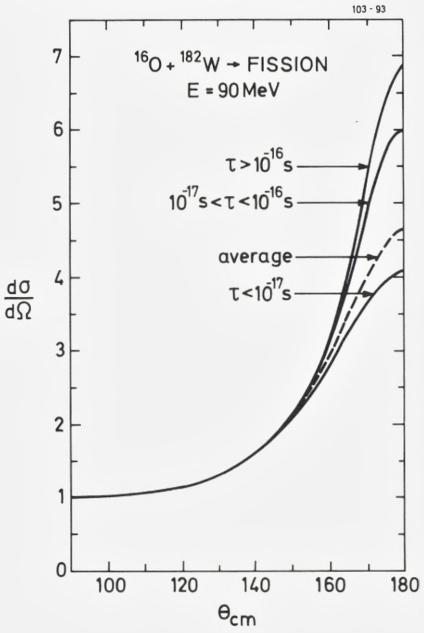

the isotope ^{182}W for ^{16}O bombarding energies of 90, 94, and 97 MeV is shown in fig. 21, and the comparison between all data and predicted values is given in table A4 in the Appendix.

The curves in fig. 21 represent weighted averages over all stages of fission and thus over a broad range of temperatures. The early-stage fission at high temperature is less anisotropic than late-stage fission at lower temperature. Since the nuclear lifetime varies rapidly with the nuclear temperature, the anisotropy and the lifetime will be strongly correlated. This is shown in fig. 22 for 90-MeV ^{16}O on ^{182}W. The fission yield has been divided into three lifetime regions, and the angular dependence of the cross section is given for each interval separately as well as for the total. At backward angles, the intermediate- and long-lifetime components are enhanced relative to the average by 25-30%. This offers an explanation for the difference between the χ_L values for the forward and backward counters which is observed (cf. fig. 16) when the analysis is made with average recoil distances for the long component consistent with the difference in projection factor.

7. Concluding Remarks

We believe that the present systematic measurements demonstrate that a new type of analysis must be adopted in the application of the blocking technique to lifetime measurements of heavy-ion-induced fission. Lifetimes cannot be extracted from the difference $\Delta\chi$ of minimum yields for blocking patterns recorded at different angles to the incident beam. An analysis in terms of several components with different lifetimes, however, can yield useful information. We have limited ourselves to two components in the present analysis, but in some cases, more information may be obtained by including a third component [34] or by introducing a continuous lifetime distribution characterized by a few parameters.

Our results, particularly for the energy dependence of the long-lifetime component, are consistent with expectations based on a simple physical picture of the fission process. It has also been possible to reproduce the data by detailed numerical calculations, including the full neutron-evaporation cascade. In this regard, it was important to combine the lifetime results with measurements of total fission cross sections and fission-fragment angular distributions. Although the set of parameters in the calculations, which reproduces the available data, is not unique, the ambiguities are greatly reduced compared to cases where only one type of data, such as total cross sections, is analyzed. In particular, the new information obtained from the lifetime measurements appears to be very useful.

We intend to continue the experiments with monoisotopic tungsten crystals. Such measurements should add further parameter constraints to the calculations, and we hope also to obtain more detailed information on the time distributions when the results are not smeared by an average over isotopes.

Acknowledgements
We would like to thank our collegues for many stimulating discussions in connection with the present research project. Of particular value were several discussions with W. J. Swiatecki. We also want to acknowledge the excellent technical assistance, both at the Chalk River Laboratories and at the Physics Institute, University of Aarhus. The Danish participation in the collaboration was made possible by funds from the Danish Committee for Accelerator Physics.

APPENDIX

The main features of the theoretical model were described in ref. 13, where it was shown that calculations based on this model qualitatively reproduce the experimental findings. We have extended the calculations with the more ambitious goal of reproducing quantitatively the experimental data, which have been supplemented with measurements of fission-fragment angular distributions. For this purpose, some improvements to the model have been introduced, and in the following discussion we shall indicate these modifications.

The first part of the appendix is a broad outline of the theoretical model used, with expressions for the most important quantities. In the second part is discussed how the parameters are determined and which of them are most important for reproducing the present data. The third part contains the results of the model calculations and a comparison with the experimental values.

A1. Theoretical Model

The fission process is assumed to proceed via the formation of a compound nucleus with a well-defined excitation energy and a spin distribution characterized by a sharp cut-off at a maximum angular momentum I_m. Three modes of decay are included, viz. fission, neutron emission, and γ emission, and the development of the distribution in excitation energy and spin of the nucleus is followed through the neutron-evaporation cascade.

A1.1 *Widths*

The partial widths for the three decay modes are calculated from the standard formulas for a statistical model, which express the widths in terms of level densities and appropriate constants and weighting functions. The neutron width may be expressed as a sum of contributions from final nuclear states with spin I' and excitation energy $E - B_n - \varepsilon$,

$$\Gamma_n(E,I) = \sum_{I'} \int_0^{E-B_n} \Gamma_n(E,I,\varepsilon,I')\,d\varepsilon, \tag{A1}$$

with

$$\Gamma_n(E,I,\varepsilon,I') = \frac{1}{2\pi\varrho_C(E,I)} \sum_{j=|I-I'|}^{I+I'} \sum_{\ell=|j-\frac{1}{2}|}^{j+\frac{1}{2}} \varrho_D(E-B_n-\varepsilon,I')\,T_{\ell j}(\varepsilon), \tag{A2}$$

where ϱ_C and ϱ_D are the level densities for the nucleus before and after the neutron emission and $T_{\ell j}(\varepsilon)$ are the neutron-transmission coefficients for orbital angular momentum ℓ, total spin j, and kinetic energy ε.

The fission width is given by

$$\Gamma_f(E,I) = \frac{1}{2\pi\varrho_C(E,I)} \int_0^E \frac{\varrho_B(\varepsilon,I)\,d\varepsilon}{1+\exp\left(-\frac{2\pi}{\hbar\omega}(E-B_f-\varepsilon)\right)}, \tag{A3}$$

which for $E > B_f$ reduces to

$$\Gamma_f(E,I) \simeq \frac{1}{2\pi\varrho_C(E,I)} \int_0^{E-B_f} \varrho_B(\varepsilon,I)\,d\varepsilon\,. \tag{A4}$$

Here ϱ_B is the level density at the saddle point for fission. Note that the dependence of the effective fission barrier on angular momentum is implicity included through this level density (cf. eq. A8). The main parameter in eq. (A3) is the fission barrier B_f. It may be expressed as a smooth contribution $\tilde{B}_f$ corrected for barrier and ground-state shell and pairing corrections,

$$B_f = \tilde{B}_f - \delta U_{gs} - \delta P_{gs} + \delta U_B + \delta P_B\,. \tag{A5}$$

The radiation width is given by

$$\Gamma_\gamma(E,I) = \frac{1}{2\pi\varrho_C(E,I)} \sum_{J=|I-1|}^{I+1} \int_0^E \varrho_C(E-\varepsilon,J) f(\varepsilon)\,d\varepsilon\,. \tag{A6}$$

In contrast to ref. 13, we have used a function $f(\varepsilon)$ given by the giant dipole expression [36a],

$$f(\varepsilon) = c_\gamma \frac{8}{3} \frac{1.4}{mc^2} \frac{e^2}{\hbar c} \frac{NZ}{A} \frac{\Gamma_G \varepsilon^4}{(\Gamma_G\varepsilon)^2 + (\varepsilon^2 - E_G^2)^2} \tag{A7}$$

The fraction of exchange force present in the nuclear force is taken as 0.5 as in ref. 37, leading to the value 1.4 in eq. (A7).

A1.2 *The level density*

The intrinsic level density $\varrho(E)$ is taken from ref. 15 for energies larger than the largest critical energy for disappearance of pairing. For smaller energies, a smoothly connected constant-temperature expression ($\varrho(E) \propto \exp(E/T)$) is used. With this assumption, the number of levels at zero excitation energy agrees reasonably well with experiments.

A spin dependence of the shell correction (as introduced in ref. 13) is not included because of its small effect and the uncertainties and complications involved.

The total level density is obtained as usual for an axial- and R-symmetric system by assuming a rotational band built on top of each intrinsic level[38], leading to

$$\varrho(E,I) = \frac{1}{2\sqrt{2\pi \mathfrak{J}_{\parallel} T}} \sum_{K=-I}^{I} \varrho\left(E - \frac{I(I+1)}{2\mathfrak{J}_{\perp}} - \frac{K^2}{2\mathfrak{J}_e}\right). \tag{A8}$$

When the rotational energies are small relative to E, this simplifies to

$$\varrho(E,I) \simeq \frac{\varrho(E)}{2\sqrt{2\pi \mathfrak{J}_{\parallel} T}} \exp\left(-\frac{I(I+1)}{2\mathfrak{J}_{\perp} T}\right) \sum_{K=-I}^{I} \exp\left(-\frac{K^2}{2\mathfrak{J}_e T}\right). \tag{A9}$$

Here, $\mathfrak{J}_{\parallel}$ and $\mathfrak{J}_{\perp}$ denote the moments of inertia parallel and perpendicular to the symmetry axis, and $\mathfrak{J}_e$ is the effective moment of inertia, $1/\mathfrak{J}_e = 1/\mathfrak{J}_{\parallel} - 1/\mathfrak{J}_{\perp}$. The temperature T is given by

$$1/T = \frac{\partial}{\partial E} \ln \varrho(E) . \tag{A10}$$

This level density is used both at the ground-state and barrier deformations. At first it may seem strange to count rotational levels at the ground state of, e.g., ^{200}Pb, which is usually assumed spherical. The argument is that fairly high spin states (25ħ-50ħ) are populated, leading to a deformed equilibrium shape. Furthermore, even for low spin values, the nucleus has a finite probability of being deformed. Since the rotational enchancement factor is very large, it is conceivable that a flat, spherical equilibrium effectively requires a level density including rotational contributions. Attempts to analyze cross sections for fission of spherical nuclei induced by light particles indicate that such a level density should always be used. This is the case even for high excitation energies ($\gtrsim 50$ MeV) where the rotations are usually expected to vanish for ground-state deformations [38].

A1.3 *Moments of inertia*

The moments of inertia have rigid-body values as expected[39] for high excitation energy, high spin, and large deformation. They are calculated from a uniform distribution with a sharp cut-off at the boundary. The shape is axially symmetric around the z axis and given by[40]

$$\varrho^2 = (c^2R^2 - z^2)(A + Bz^2/(c^2R^2)) , \tag{A11}$$

$$\frac{1}{c^3} = A + \frac{1}{5}B\,, \quad B = \frac{1}{2}(c-1) + 2h\,, \quad R = r_0 A^{1/3}\,, \tag{A12}$$

where c and h are deformation parameters. The moments of inertia are then for a system of N nucleons

$$\mathfrak{J}_{\parallel} = \frac{2}{5} mNR^2 c^5 \left\{ \frac{B^2}{21} + A^2 + \frac{2}{7} A \cdot B \right\}, \tag{A13}$$

$$\mathfrak{J}_{\perp} = \frac{1}{5} mNR^2 c^5 \left\{ A + \frac{3}{7} B \right\} + \frac{1}{2} \mathfrak{J}_{\parallel}\,. \tag{A14}$$

A1.4 *Angular distribution of fission fragments*

For a nucleus of spin I and energy E, the distribution of the emitted fission fragments with respect to the beam axis is approximately[33,41]

$$W_{E,I}(\theta) = \sqrt{\frac{2p}{\pi}} \frac{J_0(ip\sin^2\theta)\exp(-p\sin^2\theta)}{\mathrm{erf}(\sqrt{2p})}, \tag{A15}$$

where

$$p = \frac{(I+\frac{1}{2})^2}{4K_0^2}\,, \quad K_0^2 = T_B \mathfrak{J}_e(\mathrm{Barrier})\,. \tag{A16}$$

Here erf is the error function and J_0 the zero-order Bessel function. The temperature T_B corresponds to the intrinsic excitation energy at the barrier and therefore depends on spin,

$$\frac{1}{T_B} = \frac{\partial}{\partial E} \ln \varrho_B(E - B_f, I)\,. \tag{A17}$$

Expression (A15) corresponds to the relative probabilities of different projections K of the spin on the symmetry axis, which are implicitly given in eq. (A8). However, to arrive at eq. (A15), only the expansion in the last parameter in eq. (A8), $K^2/2\mathfrak{J}_e$, is necessary. The total angular distribution $W(\theta)$ is obtained by summing and integrating eq. (A15) over the spin and energy distribution P(E,I) of all stages in the evaporation cascade, weighted, of course, with the fission probability,

$$W(\theta) = \sum_{\text{Nuclei}} \sum_{I} \int dE\; P(E,I) \frac{\Gamma_f(E,I)}{\Gamma_{\text{total}}(E,I)} W_{E,I}(\theta)\,. \tag{A18}$$

A2. Parameter Determination for $^{16}O + W$

The parameters fall into two groups. One consists of parameters either fixed from independent considerations or relatively unimportant for the present data; these are discussed in the first two sections. The second group contains the parameters crucial for the present data, i.e., those about which the present experiments give information. They are discussed in the last three sections.

A2.1 *Neutron- and gamma-width parameters*

The neutron transmission coefficients are obtained from an optical model with the average parameter set recommended in ref. 42 for lower energies. They are fixed from the beginning, and no readjustment or search for better parameters has been attempted.

The giant dipole parameters in eq. (A7) are [43]

$$\Gamma_G = 5 \text{ MeV}, \quad E_G = \frac{80 \text{ MeV}}{A^{1/3}}, \quad c_\gamma = 2. \tag{A19}$$

With this choice for c_γ, we find Γ_γ values roughly in agreement with the observed average gamma width [36b] at the neutron-binding energy for nuclei below the closed shell of ^{208}Pb. Gamma emission is competitive only for the lowest excitation energies, but the magnitude of Γ_γ is important for the contribution to the fission yield from very long lifetimes, i.e., for the magnitude of the long-lifetime component.

A2.2 *General level-density parameters*

The level-density parameters[15] consist of the main parameter a, the parameter κ, the two pairing gaps Δ_n and Δ_p, the shell distance $\hbar\omega$, the shell correction δU, and the moments of inertia. For a and $\hbar\omega$, we have used the values of ref. 15, and since κ enters (weakly) only at small excitation energies, we chose $\kappa = 0.0$.

The gap parameters appear only through the critical energies and the pairing energies; we used the same set (different for the ground states and the barriers) for all nuclei. This choice, with the values selected for the other parameters, gives an average distance of D = 27 eV between $\frac{1}{2}^+$ levels in $^{195}_{82}$Pb at an excitation energy of 6.3 MeV, in agreement with the corresponding observed quantity for the nearby nucleus $^{193}_{78}$Pt. The values of a, κ, $\hbar\omega$, and Δ are:

$$\begin{aligned} &a = A/9.5 \text{ MeV}, \quad \hbar\omega = 41 \text{ MeV}/A^{1/3}, \quad \kappa = 0.0 \\ &\Delta_n^{gs} = \Delta_n^B = \Delta_p^B = 0.8 \text{ MeV}, \quad \Delta_p^{gs} = 0.5 \text{ MeV} \end{aligned} \tag{A20}$$

A2.3 *Shell corrections*

The shell-correction term is important for the energy dependence of the level density, and many prescriptions are available. We have taken δU of ref. 44 for the ground-state shell correction. It increases with the distance from the closed neutron shell N = 126 until N = 113 (A = 195), after which it stays constant at about −2 MeV. Instead of this constant value, we continued the increase by adding 0.1 MeV for A = 195, 0.2 MeV for A= 194, 0.3 MeV for A= 193, etc. This has little effect on our numerical level-density results because δU in the level density is multiplied by a small factor for small excitation energies where these nuclei play a role. However, since we use a constant smooth part $\tilde{B}_f$ of the fission barrier (see eq. A5 and A21), such a modification implies that the barriers B_f have to be decreased by the same amount, which has the important effect of increasing the long-lifetime component for the two lightest tungsten isotopes.

The barrier shell correction is presumably less dependent on nucleon number, and we have simply used a constant value $\delta U_B = -2$ MeV. It enters the barrier level density as an energy shift which, for large excitation energies, amounts to δU_B (in this case decreasing the number of levels on top of the barrier) and for small excitations approaches zero. Decreasing δU_B therefore has the effect of decreasing the fission probability at high excitation energy while leaving the fission probability at low excitation energy essentially unchanged. This means a relative increase of the late-stage fission (long-lifetime component). Thus δU_B is a very selective parameter for shifting the relative fission contribution from short to long lifetime or vice versa. Some support for the value chosen for δU_B may be found in ref. 45.

A2.4 *The smooth part of the fission barrier*

The fission barrier is obtained from eq. (A5). The shell corrections were discussed in sec. A2.3 and the pairing corrections[15] are obtained from the paring gaps*) in eq. (A20). Thus only the smooth barrier term $\tilde{B}_f$ is left to be specified. For the application described here we required a constant value (independent of A) of B_f and the experimental fission cross sections were reproduced with

$$\tilde{B}_f = 11.3 \text{ MeV}. \qquad \text{(A21)}$$

Inclusion of the pairing corrections (see eq. (A5)) in the smooth barrier reduces the value in eq. (A21) to 10.5 MeV. This may be compared to the droplet-model result [46] of 13.9 MeV. An analysis of fission cross sections similar to ours has been

*) In ref. 15, a factor $6/\pi^2$ was inadvertently omitted on the right-hand side of eq. (A24). The quantity A in this equation is the number of protons or neutrons.

published by Ignatyuk et al. [47]. Their results for the smooth barrier are smaller than the droplet-model values by approximately the same amount, e.g., 3.0 MeV for ^{200}Hg.

A2.5 *Spin distribution and moments of inertia*

The parameters in the expressions for the moments of inertia are c, h, and r_0. For the radius parameter, we take the same value for all nuclei regardless of deformation. The ground-state shape is assumed spherical. This choice is natural for the lead isotopes although we assumed rotational contributions in the corresponding level density. The ground-state moments of inertia enter only weakly in the fission probability and lifetime distribution, and the actual deformation used is therefore not critical.

For the barrier deformation we assumed the liquid-drop value, which is expected[48] for high excitation energy where the shell effects have disappeared. For low excitation energy, the shell effects should be included in the determination of the barrier deformation. However, for the lead isotopes in question, the barrier (in deformation space) is broad and relatively flat[40], and consequently, one may expect that the liquid-drop value is approached relatively quickly with increasing energy.

The values assumed were

$$\begin{aligned} &r_0 = 1.2 \text{ fm}, \quad (c,h)_{gs} = (1.0, 0.0)\,, \\ &(c,h)_B = (1.87, 0.0) \end{aligned} \tag{A22}$$

The spin distribution in the initial compound nucleus is assumed proportional to $2I+1$ with a sharp cut-off at the maximum value I_m. It is related to the complete-fusion cross section by

$$\sigma_{CF} = \pi \lambda\!\!\!^{-2} (I_m + 1)^2\,, \tag{A23}$$

where $\lambda\!\!\!^{-}$ is the de Broglie wavelength for the reduced mass and centre-of-mass energy. The Bass model[35] gives similar expressions for the complete-fusion and the total-reaction cross section with corresponding maximum spin values I^B_{CF} and I^B_R.

The experimental fission probability P_f is determined as $P_f = \sigma_f/\sigma_{CF}$, where σ_f is the measured fission cross section and σ_{CF} is given by eq. (A23). The quantity I_m thus enters both in observed and in calculated quantities. The value of I_m is especially important for the fission-fragment anisotropy (see eqs. (A15) and (A16)), but it also has a significant effect on both the calculated and the observed fission

probabilities. With the parameter set described above, I_m is chosen for each projectile energy to obtain agreement between experiment and calculation. The resulting I_m values lie between I^B_{CF} and I^B_R, determined from the Bass model.

A barrier deformation smaller than that in eq. (A22) leads to a larger $\mathfrak{I}_e$ value which, in turn, requires a larger I_m to reproduce the fission-fragment anisotropy. For example, with $c_{B_i} = 1.5$, corresponding to the low-energy barrier with shell effects included, $\mathfrak{I}_e$ is increased by a factor of 1.7 which, for the case of 97 MeV $^{16}O + ^{182}W \rightarrow ^{198}Pb$ requires $I_{m_i} = 52\hbar$, i.e., 50% larger than the Bass value. For the same case, the barrier in eq. (A22) leads to a value 14% higher than I^B_{CF}. Thus, if I_m is assumed close to the value obtained in the Bass model, the effective moment of inertia determined from experiment is that corresponding to the liquid-drop deformation.

A3. Results

A.3.1 $^{16}O + W$

Table A1 gives the input parameters used in the calculations together with other quantities of interest. This parameter set reproduces the measured fission-fragment anistotropy and fission probability and leads to a lifetime distribution consistent with what is observed. The main parameters are the smooth part of

Table A1. Statistical model parameters as functions of mass number A for the Pb isotopes in the calculations. The neutron binding energy B_n, fission barrier B_f, shell and pairing corrections δU and δP, for the ground state (gs) and the barrier (B), and the critical energy E^c, are given in MeV. The moments of inertia for the ground state and barrier deformations are given in units of $\hbar^2$/MeV.

A	B_n	B_f	δU_{gs}	δP_{gs}	δP_B	E^c_{gs}	E^c_B	$\mathfrak{I}^{gs}$	$\mathfrak{I}^B_{\|\|}$	$\mathfrak{I}^B_{\perp}$	$\mathfrak{I}^B_e$
202	8.70	14.0	−5.56	−2.53	−3.36	6.4	7.2	96.5	47.6	302.3	56.5
201	7.20	13.4	−5.00	−1.71	−2.54	4.0	7.2	95.7	47.2	299.8	56.0
200	9.10	12.8	−4.38	−2.49	−3.33	6.3	7.1	94.9	46.8	297.3	55.5
199	7.40	12.1	−3.73	−1.68	−2.51	3.9	7.1	94.1	46.4	294.8	55.1
198	9.44	11.6	−3.17	−2.46	−3.29	6.2	7.0	93.4	46.0	292.4	54.6
197	7.68	11.1	−2.66	−1.64	−2.48	3.8	7.0	92.6	45.6	289.9	54.1
196	9.75	10.7	−2.25	−2.43	−3.26	6.1	7.0	91.8	45.2	287.5	53.6
195	7.95	10.4	−1.95	−1.61	−2.44	3.7	6.9	91.0	44.9	285.0	53.3
194	9.95	10.2	−1.83	−2.39	−3.23	6.1	6.9	90.2	44.5	282.6	52.8
193	8.13	10.1	−1.73	−1.58	−2.41	3.7	6.9	89.5	44.1	280.2	52.3
192	10.14	10.1	−1.66	−2.36	−3.19	6.0	6.8	88.7	43.7	277.8	51.9
191	8.35	10.0	−1.59	−1.54	−2.38	3.6	6.8	87.9	43.3	275.4	51.4

the fission barrier $\tilde{B}_f$, the barrier shell correction δU_B, and the maximum spin I_m of the initial compound nucleus. Equally important but not varied are δU_{gs} and the effective moment of inertia at the barrier deformation.

Table A2. The maximum spin values I_R^B and I_{CF}^B, corresponding to the reaction and complete-fusion cross sections in the Bass model, are given for the reaction $^{16}O + ^{182}W \rightarrow {}^{198}Pb$. Also given are the maximum spin values I_m used in the calculations, the related complete-fusion cross sections σ_{CF}(mb), the measured fission cross sections σ_f(mb), and experimental (P_f^{exp}) and calculated (P_f^{calc}) fission probabilities. All quantities are given as functions of ^{16}O bombarding energy (MeV).

$E_{^{16}O}$	I_R^B	I_{CF}^B	I_m	σ_{CF}	σ_f	P_f^{exp}	P_f^{calc}
90	34.4	28.2	34	656	122	0.19	0.19
94	38.9	32.3	38	779	216	0.28	0.30
97	42.0	35.0	40	836	302	0.36	0.37
102	46.7	39.1	43	914	429	0.47	0.47
108	51.9	43.4	47	1027	571	0.56	0.56
115	57.3	47.8	50	1089			0.62

In table A2 we compare I_m to the Bass-model prediction as a function of energy. We note the smooth transition from the total-reaction value at low energy towards the complete-fusion value at high energy. These I_m values are also used for the other three tungsten isotopes. Table A2 also gives experimental and calculated fission probabilities, which differ at most by 7%.

Table A3. Experimental and calculated fission probabilities for the naturally occurring tungsten isotopes, for ^{16}O bombarding energies of 90 MeV and 97 MeV.

$E_{^{16}O}$		^{182}W	^{183}W	^{184}W	^{186}W
90	Calc.	0.19	0.17	0.11	0.066
	Exp.	0.19	0.16	0.12	0.066
97	Calc.	0.37	0.34	0.28	0.18
	Exp.	0.36	0.31	0.26	0.18

In table A3 is given the isotope dependence of experimental and calculated fission probabilities for bombardment with ^{16}O at 90 and 97 MeV. The agreement is within 10%. The fission-fragment anisotropy is given in table A4 for the different isotopes, and again the calculations reproduce the experimental results to within $\sim 10\%$.

Table A4. Experimental and calculated fission-fragment angular distributions in the centre-of-mass system, as functions of bombarding energy (MeV) for ^{16}O induced fission of the four W isotopes. The experimental distributions are normalized at $\theta_{cm} = 113°$ to a $(\sin\theta)^{-1}$ distribution and the calculated distributions are normalized to unity at $\theta_{cm} = 90°$.

Experiment

	A = 182		A = 183		A = 184		A = 186	
E	140°	172°	140°	172°	140°	172°	140°	172°
90	1.67	4.16	1.62	4.17	1.72	4.20	1.78	4.30
94	1.62	4.64	1.66	4.59	1.63	4.69	1.76	4.40
97	1.56	4.61	1.70	4.73	1.64	4.64	1.70	4.77
102	1.58	4.51	1.72	4.94	1.59	4.71	1.69	5.05
108	1.65	4.88	1.61	4.91	1.72	4.81	1.55	4.83

Calculation

	A = 182		A = 183		A = 184		A = 186	
E	170°	180°	170°	180°	170°	180°	170°	180°
90	4.10	4.72	4.19	4.87	4.04	4.66	3.82	4.36
94	4.46	5.25	4.55	5.39	4.53	5.41	4.41	5.23
97	4.57	5.43	4.63	5.52	4.66	5.60	4.61	5.54
102	4.65	5.52	4.70	5.61	4.75	5.71	4.77	5.77
108	4.71	5.59	4.78	5.71	4.81	5.78	4.88	5.92
115	4.70	5.58						

The lifetime distribution can be compared to experiment only for an average over isotopes. As discussed in the main text the distributions are consistent with experiment. The calculated energy dependence confirms the prediction from qualitative arguments discussed in the introduction and in sec. 6.1.

A3.2 $^{12}C + W$

The procedure described in sect. A2 was repeated for the reaction $^{12}C + W \rightarrow Hg$. The resulting parameter set was given and discussed in detail in ref. 34. The smooth part of the barrier, $\tilde{B}_f$, was first assumed constant as for the ^{16}O projectile, but a weak linear dependence on A turned out to be necessary for a good fit to the data.

The ground-state shell corrections were obtained from those for the Pb isotopes by adding 0.17 MeV due to the difference in proton number. This is 1 MeV less than expected from ref. 44. The barrier shell correction is $\delta U_B = -1.0$ MeV less negative than for the Pb isotopes.

The value of I_m, which changes with bombarding energy, was determined from the angular distribution. As for $^{16}O + W$, we found a transition from the complete-fusion value of Bass[35] at higher energies towards the total-reaction value at lower energies. The other parameters were determined as described in sect. A2 for the Pb isotopes.

A3.3 *Conclusions*

The main conclusion we can draw from these results is that the model parameters can be adjusted to reproduce the present heavy-ion data, i.e. the isotope and energy dependence of the fission probability, the anisotropy of the angular distribution and the isotope-averaged lifetime distribution.

The parameters are not unique, i.e., other sets exist which will also reproduce the data. There are two main degrees of freedom in the important set of parameters. The lifetime distribution depends only on the difference between shell corrections at the ground state and at the barrier, not on each one separately. Furthermore, with an average temperature fixed by the lifetime distribution, the anisotropy depends only on the ratio between the square of the maximum angular momentum and the effective barrier moment of inertia. We have not explored these and other degrees of freedom systematically, but it is clear that the requirement of reproducing the three different types of measurements simultaneously, for different isotopes and bombarding energies, sets narrow limits on the model parameters.

In some cases particle induced fission data for the same compound nuclei are available. Although our model can easily reproduce such data it is very difficult, if not impossible, to reproduce both sets of data with the same model parameters. As an example, one of the compound nuclei created by ^{12}C bombardment of tungsten, ^{198}Hg, has been studied also through proton induced fission of gold, and the results have been used[49] to extract the magnitude of the fission barrier for ^{198}Hg. The value obtained for B_f is about 5 MeV higher than the value found in ref. 34. One possibility is that the large negative ground-state shell corrections are strongly reduced for the high-spin states populated by heavy-ion bombardment. This explanation was suggested in ref. 34 and further support for it may be found in ref. 50.

References

1. W. M. Gibson, Ann. Rev. Nucl. Sci. *25* (1975) 465.
2. S. A. Karamyan, Yu. V. Melikov, and A. F. Tulinov, Fiz. El. Chast. Atom. Yad. *4* (1973) 456; Sov. J. Particles Nucl. *4* (1973) 196.
3. F. Brown, D. A. Marsden, and R. D. Werner, Phys. Rev. Lett. *20* (1968) 1449.
4. W. M. Gibson and K. O. Nielsen, Int. Symp. Phys. Chem. Fission SM122/129 (1969 IAEA: Vienna 861 pp.); Phys. Rev. Lett. *24* (1970) 114.
5. Yu. V. Melikov, Yu. D. Oststavnov, and A. F. Tulinov, Zh. Eksp. Teor. Fiz. *56* (1969); Sov. Phys. JETP *29* (1969) 968; Yad. Fiz. *12* (1970) 50; Sov. J. Nucl. Phys. *12* (1971) 27.
6. Yu. V. Melikov, Yu. D. Oststavnov, A. F. Tulinov, and N. G. Chechenin, Nucl. Phys. *A180* (1972) 241.
7. J. U. Andersen, K. O. Nielsen, J. Skak-Nielsen, R. Hellborg, and K. G. Prasad, Nucl. Phys. *A241* (1975) 327.
8. P. E. Vorotnikov, Yu. F. Gurtovenko, E. Kh. Kisina, V. O. Kordynkevitch, Yu. V. Melikov, N. A. Morogov, Yu. D. Oststavnov, L. N. Syutkina, A. F. Tulinov, and N. G. Chechenin, Nucl. Phys. *A281* (1977) 295.
9. J. U. Andersen, N. G. Chechenin, A. S. Jensen, K. Jørgensen, and E. Lægsgaard, Nucl. Phys. *A324* (1979) 39.
10. S. A. Karamyan, Yu. V. Melikov, F. Normuratnov, O. Otgonsuren, and G. M. Solovyeeva, Yad. Fiz. *13* (1970) 944; Sov. J. Nucl. Phys. *13* (1971) 543.
11. S. A. Karamyan, Yu. Ts. Oganesyan, and F. Normuratnov, Yad. Fiz. *14* (1971) 499; Sov. J. Nucl. Phys. *14* (1972) 279.
12. J. U. Andersen, E. Lægsgaard, K. O. Nielsen, W. M. Gibson, J. S. Forster, I. V. Mitchell, and D. Ward, Phys. Rev. Lett. *36* (1976) 1539.
13. H. Hagelund and A. S. Jensen, Physica Scripta *15* (1977) 225.
14. A. S. Jensen, *Proc. IAEA Int. Conf. on Neutron Physics and Nuclear Data for Reactors*, Harwell, U. K., Sept., 1978.
15. A. S. Jensen and J. Sandberg, Physica Scripta *17* (1978) 107.
16. H. C. Britt and A. R. Quinton, Phys. Rev. *120* (1960) 1768.
17. R. Vandenbosch and J. R. Huizenga, *Nuclear Fission* (Academic, New York, 1973) p. 234.
18. E. Lægsgaard, Nucl. Instrum. Methods *162* (1979) 93.
19. T. Sikkeland, Phys. Rev. *135* (1964) B669.
20. J. H. Barrett, Phys. Rev. *133* (1971) 1527.
21. J. Lindhard, K. Dan. Vidensk. Selsk. Mat. Fys. Medd. *34* (1965) No 14.
22. V. E. Viola, Jr., Nucl. Data Tables *A1* (1965) 391.
23. J. U. Andersen, K. Dan. Vidensk. Selsk. Mat. Fys. Medd. *36* (1967) No 7.
24. J. U. Andersen, O. Andreasen, J. A. Davies, and E. Uggerhøj, Radiat. Eff. *7* (1971) 25.
25. S. T. Picraux, in: *Ion Beam Surface Layer Analysis*, edited by O. Meyer, G. Linker, and F. Kappeln (Plenum, New York, 1976) 527.
26. Y. Hashimoto, J. H. Barrett, and W. M. Gibson, Phys. Rev. Lett. *30* (1973) 995.
27. H. E. Schiøtt, E. Bonderup, J. U. Andersen, and H. Esbensen, *Proc. 5th Int. Conf. on Atomic Collisions in Solids*, Gatlinburg, 1973 (Plenum, New York, 1975) 483.
28. J. U. Andersen and J. A. Davies, Nucl. Instrum. Methods *132* (1976) 179.
29. J. U. Andersen and L. C. Feldman, Phys. Rev. *B1* (1970) 2063.
30. S. U. Campisano, G. Foti, F. Grasso, I. F. Quercia, and E. Rimini, Radiat. Eff. *13* (1972) 23.
31. D. Gemmell, Rev. Mod. Phys. *46* (1974) 129.
32. T. Sikkeland, J. E. Clarkson, N. H. Steiger-Shafri, and V. E. Viola, Phys. Rev. *C3* (1971) 329.

33. I. Halpern and V. M. Strutinsky, *Int. Conf. on Peaceful Uses of Atomic Energy*, Geneva, vol. 15 (U.N., N.Y., 1958) 408.
34. J. U. Andersen, A. S. Jensen, E. Lægsgaard, K. O. Nielsen, J. S. Forster, I. V. Mitchell, D. Ward, and W. M. Gibson, to be published in Int. Symp. Phys. Chem. Fission, IAEA-SM/241-C7 (1979 IAEA: Jülich).
35. R. Bass, Nucl. Phys. *A231* (1974) 45.
36. J. E. Lynn, *Theory of Neutron Resonance Reactions* (Clarendon Press, Oxford, 1968) a) p. 325; b) p. 316.
37. J. E. Lynn, *Systematics for neutron reactions of the actinide nuclei*, Harwell Report 1974, AERE-R7468, p. 26.
38. S. Bjørnholm, A. Bohr, and B. Mottelson, Proc. Int. Symp. on Physics and Chemistry of Fission, Rochester, 1973; T. Døssing and A. S. Jensen, Nucl. Phys. *A222* (1974) 493.
39. M. Brack, T. Ledergerber, H. C. Pauli, and A. S. Jensen, Nucl. Phys. *A234* (1974) 185.
40. M. Brack, J. Damgaard, A. S. Jensen, H. C. Pauli, V. M. Strutinsky, and C. Y. Wong, Rev. Mod. Phys. *44* (1972) 320.
41. R. Vandenbosch and J. R. Huizenga, *Nuclear Fission* (Academic, New York, 1973) p. 184.
42. C. M. Perey and F. G. Perey, Atomic Data and Nuclear Data Tables *17* (1976) 1.
43. L. M. Bollinger, Proc. Int. Symp. on Nuclear Structure, Dubna (1968) p. 317.
44. J. W. Truran, A. G. W. Cameron, and E. Hilf, Int. Conf. on Properties of Nuclei far from the Region of Beta Stability, Leysin, Switzerland (1970) p. 275.
45. U. Mosel, Phys. Rev. *C6* (1972) 971.
46. W. D. Myers, *Droplet Model of Atomic Nuclei* (IFI/Plenum, New York, Washington, London, 1977).
47. A. V. Ignatyuk, M. G. Itkis, V. N. Okolovich, G. N. Smirenkin, and A. S. Tishin, Sov. J. Nucl. Phys. *21* (1975) 612.
48. R. Vandenbosch, Phys. Rev. *C7* (1973) 2092.
49. L. G. Moretto, S. G. Thomson, J. Routti, and R. C. Gatti, Phys. Letters *38B* (1972) 471.
50. M. E. Faber, A. Faessler, and M. Ploszajczak, Int. Symp. Phys. Chem. Fission, IAEA-SM/241-C5 (1979 IAEA: Jülich).

Indleveret til Selskabet september 1979.
Færdig fra trykkeriet april 1980

Secondary Electron Spectra from Dielectric Theory

By DAVID K. BRICE *and* PETER SIGMUND

Det Kongelige Danske Videnskabernes Selskab
Matematisk-fysiske Meddelelser **40**:8

Kommissionær: Munksgaard
København 1980

This work was supported in part by
the Danish Natural Science Research Council
and the U.S. Department of Energy, DOE,
under Contract AT(29-1) 789.

Synopsis

Angular and energy distributions of electrons excited by a heavy charged particle penetrating an electron gas have been studied theoretically for a range of electron densities. The calculations are based on the self-consistent dielectric theory of Lindhard in which the properties of the electron gas are described by a frequency and wave-vector dependent dielectric function. The excitation cross section has been investigated in the present work for a broad range of incident projectile velocities, and numerical results are presented both for doubly and singly differential forms of the excitation spectrum. An analytical approximation is developed for the case of low projectile velocities, and comparison with numerical results indicates that the analytical form is quite adequate for velocities up to near the Fermi velocity. For higher incident velocities the emitted energy spectrum is characterized by a resonance for electron energies in the range ~ 1–4 times the Fermi energy; at electron energies about 10 times the Fermi energy the spectrum approaches that given by the Rutherford cross section. The electron energy at which the resonance occurs is independent of the projectile velocity, but is a slowly varying function of the electron density. The angular position of the resonance is, however, a strong function of the projectile velocity, occurring first in the forward direction at a critical velocity, v_c, moving to higher angles with increasing projectile velocity, and limiting to lateral (90°) emission at high incident velocity. These results may form a basis for more detailed studies of electron emission in both atom-atom and atom-solid collisions.

DAVID K. BRICE[1] PETER SIGMUND[2]
H. C. Ørsted Institute,
DK-2100 Copenhagen Ø., Denmark

1: Permanent address:
Sandia Laboratories
Albuquerque, New Mexico, 87185, USA

2: Present address:
Physics Institute,
Odense University
DK-5230 Odense M, Denmark

Printed in Denmark by Bianco Lunos Bogtrykkeri A-S. ISSN 0023-3323. ISBN 87-7304-106-8

Table of contents

1. Introduction

The free electron gas is a convenient system for model studies of atomic and solid-state properties. In particular, this system offers unique possibilities of studying the interaction of energetic charged particles with matter, as far as the interaction with electrons is concerned. The free electron gas in the self-consistent picture developed by Lindhard[1] allows a treatment of the stopping of a charged particle with essentially no limitations on the range of particle velocities to be considered, thus giving qualitative insight into the partition of energy that would be quite difficult to obtain by other means.[2] When combined with the Thomas-Fermi principle, this dielectric theory provides estimates of stopping parameters that exhibit basic scaling properties as a function of atomic number.[3,4]

The dielectric theory has implications on the excitation spectrum of an electron gas. While collective excitations (plasma modes) occur in rather well-defined energy quanta, and thus show up in a number of well-studied phenomena,[5] the situation is different with regard to single-particle excitations. In a free electron gas, single-particle excitations form a continuous spectrum. Therefore most discrete systems would seem to call for a more elaborate treatment, unless attention is given to high levels of excitation and, especially, ionization. These phenomena have received less attention from the point of view of the dielectric theory than the stopping process.

In the present study, the spectrum of electrons excited by an energetic charged particle has been analyzed within the framework of the dielectric theory. Both energy and angular distributions of electrons have been evaluated as a function of the velocity of the primary particle. Therefore, the information extracted from the model is more specific than the predictions on energy loss, where primary velocity and Fermi velocity are the only variables. Both the capabilities of, and limitations to the model are expected to show up more clearly in differential quantities than in integrated ones.

Our main motivation for this study was a need for universal, and not necessarily very accurate angular and energy distributions of electrons after excitation by charged particles. Such spectra are called for in the analysis of a wide range of phenomena in radiation physics, chemistry, and biology.[6] Although quantitative studies have been made of specific systems, both experimental and theoretical,

we were missing the qualitative guidelines that the dielectric model provides in stopping theory. We started with a numerical evaluation of doubly differential electron spectra from the dielectric theory, similar to what was done by Ritchie et al. [7,8] for the energy spectrum. Later the numerical evaluation of electron spectra was followed up by an analytical study. The theory in its present form, we believe, provides insight into the qualitative behavior of secondary-electron spectra from light-ion bombardment, in particular the possible occurrence of peaks in the energy and angular distributions, the correlation between the energy and angular distribution as a function of particle velocity, and the range of angles that is accessible for secondary electrons at any given set of particle and electron energies. We had hoped to present Thomas-Fermi scaled spectra at the same time, but with an increasing amount of available analytical results we found that within the time limits imposed, it seemed most appropriate to present the free-electron results separately, and reserve applications to a later occasion.

2. Basic Equations

The basic equation governing the excitation of secondary electrons by a charged particle traversing a degenerate Fermi-Dirac gas of electrons has been derived by Ritchie.[9] His primary attention was directed toward the effects of the target on the incident projectile, and consequently the secondary electron spectrum has not been discussed in great detail. In the present section we will present a brief derivation of the basic equations for both the excitation cross section and for the single-particle contribution to the stopping cross section. Our procedure differs from that of Ritchie, but is consistent with Lindhard's derivation of the dielectric function. The derivation also makes evident the limitations of the procedure, and serves to introduce the notation which will be used throughout the paper.

A. *The Model*

We consider a point particle of charge e_1 and velocity $\boldsymbol{v}$, which traverses a degenerate Fermi-Dirac gas of electrons. The fractional energy and momentum losses suffered by the particle through its interaction with the system are assumed to be small over a time period which is long compared with pertinent electronic periods, so that $\boldsymbol{v}$ can be taken as a constant. This assumption will be quite good for a massive particle traversing the system, or for a highly energetic particle with mass comparable with the electron mass. The charge density, $\varrho(\boldsymbol{r},t)$ asso-

ciated with the perturbing particle is given by

$$\varrho(\boldsymbol{r},t) = e_1 \delta(\boldsymbol{r} - \boldsymbol{v}t) \,. \tag{2.1}$$

where δ represents the Dirac delta function.

The local electric potential $\Phi(\boldsymbol{r},t)$ which results from the charge density (2.1) includes the Coulomb field of the incident projectile as well as the induced field which results from the dynamic response of the electronic system to the perturbation. In the self-consistent treatment of Lindhard[1] the many-body problem of the interaction between an incident projectile and the electrons and between the electrons of the system themselves is resolved in the dielectric function $\varepsilon(\boldsymbol{k},\omega)$ of the system. By definition, $\varepsilon(\boldsymbol{k},\omega)$ connects $\Phi(\boldsymbol{r},t)$ and $\varrho(\boldsymbol{r},t)$ through the relation

$$\Phi(\boldsymbol{k},\omega) = 4\pi\varrho(\boldsymbol{k},\omega)/k^2\varepsilon(\boldsymbol{k},\omega) \,, \tag{2.2}$$

where $\Phi(\boldsymbol{k},\omega)$ and $\varrho(\boldsymbol{k},\omega)$ are the Fourier transforms of $\Phi(\boldsymbol{r},t)$ and $\varrho(\boldsymbol{r},t)$, respectively. For a function $g(\boldsymbol{r},t)$, the Fourier transform $g(\boldsymbol{k},\omega)$ is defined such that

$$g(\boldsymbol{r},t) = (VT)^{-1} \sum_{\boldsymbol{k},\omega} g(\boldsymbol{k},\omega) e^{i(\boldsymbol{k}\cdot\boldsymbol{r} - \omega t)}, \tag{2.3}$$

where periodic boundary conditions in the volume V and time interval T are assumed. Both V and T are taken to be large, and will ultimately be allowed to limit to infinity.

Equations (2.1)–(2.3) give the perturbing potential

$$\Phi(\boldsymbol{r},t) = \frac{4\pi e_1}{V} \sum_{\boldsymbol{k},\omega} \frac{\delta_{\boldsymbol{k}\cdot\boldsymbol{v},\omega} e^{i(\boldsymbol{k}\cdot\boldsymbol{r} - \omega t)}}{k^2 \varepsilon(\boldsymbol{k},\omega)} \,. \tag{2.4}$$

$\Phi(\boldsymbol{r},t)$ as given in Eqn. (2.4) is the effective interaction potential between the incident projectile and the electrons of the system. This field is the generalization for the system of electrons of the Coulomb interaction between two isolated charged particles.

B. *The Dielectric Function*

The dielectric function $\varepsilon(\boldsymbol{k},\omega)$ has been evaluated for the free Fermi gas by Lindhard[1] within first-order time-dependent perturbation theory. The electrons of the system are assumed to occupy states described by single-particle free-electron wave functions, $\psi(\boldsymbol{r},t)$, where

$$\psi(\boldsymbol{r},t) = V^{-1/2} e^{i(\boldsymbol{k}\cdot\boldsymbol{r} - \omega t)} \,. \tag{2.5}$$

The single-particle energies, E, are given by

$$E = \frac{\hbar^2 k^2}{2m} = \hbar\omega \tag{2.6}$$

where $\hbar$ is Planck's constant divided by 2π and m the electron mass. The system is taken initially to be in its ground state so that all states are occupied up to the Fermi energy ε_F given by

$$\varepsilon_F = \frac{1}{2} m v_F^2 = \frac{\hbar^2 k_F^2}{2m} = \frac{\hbar^2}{2m} (3\pi^2 n)^{2/3} \tag{2.7}$$

where n is the electron density in the system, and v_F and k_F are the magnitudes of the velocity and wave vector, respectively, of electrons having energy ε_F.

The results of Lindhard's analysis are conveniently expressed in terms of the variables u, z, and χ^2, defined by

$$u = \omega / k v_F \tag{2.8a}$$

$$z = k / 2k_F \tag{2.8b}$$

and

$$\chi^2 = e^2 / (\pi \hbar v_F), \tag{2.9}$$

where e is the electronic charge. In these variables

$$\varepsilon(\boldsymbol{k}, \omega) = 1 + \frac{\chi^2}{z^2} [f_1(u,z) + i f_2(u,z)] \tag{2.10}$$

where

$$f_1(u,z) = \frac{1}{2} + \frac{1}{8z} \left\{ [1-(z+u)^2] \ln \left| \frac{z+u+1}{z+u-1} \right| \right.$$
$$\left. + [1-(z-u)^2] \ln \left| \frac{z-u+1}{z-u-1} \right| \right\}, \tag{2.11}$$

and

$$f_2(u,z) = \begin{cases} \dfrac{\pi u}{2} & \text{for} \quad |z+u| < 1, \qquad (2.12a) \\ \dfrac{\pi}{8z} [1-(z-u)^2] & \text{for} \quad |z-u| < 1 < |z+u| \qquad (2.12b) \\ 0 & \text{otherwise.} \qquad (2.12c) \end{cases}$$

C. *The Transition Rates*

The excitation spectrum and the stopping cross section can be obtained from the perturbing potential, Eqn. (2.4), and electron wave functions, Eqn. (2.5), through a straightforward application of first-order time dependent perturbation theory. The use of first-order theory is valid as long as the transition rates remain small, and it is consistent with Lindhard's form of the dielectric function. It is our aim in the present work to discuss some qualitative features of the single-electron excitation spectrum, and therefore we disregard higher order effects[10], as well as many-body corrections to the Lindhard dielectric function.

In the present section we will write

$$E(\boldsymbol{k}) = E_0\,; \quad \boldsymbol{k} = \boldsymbol{k}_0\,; \quad \omega = \omega_0 = E_0/\hbar \tag{2.13a}$$

for the initial electronic states (i.e., for $|\boldsymbol{k}| < k_F$), and

$$E(\boldsymbol{k}) = E_1\,; \quad \boldsymbol{k} = \boldsymbol{k}_1\,; \quad \omega = \omega_1 = E_1/\hbar \tag{2.13b}$$

for the final states ($|\boldsymbol{k}| > k_F$). If $W(\boldsymbol{k}_1)d^3k_1$ represents the probability per unit time for excitation of electrons into states $\boldsymbol{k}_1$ in the $\boldsymbol{k}$-space volume element d^3k_1, then first-order time-dependent perturbation theory yields

$$W(\boldsymbol{k}_1)\,d^3k_1 = 2\frac{2\pi}{\hbar}\mathcal{N}_1(E_1)\,dE_1\,d\boldsymbol{\Omega}_1 \sum_{\boldsymbol{k}_0}\left|\frac{4\pi e_1 e}{Vk^2\varepsilon(\boldsymbol{k},\boldsymbol{k}\cdot\boldsymbol{v})}\right|^2 \cdot \delta(E_1 - E_0 - \hbar\boldsymbol{k}\cdot\boldsymbol{v})\,, \tag{2.14}$$

where $\boldsymbol{k} = \boldsymbol{k}_1 - \boldsymbol{k}_0$, $\mathcal{N}_1(E_1)$ is the density of states at E_1, and $d\boldsymbol{\Omega}_1$ a solid angle at $\boldsymbol{k}_1$. The extra factor of two in front of the standard expression comes from the sum over spin states which are not altered by the potential (2.4). For large V the sum in (2.14) can be expressed as an integral through

$$\sum_{\boldsymbol{k}} \rightarrow \frac{V}{(2\pi)^3}\int d^3k \tag{2.15a}$$

and, likewise

$$\mathcal{N}_1(E_1)\,dE_1 = \frac{V}{(2\pi)^3}k_1^2 dk_1\,. \tag{2.15b}$$

This yields

$$W(\boldsymbol{k}_1)\,d^3k_1 = \frac{e_1^2 e^2}{\hbar^2\pi^3}d^3k_1\int d^3k_0\left|\frac{1}{k^2\varepsilon(\boldsymbol{k},\boldsymbol{k}\cdot\boldsymbol{v})}\right|^2\delta(\omega_1 - \omega_0 - \boldsymbol{k}\cdot\boldsymbol{v})\,. \tag{2.16}$$

The integration over vectors $\boldsymbol{k}_0$ is restricted to $k_0 < k_F$. The transition rate can also be expressed as a cross section $d^3\sigma(\boldsymbol{k}_1)$ by

$$d^3\sigma(\boldsymbol{k}_1) = \frac{W(\boldsymbol{k}_1)}{nv}\, d^3k_1. \tag{2.17}$$

Eqn. (2.16) has already been derived by Ritchie (Eqn. (4.14) in ref. 9; his equation contains a spurious factor $\hbar^{-1}$).

The introduction of a cross section according to eq. (2.17) should at this point be taken as a formal step that will allow a direct comparison with the corresponding single-electron (or binary-encounter) cross sections at all stages of the theory. The physical significance of a single-electron cross section in a theory that takes into account the mutual interaction between target electrons is less evident, and we do not claim that there is any in a strict sense. Both Lindhard[1,2] and Ritchie[7-9] and coworkers avoid introducing such cross sections altogether and restrict their analysis to quantities characterizing the interaction with the medium rather than with the individual electron. Thus, any cross sections discussed in the following become physically meaningful when multiplied by the electron density n to become inverse mean free paths.

D. *The Stopping Cross Section*

Lindhard and Winther[2] have previously discussed in detail the stopping cross section $S(v)$ of the free electron gas for an incident charged particle. They take as a starting point for their discussion the electric field resulting from the potential of Eqn. (2.4) which acts to retard the motion of the incident particle.[11,1] The contribution of the single-particle excitations to the stopping cross section can also be found from the above excitation cross section.

The basic transition probability is multiplied by the energy transfer $\hbar\omega$ *before* summation over the initial states. An extra factor of $\hbar\omega = \hbar\boldsymbol{k}\cdot\boldsymbol{v}$ therefore appears in the equation corresponding to (2.16). The resulting expression is

$$S(v) = \frac{e_1^2 e^2}{nv\hbar\pi^3}\int d^3k_1 \int d^3k_0\, \frac{\boldsymbol{k}\cdot\boldsymbol{v}}{|k^2\varepsilon(\boldsymbol{k},\boldsymbol{k}\cdot\boldsymbol{v})|^2}\,\delta(\omega_1 - \omega_0 - \boldsymbol{k}\cdot\boldsymbol{v}), \tag{2.18}$$

where $k_0 < k_F < k_1$ defines the integration limits. This expression will be discussed in more detail in the following section.

3. Integrated Cross Sections

It is convenient first to study the cross section integrated over all ejection angles, i.e., the energy distribution of ejected electrons. This will be done in the present

section. In addition, the total cross section will be discussed briefly as well as the connection with the stopping power. The results of this section overlap to some extent with those of the study of Ritchie et al. [7-9]

After introduction of the vector $\boldsymbol{k}$ rather than $\boldsymbol{k}_0$ as the integration variable, (2.16) reads

$$d^3\sigma = \frac{e_1^2 e^2}{nv\pi^3\hbar^2} d^3k_1 \int d^3k \frac{\delta\left(-\frac{\hbar k^2}{2m} + \frac{\hbar \boldsymbol{k}\cdot\boldsymbol{k}_1}{m} - \boldsymbol{k}\cdot\boldsymbol{v}\right)}{|k^2\varepsilon(\boldsymbol{k}, \boldsymbol{k}\cdot\boldsymbol{v})|^2} \tag{3.1}$$

with the boundary

$$\boldsymbol{k}\cdot\boldsymbol{v} \geq \frac{\hbar}{2m}(k_1^2 - k_F^2) \geq 0 \tag{3.1a}$$

corresponding to $k_0 < k_F$. By means of spherical coordinates, and integrating, we obtain

$$d\sigma = \iint_{4\pi} d^3\sigma = \frac{2e_1^2 e^2 m}{nv\pi^2\hbar^3} k_1 dk_1 \int \frac{d^3k}{k|k^2\varepsilon(\boldsymbol{k}, \boldsymbol{k}\cdot\boldsymbol{v})|^2} \tag{3.2}$$

with

$$\frac{\hbar}{2m}(k_1^2 - k_F^2) \leq \boldsymbol{k}\cdot\boldsymbol{v} \leq \frac{\hbar}{2m}(2kk_1 - k^2) \; ; \tag{3.2a}$$

Let us now introduce Lindhard's variables z and u, Eqn. (2.9). Eqn. (3.2) becomes

$$d\sigma = \frac{e_1^2 \chi^2}{nmv^2} k_1 dk_1 \iint \frac{z\,dz\,du}{|z^2\varepsilon(z,u)|^2} \tag{3.3}$$

with boundaries on the integrals

$$uz \geq \tfrac{1}{4}(k_1^2/k_F^2 - 1) \tag{3.3a}$$

$$u + z \leq k_1/k_F \tag{3.3b}$$

$$u \leq v/v_F \; . \tag{3.3c}$$

Before analyzing (3.3), we also carry out the integration over k_1 in order to obtain the total cross section. This yields

$$\sigma = \int_{k_1 = \mathrm{Max}(k_F \cdot k_F(u+z))}^{k_F\sqrt{1+4uz}} d\sigma$$

$$= \frac{e_1^2 \chi^2 k_F^2}{2nmv^2} \iint \frac{z\,dz\,du}{|z^2\varepsilon(z,u)|^2} \{4uz \cdot \theta(1-u-z) + [1-(z-u)^2]\theta(u+z-1)\} \tag{3.4}$$

with the bounds

$$|z-u| \leq 1 \tag{3.4a}$$

$$0 \leq z \tag{3.4b}$$

$$0 \leq u \leq v/v_F. \tag{3.4c}$$

The integration region is the total accessible range for single-particle excitation; the term in the brackets of (3.4) is readily identified as $\frac{8}{\pi} z f_2(z,u)$ in the range $|z-u| < 1$. Therefore, (3.4) can be rewritten

$$\sigma = -\frac{4e_1^2 k_F^2}{\pi n m v^2} Im \int_0^\infty dz \int_0^{v/v_F} du \left(\frac{1}{\varepsilon(z,u)} - 1 \right). \tag{3.5}$$
$$|z-u| \leq 1$$

The stopping cross section S is a similar integral; it can be found by adding a factor

$$\hbar(\omega_1 - \omega_0) = \hbar \boldsymbol{k} \cdot \boldsymbol{v} = 2 m v_F^2 u z$$

in (3.5). Then,

$$(S)_{\text{Single Particle}} = \int \hbar(\omega_1 - \omega_0)\, d\sigma = -\frac{24\pi e_1^2 \hbar v_F}{m v^2} Im \int_0^\infty z dz \int_0^{v/v_F} u du \left(\frac{1}{\varepsilon(z,u)} - 1 \right) \tag{3.6}$$
$$|z-u| \leq 1$$

which is identical with Lindhard's expression[1] for the stopping cross section, except that the integration is restricted to single-particle excitations, $|z-u| \leq 1$. This was to be expected from the derivation procedure. The expression (3.6) has been studied extensively in ref. 2. The total cross section, Eqn. (3.5), can be evaluated in the same manner. A detailed study has been published recently.[8] Rather than evaluating that quantity separately, we go back to the differential quantity $d\sigma$, and mention some results concerning σ as a check on $d\sigma$ where appropriate.

Fig. 1a shows the area of integration in Eqn. (3.3) for a number of values of k_1/k_F. It is seen that the integral extends over a segment of the stripe $|u-z| \leq 1$; for $v > v_F$ the size of this segment is independent of v in the range of k_1-values limited by

$$1 \leq \frac{k_1}{k_F} \leq 2\frac{v}{v_F} - 1 \tag{3.7a}$$

and decreases towards zero in the range

$$2\frac{v}{v_F} - 1 \leq \frac{k_1}{k_F} \leq 2\frac{v}{v_F} + 1. \tag{3.7b}$$

For $v/v_F \leq 1$, the integration region depends on v for all values of k_1 (Figure 1b).

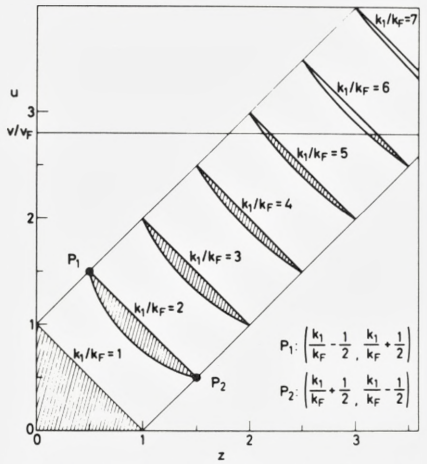

Fig. 1a. Limits of integration for Eqn. 3.3 in the (z,u) plane for $v > v_F$.

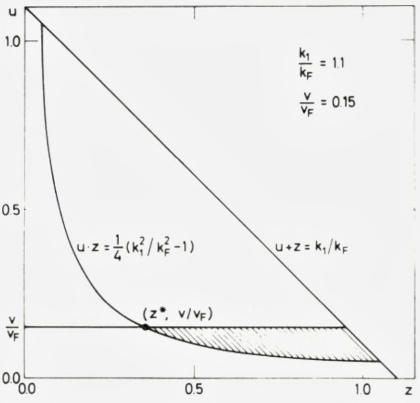

Fig. 1b. Limits of integration in the (z,u) plane for Eqn. 3.3 for $v < v_F$.

These relations provide a classification scheme for the evaluation of $d\sigma$ according to Eqn. (3.3). For practical purposes, it is convenient to include one more dimension in such a scheme, namely the role of the resonance point defined by[2]

$$\varepsilon(z_c, u_c) = 0; \quad u_c = z_c + 1 \tag{3.8}$$

The function $d\sigma$ will normally have a singularity at that value of k_1 where the point P_1 (Fig. 1a) passes through the resonance point (z_c, u_c). According to (3.3c), this is only possible for

$$v \geq u_c v_F \equiv v_c \tag{3.9}$$

Thus, v_c represents a "critical" velocity above which a singularity occurs in the excitation spectrum. From (3.8) and (2.11), we find u_c to obey the relation

$$(u_c - 1)^2 + \frac{\chi^2}{2}\left[1 - u_c \log\frac{u_c}{u_c - 1}\right] = 0. \tag{3.10}$$

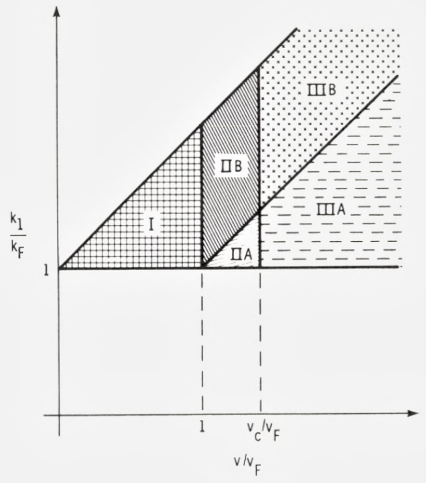

Fig. 2. Portion of (v,k_1) plane showing the classification scheme for projectile velocity and excitation k-vector. Region I, $0 < v < v_F$; region II, $v_F < v < v_c$; region III $v_c < v$.
The labels A and B indicate k_1-values for which the reduced integrated excitation spectrum, Eq. (3.22), is independent of v and dependent on v, respectively.

Now, we have three regions of particle velocity (Fig. 2). In region I, $v \leq v_F$, the integral in (3.3) depends on v, and the allowed range of k_1-values is

$$1 \leq k_1/k_F \leq 2\frac{v}{v_F} + 1 \,. \tag{3.11}$$

In region II, $v_F \leq v \leq v_c$, and region III, $v \geq v_c$, the integral (3.3) is independent of v for k_1-values in the range (3.7a), called A, and dependent on v in the range (3.7b), called B; in region III, $d\sigma$ has a singularity at

$$k_c = (2u_c - 1)k_F \,, \tag{3.12}$$

while such a singularity does not occur in region II (nor I).

The singularity in the excitation spectrum due to the resonance in $\varepsilon(z,u)$ at the point (z_c,u_c) results from the excitation of virtual plasmons with wave vector k_c and frequency $\omega_c = v_F k_c u_c$. These plasmons correspond to the shortest wavelength collective excitations which are supportable by the free electron gas.

A. *Analytical Approximation: Region I*

A simple analytic approximation is possible in region I in the limit of $v \ll v_F$. The area of integration in the $z-u$ plane as defined by Eqns. (3.3a-c) is indicated in Fig. 1b, and Eqn. (3.3) reads, to lowest order in v/v_F,

$$d\sigma_{\text{app}} \simeq \frac{e_1^2 \chi^2}{nmvv_F} k_1 dk_1 \int_{z^*}^{1} \frac{z dz}{|z^2 \varepsilon(z,0)|^2} \left(1 - \frac{z^*}{z}\right) \tag{3.13}$$

where

$$z^* = \frac{v_F}{4v} (k_1^2/k_F^2 - 1) , \tag{3.13a}$$

so that

$$d\sigma_{\text{app}} \simeq \frac{e_1^2}{2nmvv_F} k_1 dk_1 \left(\frac{1 - z^*}{\alpha^2 + \chi^2} + \frac{z^*}{\chi \cdot \alpha} \operatorname{arctg} \frac{z^* - 1}{\frac{\chi}{\alpha} + \frac{\alpha z^*}{\chi}} \right) \tag{3.14}$$

with

$$\alpha = \sqrt{1 - \chi^2/3} \tag{3.14a}$$

and

$$0 \leq z^* \leq 1 . \tag{3.14b}$$

In the evaluation of (3.14), the approximation $f_1(o,z) \simeq 1 - \frac{1}{3} z^2$ has been made.* The form (3.14) offers itself for introduction of the excitation energy above the Fermi energy

$$\varepsilon_1 = \frac{\hbar^2}{2m} (k_1^2 - k_F^2) . \tag{3.15}$$

Then

$$z^* = \frac{\varepsilon_1}{2mvv_F} \tag{3.16}$$

and

$$0 \leq \varepsilon_1 \leq 2mvv_F . \tag{3.17}$$

Integration over $d\varepsilon_1$ leads to

$$\int_{z^*=0}^{1} d\sigma_{\text{app}} = \sigma_{\text{app}} \simeq \frac{me_1^2}{2n\hbar^2\alpha^2} \left\{ \frac{\chi}{\alpha} \operatorname{arctg} \frac{\alpha}{\chi} - \frac{\chi^2}{\alpha^2 + \chi^2} \right\}, \tag{3.18}$$

an expression that can be obtained directly by evaluation of (3.4) in the limit

* This approximation is identical with the one used by Lindhard and Winther,[2] but differs from that used by Ritchie.[9]

$v/v_F \ll 1$. Eqn. (3.18) is equivalent with Ritchie's corresponding result (Ref. 9, Eqn. 6.15) when proper account is taken of the fact that his approximation for $f_1(u,z)$ leads to an $\alpha'^2 = 1-\chi^2/2$ in place of α^2 as given by our Eqn. (3.14a).[12]

Going back to the energy spectrum we write (3.14) in the form

$$d\sigma_{\text{app}} = \frac{e_1^2}{2n\hbar^2 v_F v} \frac{1}{(1+2\chi^2/3)} \cdot g\left(\frac{\varepsilon_1}{2mv_F v}\right) \tag{3.19}$$

where

$$g(z^*) = 1-z^*+z^*\left(\frac{\alpha}{\chi}+\frac{\chi}{\alpha}\right)\operatorname{arctg}\frac{z^*-1}{\frac{\chi}{\alpha}+\frac{\alpha z^*}{\chi}} \tag{3.20}$$

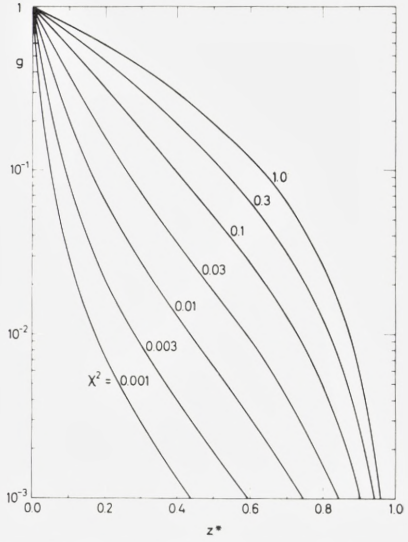

Fig. 3. Normalized low velocity excitation cross section, Eqns. (3.19) and (3.20).

has been plotted in Fig. 3. Note the very simple scaling properties as a function of the primary velocity $v(z^* \propto v^{-1})$. In particular, note that for a wide range of electron densities $(0.03 \leq \chi^2 \leq 0.3)$ the curves for g are almost linear on the semilogarithmic plot of Fig. 3. Figs. 4.a-c shows the ratio of the actual (numerically evaluated) cross section (3.3) and the analytical approximation formula (3.14′) for three different values of the density parameter χ^2, and three values of the ratio v/v_F. We conclude that for rough estimates, the analytical approximation will be satisfactory at all allowed values of the electron energy at values of v not too close to the Fermi velocity.

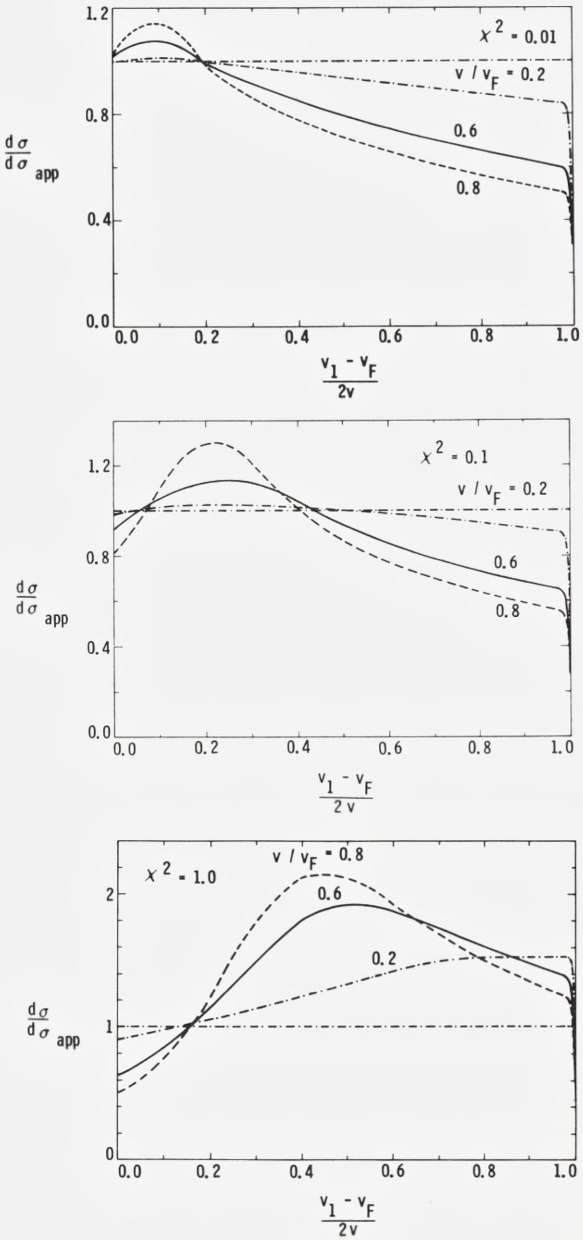

Fig 4. Excitation cross section normalized to the analytical approximation for low incident projectile velocities,
a) $\chi^2 = 0.01$,
b) $\chi^2 = 0.1$,
c) $\chi^2 = 1.0$.

B. *Analytical and Numerical Results: Region II & III*

For $v > v_F$, it is convenient to compare our results with the Rutherford cross section averaged over the Fermi distribution of initial electron velocities. This averaged cross section $d\sigma_R$ is found be setting $\varepsilon \equiv 1$. Eqn. (3.3) yields, then

$$d\sigma_R = \frac{2\pi e_1^2 e^2}{mv^2} \frac{d\varepsilon_1}{\varepsilon_1^2} g_1(\varepsilon_1) \tag{3.21}$$

with

$$g_1(\varepsilon_1) = \begin{cases} 1 & \ldots 0 \le \varepsilon_1 \le 2mv^2 - 2vp_F \\ \left(\frac{v}{v_F}\right)^3 + \frac{3}{16}\left(\frac{\varepsilon_1}{\varepsilon_F}\right)^2 \frac{p_F}{mv - p_1} + & \\ + \frac{1}{4}\left(\frac{\varepsilon_1}{\varepsilon_F}\right)^2 \frac{p_F(p_1 + 2p_F)}{(p_1 + p_F)^2} & \ldots 2mv^2 - 2vp_F \le \varepsilon_1 \le 2mv^2 + 2vp_F \\ 0 & \ldots \varepsilon_1 \ge 2mv^2 + 2vp_F \,. \end{cases} \tag{3.21a}$$

ε_1 is defined in (3.15), and

$$p_1 = \hbar k_1 \tag{3.21b}$$

$$p_F = \hbar h_F \,.$$

In the region where $g_1(\varepsilon_1) = 1$, (3.21) is identical with the conventional Rutherford spectrum for target electrons initially at rest except that the electron energy here is measured from ε_F. The smearing of the edge ($g \neq 1$) is then caused by the ground-state motion in the Fermi gas. The function $g_1(\varepsilon_1)$ has been plotted in Fig. 5 with the expression

$$x = \frac{\varepsilon_1 - (2mv^2 - 2vp_F)}{4vp_F} \tag{3.21c}$$

as the independent variable. It is seen that for $v > 2v_F$, this function is essentially independent of v.

In the more general case, we can write

$$\frac{d\sigma}{d\sigma_R} = \frac{3}{8}\left(\frac{\varepsilon_1}{\varepsilon_F}\right)^2 \iint \frac{z\,dz\,du}{|z^2 \varepsilon(z,u)|^2} \,, \tag{3.22}$$

where the Rutherford cross section $d\sigma_R$ is the expression (3.21) for $g_1 \equiv 1$. This form does not contain the velocity at all in regions IIA and IIIA, and is therefore a universal function of ε_1, dependent on the density parameter χ^2 only. In

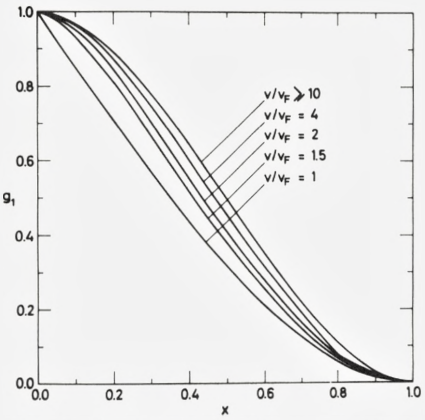

Fig. 5. Cutoff region for $d\sigma_R$, Eqns. (3.21) and (3.21a).

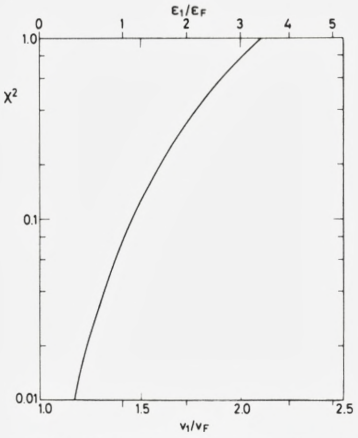

Fig. 7. Peak electron velocity (v_1/v_F) versus electron density, expressed by $\chi^2 = e^2/\pi\hbar v_F$, cf. eqn. (3.25).

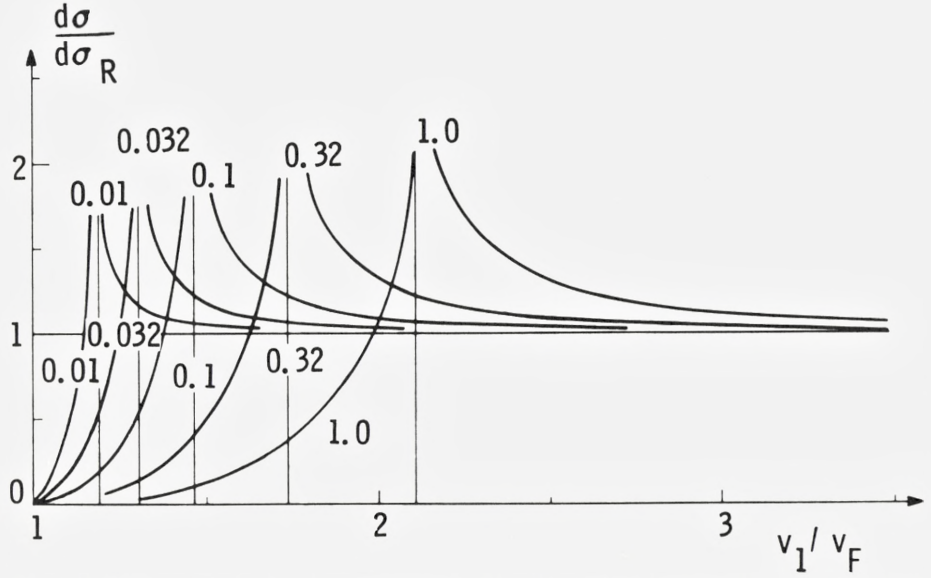

Fig. 6. Excitation cross section $d\sigma$, normalized to $d\sigma_R$, for a series of values of the electron density (cf. eqn. 3.22). For this plot $g_1 = 1$. The numerical integration has been performed by J. Schou.

regions IIB and IIIB, the universal function is to be multiplied by some function $g^1(\varepsilon_1, v; \chi^2)$, with $0 \leq g^1 \leq 1$ and g^1 monotonically decreasing with increasing ε_1. Moreover, for large v (region III) we must have

$$g^1(\varepsilon_1, v; \chi^2) \longrightarrow g_1(\varepsilon_1) \tag{3.23}$$

since $\varepsilon \longrightarrow 1$ at large z, i.e., large values of k.

Fig. 6 shows the expression (3.22), evaluated numerically for $v/v_F \gg 1$. Obviously, $d\sigma$ can be determined directly from Fig. 6 in the regions IIA and IIIA where $g_1 = 1$.

Fig. 6 shows that substantial ($\gtrsim 25\%$) deviations from straight Rutherford scattering occur at electron energies

$$\varepsilon_1 \lesssim 10\varepsilon_F , \tag{3.24}$$

the deviations being somewhat dependent on the density parameter χ^2. Most spectacular, of course, is the peak at the position

$$\varepsilon_{1c} = 4u_c(u_c - 1)\varepsilon_F , \tag{3.25}$$

following from (3.12), with u_c given by (3.10). This relation has been plotted in Fig. 7. It is seen that the peak position varies slowly with χ^2, and so does the detailed shape of the peak.

Ritchie et al.[7,8] have previously pointed out that the cross section $d\sigma/d\sigma_R$ is a universal function of ε_1, independent of projectile velocity, for $\varepsilon_1 \leq 2mv^2 - 2vp_F$,

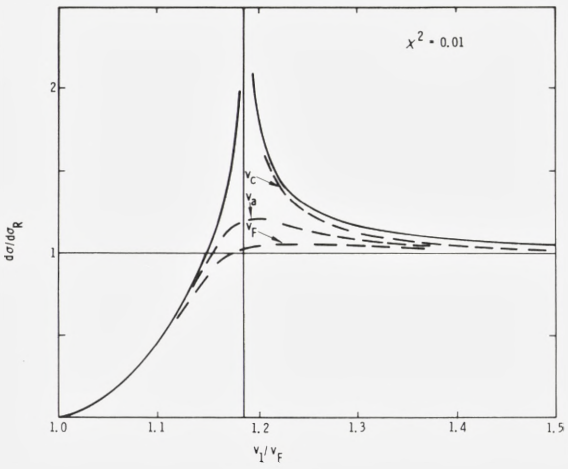

Fig. 8. Excitation cross sections, $d\sigma/d\sigma_R$, in region II. a) $\chi^2 = 0.01$, b) $\chi^2 = 0.1$, c) $\chi^2 = 1.0$.

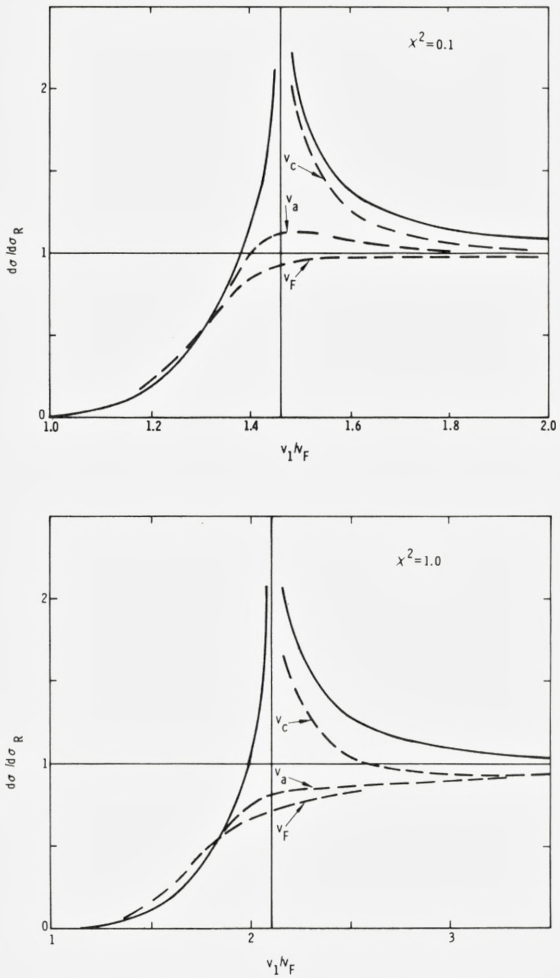

and have evaluated an expression similar to (3.22) for incident electrons. Their spectra also show a peaked behavior with the peak occurring at the position indicated by (3.25). *

Figs. 8a-c show electron spectra, evaluated numerically, and normalized to

*See, for example, Fig. 4 of the second paper of Ref. 7 where the value $r_s = 2.07$ corresponds to $\chi^2 = 0.343$.

Eqn. (3.21), i.e., including that region for which $g_1 < 1$. Curves are shown (dashed) for $v = v_F$, v_a, and v_c, where $v_a = (v_F + v_c)/2$. Also shown are the universal curves from Fig. 6 (solid). (Note the different horizontal scales on the various parts of Fig. 8). The velocity v_F is the boundary velocity between regions I and II, v_c is the boundary velocity between regions II and III, and v_a lies in the center of region II. For the more dense gases ($\chi^2 \leq 0.1$) the presence of a resonance is already noticed at $v = v_a$, although the singularity in the spectrum occurs only for $v \geq v_c$. Also, for these cases it is seen that with v in region III the actual cross section will differ by less than 10% from that determined from the universal curves (providing that the function g_1 is included in $d\sigma_R$). For $\chi^2 > 0.1$ at $v = v_c$, deviations $\sim 25\%$ are seen between $d\sigma/d\sigma_R$ and the universal curve; therefore v must be somewhat greater than v_c before the universal curve becomes an accurate representation of $d\sigma/d\sigma_R$. It should be noted, however, that these deviations are important only for region IIIB in which $d\sigma$ is a rapidly decreasing function of v_1.

4. Doubly Differential Cross Section

In this section, the full angular and energy distribution of excited electrons is analyzed on the basis of eqs. (3.1) and (3.1a). The procedure is very similar to the one sketched in Section 3. We first introduce spherical coordinates for both $\boldsymbol{k}$ and $\boldsymbol{k}_1$, with polar angles θ and θ_1 against $\boldsymbol{v}$ as the axis. Then, eqn. (3.1) reads

$$d^2\sigma = \frac{\chi^2 e_1^2 k_1\, dk_1\, d\eta_1}{2\pi n m v^2} \int \frac{z\,dz\,du\,d\varphi}{|z^2 \varepsilon(z,u)|^2} \cdot \delta\left(\cos\theta \cos\theta_1 + \sin\theta \sin\theta_1 \cos\varphi - \frac{k_F}{k_1}(z+u)\right) \tag{4.1}$$

where z, u, and χ^2 have been introduced in Eqns. (2.8) and (2.9), φ is an azimuth, and $\eta_1 = \cos\theta_1$. We also have

$$u = \frac{v}{v_F} \cos\theta\,, \tag{4.2a}$$

and the limit of integration (3.1a) reads

$$4zu \geq \frac{k_1^2}{k_F^2} - 1 \geq 0\,. \tag{4.2b}$$

The integration over φ can be carried out in (4.1), whereafter $d^2\sigma$ reads

$$d^2\sigma = \frac{\chi^2 e_1^2 k_1\, dk_1\, d\eta_1}{\pi n m v^2} \int \frac{z\,dz\,du}{|z^2 \varepsilon(z,u)|^2} \cdot \left\{(1-\eta^2)(1-\eta_1^2) - \left(\eta\eta_1 - \frac{k_F}{k_1}(z+u)\right)^2\right\}^{-1/2} \tag{4.3}$$

with the extra integration condition that the square root be real, i.e.,

$$(1-\eta_1^2)\left[1-\frac{k_F^2}{k_1^2}(z+u)^2\right] \geq \left[\eta-\eta_1\frac{k_F}{k_1}(z+u)\right]^2 \tag{4.4}$$

The condition (4.2a) provides a hyperbolic boundary for the integration in the $z-u$ plane, curve C_1 in Fig. 9, while condition (4.4) provides an elliptical

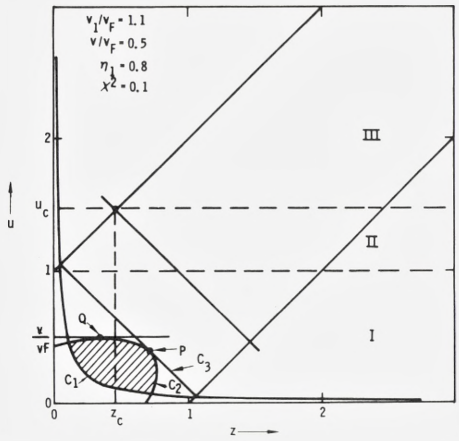

Fig. 9. Limits of integration for Eqn. 4.1 in the (z,u) plane. C_1 corresponds to Eqn. (4.1a), C_2 corresponds to condition (4.4), and C_3 corresponds to condition (3.3b) (Fig. 1).

boundary, curve C_2. We note that the ellipse is tangent to the line $z+u=v_1/v_F$ at point P and also to the line $u=v/v_F$ at point Q, and thus the integration area for $d^2\sigma$ lies *within* the integration area for $d\sigma$ (Fig. 1a), but is tangent to those boundaries. The points P and Q are given by

$$z(P)=\frac{v_1}{v_F}-\eta_1\frac{v}{v_F}, \quad u(P)=\eta_1\frac{v}{v_F} \tag{4.5a}$$

and

$$z(Q)=\frac{v_1}{v_F}\eta_1-\frac{v}{v_F}, \quad u(Q)=v/v_F\,. \tag{4.5b}$$

It is thus clear that the elliptical boundary determines the upper bound on the u-integration.

For fixed v, v_1, Eqns. (4.5a and b) indicate that the points P and Q move along their respective tangent lines as η_1 is varied. This motion is accompanied by rotation and change in magnitude of the axes of the ellipse so that from the standpoint of an observer stationed on either of the tangent lines the ellipse would

appear to roll along the tangent line as η_1 varies. This rolling motion allows the integration area to vary in such a way with η_1 so as to eventually cover the entire boundary region given in Fig. 1a). It is noted that for $\eta_1 = 1$ the points P and Q are identical and the integration area degenerates to a straight line. The cross section $d^2\sigma$ does not become zero in this case, however, because of the integrable singularity in the integrand.

The area of integration in Fig. 9 is only slightly smaller than that for $d\sigma$ (Fig. 1a) so long as P and Q are well separated and P remains within the two straight lines that bound the region of single-particle excitations, $u = z \pm 1$, i.e.,

$$2v\eta_1 - v_F \lesssim v_1 \lesssim 2v\eta_1 + v_F \tag{4.6a}$$

or

$$\frac{v_1 - v_F}{2v} \lesssim \eta_1 \lesssim \frac{v_1 + v_F}{2v}. \tag{4.6b}$$

The integration area decreases rapidly outside this range. An interesting special case, which depends on the form of $\varepsilon(z,u)$, is the position of the resonance. According to (3.12) it occurs at

$$k_c/k_F = 2u_c - 1 \ ;$$

in order to specify the angular region where a peak may be observed, we note that the integration area in Fig. 9 includes the resonance point (z_c, u_c), only when the point P coincides with the resonance point, i.e., according to (4.2)

$$\eta_c = v_F u_c / v \ . \tag{4.7}$$

However, because of the rolling movement of the ellipse one may expect the resonance to be broad as a function of η_1 at a given v_1/v_F in the region near η_c.

We now consider the case where the ellipse becomes tangent to the hyperbola at a single point, i.e., where the two points of intersection degenerate to one. In this case, the integration area has approached zero. This determines the bounds on electron velocity and ejection angle at a given primary velocity. Solving (4.2a) and (4.4) for u^2, and setting the discriminant equal to zero yields

$$\frac{v_1}{2v} - \frac{(2v + v_F)v_F}{2vv_1} < \eta_1 < \frac{v_1}{2v} + \frac{(2v - v_F)v_F}{2vv_1} \ . \tag{4.8}$$

For $v_1 > 2v - v_F$ the right hand side of (4.8) is greater than 1 and the upper bound on η_1 is 1 in this case. This relation is illustrated in Fig. 10. The reader may keep

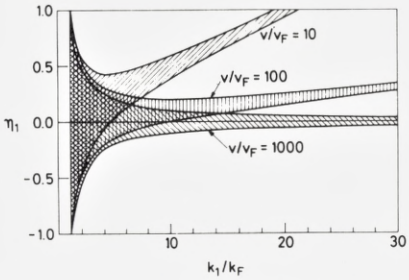

Fig. 10. Values of the excitation velocity, v_1, and cosine of the emission angle, η_1, which are allowed by conservation of energy and momentum.

in mind that it is based only on conservation laws as well as the Fermi distribution at zero temperature, while the dielectric function need not be specified. Thus, no spectral information is contained in Fig. 10 except that the intensity is zero outside the shaded area at any given velocity v.

A. *Analytical Approximation: Region I*

An analytical approximation is possible on Region I in the limit of $v \ll v_F$, as was the case for $d\sigma$. Ignoring u in comparison with z, and working in the (z,η) rather than the (z,u) — plane, we find from (4.3),

$$d^2\sigma = \frac{\chi^2 e_1^2 k_1\, dk_1\, d\eta_1}{\pi n m v v_F} \int \frac{z\,dz}{|z^2 \varepsilon(z,0)|^2} \cdot \int \frac{d\eta}{\sqrt{(1-\eta_1^2)(1-z^2)-(\eta-\eta_1)^2}} \tag{4.9}$$

where the area of integration corresponds to the one indicated in Fig. 9, but with the simplifying feature that the ellipse C_2 has its axes parallel to the diagonals on the (z,u) plane. Therefore, (4.9) reads

$$d^2\sigma = \frac{e_1^2 \chi^2}{\pi n m v v_F} k_1\, dk_1\, d\eta_1 \left\{ \pi \int_{z_+}^{1} \frac{z\,dz}{|z^2 \varepsilon(z,0)|^2} + \int_{z_-}^{z_+} \frac{z\,dz}{|z^2 \varepsilon(z,0)|^2} \arccos \frac{r - z\eta_1}{\sqrt{(1-\eta_1^2)(1-z^2)}} \right\} \tag{4.9a}$$

after integration, where

$$r = \frac{v_1 - v_F}{2v}, \tag{4.9b}$$

and z_- and z_+ represent the z coordinates of the upper and lower point of intersection, respectively, of the hyperbola and the ellipse as indicated in Fig. 9.

Again we approximate

$$z^2 \varepsilon(z,0) \rightarrow \alpha^2 z^2 + \chi^2$$

Fig. 11. Low velocity ($v \ll v_F$) values $d^2\sigma/d^2\sigma_{app}$ *vs* $r = (v_1 - v_F)/2v$ for several values of η_1, cf. eqn. (4.10) for $d^2\sigma_{app}$. a) $\chi^2 = 0.01$, b) $\chi^2 = 0.1$, c) $\chi^2 = 1.0$.

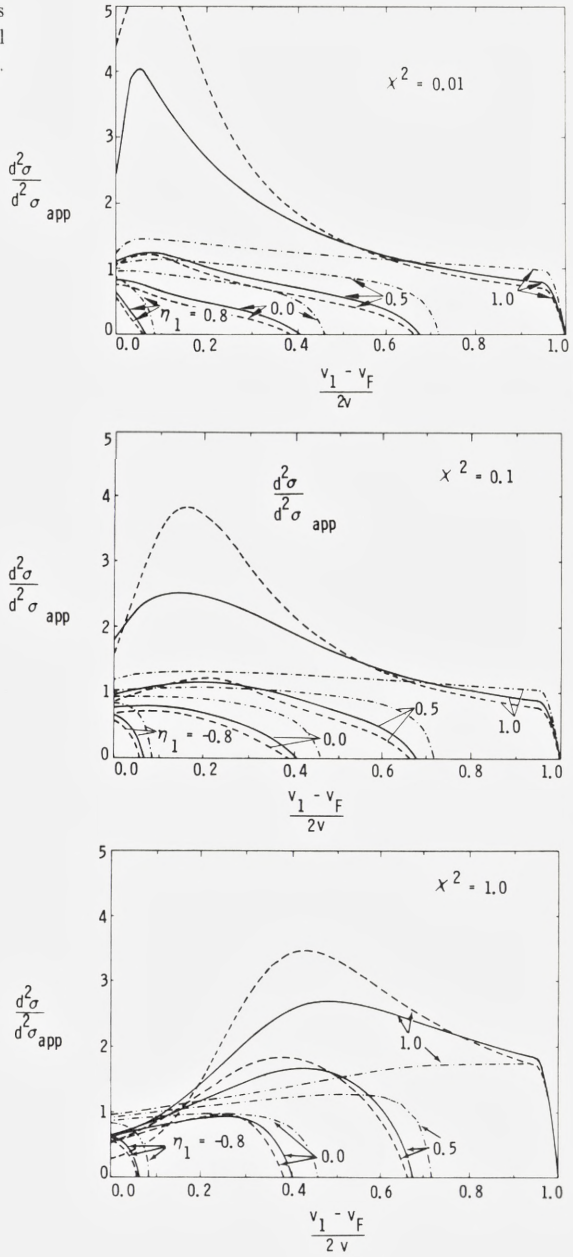

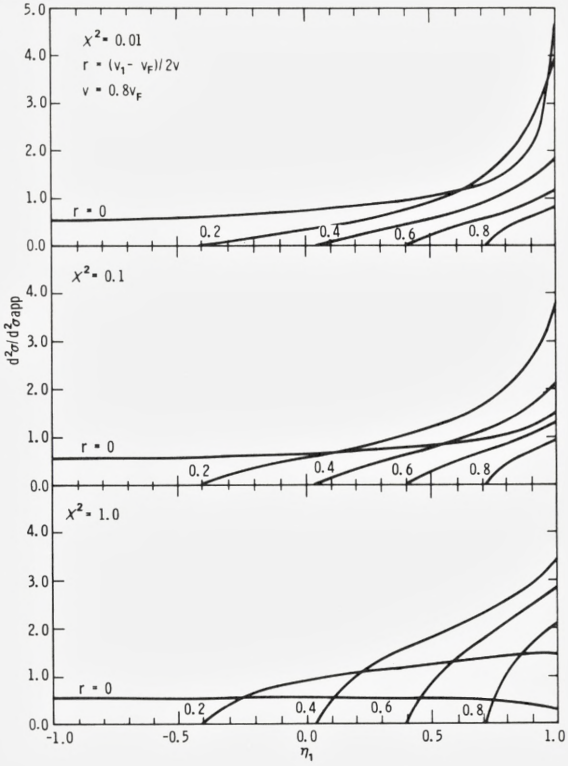

Fig. 12. Low velocity ($v \ll v_F$) values of $d^2\sigma/d^2\sigma_{\text{app}}$ *vs* η_1, for several values of $r = (v_1 - v_F)/(2v)$.

where α is given by (3.14a). Then, the integration in (4.9a) can be carried out. The resultant expression for $d^2\sigma$ is

$$d^2\sigma_{\text{app}} \simeq \frac{3\pi^2}{16} \frac{e_1^2 \hbar}{mv\varepsilon_F^2} \frac{d\varepsilon_1 \, d\eta_1}{(\alpha^2 + \chi^2)} [1 - g_2(r, \eta_1)] \tag{4.10}$$

for $-1 + 2r \leq \eta_1 \leq 1$; $r \leq 1$,

and where

$$g_2(r, \eta_1) = \frac{(\alpha^2 + 2\chi^2)r - \chi^2 \eta_1}{[(\alpha^2 r + \chi^2 \eta_1)^2 + \chi^2(\alpha^2 + \chi^2)(1 - \eta_1^2)]^{1/2}} . \tag{4.10a}$$

We note also that within this approximation ($v \ll v_F$)

$$\varepsilon_1 = 4\varepsilon_F r v / v_F , \tag{4.10b}$$

i.e., r is proportional to the excitation energy ε_1 above the Fermi level. Figs. 11a-c show spectra, evaluated numerically, normalized to the analytical approximations (4.9) for four different values of η_1, and three values of v/v_F. These curves are analogous to the integrated spectra in Figs. 4a-c, respectively. In Figs. 11, the three values of v/v_F are also 0.2, 0.6, and 0.8, corresponding to the dash-dot, solid, and dashed curves, respectively. The drop to zero on the leading edge of each spectrum occurs because $d^2\sigma_{\text{app}}$ does not go to zero at the right-hand boundaries indicated in Fig. 10, while the exact spectra do.

While the integrated spectra of Figs. 4 do not show large deviations from $d\sigma_{\text{app}}$, the doubly differential spectra of Figs. 11 show considerable departure from $d^2\sigma_{\text{app}}$ for both the forward and backward directions. Despite this, the approximate cross section, Eqn. (4.8), can be quite useful in obtaining spectra for other values of χ^2 by interpolation between curves such as those displayed in Figs. 11. For example, although the numerical values of the absolute cross section differ by more than two orders of magnitude for $\chi^2 = 1$ and $\chi^2 = 0.01$, the *relative* cross sections of Figs. 11a-c differ by a factor less than 2 for most values of η_1, r, and v. This is made particularly evident when angular distributions are compared as in Figs. 12a-c. We thus conclude that the approximate cross section, $d^2\sigma_{\text{app}}$, is quite useful in normalizing the spectra in region I, and that it may be acceptable for many purposes even for velocities v approaching the Fermi velocity.

B. *Analytical and Numerical Results: Regions II and III*

As in the case of the integrated cross section it proves convenient to compare the numerical results for $d^2\sigma$ with the Rutherford cross section, appropriately averaged over the Fermi sphere of initial electron velocities. This cross section $d^2\sigma_R$ is obtained from (4.1) when $\varepsilon = 1$. The resultant expression for $d^2\sigma_R$ is somewhat complicated, but it can be compactly written in terms of several characteristic energies associated with the excitation event. These are

$$\varepsilon_e = \tfrac{1}{2} m v_1^2 = \varepsilon_1 + \varepsilon_F \,, \tag{4.11a}$$

$$\varepsilon_p = \tfrac{1}{2} m v^2 \tag{4.11b}$$

$$\varepsilon_r = \varepsilon_p + \varepsilon_e - 2\eta_1 (\varepsilon_e \varepsilon_p)^{1/2} = \frac{m}{2} (\boldsymbol{v} - \boldsymbol{v}_1)^2 \tag{4.11c}$$

and

$$\varepsilon_0 = \varepsilon_p + \varepsilon_r - 2(\varepsilon_p \varepsilon_r)^{1/2} = \frac{m}{2} (v - |\boldsymbol{v} - \boldsymbol{v}_1|)^2. \tag{4.11d}$$

Here, ε_e is the kinetic energy of an excited electron and ε_p the energy of an electron at the projectile velocity, ε_r is the excited electron energy in a system moving with the projectile velocity, and ε_0 is the minimum energy an electron can have in order to be excited to the velocity v_1. The expression which results for $d^2\sigma_R$ is then

$$d^2\sigma_R = \frac{3\pi e_1^2 e^2 (\varepsilon_e \varepsilon_p)^{1/2} g_3(\varepsilon_e, \varepsilon_p, \varepsilon_0, \eta_1)}{4(\varepsilon_F \varepsilon_r)^{3/2}} d\varepsilon_e d\eta_1 \tag{4.12}$$

where

$$g_3 = \varepsilon_e(1-\eta_1^2)[(\varepsilon_e-\varepsilon_F)^{-2}-(\varepsilon_e-\varepsilon_0)^{-2}]-[1-\eta_1(\varepsilon_e/\varepsilon_p)^{1/2}][(\varepsilon_e-\varepsilon_F)^{-1}-(\varepsilon_e-\varepsilon_0)^{-1}]. \tag{4.13}$$

It can be shown that in the limit as $\varepsilon_F \longrightarrow 0$

$$d^2\sigma_R \longrightarrow d\sigma_R \cdot \delta(\eta_1 - v_1/2v)\ , \tag{4.14}$$

where $d\sigma_R$ is the expression given in (3.21) with $g_1 = 1$, and where proper account is taken in the limiting process of the fact that the cross hatched areas in Fig. 10 limit to straight lines as $\varepsilon_F \longrightarrow 0$. The cross section (4.12) can also be obtained by appropriately averaging the classical binary-encounter cross section (Ref. 13, eqn. 15) over a Fermi distribution of initial electron velocities.

The results in section 3 suggest that (4.12) should be an accurate description of $d^2\sigma$ for sufficiently large excitation energy, and comparison with numerically evaluated spectra bears this out. Figures 13a-c show such comparisons for $d^2\sigma$ as a function of electron velocity, v_1, at $\eta_1 = \eta_c$ as defined by (4.6). The projectile velocity, v, was selected for these calculations such that the values of η_c are 0.25, 0.5, and 0.75, for plots a) through c), respectively. These spectra correspond to Fig. 6 for the integrated cross section, $d\sigma$.

One notes that the width of the resonance is relatively independent of the location of the critical angle, and thus that the shape of the resonance is essentially independent of the projectile velocity, as long as v is greater than the critical velocity, v_c (Eqn. (3.9)). This property is further illuminated by the angular distributions one obtains at the critical excitation energy, ε_{1c}, Eqn. (3.25), as shown in Figs. 14a-c, respectively. There it is seen that the angular width of the singularity is almost independent of the projectile velocity. Fig. 15 shows the combined energy and angular dependence of the cross section in the (v_1, η_1) plane. It is nonzero in the cross hatched area defined by Fig. 10, above which is plotted $d^2\sigma/d^2\sigma_R$, for $\chi^2 = 0.1$. The singularity is indicated by the arrow at (x_c, η_c).

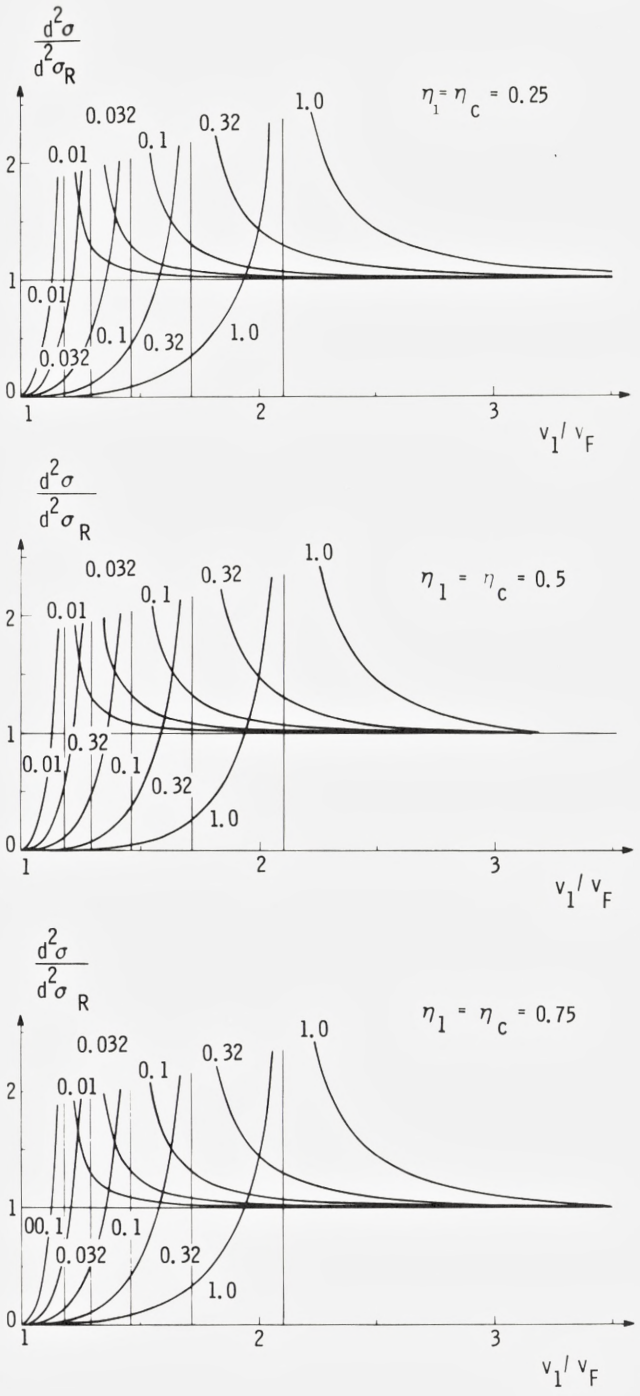

Fig. 13. Normalized double differential excitation cross sections, $d^2\sigma/d^2\sigma_R$, *vs* v_1/v_F for incident projectile velocities such that η_c = a) 0.25, b) 0.5, and c) 0.75.

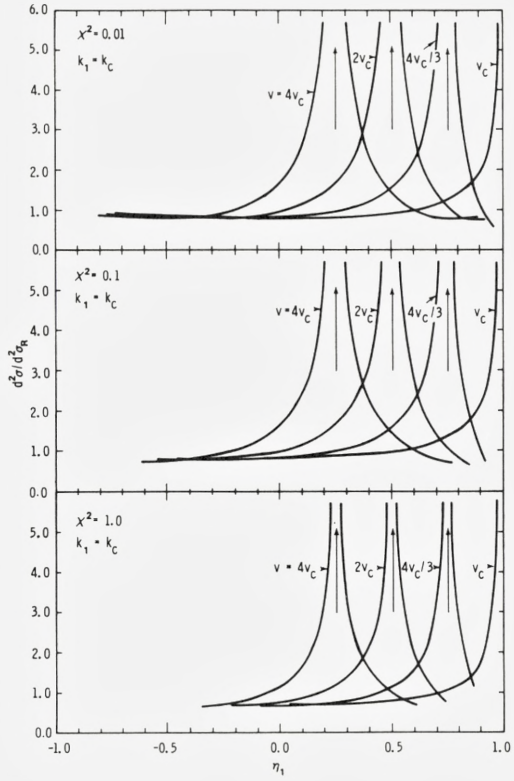

Fig. 14. Normalized double differential excitation cross sections, *vs* η_1 at the critical excitation energy. Incident projectile velocities are such that $\eta_c = 0.25$, 0.5, 0.75, and 1.0. a) $\chi^2 = 0.01$, b) $\chi^2 = 0.1$, c) $\chi^2 = 1.0$.

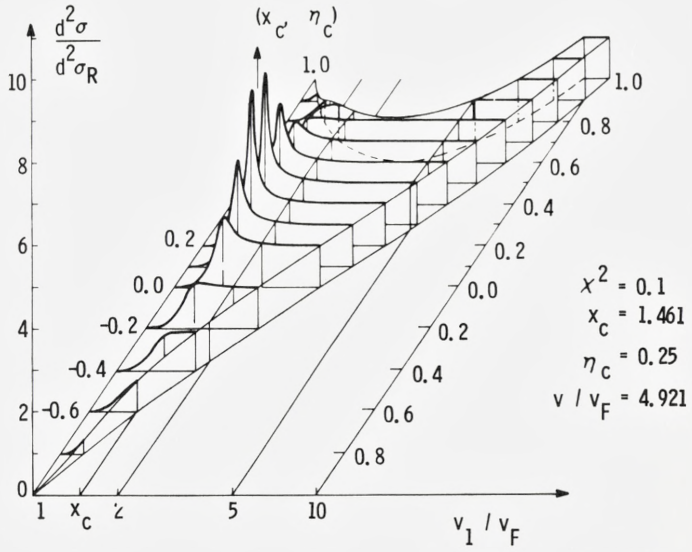

Fig. 15. Three dimensional plot of $d^2\sigma/d^2\sigma_R$ showing both the v_1 and η_1 dependence of the normalized cross section.

From Figs. 13, 14, and 15 it appears that qualitatively we may describe the relative cross section $d^2\sigma/d^2\sigma_R$ as the sum of two parts. One part increases slowly with excitation energy, ε_1, from zero at the Fermi surface to a value approximately equal to 1 for energies greater than ε_{1c}. The other contribution comes from the resonance whose location in the spectrum is determined by Eqns. (3.25) and (4.6), and the shape of which is essentially independent of projectile velocity. This qualitative description also indicates that relatively accurate cross sections can be extracted from Figs. 13 and 14, even for velocities below the critical velocity, by simply translating the angular distributions in η_1 so that the singularity falls at the location determined by (4.6). It should be noted that for $v < v_c$, (4.6) yields values of $\eta_c > 1$, so that the angular distributions are truncated in this case at a value of η_1 which is dependent on v.

5. Summary and Discussion

Single-particle excited-electron spectra have been calculated for heavy atomic projectiles penetrating a free-electron gas. The interactions among the electrons of the gas have been included through the dielectric function of Lindhard. The calculations have been carried out for a broad range of electron densities.

For low incident projectile velocities it proves possible to derive analytical approximations to both single and double differential spectra analogous to Lindhard's low-velocity approximation to the stopping power. The analytical expressions are reasonably accurate for incident velocities not too close to the Fermi velocity of the target electrons. Further, the analytical formulae form a convenient base for the normalization of numerical results, and simplify the process of interpolation between the results presented here.

The low-velocity spectra exhibit characteristic scaling properties expressed by Eqs. (3.19) and (4.10) for the single and double differential cross section, respectively. Apart from normalization, both spectra depend on the excitation energy through the variable

$$r = \varepsilon_1/(2mv_F v)\,, \tag{5.1}$$

and the cross section at $\varepsilon_1 = 0$ is proportional to the reciprocal projectile velocity. These relationships are well corroborated experimentally in low-velocity ion-atom collisions.[14] A more quantitative check on the details of the predicted spectra hinges on a proper averaging procedure over the electron density distribution of the collision partners according to the Thomas-Fermi principle, and is outside the scope of the present paper.

In the limit of very high projectile velocity, the electron spectra follow the laws of classical Coulomb scattering—due account being taken for the initial Fermi distribution of electron velocities—except for excitation energies of the order of the Fermi energy and below, where the behavior is influenced by the mutual interaction between the electrons. A characteristic feature is the occurrence of a resonance at a fixed excitation energy at $\sim$1-4 times the Fermi energy, dependent only on the density of the electron gas. Inspection of the double differential electron spectra shows that this resonance occurs at an ejection angle θ_c given by Eq. (4.7),

$$\cos \theta_c = u_c \cdot \frac{v_F}{v}, \tag{5.2}$$

the parameter $u_c (\sim 1.5)$ being determined by Fig. 7 as a function of electron density. It has been shown recently [15] that Eq. (5.2) can be interpreted as a preferential electron ejection in the direction of the Mach angle of the polarization wake[11,16,17] excited by the penetrating particle. The width of the resonance in energy and direction depends on the electron density, and turns out to be roughly proportional with the excitation energy at which the resonance occurs. In atomic systems, the resonance is expected to be broadened due to the finite volume of the atomic electron gas. Resonances of this type do not seem to have been identified experimentally so far.

With regard to predicted spectra for the case of the free Fermi gas, the limiting energies and angles of ejection are given by Fig. 10 as a function of electron velocity, and Figs. 5 and 6 determine the deviations of single differential spectra from straight Coulomb scattering. Similarly, Figs. 13a-c and 14a-c determine the corresponding deviation of the double differential cross section in energy and angular variables, respectively. Numerical tabulations are available.[18] The latter may become useful in particular for intermediate projectile velocities.

Acknowledgements

This work has been supported by a grant of the Danish Natural Science Research Council, which enabled one of us (DKB) to carry out the research reported here. DKB would also like to extend his appreciation to the faculty and staff of Physical Laboratory II of the H. C. Ørsted Institute of the University of Copenhagen for making his stay there an enjoyable and productive experience. Both authors would like to thank lic. scient. Jørgen Schou for assisting in part of the computational work.

References

1. J. Lindhard, Mat. Fys. Medd. Dan. Vid. Selsk. *28*, No. 8 (1954).
2. J. Lindhard and Aa. Winther, Mat. Fys. Medd. Dan. Vid. Selsk. *34*, No. 4 (1964).
3. J. Lindhard, and M. Scharff, Mat. Fys. Medd. Dan. Vid. Selsk. *27*, No. 15 (1953).
4. E. Bonderup, Mat. Fys. Medd. Dan. Vid. Selsk. *35*, No. 17 (1967).
5. See, for example, *Elementary Excitations in Solids* by D. Pines, W. A. Benjamin, New York (1963).
6. Radiation Research, Biomedical, Chemical and Physical Perspectives, O. E. Nygaard et al, editors, Academic Press (1975).
7. V. E. Anderson and R. H. Ritchie, IEEE Transactions of Nuclear Science *18*(6), 141 (1971); R. H. Ritchie, C. J. Tung, V. E. Anderson, and J. C. Ashley, Radiat. Research *64*, 181 (1975); C. J. Tung and R. H. Ritchie, Phys. Rev. B *16*, 4302 (1977).
8. C. J. Tung, R. H. Ritchie, J. C. Ashley, and V. E. Anderson, ORNL-TM-5188 (1976).
9. R. H. Ritchie, Phys. Rev. *114*, 644 (1959).
10. H. Esbensen, Thesis, University of Aarhus (1977).
11. Aa. Bohr, Mat. Fys. Medd. Dan. Vid. Selsk. *24*, No. 19 (1948).
12. Equation 6.15 in reference 9 contains a number of typographical errors (R. H. Ritchie, private communication). When these errors are corrected this equation is identical to our equation 3.18, apart from the different α-value as indicated in the text.
13. E. Gerjuoy, Phys. Rev. *148*, 54 (1966).
14. J. Østgaard Olsen and N. Andersen, private communication.
15. W. Schäfer, H. Stöcker, B. Müller, and W. Greiner, Z. Physik *A288*, 349 (1978).
16. N. Bohr, Mat. Fys. Medd. Dan. Vid. Selsk. *18*, no. 8 (1948).
17. J. Neufeld and R. H. Ritchie, Phys. Rev. *98*, 1632 (1955).
18. D. K. Brice, unpublished.

Indleveret til Selskabet juli 1979.
Færdig fra trykkeriet februar 1980.

Straggling in Energy Loss of Swift Hydrogen and Helium Ions in Gases

By F. BESENBACHER, H. H. ANDERSEN,
P. HVELPLUND, *and* H. KNUDSEN

Det Kongelige Danske Videnskabernes Selskab
Matematisk-fysiske Meddelelser **40**:9

Kommissionær: Munksgaard
København 1981

Synopsis

Straggling in energy loss for 40-keV to 1-MeV hydrogen ions and 100-keV to 2.4-MeV helium ions in a variety of atomic and molecular gases has been measured with an accuracy of 5–7 %. When straggling data for hydrogen and helium penetrating the same monatomic gas are compared, significant deviations from the Z_1^2 scaling contained in the Bohr expression for energy straggling Ω_B^2 are observed. These deviations are explained by an atomic correlation term stemming from the bunching of electrons into atoms and by an additional straggling term Ω_C^2 resulting from charge-state fluctuations. It is shown that the importance of charge-exchange straggling has been substantially overestimated in the past. For hydrogen ions penetrating heavy monatomic gases, the straggling increases with increasing energy and approaches the high-energy Bohr limit, in agreement with theory. The qualitative agreement between these hydrogen results and the electron-gas calculations by Bonderup and Hvelplund and by Chu is, however, markedly improved by inclusion of the atomic correlation term. For hydrogen and helium targets, an excess over the Bohr value, caused by finite values of the electron velocities compared to that for the projectile, is observed at velocities, where the electronic stopping power has its maximum. For molecular gases, a further increase in straggling is seen, caused by bunching of atoms into molecules, which leads to a further increase in the fluctuations of the number of collisions with electrons.

Institute of Physics, University of Aarhus
DK-8000 Aarhus C, Denmark.

Printed in Denmark by Bianco Lunos Bogtrykkeri A/S. ISSN 0023-3323. ISBN 87-7304-113-0.

Contents

§ 1. Introduction

When an initially monoenergetic ion beam penetrates matter, the average energy loss is accompanied by a spreading of the energy of the ion beam due to the statistical nature of the collision processes. A measure of this energy broadening is given by the mean-square deviation Ω^2 of the resulting energy-loss distribution, also known as the energy straggling.

While the average energy loss per path length, the so-called stopping power, of energetic hydrogen and helium ions has been extensively studied and can be predicted to within 3–10 % for all elements from recent tabulations (Andersen and Ziegler (1977) and Ziegler (1978)), the straggling in energy loss has received much less attention, probably because straggling measurements involve more experimental complications than do stopping-power measurements, and most of the published experimental straggling results are thus rather uncertain. However, as Rutherford-backscattering and nuclear-reaction analysis have become important microanalytical techniques for discerning atomic mass, resolving depth, and perceiving crystalline structure of the near-surface region of materials, precise data on energy straggling are desirable since electronic energy-loss straggling is indeed one of the main features limiting the depth resolution of both these ion-beam-analysis teckniques.

The fact that the majority of experimental straggling results have been obtained using solid targets has obscured our understanding and description of the straggling processes since specific solid-state effects stemming from target inhomogeneities such as nonuniform film thickness, porosity, surface contamination, and crystal structure can obscure the measured straggling in an uncontrolable way. Measurements with gaseous targets provide a much better basis for quantitative comparison between theory and experiment, and we have therefore performed an accurate, systematic investigation of the straggling in energy loss for hydrogen and helium ions on a variety of atomic and molecular gases (H_2, He, N_2, O_2, CO_2, Ne, Ar, Kr, and Xe) at ion energies of 40 keV $\lesssim E_H \lesssim$ 1 MeV and 100 keV $\lesssim E_{He} \lesssim$ 2.4 MeV.

The present paper belongs to a series of three, which describes the results of an experimental study of the penetration of swift hydrogen and helium ions through gases [Besenbacher (1977)]. The stopping-power results and a detailed discussion of the experimental setup was presented in the first paper [Besenbacher et al. (1979)], hereinafter referred to as I. In the second paper [Besenbacher et al. (1980)], referred to as II, a comprehensive discussion of the theoretical descrip-

tion of straggling in energy loss of energetic hydrogen and helium ions was presented. The present paper deals mainly with a presentation of the experimental straggling results, some of which have been published in a recent letter [Besenbacher et al. (1977)] and in II.

Following a review of the theory of electronic energy straggling for light, swift ions in § 2, we shall give a brief description of the experimental procedure and data treatment in § 3 together with a discussion of how the measured straggling results are influenced by the small contribution from nuclear collisions. Finally, in § 4, the experimental results are presented and discussed in connection with a comparison with theory.

§ 2. Theory

A general description of the statistical nature of the energy-loss processes in targets with randomly distributed atoms has been given by Bohr (1948). For a monoenergetic beam suffering, an energy loss, which is small compared to the initial energy (the thin-absorber approximation), Bohr divided up the collisions of the projectile into various types of processes i, each one corresponding to a small interval of energy transfer $(T_i, T_i + dT_i)$. If n_i denotes the fluctuating number of processes of type i, the average energy loss and the average square fluctuation in energy loss is given by

$$\overline{\Delta E} = \sum_i \overline{n_i} T_i = N \Delta R \int d\sigma(T) = N \Delta R S \tag{1}$$

and

$$\Omega^2 = \overline{(\Delta E - \overline{\Delta E})^2} = \sum_i \overline{(n_i - \overline{n_i})^2} T_i^2 = \sum \overline{n_i} T_i^2 = N \Delta R \int d\sigma(T) T^2 \tag{2}$$

Here, $N\Delta R$ is the target density, $d\sigma$ is the cross section for an energy transfer T, and S is the stopping cross section. The two important assumptions underlying Eqs. (1) and (2) are that processes of different type are statistically independent and that the number of processes of a given type follows Poisson statistics.

As argued by Bohr (1948) and Vavilov (1957), the energy-loss distribution is expected to be a Gaussian provided all the individual contributions to the energy loss are small compared to Ω, i.e., $\Omega \gtrsim 3T_{max}$, where T_{max} is the maximum energy transfer in a single collision with a free electron. This inequality, together with the requirement that $\Delta E \ll E$, leads to the following condition on the target density,

$$E/S \gg N \Delta R\,[\text{atoms/cm}^2] \gtrsim 2 \times 10^{20} \frac{1}{Z_2} \left(\frac{E[\text{MeV}]}{Z_1 M_1 [\text{amu}]} \right)^2, \tag{3}$$

where Z_1, M_1, and E denote the atomic number, mass, and energy of the projectile and Z_2 the atomic number of the target atoms. This requirement defines a broad, experimentally accessible and interesting region, in which comparison between experimental data and theoretical results is most easily performed since the resulting Gaussian energy-loss distribution is characterized by $\overline{\Delta E}$ and Ω only. The general case, for which the inequalities in Eq. (3) are not necessarily fulfilled, has been treated by Bohr (1948) and, in particular, by Williams (1929), Landau (1944), Vavilov (1957), and Tschaläar (1968). In the limit of very thin ($\Omega \ll T_{max}$) and very thick ($\Delta E \sim E$) absorbers, highly asymmetric energy-loss distributions are obtained.

For the light, swift ions considered in this experiment, the slowing-down is mainly caused by collisions with electrons. Assuming as a first approximation that all the target electrons contribute to the straggling as free electrons initially at rest, we may insert in Eq. (2) as the differential cross section the Thomson formula for the scattering of a projectile with velocity v by a free electron,

$$d\sigma = -\frac{2\pi Z_1^2 e^4}{mv^2}\,\frac{dT}{T^2}\,, \tag{4}$$

where $-e$ and m denote the charge and mass of the electron. As opposed to the calculation of the average energy loss, the Rutherford cross section may provide a reasonable approximation to be used in the calculation of energy straggling since this quantity is dominated by the more violent collisions, for which atomic binding and screening are less important. By inserting Eq. (4) into Eq. (2), we obtain Bohr's remarkably simple nonrelativistic high-energy limit,

$$\Omega^2 = \Omega_B^2 = 4\pi Z_1^2 e^4 Z_2 N \Delta R\,. \tag{5}$$

So far, the orbital velocities v_e of the electrons have been completely neglected as compared to the projectile velocity v. For small but finite values of v_e/v, a correction term to the simple Bohr formula appears, and in the quantal-perturbation limit $v \gg 2Z_1 v_0$, where $v_0 = e^2/\hbar$, the following formula is obtained [Fano (1963)],

$$\frac{\Omega_F^2}{\Omega_B^2} = 1 + \frac{\frac{1}{Z_2}\,S(1)}{mv^2}\log\frac{2mv^2}{I_1}\,. \tag{6}$$

Here, the average excitation energy I_1 is given in terms of the atomic dipole oscillator strengths f_{0i} and the corresponding transition frequencies ω_{0i} by

$$\log I_1 = \frac{\sum_i f_{0i}\hbar\omega_{0i}\log\hbar\omega_{0i}}{\sum_i f_{0i}\log\hbar\omega_{0i}}\;;\;\sum_i f_{0i} = Z_2\,, \tag{7}$$

while the parameter S(1) defined as the zero moment over the dipole oscillator-strength distribution according to Fano (1963) can be written as

$$S(1) = \sum_i \hbar\omega_{0i} f_{0i} = \frac{2m}{3} < \left| \sum_i v_i \right|^2 >_0 , \tag{8}$$

where v_i is the velocity of the i'th atomic electron and $< >_0$ denotes the ground-state expectation value. The validity of Eq. (8) is discussed in some detail in Sec. 4.3.

As the velocity of the projectile decreases, the velocity of the inner electrons may even exceed the projectile velocity, especially for heavy substances. According to Bohr (1948), an approximate way of accounting for the straggling in this situation is to neglect the contribution to the straggling from the inner electrons and replace the total electron density NZ_2 in Eq. (5) by the density of electrons with velocities lower than v. For this density, Bohr inserted the value $N(v_e < v) \sim NZ_2^{1/3}(2v/v_0)$, and at lov velocities, this implies a significant reduction in the straggling compared to the Bohr value.

Bohr's treatment was improved by Lindhard and Scharff (1953). They treated the target as a collection of free electron gases, and the straggling pertaining to an atom was obtained as an average over the electron cloud of the straggling $\Omega^2(\varrho, v)$ for a gas of constant density ϱ (see Eq. (7) in II). In order to calculate $\Omega^2(\varrho, v)$, the electron cloud of the target atom is divided into an outer and an inner region, where the outer electrons are roughly those corresponding to a local Fermi velocity lower than v. Assuming that the contributions from the outer and inner electrons are given by the asymptotic expressions for an electron gas and using the Bohr model for the atomic density $\varrho(r)$, Lindhard and Scharff (1953) arrived at the following formula,

$$\frac{\Omega^2_{LS}}{\Omega^2_B} = \begin{cases} \dfrac{L(x)}{2} & \text{for } x \lesssim 3 \\ 1 & \text{for } x \gtrsim 3 \end{cases} . \tag{9}$$

Here, x is a reduced energy variable, $x = (v/v_0)^2/Z_2$, and L(x) is defined in terms of the electronic stopping cross section through the relation

$$S_e = \frac{1}{N}\left(-\frac{dE}{dR}\right) = \frac{4\pi Z_1^2 e^4}{mv^2} Z_2 L(x) . \tag{10}$$

Bonderup and Hvelplund (1971) have refined the Lindhard-Scharff model by using a more accurate expression for the straggling contributions from the various parts of the electron cloud and the more realistic Lenz-Jensen model for the atomic-electron density. Similar calculations with Hartree-Fock-Slater elec-

tron densities have been performed by Chu (1976). These calculations were based on the following expression for $\Omega^2(\varrho,v)$, (Bonderup and Hvelplund (1971)).

$$\frac{\Omega^2_{BH}(\varrho,v)}{\Omega^2_B} = \begin{cases} 1+\left[\frac{1}{5}\left(\frac{v_F}{v}\right)^2+\frac{\hbar\omega_0}{2mv^2}\right]\log\left(\frac{v}{v_F}\right)^2; & v \gtrsim v_F \quad (11a) \\ (1+13\chi^2)^{-1/2}\left(\frac{v}{v_F}\right)^2; & v \lesssim v_F\,, \quad (11b) \end{cases}$$

where $v_F(\varrho)$ is the local Thomas-Fermi velocity, $\omega_0(\varrho)$ is the local plasma frequency, and $\chi^2 = v_0/\pi v_F$ is a dimensionsless quantity proportional to the third root of the density. The term with the plasma frequency stems from resonance collisions due to collective excitations, but the main contribution in the limit $v \gtrsim v_F$ comes from single-particle collisions.

However, as pointed out by Bonderup and Hvelplund (1971) and discussed in greater detail in II, it is important to realize that, within the Lindhard-Scharff (LS) model, the projectile-electron excitations are assumed to lead to the same basic, statistically independent excitations in the atom as in the electron gases by means of which the electron cloud is described. In a real atomic gas target, the electrons are bunched into atoms, leaving part of the space empty. This spatial correlation of the atomic electrons leads to stronger fluctuations in the number of collisions with electrons and thus to an increase in energy straggling. A similar type of correlation results when the target is a dilute gas of diatomic molecules. In this case, the electrons are not only bunched into atoms, but the atoms are also bunched together into molecules, leading to a further increase of the fluctuation in the number of collisions with electrons. These molecular correlation effects have been discussed extensively by Sigmund (1976, 1978) from a somewhat different point of view. Another type of correlation effect may stem from charge-state fluctuations in a gas target, when the charge of the ion fluctuates in such a manner that a given charge state persists during several ion-atom collisions. Since the energy loss depends on the charge state, the losses in successive collisions with atoms become correlated, and an additional straggling contribution Ω^2_B results. Spatial and charge-state correlations were discussed in detail in II, and only the main results will be stated here.

As shown in II, the straggling for a light, swift ion colliding with an atom, which contains many electrons, can, if charge-state fluctuations are neglected, be written as

$$\Omega^2 = \Omega^2_{LS} + \Omega^2_A \quad (12)$$

with the atomic correlation term Ω^2_A given by

$$\Omega^2_A = N\Delta R \int d^2\boldsymbol{p}\,[\varepsilon(\boldsymbol{p})]^2\,. \quad (13)$$

Here, $\varepsilon(\boldsymbol{p})$ is the average energy loss to an atom at fixed impact parameter with respect to the nucleus. In II, it was found convenient to introduce an atomic area,

$$\pi r_A^2 = \frac{[\int d^2\boldsymbol{p}\varepsilon(\boldsymbol{p})]^2}{\int d^2\boldsymbol{p}[\varepsilon(\boldsymbol{p})]^2}, \tag{14}$$

such that Eq. (14) can be written as

$$\Omega_A^2 = N\Delta R\frac{S^2}{\pi r_A^2}. \tag{15}$$

Equation (12) reduces to the Lindhard-Scharff expression in the high-velocity limit, where the probability for electron excitation is small. In the opposite extreme to the LS limit, i.e., at sufficiently low projectile velocities, the penetration of the atom leads to the excitation of several electrons. For a fixed impact parameter, the fluctuation in energy loss may then be neglected, and the entire straggling derives from the statistical distribution of impact parameters, i.e., is given by Eq. (13).

For heavy ions at low velocities, $v < v_0 Z_1^{2/3}$ (v_0 is the Bohr velocity), Firsov (1959) has calculated $\varepsilon(\boldsymbol{p})$ within a Thomas-Fermi treatment. Inserting the Firsov result $\varepsilon_F(\boldsymbol{p})$ in Eq. (13), we get the entire straggling for heavy ions in this low-velocity limit (Hvelplund (1971) and II).

$$\frac{\Omega_{HF}^2}{N\Delta R} = \int_0^\infty \varepsilon_F^2(p)2\pi p dp = (Z_1+Z_2)^{8/3}\left(\frac{v}{v_0}\right)^2 8\times 10^{-15}\,eV^2cm^2/atom. \tag{16}$$

For hydrogen and helium ions, on the other hand, a detailed knowledge of $\varepsilon(\boldsymbol{p})$ is still lacking, and this complicates a calculation of the atomic area πr_A^2, and thereby of the atomic correlation term Ω_A^2. However, as discussed in some detail in II, simple estimates based on the Lindhard-Scharff model [Lindhard and Scharff (1953), Lindhard and Winther (1964), and Bonderup (1967)], for energy loss show (i) that πr_A^2 depends only weakly on Z_2, (ii) that for energies around the stopping-power maximum where Ω_A^2 has its maximum value, πr_A^2 is $\sim 8\text{-}10\pi a_0^2$ (a_0 is the Bohr radius) and (iii) that the energy dependence of πr_A^2 is probably rather weak. In II it was therefore tentatively suggested that the simple formula (15) with an atomic area $\pi r_A^2 \simeq 10\pi a_0^2$ may account for the increase in straggling for an atomic-gas target due to the bunching of the electrons. This suggestion is supported at least for protons and α particles by comparison with the comprehensive set of straggling results presented here, a fact that will be discussed in detail in § 4.1.

If, instead, the projectile penetrates a target of homonuclear diatomic mole-

cules with internuclear distance d, the total straggling is obtained by adding to Eq. (12) a further correlation term Ω_M^2, which results from the bunching of the atoms into molecules. For the simple case, where the molecular axis is aligned with respect to the beam axis, the molecular term Ω_M^2 equals Ω_A^2. A misalignment reduces the molecular term, and a simple geometrical argument presented in II as well as a more refined calculation [Sigmund (1976)] yields the following molecular correlation term,

$$\Omega_M^2 = \begin{cases} N\Delta R \dfrac{S^2}{2\pi d^2}, & d \gg r_A \qquad (17a) \\ \Omega_A^2 = N\Delta R \dfrac{S^2}{\pi r_A^2}, & d < r_A \qquad (17b) \end{cases}$$

Concerning the straggling contribution stemming from charge-state fluctuations, the discussion will be restricted to target thicknesses, for which several charge-changing collisions occur, and to cases where only two charge states q_1 and q_2 are important. This is the situation for helium ions at the energies and target thicknesses used in the present work. If S_1 and S_2 denote the stopping cross section for the projectile in the two charge states and α is the fractional time spent in charge state 1, the average-square fluctuation in ΔE due to fluctuations in α is given by

$$\Omega_C^2 = (N\Delta R)^2 (S_1 - S_2)^2 (\overline{\alpha^2} - \bar{\alpha}^2) . \qquad (18)$$

The average-square fluctuations in α is determined by the capture and loss cross sections σ_{12} and σ_{21}, and a calculation presented in II yields

$$\Omega_C^2 = N\Delta R \, (S_1 - S_2)^2 \frac{2\sigma_{12}\sigma_{21}}{(\sigma_{12} + \sigma_{21})^3} . \qquad (19)$$

This result is similar to that stated by Vollmer (1974) and by Efken et al. (1975).

§ 3. Experimental procedure and data treatment

In the present work, an extensive investigation of energy loss and straggling in energy loss for hydrogen ions of 40-keV to 1.5-MeV energy and helium ions of 100-keV to 2.4-MeV energy penetrating thin layers of various gases (H_2, He, N_2, CO_2, O_2, Ne, Ar, Kr, Xe) has been carried out.

Since details of the experimental procedure and data treatment were presented in I, only a brief description will be given here.

A magnetically analyzed hydrogen or helium beam passes through a differentially pumped, 504-mm long gas cell via 0.2-mm diameter apertures. For energies below 300 keV, measurements were performed at a 400-kV Van de Graaf accelerator and a 100-kV electromagnetic isotope separator. The energy-degraded beam was energy-analyzed by means of an electrostatic analyzer and detected

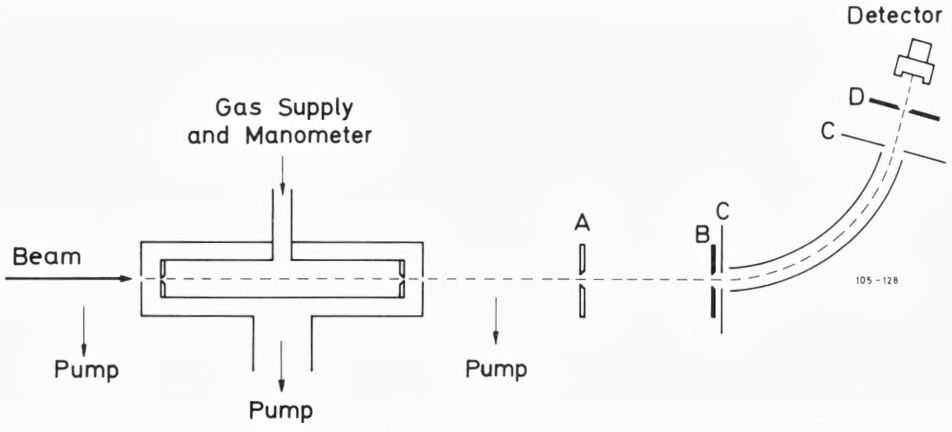

Fig. 1: Experimental setup used at the 400-kV Van de Graaff accelerator and at the 100-kV isotope separator.

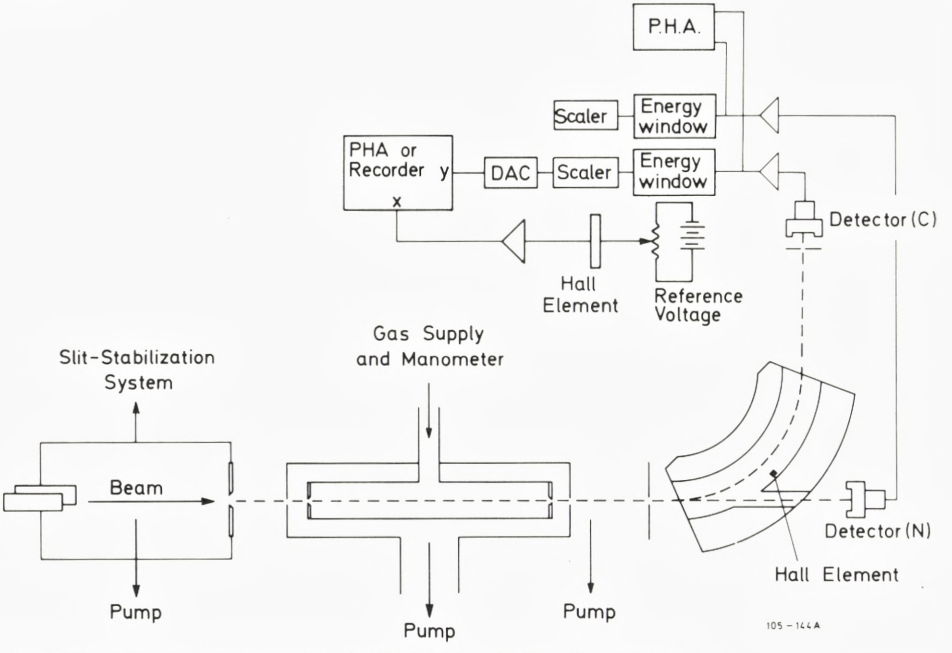

Fig. 2: Experimental setup used at the 2-MV Van de Graaff accelerator.

by a standard Si surface-barrier detector, as shown in Fig. 1. The energy-loss distributions were measured by sweeping the beam across the exit aperture D by means of the electrostatic analyzer. In this way, the beam intensity is averaged in time, and no beam normalization is needed. For energies above 200 keV, measurements were performed at a 2-MV Van de Graaff accelerator, and the beam transmitted through the gas cell was momentum-analyzed, using a double-focussing sector magnet, and detected by a solid-state detector (Fig. 2). Detector N counted neutrals and was used for normalization. Thus fluctuations in the beam current did not influence the measurements. The use of energy-dispersive detectors allowed elimination of beam contamination and slit-edge-scattered particles. The pressure in the gas cell was measured with a membrane manometer, and the pressure was kept stable within less than 1 % via a motor-driven, servo-controlled needle valve. The purity of all gases used was better than 99.5 %.

In all cases except for hydrogen ions penetrating H_2 at energies above 200 keV, the gas-cell pressure ($0.1 \lesssim P_G \lesssim 2$ torr) was chosen to satisfy the inequalities (3), which give Gaussian energy-loss distributions. This was confirmed experimentally by plotting the distribution on graph paper with a cumulative Gaussian scale, as shown by the example given in Fig. 3.

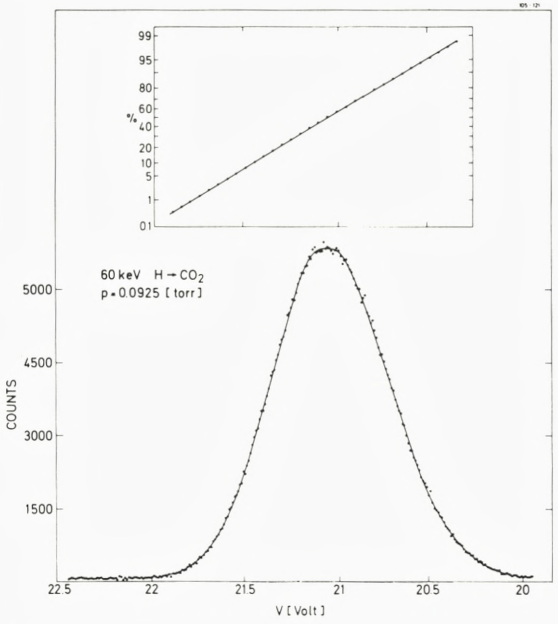

Fig. 3: Energy distribution of an incident 60-keV H^+ beam after it emerges from a 1.51×10^{17} molecules/cm^2 CO_2 layer. The main part of the distribution is plotted on probability paper, from which it is concluded that the energy-loss distribution is Gaussian.

From the measured energy-loss or momentum distribution, the average energy loss and the standard deviation are easily obtained as

$$\overline{\Delta E} = E_i - \frac{E_1 + E_2}{2} \tag{20}$$

and

$$\Omega_E = \frac{E_1 - E_2}{2\sqrt{2\log 2}} \tag{21}$$

where E_i is the incident energy and E_1 and E_2 are the energies corresponding to the half-maximum positions for either the momentum or the energy-loss distribution. The energy spectra obtained with no target gas were also approximately Gaussian with a mean-square deviation Ω_i, corresponding to an energy resolution (FWHM/E_i) of 0.74 % and 0.10 % for the electrostatic and the magnetic analyzers, respectively. Consequently, the straggling can be obtained from the formula

$$\Omega^2 = \Omega_E^2 - \Omega_i^2 \,. \tag{22}$$

In all the cases reported here, Ω_i is small compared to Ω_E. The target density $N\Delta R$ in molecules/cm^2 is calculated from Eqs. (15) and (16) in I, and the straggling parameter $\Omega^2/N\Delta R$ is assigned to the mean energy $E_{av} = E_i - \Delta E/2$.

For asymmetric energy distributions, which were found only for hydrogen penetrating H_2 at energies $E \gtrsim 200$ keV, the moments $M_1 = \overline{\Delta E}$ and $M_2 = \Omega^2$ were found by numerical integration of the energy-loss distribution $W(\Delta E)$ according to

$$M_1 = \frac{\int_0^\infty \Delta E\, W(\Delta E)\, d(\Delta E)}{\int_0^\infty W(\Delta E)\, d(\Delta E)} \tag{23}$$

$$M_2 = \frac{\int_0^\infty (\Delta E - \overline{\Delta E})^2\, W(\Delta E)\, d(\Delta E)}{\int_0^\infty W(\Delta E)\, d(\Delta E)} \tag{24}$$

To verify that the straggling Ω^2 is proportional to the target density $N\Delta R$, Ω^2 was plotted versus $N\Delta R$ for different energies and gases, and a typical example is shown in Fig. 4.

In the present energy region, it is not possible to correct in a simple way the measured straggling data for contributions from nuclear collisions as is the case for stopping-cross-section data. The reason is that compared to average energy

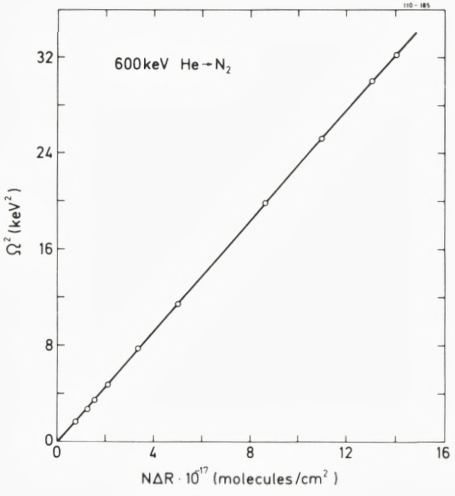

Fig. 4: The energy straggling Ω^2 versus target density for He in N_2.

loss, straggling depends more strongly on close collisions, and hence the separation of the elastic and inelastic collisions becomes more ambiguous. In order to estimate the contribution from nuclear collisions to the measured straggling, we shall consider the following example, which represent one of the cases with the largest contribution from nuclear collisions,

113.4 keV He → He	$N\Delta R = 1.24 \cdot 10^{18}$ atoms/cm^2
$\Omega_e = 0.792$ keV	$\Omega_n = 1.137$ keV
$T_{max,e} = 0.062$ keV	$T_{max,n} = 113.4$ keV

Here, indices e and n refer to electronic and nuclear collisions, respectively, and Ω_n is calculated from Bohr's nuclear-straggling formula (Bohr (1948)), which is analogous to formula (5). The spectrum originating from the electronic collisions will be a Gaussian distribution, while the nuclear collisions give rise to a strongly asymmetric distribution with a low-energy tail. However, particles which have experienced the most violent nuclear collisions are scattered out of the angularly narrow, forward-directed, analyzed beam, thus reducing the "nuclear tail" considerably. According to Hvelplund (1971), the particles accepted by the analyzer will approximately be those which have suffered collisions with an energy transfer $T \lesssim T_n^*$ where T_n^* is the nuclear-energy transfer, corresponding to a deflection angle φ^* that divides the angular distribution into a Gaussian peak and a tail. In Fig. 5, T_n^* and the corresponding impact parameter p_{min} are shown for the case considered here. If the measured straggling is given by

$$\frac{\Omega^2_{exp}}{N\Delta R} = \int_{p_{min}}^{\infty} (T_n + T_e)^2 2\pi p dp, \tag{25}$$

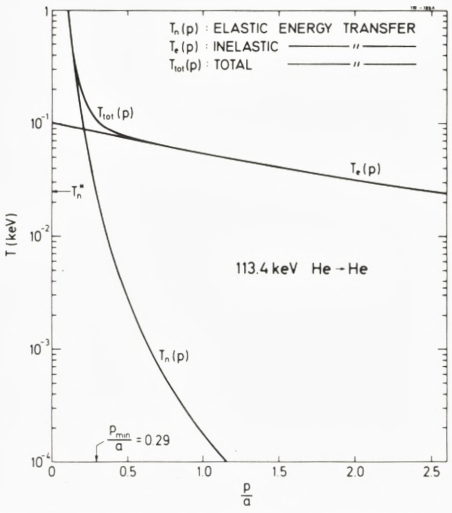

Fig. 5: Energy transfer in a single collision as a function of impact parameter. Inelastic transfer is calculated from Firsov's (1959) $T_e(p)$. The elastic energy transfer is calculated from a power potential $V(r) \propto r^{-2}$ (Lindhard et al. (1968)). T_n^* and p_{min} refer to maximum elastic energy transfer and the corresponding impact parameter for atoms still belonging to the forward-directed beam, cf. text. The TF screening radius is given by $a = 0.8853\, a_0 (Z_1^{2/3} + Z_2^{2/3})^{-1/2}$.

then for the actual case $\Omega_{exp} > T_e(p_{min}) + T_n^*$, and hence the energy distribution for the forward-directed beam should be Gaussian, in agreement with the experimental findings. From Fig. 6 it is found that the contribution from the nuclear collisions (area I_2) to the measured straggling Ω_{exp}^2 is roughly 2 %, whereas the excluded straggling term from electronic collisions with $p < p_{min}$ (area I_1) is approximately 4 %.

It can thus be concluded that the measured straggling can be attributed mainly to electronic collisions, and no corrections for nuclear straggling have been applied.

Based on the systematic and statistical experimental errors quoted in I and an assumed 10 % uncertainty in Ω_i^2 (stemming from the assumption that the primary energy distribution is Gaussian and from the actual value of Ω_1^2), we estimate the total uncertainty in the measured straggling $\Omega^2/N\Delta R$ to be 5–7 %.

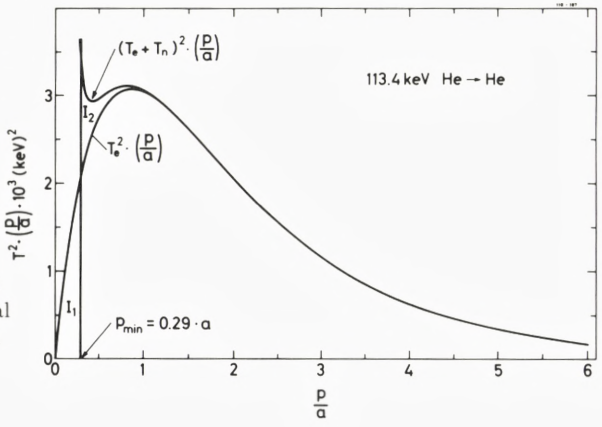

Fig. 6: The energy transfer squared times the reduced impact parameter for the specific case considered in Fig. 5, plotted versus the reduced impact parameter. According to formula (25), the contribution to the straggling from nuclear collisions is given by the area I_2 and the straggling term stemming from small impact parameters, which we exclude in the present experimental setup, is given by the area I_1. Concerning T_e, T_n, and p_{min}, see Fig. 5.

§ 4. Experimental results and comparison with theory

4.1 *Deviations from* Z_1^2 *Scaling for* H *and* He *Ions in Monatomic Gases*

Since the contributions to the Lindhard-Scharff straggling term in Eq. (13) mainly stems from close collisions with electrons, Ω_{LS}^2 is proportional to Z_1^2 even in an energy region where the electronic stopping power may deviate from the Z_1^2 perturbation scaling. The corrections to Ω_{LS}^2, however, show a different dependence on Z_1 since they are proportional to S_e^2 and thus to $\sim Z_1^3 - Z_1^4$. It is therefore possible to obtain a semi-emperical determination of the atomic-correlation term Ω_A^2 due to bunching of electrons into atoms by comparing experimental hydrogen- and helium-straggling results for the same monatomic gas. As argued for in II, such a semiempirical procedure is preferable because of the problems involved in performing a stringent theoretical calculation of Ω_A^2.

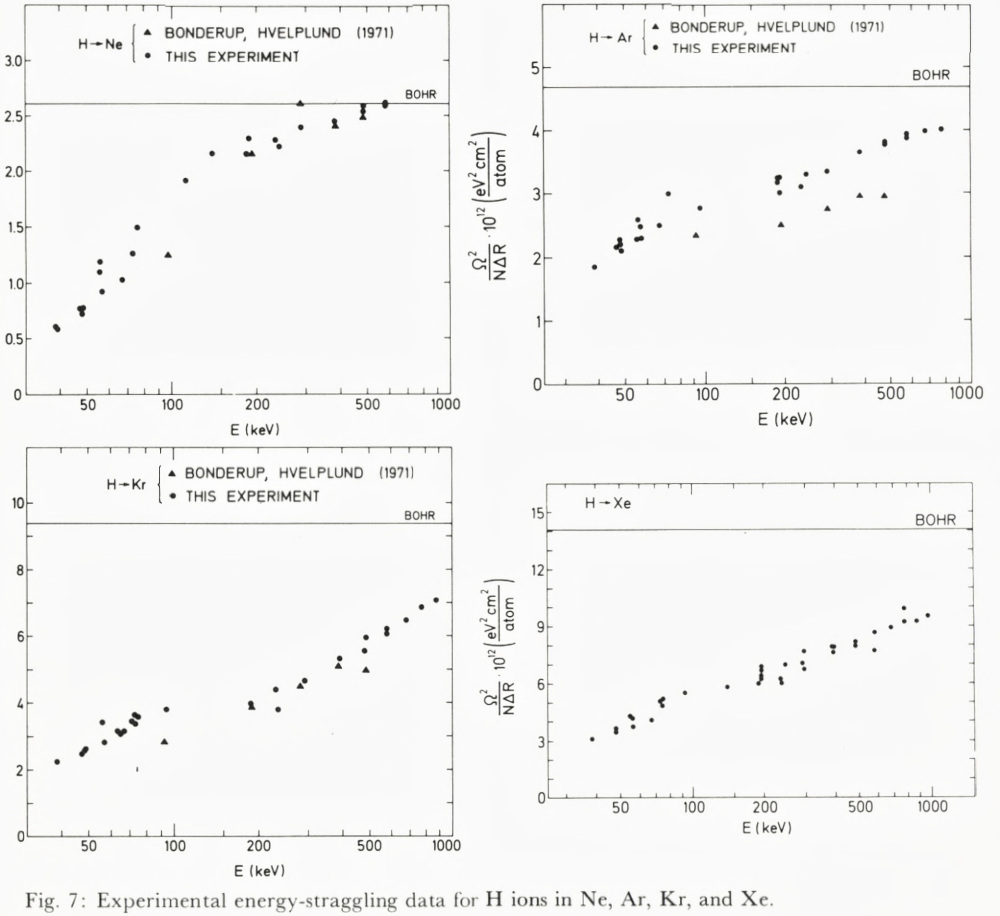

Fig. 7: Experimental energy-straggling data for H ions in Ne, Ar, Kr, and Xe.

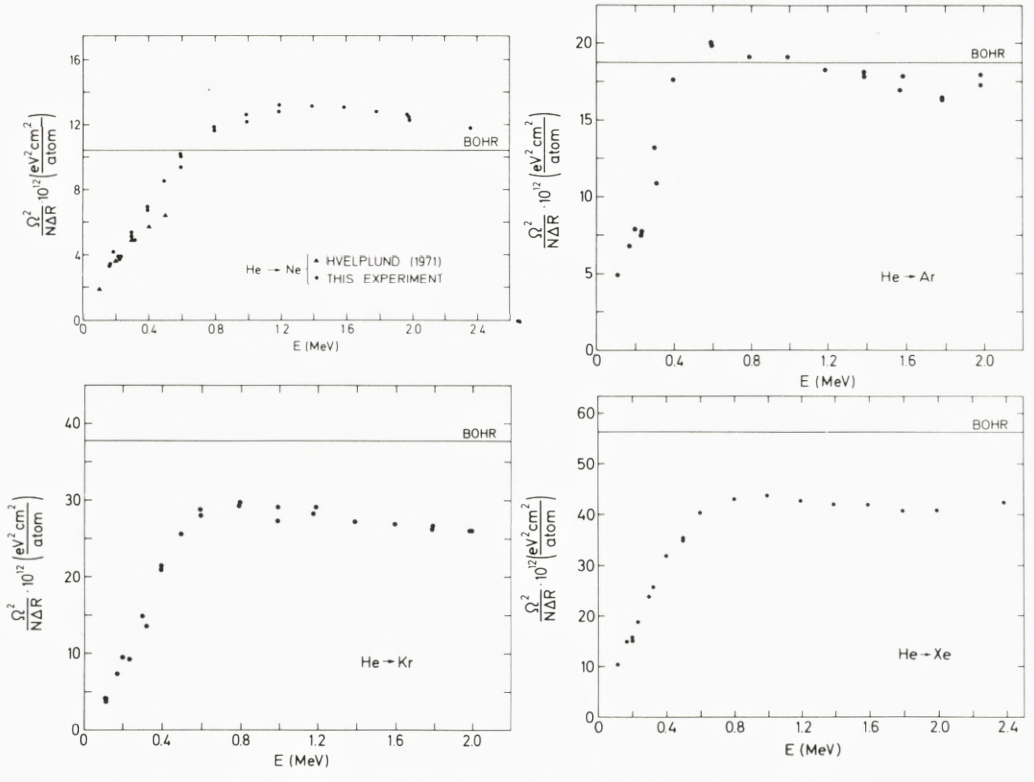

Fig. 8: Experimental energy-straggling data for He ions in Ne, Ar, Kr, and Xe.

The experimental straggling parameters $\Omega^2/N\Delta R$ for hydrogen and helium ions penetrating Ne, Ar, and Xe are plotted in Figs. 7 and 8 as a function of the mean energy E_{av}. While the hydrogen data increase monatomically and approach the Bohr value for increasing energy, as expected from theory, the helium data show a local maximum at $E_{He} \sim 1$ MeV. In Fig. 9, the hydrogen and helium results Ω^2/Ω_B^2 are plotted versus energy per nucleon for Ne, Ar, Kr, and Xe, while similar results for a helium target are shown in Fig. 15. A significant deviation of the Ω^2 values from the Z_1^2 scaling contained in the Bohr straggling formula Ω_B^2 (Eq. (5)) is revealed. The difference between the averaged helium and hydrogen results in Figs. 9 and 15, which is plotted as points in Figs. 10 and 16, can, as argued above, be attributed to corrections to the Lindhard-Scharff term, i.e., to straggling terms resulting from the bunching of electrons into atoms and from charge-state fluctuations.

The contribution from charge-state fluctuations for helium ions can be obtained from Eq. (20) and is shown in Figs. 10 and 16 as the lower solid line. For

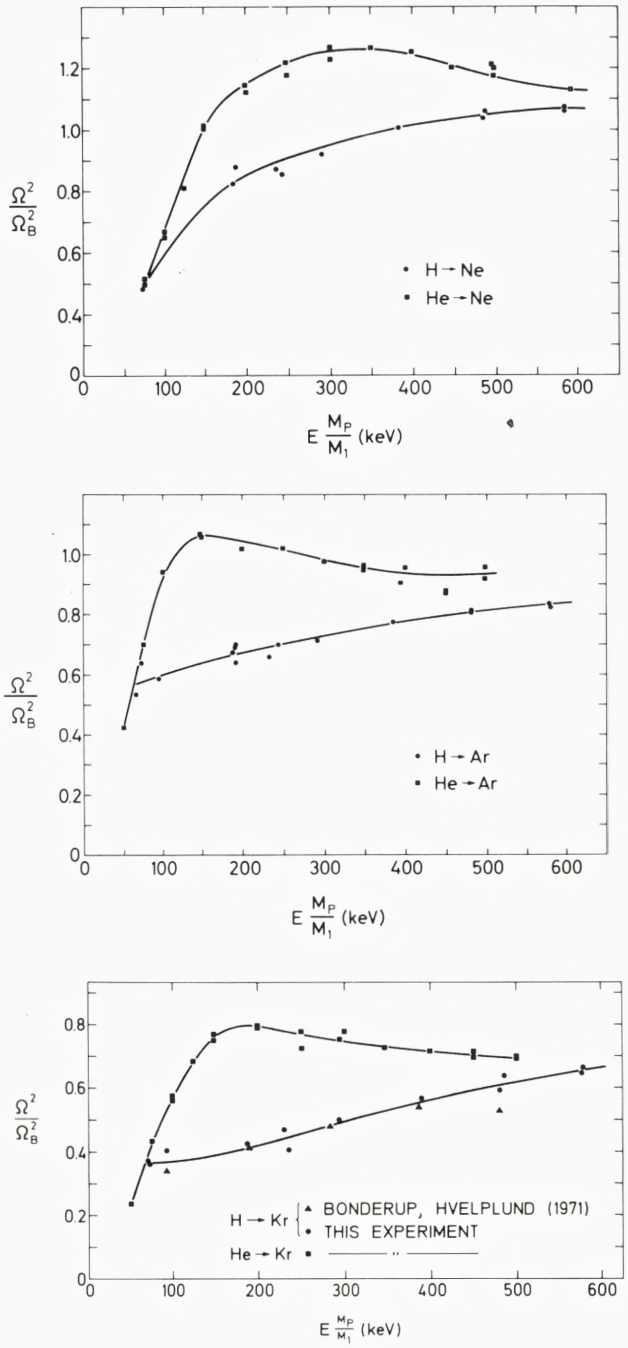

Fig. 9: Energy straggling for H and He ions in Ne, Ar, Kr, and Xe versus energy per nucleon. The solid lines through the experimental results are drawn only to guide the eye.

Fig. 9 continued on p. 20.

Fig. 9 (continued from p. 19).

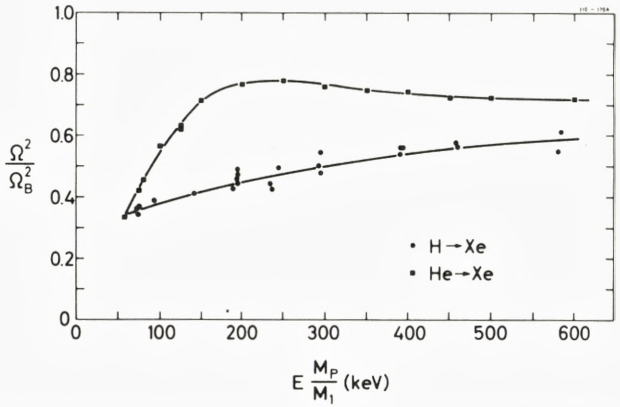

the capture and loss cross sections in Eq. (20), the experimental values for Kr, Ar, and He of Pivovar et al. (1962a, 1962b) and of Hvelplund et al. (1976, 1980) are used while no data are available for Ne and Xe. A simple estimate of the partial stopping cross section $S_e(He^+)$, i.e., the stopping cross section of a helium ion in the fixed charge state He^+ (Cuevas et al. (1964)) can be obtained from our measured helium-stopping cross sections (I) through the equation

$$S(He) = F_{1\infty} S_1(He^+) + F_{2\infty} S_2(He^{++}) , \tag{26}$$

for $E_{He} \gtrsim 400$ keV, for which the neutral component is negligible. Here, the equilibrium charge-state fractions are given by $F_{1\infty} = \sigma_{21}(\sigma_{12} + \sigma_{21})^{-1}$ and $F_{2\infty} = \sigma_{12}(\sigma_{12} + \sigma_{21})^{-1}$, while the partial α-stopping cross section $S_2(He^{++})$ can be set equal to four times the measured proton-stopping cross section S_p (I). The uncertainty in the derived straggling contribution Ω_C^2/Ω_B^2 is ~15–25 %, stemming from uncertainties in the applied experimental quantities. For the heavy monatomic gases, it is seen in Fig. 10 that Ω_C^2 is negligible for $E\frac{M_p}{M_1} \gtrsim 300$ keV and that Ω_C^2/Ω_B^2 cannot alone account for the experimental helium-hydrogen difference.

In previous investigations of the influence of charge-exchange straggling [Besenbacher et al. (1977) Bednyakov et al. (1977), Efken et al. (1975), Sofield et al. (1978), Crowern et al. (1979), Schmidt-Böcking and Hornung (1978), Vollmer (1974)], it has been assumed that the partial stopping cross section of an ion in a fixed charge state q can be written as $S_q = q^2 S_p$, which for the factor in Eq. (19) yields $(S_1 - S_2)^2 = (q_1^2 - q_2^2)^2 S_p^2$. For helium ions, this means that $S_1(He^+) = S_p$, which is appropriate for distant collisions only, and consequently, $S_1(He^+)$ is underestimated. The assumption thus leads to values of Ω_C^2/Ω_B^2, presented by the upper full-drawn curves in Figs. 10 and 16, which overestimate the influence of charge-state fluctuations considerably.

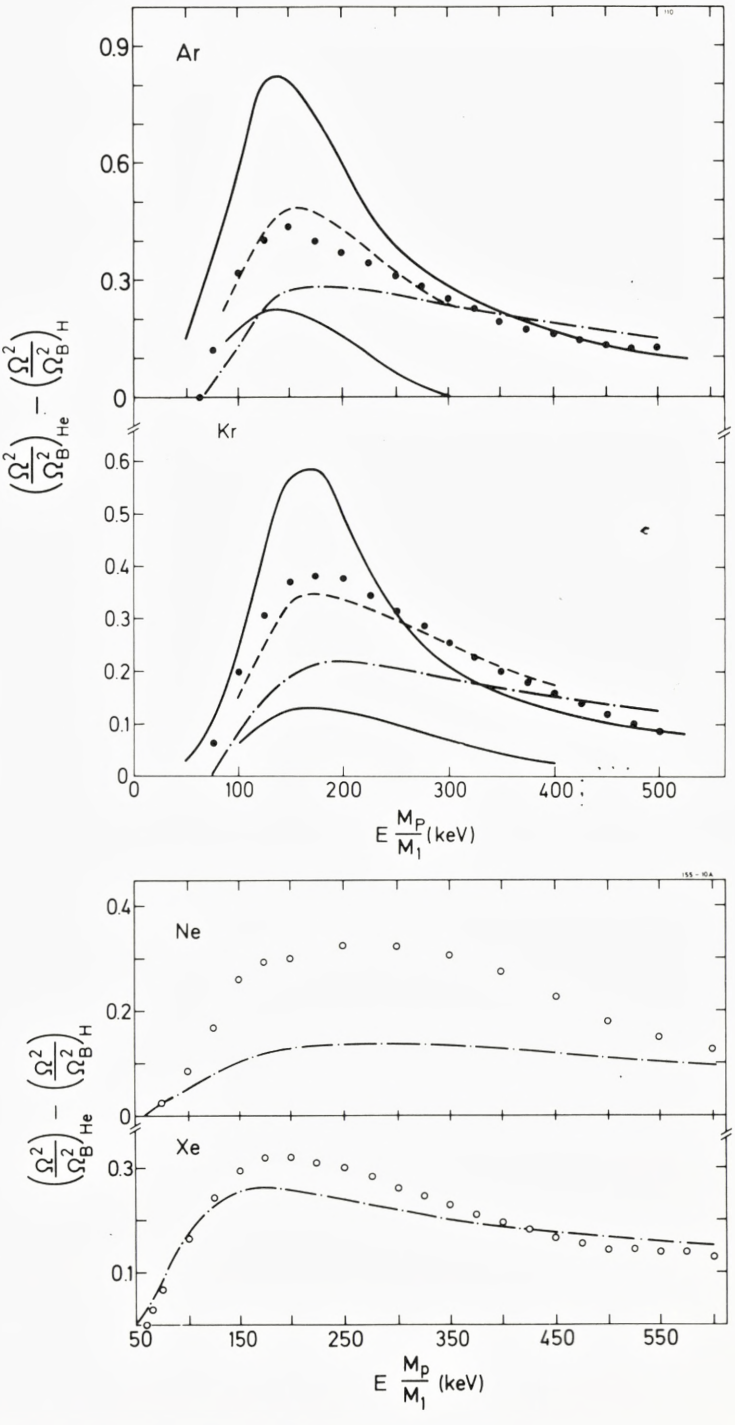

Fig. 10: The deviation from the Z_1^2 scaling of energy straggling for H and He ions in Ar, Kr, Ne, and Xe versus energy per nucleon. The points display the difference between the experimental He and H results from Fig. 9. The contribution from charge-state fluctuations Ω_C^2 (Eqs. (19) and (26) for He ions, measured in units of Ω_B^2 (He), is given by the lower, solid curve, whereas the upper solid curve shows the incorrect value of Ω_C^2 calculated previously under the assumption that the stopping cross section for He^+ is equal to that for protons. The difference between the atomic-correlation terms in units of Ω_B^2 for He and H ions is represented by the dot-and-dash curve for an atomic area of $10\pi a_0^2$. When the contribution from charge-state fluctuations is added, the dashed curve results.

The difference between the atomic correlation terms Ω_A^2/Ω_B^2 for helium and hydrogen ions is shown as the dot-and-dash curve in Figs. 10 and 16. For Ω_A^2 we have used Eq. (15) with the experimental-stopping cross section (I) and an atomic area πr_A^2 of $10\pi a_0^2$. Adding to this curve the contribution from charge-state fluctuations, we obtain the dashed curve, which is seen to be in overall good agreement with the experimental data. This fact lends strong support to the theoretically predicted expression for the atomic correlation term (Eq. (15) with an atomic area $\pi r_A^2 \simeq 10\pi a_0^2$, approximately independent of energy and Z_2.

For a xenon target, the helium-hydrogen difference is nearly completely described by Ω_A^2; for the medium elements such as Kr, Ar, and Ne, the relative importance of Ω_C^2 increases with decreasing atomic number, and for helium, the difference can on the whole be accounted for by Ω_C^2. The experimental results thus support the expectation that the relative importance of the atomic bunching term Ω_A^2 decreases with decreasing number of target electrons since from Eqs. (15) and (5), we have that Ω_A^2/Ω_B^2 is roughly proportional to Z_2.

While the helium-hydrogen difference in Fig. 10 approaches zero at high energies, negative values are obtained at low energies (see, e.g., the argon and krypton data in Figs. 9 and 10). This at first somewhat surprising result is explained by the energy dependence of the stopping, cross sections and thereby of the atomic correlation term Ω_A^2, Eq. (15). For energies $E\frac{M_p}{M_1} \sim 50$–100 keV, S_H and consequently Ω_A^2 for hydrogen ions reach their maximum values and are approximately constant while S_{He} and hence Ω_A^2 for helium ions decrease with energy as $E^{1/2}$ and E, respectively, and at 50 keV, $(\Omega_A^2/\Omega_B^2)_H$ is in fact larger than $(\Omega_A^2/\Omega_B^2)_{He}$. This explains the steep slope of the dot-and-dash curves in Fig. 10 at the low energies. In Fig. 11, the straggling data for helium and hydrogen ions in Ar have been corrected for the influence of the atomic-straggling term Ω_A^2 due to the bunching

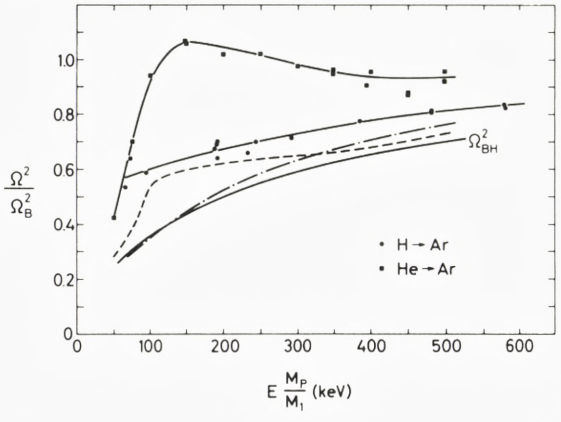

Fig. 11: The experimental-straggling results from Fig. 9 for H and He ions in Ar corrected for the influence of the atomic-straggling term Ω_A^2 given byg Eq. (15) with an atomic area of $10\pi a_0^2$. The corrected He (dashed curve) and H (dot-and dash curve) results are compared with the electron-gas calculations by Bonderup and Hvelplund (1971) (Ω_{BH}^2).

of the electrons into atoms. These corrected helium (dashed curve) and hydrogen (dot-and-dash curve) results agree mutually and with the Bonderup and Hvelplund results (solid curve) both at low and at high energies. The increase of the helium results over the hydrogen results at $E\frac{M_p}{M_1} \sim 50$–100 keV is due to the influence of charge-state fluctuations. Similar curves can be obtained for the other rare gases.

We may complete this section by concluding that the importance of charge-exchange straggling has been overestimated substantially in the past, and that the deviation from the Z_1^2 scaling of Ω^2, resulting in a significant difference between the helium- and hydrogen-straggling results may be accounted for by the atomic bunching term given by Eq. (15) with an empirically determined area of $10\pi a_0^2$ and the charge-exchange straggling expression given by Eqs. (19) and (26).

4.2 *Straggling for Hydrogen Ions in the Monatomic Heavy Gases*

In Fig. 12, the experimental straggling results for hydrogen in Ne, Ar, Kr, and Xe are compared with the electron-gas calculations Ω_{BH}^2 by Bonderup and Hvelplund (1971) shown by the dashed curves. The experimental results are in qualitative agreement with the theoretically predicted reduction in straggling compared to the Bohr value for decreasing velocities, but the quantitative agreement

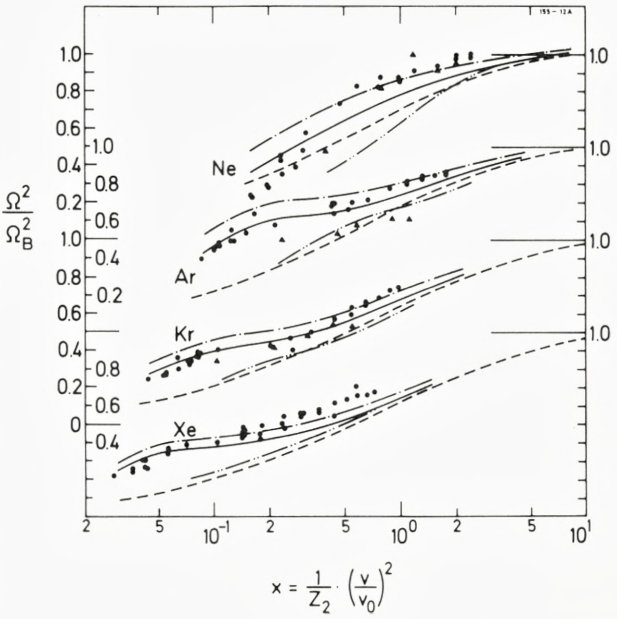

Fig. 12: Energy straggling for protons in Ne, Ar, Kr, and Xe versus the reduced-energy parameter x, normalized to the asymptotic Bohr value (Eq. (5)). The experimental data (•) from Fig. 7 and (▲) from Bonderup and Hvelplund (1971) are compared with the theoretical results. Dashed curves: theoretical values by Bonderup and Hvelplund (1971); solid curves: the sum of the BH results and the atomic correlation term, Eq. (15) for an atomic area of $10\pi a_0^2$; double dot-and-dash curve: theoretical values of Chu (1976); dot-and-dash curve: equivalent to the solid curve except that the BH results are modified, as explained in text.

is rather bad. For the heavier atoms, the discrepancy increases for decreasing x. Adding, however, the atomic correlation term Ω_A^2 given by Eq. (15) with an atomic area of $10\pi a_0^2$ to Ω_{BH}^2, the solid curves in Fig. 11 are obtained, and it is seen that Ω_A^2 on the whole accounts for the discrepancy between Ω_{BH}^2 and the experimental results for Ar, Kr, and Xe, while the agreement in the case of Ne is still relatively poor. However, for the lighter rare gases such as Ne and He, the more realistic Hartree-Fock-Slater electron densities applied by Chu (1976) are superior to the Lenz-Jensen densities underlying the Bonderup-Hvelplund (1971) calculations, and from Fig. 12 it is in fact seen that for Ne, the energy dependence of the measured straggling is in somewhat better agreement with Ω^2_{Chu} (the double dot-and-dash curve). For the heavier elements Ar and Kr, Ω^2_{Chu} and Ω_{BH}^2 are in very good agreement, while Ω^2_{Chu} is systematically 0.05 Bohr units higher than Ω_{BH}^2 for Xe, probably because this element is positioned in a maximum of the Z_2 oscillatory structure in Ω^2 revealed by Chu (1976).

From Fig. 12 the only remaining systematic deviation between theory and experiment appears to be an underestimate of the predicted straggling at higher x values, corresponding to energies above the stopping-power maximum. Since Ω_A^2 in this energy region becomes small, the deviations may be due to uncertainties in Ω_{BH}^2 (Eq. (11)), some of which we shall discuss in the following.

In the straggling calculations by Bonderup and Hvelplund (1971), the target was considered as a collection of free electron gases, and the straggling contribution from an atom was obtained as an average over the electron cloud of the straggling for a gas of constant density. One of the advantages of considering the case of straggling in a free gas of electrons is that one is concerned with a simple scattering phenomenon: An equilibrium situation is established where the projectile is screened by the electron gas or, equivalently, free electrons are scattered in a self-consistent, steady-state screened Coulomb potential. The influence of the screening on the straggling contribution from the outer atomic electrons ($v_e < v$) is of minor importance since for these electrons, the pure Coulomb potential results in the Bohr expression (Eqs. (4) and (5)), which deviates only slightly from the electron-gas expression in Eq. (11a).

However, since the relative contribution from the inner electrons increases with decreasing x (e.g., for $Z_2 = 18$, $\Omega^2_{inner}/\Omega^2_{total}$ takes on the values 0.63, 0.46, and 0.27 at x values of 0.125, 0.41, and 1.52, respectively), the calculated straggling at low x is rather sensitive to the detailed screening prescription used for the contribution from the inner electrons. It might be questionable whether the steady-state screening leading to the explicit dependence of Ω^2_{inner} on the parameter χ^2 in Eq. (11b) is established in a collision with a single atom. One can obtain an overestimate of the straggling contribution from inner electrons by letting the electrons scatter in a pure Coulomb potential around the projectile.

Mathematically, this is equivalent to a replacement of the quantity χ^2 in Eq. (11b) by unity since χ^2 is equal to the ratio $(\lambda\!\!\!^{-}_F/2a)^2$, where $\lambda\!\!\!^{-}_F$ is the wavelength of an electron at the Fermi surface and a is the static screening length in an electron gas ($\lambda\!\!\!^{-}_F = \hbar/mv_F$).

Another type of uncertainty exists in the high-velocity limit of the electron-gas expression given by Eq. (11a). The electrons in an atom are influenced by both the polarization force corresponding to a local plasma frequency ω_0 and an orbital force corresponding to the revolution frequency ω_{rev}. Since $\omega_{rev} \simeq \omega_0$ in the simple Bohr atomic model, Lindhard and Scharff (1953) accounted approximately for the binding of the electrons in the atomic system by multiplying the plasma frequency in the electron-gas calculation by the factor $\sqrt{2}$.

To get an estimate of the uncertainties underlying the electron-gas calculations, those of Bonderup and Hvelplund (1971) have been repeated with the two above modifications of the expressions for the straggling contributions from the outer and inner electrons, and as a result, the solid curves in Fig. 12 are replaced by the dot-and-dash curves. Of the two substitutions, $\omega_0 \rightarrow \sqrt{2}\omega_0$ is the least important, and it only gives rise to a 3 % increase in Ω^2_{BH} at the highest x values. The dot-and-dash curves are in good agreement with the experimental results at the high x values but overestimate the straggling at the low ones, and thus the overall agreement is not improved. The results, however, may indicate that the discrepancies between the experimental results and the theoretical estimates, which are $\sim$10–20 %, are within the accuracy of the electron-gas calculations.

4.3 *Straggling in Light, Monatomic Substances*

The straggling results for hydrogen penetrating helium are shown in Fig. 13, and the data disclose a characteristic "overshoot" above the Bohr value. In Fig. 13 are also plotted the results of the electron-gas calculations by Bonderup and Hvelplund (1971) (dashed curve), and by Chu (1976) (double dot-and-dash curve), together with Fano's straggling formula (6) (solid curve). The parameters I_1 and S(1), which enter this formula, have been calculated by Inokuti et al. (1978) for atomic systems, and in the case of helium, they obtain $I_1 = 80.1$ eV and $S(1) = 104.9$ eV.

The Fano formula is the result of a perturbation calculation, i.e., the probability of an electron excitation is assumed to be small. In principle, all straggling contributions are included in the Fano formula, but in practice, only one-electron excitations are taken into account [Dehmer et al. (1975) and Inokuti et al. (1978)] in calculations of I_1 and S(1). However, as mentioned in Sec. 4.1, the relative importance of the atomic bunching term, which in the Fano treatment can be interpreted as the contribution from multi-electron excitations, decreases with

decreasing Z_2. For helium, the corrections to the Fano curve, with only single-electron excitations included, are therefore expected to be small, but for heavier target elements such as argon, the correction might be important.

For energies $E \gtrsim 300$ keV, the experimental results are in good agreement with Fano's formula, while it fails at low energies, where the assumption $v > v_e$ is no longer fulfilled.

As was the case for neon, the calculations by Chu are superior to those by Bonderup and Hvelplund, and on the whole, the energy dependence of Ω^2_{Chu} agrees with that of the experimental results. The comparison of absolute values is, however, less satisfactory. As shown by the double-dashed curve, this discrepancy cannot be removed through an application of the modified electron-gas expression described above, and the addition of the small atomic correlation term.

In order to understand the difference between Ω^2_{Fano} and Ω^2_{Chu} or Ω^2_{BH}, one has to compare the asymptotic straggling formulas (6) and (11a). The Fano formula is based upon the sum rules for the generalized and the dipole oscillator strengths $F_{0i}(\boldsymbol{q})$ and f_{0i}, and for large and small momentum transfers $\hbar\boldsymbol{q}$, these sum rules are given by

$$\sum_i \hbar\omega_{0i} F_{0i}(\boldsymbol{q}) = \frac{\hbar^2 \boldsymbol{q}^2}{2m} + \frac{4}{3} < K >_0, \quad \text{q large} \tag{27a}$$

$$S(1) = \sum_i \hbar\omega_{0i} f_{0i} = \frac{4}{3}\left[< K >_0 + \frac{m}{2} \sum_i \sum_{j \neq i} < \boldsymbol{v}_i \boldsymbol{v}_j >\right], \quad \text{q small} \tag{27b}$$

where $< K >_0$ is the mean kinetic energy of an electron in the ground state of the target system. Using these sum rules, Fano calculated the contribution from the close and distant collisions, but in the combination of the two contributions to the final formula (6), it was assumed that

$$< K >_0 = \sum_i \hbar\omega_{0i} f_{0i} = S(1) \tag{28}$$

As illustrated by the example of an electron gas, the neglect of the correlation term in Eq. (27b) may be quite serious for the evaluation of the correction to the Bohr formula. In this case, all of the dipole oscillator strength is contained in the plasmon excitation, and the left and right-hand side of Eq. (28) are equal to $2mv_F^2 = (0.12/\chi^2)^{1/2} \cdot \hbar\omega_0$ and $\hbar\omega_0$, respectively. Applying the correct sum rules Eq. ((27)) for an electron gas, we obtain, as expected, the two terms in the square brackets of Eq. (11a). In the high-density limit, $\chi \to 0$, the second term in Eq. (11a) may be neglected, and the constants in front of the logarithms in Eqs. (11a) and (11b) differ by a factor of 2.

In the asymptotic expression (6), shell corrections and other terms of order $< v_e^2 > / v^2$ have been neglected as compared to the logarithm. This may not be a

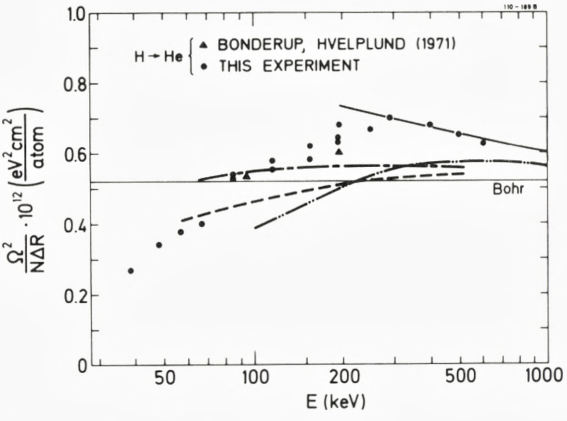

Fig. 13: Experimental energy-straggling data for H ions in He compared with theoretical results. Upper solid curve: the asymptotic Fano straggling formula (6); dashed curve: theoretical values by Bonderup and Hvelplund (1971); double dot-and-dash curve: theoretical values by Chu (1976); — - — curve: Ω^2_{BH}, modified (as explained in text), plus the atomic correlation term, which, in the case of He, is given approximately by Eq. (15) times 0.5 with πr_A^2 equal to $10\pi a_0^2$, cf. II.

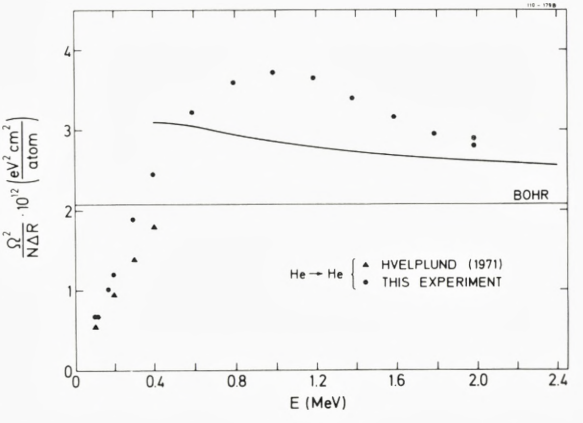

Fig. 14: Experimental energy-straggling data for He ions in He compared with the asymptotic Bohr (1948) (Eq. (5)) and Fano (Eq. (6) straggling formulas (upper solid curve).

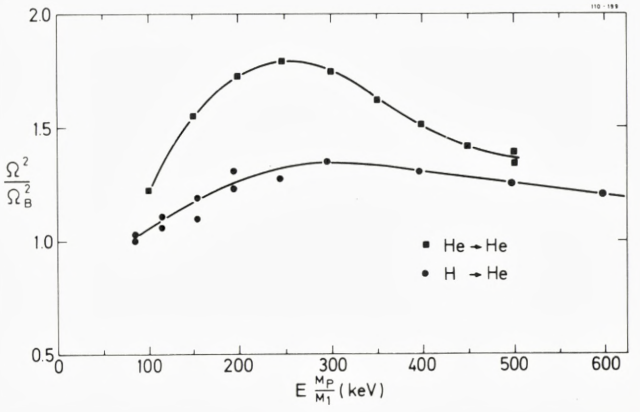

Fig. 15: Energy straggling for H and He ions in He versus energy per nucleon. Solid curves through the experimental data are drawn only to guide the eye.

very good approximation at the relatively low projectile velocities, at which the correction to the Bohr formula becomes significant. Again, the electron gas provides a convenient illustration. The energy I_1 appearing in Eq. (6) is equal to $\hbar\omega_0$, as obtained from the defining equation (7), and at normal atomic electron densities, this energy is quite low as compared to the value $2mv_F^2$ implied by Eq. (11a). To obtain this expression, which was found to be in good agreement with the exact values evaluated numerically by Bonderup and Hvelplund (1971), it was necessary to include terms of order one as compared to terms of order $\log(v/v_F)$ in the expansions. The good agreement between the experimental results and Eq. (6) may therefore be somewhat fortuitous. On the other hand, the statistical description underlying the electron-gas calculations, i.e., Ω^2_{Chu} and Ω^2_{BH}, is probably rather inaccurate for a very light atom such as helium.

In Fig. 14, the experimental straggling results for helium ions transmitted through a helium target are compared to the asymptotic Fano formula (solid curve). Both the energy dependence and the absolute magnitude of the discrepancy between theory and experiment deviate significantly from the values for hydrogen ions shown in Fig. 13. To understand the deviation, we proceed as in Sec. 4.1 by plotting in Fig. 15 the experimental values of Ω^2/Ω^2_B as a function of energy per nucleon for helium ions and for protons, and the difference between the two averaged curves in Fig. 15 is plotted as points in Fig. 16. As expected, these difference values for helium mainly contain contributions from charge-state fluctuations (lower solid curve), and the atomic correlation term (dot-and-dash curve) only amounts to a small correction. The figure has been discussed in detail in Sec. 4.1.

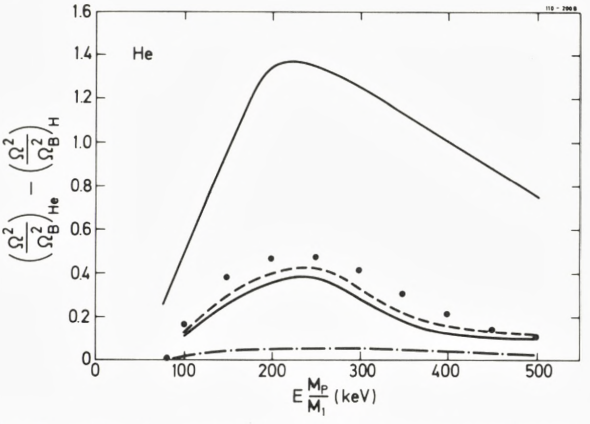

Fig. 16: The deviation from the Z_1^2 scaling of energy straggling for H and He ions in He versus energy per nucleon. The points display the difference between the experimental He and H results in Fig. 15. The contribution from charge-state fluctuations Ω_C^2 (Eqs. (19) and (26)) for He ions, measured in units of Ω_B^2(He), is given by the lower solid curve, whereas the upper solid curve shows the incorrect value of Ω_C^2 calculated previously under the assumption that the stopping cross section for He^+ is equal to that for protons. The difference between the atomic correlation terms (for He given by Eq. (15) times 0.5, cf. II, and zero for H_2) in units of Ω_B^2 for He and H ions is represented by the dot-and-dash curve for an atomic area of $10\pi a_0^2$. When the contribution from charge-state fluctuations is added, the dashed curve results.

4.4 *Molecular Correlation Effects*

In Figs. 17 and 18 are shown the experimental straggling data for hydrogen and helium ions in N_2, O_2, and CO_2. To investigate the molecular correlation effect, we need information on the straggling in targets where the molecules have been dissociated into their constituent atoms. Experimentally, it is extremely difficult to obtain such dissociated targets, and therefore neon was chosen as an atomic reference in the evaluation of molecular correlation effects. According to Bonderup and Hvelplund (1971), the Z_2 dependence of the straggling normalized to the asymptotic Bohr value is very weak when plotted as a function of the reduced variable x, and it is therefore a good approximation to use neon as an atomic reference for N_2, O_2, and CO_2.

In Figs. 19 and 20, the straggling results for the molecular and atomic targets are therefore shown as a function of x. It is evident that the molecular targets cause a consistently higher straggling than the atomic ones, and the difference between the curves may be interpreted as a molecular correlation effect.

For N_2 and O_2 in Figs. 19 and 20, the molecular bunching term Ω_M^2, calculated from the asymptotic formula (17a) with experimental stopping cross sections taken from I, is indicated by arrows. It is seen that both the energy dependence and the absolute value of the correction term are in fairly good agreement with experimental data.

However, the applicability of the asymptotic formula (17a) is questionable since the assumption underlying this expression is far from being fulfilled. This is seen by a comparison of the internuclear distances in nitrogen and oxygen ($d(N_2) = 1.1$ Å and $d(O_2) = 1.21$ Å) with the atomic radius $r_A = 1.65$ Å for an atomic area of $10\pi a_0^2$. Nevertheless, if it is correct that the smaller of the two values in Eq. (17) gives a reasonable estimate of the molecular correlation term Ω_M^2, the asymptotic formula (17a) is, in fact, the appropriate expression for Ω_M^2 in the case of oxygen, and it only overestimated Ω_M^2 for nitrogen by $\sim 10\,\%$.

According to Sigmund (1976), the description of the molecular correlation effect in diatomic molecules can easily be generalized to polyatomic molecular targets, for which the straggling correction per molecule takes on the form

$$\Omega_M^2 = \sum_{i \neq j} \frac{S_i S_j}{2\pi d_{ij}^2} N\Delta R\,, \tag{29}$$

where the sum extends over the constituent atoms $i = 1, 2, \ldots$ of the molecule. This correction term is indicated in Figs. 19 and 20 for CO_2, and again, reasonably good agreement with the experimental results is found.

It should be noticed that for CO_2, which is a linear molecule, the same type of correlation term as that in Eq. (29) is obtained if the somewhat different treatment of correlation effect described in II is used. Generally, for nonlinear polyatomic molecules, Eq. (29) may overestimate the influence of molecular correlations.

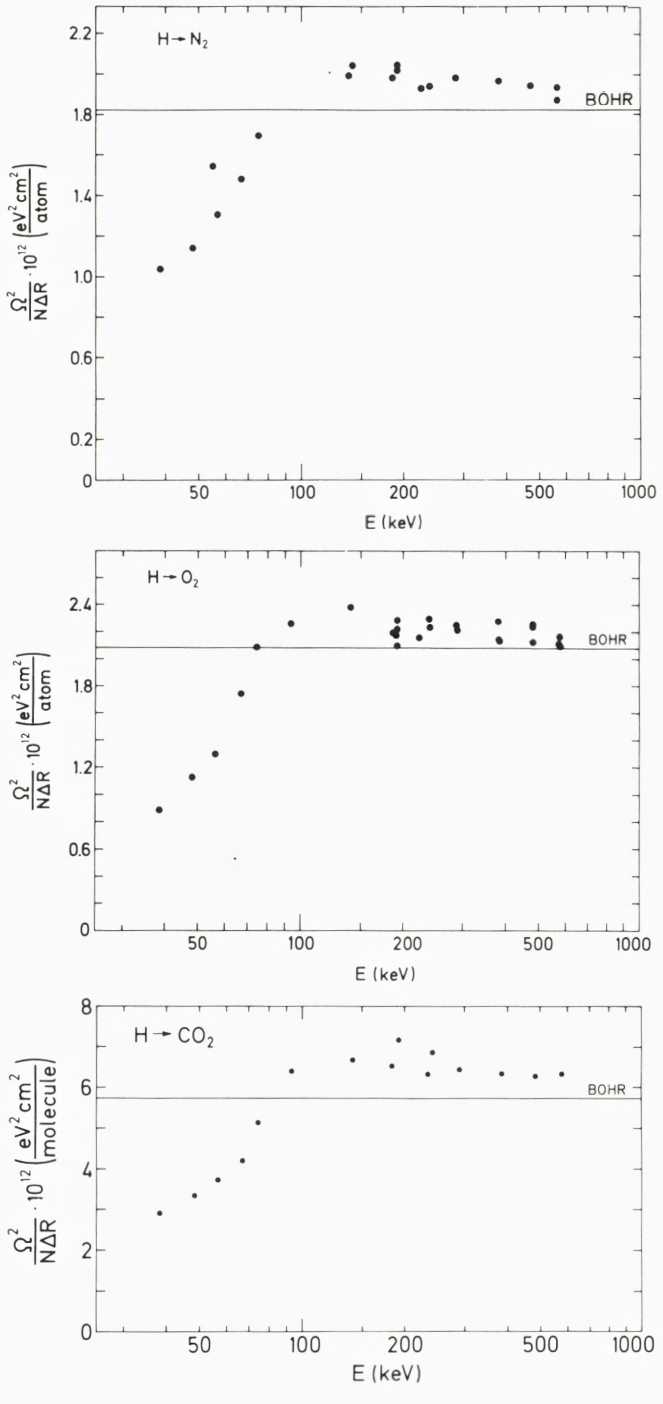

Fig. 17: Experimental straggling data for H ions in N_2, O_2, and CO_2.

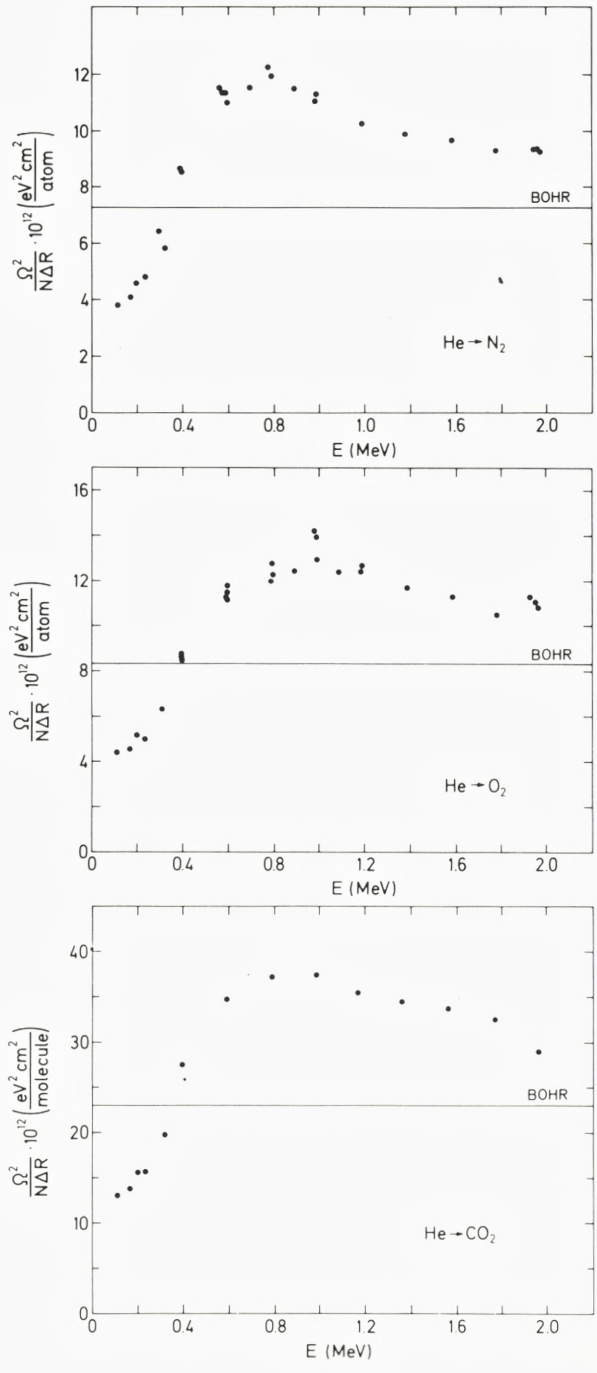

Fig. 18: Experimental energy-straggling data for He ions in N_2, O_2, and CO_2.

Fig. 19: Straggling results for protons in N_2, O_2, and CO_2 from Fig. 17 are compared with straggling results for protons in Ne from Fig. 7. Solid curves drawn through the experimental results are drawn only to guide the eye, whereas the arrows indicate the asymptotic molecular-correlation term Ω_M^2 (Eqs. (17a) and (29)).

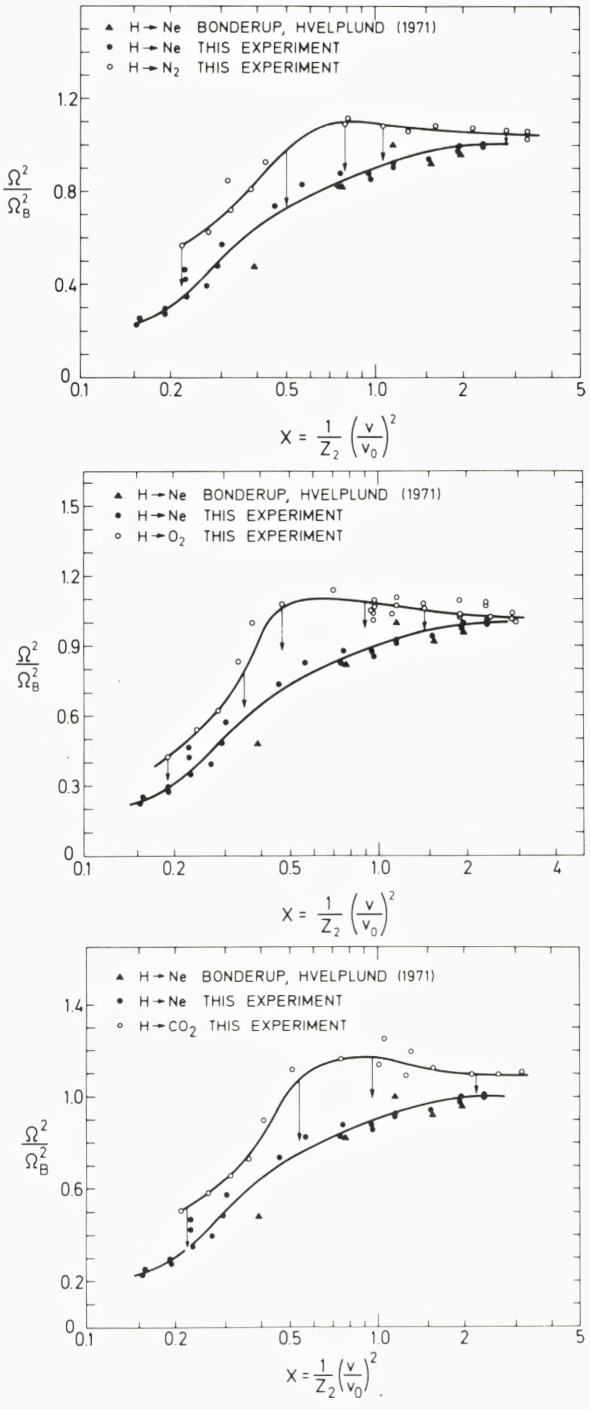

Fig. 20: Straggling results for He ions in N_2, O_2, and CO_2 from Fig. 18 are compared with the straggling results for He ions in Ne from Fig. 8. The solid curves through the experimental results are drawn only to guide the eye, whereas the arrows indicate the asymptotic molecular correlation term Ω_M^2 (Eqs. (17a) and (29)).

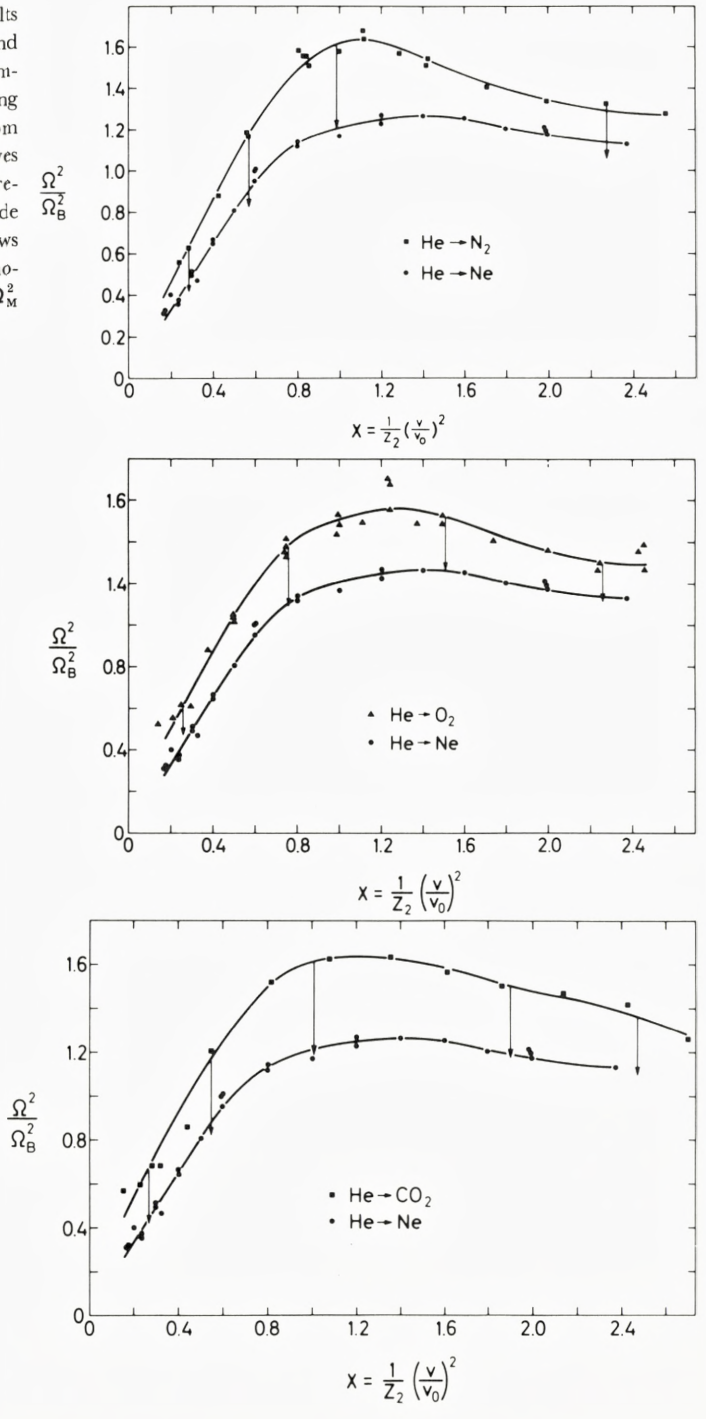

4.5 *Straggling in Hydrogen*

The straggling results for hydrogen ions transmitted through a hydrogen target are shown in Fig. 21 together with the results from the asymptotic Fano formula

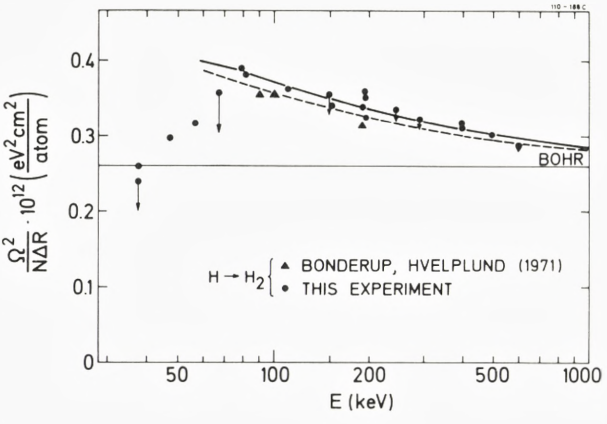

Fig. 22: Experimental energy-straggling results for protons penetrating a H_2 target compared with the asymptotic straggling formulas of Bohr (Eq. (5)) and Fano (Eq. (6)), the latter calculated for molecular (solid curve) and atomic targets (dashed curve). Arrows indicate the molecular correlation term Ω_M^2 given by Eq. (17b).

(6) for molecular (the full-drawn curve) and atomic (the dashed curve) hydrogen. The values of $S(1)$ and I_1 for molecular and atomic hydrogen have been calculated by Zeiss et al. (1977) and Inokuti et al. (1978), respectively, and they are shown in the table below.

	I_1 (eV)	$\frac{1}{Z_2} S(1)$ (eV)
H_2	29.13 eV	22.79 eV
H	24.07 eV	18.13 eV

The difference in I_1 and $S(1)$ reflects the change in electron density and thereby in the oscillator-strength distribution upon molecular formation.

When H_2 molecules are considered as the basic target elements in the straggling calculation, molecular correlation effects caused by two-electron excitations in an H_2 molecule are in principle included in the Fano formula, but as for He not in practice since the I_1 and $S(1)$ values for H_2 only include one-electron excitations. However, according to the discussion in Secs. 4.1 and 4.3, the molecular bunching term Ω_M^2 is small for hydrogen, and the good agreement between the experimental data and formula (6) for energies as low as 80 keV therefore supports the Fano formula.

To indicate that the molecular correlation term Ω_M^2 actually is fairly small

for hydrogen, Ω_M^2 calculated from Eq. (17b) is shown in Fig. 21. Equation (17b) is used since the intermolecular distance is only 0.74 Å and the asymptotic formula (17a) would overestimate Ω_M^2 by a factor of ~ 2.5.

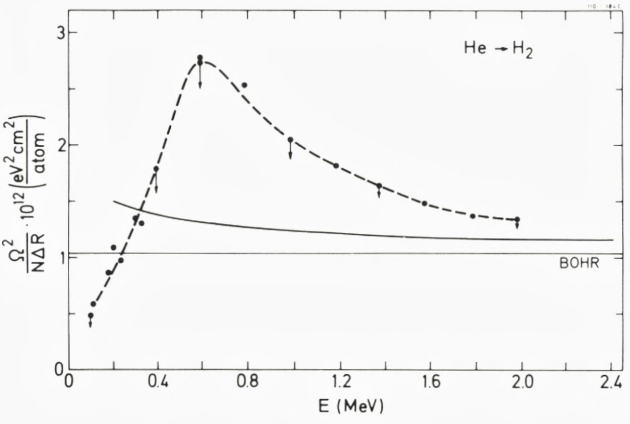

Fig. 22: Experimental energy-straggling results for He ions in H_2 compared with the asymptotic straggling formulas by Bohr (Eq. (5)) and Fano (Eq. (6)). Arrows indicate the molecular correlation term Ω_M^2 given by Eq. (17b).

In Fig. 22, the experimental straggling results for helium ions penetrating hydrogen are compared with the results from the asymptotic Fano formula (6) for molecular hydrogen. A combination of three different effects leads to an increase of the straggling to a factor of as much as 2.6 above the atomic Bohr value. Of the three effects, i.e., (i) the "overshoot" in Eqs. (6) and (11a) caused by the non-vanishing electron velocities, (ii) the molecular correlation effect, and (iii) the charge-state-fluctuation effect, the latter being by far the dominating one for a hydrogen target. This is seen from Fig. 23, where the difference between the averaged helium and hydrogen results in Figs. 21 and 22 in units of Ω_B^2 is compared to the contribution from the different effects. In the calculation of Ω_C^2 from Eqs. (19) and (26), the capture and loss cross sections by Hvelplund et al. (1976, 1980) have been applied. The agreement between the experimental results and the dot-and-dash curve, which is the sum of the contributions from Ω_C^2, Ω_M^2, and Ω_F^2 (Eq. (6)), is reasonable but certainly not as good as for the helium case in Fig. 16.

4.6 *Connection to Other Measurements*

As argued in II, the straggling of light, swift ions may be theoretically simpler in a solid than in a gas. In a solid, the effective atomic diameter $2r_A \sim 3.3$ Å is of the order of the interatomic distance and the fluctations in the number of ion-atom encounters, and thus the atomic correlation term Ω_A^2 will be small as com-

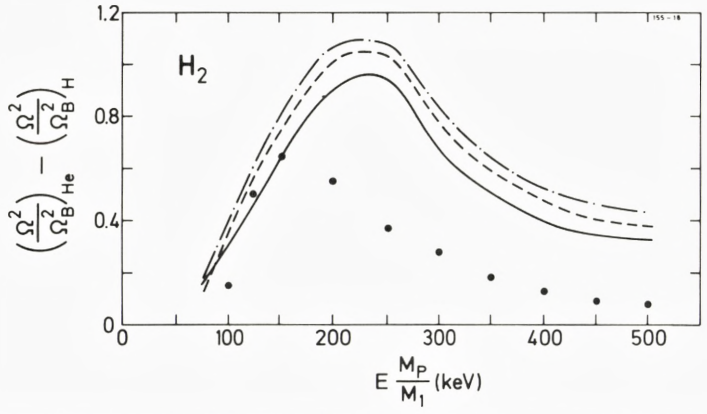

Fig. 23: The deviation from the Z_1^2 scaling of energy straggling for H and He ions in H_2 versus energy per nucleon. The points display the difference between the experimental H_2 results in Figs. 21 and 22. The contribution from charge-state fluctuations Ω_C^2 (Eqs. (19) and (26) for He ions measured in units of Ω_B^2(He) is given by the solid curve. When the contribution from molecular correlation effects Ω_M^2 (Eq. (17b) is added, the dashed curve results. When finally the contribution from the Fano formula (Eq. (6)) is added, the dot-and-dash curve results.

pared to that in a gas of the same area density $N\Delta R$. Similarly, charge-state fluctuations in a gas, resulting in the straggling term Ω_C^2, is for a solid reduced to a significantly smaller fluctuation of the screening cloud travelling with the ion. Thus we would expect the straggling in a metal to agree approximately with the electron-gas results, an expectation which is actually borne out by recent measurements by Heine et al. (1979) on aluminium (Fig. 6 in II).

Generally, however, straggling data for hydrogen and helium ions in solids deviate from the theoretical electron-gas estimates, and measurements on the same target by different groups may even deviate by as much as a factor of two (Fig. 7 in II). One of the reasons why it is so difficult to deduce any systematics from straggling measurements in solids is probably that the target inhomogeneities such as, e.g., non-uniform film thickness and texture effects tend to increase the straggling in an uncontrollable way. It is worthwhile to point out, however, that in many applications of straggling results to ion-beam analysis of solids, the difficulties, which hamper accurate, reliable, and reproducible measurements on thin solid films, often are reduced, and thus a precise knowledge of the basic straggling term Ω_{Ls}^2 caused by fluctuations in electron excitation is still of great importance. Experimentally, such information can be obtained for solids only if a proper check and/or correction for foil inhomogeneities is performed. Unfortunately, only very few experiments on solids have been made with proper control of the target conditions, and we shall abstain from a further discussion of straggling

data for light ions in solids and concentrate upon the straggling data for gaseous targets.

Hvelplund (1968, 1971, 1975) and Bonderup and Hvelplund (1971) performed an extensive investigation of energy straggling suffered by keV ions penetrating gas targets. A comparison with Hvelplund's straggling results for hydrogen ions transmitted through H_2, He, Ne, Ar, Kr, and for helium ions penetrating He and Ne is made in the respective figures of this work. For the cases of $H \rightarrow H_2$, He, Ne, Kr, Hvelplund's straggling data agree with the present ones within the uncertainties, while in the case of $H \rightarrow Ar$ and $He \rightarrow He$, Ne at the highest energies, the two sets of data deviate by approximately 20 %. The reason for this discrepancy is not understood, but it may be mentioned that also the stopping-power data in Ar by Bonderup and Hvelplund appear to be low (see I).

Mason et al. (1966), Ramirez et al. (1969), and Haque and Hora (1972) have measured straggling for protons and α particles in gases. In these experiments, the mean energy loss is considerable compared to the initial energy, and a comparison with the present measurements becomes difficult. (If $\overline{\Delta E}$ is comparable to E_i, the measured straggling $\Omega^2/N\Delta R$ will be larger than that for negligible energy loss provided the stopping power is a decreasing function of energy, Tschalär (1968).) An exception to the above situation is the $He \rightarrow He$ data by Ramirez et al. (1969), where $\Delta E/E_i$ is only ~ 18 %. For energies of $1.5 \lesssim E_{He} \lesssim 3.5$ MeV, Ramirez et al. (1969) found that Ω/Ω_B is approximately a constant equal to 2.5, decreasing slowly with increasing energy. This result deviates drastically from the present findings shown in Fig. 14.

Cameron et al. (1977) have measured straggling for low-energy α particles in helium. Comparing their data for the lowest energy losses with those shown in Fig. 14, good agreement is found for energies below 400 keV, while for higher energies, the discrepancy increases with energy, resulting in a difference of a factor of 3 in Ω^2 for $E = 1070$ keV.

Concerning the above discrepancies in the helium data, it might be mentioned that in the experiments by both Cameron et al. and Ramirez et al., the energy spread of the incident α-particle beam is not negligible as compared to that resulting from the penetration of the helium gas, and this might obscure the straggling results.

Recently, there has been a growing interest in straggling for heavy ions because of its importance for many heavy-ion-accelerator experiments. Efken et al. (1975) have measured energy-loss straggling of N, Ne, and Ar ions in He, N_2, SF_6, and Ar-gas targets and in carbon foils at energies of 5–15 MeV. All these measurements were performed in the thin-absorber limit $\overline{\Delta E}/E_i \lesssim 0.1$. For monatomic targets, the measured straggling was significantly higher (1.5–2.5) than the straggling due to fluctuations in electron excitations, calculated from

the Vavilov theory (Vavilov (1957)). Efken et al. attributed this discrepancy to the straggling contribution Ω_C^2 caused by charge-state fluctuations and, using either formula (19) or Monte-Carlo calculations to predict Ω_C^2, they were able to explain their experimental findings qualitatively.

However, their measurements belong to the velocity-proportional stopping region $v \lesssim v_0 Z_1^{2/3}$, and thus the Vavilov theory is not applicable since the assumption underlying the Vavilov theory and the Bohr formula (Eq. 5) is similar, i.e., all of the target electrons contribute to the straggling as free electrons at rest, and the cross section is given by the Thomson formula (Eq. 4). In the low-velocity region, the straggling due to fluctuations in electron excitations is small as mentioned in Sec. I and discussed in detail in II. The straggling results mainly from the statistical distribution in impact parameters in the ion-atom collisions, and within the Firsov model, it is given by Eq. (16).

In Fig. 24, the experimental straggling data for heavier ions at low and medium velocities by Efken et al. (1975), Hvelplund (1971), Andersen et al. (1978), Sofield et al. (1978), and Cowern et al. (1979) are compared with the Hvelplund-Firsov low-velocity straggling formula (16) and the high-energy Bohr formula (5). When the straggling in Bohr units is plotted versus the parameter $[(Z_1+Z_2)^{8/3}/(Z_1^2 Z_2)]\left(\frac{v}{v_0}\right)^2$, formula (16) leads to a universal straight line.

From Fig. 24 it is seen that the straggling data by Efken et al. (1975) on atomic targets, and also the molecular results, when corrected for the molecular-correction term Ω_M^2, agree with the general trend of the straggling results by Hvelplund (1971) and Andersen et al. (1978) and with Eq. (17) to within a

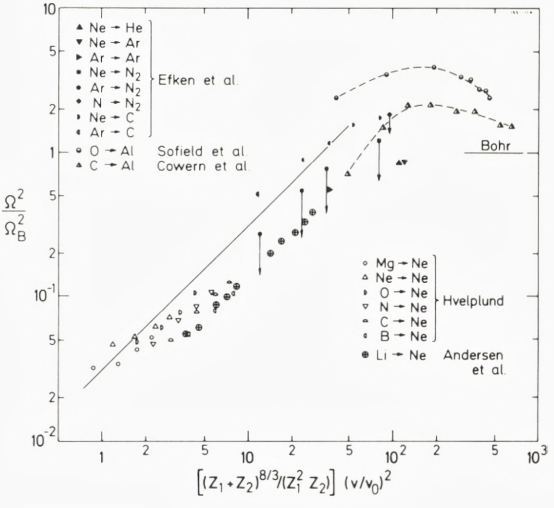

Fig. 24: The experimental straggling results for heavy ions at low and medium velocities by Efken et al. (1975), Hvelplund (1971), Andersen et al. (1978), Sofield et al. (1978), and Cowern et al. (1979) are compared with the Hvelplund-Firsov low-velocity straggling formula (16), and the high-energy Bohr formula (5). The dashed curves through the data of Sofield et al. and Cowern et al. are made only to guide the eye, whereas the arrows indicate the molecular correlation term Ω_M^2.

factor of 1–2. It therefore seems unneccessary to incorporate the straggling term Ω_C^2 to explain the experimental gas data by Efken et al.

In Fig. 24 are also shown the straggling results of Efken et al. for Ne and Ar ions on thin carbon foils. These solid-target results are systematically higher than the results on atomic gas targets. According to the authors, this may be due to the influence of foil inhomogeneities.

First, in Fig. 24 are shown the experimental straggling results of the Harwell group [Sofield et al. (1978) and Cowern et al. (1979)] for nearly fully stripped ^{16}O and ^{12}C ions penetrating aluminum foils. For the lowest energies, the experimental results again agree with Eq. (17) to within a factor of 1–2. At the highest energies, the data are significantly higher than the predictions based on the Livingstone-Bethe formula (Livingstone and Bethe (1937)), which is a semi-empirical version of the perturbation formulas, Eqs. (6) and (7), with the atomic quantities expressed in terms of ionization potentials and effective charges for the various electronic shells. The deviations from the Livingstone-Bethe formula was attributed to the straggling contribution Ω_C^2 from charge-state fluctuations, and on the assumption that Ω_C^2 is given by Eq. (19) and that the partial stopping cross sections can be written as $S_q = q^2 S_p$, experimental values of the electron-capture and -loss cross sections σ_{56} and σ_{65} were determined for ^{12}C.

However, the results may be vitiated by large uncertainties. First, the assumption that the stopping-power scales as the average square of the charge state may lead to an overestimate of the influence of charge-exchange straggling Ω_C^2 even though one may expect the error to be smaller than in the helium-ion case discussed above. Also the applicability of the Bethe-Livingstone perturbation formula might be questionable since the parameter $\kappa_B = 2Z_1 v_0/v$ is of the order of unity. A better way to obtain information on Ω_C^2 would be to compare the ^{12}C results with experimental-straggling results for a lighter ion, which is in a fixed charge state, i.e., to use a method similar to that used in Sec. 4.1.

Second, the measurements may be obscured by straggling contributions from foil inhomogeneities on a microscopic scale. Such effects were carefully checked by the Harwell group by means of a 25-μm diameter proton beam and a 2×0.1-μm Tallystep profiler, and it was concluded that thickness variations over distances larger than the lateral resolution of 2×10^5 Å and 2×10^4 Å for the methods contribute to the straggling by less than 10 %. It is, however, noteworthy that the energy dependence of the straggling is nearly identical to the energy dependence of the stopping power, which is exactly what is expected for a contribution $\Omega^2_{\Delta t}$ from thickness variations since $\Omega^2_{\Delta t} = (dE/dx)^2 \Delta t^2$, where Δt is the standard deviation of the foil-thickness distribution. It may therefore still be worthwhile to check for foil-inhomogeneity effects by comparing the straggling in the foils for different light ions such as protons, α particles, and lithium ions, for which

the influence of charge-state fluctuations is negligible. The applicability of this method, which has a high lateral resolution, has been demonstrated by the Oak Ridge group (see II for further details).

Finally, in our opinion, the ultimate test of the influence of charge-exchange straggling for heavy ions would be obtained from measurements with ^{12}C in a gas target since the electron-capture and -loss cross sections are either known or can be measured separately, and the problems with target inhomogeneities disappear.

Acknowledgements

The authors are indebted to J. U. Andersen, E. Bonderup, M. Inokuti, J. Lindhard, and P. Sigmund for their continuous interest in the present work and for the help and guidance received from them in numerous discussions. The assistance extended to us from the technical stoff, particularly V. Toft, is gratefully acknowledged. Finally, we wish to thank Alice Grandjean for her competent assistance in the preparation of the manuscript for the present article.

References

H. H. Andersen, F. Besenbacher, and H. Knudsen, Nucl. Instrum. Methods *149* (1978) 121.

H. H. Andersen and J. F. Ziegler, *Hydrogen Stopping Powers and Ranges in All Elements* (Pergamon, New York, 1977).

A. A. Bednyakov, U. V. Bulgakov, V. S. Nikolaev, V. P. Sobakin, and V. L. Chernov, Phys. Letters *62A* (1977) 183.

F. Besenbacher, Thesis (University of Aarhus, 1977) (unpublished).

F. Besenbacher, H. H. Andersen, P. Hvelplund, and H. Knudsen, Kgl. Danske Vidensk. Selsk., Mat.-Fys. Medd. *40*, No 3 (1979) (I).

F. Besenbacher, J. U. Andersen, and E. Bonderup, Nucl. Instrum. Methods *168* (1980) 1 (II).

F. Besenbacher, J. Heinemeier, P. Hvelplund, and H. Knudsen, Phys. Letters *61A* (1977) 15.

N. Bohr. Kgl. Danske Vidensk. Selsk., Mat.-Fys. Medd. *18*, No 8 (1948).

E. Bonderup, Kgl. Danske Vidensk. Selsk., Mat.-Fys. Medd. *35*, No 17 (1967).

E. Bonderup and P. Hvelplund, Phys. Rev. A *4* (1971) 562.

J. M. Cameron, R. H. McCamis. G. A. Miller, G. A. Moss, G. Roy, and A. W. Stetz, Nucl. Instrum. Methods *145* (1977) 405.

W. K. Chu, Phys. Rev. *A 13* (1976) 2057.

J. Cuevas, M. Garcia-Munoz, P. Torres, and S. K. Allison, Phys. Rev. A *135* (1964) 335.

N. E. B. Cowern, C. J. Sofield, J. M. Freeman, and J. P. Mason, Phys. Rev. A *19* (1979) 111.

J. L. Dehmer, M. Inokuti, and R. P. Saxon, Phys. Rev. A *12* (1975) 102.

B. Efken, D. Hahn, D. Hilscher, and G. Wüstefeld, Nucl. Instrum. Methods *129* (1975) 219.

U. Fano, Ann. Rev. Nucl. Sci. *13* (1963) 1.

O. B. Firsov, Zh. Eksp. Teor. Fiz. *36* (1959) 1517 [Engl. transl. Sov. Phys. JETP *9* (1959) 1076].

A. K. M. M. Haque and R. M. Hora, Nucl. Instrum. Methods *104* (1972) 77.

P. Hvelplund, Thesis (University of Aarhus, 1968) (unpublished).

P. Hvelplund, Kgl. Danske Vidensk. Selsk., Mat.-Fys. Medd. *38*, No 4 (1971).

P. Hvelplund, Phys. Rev. A *11* (1975) 1921.

P. Hvelplund et al. (1980) (private communication).

P. Hvelplund, J. Heinemeier, E. Horsdal Pedersen, and F. R. Simpson, J. Phys. B: Atom. Molec. Phys. *9* (1976) 4911.

M. Inokuti, T. Baer, and J. L. Dehmer, Phys. Rev. A *17* (1978) 1229.

L. Landau, J. Phys. USSR *8* (1944) 201.

J. Lindhard and M. Scharff, Kgl. Danske Vidensk. Selsk., Mat.-Fys. Medd. *27*, No 15 (1953).

J. Lindhard and A. Winther, Kgl. Danske Vidensk. Selsk. Mat. Fys. Medd. *34*, No. 4 (1964).

J. Lindhard, V. Nielsen, and M. Scharff, Kgl. Danske Vidensk. Selsk. Mat.-Fys. Medd. *35*, No. 10 (1968).

M. S. Livingstone and H. A. Bethe, Rev. Mod. Phys. *9* (1937) 245.

D. L. Mason, R. M. Prior, and A. R. Quinton, Nucl. Instrum. Methods *45* (1966) 41.

L. I. Pivovar, V. M. Tubaev, and M. T. Novikov, Zh. Eksp. Teor. Fiz. *41* (1961) 26; ibid. *42* (1962) 1490 [Engl. transl. Sov. Phys. JETP *14* (1962) 20; ibid. *15* (1962) 31].

J. J. Ramirez, R. M. Prior, J. B. Swint, A. R. Quinton, and R. A. Blue, Phys. Rev. *179* (1969) 310.

H. Schmidt-Böcking and H. Herming, Z. Phys. *A286* (1978) 253.

P. Sigmund, Phys. Rev. A *14* (1976) 996.

P. Sigmund, Kgl. Danske Vidensk. Selsk. Mat. Fys. Medd. *40*, No 5 (1978).

C. J. Sofield, N. E. B. Cowern, R. J. Petty, J. M. Freeman, and J. P. Mason, Phys. Rev. A *17*, 859 (1978).

C. Tschalär, Nucl. Instrum. Methods *61* (1968) 141; ibid. *64* (1968) 237.

P. V. Vavilov, Zh. Eksp. Teor. Fiz. *32* (1957) 920 [Engl. transl. Sov. Phys. JETP *4* (1957) 749].
O. Vollmer, Nucl. Instrum. Methods *121* (1974) *373*.
E. J. Williams, Proc. Roy. Soc. A *125* (1929) 420; ibid. A *130* (1931) 328.
J. F. Ziegler, *Helium Stopping Powers and Ranges in All Elements* (Pergamon, New York, 1978).
G. D. Zeiss, W. J. Meath, J. C. F. MacDonald, and D. J. Dawson, Radiat. Research *70* (1977) 284.

Indleveret til Selskabet november 1980.
Færdig fra trykkeriet august 1981.

The 'Astronomical' Chapters of the Ethiopic Book of Enoch (72 to 82)

TRANSLATION AND COMMENTARY
by OTTO NEUGEBAUER

With Additional Notes on the Aramaic Fragments
by Matthew Black

Det Kongelige Danske Videnskabernes Selskab
Matematisk-fysiske Meddelelser **40**: 10

Kommissionær: Munksgaard
København 1981

Summary

Ethiopic literature has preserved the "*Book of Enoch*" which is, as we know, closely related to the Jewish sect that is represented in the "*Dead Sea Scrolls*". Ten chapters of this work are concerned with *astronomical* concepts of a rather primitive character (variation in the length of daylight, illumination and rising amplitude of the moon, wind-directions, etc.), dominated by simple arithmetical patterns.

The present paper gives a new translation of these chapters, followed by notes where the meaning of the text is not self-explanatory. An appendix, with additional notes, deals with related source material in the *Qumran astronomical scrolls*.

Otto Neugebauer
Professor
Brown University, Box 1900
Providence
Rhode Island 02912, USA

Matthew Black
Professor
40 Buchanan Gardens
St. Andrews
Fife, Scotland

Bibliographical Abbreviations

Charles, Enoch: R. H. Charles, The Book of Enoch, 2nd ed., Oxford 1912.
Dillmann, Henoch: A. Dillmann, Das Buch Henoch, Leipzig 1853.
Flemming, Henoch: J. Flemming, Das Buch Henoch, Leipzig 1902.
Knibb, Enoch: M. A. Knibb, The Ethiopic Book of Enoch, 2 vols., Oxford 1978.
Martin, Le Livre d'Henoch, F. Martin, Paris 1906.
Milik, Enoch: J. T. Milik, The Books of Enoch, Oxford, 1976.
Neugebauer, EAC: O. Neugebauer, Ethiopic Astronomy and Computus, Österr. Akad. d. Wiss., Philos.-Hist. Kl., SB 347 (1979).
P-Sm Payne Smith, Thesaurus Syricus, Oxford, 1879.
Th W NT Theologisches Wörterbuch zum Neuen Testament.

Printed in Danmark by Bianco Lunos Bogtrykkeri A-S. ISSN 0023-3323. ISBN 87-7304-1173

Introduction

It has long been recognized that the astronomical chapters of the Book of Enoch constitute a composition of their own without much direct contact with the other parts of the treatise. This does not mean, however, that the astronomical book is unrelated to the rest of the Book of Enoch. On the contrary, its contents reflect faithfully, but in greater detail, the simple cosmologic concepts that prevailed in the communities which produced the Enochian literature.

I do not think, however, that one should consider the astronomical chapters as a literary unit composed by one author who followed some stylistic reasoning. It seems obvious to me that the text, as we have it, consists of two major versions, both covering essentially the same material, to which are added several still more fragmentary pieces. What we have is not the work of one author (or "redactor") but a conglomerate of closely related versions made by generations of scribes who assembled, to the best of their knowledge, the teaching current in their community about the structure and the laws of the cosmos. It is also important to note that purely calendaric rules on fasts and feasts are conspicuously absent, in marked contrast to the later Ethiopic "computus" of Judaic and Christian origin.

It is, of course, possible that there existed originally one treatise written to codify the astronomical doctrines of a religious sect. Such a treatise would then have reached us only in several more or less modified versions, two of which are reflected in the present chapters **72** to **76** and **77** to **79**,1 respectively. Fragments from additional versions are preserved in **79**,2 to **80**,1 while the description in **82** of the angelical hierarchy of the stars evidently belongs to a quite different source. Furthermore it should be remembered that innumerable fragments of Enochian "astronomy" (concerning the variation of the length of daylight, the "gates," the winds, etc.) are scattered all through the Ethiopian "computus"-treatises.

The several chapters of our treatise are grouped around only a small number of topics: solar year and lunar months, winds, the hierarchy of the stars, always hemmed in by a rigid schematism unrelated to reality. First the reader is told about the division of the "solar" year into four seasons of 30+30+31 days each. Then comes the variation of the length of daylight, based on a linear progression with extrema in the ratio 2:1. Then the lunar phases are also described by a linear pattern, assuming day 14 or day 15, respectively, as full moon dates. The variable

illumination of the moon is expressed either in terms of the moon's illuminated area (from 1 to 14 parts) or in relation to the sun's brightness, thus increasing from 1/98 (i.e. $1/7 \cdot 14$) to 1/7 (at full moon). Finally lunar months, alternatingly full and hollow, are related to the (schematic) solar year (but without any trace of a cyclic adjustment) and to the rising and setting in the "gates" at the eastern, respectively western, horizon. Unrelated to these gates are the twelve gates for the winds, four of which are beneficial, while eight bring discomfort and destruction. In contrast the stars are astronomically totally insignificant, being nothing but a replica of the division of the solar year. Neither constellations nor the zodiac nor planets are ever mentioned. This remains the rule also for the Ethiopic computus until the Arab conquest.

The search for time and place of origin of this primitive picture of the cosmic order can hardly be expected to lead to definitive results. The use of 30-day schematic months could have been inspired, e.g., by Babylonian arithmetical schemes (of the type of "Mul-Apin"), or by the Egyptian calendar. But the number and location of the epagomenal days was obviously chosen under the influence of the Jewish seven-day week and has no parallel elsewhere. The linear pattern for the variation of the length of daylight as well as the ratio 2:1 of its extrema suggests an early Babylonian background. But there is no visible trace of the sophisticated Babylonian astronomy of the Persian or Seleucid-Parthian period.

Dillmann's statement[1] that the astronomical part of the Book of Enoch is based on concepts extant in the Old Testament is simply incorrect: the Enoch year is not an old semitic calendaric unit; the schematic alternation between hollow and full months is not a real lunar calendar, and there exists no linear scheme in the Old Testament for the length of daylight, or patterns for "gates", for winds, or for "thousands" of stars, related to the schematic year. The whole Enochian astronomy is clearly an *ad hoc* construction and not the result of a common semitic tradition.

Summary of the Contents of Ch. **72** *to* **82**

First Version: **72** to **76** (with **74** probably being an intrusion)

72,2–5: Gates and Windows; winds drive the chariot of the sun (cf. **73**,2 and also **18**,4)

6–36: length of daylight, $M:m = 12:6$; year of $4 \cdot 91^{d} = 364^{d}$

37: brightness and size of sun and moon (cf. **73**,3; **78**,3,4)

73,1–3: winds drive the chariot of the moon (cf. **72**,5); brightness of sun and moon (cf. **72**,37; **78**,4)

4–8: increase of the area of illumination and of brightness of the moon from day 1

1: Dillmann, Henoch, p. 220.

to day 14 (incomplete); first visibility on the preceding day 30(i.e., after a hollow month)
74,1–4: illumination of the moon during 15 days (i.e., for a full month)
5–9: Gates and moon rise (incomplete)
10–16: garbled description of an octaeteris
75,1–7: stars ("thousands") and seasons (cf. **82**,4–20)
8,9: circumpolar stars
76,1–13: the 12 gates of the winds and their qualities (cf. the short version **33** to **36**)
14: concluding words to Methuselah (cf. **79**,1)

Second Version: **77** to **79**,1
77: Mythical geography
78,1: two-division of the year (cf. **78**,15,16; **79**,4,5)
2–5: lunar phases; size and brightness of sun and moon (cf. **72**,33–37); Gates
6–14: lunar visibility, waning moon; hollow and full months (cf. **73**,4–8 and **74**,1–4)
15,16: two-division of the lunar year (cf. **78**,1; **79**,4,5)
17: visibility of the moon during night and daytime
79,1: concluding words to Methuselah (cf. **76**,14)

Additional Fragments: **79**,2 to **80**,1; **82**,4–20 (**80**,2 to **82**,3 intrusion: apocalyptic)
79,2,3: Gates and lunar phases
4,5: two-division of the Enoch-year (cf. **78**,1,15,16) and Enoch epact
6,**80**,1: concluding speech of Uriel
82,4–20: hierarchy of stars ("thousands"), their leaders during the Enoch year (cf. **75**,1).

It seemed tempting to utilize in this commentary to the astronomical chapters of the Book of Enoch the numerous parallels and variants found in the Ethiopic "computus" treatises.[2] Since, however, practically all of these texts are unpublished and since only a detailed study could bring order and relative completeness to this huge mass of material,[3] I have usually abstained from referring to such "secondary" sources, though they may well contain information more reliable than the Book of Enoch in its present condition. I made good use, however, of the possibility of discussing my interpretations of the text with Professor Ephraim Isaac at the Institute for Advanced Study in Princeton.

In many ways every student of Enoch is indebted to Dillmann's pioneering work. When deviating from it in some technical details, however, I did not find it necessary always to quote Dillmann's translation and notes. In particular I did not refer to all the cases where the mix-up between the "gates" in the horizon and the modern concepts of orbital motion in the ecliptic produced misleading explanations. The insight into its archaic primitiveness is the key to understanding Enochian "astronomy."

2: Cf. for these texts my EAC.
3: The majority of printed catalogues deals only in a very unreliable fashion with treatises of this type.

Chapter **72**

1. Book on the Motion of the Luminaries of the Heaven, how each one of them stands in relation to their number, to their powers and their times, to their names and their origins and their months, as the holy angel Uriel, who is their leader, showed to me when he was with me. And he showed to me their whole description as they are, and for the years of the World to eternity, until the creation will be made anew to last forever.

2. This is the first law of the luminaries: the light (called) Sun has its exit among the gates of heaven in the east and it sets among the gates of heaven in the west.

3. And I saw six gates from which the sun rises and six gates where the sun sets; and (also) the moon rises and sets in these gates, as well as the leaders of the stars together with those which they lead. Six (gates) are in the east and six in the west and all of them are arranged in sequence. And there are many windows to the right and to the left of these gates.

4. And first comes out the great light called Sun and its roundness is as the roundness of heaven and it is all filled with fire that illuminates and heats.

5. And the chariot in which it rises the winds drive. And the sun goes down from the heaven and it turns toward north in order to travel toward the east; and it is guided in such a way that it enters in the (proper) gate and shines (again) in heaven.

6. In this way (the sun) emerges in the first month from the great gate, the fourth of these six gates in the east.

7. And in this fourth gate from which the sun emerges in the first month there are twelve window-openings from which flames come forth when (these windows) are opened in their (proper) times.

a. [8] When the sun rises in the sky it rises from this fourth gate (during) 30 days; and the sun sets exactly in this (fourth) gate in the west. [9] And in these days the day increases over the (preceding) day and the night decreases from the (preceding) night during 30 days. [10] And on this (30th) day the day is two ninths, (i.e. two) "parts", longer than the night, the day being exactly 10 parts and the night exactly 8 parts. [11] And the sun rises from the fourth gate and sets in the fourth (gate).

b. (Then) the sun moves to the fifth gate in the east, for 30 days, and it rises from it and it sets in the fifth gate. [12] And then the day increases two parts and the day amounts to eleven parts and the night decreases and amounts to seven parts.

c. [13] And (the sun) returns to the east and enters the sixth gate and it rises and sets in the sixth gate (during) 31 days according to its (the gate's) characteristics (for the season). [14] And during these days the day increases over the night (until) the day is twice (as long as) the night, such that the day amounts to twelve parts

and the night decreases and amounts to six parts. [15] Then the sun sets out to shorten the day and to lengthen the night.

d. And when the sun returns to the east it enters the sixth gate and it rises from it and it sets (in it during) 30 days. [16] And when the 30 days are completed the day has decreased exactly one part and the day is eleven parts and the night is seven parts. [17] And then the sun leaves this sixth gate in the west and

e. travels toward east to rise in the fifth gate (during) 30 days and it sets also in the west in the fifth gate. [18] And on this day the day has decreased two parts and the day is ten parts and the night is eight parts. [19] And the sun rises from the fifth gate and it sets in the fifth gate in the west.

f. (And then) it rises in the fourth (during) 31 days (according to) its (the gate's) characteristics (for the season), and it sets in the west. [20] On this day the day equals the night and they are the same and the night is nine parts and the day is nine parts. [21] And the sun rises from this (fourth) gate and it sets in the west.

g. And (then) it returns to the east and it rises from the third gate (during) 30 days and it sets in the west in the third gate. [22] And on these days the night increases over the day and the night increases over the (preceding) night and the day decreases from the (preceding) day until 30 days and the night is exactly ten parts and the day eight parts. [23] And the sun rises from this third gate and it sets in the west in the third gate.

h. And (then) it returns toward the east and the sun rises (during) 30 days in the second gate in the east and it sets also in the second gate in the western sky. [24] And on this day the night is eleven parts and the day seven parts. [25] And in these days the sun rises from this second gate and sets in the west (also) in the second gate.

i. And (then) it returns to the east to the first gate (during) 31 days and it (also) sets in the first gate in the western sky. [26] And on this day the night has increased to become twice (the length of) the day and the night is exactly 12 parts and the day is 6 parts.

k. [27] [And the sun has (thus) completed its appearances (in all gates) and then returns to these (same) appearances and it rises (again) in all its gates (during) 30 days and it sets opposite to them in the west.]

l. [28] And (during) these days the night has decreased by a ninth part (of its mean length), that is by one part; and the night consists of eleven parts and the day of seven parts.

m. [29] And the sun returns and enters the second gate in the east [and it returns to these appearances] during 30 days, rising and setting (in the second gate). [30] And in these days the night decreases in its length and the night is ten parts and the day eight parts. [31] And in these days the sun rises from the second gate and sets in the west.

TABLE I*

[a] ⊙ rises and sets in G_4 for 30^d; d increases, n decreases. Finally $d = n + 2$, thus $d = 10$, $n = 8$. Sunrise and sunset in G_4.

[b] ⊙ returns to E, in G_5 for 30^d; d increases by 2 to $d = 11$, n decreases to $n = 7$.

[c] (⊙) returns to E, enters G_6; rises and sets in G_6 for 31^d, as appropriate; d increases to $d = 2n$, thus $d = 12$, $n = 6$.
⊙ begins to shorten d and lengthen n:

[d] ⊙ returns to E, enters G_6; rises and sets in it for 30^d. After completion of these 30^d, d has decreased by 1, thus $d = 11$, $n = 7$.
⊙ leaves G_6 in the W and

[e] travels to E, to rise and to set in G_5 for 30^d. Finally d has decreased by 2, thus $d = 10$, $n = 8$. Sunrise and sunset in G_5.

[f] ⊙ rises in G_4 for 31^d, as appropriate, sets in W. (Finally) $d = n$, thus $n = 9$, $d = 9$. Sunrise and sunset in G_4.

[g] ⊙ returns to E, rises and sets in G_3 for 30^d. Now n increases over d; n increases, d decreases, until (after) 30^d $n = 10$, $d = 8$. Sunrise and sunset in the W in G_3.

[h] ⊙ returns to E, rises in G_2 for 30^d, sets in the W in G_2. Finally $n = 11$, $d = 7$. Sunrise and sunset in the W in G_2.

[i] ⊙ returns to E, [rises and] sets in the W in G_1 for 31^d. Finally n has increased to $n = 2d$, thus $n = 12$, $d = 6$.

[k] {⊙ completed its appearances (in all gates), now returns to these appearances, rising in all gates for 30^d and sets in the W.}

[l] [⊙ rises in G_1 for 30^d Finally] n has decreased by 1, thus $n = 11$, $d = 7$.

[m] ⊙ returns to E, [rising] in G_2 returns to appearances, rising and setting for 30^d; n decreases, thus (finally) $n = 10$, $d = 8$. Sunrise and sunset in the W in G_2.

[n] ⊙ returns to E, rising in G_3 for 31^d, setting in the W; n decreases to 9, thus $d = 9$ and $n = d$. {The year is 364^d long.}

* ⊙ . . . sun, G . . . gate (its number as subscript), E/W . . . East/West, d . . . day, n . . . night { } . . . intrusion

n. And (then) it returns to the east and it rises in the third gate (during) 31 days and it sets in the western sky. [32] And in these days the night decreases and it is 9 parts and the day is 9 parts and the night equals the day. [And the year is exactly 364 days (long)].

33. And the length of the day and the night and the shorteness of day and night vary with the circuit of the sun,

34. because its course becomes longer day after day or shorter night after night.

35. And this is the rule for the circuit of the sun, when it returns (to the east) and rises (again). This great luminary is called "sun" for all eternity.

36. And what rises is the great luminary and it is named according to its appearance as the Lord has commanded.

37. And it rises and similarly it sets and it does not diminish (in brightness) and it does not rest, but travels day and night. And its light is seven times as bright as the (light of the full) moon but with respect to their size the two are equal.

Notes to Chapter **72**. *Sun and Moon*

The composition of this chapter is very simple: its core is formed by twelve strictly parallel verses that describe the variation of the length of daylight and night during the year. To this tabulation is added a general introduction (2 to 7) about the six "gates" on the eastern and western horizon where the sun rises and sets. Similarly the tabulation is followed by some general remarks (33 to 37) about the sun and its role in the universe.

This structure of the chapter has been obscured by dividing the text into twenty-five verses unrelated to the original tabulation. I have therefore compiled a table (opposite) which shows the original pattern. Needless to say, there are many small variations from sentence to sentence. A serious disturbance occurred in verse 28 where a gloss (27) intruded into the text (with a repercussion still visible in 29). But Table I makes it easy to restore the basic scheme for each month:

> "The sun returns (from the preceding gate) to the east and enters the next gate in which it rises – and sets in the west – for 30 (or 31) days. During that time the days increase/decrease and the nights decrease/increase such that the day becomes . . . (parts), the night . . . (parts). Sunrise – and sunset in the west – takes place in this gate".

Twelve such sentences are the exact equivalent of our Table II or of the graph Fig. 1. Similar verbal presentations of tabular material are not only found frequently in Ethiopic computus texts but also in Aramaic fragments (Milik,

TABLE II

month 1 in gate 4	during	30 days, ending in	10^p of daylight,	8^p of night
2	5	30	11	7
3	6	31	12	6
4	6	30	11	7
5	5	30	10	8
6	4	31	9	9
7	3	30	8	10
8	2	30	7	11
9	1	31	6	12
10	1	30	7	11
11	2	30	8	10
12	3	31	9	9

Enoch, pp. 278–281). I have no doubt that the same genesis underlies also the next chapter.

72.1. Preamble, giving a summary of topics concerning the celestial luminaries. The expression ḫezabihomu, literally "their tribes, populations", obviously refers to the hierarchical grouping of the stars. Similarly śelṭanomu means "their powers", exercised by the stars over the division of the year, the seasons and the epagomenal days. Cf. for all these influences **75**,1–7 and **82**,4–20.

72,2,3. In the course of the year sun and moon rise and set in six "gates" on the eastern, respectively western, horizon. To the right and to the left of these gates are "windows", presumably for the stars (whereas in **36**,2,3 "small gates" are assigned to them). It should be noted that "right" and "left" are not the same as "south" and "north" since these associations are reversed with the change of direction of the observer.

Verse 3. "Arranged in sequence" probably refers to the numbering of the gates from one to six or from south to north.

72,4. The "roundness" (kebabu) of the sun corresponds to the roundness of the heavenly cupola. Neither "Umkreis" (Dillmann) nor "disc" (Knibb) are suitable descriptions of the sky.

72,5. Here we are told that the chariot of the sun (and of the moon, cf. **72**,2) is blown by winds, and that the sun, after setting in the west, returns via the north to the east. Independent of this motion of the luminaries is the (daily) rotation of the heaven, i.e. of the stars, which is also caused by winds (**18**,4). A slightly different picture is found in **41**,5 where sun and moon are said to come out from, and return to, "chambers" (mazāgebt). Similar differences are recognizable for the stars: "windows" in **72**,2,3, "gates" in **36**,2,3.

Fig. 1.

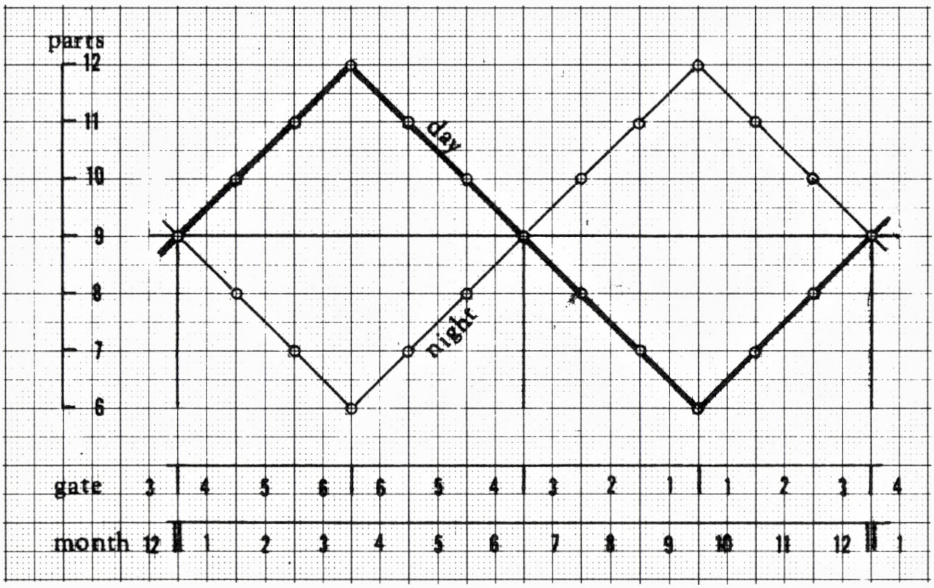

72,6 to 32. The essential content of these verses is summarized in Table II and in the graph of Fig. 1. Note that the linear pattern for the length of daylight and night ignores the epagomenal days (as is admitted in **75**,1).

The variation of the length of daylight and night during the solar year is here described by a numerical sequence that alternates, with constant difference, between a maximum M and a minimum m. If one chooses the simplest increment, i.e. if one makes the monthly difference "1 part" (p), then one has $M = m + 6$. If one furthermore assumes that $M = 2m$, then one finds finally $m = 6^{p}$, $M = 12^{p}$ (and always daylight + night = 18^{p}). This is exactly what we have in our text.

The use of such an alternating sequence (known as "linear zigzag function") suggests a Babylonian origin, since functions of this type play a fundamental role in Babylonian astronomy. For the length of daylight we find in cuneiform texts two ratios: one $M:m = 3:2$, the other (in earlier texts, e.g. in the series "Mul-Apin") $M:m = 2:1$. In the first case the units of time are "large hours" (i.e. 4 of our hours), in the second case we deal with "manas", i.e. weights of water, outflowing from a cylindrical water clock.[4]

In our texts the "parts" are never connected with any meteorological unit, neither hours, nor weights or volumes. Hence borrowing from Mesopotamia

4: Cf. Neugebauer, The Water Clock in Babylonian Astronomy, *Isis* 37 (1947), pp. 37–43.

remains only a possibility, though supported by another (slightly conjectural) feature, an 18-division of the day (counted in manas) in Mul-Apin.[5]

Of course a borrowing from comparatively early Babylonian material cannot be used as a chronological criterion for the time of composition of the astronomical section of the Book of Enoch. Methods of this kind have a life-span of many centuries and easily survive the development of more advanced methods.

72,6 to 11. In month 1 the sun emerges from gate 4 and the length of daylight increases during this month from 9^p to 10^p. Note that this implies that the year begins at the vernal equinox (as in Babylonia) whereas the Ethiopic calendar follows the Alexandrian year that begins with the month Thoth, roughly September.

Why is gate 4 called "large"? Dillmann[6] thinks of a comparison with the 12 windows which eject flames (**72**,7). Are other gates not provided with such windows?

Verse 11. After 30 days the sun returns (yegabe') from gate 4 in the west (via the north) to gate 5 in the east.

72,13 and 19. The translation of te'emerta zi'ahā as "its sign" is misleading since it could be taken as a reference to zodiacal signs[7] (which do not exist in Enoch's astronomy). The purpose of this remark, however, is to explain that 31 days of the sun's risings in the same gate is indicative for the position of the equinoxes and solstices. The Greek equivalent of te'emert is σημεῖον used in a technical sense,[8] in particular in relation to meteorological and calendaric dates (ἐπισημαίνειν).[9] Hence we may say that the rising of the sun in a specific gate is "indicative" or "characteristic" for the seasons. Cf. also **75**,6 and **82**,16 and 19.

Verse 19. As Fig. 1 (p. **11**) shows, the autumnal equinox occurs when the sun rises at the beginning of gate 3 in month 7.

72,27. Dillmann rendered 'ar'estihu by "Bahnabschnitte" (hence Knibb: "division of journey" – instead of "orbital segments"). It seems to me, however, that no reference to the sun's "orbit"[10] – at any rate a much too modern concept – is intended. In my opinion what is meant is simply the appearances (literally the "heads", the "beginnings") in the consecutive gates. This interpretation is supported by a variant in Ṭānā 9: 'ar'ayāhu, indicating something like "appearances". Cf. also next section.

5: This connection between Mul-Apin and the Book of Enoch was suggested many years ago by A. J. Sachs (cf. Neugebauer, *l.c* note 4, p. 40).

6: Dillmann, Henoch, p. 222.

7: So expressly by Charles.

8: Cf. e.g., also Matth. 16,3 σημεῖα τῶν καιρῶν "the signs of the time".

9: Cf. e.g., Ptolemy's work Φάσεις ἀπλανῶν ἀστέρων καὶ συναγωγὴ ἐπισημασίων (Opera minora, pp. 2–67). Cf. also RE Suppl. 7 col. 176–198 [Rehm].

10: Not to ask: the daily orbit? the yearly orbit? what are "Bahnabschnitte"?

72,33 to 35. The variability of the length of daylight and night is caused by the variability of the sun's positions in the gates (cf. verse 27), i.e. by the changing rising amplitude, as is indeed the case.

A number "60" (of risings and settings?) in verse 35 is omitted in several manuscripts (among them Ṭānā 9). This seems to be the better version.

72,37. The sun's brightness never changes (in contrast to the moon) and it is sevenfold the moon's greatest brightness[11] (cf. **73**,3 and **78**,4). Their apparent sizes, however, are equal (cf. **78**,3).[12]

Chapter **73**

1. And after the rule (concerning the sun) I saw another rule about the smaller luminary, called Moon.

2. And its roundness is as the roundness of heaven and the chariot on which it travels is driven by winds; and light is given to it in measure.

3. And each month its place of rising and of setting varies (through all gates) but its days are as the days of the sun. And when its light is evenly spread (over its disc) then it amounts to one seventh of the light of the sun.

4. And thus (the lunar month) begins, when (the moon) itself moves away (from the sun) toward east on the 30th day, and (when) on this day it becomes visible it is for you the beginning of the (lunar) month on the thirtieth day, (when the moon is setting) together with the sun in the gate from which the sun rises, [5] (but) at a distance (from the sun) of half of a seventh part.

And its whole disc is empty (i.e.) without light, excepting its seventh part of a fourteenth part (i.e. 1/98) of the light (of the sun).

6. And on (this) day (the moon) takes on a seventh part of one half (i.e. 1/14) of its light, and (thus) its light is the seventh of a seventh part and one half of it (i.e. 1/98 of the light of the sun).

7. (The moon) sets with the sun and when the sun rises, the moon rises with it and it takes on one half part (of 1/7) of its light. And in this night, at the beginning of the (lunar) day, which is the first day of the month, the moon sets with the sun, and it is dark in this night. – A seventh of a seventh part and one half.

8. And the moon rises and comes out on this day with exactly the seventh part (of its total light) and recedes from the rising of the sun and it (the moon) is

11: Dillmann (Henoch p. 226) suggests a derivation of this ratio from Isaiah 30.26. This passage (and similarly Enoch **91**,16), however, does not compare the sun with the moon but deals with some future events in the universe.

12: This is very nearly correct, as is common knowlege in ancient astronomy (based on evidence from solar eclipses).

illuminated during the remaining (part) of its day a sixth (?) and a seventh part (of the light of the sun).

Notes to Chapter **73**. *The Moon's Variable Illumination*

The original arrangement in this chapter was probably similar to the arrangement in the preceding chapter: a central tabulation preceded (and perhaps also followed) by general remarks. In the extant version, however, only the introduction is preserved (verses 1 to 3) while the tabulation breaks off after day 2. No doubt originally all days until full moon (day 14) had been listed. Instead we find now a disorganized chapter (**74**) which obviously does not belong to the original composition.

73,1 to 3. The moon's chariot is driven by winds (cf.**72**,5) and the roundness of the moon is as the roundness of the heavens.[13] Light is given to the moon (from the sun) and produces at full moon one-seventh of the sun's brightness (cf. **72**,37 and **78**,4). The rising and setting points of the moon change rapidly, but the number of "days" in a lunar calendar is the same as the corresponding number of solar days (**73**,3); for example, day 14 has the same distance from day 1 in a lunar calendar as a solar day 14 from solar day 1, in spite of the variability of the moments of moon-rise and moon-set in relation to sun-set. – For **73**,2 cf. also **78**,4.

73,4 to 8. In these verses we have a fragmentary description of a linear scheme for the increasing illumination of the moon during the first half of the lunar month. This increase is expressed in two scales: first, in absolute terms from 1^p to 14^p (hence proportional to the illuminated area),[14] and, secondly, in terms of solar brightness, hence increasing from $1/14 \cdot 1/7 = 1/98$ on the first day to $1/7$ at full moon (cf. **73**,3). Our text represents only a fragment of this scheme, which concerns the first two days. But the whole scheme is preserved in several computus texts (cf. EAC, p 196) the only difference being that a "full month", i.e. a 15-day increase, is contemplated.

Some trouble has been caused by an unfortunate terminology used in this section: the term ṣebāḥ "morning" here stands for "day" (as we sometimes count "summers" as "years", or winters" (keramt) in Ethiopic). To retain in astronomical context the literal meaning of an idiom of this type leads to senseless translations; e.g., "on that night at the beginning of its morning, at the beginning of the moon's

13: Knibb's MS has "sun" instead of "heaven". The parallel with **72**,4 shows that "heaven" is the better version.

14: The "parts" ('eda) here have nothing to do with the "parts" (kefla) in **72**,6 to 32.

day",[15] instead of "on that night, at the beginning of the (lunar) day, which is the first day of the month".

73,4. To say that a lunar month begins on "day 30" characterizes its predecessor as a hollow month.[16] At the beginning of the new month the moon has obtained enough (easterly) elongation from the sun to be visible at sunset. At conjunction, however, the moon is still nearer to the sun and thus rises and sets (invisibly) in the same gate as the sun. (Of course, all this is only that simple in the schematic lunar calendar which ignores, of necessity, all complexities of the actual lunar motion).

The conclusion of this verse is incorrectly assigned in part to the next verse. It contains the statement that the elongation of the moon from the sun at the evening of first visibility is 1/14 of the total elongation (reached at full moon). The use of reḫeqa in the technical sense of "elongation" is well attested in computus treatises. We read, e.g., in BM Add 24995 (28[a] II,1): "On the second day (the moon) recedes (yerḫeq) from the sun and becomes visible at 8 kekros and illuminates 2 parts of 15 (of its greatest) light (at full moon) and 1 part of 98 (parts) of the light of the sun". Incidentally, this close parallelism supports our conclusion that verses **73**,4 to 8 are only a fragment of a complete table for the moon's illumination, both absolute and in relation to the sun.

73,5. The numerical data for day 1 are: darkness of the moon's disc excepting $1/2 \cdot 1/7$ of its area that shines with the brightness of $1/7 \cdot 1/14$ (=1/98) of the sun's light.

73,6 to 8. The numbers in these verses are obviously corrupt as the many variants show, in part probably caused by the usual confusion of sixes and sevens. Both translation and notes are therefore only tentative and show not much more than that we are dealing with the description of the moon's increasing illumination. The text ends abruptly after verse 8.

73,6. The daily increment of the moon's illuminated area is 1/14. Its brightness on the first day of the lunar month amounts to $1/7 \cdot 1/7 \cdot 1/2$ (=1/98) of the sun's light.

73,7 and 8. On day 1 the moon is still near conjunction and therefore (nearly) rises and sets at the same time as the sun (cf. **73**,4). The number $1/7 \cdot 1/7 \cdot 1/2$ at the end of verse 7 is perhaps a meaningless duplication from verse 6.

Turning to day 2 (in verse 8) the moon's illuminated area is 2/14 = 1/7. It follows again a remark about the increasing elongation, but one should expect a

15: Knibb, p. 172 (**73**,7). Cf. also *Gen.* 50,3 and *Num.* 13, 25 in the Ethiopic Bible (E. Isaac). "Mornings" for "days" is also well attested in computus texts.

16: This is standard terminology in Babylonian astronomy, cf. F. X. Kugler, *Die Babylonische Mondrechnung*, Freiburg 1900, p. 36.

motion "away from the sun toward east" (as in verse 4) instead of a "receding from the rising sun". Perhaps this is simply a scribal error. Why the "remaining part of the day" is mentioned in the present context I do not know. For the brightness of the crescent on day 2 one should expect $1/7 \cdot 1/7$ (of the sun's brightness) and, indeed, some variants contain these numbers.

Chapter **74**

1. And I saw another circuit and (another) rule for it (the moon), whereby according to that rule it produces the cycle of the months.

2. All this showed to me Uriel, the holy angel, who is the leader of all of them. And I wrote down their positions as he showed them to me and I wrote down their respective months and the phases of their illumination until full moon on the fifteenth day.

3. And in steps (of fractions) of sevenths (lit. single seventh parts) the full moon is completed in the east and in steps (of fractions) of sevenths complete darkness is reached in the west.

4. In certain months (the moon) changes (the location of) its settings (with the sun, but) in certain months it goes its own individual way.

5. In two months (the moon) sets with the sun in these two middle gates, that is in the third and fourth gate.

6. (The moon) comes out (from the same gate) during seven days and it turns and moves back to the gate from which the sun rises, and it completes its light. And (the moon) recedes from the sun and enters for eight days the sixth gate from which the sun rises.

7. And when the sun rises from the fourth gate (the moon) comes out (from the sixth gate) during seven days until it rises from the fifth (gate) and it returns again during seven days to the fourth gate and it completes its light and it recedes (from the sun) and it enters the first gate (during) eight days.

8. And again it returns (after) seven days to the fourth gate from which the sun rises.

9. Thus I saw their positions when the months begin at sunset. – It seems pointless to attempt to give an accurate translation of the confused nonsense which some scribes produced from some trivial arithmetical relations (for which cf. the notes on p. 19). Readers who wish to see some rendering of these scrambled verses may look up Charles Enoch pp. 149–161 or Knibb Enoch pp. 173–4.

10. We are dealing with five ("solar") years of 364 days each.

11. Five lunar years fall short of five solar or sidereal years by (50 days, similarly three lunar years by) 30 days.

12. In this way the length of the lunar years is not too long and not too short by a single day in all eternity in relation to the years of 364 days each.

13. Three years are 1092 days long, five years 1820 days, thus eight years 1912 days.

14. to 16. Three lunar years are 1062 days long, thus 30 days shorter than three solar years. Similarly for five and eight years.

17. And the year is correctly completed in relation to its position within (the era of) the World and to the positions of the sun that rises and sets in its gates for 30 days (each).

Notes to Chapter **74**. *The Lunar Year*

This chapter contains a fragmentary description of the shift from gate to gate of sun and moon, based on a simple arithmetical scheme that is well known from computus treatises.[17] The present text, however, covers only the discussion for the first month. The remaining tabulation is replaced by a badly bungled attempt to describe an octaeteris that would relate a lunar year to the Enoch-year. It is quite evident that these verses (10 to 17) are a later addition.

74,1 and 2. A reference to the angel Uriel supports our impression that this chapter was originally not connected with the preceding or following chapter. Also full moon is here associated with day 15, not with day 14, as in chapter **73** (but cf. **78**,6,7).

74,2 to 4. The text as it stands is not very clear. What was intended to be expressed may be formulated as follows: Enoch writes down the pattern for the gates traversed by sun and moon during the lunar year. In each month the moon is waxing and waning: first its light increases until 1/7 of the sun's brightness is reached at full moon, visible in the east when the sun sets in the west; then the moon returns to darkness at conjunction which normally takes place in the same gate with the sun, though occasionally the moon may appear in an adjacent gate (as can actually be the case).

74,5. The gates 3 and 4 correspond to the equinoxes (cf. Fig. 1, p. **11**).

74,6. We have here a general description of the relationship between the days of a lunar month and the gates: the moon comes out through one of the outermost gates during seven (or eight) days; there it turns and moves back to the gate from which the sun rises during this month, and its light becomes full (at sunset); then the moon recedes again from this gate.

At the end of this verse the words "enters for eight days the sixth gate" do not belong here and should be deleted.

74,7 to 9. The tabulation begins with month 1 at the vernal equinox. Con-

TABLE III

Months	1	2	3	4	5	6	7	8	9	10	11	12	1	Months
Gates														Gates
4	2													4
5	2	2												5
6	8	8	4	4										6
5	2	2	2	2	2									5
4	1	1	2	2	1	2								4
3	1	1	1	1	1	1	2							3
2	2	2	2	2	2	2	2	2						2
1	8	7	8	7	8	7	8	7	4	4				1
2	2	2	2	2	2	2	2	2	2	2	2			2
3	1	1	1	1	1	1	1	1	2	2	1	2		3
4	1	1	2	2	1	1	1	1	1	1	1	1	2	4
5		2	2	2	2	2	2	2	2	2	2	2	2	5
6			4	4	8	8	8	8	8	7	8	8	8	6
5					2	2	2	2	2	2	2	2	2	5
4						1	1	1	1	1	1	1	1	4
3							1	2	2	2	1	1	1	3
2								1	2	2	2	2	2	2
1									4	4	8	7	8	1
2											2	2	2	2
3												1	1	3
4													1	4
Days	30	29	30	29	30	29	30	29	30	29	30	29	30	Days

junction takes place in gate 4, then the moon's rising and setting moves on to gate 6 for a period of seven days. Moving back[18] to gate 4 we have full moon, followed by another delay (of 8 days) in gate 1. Thus the complete scheme for this month would look about as follows (cf. also Table III):

gates:	4	5	6	5	4	3	2	1	2	3	4	
	sun				sun						sun	
during days:	[2]	[2]	7	[2]	[1]	[1]	[2]	8	[2]	[1]	[1]	total: 29

The continuation of this tabulation is omitted just as in the preceding chapters.

74,10 to 17. These verses constitute an abortive attempt to describe an octaeteris. The scribe had obviously only a very vague idea of the working of such a cycle, remembering only a separation of 8 years into two groups, one of 5

years (with 2 intercalary full months – hence his 30 days in **74**,11) and one of 3 years (with 1 intercalary month).[19] However instead of operating with Alexandrian years he assumes Enoch years; and because this does not lead to any reasonable relationship, he ends up with some correct but irrelevant numerical identities, based on the comparison of 5+3 Enoch years with 5+3 lunar years:

$5 \cdot 364 = 1820$ days	$5 \cdot 354^{d} = 1770 = 1820 - 50$ days
$3 \cdot 364 = 1092$ days	$3 \cdot 354^{d} = 1062 = 1092 - 30$ days
$8 \cdot 364 = 2912$ days	$8 \cdot 354^{d} = 2832 = 2912 - 80$ days

I surmise that this whole group of verses is a late addition, written under the influence of some computus treatise, where a mix-up of Alexandrian and Enoch years is quite common.

Chapter **75**

1. And their leaders, at the head of (each) thousand (stars), who are appointed (to rule) over the whole creation and over all stars (have to do also), with the four additional (days), without deviating from their positions, corresponding to the computus of the year. And they render service (also) on these four days which are not counted in the computus of the year.

2. And with respect to these (four days) people err since these luminaries do true service (also) in the (following) positions of the cosmos: once in the first gate and once in the third gate and once in the fourth gate and once in the sixth gate, so that the accuracy (of return) of the world is achieved after 364 (days) (with respect to the) positions of the cosmos.

3. Thus the signs, the times, the years, and the days were shown to me by the angel Uriel whom the eternal Lord of glory has appointed (to rule) over all the heavenly luminaries in heaven and in the world, such that they rule on the face of the sky and are seen from the earth and are made the guides of day and night, (namely) the sun and the moon and the stars and all the servants who return on all chariots of heaven.

4. Likewise Uriel showed me twelve openings, openings in the disc of the

17: Cf. Table III (p. 18), taken from EAC, p. 160. The positions of the numbers are not rigidly the same in all manuscripts; 7 and 8 as well as 1 and 2 can interchange places, as long as the proper totals 29 or 30 are preserved.

18: The assignment of seven days to the return to gate 4 (instead of 2 days) is a scribal error, perhaps caused by a similar passage in verse 8.

19: Cf. EAC, p. 83ff.

chariots of the sun in the sky, from which come forth over the earth the rays of the sun and its heat when they are opened at the proper time.

5. And (there are openings) for the winds and for the wind (that brings) dew, when the openings of heaven are opened at the boundaries (of the earth).

6. I have seen twelve gates in the heaven at the boundaries of the earth from which come out sun and moon and stars, and all the works of heaven from the east and from the west.

7. And (I saw) many window openings to the right and to the left and (each) one window emits heat at its time according to the gates from which the stars rise, as they are ordered, and in which they set according to their (the gates') numbers.

8. And I saw chariots in the heaven travelling in the world above the gates, where the stars revolve which never set.

9. And one of these (circuits) is larger than all of them and it is one which circles the whole world.

Notes to Chapter **75**. *The Stars*

75,1,2. The stars convey cosmic order to the calendar by their organization, which agrees exactly with the divisions of the Enoch year (ḥasāba ʿāmat), including the epagomenal days at the end of each season. Some people commit an error by ignoring these epagomenal days; this could refer to the lunar calendar of the Jews (which has no intercalary days), or to the Egyptian calendar (with five epagomenal days at the end of the year), or even to the schematic year of "Mul-Apin", which contains only twelve 30-day months.

In fact, however, the epagomenal days are "not counted in the computus of the year" since it would disturb the linearity of the scheme for the variation of the length of daylight (cf. note to **72**,6 to 32, p. **11**). This admission of a contradiction between theory and practice is obviously due to a gloss that intruded into the text.

The divisions between the seasons are marked by the rising of the sun in one of the following gates: winter solstice in gate 1, the equinoxes in gates 3 and 4 (autumnal and vernal equinox respectively, as is seen from the trend in the variation of the length of daylight – cf. **72**,6 to 32, p. **11**, Fig. 1), the summer solstice in gate 6. Cf. also **82**,6 and **74**,5. At these points the cosmos returns accurately to its previous position, 364 days earlier. Hence the (assumed) symmetry of the seasons of the solar year is taken as the ultimate basis for the calendar, and the stars reflect the same order.

75,3. The angel Uriel shows to Enoch all the things "about the signs and about

the times" (late'emert wala'azmān); this could refer to the role of the stars as indicators of the climatic changes from season to season (cf. above, **72**,13 p. **12**).

Sun, moon, and stars move "on the face of heaven" and thus are visible from the earth. The "servants[20] who return (ya'awdu – not, in this case, "revolve") on all chariots of heaven" are perhaps responsible for the return of the celestial bodies from their settings in the west to the eastern gates via the north (cf. **72**,5; **78**,5).

75,4. Once more Uriel explains the purpose of the gates and of the chariots: "twelve openings in the disc of the chariot of the sun ... from which the rays of the sun ... and heat ... come out". This picture has no parallel in the rest of the text and I suspect some confusion with the gates traversed by the sun (cf. also verse 7) or with the twelve windows from which flames are ejected (**72**,7).

75,5. Probably an intrusion,[21] in part duplicating verse 6.

75,6,7. Again 12 gates, east and west, but now not only for sun and moon but also for the stars. This makes little sense since the stars rise in all points of the eastern horizon. Then there are "windows" to the right and to the left (cf. **72**,3,7) from which heat comes out – a moment before (in **75**,4) the openings in the solar chariot performed this function – and also stars.

In verse 6 the "works of heaven" (gebrāta samāy) probably means the meteorological phenomena connected with the seasons. The "numbers" in verse 7 probably refer to the numbering of the gates, thus guaranteeing the proper positions of risings and settings.

75,8,9. There are chariots (obviously for stars) "above[22] the gates" for those stars which never set, i.e. circumpolar stars. One of their circuits is the greatest, encircling the whole (always visible) world.[23]

Chapter **76**

1. And I saw at the boundaries of the earth twelve gates, open to all winds, from where the winds come out and blow over the earth.

2. Three of them are open at the front of heaven (i.e. in the east) and three in

20: Dillmann's "dienstbare Geschöpfe" (in his time an idiom reminiscent of household help) became "serving creatures" in Knibb's translation.

21: Cf. Dillmann, Henoch, p. 233/4.

22: Some manuscripts add here "and below them", which makes no sense. Unfortunately Knibb accepted this version (following Dillmann but not Flemming).

23: Dillmann's "durchkreutzt die ganze Welt" (hence Knibb's "goes round through the whole world") is senseless. Obviously Dillmann was not familiar with the concept "greatest always visible circle". In his notes (p. 234) he even considers the "Morgenstern" or the Great Bear. In Greek astronomy this circle is known as the 'arctic circle.'

the west, and three at the right side of heaven, and three on the left side.

3. And the three first ones are in the direction of east, and (then) three are in the direction of north, and then those on the left, in the direction of south, and three in the west.

4. From four of them winds of blessing and prosperity come out, (but) through eight of them come winds (causing) calamities; when they are sent out they bring devastation over the whole earth and the water on it, and to all that inhabit it, to all that is in the water or on dry land.

5. And the first wind that comes out from these gates is called easterly. From the first gate in the direction of east, inclined toward south, devastation, drought, and heat and destruction come out.

6. And in the second gate, the middle one, (the wind) comes out straight; and from it rain and fruitfulness and prosperity and dew come out. And from the third gate, in the direction toward north, cold and drought come out.

7. And then the winds in the direction from south come out from three gates. First, from the first gate, that is inclined toward east, a hot wind comes out.

8. And from the middle gate, next to it, beautiful fragrance and dew and rain and prosperity and health come out.

9. And from the third gate, in the direction toward west, dew and rain and locusts and devastation come out.

10. And then the winds in the direction from north, (also) called baḥr (Sea),... From the seventh gate, (inclined) toward east, dew and rain, locusts and devastation come out.[24]

11. And from the middle gate, in a straight direction, health and rain and dew and prosperity come out. And from the third gate, (inclined) toward west, mist and hoar-frost and snow and rain and dew and locusts come out.

12. And then the fourth (group of) winds, in the direction toward west: from the first gate, in the direction of north, dew and rain and hoar-frost and cold and snow and frost come out.

13. And from the middle gate dew and rain, prosperity and blessing come out. And from the next gate, in the direction toward south, drought and devastation, burning and destruction come out from it.

14. And thus (the description of) the twelve gates in the four (quarters) of heaven is completed; and I have shown to you, my son Methusaleh, all their laws, (and all their) calamities and benefactions.

24: The text of this verse is corrupt but there is no doubt about the essential points, the order of the gates and the quality of the winds. A remark "inclined toward south" (and similarly "...toward north" in the next verse) makes no sense. The cause of all this trouble is probably the replacement of the eight-point rose of winds by twelve points, i.e. the duplication of the intermediate directions. Cf. the commentary (p. 24).

Fig. 2.

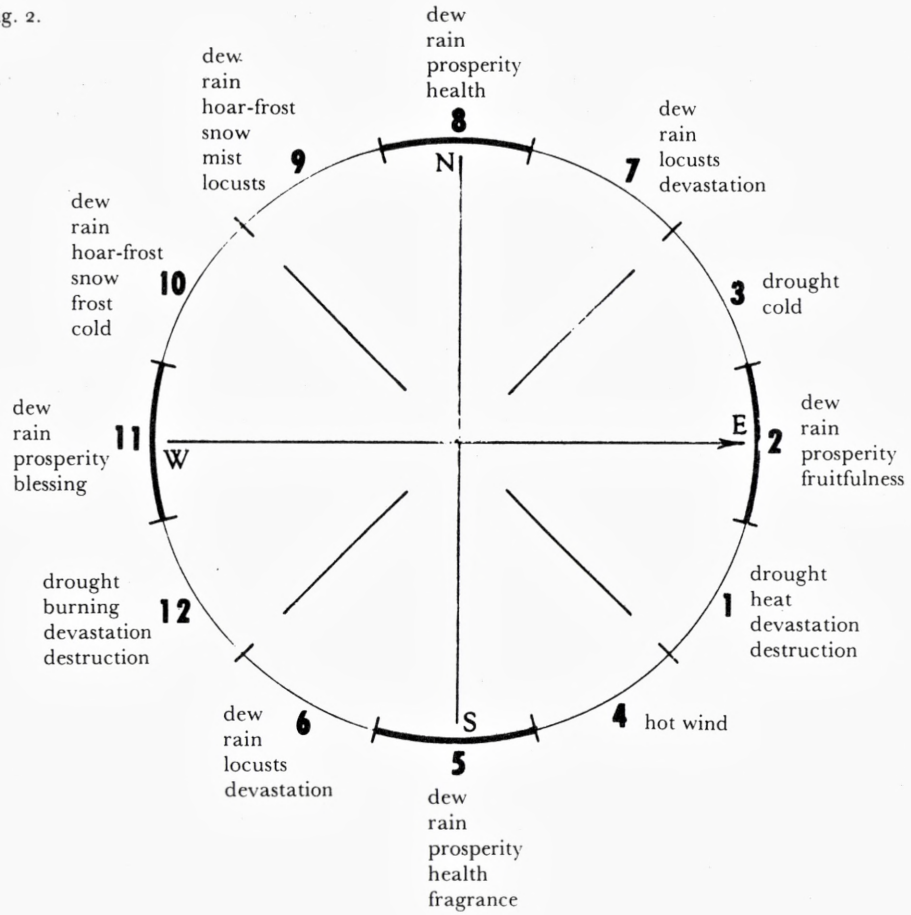

Notes to Chapter **76**. *The Winds*

The Ethiopian rose of winds consists of a sequence of twelve openings, again called "gates", which encircle the whole horizon. The winds from the four cardinal directions are supposed to be beneficial, in contrast to the winds from the remaining eight gates that bring discomfort and devastation (cf. Fig. 2).[25] Lists of this type are also found in many Ethiopic "computus" treatises. An abridged version is preserved in **34**,2 to **36**,1 of the Book of Enoch.

25: The accuracy of the 12-division of the horizon as shown in Fig. 2 should not be taken seriously. No numerical data are ever associated in our texts with these "gates".

One might think that long experience with climatic conditions would be condensed in such lists. In fact, however, we have here again only a schematic pattern, as far removed from empirical data as the arithmetical schemes for the length of daylight or the shadow tables. In all these cases scribal tradition has wiped out any connection with reality, if one ever existed.

The purely schematic character of qualities enumerated in the present section is easily recognizable in spite of some omissions or additions.[26] This is quite obvious in the case of winds from the cardinal directions. All of them bring "dew, rain, prosperity" to which is added one more gift:

E: fruitfulness S and N: health W: blessing.

Only the southern wind has a fifth quality ("fragrance").

This list for the principal wind-directions strongly suggests that each wind should be associated with exactly four qualities. This is indeed confirmed for the destructive winds, listed here in the order of the text:

E	1	drought, heat, devastation, destruction
	3	drought, cold
S	4	hot wind
	6	dew, rain, locusts, devastation
N	7	dew, rain, locusts, devastation
	9	dew, rain, hoar-frost, snow (mist, locusts)
W	10	dew, rain, hoar-frost, snow (frost, cold)
	12	drought, burning, devastation, destruction.

Excepting E 3 and S 4 and the rather senseless additions (shown in parentheses) in N 9 and W 10, we always have exactly four qualities mentioned. But this list reveals one more structural pattern. The third wind in one group has the same qualities as the first wind in the next: S 6 = N 7, N 9 = W 10, W 12 = E 1, thus closing the cycle. Only E 3 and S 4 are exceptions, which is not surprising since both entries are obviously defective.

Summarizing these regularities we can now say that the twelve-wind arrangement contains four beneficial gates and only four qualities for the remaining eight gates. This suggests an historical evolution from an 8-point rose of winds to a 12-point arrangement, the latter probably recommending itself by the formal similarity to the 6 + 6 "gates" for the risings and settings of sun and moon. Both eight-division and twelve-division are well known in hellenistic and Roman schemes, e.g., in geographical or architectural context.[27]

26: The order of the qualities listed in Fig. 2 for each individual wind can differ from the order (or rather disorder, which tends to obscure parallelisms) in the text.

27: Cf. (with caution) RE 8A, 2 cols. 2351f. and 2378 for the 12-division and col. 2364 for 8-division [Böker].

Fig. 3.

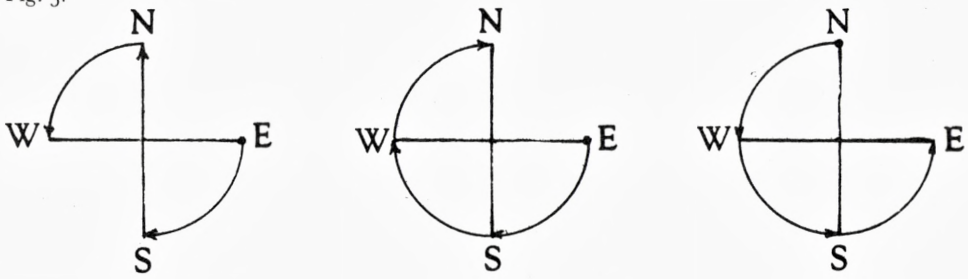

76,1 to 13 77,1 to 3 34 to 36

Finally, a remark should be made about the order in the text of enumerating the gates for the winds. Since little consistency is found in computus texts in matters of orientation, it is not surprising to meet the same situation in the present treatise. Fig. 3 illustrates two instances from the "astronomical" book (Ch. **76** and **77**) and compares them to the short version in Ch. **34** to **36**. In **76** and **77** the speaker faces east, the "front of heaven" (gaṣa samāy), thus north is "left" and south is "right". In **34** to **36**, however, the enumeration starts with north and proceeds counter-clockwise. In the astronomical sections the enumeration is either clockwise or E-S-N-W, as shown in Fig. 3, revealing one of the differences between the two versions to which **76** and **77**, respectively, belong.

On the other hand the existence of an overall common background is visible in the fact that the only qualities associated with a wind-direction in **34** to **36** are "dew, rain, hoar-frost, snow (hail)", ascribed in **34**,2 to the north (in general) and in our chapter to N 9 = W 10 (cf. above).

Concluding words to Methuselah (**76**,14) mark the end of the first version of the "astronomical" book, similar to **79**,1 for the second version.

Verse 7 is corrupt, as is evident from the restriction to only one quality (heat = moq, in some MSS misread to mot = death). Several computus treatises have here nafās meweq zasemu netug (or natig[28]), "hot wind called netug/natig". A similar gloss disturbed verse 10 by giving the north wind a special name, bāḥr = sea or ocean. With bāḥr is commonly associated as its counterpart the wind libā, i.e. λίψ, a southerly wind. Perhaps netug is a substitution for λίψ and is derived from νότος, the south wind.

In **77**,2 netug is assigned to the west and derived from the meaning "diminish." I suspect, however, that the transformation of this wind from the SE to the W is caused by this etymology, rather than explaining it. The shift from the eight-point rose of winds (still reflected in the restriction to only eight names – cf. EAC,

28: Cf. Littmann, Zeitschr. f. Assyriol. 16 (1902), p. 384.

p. 199, Fig. 4) to the twelve-point scheme (above Fig. 2) could only augment the confusion of directional terminology.

In fact the name bāḥr, "north," being unrelated to any great sea, may also be the result of a learned scribal interpretation of βόρεας. All these explanations are glosses, introduced by zasemu "which is called . . .", based on the same principle of assimilation of foreign words to semitic roots, exemplified by the change of τῶν θεῶν to ṭentyon and explained by the scribes as meaning "at the beginning".

Chapter **77**

1. The first quarter is called east because it is the chief (quarter); and the second is called south because there the Most High descends {and there in particular descends the one blessed in eternity}[29].

2. And the quarter in the west is called netug (diminished) because all celestial luminaries decrease there and go down.

3. And the fourth quarter which is called north is divided into three parts. The first of them is the habitat for man, the second (contains) the oceans and gorges and forests and rivers, darkness and mist. The third part (contains) the Garden of Justice.

4. I saw seven high mountains, higher than all mountains on the earth, and hoar-frost comes from them. {And days and seasons and years traverse them.}[29]

5. I saw seven rivers on the earth, greater than all other rivers; one of them, coming from the west, sheds its waters into the Great Sea.

6. And two (of them) come from the north to the sea and shed their waters into the Erythrean Sea in the east.

7. And the remaining four (rivers) come from the northern side toward the sea, two to the Erythrean Sea, and two empty into the Great Sea – and (some) say: into the desert.

8. I (also) saw seven large islands in the sea and on land; two on land and five in the Great Sea.

Notes to Chapter **77**. *Mystical Geography*

77,1 to 3. The cardinal directions are here enumerated in the order E-S-W-N, in contrast to **76** and **33** to **36** (cf. Fig. 3, p. 25). As in **76**,2 we are facing east. For the wind netug, cf. the note to **76**,7 (p. 25).

29: Probably a gloss.

The description in verse 1 of the south as "where the Most High descends" is explained in an Amharic (unpublished) commentary as a reference to Mt. Sinai (communication by Prof. Ephraim Isaac). In verse 3 one might expect the human habitat to be located between ocean and paradise, not to the west of the ocean.

77,4 to 8. In verse 4 the traditional translation of yaḥalf[30] as "schwinden dahin" (Dillmann, Flemming), "pass away and vanish" (Charles), makes no sense in the present context. I therefore suggest a translation "days and seasons and years traverse (them)", meaning that the sun, the cause of days, seasons, and years, traverses the space above the mountains.

The tendency of this geography is too mythological to allow accurate identifications. It seems plausible, however, to take the Erythrean Sea for the Persian Gulf into which the Euphrates and Tigris empty their waters. The two islands "on land" (verse 8) could be land between rivers, as Dillmann suggested (p. 238), Mesopotamia and Meroe. Milik assumed[31] a Greek version meaning "near (ἐπὶ) land."

Chapter **78**

1. The names for the sun are as follows: the first ʾOryārīs and the second Tomās.

2. The moon has four names: the first name is ʾAsonyā, the second ʾEblā, the third Benāsē, and the fourth ʾErāʿe.

3. These are the two great luminaries. Their roundness is as the roundness of the heavens and the amount of the roundness of the two is the same.

4. In the disc of the sun is combined seven times what is of light in the moon, and according to measure (light) is injected (from the sun into the moon) until the seventh part (of the light of the sun) has been transmitted.

5. And they set and they enter the gates in the west, and they return via the north to the eastern gates and (thus) come out (again) at the front of the sky (i.e. in the east).

6. And when the moon rises it becomes (first) visible on the sky when it contains the light of one-half of one-seventh part (of its total) and in fourteen (steps) it completes its full light.

7. And fifteen (parts of) light are put into it until in fifteen (days) its light is completed according to the character of the year and it makes fifteen parts while the moon is at its fourteenth part.

8. And when (the moon) is waning it decreases on the first day (to) fourteen

30: Some MSS (but not Ṭānā 9) have here wayaḥawer: "and proceed," "go", etc.
31: Milik, *Chronique d'Égypte* 46 (1971), p. 333.

parts of its light, on the second day it decreases to thirteen parts, on the third it decreases to twelve parts and on the fourth it decreases to eleven parts, and on the fifth it decreases to ten parts and on the sixth it decreases to nine parts, and on the seventh it decreases to eight parts, and on the eighth it decreases to seven parts, and on the ninth it decreases to six parts, and on the tenth it decreases to five parts, and on the eleventh it decreases to four parts, and on the twelfth it decreases to three parts, and on the thirteenth it decreases to two (parts), and on the fourteenth it decreases to half of one-seventh of its total light, and on the fifteenth is consumed what remains of the total.

9. And in certain months the moon (is visible) for each one of twenty-nine days and at times for twenty-eight days.

10. Then Uriel showed me another rule how light is put into the moon and where it is put into it from the sun.

11. The whole time in which (the illumination of) the moon progresses, light is transmitted to it, facing the sun, until the fourteenth day when its light is complete. And when the (lunar disc) is completely aflame (then) its light in the sky is complete.

12. On the first day it is called New Moon because on the day light appears on it (for the first time).

13. And (the light) becomes exactly complete on the day when the sun sets in the west and when in the east (the moon) rises at (the beginning of) night. And the moon is illuminated all night until the sun rises opposite it and the moon is seen opposite the sun.

14. And where the light for the moon entered it, there again it wanes until all its light is consumed and the days of the (lunar) month are used up and the moon's disc remains empty without light.

15. And in three months their duration amounts to thirty days and in three months it amounts to twenty-nine days each, in which it makes its recession, in the first time and in the first gate, in 177 days.

16. And in the time of its waxing it becomes visible in three months for thirty days each, and it becomes visible in three (other) months for twenty-nine days each.

17. At night it is visible for twenty(nine) (days) each like a man and at daytime (it is) like the sky because without its light there is nothing else in it.

79,1. And now, my son, I have shown you everything and completed is (the story about) the law of all the stars in the sky.

Notes to Chapter **78**. *Lunar Phases*

Much in this chapter duplicates the preceding versions.

78,1. A two-division of the year in reflected in the attribution of two names to the sun. For the etymology, cf. Charles, Enoch, p. 166, notes; also Milik Chronique d'Égypte 46 [1971] p. 338, commentary to line 7.

78,2. Corresponding to its four major phases the moon is given four names; cf. Charles, Enoch, p. 166/7, notes.

78,3 to 5. Equality of the apparent diameters of sun and moon (cf. **72**,37) and brightness 7:1 (cf. **72**,37 and **73**,3). Setting of the luminaries in the western gates and return via the north (cf. **72**,5 and **75**,3) to the east.

78,4. The transfer of light "according to measure" (here and in **73**,2) probably means the steady increase of illumination, proportional to time.

78,6 to 9. Verses 6 and 7 deal in a general fashion with the waxing moon, allowing either day 14 or day 15 as full moon date. What the character of the "year" has to do in this context (verse 7) I do not understand. Error for "month" (hollow/full)?

Verse 8 concerns the waning moon, describing the day-by-day decrease of the moon's illuminated area in terms of "parts", from 14 on the first day to invisibility on the 15th day. For a fragment of a Greek version cf. Milik, *Chronique d'Égypte* 46 (1971), p. 339.

Verse 9 offers the possibility that a "month" may contain 29 or 28 days (of visibility), being either full or hollow.

78,10 to 14. Once more a general description of the lunar phases, introduced by Uriel. In verse 11 one should not say that the moon is "opposite" the sun during the whole time of waxing in order to avoid misinterpretation as "opposition" (which is the proper term in verse 13). Prof. E. Isaac suggests, therefore, translating baqedma ḍaḥay as "facing the sun".

Verse 14 states correctly darkness of the waning moon begins on the same side (the western rim) on which the illumination of the waxing moon begins.

78,15,16. The lunar year is schematically divided into two halves, each containing three full and three hollow months, thus a total of 177 days. Apparently in analogy to the two halves of a lunar month these two halves of the lunar year are denoted as "waning" and "waxing" (why in that order?). Cf. also **79**,3,4.

78,17. During 2[9] nights,[32] when the moon is visible, "it looks like a man". At daytime, however, the moon is invisible, apparently because it has no corporality, being only a receptacle of the solar light. Cf. also the Aramaic version.[33]

79,1. Final words of Methuselah, similar to the end of the first version (**76**,14).

32: The reading 20 in the MSS is obviously a scribal error, unfortunately not emended by Dillmann and thus retained ever since. The Aramaic version has no number.

33: Milik, Enoch, p. 295/5. Cf. also Claire Préaux, La lune dans la pensée grecque, Ch. III. (Académie Royale de Belgique, Mémoires de la Classe des Lettres, 2e sér. t. 61, fasc. 4 [1973]).

Chapter **79**

2. And he (Uriel) showed me every one of their rules for every day and for every season with its power, and for every year, and about the places of exit (i.e. the gates), and concerning the rules for every month and for every week;

3. and the decrement of the moon that accumulated in the sixth gate, because in the sixth gate its (the moon's)light is completed. The beginning of the decrement

4. that accumulates (is) in the first gate (and it is counted) at its (proper) time, (i.e.) when 177 days are completed – or, after the reckoning with weeks, 25 (weeks) and two days.

5. And how it (the moon) falls behind in relation to the sun – or, after the reckoning with the stars, exactly five days in one single (period of) time, (i.e. half a lunar year) and when this position which you see has been traversed (by the stars).

6. Such is the appearance and the picture for each luminary shown to me by the great angel Uriel who is their leader.

80,1. And in these days the angel Uriel spoke to me and said to me: see, I have shown to you, O Enoch, everything and I have revealed to you everything to be seen about the sun, the moon, and everything about those who guide the stars in heaven and all who turn (back) their works, (and about) their times, and their places of exit (i.e. the gates).

Notes to Chapter **79**. *The Lunar Year*

79,2. "He showed me" refers, of course, to the angel Uriel, not to Methuselah, who was addressed in **79**,1. Cf. also **79**,6–**80**,1.

The "power" of each season (lit. "time") refers to the stars which during stretches of 91 days represent the seasons, as we are told in **82**,15 to 20.

79,3,4. The verses 3 to 5 assume a two-division of the lunar year, similar to **78**,15,16. Details remain obscure since the text is obviously corrupt.

In the present context "sixth gate" and "first gate" do not refer to the numbering of the gates from south to north but probably mean here "a sixth gate" and "a first gate", thus describing an interval of six gates traversed by the sun, i.e. the time of half a lunar year (cf. **78**,15).

During this time the lunar months develop a "decrement" (tāḥṣāṣita) with respect to the calendar months. How the changing illumination of the moon got involved with this problem I do not know. Actually this whole chapter is only an expanded (and therefore more obscure) version of **78**,15.

79,5. One half lunar year is now compared to one half of the Enoch-year. The

latter is considered to be a "sidereal" year. Indeed, "the law of stars" is identical with the order of the Enoch-year (cf. **75**,1,2 and **82**). The difference in question is, of course, 5 days; cf. also **74**,10 to 17.

The "position traversed" (by the stars) marks the completion of the two seasons; cf. **82**,9 and 10.

79,6; **80**,1. Concluding speech of the angel Uriel, referring to his teaching about sun, moon, and stars (cf. also **82**,7,8), i.e. the topics which constitute the core of the "astronomical" Book of Enoch. The remaining topics (including the winds?) appear to be later accretions.

The "turning back" probably refers to the return of the celestial bodies to the east after their setting; cf. for parallels **75**,3 (p. 19).

80,2 to **82**,3 is an intrusion of non-astronomical material: apocalyptic and again concluding words to Methuselah.

Chapter **82**

4. Blessed are all the righteous ones, blessed are those who walk in the path of righteousness and do not err, like the sinners, in counting all their days in which the sun travels in the sky, entering in and coming out from the doors for thirty days, together with the leaders of the thousands of the orders of the stars, together with the four (days) that are added in order to separate the intervals (of the year, i.e.) the four intervals, the parts of the year, which lead them and with which they make their entry on four days.

5. There are people who err concerning them (the epagomenal days) by not counting them in the reckoning of the year, for such people err and do not know them correctly,

6. although they belong to the computus of the year and are truly recorded forever: one in the first gate and one in the third and one in the fourth and one in the sixth (gate) and the year is completed in 364 days.

7. For (this) account is true and the computation exact as (here) recorded, since (everything) concerning the luminaries, the months and the festivals and the (years) and the days Uriel has shown to me and revealed it as he was ordered by the Lord of the whole creation of the world and about the host of heaven.

8. And he has power in heaven over night and day, so as to make light visible to men, sun and moon and stars and all the powers of heaven which revolve in their circuits.

9. And this is the law of the stars which set in their (proper) places, and at their times and their festivals and at their months.

10. And these are the names of their leaders, who watch them that they enter at their times, who guide them in their positions and their order, in their times and their months and their powers and their positions.

11. Their four leaders who separate the four parts of the year enter first; after them (enter) the twelve leaders of the orders who separate the months; and the 360 heads over thousands (of stars) are the ones who separate the days; and for the four epagomenal days those are the leaders who separate the four parts of the year.

12. And concerning these heads over thousands: always one (of the four main leaders) is placed at the position between the leaders (of thousands) and their followers; but these (single) leaders separate (the seasons).

13. And these are the names of the leaders who separate the four fixed parts of the year: Melk'ēl, Hel'ememēlēk, Mel'ēyal, Nārēl.

14. And the names of those whom they lead are 'Adnār'ēl, 'Iyāsusa'ēl, and 'Iyelumē'ēl. These three follow the leaders of the orders (of thousands); (then again) one (of the four main leaders) follows the three leaders of the orders which (in turn) follows after those (main) leaders (who are placed) at the positions which separate the four seasons of the year.

15. At the beginning of the year Melk'ēl rises first and rules – to whom is (also) given the name "Southern Sun". And the total of days during which he exercises his power is 91 days.

16. And these are the signs of the days which are to be seen on earth in the days of his period of rulership: sweat, heat, and dryness (?). And all trees bear fruit, and leaves appear on all trees (and there will be) good harvest, and rose-flowers and all the flowers which blossom in the fields; but the trees of winter are withered.

17. And these are the names of the leaders who are the subordinates: Berke'ēl, Zēlebsā'ēl, and another one who is added, (as) head of thousands, called Hēloyāsēf; and completed are the days of rulership (over this season) with this one.

18. And the second leader after him is Hel'ememēlēk whom they (also) call "Luminous Sun"; and the total of the days of his light are 91 days.

19. And these are the signs of these days on earth: heat and drought; and the trees bring their fruit to ripeness and maturity and make their fruit dry; and the sheep mate and become pregnant; and men gather all the fruits of the earth, and everything which is in the fields, and the vats of wine. (And this) will take place in the days of his rulership.

20. And these are the names, and the orders and the subordinates, the leaders of thousands: Gēda'ēyāl, Kē'ēl, and Hē'ēl and the name of one who is added to them as a head of thousands called 'Asfā'ēl, and completed are the days of rulership with this one.

Notes to Chapter **82**. *The Hierarchy of the Stars*

As before, e.g. in **75**,1 and 2, the arrangement of the stars follows exactly the pattern of the Enoch-year.

82,4,5. There are "leaders of thousand (stars)", responsible for each month of 30 days and four leaders of higher rank who are associated with the four epagomenal days. Again people are mentioned who do not deal correctly with these days (cf. **75**,2).

In verse 4 'anqaṣ "door" (also "division," "chapter" and "cycle") probably means here not the gates but the divisions between the seasons.

82,6. The epagomenal days are associated with gates 1, 3, 4, 6, i.e. with the solstices and equinoxes (cf. **75**,2).

82,7,8. All this is handed down on the authority of the angel Uriel, who is set over the luminaries, sun, moon, and stars. Cf. the similar epilogue in **80**,1.

What follows in the remaining verses of Chapter **82** is obviously an addition taken from a different source.[34] It contains one of those lists of freely invented names which enhance the authority of cosmologic revelations. The text as we have it is slightly in disorder, which is not surprising for a meaningless list of (angel-) names. Nevertheless it seems to be clear that the original structure was simple enough: first are listed the leaders of the four seasons, then the twelve subordinate commanders for the single months. The text is incomplete only in the case of the last season, perhaps owing to an early mutilation of the manuscript.

82,9,10. Introductory remarks to the following (but not "headings" as Dillmann, p. 249, says).

82,11. Different ranks are given to the "leaders" (marāḥyān) of the stars. There are four leaders of the seasons, associated with the four epagomenal days, each one on duty for 91 days; then follow four groups of three leaders of the "orders" (śer'atāt) corresponding to the twelve months of 30 days each; finally, the "leaders of the thousand (stars)", concerned with the 360 single days. These leaders are presumably angels. Dillmann expressed their ranks by hellenistic titles: 4 toparchs, 12 taxiarchs, 360 chiliarchs.[35]

82,12,13. The names of the leaders of the seasons, represented by the epagomenal days, are:

Melkiel Helemmemelek Meleyal Narel

82,14,15. The first season, spring, is ruled over by Melkiel. The subordinate leaders are:

Adnarel Iyasusael Iylumiel.

34: Also Dillmann, Henoch, p. 239 (and p. 248) assumes the "Unächtheit" of **82**,9 to 20.
35: Dillmann, p. 52, notes; p. 248, n. 1.

It is the function of the fixed stars to signal by their (heliacal) rising the beginnings of months and seasons. The cyclic order of these phenomena is expressed in the text by indicating that the season-stars can be considered either as preceding or following the three subordinate stars which initiate the three months of each season. The second half of verse 14 seems to express in a clumsy fashion the fact that it is immaterial in a circular sequence of stars to distinguish between leading and following positions.

82.15 and 18. The names "Southern Sun" and "Luminous Sun", associated with seasonal leaders, do not fit very well, respectively, spring and summer, where they are mentioned.

82,16,19. The "signs" are here clearly referring to climatic and agricultural characteristics (cf. **72**,13).

82,17,18. The second season has the following subordinate rulers:

Berkeel Zelebsael Heloyasef.

82,20. The subordinate rulers of the third season are:

Gedaeyal Keel Heel.

Only the name Asfael is preserved for the last season.[36] Here the text ends abruptly.

Although the text of this verse, as we have it, is in disorder, the preserved words nevertheless suffice to show that the original version was an exact parallel to **82**,17: the names of two subordinate leaders are given, followed by a third one who brings the three months of the season to a conclusion.

Additional Notes on the Aramaic Fragments

by Matthew Black

72.1 With šelṭānomu cf. שלטן **82**.10, Enastr^{b}28.2, Milik, *Enoch*, p. 295 (ל]טנהון[ב ו?).

72.27 Milik, Enoch, p. 282, equates 'ar'estihu with חרתיה 'its sections' at Enastr^{b}iii.2.

72.4–8 This linear scheme is found in the Aramaic fragments (Milik, Enoch, p. 278 f.; EAC, p. 195 f.). That the Ethiopic texts go back ultimately to this Aramaic Enoch is amply demonstrated by the surviving fragment of En **78**.6–8, 9–12 etc. (Milik, Enoch, p. 292 f.). The terminology of these texts has given rise

36: Charles, Enoch, p. 178, n. 20, considers the name Asfael as "merely an inversion" of Heloyaseph (of the second season). There is, of course, no reason visible for such a reduction of the number of leaders (not to mention the inept execution of the "inversion").

to a certain amount of confusion in the Ethiopic, e.g. the fractions 1/2 of 1/7th (1/14th) or 6/7ths and 1/2 (13/14ths) (see note on 73.6). For the general pattern of the Aramaic texts, consult Milik, Enoch, p. 274f. and EAC, p. 196, n. 6.[37]

73.6 The correct translation of 1/14 is found at **78**.6, manfaqa sāb'eta'eda, lit. 'half of a seventh part': so Enastr^{b}6.8, פלג שביע חד (Milik, Enoch, p. 284).

76.3–10 are preserved (fragmentarily) at Enastr^{c}1.ii.1–10(Milik, Enoch, p. 284f.).

76.3 Enastr^{c}1.ii.1 (Milik, Enoch, p. 285) has 'and the three (gates) which are after them are on the north (lit. the left)': (ותלתה די בתריהון על שמול) This corresponds to the clause in Ethiopic, 'and then those on the left'. Charles bracketed this clause (Charles, Enoch, p. 163) as 'nonsense'. It is undoubtedly original: the preceding clause 'and (then) three are in the direction of the north' seems to be a doublet. In this verse the Ethiopic text follows the order ENSW which does not correspond to the order ESNW in verses 5–14;[38] for a discussion of this problem and possible explanations, see Charles Enoch, p. 163, Martin Le Livre d'Hénoch, p. 176, Knibb, Enoch, p. 176. (Milik claims (p. 286) that it is the order [S] N [W] which is found in the Aramaic, but there is no evidence in the fragment for this – only the north is mentioned.)

76.4–5 Cf. Enastr^{c}1.ii.2, Milik, Enoch, p. 285. The Aramaic has a fuller form of text. For these destructive winds, see above, p. 23.

76.6 relates to the favourable East wind (above, p. 23). Enastr^{c}1. ii.5: '... by the second gate comes forth the east wind, the chief (of winds) (נפקא רוח קדים [קד]מיא)'. Milik reconstructs (p. 285) רוח קדים קדימא, 'the east-east wind', comparing line 6 רוח קדים גרבה, 'the east-north wind' which comes from the third eastern gate. But 'east-east' is a meaningless tautology. At **77**.1 Eth. the wind is called 'east' because it is qadāmāwi, 'chief, first': here Enastr^{c}1.ii.15 reads קדמיא and the line is restored by Milik: '[And they call the east (quarter) East] because it is the first (בדי הוא קדמיא) (Eth. has translated 'quarter' as 'wind': see below, note on **76**.13, **77**.1.) This east wind is said to be 'in the middle', i.e. between the two destructive winds of gates 1 and 3, and according to Eth. it 'comes forth in a straight line', i.e. blowing due E–W,

37: The expression rendered in EAC 'keeping (in darkness) a remainder of 2/7 (= 4/14)' is a curious one in the original. It occurs twice in this passage Enastr^{b}7.iii.4 and 8: thus line 4 נפק . . . ושלט בשאר יממא דן שביעין תרין ופלג . . . rendered by Milik 'it (the moon) emerges ... and it keeps during the rest of this day two sevenths (parts of its light) and a half'. Milik explains ושלט (p. 282), 'lit. 'and it reigns (over such and such a fraction of its light)'. May we not rather have here the lost root שלט behind Heb. שֶׁלֶט 'a shield', and meaning 'to cover' velare? (cf. Th WNT s.v. ἐξουσία Bd. II., p. 570 (Foerster).) We should then translate: 'it emerges and covers during the rest of this day 5/14'.

38: See EAC p. 198 for Ethiopic directional terminology.

unlike the two other east winds which are deflected to the south or the north. (See Flemming-Radermacher, p. 99.)

76.13 Enastr^{c}1.ii.14, Enastr^{b}23.1 (cf. Milik, Enoch, pp. 228, 289, 290) [א]בדן ומות [. . .] וחרבן 'devastation, death, [heat?] and destruction'. Cf. **76**.5 where several manuscripts read mot ('death') for moq ('heat'); mot may have fallen out of Eth. by haplography. (The reading מות seems reasonably certain.)

76.14 Enastr^{c}1.ii.14, Enastr^{b}23.2 'And (the description of) the twelve gates of the four quarters of heaven (רוחי שמיא) is completed; their full number and explanation I have shown to you, my son Methuselah'. Eth.'s 'four gates' (ḫewāḫewe) is a scribal error for nafāsāt = רוחות 'quarters' (Flemming Henoch, p. 103). (Milik reads שלמהון ופרשהון as a hendiadys 'their complete explanation'.)

77.1 Cf. Enastr^{c}1.ii.13–20, Enastr^{b}23, Milik, Enoch, p. 287 f. *The first quarter is called east.* That nafās translated 'region, quarter' is clear from Enastr^{b}23.4 'And the great quarter (רוח רבא) (they call) the west quarter רוח מערבא ... *because it is the chief (quarter).* Enastr^{c}1.ii.14 ('The east they call East) because it is the chief (quarter) (בדי הוא קדמיא). For the word-play on קדם, Dillmann, Henoch, p. 236: קדמיא can mean both 'first, chief' or 'in front' – The East is 'in front'. *the Most High descends.* Enastr^{b}23.2 בדיל לתמן דאר רבא 'because there the Great One dwells'. The Aram. assumes an etymology from Heb. דר רם; the translator reads the text as ירד רבא καταβαίνει ὁ ὕψιστος. Cf. Dillmann, Henoch, p. 236, Knibb, Enoch, p. 179.

77.2 *because all celestial luminaries decrease there* ... Enastr^{b}23.5 is defective in this clause: I suggest with Eth. בדי [לתמן חסרו נהור]י שמיא[39]. The reading מאין '(celestial) bodies' is corrected three times at Enastr^{c}1.ii.17,18: the first correction מאנין gives the true reading (the word occurs again at line 17 מאני שמיא [(written מאאן)]: '(celestial) bodies setting and bodies entering'. (Milik reads interrogative מנ(א)ין 'whence' but translates 'there'.) The whole verse then reads: 'And the West is called the great quarter, because there the heavenly luminaries wane, (celestial) bodies setting and (celestial) bodies entering, and all the stars; and on this account it is called West (lit. 'setting').' Presumably 'great' because it has to accommodate all the heavenly host after they set.

77.3a Enastr^{c}1.ii.18–19, Enastr^{b}23.6–9 has a much longer text, relatively fully preserved; for the text see Milik, Enoch, pp. 288, 289. I read Enastr^{c}1.ii.18 בדי מאנין זרחין 'because (celestial) bodies arise' as above at Enastr^{b}23.7. 'And the north (they call) North because in it all the celestial bodies (lit. vessels)

39: Syr ܣܗܪ ܕܢܘܗܪ (P Sm col 1341) luna decrescens.

hide and assemble and revolve and proceed to the East of heaven. And the east (they call) East because from there the celestial bodies (מאני שמיא) arise; and also (they call it) *mizraḥ* because (there celestial) bodies arise זרחין, דרחין), moons . . . to appear . . .' (For Milik's conjectural supplement, see p. 288.)

77.3b For the second part of the verse, cf. Enastr^{c}1.ii.19, Enastr^{b}23.9; on the analogy of v.4 perhaps supplement [וחזית תלת פלגות] 'And I saw three divisions of the earth, one of them for the traffic of men, and one of them for [all seas and rivers], and one of them for the deserts [and the . . .] and the Paradise of Justice.' Milik supplies (after 'for the deserts') ולשבע 'and for the Seven (ultra-terrestrial regions)', a fascinating but unsupported guess (p. 291).

77.4 A few letters only are preserved in the first part of the verse (Milik, p. 289), but [ונ]חת עליהון תלגא is certain ·and snow comes down upon them'.

78.1 Milik's observation (Chronique d'Egypte, 46 (1971), p. 338) that the two names for the sun correspond to the two seasons of the year seems correct, but the order is not the 'dry' season followed by the 'wet' season, but probably the other way round (cf. Charles, Enoch, p. 167), winter and spring (early summer), the 'wet' season' Oryāres אורי חרס followed by summer, the 'dry' or 'hot' season (Tomās חמה?). 'Asonyā ('Asenyā) for the moon may be connected with Accadian sin, sen, 'moon' (cf. sivan, month of the moon-god, Sinai, etc.). 'Eblā can only be לבנה 'the white one', 'Ērā' ירח 'moon', and Benāsē is probably corrupt in the first syllable (Dillmann) unless it stands for בן ־ אנש, 'man' (cf. **78**.17).

78.6–8 cf. Enastr^{c}1.iii.3–9 (Milik, Enoch, p. 292). In line 1 בשמיא (corresponding to basamāy) is barely identifiable in the photograph and nothing else is now recoverable from the traces of other letters visible. At line 2 מין[משל . . .] בכול יום ויום ? עד יום ארבעת עשר ומש[למין בה כול נהורה] is all that can be recovered with certainty, but the Aram. text is evidently fuller than Eth.: the meaning seems to be that 'they (the added fractions) fill up (the light) each day and complete in it (the 14th day) all its light'. The last few words can be confidently restored from verse 7 where Enastr^{c}1.iii.5 has preserved a text: עד יום חמשת עשר ומשלמין בה נהורה 'Until the 15th day and they (the fractions) complete in it its light.'

78.7 cf. Enastr^{c}1.iii.6, read and translated by Milik: ודבר ירחיא בפלגי שבעין 'And it (the moon) accomplishes (lit. guides) (its) phases by halves of sevenths.' The reading דבר is certain (cf. Knibb): the word occurs again at **78**.5 as a noun (Enastr^{b}26.3, Milik, p. 294); cf. Tg דברא Jud. 5.21. If we assume that ירח 'month' can mean 'phase of the moon' (Milik), an alternative construction would be to take דבר as a noun and render 'and the course of the moon's phases is by halves of sevenths'.

78.8 Enastr^{c}1.iii.8 reads [ובי]ומא רב[יעי חד מן חד עשׂ[ירי]א 'and on the fourth day (the moon decreases) by one part from eleven parts', i.e. to ten parts (not as Milik 'eleven parts'). This firm text enables us to restore the earlier sequence which should be correctly rendered: 'And on the first day (the moon decreases) by one part from fourteen parts', i.e. to thirteen parts (not as Milik fourteen parts).

78.10 *Then Uriel showed me another rule.* Milik equates the fragment Enastr^{b}25.1–4 with this verse but the identification is doubtful. All that is now visible in the photograph are the words: [. . .]שבון אחרן אחזית לה די אזל [. . .]. 'Another calculation I was shown with regard to it (the moon?).' חשבון 'calculation' is certainly right (cf. **79**.1 Enastr^{b}26.7) and אחזית is to be construed as an inner passive of the Ophal (cf. Milik, Enoch, p. 202). (Milik supplements ['And Uriel demonstrated to me] a further calculation by having shown it unto me that . . .', but this is forcing the syntax to support the identification.) In line 1 שניא 'years' is visible but there is nothing corresponding in Eth. There are several other passages where similar words are found, e.g. **73**.1 '. . . I saw another law', **74**.1 'I saw another course, a law . . .'. (The verb אזל is probably auxiliary, but the main verb is lost.)

78.17 *At night it is visible . . . nothing else in it.* This verse is fragmentarily preserved at Enastr^{b}26.4–6 but in a longer form of text. (Enastr^{b}26.3 is reproduced in Eth. at **79**.3, but Enastr^{b}26.4–6 go together and belong to the text behind **78**.17 Eth.) Enastr^{c}26.4–5 reads: [. . .] בה כדמות חזי דמי כדי נהורה בה . . . האי]ר בלילא מן קצ[ת דמי חזוא דן כדמות אנש . . . in it (?) it resembles the likeness of a mirror when the light shines on it. On some nights (מן קצת) this appearance resembles the image of a man'. There is a play on the noun חזי, חזיא 'mirror' (Heb. חזיא מראה Tg. Ex. 38.8) and חזוא 'vision, appearance, (Milik's 'like an image of vision' makes little sense). I take האיר as a Haphel of אור (cf. the use of אורתא for 'moon-light'; אר Hoftijzer, p. 23). Has this line 4 fallen out of the original behind Eth. by h m t or a similar form of scribal error (note the common phraseology of lines 4 and 5). מן קצת = *partim* (Dan 2.42) must refer in this context to the appearance of 'the man in the moon' for only a part of the full times of the moon's waxing or waning. There is nothing in the Aram. text about 'twenty (nine) days', which could have arisen in the Eth. text from the Greek κατεικάζει = דמי read as κατ' εἴκοσι, baba'ešrā. All that remains of the rest of the verse in Aram. is ובימא מן ה בלחודהי[. . .]. The second phrase is read as a repeated מן קצת by Milik. The last phrase looks like נהורה בלחודוהי 'light by itself'; perhaps the original read 'and in the day-time, for part (of the time), it resembles the sky for there is no light in it by itself: ובימא מן[קצת דמי כדמות שמיא די לית בה נהור]ה בלחודוהי . The meaning would be that

the moon 'resembles the sky' in the sense that its now invisible disc is blue 'like the sky'. (There is no evidence to support Milik's 'like the sun in the sky'.)

79.1 Enastr[b] 26.6 וכען מחזא אנה לך ברי 'And now I am showing to you, my son ...'

79.3–4 Fragments of the original of these verses have been preserved at Enastr[b] 26.2–4: בתרעא שתיתיא בה 'in the sixth gate ...' ומין [. . . ו] תרין ומחסר מן דבר שמשא [4](twenty five weeks) and two days. [5]And it (the moon) falls behind the course of the sun ...' (For the rest of this fragment see on **78**.17.)

82.9 Fragments of verses 9–13 are preserved at Enastr[b] 28.1–5 (Milik, Enoch, p. 295). It is pointless to try to reconstruct an original text on the basis of the few words and phrases preserved: the most we can do is to identify the terminology and its Eth. equivalent. Thus lines 1 and 2 preserve five nouns two of which occur in Eth. verse 9, two in verse 10: למעדיהון לחדשיהון לדגליהון . . . [ו]בש[לטנהון לכל מסרתהון. The first two words correspond to Eth's 'their festivals and at their months'. (There is no astronomical justification for taking מעדין as 'signs of the Zodiac', Milik, p. 295,187f.) Eth.'s 'months' should be understood, in the light of Aram. חדשיהון as 'their new moons', closely associated with 'festivals'. The last term דגליהון probably corresponds to šer'atātihomu of verses 10, 11 in the sense of τάγματα 'order, classes', especially in a military sense 'battalions'. See Milik, Enoch, p. 147, Knibb, Enoch, p. 188f. The two terms in line 10 correspond to šelṭānātihomu 'their powers' and either to meqwāmātihomu or makānātihomu, 'their positions' or 'their places'. See Milik, p. 187 for מסרת. At lines 3 and 4 the fragment has [. . . ן ראשין ד and [. . . רשין בי[מפ] corresponding to Eth. marāḥyan zašer'atāt 'leaders of the orders' ([ד]גלין ראשין probably translated first as ταξιάρχαι); the remaining fragment corresponds to 'ella yelēleyewomu la'awerah, 'who separate the months' ([די מפ]רשין) בין ירחיא. Line 5 corresponds to verse 13 [וא]לין שמהת 'and these are the names ...'

82.16ff. A description of spring, summer and winter occurs at Enastr[d] 1.1 (Milik, Enoch, p. 296) with expressions recalling En 2.1–5 and En 3 (En[a] 1.ii.3ff.) and En **82**.16ff. Milik detects in this piece the missing original of the description of autumn and winter which should have followed **82**.20. Certainly some original Aramaic description of the seasons, preserved more fully at En[a] 1.ii.3ff., has served to provide the foundation of the poetic account of the seasons at En 2 and 3. En[d] i [. . .]ומטר מחתין על ארעא וזרע[ונין . . . line 2 '... and rain descend upon the earth, and plants (?) ...' Cf. Eth. En 2.3 '... and clouds and dew and rain rest upon it (the earth)'. (Has מחתין, Aph. ptc. נחת been read as מניחין Aph. ptc. נוח = 'a'raf?)

[. . .]עשב ארעא יעא ונפק ויעל[י . . .] line 3

'. . . the herbage of the earth sprouts, comes forth and blossoms.' Cf. 82.16.

ושתוא הוה ועלי כל אילנוא [מתבישין ונפלין lines 4–6[40]
ברא מן ארבעה] עשר אילנין די לא חזה להון [לאתעריא
לאתערטלה . . .]על[יהו]ן מתקימין

'But winter comes and the leaves of all the trees [wither and fall except for four]teen trees from whom it is unseemly [to be stripped bare . . .] their leaves abide . . . Cf. Eth. En 3 '. . . the trees appear withered . . . with the exception of fourteen trees which are not stripped bare (but) which abide with the old (foliage) till the new appears after two or three years.' (cf. En[a]1.ii. 5–6)

40: Restored from En 2.2, En 3.

Subject Index

Indleveret til Selskabet januar 1981.
Færdig fra trykkeriet november 1981.

Self-Mass and Equivalence in Special Relativity

By J. KALCKAR, J. LINDHARD *and* O. ULFBECK

Det Kongelige Danske Videnskabernes Selskab
Matematisk-fysiske Meddelelser **40**: 11

Kommissionær: Munksgaard
København 1982

Contents

Synopsis

We study dynamical aspects of equivalence between mass and energy, for systems of interacting particles. The starting-point consists in the classical formulae for electromagnetic self-momentum, self-energy and self-force. These formulae possess puzzling terms which have been subject to various explanations, like compensating Poincare stresses, or were bypassed through attempts of redefinition of the classical electron model. By means of a comprehensive study of acceleration processes we show that there is a crucial error in the usual derivations of self-force. We derive a basic acceleration equation for a point-like system, with detailed equivalence. It also follows that the standard formulae for self-energy and self-momentum are, at best, misleading. Next, we study how systems are to be described in an accelerated, rigid coordinate frame – the Møller box. In considerable detail we investigate classical and quantal equations of motion for fields and for particles in the Møller box, including the Dirac equation for the hydrogen atom, arriving at equivalence. Finally we discuss properties of composite systems as compared with properties of particles.

JØRGEN KALCKAR, OLE ULFBECK
Niels Bohr Institute
University of Copenhagen

JENS LINDHARD
Institute of Physics
University of Aarhus
Denmark

Printed in Denmark by Bianco Lunos Bogtrykkeri A/S, ISSN 0023-3323. ISBN 87-7304-124-6

§1. Introduction

The present paper contains a study of equivalence between mass and energy, for a system of interacting particles. This question may appear trivial from the point of view of general principles in special relativity, for there can be no doubt about the validity of equivalence as a basic statement. But if we turn to actual calculations on systems with Coulomb interaction, we find that the resulting self-energies and self-momenta do not correspond to equivalence, and lack four-vector properties[1]. This is certainly surprising to the uninitiated, for one would expect beforehand that the Maxwell equations must give equivalence unambiguously and in a straightforward manner, since special relativity, in a sense, is suspended in the Maxwell equations. It should be added that the results in question have often been treated in connection with the problem of electron self-energies where they apparently required the presence of non-electromagnetic forces. Because of the complications, some authors have preferred to *define* an electromagnetic energy-momentum four-vector for the electron[1,9]. This will hardly do, however. The basic classical case is not an electron, but a macroscopic system, for which one is not free to define the electromagnetic self-energy or self-momentum.

These preliminary comments will be enlarged upon in the remainder of this chapter. But they indicate the aim of the present paper. In fact, we hope to convince the reader that simple acceleration processes, if studied with care, reveal that there is not only equivalence, but even *detailed* equivalence: each individual term of, e.g., the interaction energy, has separate equivalence. The basic conclusions in this respect are contained in §2, where the connection between mass, forces and acceleration is studied. A central issue is the question of comparison of forces acting in different points of a system. In §3 is presented the more systematic treatment of accelerated frames of reference. Next, in §4, we calculate the various contributions to self-mass in a number of classical and quantal cases, including the Dirac equation for a hydrogen atom.

As outlined, our study has an immediate background. But it is also a necessary step in a more general pursuit: the endeavour to understand composite systems

and elementary particles, including the connection between them and between their classical and quantal descriptions. At the end of this paper, in § 5, we outline general viewpoints on this matter.

Basic equivalence

The equivalence between energy and inertial mass was first established by Einstein[2] (cf. also v. Laue[3]). He considered the change suffered by a system emitting electromagnetic radiation. The usual derivation consists in showing, first, that the energy E and momentum **P** of any closed system constitute a four-vector. The basis for this result is the special principle of relativity, combined with conservation of energy and momentum for initial and final states of a collision process (corresponding to Einstein's idealized experiments). Second, the four-vector may be written as

$$E = E'\gamma, \tag{1.1}$$

$$\mathbf{P} = \frac{E'}{c^2}\gamma\mathbf{v}, \tag{1.2}$$

where E' is a constant, and

$$\gamma = \frac{1}{(1-\mathbf{v}^2/c^2)^{1/2}}\,.$$

Now, on the one hand, E' in (1.1) has to be the energy of the system in the rest frame. On the other hand, E'/c^2 in (1.2) must be the mass M of the system, belonging to the non-relativistic limit $v \ll c$, and so we obtain equivalence,

$$M = \frac{E'}{c^2}. \tag{1.3}$$

Equivalence is therefore derived by comparing initial and final states of an elastic or inelastic process. The proof concerns not only a stable system; it includes unstable systems. Although it appears that the proof of equivalence is concerned with only the total energy of a system, still there are evidently cases where part of the energy must have equivalence. Moreover, one can divide the total energy of a system into well-defined average contributions from various forms of energy, as exemplified by the virial theorem. Beforehand, one would expect individual equivalence from these clearly separated contributions. Thus, it is natural to investigate the possible validity of *detailed* equivalence, as formulated in the preamble.

The previous results may be put on a more comprehensive form if we introduce the Lagrangian of the system. In fact, the above momentum-energy four-vector

with its derivation from collisions, must be connected to a variational principle, albeit with limited validity. In an inertial frame where the system has velocity $\mathbf{v}$, the corresponding Lagrangian must be

$$L = -E'\left(1-\frac{\mathbf{v}^2}{c^2}\right)^{1/2}. \tag{1.4}$$

In this formula the internal energy E' is a constant of the motion for a given internal state of the system. If we now observe the given system from another frame, where it has velocity $\mathbf{v}+\delta\mathbf{v}$, the change δL becomes

$$\delta L = \delta\mathbf{v}\cdot\mathbf{P}, \tag{1.5}$$

where $\mathbf{P}$ is given by (1.2). Furthermore, the quantity $E = -L+\mathbf{v}\cdot\mathbf{P}$ corresponds to (1.1).

In (1.5) we are concerned with a variation where the internal state of the system is kept unchanged. Thus, we have obtained equivalence, $E' = Mc^2$, by being able to separate the external velocity variable, $\mathbf{v}$ in (1.4), from the internal variables of the system, concealed in the constant E'. Moreover, for soft collisions – if the internal state of the system is not changed during a collision – the equation of motion will be based on (1.4), i.e. the kinetic contribution to the total Lagrangian.

In itself, eq. (1.4) reasserts the surmises about detailed equivalence made above. Thus, when the system is in internal statistical equilibrium, and E' separates into definite terms according to the virial theorem, these terms should contribute separate mass terms in the account of the system.

The classical electron model

Already before the advent of special relativity, Poynting's theorem of density of field energy was utilized in several calculations of self-energy and self-momentum of a charged body (cf. e.g. Jammer[4]). The foremost contribution was made by Lorentz[5]. The results were hardly changed at all by special relativity. We shall illustrate the situation in terms of the so-called classical electron model, as quoted in numerous monographs (e.g., Jackson[1], Pais[6], Feynman[7]).

Consider then a stable spherical shell with radius a, on which a total charge Q is uniformly distributed. In a inertial frame K the shell moves with velocity $\mathbf{v}$. According to standard results, the densities of momentum and energy of an electromagnetic field are given by the field strengths

$$\mathbf{g}(\mathbf{r},t) = \frac{1}{4\pi c}\mathbf{E}(\mathbf{r},t)\times\mathbf{B}(\mathbf{r},t), \tag{1.6}$$

$$u(\mathbf{r},t) = \frac{1}{8\pi}(\mathbf{E}^2(\mathbf{r},t) + \mathbf{B}^2(\mathbf{r},t)). \tag{1.7}$$

In these equations we introduce the field belonging to the shell, as observed in the frame K. By integrating over all space we find a momentum $\mathbf{P}_{el}$, and an energy E_{el} (cf. Jackson[1], Becker and Sauter[8], Rohrlich[9])

$$\mathbf{P}_{el} = \int d^3r\ \mathbf{g}(\mathbf{r},t) = \frac{4}{3}\frac{Q^2}{2a}\gamma\mathbf{v}, \tag{1.8}$$

$$E_{el} = \int d^3r\ u(\mathbf{r},t) = \frac{Q^2}{2a}\gamma\left(1+\frac{1}{3}\frac{\mathbf{v}^2}{c^2}\right). \tag{1.9}$$

In particular, it is seen that, in the rest frame, the momentum is $\mathbf{P}'_{el} = 0$, and the energy $E'_{el} = Q^2/2a$. Therefore it follows that not only is equivalence lacking, but also $\mathbf{P}_{el}$, E_{el}, $\mathbf{P}'_{el}$, and E'_{el} fail to transform like the four-vector (1.1), (1.2). As is well known, this curious result cannot be rejected out of hand, the reason being that $\mathbf{P}_{el}$ and E_{el} do no represent the *total* momentum and energy of the shell. The shell in question must in any case be stabilized by other, nonelectromagnetic, forces. These forces, or Poincaré stresses, should then compensate the erratic behaviour of (1.8), (1.9), giving a correct total four-vector.

The results (1.8) and 1.9) are obtained somewhat indirectly, in a sense. Their basis, i.e. the densities (1.6) and (1.7), was derived in turn by studying the action of forces from material charges on an electromagnetic field. Therefore, by omitting the intermediate step (1.6), there should be a more direct, but apparently equivalent, way of obtaining the self-mass due to Coulomb interaction. In fact, one can instead find the electromagnetic self-force of an accelerated shell of charge. An early calculation of this kind was performed by Born[10] (cf. also Heitler[11], and Jackson[1]). If the shell is momentarily at rest, but accelerated, at time $t = 0$, one may find the electric field $\mathbf{E}_s(\mathbf{r},t)$ caused by it. We assume that the acceleration is small, or $ga/c^2 \ll 1$. It follows that $\mathbf{E}_s(\mathbf{r},t)$ is linear in $\mathbf{g}$. Let further $\varrho(\mathbf{r})$ denote the internal charge distribution of the shell. The total self-force $\mathbf{F}_s$ is then linear in the acceleration

$$\mathbf{F}_s = \int d^3r\,\varrho(\mathbf{r})\,\mathbf{E}_s(\mathbf{r},t=0)\ . \tag{1.10}$$

By these means the self-mass was calculated as the ratio F_s/g, the result being in agreement with (1.8).

It thus looks as if the previous result (1.6) has been vindicated in an elementary way by the self-force (1.10). The latter becomes our starting-point, however. For although it concerns non-relativistic motions and an apparently innocent acceleration process, still this process contains unexpected relativistic pitfalls, and (1.10) is not connected to the self-mass, as we shall see ind § 2.

§2. Self-Mass and Self-Force of Accelerated Systems

In this chapter we attempt to find the way in which inertial mass can be determined by means of acceleration processes. Since we know that there may be hidden difficulties in this problem, we try to be careful – and thereby perhaps overly cautious – in deriving the relativistic connection between acceleration, forces, and mass. We do it in two steps. First, we look for the physically simplest acceleration process for a system of finite size. Next, we find the expression for the mass of a system, given in terms of its acceleration and the forces acting on it. We will then be ready to find actual self-masses for charged systems, and have also prepared the way for the more systematic treatment in the following chapters.

The problem at hand can be exemplified by an elastic body originally at rest, and in equilibrium, in an inertial frame. We want to transfer it to another inertial frame, where it should finally be at rest and in the same state of equilibrium as before. The simplest way in which to bring about this change is to have an adapted acceleration of the various parts of the system, such that it is moved as if it were rigid. In fact, by means of the idealized process of rigid acceleration we avoid producing internal stress or excitations in the system, as well as growing deformations. It would of course be possible to employ acceleration processes other than the rigid one; they would be more complicated, however, and would need the rigid acceleration as a standard of reference.

Rigid acceleration

As our first step we therefore consider the kinematical consequences of rigid acceleration of a static system. Then there exist successive frames in which the velocities of all constituent particles vanish simultaneously. Consequently the time, t_i, at which the i'th particle obtains a given velocity, $\mathbf{v}_0$, in the inertial

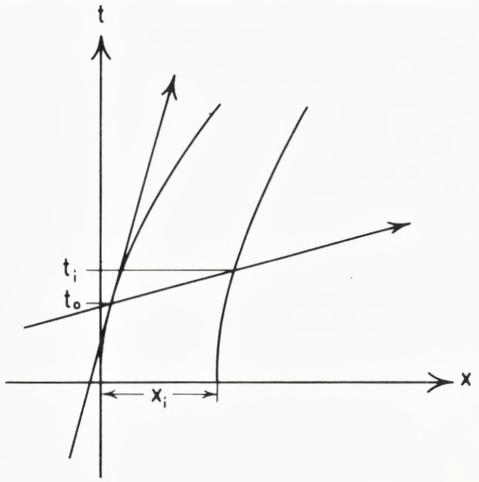

Fig. 1. Space-time diagram showing world lines of system of accelerated particles. In the inertial frame K the time t_i at which the i'th particle obtains a given velocity, $\mathbf{v}_0$, depends on its position x_i relative to the reference point. The instances t_i and t_0 are simultaneous in the rest frame, i.e. the oblique line corresponds to simultaneity in this frame.

frame K depends on its position, $\mathbf{r}_i$ (see Fig. 1). For constant acceleration, $\mathbf{g}_i$, of the i'the particle we then have, since we consider small time intervals and velocities,

$$\mathbf{v}_0 = \mathbf{g}_i t_i \,. \tag{2.1}$$

Let us measure positions relative to some reference point chosen arbitrarily within the system, and let t_0 denote the time during which the reference point has been accelerated with acceleration $\mathbf{g}_0$. Since the instances t_0 and t_i in the frame K must correspond to simultaneity in the rest frame, they are to first order in v/c related by the equation

$$t_i = t_0 + \frac{\mathbf{v}_0 \cdot \mathbf{r}_i}{c^2} = t_0\left(1 + \frac{\mathbf{g}_0 \cdot \mathbf{r}_i}{c^2}\right). \tag{2.2}$$

It therefore follows that the accelerations of the various points $\mathbf{r}_i$ must obey the relation

$$\mathbf{g}_i = \frac{\mathbf{g}_0}{1 + \mathbf{g}_0 \cdot \mathbf{r}_i / c^2} \,. \tag{2.3}$$

Thus, the acceleration of the points $\mathbf{r}_i$ decreases in the direction of $\mathbf{g}_0$. This effect exactly corresponds to the Lorentz contraction of the system as measured from the frame K.

Mass determined from forces and acceleration

As a second step, let us study the connection between force, acceleration, and mass. The fundamental relation between the three is obtained in the idealized case of a point particle. In fact, consider a point particle at rest, and with mass m. If it acquires a small acceleration $\mathbf{g}$, the applied force must be $\mathbf{F} = \mathbf{g}m$. Moreover, during a time δt, its change of momentum and velocity are, respectively, $\delta\mathbf{p} = \mathbf{F}\delta t$ and $\delta\mathbf{v} = \mathbf{g}\delta t$. This result has an immediate consequence. For suppose that, by applying the above force $\mathbf{F}$ in one point of a composite system, we obtain the acceleration $\mathbf{g}$ of this point, while the system remains, internally, in a stationary state. Since the momentum transfer and velocity change remain as before, the composite system must have the same mass m as the above particle. Presumably, part of its mass is then due to deformation energy caused by the acceleration. These seemingly trivial conclusions give one important clue to self-mass problems, as shown in an example at the end of this chapter.

Having verified the basic results belonging to a point force, we next consider acceleration of a system where forces are applied in several points. It follows from, e.g., eq. (2.3) that in special relativity there must be a somewhat intricate connection between forces on a system, its acceleration, and its total mass. Because of this, and because of the important consequences, we treat the problem at hand in an elementary and somewhat elaborate manner. We also want to show that

one is not concerned with new definitions, but instead with an inherent physical property of accelerated systems: although the velocities are non-relativistic, we sometimes have to introduce a relativistic correction to the usual conception of forces.

Consider then a set of point masses m_i, at $\mathbf{r}_i$, initially at rest and with no mutual forces. By means of suitable external forces we can accelerate the masses together, according to (2.3). We must act on them with the individual forces $\mathbf{F}_i$, located at $\mathbf{r}_i$,

$$\mathbf{F}_i = \mathbf{g}_0 \frac{m_i}{1 + \mathbf{g}_0 \cdot \mathbf{r}_i / c^2}, \tag{2.4}$$

where the acceleration at $\mathbf{r} = 0$ is $\mathbf{g}_0$. Now, if we compute the total force $\mathbf{F}$, we obtain

$$\mathbf{F} = \sum_i \mathbf{F}_i = \sum_i \mathbf{g}_0 \frac{m_i}{1 + \mathbf{g}_0 \cdot \mathbf{r}_i / c^2}, \tag{2.5}$$

which quantity is not proportional to the total rest mass, $M = \sum_i m_i$. Instead, the exact expression for the mass M is, by (2.4),

$$\mathbf{g}_0 M = \sum_i \mathbf{F}_i \left(1 + \frac{\mathbf{g}_0 \cdot \mathbf{r}_i}{c^2}\right). \tag{2.6}$$

In point of fact, we have here normalized all forces to the point $\mathbf{r} = 0$, with acceleration $\mathbf{g}_0$. At first, eq. (2.6) might appear to be an unnecessary elaboration, for if $\mathbf{g}_0$ is imagined to be sufficiently small, it looks as if the factors $(1 + \mathbf{g}_0 \cdot \mathbf{r}_i / c^2)$ can be replaced by unity. That will also be true in many cases, but for self-forces it is in error, because they contain large leading interaction terms, which would cancel if this replacement were made.

The conception of rigid acceleration may appear a little artificial for non-interacting point masses. But the idea is, as before, that we can replace this system by an actual system of interacting masses, e.g., an elastic body. In order not to deform the body more and more during the acceleration, we must keep to the prescribed rigid acceleration. As before, the total mass of the elastic body must be the same as that of the non-interacting point masses, if the accelerations and forces are the same. The formula (2.6) is therefore the general expression for the mass of the system, calculated in the simplest consistent situation.

Electromagnetic self-mass

Suppose that a system consists of charged particles, with individual masses m_i. At time $t = 0$ in the frame K the particles are all at rest with separations r_{ik} and electrostatic energy

$$U = \frac{1}{2} \sum_{i,k}^{i \neq k} \frac{q_i q_k}{r_{ik}} , \tag{2.7}$$

where q_i is the charge of the i'th particle. We assume that the particles are all accelerated according to (2.3), i.e. with rigid motion. By means of the Lienard-Wiechert potentials we can find, for $t = 0$, the total electric field at $\mathbf{r}_i$, as generated by all the other particles. It is readily shown to be[1,12], to first order in the accelerations $\mathbf{g}_k$,

$$\mathbf{E}(\mathbf{r}_i) = \sum_{k \neq i} q_k \left\{ \frac{\mathbf{r}_{ik}}{r_{ik}^3} - \frac{1}{2 r_{ik} c^2} \left(\mathbf{g}_k + \frac{(\mathbf{g}_k \cdot \mathbf{r}_{ik}) \mathbf{r}_{ik}}{r_{ik}^2} \right) \right\}, \tag{2.8}$$

where $\mathbf{r}_{ik} = \mathbf{r}_i - \mathbf{r}_k$, and $\mathbf{g}_k$ is given by (2.3). Note that the first term in the brackets is the dominating Coulomb force.

The self-forces are $q_i \mathbf{E}(\mathbf{r}_i)$, and by applying, in principle, external forces $\mathbf{F}_i = -q_i \mathbf{E}(\mathbf{r}_i) + m_i \mathbf{g}_i$, we maintain the stipulated acceleration. The total mass is now given by (2.6) and (2.8), i.e.

$$\mathbf{g}_0 M = \mathbf{g}_0 \sum_i m_i - \sum_{i,k}^{i \neq k} q_i q_k \left\{ \frac{\mathbf{r}_{ik}}{r_{ik}^3} - \frac{1}{2 r_{ik} c^2} \left(\mathbf{g}_k + \frac{(\mathbf{g}_k \cdot \mathbf{r}_{ik})}{r_{ik}^2} \mathbf{r}_{ik} \right) \right\} \left\{ 1 + \frac{\mathbf{g}_0 \cdot \mathbf{r}_k}{c^2} \right\}. \tag{2.9}$$

The right-hand side of (2.9) contains g_0 to first power, and higher powers. The latter terms are to be omitted, however, since we disregarded higher order terms in (2.8). But then the multiplying factor $1 + \mathbf{g}_0 \cdot \mathbf{r}_i / c^2$ is needed only for the dominating Coulomb term, and we may also put $\mathbf{g}_k = \mathbf{g}_0$ in the second term within the brackets. Finally, a cancellation occurs for all terms directed along $\mathbf{r}_{ik}$. We can then divide out the common factor $\mathbf{g}_0$, and obtain the inertial mass

$$M = \sum_i m_i + \frac{1}{2c^2} \sum_{i,k}^{i \neq k} \frac{q_i q_k}{r_{ik}} = \sum_i m_i + \frac{U}{c^2}. \tag{2.10}$$

Hereby we have found separate equivalence in a simple example of Coulomb interaction. Equivalence even applies for each individual pair of particles.

As expected, the calculation for the Coulomb interaction is independent of the presence of other compensating forces, whose contribution to self-mass may be obtained separately, if the corresponding field equations are known. But even if the compensating forces are only known on an approximate, non-relativistic form, we can obtain their contribution to the self-mass. At the same time, our basic equation (2.6) gives a condition to be fulfilled by the retarded solution of these forces, to first order in relative velocities.

We omitted the deformation energy caused by the acceleration, and its equivalence. This is mainly because the acceleration did not correspond to a normal physical situation. The external forces introduced were artificial, in that

they exactly took care of maintaining the configuration of the particles within the undisturbed system. In actual acceleration processes one can instead be concerned with an external electric field which is constant in space and time. Then, the configuration of the particles will be changed slightly from that of the undisturbed system. Hereby, deformation energy, and its equivalence, can be obtained. In many cases, such deformation terms are of higher order in g_0, and therefore do not affect the basic result (2.10). We shall presently discuss a simple example where deformation energy plays a major role.

Basic equation of motion

From the previous results it is easy to formulate the basic equation of motion of charged system momentarily at rest, and placed in a weak external electric field $\mathbf{E}_{ext}(\mathbf{r},t)$ varying slowly in space and time. By a slow variation in space we mean that the relative change of $\mathbf{E}_{ext}(\mathbf{r},t)$ is small within the system. We suppose that the field varies sufficiently slowly so that the system remains in a quasistationary state. Eq. (2.9) provides an expression for the acceleration $\mathbf{g}_0$ of a standard point $\mathbf{r}_0$, times the total mass M as arising from Coulomb interaction and from other energy contributions in the system. Next, according to (2.6) the product $\mathbf{g}_0 M$ is equal to the weighted sum of external forces,

$$\mathbf{g}_0 M = \sum_i F_i \left(1 + \frac{\mathbf{g}_0 \cdot (\mathbf{r}_i - \mathbf{r}_0)}{c^2}\right) = \sum_i q_i \mathbf{E}_{ext}(\mathbf{r}_i, t) \left(1 + \frac{\mathbf{g}_0 \cdot (\mathbf{r}_i - \mathbf{r}_0)}{c^2}\right). \quad (2.11)$$

Here, we expand $\mathbf{E}_{ext}$ in powers of $\mathbf{r}_i - \mathbf{r}_0$, and include only first order terms on the right hand side. But since the standard point $\mathbf{r}_0$ may be freely chosen, we place it at the charge centre, $\mathbf{r}_0 = \mathbf{r}_c \equiv \sum_i q_i \mathbf{r}_i / q$, where $q = \sum_i q_i$ is the total charge of the system. For it then turns out that first order terms in $\mathbf{r}_i - \mathbf{r}_0$ disappear, and we are left with $q\mathbf{E}_{ext}(\mathbf{r}_c, t)$ on the right hand side of (2.11). The equation of motion is now simply, in the momentary rest frame,

$$\mathbf{g}_c M = q\mathbf{E}_{ext}(\mathbf{r}_c, t), \quad (2.12)$$

where $\mathbf{r}_c$ is the charge centre, and $\mathbf{g}_c$ its acceleration. Moreover, q is the total charge, and M the total mass of the system. Thus, the result (2.12) represents a precise basic equation of motion of a charged system. It gives an essential modification of the so-called Abraham-Lorentz equation; the standard factor 4/3 multiplying the electromagnetic mass has disappeared, because equivalence reigns in M. In addition, eq. (2.12) contains the subtlety that the system is represented by one definite point, i.e. the charge centre $\mathbf{r}_c$. Consequently, eq. (2.12) can be used as an equation of motion for, say, a uranium nucleus in an external electric

field, or, for a classical electron model. One may immediately correct the equation by a familiar term containing radiation damping, if so desired.

Although, as mentioned, eq. (2.12) is widely applicable, let us register main corrections to it, or assumptions contained in it. We have assumed that the external field varies slowly in time. The time variation of $\mathbf{E}_{ext}$ will, first, give rise to adiabatic changes of M and, second, to non-adiabatic mass excitations. Third, we have already mentioned that a time variation of $\mathbf{g}_c$ leads to radiation damping. Finally, if $\mathbf{g}_c$ quickly changes direction, the mass centre need not remain behind the charge centre, and rotations may be induced. In order to study that, systems with spin must be included in the description, but that is outside the scope of the present paper.

Shortcomings of standard formulae

At this stage it is convenient to compare with the standard derivation of self-force as alluded to in §1, and performed by Heitler, for instance. In that description, the self-fields are again given by (2.8), but with $\mathbf{g}_k = \mathbf{g}_0$, which does not lead to immediate errors. Next, the total force is calculated, corresponding to (1.8) and (2.5), and erroneously identified with the mass times the acceleration $\mathbf{g}_0$. Thus, from (2.8) and (1.8)

$$\mathbf{F} = \sum_i \mathbf{F}_i = \sum_i m_i \mathbf{g}_0 + \sum_{i,k}^{i \neq k} \frac{1}{2 r_{ik} c^2} \left(\mathbf{g}_0 + \frac{(\mathbf{g}_0 \mathbf{r}_{ik})}{r_{ik}^2} \mathbf{r}_{ik} \right), \tag{2.13}$$

where the dominant Coulomb terms have cancelled out, in contrast to (2.9).

For a spherical symmetric charge distribution, with electrostatic energy U, the expression (2.13) leads to

$$\mathbf{F} = \left(\sum_i m_i + \frac{4}{3} \frac{U}{c^2} \right) \mathbf{g}_0 , \tag{2.14}$$

In case the charge distribution is merely symmetric about the direction of $\mathbf{g}_0$, the factor 4/3 is seen to be replaced by a number $1 + \xi$, where $0 \leq \xi \leq 1$. For a general distribution, however, the force $\mathbf{F}$ need not even point in the direction of $\mathbf{g}_0$. We have hereby clarified in some detail the shortcomings of the Galilean concept of a total force and its association with total mass, in special relativity.

Next, let us consider the standard formulae for self-momentum and self-energy of a charged system, i.e. (1.8) and (1.9). Although they are connected to the above-mentioned standard self-force calculation, their short-comings are of a more elusive kind. Still, in order to elucidate their basic contents, we can observe the following. If a system has internal Coulomb energy U, then the standard self-momentum corresponding to (1.8) can be $\mathbf{P}_{el} = (U/c^2) \mathbf{v} \cdot \gamma \cdot (1 + \xi)$, where

$\xi = 1/3$ for a spherically symmetric charge distribution. Similarly, the standard self-energy becomes $E_{el} = U \cdot \gamma \cdot (1 + \xi v^2/c^2)$, corresponding to (1.9). Therefore, if we form the difference $\mathbf{v} \cdot \mathbf{P}_{el} - E_{el}$, we invariably get a quantity independent of ξ, namely

$$L_{el} = -E_{el} + \mathbf{v} \cdot \mathbf{P}_{el} = -U \cdot \left(1 - \frac{\mathbf{v}^2}{c^2}\right)^{1/2}. \tag{2.15}$$

In point of fact, we have recovered eq. (1.4), i.e. the Lagrangian belonging to equivalence. Moreover, it is apparent that, instead of making the indirect derivation of (2.15) via E_{el} and $\mathbf{P}_{el}$, we could have obtained it directly by integration of the invariant Lagrangian density in space, as belonging to the field and to its interaction with matter, or $\mathscr{L}_{field} + \mathscr{L}_{int}$.

Returning to the Lagrangian in (2.15), we have already seen, in (1.5), that if we vary L_{el} with respect to $\mathbf{v}$, keeping the internal state unchanged, we arrive at the momentum $\mathbf{P} = (U/c^2)\gamma \cdot \mathbf{v}$, leading to equivalence. In fact, this implies *detailed* equivalence, the Coulomb contribution being only part of the total internal energy.

Next, it also becomes clear how the standard momentum $\mathbf{P}_{el}$ can be connected to (2.15): when $\mathbf{v}$ is varied, there is assumed to be an associated variation of the internal state – i.e. of U. Thus, $\mathbf{P}_{el}$ will result if we let U vary proportionally to $(1 - v^2/c^2)^{\xi/2}$, when L_{el} is varied with respect to $\mathbf{v}$. The factor in question must be due to a Lorentz transformation of the internal variables of the system.

We have thus realized that the standard momentum and energy (1.8) and (1.9), arise from an unwarranted variational procedure, whereby they lose connection to our basic concepts of momentum and energy of an isolated system, as described in §1. Such results arise in general from arbitrary transformations of internal variables of a system, where momenta become abstract quantities, without direct physical significance.

Self-mass for point force

The present discussion of the central ingredients in equivalence calculations is perhaps best concluded by means of an example serving a triple purpose. First, it concerns an external point force, implying the simplest possible connection to mass and acceleration. Second, the equivalence in question applies to deformation energies, not studied explicitly above. Third, Poincaré stresses cannot be introduced.

Let two mutually repelling charges, q_a and q_b, be accelerated from rest along their line of connection, $\mathbf{r}_{ba}$. An external force $\mathbf{F}_a$ acts on particle a, while particle b in turn is made to accelerate by the Coulomb repulsion from particle a. The

force and distance r_{ab} are balanced such that the particles are accelerated in rigid motion. The internal energy of the system, $q_a q_b / r_{ab}$, is purely an energy of deformation. The internal electric fields are given by (2.8), and so the equations of motion of the two particles become

$$m_a \mathbf{g}_a = \frac{q_a q_b}{r_{ab}^3} \mathbf{r}_{ab} - \frac{q_a q_b}{r_{ab} c^2} \mathbf{g}_b + \mathbf{F}_a \,, \tag{2.16}$$

$$m_b \mathbf{g}_b = \frac{q_a q_b}{r_{ab}^3} \mathbf{r}_{ba} - \frac{q_a q_b}{r_{ab} c^2} \mathbf{g}_a \,, \tag{2.17}$$

where all vectors are collinear, while m_a and m_b are mechanical masses. Further, the condition of rigid acceleration determines $\mathbf{g}_b$ in terms of $\mathbf{g}_a$ and $\mathbf{r}_{ba}$, cf. (2.3),

$$\mathbf{g}_b = \frac{\mathbf{g}_a}{1 + \mathbf{g}_a \cdot \mathbf{r}_{ba} / c^2} \,. \tag{2.18}$$

We multiply (2.17) by $1 + (\mathbf{g}_a \cdot \mathbf{r}_{ba})/c^2$, add (2.16), and obtain to first order in $\mathbf{g}_a$

$$\mathbf{F} = \mathbf{g}_a \left(m_a + m_b + \frac{q_a q_b}{r_{ab}} \frac{1}{c^2} \right). \tag{2.19}$$

Since the mass M of the system must be given by $M \mathbf{g}_a = \mathbf{F}_a$, we find

$$M = m_a + m_b + \frac{q_a q_b}{r_{ab}} \frac{1}{c^2} \,. \tag{2.20}$$

In the simplest imaginable case we have thus obtained equivalence, and for a deformation energy in fact.

Let us next turn to the standard procedure, where the total self-force is calculated, cf. (2.13) or (1.10). It corresponds to adding the right-hand sides of (2.16) and (2.17), omitting $\mathbf{F}_a$. The self-mass becomes erroneous, or $2q_a q_b/(r_{ab} c^2)$, like in (2.13). We might similarly, as done by Heitler, add (2.16) and (2.17) with the Galilean demand $\mathbf{g}_b = \mathbf{g}_a$, and obtain a wrong value of the force $\mathbf{F}_a$. In any case, there are here no compensating Poincaré stresses, which can repair the error.

Whereas, in the present chapter, we have arrived at the proper treatment belonging to coordinates (inertial frames) where equations of motion are simple but self-mass calculations delicate, the theme in the following will be reversed. In fact, we shall introduce coordinates (Møller box) where self-mass calculations become extremely simple; our task will be to obtain the equations of motion. Thereby, the discussion becomes lengthy, containing transformations of equations of motion in various classical and quantal cases.

§ 3. Systematic Description by Means of Accelerated Reference Frame

Basic properties of Møller box

The previous chapter contained a preliminary analysis of simple acceleration processes for which the intrinsic state remained stationary in the instantaneous rest frame. A systematic analysis of such processes must be based on a description of the system in an accelerated rigid frame of reference, always coinciding with the instantaneous rest frame. A coordinate system of this kind, where each point has a time independent acceleration in its momentary rest frame, we shall refer to as a Møller box *).

Before embarking on a detailed discussion of the Møller box, we may point out some of its salient features. First, the physical laws in the box are independent of time, i.e. there is invariance against time displacement and time-reflection. Second, there is an inborn simultaneity, like in a static gravitational field. Third, it also follows that a charge at rest in the Møller box gives rise to a purely electrostatic field in this frame. This feature corresponds to the fact that for a static charge in the box, performing a hyperbolic motion in an inertial frame, the retarded and advanced fields are identical within the box. Fourth, in the inertial frame we had to distinguish between, on the one hand, that weighted sum of forces which leads to the total mass of a system and, on the other hand, the total force. In the Møller box these concepts are united in the sense that the total force required to keep a body at rest in the box is proportional to the total mass of the body.

When introducing the Møller box it is useful to consider first the hyperbolic motion of a single particle. Let a particle in an inertial frame K be accelerated along the X-axis, with the constant acceleration g_0 in its rest frame. It is convenient to introduce the length $\lambda = c^2/g_0$ and write for the trajectory

$$X_0 = \lambda \cosh \frac{ct}{\lambda}, \quad Y_0 = Z_0 = 0, \tag{3.1}$$

$$cT_0 = \lambda \sinh \frac{ct}{\lambda}.$$

Thus, the coordinates cT_0 and X_0 lie on the hyperbola

$$X_0^2 - c^2 T_0^2 = \lambda^2. \tag{3.2}$$

*) Accelerated rigid frames of reference are discussed in some detail by C. Møller in his monograph on relativity[13]. We have adopted the name Møller box for the particular frame discussed in the text. The wording *box* is meant to indicate that we are considering a space-time domain of finite extension.

Here (T_0, X_0, Y_0, Z_0) are the particle coordinates in the inertial frame K, and t denotes proper time for the particle. For this motion the four-velocity

$$U_0 = \left(\frac{d(cT_0)}{dt}, \frac{dX_0}{dt}, 0,0\right) = \frac{1}{\lambda}(X_0, cT_0, 0,0) \tag{3.3}$$

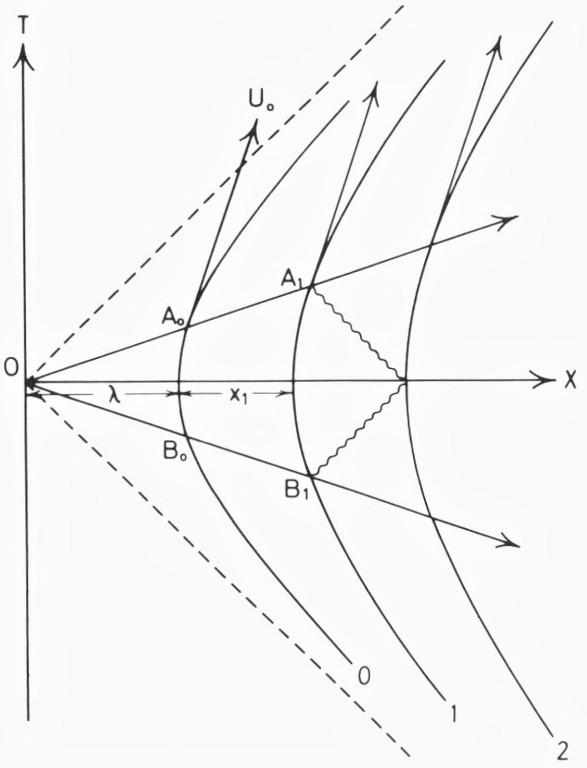

Fig. 2. The world lines of the reference points 0,1 and 2 in the Møller box are scaled hyperbolae with the light cone through the origin as the common asymptote. Successively steeper lines through the origin correspond to progressive time in the Møller box. Proper time on the hyperbola labelled 0 has been chosen as the common standard time in the box, and distances are measured from this hyperbola. The wavy lines represent the world line of a light signal exchanged between the observers 1 and 2.

is always perpendicular to the radius vector from the origin $(cT_0, X_0, 0,0)$. It is therefore clear from Figure 2 that if another particle is to remain at rest relative to the first at the distance x_1, its world line will be given by

$$(cT_1, X_1, 0,0) = \left(1+\frac{x_1}{\lambda}\right)(cT_0, X_0, 0,0) \tag{3.4}$$

i.e. it will also perform a hyperbolic motion, but with rest acceleration $g_0(1+g_0x_1/c^2)^{-1}$. Thus we are led to the introduction of the accelerated rigid frame, the Møller box, with coordinates (t,x,y,z), by the transformation from the variables (T,X,Y,Z) in the inertial frame K:

$$\begin{aligned} X &= (x+\lambda)\cosh\frac{ct}{\lambda}, \quad Y = y, \quad Z = z, \\ cT &= (x+\lambda)\sinh\frac{ct}{\lambda}, \end{aligned} \tag{3.5}$$

corresponding to the line element

$$ds^2 = c^2 dT^2 - d\mathbf{R}^2 = \left(1 + \frac{x}{\lambda}\right)^2 \cdot c^2 dt^2 - d\mathbf{r}^2 . \tag{3.6}$$

For $T = t = 0$ we have $X = x + \lambda$, where we have selected a standard hyperbola from which we measure distances along the x-direction in the box. The proper time t of the standard hyperbola $x = 0$ has been chosen as the common standard time variable in the box. Hence, outside the standard hyperbola, local proper time deviates from standard time. In fact, the relation between standard time t and local proper τ at the position x is given by

$$d\tau = \left(1 + \frac{x}{\lambda}\right) dt . \tag{3.7}$$

The choice of the standard time t in the Møller box makes explicit the invariance against time displacement and time reflection inherent in this static reference frame. Therefore, this way of synchronizing events corresponds to the inborn simultaneity in the box. This can be illustrated by considering a light signal moving along the x-axis between two observers 1 and 2 at rest in the box (see figure 2). We assume that the light signal is sent back at time $T = 0$. We notice that since each hyperbola corresponds to the locus of constant distance from O in Minkowski space, they are symmetric with respect to the radius vectors in this space. We have therefore drawn the figure such that the inherent symmetry of the hyperbolae is made explicit with respect to the axis $T = 0$. Events on the line OB_0B_1 are simultaneous with the departure of the light signal from the first observer, and events on the line OA_0A_1 are simultaneous with its return. It is obvious from the figure that if the events are synchronized to proper time of the standard hyperbola $x = 0$, the time of arrival to the second observer will be halfway between the time of departure from the first observer and the time of return. This result is also directly borne out by evaluation of the standard time intervals in question, which are found to be $(\lambda/c)\log[(x_2 + \lambda)/(x_1 + \lambda)]$, x_1 and x_2 being the coordinates of the two observers.

It follows from the transformation (3.5) that a particle at rest in the Møller box at position x at time $T = t = 0$ has acceleration

$$g(x) = \frac{c^2}{\lambda + x} = \frac{g_0}{1 + g_0 x/c^2} \tag{3.8}$$

in the inertial frame. This is of course the result (2.3) already deduced for the rigid acceleration in the inertial frame. In contrast, a particle at rest at $T = t = 0$ in the inertial frame at the same position $X = x + \lambda$, in the Møller box has an acceleration

$$\frac{d^2x}{dt^2} = -g_0\left(1+\frac{g_0 x}{c^2}\right). \tag{3.9}$$

Thus (3.9) expresses the acceleration of a freely falling particle in the coordinates of the Møller box. It has of course the opposite sign of (3.8), but, more important, its magnitude increases in the direction of g_0 in contrast to $g(x)$.

The line element (3.6) implies a simple scaling law for velocities. In particular, the velocity of light in the box is given by

$$c(x) = c\cdot\left(1+\frac{g_0 x}{c^2}\right). \tag{3.10}$$

In fact, whereas the velocity of light in local units is alsays c, it must be changed by the factor in (3.7) when we measure in standard time.

Electrostatic interactions in Møller Box

In this section we shall be concerned with charged particles moving in static potentials*). The field equations for static potentials in the Møller box are derived from the action principle

$$\delta S_f + \delta S_{int} = 0, \tag{3.11}$$

where the contributions to the action from the field and the interaction are obtained from the general expressions (A13) and (A14):

$$S_f = -\frac{1}{8\pi}\int dt\int d^3r\,\frac{(\nabla\varphi)^2}{(1+x/\lambda)}, \tag{3.12}$$

$$S_{int} = -\int dt\int d^3r\,\varrho(\mathbf{r})\,\varphi(\mathbf{r}). \tag{3.13}$$

If (3.11) corresponds to variation of the potential φ for fixed charge distribution ϱ, one obtains to first order in $\lambda^{-1} \equiv g_0/c^2$ the result

$$\Delta\varphi(\mathbf{r}) - \frac{1}{\lambda}\frac{\partial\varphi(\mathbf{r})}{\partial x} = -4\pi\left(1+\frac{x}{\lambda}\right)\varrho(\mathbf{r}). \tag{3.14}$$

*) For the sake of completeness, a discussion of electrodynamics and the equations of motion of charged particles in the Møller box is given in appendix A, while the static potentials are solved in appendix B.

Consider the potential $\varphi(\mathbf{r};\mathbf{r}_1)$ in the point $\mathbf{r}$ generated by the charge density $\varrho(\mathbf{r}) = q_1\delta(\mathbf{r}-\mathbf{r}_1)$, i.e. by a single charge q_1 at rest in the point $\mathbf{r}_1$. According to (3.14) this potential is to first order in $1/\lambda$

$$\varphi(\mathbf{r};\mathbf{r}_1) = \frac{q_1}{|\mathbf{r}-\mathbf{r}_1|}\left(1+\frac{x+x_1}{2\lambda}\right). \tag{3.15}$$

In order to appreciate the significance of the second term in the brackets in (3.15), consider a second charge q_2 at rest at the position $\mathbf{r}_2$. We notice that the density of the interaction energy of two charges depends on the values of the two charges only through their product. We therefore expect that the position of the centre-of-mass of the interaction energy is always the same as for two identical charges, namely midway between them. Thus, in the interaction energy $q_2\,\varphi(\mathbf{r}_2;\mathbf{r}_1)$ we can interpret the term

$$\delta E_{int} = \frac{q_1 q_2}{|\mathbf{r}_2-\mathbf{r}_1|c^2} g_0 \frac{x_2+x_1}{2} \tag{3.16}$$

as the potential energy of a mass $q_1q_2/c^2|\mathbf{r}_2-\mathbf{r}_2|$ located at the midpoint between the charges in the artificial gravitational field g_0. The energy (3.16) therefore represents the work required to lift a mass equivalent to the Coulomb energy from the reference level $x = 0$ to the height $(x_1+x_2)/2$. Hence we expect that the sum of the mutual forces be equal to $(q_1q_2/c^2|\mathbf{r}_2-\mathbf{r}_1|)g_0$. This is indeed in accordance with (3.15), from which it follows that

$$q_2\frac{\partial\varphi(\mathbf{r}_2;\mathbf{r}_1)}{\partial x_2} + q_1\frac{\partial\varphi(\mathbf{r}_1;\mathbf{r}_2)}{\partial x_1} = \frac{q_1q_2}{|\mathbf{r}_2-\mathbf{r}_1|c^2}g_0\,. \tag{3.17}$$

This relation, which embodies the equivalence between electrostatic energy and mass, will be crucial in the following discussion. It corresponds to the weighted addition of forces (2.6), applied to the Coulomb case (2.8), but in the Møller box it emerges as a direct consequence of the term (3.16) in the interaction energy.

The equations of motion in the Møller box, for a particle of mass m and charge q moving in a static potential φ, is obtained from the action principle

$$\delta S_{kin} + \delta S_{int} = 0, \tag{3.18}$$

with

$$S_{kin} = -mc^2\int d\tau = -mc^2\int dt\left\{\left(1+\frac{x}{\lambda}\right)^2 - \frac{\mathbf{v}^2}{c^2}\right\}^{1/2}, \tag{3.19}$$

$$S_{int} = -\int dt\, q\varphi(\mathbf{r}(t))\,. \tag{3.20}$$

If (3.18) corresponds to variation of the particle coordinates for fixed potential, one obtains the equations of motion of the particle. They correspond to the Lagrangian

$$L = -mc^2 \left\{ \left(1 + \frac{x}{\lambda}\right)^2 - \frac{\mathbf{v}^2}{c^2} \right\}^{1/2} - q\varphi(\mathbf{r}) \,. \tag{3.21}$$

Equivalence for kinetic energy

The first term in the Lagrangian (3.21) turns out to contain separate equivalence for kinetic energy. In order to illustrate this property let us consider a ball of mass m, bouncing between ceiling and floor of a small rectangular enclosure which is kept at rest in the Møller box, with its floor at the reference level $x = 0$, and with its edges parallel to the coordinate axis. Let the ball jump from the floor with momentum $p_x(1)$ in the x-direction and hit the ceiling after a time T with momentum $p_x(2)$ along this direction. We assume that the enclosure is so small that the kinetic energy of the ball can be regarded as constant during its motion. Consequently the net momentum transfer per unit time from the ball to the box is

$$\frac{p_x(2) - p_x(1)}{T} = \frac{1}{T}\int_0^T dt \frac{dp_x}{dt} = \frac{1}{T}\int_0^T dt \frac{\partial L}{\partial x} = -\frac{mg_0}{(1 - \mathbf{v}^2/c^2)^{1/2}} \,, \tag{3.22}$$

where we have used the equation of motion corresponding to the first term of the Lagrangian (3.21). In order to keep the enclosure at rest in the Møller box, the presence of the bouncing ball thus requires an extra force $\delta\mathcal{F}$ so as to support the floor of the enclosure

$$\delta\mathcal{F} = \frac{m}{(1 - \mathbf{v}^2/c^2)^{1/2}} \mathbf{g}_0 \,. \tag{3.23}$$

This force is the same in the Møller box as in the particular inertial frame, which momentarily coincides with the enclosure, since standard time coincides with proper time at the location $x = 0$.

However straightforward this demonstration of separate equivalence for kinetic energy may appear, one should note that it stands in contrast to the conventional treatment of similar examples. In fact, in the latter approach equivalence can only be stablished by explicitly taking into account the stresses set up in the walls by the bouncing ball, and would not apply to the kinetic energy separately.

§ 4. Equivalence for Atomic Binding Energies

So far we have discussed quite idealized systems in which there was either electrostatic or kinetic energy present. As a simple example of a more realistic physical system with both kinetic and potential energy, we consider a hydrogen atom and enquire into the total force necessary to keep the nucleus at rest at the position $\mathbf{r}_n = 0$ in the Møller box. This force is the same in the Møller box as in that inertial frame in which the nucleus is momentarily at rest, since standard time coincides with proper time at the position $\mathbf{r} = 0$. For simplicity we treat the atom as a one-particle system, i.e. we neglect the motion of the heavy nucleus around the mass centre.

The atom is assumed to be in a stationary state in the Møller box. Within quantum mechanics, this means that the wave function corresponds to a definite energy in the Møller box and the associated charge distribution of the electron is static in this frame. In the case of classical mechanics we are dealing with definite orbits, time-averages over which correspond to quantum mechanical expectation values. One would expect that the question of equivalence be independent of whether a quantal or a classical description is used in accounting for the stability of the system. This is indeed borne out by the following discussion.

Classical hydrogen atom

The external force, $\mathcal{F}$, required to keep the nucleus with charge Ze and mass m_n at rest in the box, must compensate the fictitious gravitational force $-m_n \mathbf{g}_0$ acting on the nucleus in the accelerated frame, as well as the reaction force on the nucleus from the electron of charge $-e$ and mass m_e.

According to the Lagrangian (3.21) the time average, F_x, of this reaction force over a time T, long compared to the orbital periods of the atom, is

$$F_x = \frac{1}{T}\int_0^T dt\, Ze \left.\frac{\partial \varphi(\mathbf{r}_n;\mathbf{r}_e(t))}{\partial x_n}\right|_{\mathbf{r}_n=0}, \tag{4.1}$$

where $\mathbf{r}_e(t)$ is the coordinate of the electron. From the relation (3.17) and the Lagrangian (3.21) we find for the integrand in (4.1)

$$\begin{aligned} Ze\frac{\partial \varphi(\mathbf{r}_n;\mathbf{r}_e)}{\partial x_n} &= \frac{Ze(-e)}{\lambda|\mathbf{r}_e-\mathbf{r}_n|} - (-e)\frac{\partial \varphi(\mathbf{r}_e;\mathbf{r}_n)}{\partial x_e} \\ &= -\frac{Ze^2}{\lambda|\mathbf{r}_e-\mathbf{r}_n|} + \frac{\partial L}{\partial x_e} + \frac{\partial}{\partial x_e} m_e c^2 \left\{\left(1+\frac{x_e}{\lambda}\right)^2 - \frac{\mathbf{v}_e^2}{c^2}\right\}^{1/2}. \end{aligned} \tag{4.2}$$

Because of the equations of motion, the term

$$\frac{\partial L}{\partial x_e} = \frac{d}{dt}\frac{\partial L}{\partial v_{ex}}$$

does not contribute to the time average (4.1). Hence, keeping only terms of order $1/\lambda$, we obtain an average reaction force

$$F_x = -\frac{1}{T}\int_0^T dt\left[\frac{m_e c^2}{(1-\mathbf{v}_e^2/c^2)^{1/2}} - \frac{Ze^2}{|\mathbf{r}_e - \mathbf{r}_n|}\right]\frac{g_0}{c^2}. \tag{4.3}$$

We notice that the integrand in (4.3) is the energy of the electron multiplied by g_0/c^2, and accordingly time independent. Thus the total force required to keep the atom at rest is

$$\mathcal{F} = \left[m_n + \frac{m_e}{(1-\mathbf{v}_e^2/c^2)^{1/2}} - \frac{Ze^2}{|\mathbf{r}_e - \mathbf{r}_n|c^2}\right]\mathbf{g}_0\,, \tag{4.4}$$

or

$$\mathcal{F} = \left(m_n + m_e - \frac{B}{c^2}\right)\mathbf{g}_0\,, \tag{4.5}$$

where B is the binding energy of the atom. The relation (4.5) expresses the equivalence between binding energy and mass for a classical hydrogen atom to all orders in v/c. The limitations to this result are solely due to the possible radiation from the system, proportional to some power of e^2. The classical orbits depend on the charges through their product only. We can therefore consider (4.5) as an exact result for a given orbital configuration of the atom, corresponding to the limit $e^2 \to 0$ for fixed value of the product Ze^2, in which limit the radiation is negligible.

Quantal hydrogen atom

The above discussion of a classical hydrogen atom can be carried over to the quantal case by passing from a Langrangian to a Hamiltonian description and replacing time averages by expectation values. Whereas the motion of the nucleus is still treated in classical terms, the state of the electron is now described by the Hamiltonian operator constructed from the Lagrangian (3.21):

$$\begin{aligned} H &= \frac{1}{2}\left\{\left(1+\frac{x_e}{\lambda}\right)c[m_e^2c^2+\mathbf{p}_e^2]^{1/2} + c[m_e^2c^2+\mathbf{p}_e^2]^{1/2}\left(1+\frac{x_e}{\lambda}\right)\right\} - e\varphi(\mathbf{r}_e;\mathbf{r}_n) \\ &\equiv H_0 - e\varphi(\mathbf{r}_e;\mathbf{r}_n)\,. \end{aligned} \tag{4.6}$$

Here the operators $\mathbf{r}_e$ and $\mathbf{p}_e$ refer to the electron and satisfy the usual commutation relation, whereas $\mathbf{r}_n$, the coordinate of the nucleus, is a c-number. The first term, H_0, has been symmetrized in an obvious manner, and the potential $\varphi(\mathbf{r}_e;\mathbf{r}_n)$

generated by the nucleus, is given by (3.15). We use here the Hamiltonian (4.6) in order to emphasize the analogy to the classical treatment. As indicated below, similar considerations can be applied to the Dirac Hamiltonian, whereby effects associated with the electron spin are included.

In close analogy to (4.2) we obtain from (4.6)

$$Ze\frac{\partial\varphi(\mathbf{r}_n;\mathbf{r}_e)}{\partial x_n} = -\frac{Ze^2}{\lambda|\mathbf{r}_e-\mathbf{r}_n|} + e\frac{\partial\varphi(\mathbf{r}_e;\mathbf{r}_n)}{\partial x_e} = -\frac{Ze^2}{\lambda|\mathbf{r}_e-\mathbf{r}_n|} - \left[\frac{\partial}{\partial x_e}, H-H_0\right]. \quad (4.7)$$

Since the expectation value of $\left[\frac{\partial}{\partial x_e}, H\right]$ in the last term of (4.7) vanishes in a stationary state, we get for the expectation value, F_x, of the reaction force

$$F_x = -<\psi\left|Ze\frac{\partial\varphi(\mathbf{r}_n;\mathbf{r}_e)}{\partial x_n}\right|\psi> = -<\psi\left|c[m_e^2c^2+\mathbf{p}_e^2]^{1/2} - \frac{Ze^2}{|\mathbf{r}_e-\mathbf{r}_n|}\right|\psi> \frac{g_0}{c^2}$$

$$= -\left(m_e - \frac{B}{c^2}\right)g_0 . \quad (4.8)$$

Thus, the total force required to keep the atom at rest is given by eq. (4.5).

The Dirac equation

In order to establish the form of the Dirac equation in the Møller box we notice that for any value of the standard time t, the wave function $\psi(t)$ in the Møller box is equal to the wave function $\psi_{K(t)}(T)$ in that inertial frame $K(t)$ which at time t coincides with the box

$$\psi(t) = \psi_{K(t)}(T) . \quad (4.9)$$

Here T is the time measured in the inertial frame $K(t)$ and, according to (3.7), the time intervals dt and dT are related by

$$dT = \left(1+\frac{x}{\lambda}\right)dt . \quad (4.10)$$

The time variation of $\psi(t)$ is due partly to the change of inertial frame $K(t)$ with time and partly to the intrinsic time variation of the state. In order to find the change with time, t, of the wave function at a fixed space point in the box, let us consider the three events pictured in Fig. 3. Here the events 1 and 2 refer to one and the same space point in the box, but are separated by the time interval δt in this frame. Similarly 2 and 3 are simultaneous in the box, whereas 1 and 3 refer to one and the same space point in the inertial frame $K(t)$, but are separated by the time interval δT in this frame.

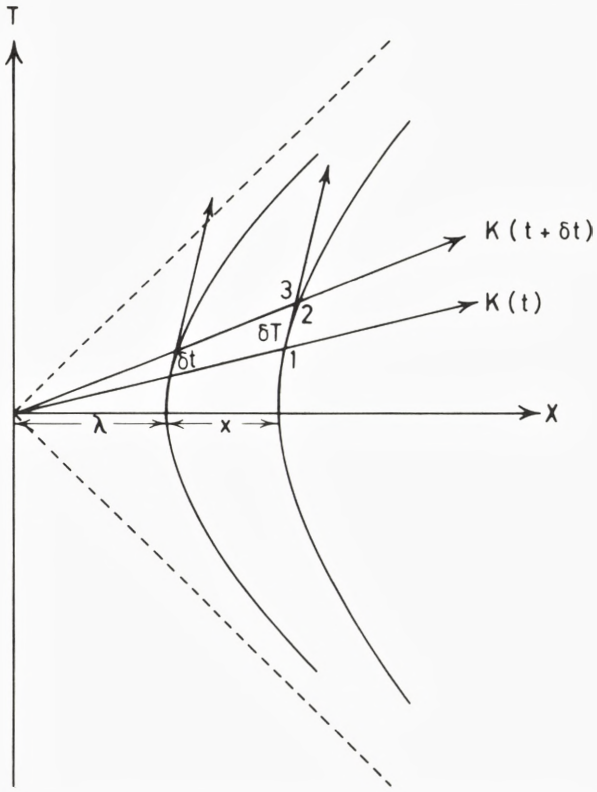

Fig. 3. Space-time diagram showing the events 1, 2 and 3, mentioned in the text, and two successive rest frames $K(t)$ and $K(t+\delta t)$. The events 1 and 2 refer to one and the same space point in the Møller box, whereas 1 and 3 refer to one and the same space point in the the inertial frame $K(t)$.

For the sake of simplicity we use as variables in the wave function the numbers referring to the appropriate space-time points. With this notation we get

$$\psi(2)-\psi(1)\equiv\psi_{K(t+\delta t)}(2)-\psi_{K(t)}(1)=\left(\psi_{K(t+\delta t)}(2)-\psi_{K(t)}(3)\right)+\left(\psi_{K(t)}(3)-\psi_{K(t)}(1)\right) \tag{4.11}$$

Since the separation between the points 2 and 3 is of the order $g_0(\delta t)^2$, we get to first order in δt

$$\psi(2)-\psi(1)=\left(\psi_{K(t+\delta t)}(2)-\psi_{K(t)}(2)\right)+\frac{\partial\psi_{K(t)}}{\partial T}\delta T. \tag{4.12}$$

Because the inertial frame $K(t+\delta t)$ moves with the infinitesimal velocity $\mathbf{v}=\mathbf{g}(x)\delta T=\mathbf{g}_0\delta t$ relative to the inertial frame $K(t)$, we obtain

$$\psi_{K(t+\delta t)}(2)\simeq\exp\left(\frac{-\boldsymbol{\alpha}\mathbf{v}}{2c}\right)\psi_{K(t)}(2)\simeq\left(1-\frac{\boldsymbol{\alpha}\mathbf{g}}{2c}\delta t\right)\psi_{K(t)}(2) \tag{4.13}$$

Here the matrix $\exp(-\frac{1}{2}\boldsymbol{\alpha}\mathbf{v}/c)$, where $\boldsymbol{\alpha}$ denotes the usual Dirac matrices,

transforms the wave function from the inertial frame K(t) to K(t+δt). Combining (4.10), (4.12) and (4.13), we obtain

$$i\hbar\frac{\partial\psi}{\partial t}=-i\hbar\frac{\boldsymbol{\alpha}\mathbf{g}_0}{2c}\psi+\left(1+\frac{x}{\lambda}\right)i\hbar\frac{\partial\psi}{\partial T}=-i\hbar\frac{\boldsymbol{\alpha}\mathbf{g}_0}{2c}\psi+\left(1+\frac{x}{\lambda}\right)H_D\psi\,. \tag{4.14}$$

Here H_D is the Dirac Hamiltonian in the inertial frame K(t),

$$H_D=c\boldsymbol{\alpha}\left(\mathbf{p}+\frac{e}{c}\mathbf{A}_{K(t)}\right)+\beta mc^2-e\varphi_{K(t)}\,, \tag{4.15}$$

where $(\varphi_{K(t)}, \mathbf{A}_{K(t)})$ is the four-potential in the frame K(t), and where the electron charge is $-e$. The Møller box coincides with K(t) at time t, and therefore

$$\mathbf{p}=-i\hbar\nabla_{\mathbf{r}}, \tag{4.16}$$

where $\mathbf{r}$ denotes the spatial coordinates in the box. From the equations (4.14)-(4.16) it follows that the Dirac equation in the Møller box takes the form, valid to all orders in $1/\lambda$,

$$i\hbar\frac{\partial\psi}{\partial t}=\frac{1}{2}\left[\left(1+\frac{x}{\lambda}\right)H_D+H_D\left(1+\frac{x}{\lambda}\right)\right]\psi\,. \tag{4.17}$$

From eq. (4.17) one may derive the continuity equation

$$\frac{\partial}{\partial t}(\psi^+\psi)+\mathrm{div}_{\mathbf{r}}\left(\psi^+\left(1+\frac{x}{\lambda}\right)c\boldsymbol{\alpha}\psi\right)=0\,. \tag{4.18}$$

Therefore, the quantity $(-e\psi^+\psi)$ is the charge density in the Møller box and $(-e\psi^+(1+x/\lambda)\boldsymbol{\alpha}c\psi)$ is the charge current density.

In order to apply the Dirac equation to a hydrogen atom with the nucleus at rest at $\mathbf{r}=0$, we have to find the potentials $\varphi_{K(t)}$ and $\mathbf{A}_{K(t)}$ generated by the nucleus. Because the inertial frame K(t) is the momentary rest frame of the nucleus at time t, the retarded potentials are to first order in the acceleration given by (cf. ref. 12, p. 167)

$$\begin{aligned}\varphi_{K(t)}&=\frac{Ze}{r}+\frac{Ze}{2c^2}\frac{d^2r}{dT^2}\,,\\ \mathbf{A}_{K(t)}&=0\,,\end{aligned} \tag{4.19}$$

where $r=|\mathbf{r}_e-\mathbf{r}_n|$ and d^2r/dT^2 refers to the inertial frame K(t), i.e.

$$\frac{d^2r}{dT^2}=-\frac{\mathbf{g}_0\cdot(\mathbf{r}_e-\mathbf{r}_n)}{r}\,. \tag{4.20}$$

Thus we obtain

$$\varphi_{K(t)} = \frac{Ze}{|\mathbf{r}_e - \mathbf{r}_n|}\left(1 - \frac{\mathbf{g}_0 \cdot (\mathbf{r}_e - \mathbf{r}_n)}{2c^2}\right),$$
$$\mathbf{A}_{K(t)} = 0\,. \tag{4.21}$$

From (4.15) and (4.17) we then get

$$i\hbar \frac{\partial \psi}{\partial t} = \left\{\frac{1}{2}\left(1 + \frac{\chi_e}{\lambda}\right)(c\boldsymbol{\alpha}\cdot\mathbf{p}_e + \beta m_e c^2) + \frac{1}{2}(c\boldsymbol{\alpha}\cdot\mathbf{p}_e + \beta m_e c^2)\left(1 + \frac{\chi_e}{\lambda}\right) - e\varphi(\mathbf{r}_e;\mathbf{r}_n)\right\}\psi \tag{4.22}$$

Here the potential

$$\varphi(\mathbf{r}_e;\mathbf{r}_n) = \left(1 + \frac{\chi_e}{\lambda}\right)\varphi_{K(t)}(\mathbf{r}_e;\mathbf{r}_n) \tag{4.23}$$

is seen to be identical with the electrostatic potential in the Møller box as given, to first order in $1/\lambda$, by (3.15). The Hamilton in (4.22) is just what one would obtain by simply replacing the square root in the Hamiltonian (4.6) by $(c\boldsymbol{\alpha}\cdot\mathbf{p}_e + \beta m_e c^2)$.

Since $(-e\psi^+\psi)$ is the charge density of the electron in the atom, we can immediately write down the expectation value, F_x, of the reaction force on the nucleus from the electron in a stationary state. By steps analogous to those of eq. (4.7), we obtain

$$\begin{aligned} F_x &= -\langle\psi\left|Ze\frac{\partial\varphi(\mathbf{r}_n;\mathbf{r}_e)}{\partial x_n}\right|_{\mathbf{r}_n=0}|\psi\rangle = \\ &= -\langle\psi\left|\frac{Ze^2}{\lambda|\mathbf{r}_e - \mathbf{r}_n|}\right|\psi\rangle + \langle\psi\left|e\frac{\partial\varphi(\mathbf{r}_e;\mathbf{r}_n)}{\partial x_e}\right|\psi\rangle \\ &= -\langle\psi\left|c\boldsymbol{\alpha}\cdot\mathbf{p}_e + \beta m_e c^2 - \frac{Ze^2}{|\mathbf{r}_e - \mathbf{r}_n|}\right|\psi\rangle\frac{g_0}{c^2} \\ &= -\left(m_e - \frac{B}{c^2}\,g_0\right). \end{aligned} \tag{4.24}$$

Thus the total force required to keep the atom at rest is given by the expression (4.5), where B, the binding energy of the electron, now includes spin-orbit coupling, the Darwin term and all other effects contained in the Dirac Hamiltonian.

It is also possible to demonstrate equivalence for a hydrogen-like atom described by the Klein-Gordon equation. Since the argumentation is somewhat different from the cases considered so far, the Klein-Gordon equation is treated separately in appendix C.

Thomas-Fermi atom

In the previous analysis we have considered equivalence for electrostatic energies and kinetic energies of a single particle bound in an atom. When we turn to more general systems, consisting of several moving charged particles, one might attempt to base the discussion on a mechanical description in terms of the coordinates and velocities of the particles only. It has turned out, however, that this description can in general only be carried to terms proportional to $1/c^2$, within an expansion in powers of $1/c$. The corresponding Lagrangian is the familiar one introduced by Darwin (cf. Landau and Lifshitz[12]). Equivalence may be demonstrated within this scheme, but a strong limitation is then imposed on the internal velocities of the system as well as on the velocity belonging to Lorentz transformations. Such limitations are avoided in a self-consistent description of the system, in which each particle interacts with a common four-potential, the latter being generated by the particles themselves. As a first step towards such general dynamical descriptions we shall study equivalence for the simple case of a non-relativistic Thomas-Fermi atom.

The first step is to establish, within the Møller box, the equilibrium condition for the electron distribution in an atom, the nucleus of which is at rest at $\mathbf{r}_n = 0$. The local Fermi momentum of a degenerate electron gas is

$$p_F(\mathbf{r}) = (3\pi^2)^{1/3}\hbar n^{1/3}(\mathbf{r}), \tag{4.25}$$

where $n(\mathbf{r})$ is the density of electrons. Thus, the electron charge density is

$$\varrho_e(\mathbf{r}) = -en(\mathbf{r}), \tag{4.26}$$

and the total charge density of the system is

$$\varrho(\mathbf{r}) = \varrho_e(\mathbf{r}) + Ze\,\delta(\mathbf{r}-\mathbf{r}_n)\,. \tag{4.27}$$

For a free atom at rest, the total Hamiltonian of the system then takes on the familiar form (cf. Gombás[14])

$$H = \int d^3r\left(mc^2 + \frac{3}{5}\frac{p_F^2(\mathbf{r})}{2m}\right)n(\mathbf{r}) + \int d^3r\,\frac{Ze\varrho_e(\mathbf{r})}{|\mathbf{r}-\mathbf{r}_n|} + \frac{1}{2}\int d^3r\int d^3r'\,\frac{\varrho_e(\mathbf{r})\varrho_e(\mathbf{r}')}{|\mathbf{r}-\mathbf{r}'|}, \tag{4.28}$$

where m is the electron mass.

For the total electric potential $\varphi(\mathbf{r})$, generated by the charge distribution (4.27), we have according to (3.15)

$$\varphi(\mathbf{r}) = \int d^3r'\,\frac{\varrho(\mathbf{r}')}{|\mathbf{r}-\mathbf{r}'|}\left(1+\frac{x+x'}{2\lambda}\right). \tag{4.29}$$

The effective Lagrangian for the individual electron, moving in the total

potential φ, is given by (3.21), and the corresponding Hamiltonian for a single electron is to lowest order in v^2/c^2

$$H_e = \left(1+\frac{x}{\lambda}\right)\left(mc^2+\frac{\mathbf{p}^2}{2m}\right)-e\varphi(\mathbf{r}) . \tag{4.30}$$

All electron states up to the Fermi momentum $p_F(\mathbf{r})$ are occupied, and in equilibrium the maximum energy, E_{max}, that an electron can have at any point, is constant throughout the atom

$$\left(1+\frac{x}{\lambda}\right)(mc^2+\mu(\mathbf{r}))-e\varphi(\mathbf{r}) = E_{max} , \tag{4.31}$$

where we have introduced the potential

$$\mu(\mathbf{r}) = \frac{p_F^2(\mathbf{r})}{2m} = (3\pi^2)^{2/3}\frac{\hbar^2}{2m}n^{2/3}(\mathbf{r}) . \tag{4.32}$$

Combining (4.32) with the generalized Poisson equation (3.14), one may obtain the Thomas-Fermi equation in the Møller box.

In order to derive the reaction force on the nucleus due to the electrons, we note that from the potential (4.29), one obtains as a generalization of the relation (3.17)

$$\int d^3r\,\varrho(\mathbf{r})\frac{\partial\varphi(\mathbf{r})}{\partial x} = \frac{1}{2\lambda}\int d^3r'\,\frac{\varrho(\mathbf{r})\varrho(\mathbf{r}')}{|\mathbf{r}-\mathbf{r}'|} . \tag{4.33}$$

This relation is valid for any static charge distribution and may in particular be applied to the charge distribution $\varrho_n(\mathbf{r})$ of the nucleus and the potential φ_n that it generates

$$\int d^3r\,\varrho_n(\mathbf{r})\frac{\partial\varphi_n(\mathbf{r})}{\partial x} = \frac{1}{2\lambda}\int d^3r\int d^3r'\,\frac{\varrho_n(\mathbf{r})\varrho_n(\mathbf{r}')}{|\mathbf{r}-\mathbf{r}'|} . \tag{4.34}$$

Next, we write the total potential φ in (4.33) as

$$\varphi(\mathbf{r}) = \varphi_n(\mathbf{r})+\varphi_e(\mathbf{r}), \tag{4.35}$$

where $\varphi_e(\mathbf{r})$ is the potential generated by electron charge distribution $\varrho_e(\mathbf{r})$. Subtracting (4.34) from (4.33) we obtain

$$\int d^3r\,\varrho_n(\mathbf{r})\frac{\partial\varphi_e(\mathbf{r})}{\partial x}+\int d^3r\,\varrho_e(\mathbf{r})\frac{\partial\varphi(\mathbf{r})}{\partial x} = \tag{4.36}$$

$$= \frac{1}{\lambda}\int d^3r\int d^3r'\,\frac{\varrho_n(\mathbf{r}')\varrho_e(\mathbf{r})}{|\mathbf{r}-\mathbf{r}'|}+\frac{1}{2\lambda}\int d^3r\int d^3r'\,\frac{\varrho_e(\mathbf{r})\varrho_e(\mathbf{r}')}{|\mathbf{r}-\mathbf{r}'|} .$$

In this relation we may approximate the charge distribution $\varrho_n(\mathbf{r})$ of the nucleus by a delta function in accordance with (4.27). For the reaction force on the nucleus from the electron distribution we thus get

$$F_x = -Ze\frac{\partial \varphi_e(\mathbf{r})}{\partial x}\Big|_{\mathbf{r}_n=0}$$

$$= \int d^3r\, \varrho_e(\mathbf{r})\frac{\partial \varphi(\mathbf{r})}{\partial x} - \frac{1}{\lambda}\int d^3r\frac{Ze\,\varrho_e(\mathbf{r})}{|\mathbf{r}-\mathbf{r}_n|} - \frac{1}{2\lambda}\int d^3r\int d^3r'\frac{\varrho_e(\mathbf{r})\,\varrho_e(\mathbf{r}')}{|\mathbf{r}-\mathbf{r}'|}\,. \tag{4.37}$$

Expressing the potential φ in terms of μ, cf. the equilibrium condition (4.31), and using (4.32), we find

$$\int d^3r\varrho_e(\mathbf{r})\frac{\partial \varphi}{\partial x} = -\int d^3r\; n(\mathbf{r})\frac{\partial}{\partial x}\left\{\left(1+\frac{x}{\lambda}\right)(\mu(\mathbf{r})+mc^2)\right\}$$

$$= -\int d^3r\left\{n(\mathbf{r})\frac{1}{\lambda}\left(\mu(\mathbf{r})+mc^2\right) + (1+\frac{x}{\lambda})\;\frac{1}{3\pi^2}\left(\frac{2m}{\hbar^2}\mu\right)^{3/2}\frac{\partial \mu}{\partial x}\right\}$$

$$= -\frac{1}{\lambda}\int d^3r\; n(\mathbf{r})\left(mc^2+\frac{3}{5}\mu(\mathbf{r})\right), \tag{4.38}$$

where the last equation follows by partial integration. Inserting this expression in (4.37), the reaction force, F_x, becomes:

$$F_x = -\frac{H}{c^2}g_0 = -\left(Nm-\frac{B}{c^2}\right)g_0\,, \tag{4.39}$$

where H is the Thomas-Fermi Hamiltonian (4.28) and N the total number of electrons. For the total force required to keep the atom at rest, we thus again obtain the expression (4.5), where B is the binding energy of the Thomas-Fermi atom.

§ 5. Conclusions and General Outlook

In the previous chapters we have verified that there is equivalence between inertial mass and self-energy. The study was performed in considerable detail, including electrostatic interactions and kinetic energies, for hydrogen-like systems and the Thomas-Fermi model, within both classical mechanics and relativistic quantum mechanics. Moreover, there was detailed equivalence, i.e. equivalence for each term and for each element of the interaction energy. It was not necessary for the treatment that the system were stable. Without doubt, these are satisfactory results since they imply that all terms of a calculation of self-energies have a separate and simple significance.

The equivalence could be made specific in terms of the basic equation of motion (2.12) for a charged, composite system, $\mathbf{g}_c M = q\mathbf{E}_{ext}(\mathbf{r}_c, t)$. Thus, not only did the mass M contain detailed equivalence, but also the system, and its acceleration, could be represented by one point: the centre of charge $\mathbf{r}_c$. Higher order terms, like radiation damping, may afterwards be built into the above equation of motion. In connection with these results we showed that there is an error in the standard Born-Heitler calculation of self-mass from total self-force. As to the conventional formulae for self-momentum and self-energy, i.e. (1.8) and (1.9), we found that they resulted from an unwarranted variation of a constant term in the Lagrangian (2.15), and therefore could not be compared with the proper momenta and energies. It was apparent that if one kept to a Lagrangian formulation in describing a system, the undesirable expressions (1.8) and (1.9) were avoided, the need for Poincaré stresses did not arise, and detailed equivalence was explicit.

There is a more general background to our work, concerned with the consistency and aim of the description. As promised in the brief introductory remarks in §1, we shall now discuss this background.

We have been concerned with composite systems, and with their primary property, i.e. their mass. It was supposed that we can speak consistently about such systems. But already in the wording *composite* systems it is implicit that a simpler concept exists. In point of fact, we have an idealized concept, that of a *particle*, sometimes referred to as an *elementary* particle, or a *point* particle. From old, a particle is conceived as an unchangeable building stone of matter. On the one hand, we then visualize a composite system as a swarm of particles interacting with each other. On the other hand, we have to compare the properties of this swarm with the properties of one particle, asking for the likeness between the two, as well as for their difference in behaviour.

For the purpose of this comparison, consider a composite system, be it a molecule, a liquid drop, a crystal, or an atomic nucleus, and note the following. If we act upon the system by means of comparatively weak forces, the forces varying sufficiently slowly in space and time, then the behaviour of the system will be as if it were a particle. This means that it has a certain mass, charge, inner angular momentum, magnetic dipole moment, etc. It can possibly be represented as a point in space as was shown in the equation of motion (2.12), just in the way a particle – if we are cautious – can possibly be described as a point in space. By acting on the system with such moderate forces, we can measure the properties of the system, properties which are conserved when the system remains isolated. In this comparison to a point particle we need not require that the system be absolutely stable when isolated. We can allow it to be unstable,

like a uranium nucleus with a probability of fissioning, or like a liquid drop which may evaporate. In such cases we can think of it as having conservation within sufficiently short time intervals, or with a certain width of its energy. Note in this connection that, in the main, it is permissible to use classical mechanics as well as quantum theory in the description of the system, although, of course, quantum mechanics will give a more precise account of the physical properties.

Thus, in the limiting case of weak and slowly varying external fields, we find that we must be able to describe a composite system and a particle in a like manner. It lies near at hand to demand that we are also able *to account for* their properties in a like manner. In a way, this hypothesis corresponds to the historical development of particle physics where successively, molecules, atoms, and atomic nuclei, etc., have been described as elementary particles. But it is more essential that actual calculations of basic properties of systems comply with our demand, in so far as we are able to calculate these properties. Correspondingly, the problem of equivalence of mass and energy must be our primary concern.

Consider then calculations of self-energies and self-masses for, on the one hand, composite systems, and, on the other hand, particles. In the case of composite systems this calculation is prescribed: we treat its constituents, e.g., electrons and atomic nuclei, as elementary particles, and only their interactions and their motion contribute to the additional self-energy and mass. It is important to notice that constituents of a composite system – constituents like the above atomic nuclei – often can be regarded as composite systems themselves, and so the division into constituents can be somewhat free. This possibility of a variable division into constituents leads to the further expectation that each separate interaction contribution, or kinetic energy contribution, should show equivalence. We described this as the demand of *detailed* equivalence, and we verified that it is fulfilled.

If we demand a systematic account, the above ought to be compared with self-energies for particles, such as the self-energy of an electron. The latter concept is not quite simple, however, and that mainly on three counts. First, the basic method of finding self-energies belongs primarily to composite systems, and we can merely maintain that the proper procedure for a supposedly elementary particle must not be in discord with the former. Second, the leading term in the electron self-energy is apparently divergent, whereas the physically observable parts of the self-energy, like the Lamb effect, appear only in higher order terms in expansions in powers of $1/c$. But our primary concern, for composite systems, was not to evaluate cumbersome higher order terms. Third, there is an interesting complication because of the spin and magnetic moment of the electron; in order to make a comparison, one must first analyse composite systems with spin, or inner angular momentum. We have made this study and found that a classical

system with spin must be described by at least two points, the centre of motion and the centre of charge. An account of these questions will be given in a separate publication.

Acknowledgments

This paper has been under way during one decade. The contents of it, and its aim, has changed considerably in that period. Part of the subject, systems with spin, has been reserved for a future publication. We are grateful to many friends for debates on equivalence as well as subjects akin to it. We have, in particular, profited much from discussions with E. Eilertsen, P. Kristensen, Vibeke Nielsen, W. J. Swiatecki, and A. Winther.

We are especially indebted to Lise Madsen for competent and careful preparation of the paper.

Appendix A

Electrodynamics in Møller Box

The line element (3.6) in the Møller box corresponds to a diagonal metric tensor g_{ik}. If we put $(x^0, x^1, x^2, x^3) = (ct, x, y, z)$, we have

$$g_{00} = \left(1 + \frac{x}{\lambda}\right)^2,$$

$$g_{11} = g_{22} = g_{33} = -1, \tag{A1}$$

$$\sqrt{-g} = 1 + \frac{x}{\lambda},$$

where g is the determinant of g_{ik}.

The field equations are derived from the action principle

$$\delta S_f + \delta S_{int} = 0, \tag{A2}$$

where, with general covariant notation, the contributions to the action from the field and the interaction are, respectively,

$$S_f = \frac{1}{16\pi c}\int d^4x \sqrt{-g}\, F^{ik} F_{ik} \tag{A3}$$

and

$$S_{int} = -\frac{1}{c^2}\int d^4x \sqrt{-g}\, j^i \mathcal{A}_i. \tag{A4}$$

Here the field tensor is given in terms of the four-potentials by

$$F_{ik} = \frac{\partial}{\partial x^i}\mathcal{A}_k - \frac{\partial}{\partial x^k}\mathcal{A}_i, \tag{A5}$$

and hence the action S_f is invariant with respect to the gauge transformation

$$\mathcal{A}_i \rightarrow \mathcal{A}_i + \frac{\partial}{\partial x^i}\Lambda(\mathbf{r}, t), \tag{A6}$$

where $\Lambda(\mathbf{r}, t)$ is an arbitrary scalar function of the coordinates.

The condition that also the action S_{int} be invariant against the transformation (A6) yields the conservation law

$$\frac{\partial}{\partial x^i}(\sqrt{-g}\, j^i) = 0. \tag{A7}$$

Therefore, we introduce the conserved current $(\varrho c, \mathbf{s})$ as

$$j^i = \frac{1}{\sqrt{-g}}(\varrho c, \mathbf{s}), \tag{A8}$$

so that the total charge

$$q = \int d^3 r \, \varrho(\mathbf{r}, t) \tag{A9}$$

is a constant.

If a point charge q_1 is located at the position $\mathbf{r}_1(t)$, the current density takes the form

$$j^i = \frac{q_1}{\sqrt{-g}} \frac{dx^i}{dt} \delta(\mathbf{r} - \mathbf{r}_1(t)) . \tag{A10}$$

From (A4) and (A8) we have

$$S_{int} = -\int dt \int d^3 r \left(\varrho \mathcal{A}_0 + \frac{1}{c} s^\lambda \mathcal{A}_\lambda \right) \tag{A11}$$

where $\lambda = 1, 2, 3$.

Since the space integral in (A11) represents the interaction energy, we must introduce the scalar potential φ and the vector potential $\mathbf{A}$ through the relation

$$(\mathcal{A}_0, \mathcal{A}_1, \mathcal{A}_2, \mathcal{A}_3) = (\varphi, -A_x, -A_y, -A_z) , \tag{A12}$$

so that

$$S_{int} = -\int dt \int d^3 r \left(\varrho \varphi - \frac{1}{c} \mathbf{s} \cdot \mathbf{A} \right). \tag{A13}$$

From eq. (A5) follows the homogeneous Maxwell equations

$$\frac{\partial}{\partial x^i} F_{kl} + \frac{\partial}{\partial x^k} F_{li} + \frac{\partial}{\partial x^l} F_{ik} = 0 , \tag{A14}$$

whereas the inhomogeneous equations are obtained from the action principle (A2), when the variation is carried out for fixed charge and current distributions. The result is (cf. ref. 12)

$$\frac{1}{\sqrt{-g}} \frac{\partial}{\partial x^k} (\sqrt{-g} \, F^{ik}) = -\frac{4\pi}{c} j^i . \tag{A15}$$

The conservation law (A7) is of course one consequence of the Maxwell equations (A15).

The physical significance of the potentials φ and $\mathbf{A}$ is expressed by the equations of motion for a charged particle in an external field. These equations are found from the action principle

$$\delta S_{kin} + \delta S_{int} = 0 , \tag{A16}$$

where a variation of the particle coordinates is carried out for fixed potentials.

Here

$$S_{kin} = -mc^2 \int dt \left\{ \left(1 + \frac{x}{\lambda}\right)^2 - \frac{\mathbf{v}^2}{c^2} \right\}^{1/2}, \tag{A17}$$

$$S_{int} = -\int dt\, q \left\{ \varphi(\mathbf{r}(t)) - \frac{\mathbf{v}}{c} \mathbf{A}(\mathbf{r}(t)) \right\}, \tag{A18}$$

where m is the mass of the particle and q its charge. The corresponding Lagrangian is

$$L = -mc^2 \left\{ \left(1 + \frac{x}{\lambda}\right)^2 - \frac{\mathbf{v}^2}{c^2} \right\}^{1/2} - q\varphi(\mathbf{r}, t) + \frac{q}{c} \mathbf{v} \cdot \mathbf{A}(\mathbf{r}, t), \tag{A19}$$

and hence the equations of motion become

$$\frac{d}{dt} \frac{m\mathbf{v}}{\{(1+x/\lambda)^2 - \mathbf{v}^2/c^2\}^{1/2}} = \frac{-m(1+x/\lambda)\mathbf{g}_0}{\{(1+x/\lambda)^2 - \mathbf{v}^2/c^2\}^{1/2}} + q\left(\mathbf{E} + \frac{\mathbf{v}}{c} \times \mathbf{B}\right), \tag{A20}$$

where we have introduced the electromagnetic fields

$$\mathbf{E} = -\nabla\varphi - \frac{1}{c} \frac{\partial \mathbf{A}}{\partial t}, \tag{A21}$$

$$\mathbf{B} = \nabla \times \mathbf{A}. \tag{A22}$$

In terms of these quantities the field action (A3) takes the simple form

$$S_f = \frac{1}{8\pi} \int dt \int d^3r \left(\frac{\mathbf{E}^2}{1+x/\lambda} - (1+x/\lambda)\mathbf{B}^2 \right). \tag{A23}$$

It can be convenient to express the Maxwell equations (A14) and (A15) in the following three-dimensional notation

$$\begin{aligned} &\text{div } \mathbf{B} = 0 \quad , \\ &\text{rot } \mathbf{E} = -\frac{1}{c} \frac{\partial \mathbf{B}}{\partial t} \quad , \\ &\text{div } \mathbf{D} = 4\pi\varrho \, , \\ &\text{rot } \mathbf{H} = \frac{1}{c} \frac{\partial \mathbf{D}}{\partial t} + \frac{4\pi}{c} \mathbf{s} \, , \end{aligned} \tag{A24}$$

where we have introduced the abbreviations

$$\mathbf{D} = \frac{1}{1+x/\lambda} \mathbf{E}, \tag{A25}$$

$$\mathbf{H} = \left(1 + \frac{x}{\lambda}\right) \mathbf{B}. \tag{A26}$$

Appendix B

Static Potentials in Møller Box

In this appendix we derive the potential generated by a charge at rest in the box. By introducing (A21) and (A25) into (A24), one obtains the generalized Poisson equation for the potential φ,

$$\Delta\varphi - \frac{1}{\lambda + x}\frac{\partial\varphi}{\partial x} = -4\pi q_1 \left(1 + \frac{x}{\lambda}\right)\delta(\mathbf{r} - \mathbf{r}_1)\,, \tag{B1}$$

where the charge q_1 is at rest at the position $\mathbf{r}_1$. In the text we only use the solution of this equation to first order in $1/\lambda$ as given by (B12). But for the sake of completeness we here give the exact solution of (B1), subject to the boundary condition that it vanishes at infinity in the box. This solution is a somewhat complicated analytical expression, which can, however, be given a simple geometrical representation.

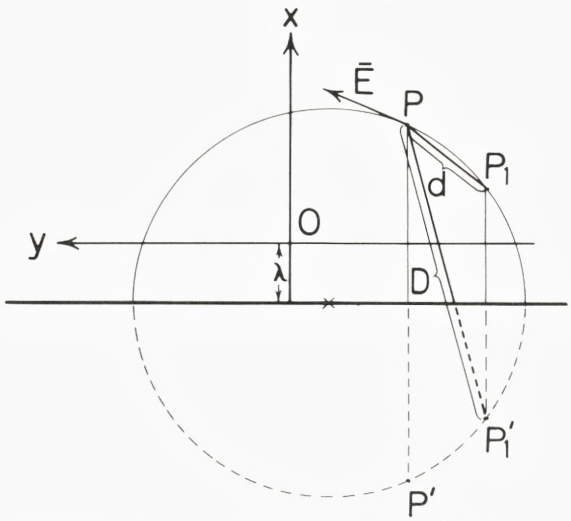

Fig. 4. Geometrical construction of potential and field from fixed charge in the Møller box. The x-axis in the box is chosen in the direction of $\mathbf{g}_0$. The thick line, at $x = -\lambda$, represents the bottom of the box. i.e. the region below this line does not belong to the box. The circle is drawn through the charge point P_1 and the field point P as well as through their mirror images, P_1' and P' beyond the bottom of the box. The field strength $\mathbf{E}$ is tangential to the circle at the point P.

Let P_1 represent the point in which the charge is located and P the field point (see Fig. 4). We draw a circle through these two points and their mirror images, P_1' and P', beyond the bottom of the box, at $x = -\lambda$. Denote the vectors from P_1 to P and from P_1' to P by $\mathbf{d}$ and $\mathbf{D}$, respectively. We shall prove that the solution of (B1) may be written

$$\varphi(\mathbf{r};\mathbf{r}_1) = \frac{q_1}{2\lambda}\left(\frac{d}{D} + \frac{D}{d}\right), \tag{B2}$$

where $d = |\mathbf{d}|$ and $D = |\mathbf{D}|$.

The right hand side of (B2) tends to the constant q_1/λ at infinity and at the bottom of the box. It is seen from Fig. 4 that d and D are given by

$$d = \{(x-x_1)^2 + (y-y_1)^2 + (z-z_1)^2\}^{1/2} \tag{B3}$$

$$D = \{(x+\lambda+x_1+\lambda)^2 + (y-y_1)^2 + (z-z_1)^2\}^{1/2}. \tag{B4}$$

In order to show that (B2) is a solution of (B1), we observe that the Laplacian acting on d/D becomes

$$\Delta\frac{d}{D} = \frac{1}{D}\cdot\Delta d + d\,\Delta\frac{1}{D} + 2(\nabla d)\cdot\left(\nabla\frac{1}{D}\right) = -4\pi d\,\delta(\mathbf{D}) + \frac{1}{dD} - \frac{d}{D^3} + \frac{4(x_1+\lambda)^2}{dD^3}, \tag{B5}$$

and similarly

$$\Delta\frac{D}{d} = -4\pi D\,\delta(\mathbf{d}) + \frac{1}{dD} - \frac{D}{d^3} - \frac{4(x_1+\lambda)^2}{Dd^3}. \tag{B6}$$

Furthermore,

$$\begin{aligned}\frac{1}{\lambda+x}\frac{\partial}{\partial x}\frac{d}{D} &= \frac{1}{\lambda+x}\left(\frac{x-x_1}{dD} - d\,\frac{x+\lambda+x_1+\lambda}{D^3}\right),\\ \frac{1}{\lambda+x}\frac{\partial}{\partial x}\frac{D}{d} &= \frac{1}{\lambda+x}\left(\frac{x+\lambda+x_1+\lambda}{dD} - D\,\frac{(x+\lambda)-(x_1+\lambda)}{d^3}\right).\end{aligned} \tag{B7}$$

Finally, making use of the relation

$$D^2 - d^2 = 4(x+\lambda)(x_1+\lambda), \tag{B8}$$

we obtain

$$\left(\Delta - \frac{1}{\lambda+x}\frac{\partial}{\partial x}\right)\frac{q_1}{2\lambda}\left(\frac{d}{D}+\frac{D}{d}\right) = -4\pi\frac{q_1}{2\lambda}\left(D\,\delta(\mathbf{d}) + d\,\delta(\mathbf{D})\right). \tag{B9}$$

Since $\delta(\mathbf{D})$ vanishes everywhere within the box, we have verified that, apart from an additive constant, (B2) is the solution of (B1) with the desired boundary condition. It is easily seen that the electric field $\mathbf{E}$ at the point P is tangential to the circle and of magnitude

$$E(P) = q_1\left(1+\frac{x_1}{\lambda}\right)\left(\frac{1}{d^2} - \frac{1}{D^2}\right). \tag{B10}$$

Incidentally it may be remarked that a light ray, sent from the point P_1 to the point P, travels along the circle shown on the figure.

In order to obtain the potential to first order in $1/\lambda$ we expand as follows

$$D = 2\lambda + x_1 + x \ldots . \tag{B11}$$

Hence the potential becomes

$$\varphi \simeq \frac{q_1}{2\lambda}\frac{D}{d} \simeq \frac{q_1}{|\mathbf{r}-\mathbf{r}_1|}\left(1+\frac{x+x_1}{2\lambda}\right), \tag{B12}$$

which is the form used in the text.

The above result for the potential may also be derived by transforming the potentials, generated by a charge in hyperbolic motion, from the inertial frame to the Møller box and performing a gauge transformation. The potentials in the inertial frame were originally derived by Born[10].

Appendix C

Klein-Gordon Equation in Møller Box

Let K(t) denote the particular inertial frame which coincides with the Møller box at time t. In this frame, the Klein-Gordon equation for a spinless particle of charge q and mass m in an external potential $\mathcal{A}$ may be written as

$$\left(P_l - \frac{q}{c}\mathcal{A}_l\right)\left(P^l - \frac{q}{c}\mathcal{A}^l\right)\psi_{K(t)}(T) = m^2c^2\psi_{K(t)}(T)\,, \tag{C1}$$

where $\psi_{K(t)}(T)$, the wave function in the frame K(t), is a scalar quantity. With the identification

$$P_l = i\hbar\frac{\partial}{\partial X^l}\,, \tag{C2}$$

and imposing the Lorentz condition we obtain

$$\left(-\hbar^2\,\Box - 2\frac{q}{c}i\hbar\,\mathcal{A}^l\frac{\partial}{\partial X^l} + \frac{q^2}{c^2}\,\mathcal{A}^l\mathcal{A}_l\right)\psi_{K(t)}(T) = m^2c^2\psi_{K(t)}(T). \tag{C3}$$

We now notice that the wave function in the Møller box $\psi(t)$ is equal to the wave function $\psi_{K(t)}(T)$

$$\psi(t) = \psi_{K(t)}(T)\,. \tag{C4}$$

Moreover, since $\psi_{K(t)}$ is a scalar, the product $\mathcal{A}^l\,\partial\psi_{K(t)}/\partial X^l$ is an invariant. Therefore the Klein-Gordon equation in the Møller box is simply obtained by expressing this invariant and the d'Alembertian in non-Euclidean coordinates. For the latter operator we have the general expression (cf. ref. 12, §86)

$$\Box = \frac{1}{\sqrt{-g}}\frac{\partial}{\partial x^i}\sqrt{-g}\,g^{ik}\frac{\partial}{\partial x^k}\,. \tag{C5}$$

With the metric (A1) in the Møller box, this operator becomes

$$\begin{aligned}\Box &= \frac{1}{(1+x/\lambda)^2}\frac{1}{c^2}\frac{\partial^2}{\partial t^2} - \left(\Delta + \frac{1}{\lambda+x}\frac{\partial}{\partial x}\right)\\ &\simeq (1-2x/\lambda)\frac{1}{c^2}\frac{\partial^2}{\partial t^2} - \left(\Delta + \frac{1}{\lambda}\frac{\partial}{\partial x}\right),\end{aligned} \tag{C6}$$

where the last expression is valid to first order in $1/\lambda$. We shall only consider the case of a static potential in the Møller box, i.e. $\mathcal{A} = (\varphi,0,0,0)$. Hence we obtain

$$\mathcal{A}^l\frac{\partial}{\partial x^l} = g^{00}\mathcal{A}_0\frac{\partial}{\partial x^0} = \frac{1}{(1+x/\lambda)^2}\varphi\frac{1}{c}\frac{\partial}{\partial t} \simeq (1-2x/\lambda)\varphi\frac{1}{c}\frac{\partial}{\partial t}\,. \tag{C7}$$

Similarly,

$$\mathcal{A}^i \mathcal{A}_i = g^{00} \mathcal{A}_0^2 \simeq (1 - 2x/\lambda)\varphi^2 . \tag{C8}$$

Multiplying eq. (C3) from the left with the factor $(1+2x/\lambda)$, we obtain to first order in $1/\lambda$

$$\left\{-\hbar^2 \frac{1}{c^2}\frac{\partial^2}{\partial t^2} - \frac{2q}{c} i\hbar\varphi \frac{1}{c}\frac{\partial}{\partial t} + \frac{q^2}{c^2}\varphi^2 + \left(1+2\frac{x}{\lambda}\right)\left(\Delta + \frac{1}{\lambda}\frac{\partial}{\partial x}\right)\right\}\psi = \left(1+2\frac{x}{\lambda}\right) m^2 c^2 \psi, \tag{C9}$$

or

$$\left(i\hbar\frac{\partial}{\partial t} - q\varphi\right)^2 \psi = \left\{m^2 c^4 \left(1+2\frac{x}{\lambda}\right) - \left(1+2\frac{x}{\lambda}\right)\hbar^2 \Delta - \frac{\hbar^2}{\lambda}\frac{\partial}{\partial x}\right\}\psi . \tag{C10}$$

It is convenient to rewrite this equation in a more symmetric form by introducing an auxiliary function

$$\Psi = \frac{1}{(1+x/\lambda)^{1/2}}\,\psi . \tag{C11}$$

Thereby we get from (10), again to first order in $1/\lambda$,

$$\left(i\hbar\frac{\partial}{\partial t} - q\varphi\right)^2 \Psi = \left\{m^2 c^4 \left(1+2\frac{x}{\lambda}\right) + c\mathbf{p}\left(1+2\frac{x}{\lambda}\right)c\mathbf{p}\right\}\Psi , \tag{C12}$$

where $\mathbf{p} = -i\hbar\boldsymbol{\nabla}$. We note that to this order eq. (C12) may be written

$$\left(i\hbar\frac{\partial}{\partial t} - q\varphi\right)^2 \Psi = H_0^2 \Psi , \tag{C13}$$

where H_0 is given by (4.6).

To the Klein-Gordon equation belongs a conserved four-current density $(\varrho, \mathbf{s})$. According to (C11) it is to first order in $1/\lambda$ given by

$$\begin{aligned} \varrho &= \frac{i\hbar}{2mc^2}\left(\Psi^* \frac{\partial \Psi}{\partial t} - \Psi \frac{\partial \Psi^*}{\partial t}\right) - \frac{q\varphi}{mc^2}|\Psi|^2 , \\ \mathbf{s} &= -\frac{i\hbar}{2m}\left(\Psi^*\left(1+2\frac{x}{\lambda}\right)\boldsymbol{\nabla}\Psi - \Psi\left(1+2\frac{x}{\lambda}\right)\boldsymbol{\nabla}\Psi^*\right). \end{aligned} \tag{C14}$$

These quantities obey the continuity equation $\partial\varrho/\partial t = -\operatorname{div}\mathbf{s}$ because of (C12).

Consider a hydrogen-like system, where a particle of charge q_2 moves in the potential φ given by (3.15). The demonstration of equivalence in this case differs slightly from the derivations in § 4 for two reasons. First, the wave function belonging to a stationary state of the atom is not an eigenstate of a Hamiltonian as in the cases studied in the text. Second, the conserved density is not $|\Psi^2|$, but is given by (C14).

In a stationary state we have

$$\Psi(\mathbf{x},t) = \Psi(\mathbf{x})e^{\frac{-i}{\hbar}Et}. \tag{C15}$$

Thus the density ϱ takes the form

$$\varrho = \frac{E - q_2\varphi}{mc^2}|\Psi|^2, \tag{C16}$$

where Ψ satisfies the equations (C12) or (C13) with $i\hbar\partial/\partial t$ replaced by E.

We assume that the integral of the density ϱ, in (C16), is normalized to unity, and thus the charge density of the particle is equal to $q_2\varrho(\mathbf{r}_2)$. Hence we get for the expectation value, F_x, of the reaction force from the particle on the charge centre q_1 situated at the position $\mathbf{r}_1 = 0$

$$\begin{aligned} F_x &= -q_1 \overline{\frac{\partial\varphi(\mathbf{r}_1;\mathbf{r}_2)}{\partial x_1}}\bigg|_{\mathbf{r}_1=0} \equiv -\int d^3r_2\, q_1\varrho(\mathbf{r}_2)\left(\frac{\partial\varphi(\mathbf{r}_1;\mathbf{r}_2)}{\partial x_1}\right) \\ &= -\int d^3r_2\,\varrho(\mathbf{r}_2)q_2\left(\frac{1}{\lambda}\varphi(\mathbf{r}_2;\mathbf{r}_1) - \frac{\partial\varphi(\mathbf{r}_2;\mathbf{r}_1)}{\partial x_2}\right). \end{aligned} \tag{C17}$$

Noticing the relationships

$$\begin{aligned} \int d^3r_2\varrho q_2\frac{\partial\varphi}{\partial x_2} &= -\int d^3r_2|\Psi|^2\frac{\partial}{\partial x_2}\frac{(E-q_2\varphi)^2}{2m_2c^2} \\ &= -\int d^3r_2\Psi^*\left[\frac{\partial}{\partial x_2}, \frac{H_0^2}{2m_2c^2}\right]\Psi \\ &= -\frac{1}{\lambda}\int d^3r_2\Psi^*\frac{(E-q_2\varphi)^2}{m_2c^2}\Psi \\ &= -\frac{1}{\lambda}\int d^3r_2\varrho(\mathbf{r}_2)(E-q_2\varphi), \end{aligned} \tag{C18}$$

we obtain equivalence in (C17)

$$F_x = -\frac{1}{\lambda}E\int d^3r_2\varrho(\mathbf{r}_2) = -\frac{E}{c^2}g_0. \tag{C19}$$

References

1. Jackson, J. D., Classical Electrodynamics, Chapter 17, Wiley, New York (1962).
2. Einstein, A., Ann. d. Phys. *17*, 891 (1905), Ann. d. Phys. *18*, 639 (1905). Reprinted in English translation in "The Principle of Relativity", Dover Publications (1952).
3. v. Laue, M., Inertia and Energy, in "Albert Einstein, Philosopher-Scientist", (Ed. A. Schilpp) The Library of Living Philosophers, Evanstone, Illinois (1949).
4. Jammer, M., Concepts of Mass, Chapter 11, Harvard University Press (1961).
5. Lorentz, H. A., The Theory of Electrons, Teubner Verlag, Leipzig (1916). Reprinted in Dover Publications (1952).
6. Pais, A., Developments in the Theory of the Electron. Institute for Advanced Studies and Princeton University (1948).
7. Feynman, R. P., Lectures on Physics II (Chapt. 28), Addison-Wesley, Reading, Mass. (1964).
8. Becker, R. and Sauter, F., Theorie der Elektrizität, Teubner Verlag, Stuttgart (1957).
9. Rohrlich, F., Am. J. Phys. *28*, 634 (1960), Ibid. *38*, 1310 (1970), and Classical Charged Particles, Addison-Wesley, Reading, Mass. (1965).
10. Born, M., Ann. d. Phys. *30*, 1 and 840 (1909).
11. Heitler, W., The Quantum Theory of Radiation, Oxford University Press, Oxford (1954).
12. Landau, L. and Lifshitz, I. M., Classical Theory of Fields, 3. ed. Pergamon Press, Oxford, New York (1973)
13. Møller, C., The Theory of Relativity, Oxford University Press, Oxford (1972).
14. Gombás, P., Die Statistische Theorie des Atoms und ihre Anwendungen, Springer Verlag, Wien (1969).

Indleveret til Selskabet december 1981.
Færdig fra trykkeriet juni 1982

Additive Theory for $\mathbf{F}_q[x]$ by Probability Methods

By JØRGEN CHERLY

Det Kongelige Danske Videnskabernes Selskab
Matematisk-fysiske Meddelelser **40**:12

Kommissionær: Munksgaard
København 1983

Synopsis

Let $\mathbf{F}_q$ be a finite field and let $\mathbf{F}_q[x]$ denote its polynomialring. Let $AC\mathbf{F}_q[x]$ denote a sequence of polynomials and $A(n)$ the counting number Card $\{f \in A | \partial f \leq n\}$ where ∂f denotes the degree of f.

A sequence $AC\mathbf{F}_q[x]$ is said to be an asymptotic basis of order 2 if all polynomials of sufficiently high degree lie in $A+A = 2A$ and an asymptotic complementary sequence is defined analogously.

Let further P denote the sequence of irreducible polynomials in $\mathbf{F}_q[x]$. The subject of this paper is to translate two principal results of a chapter of the book of H. Halberstam and K. F. Roth to the case of a polynomialring over a finite field.

We shall use an idea of Erdös to make the space of polynomial sequences into a probability space.

We then prove the following two existence theorems by showing that the property one looked for holds with probability 1.

There exist:

— a thin asymptotic basis of order two

— an asymptotic complementary sequence to P such that the counting number $B(n) \ll n^2$.

JØRGEN CHERLY
Université de Bordeaux I
Mathematiques et Informatique
351, cours de la Liberation
33405 Talence Cedex

Det Kongelige Danske Videnskabernes Selskab 1983
Printed in Denmark by Bianco Lunos Bogtrykkeri A/S. ISSN 0023-3323. ISBN 87-7304-138-6

§1. Introduction .

Let $\mathbf{F}_q$ be a finite field of $q = p^m$, $m \in N$ elements and let $\mathbf{F}_q[x]$ denote its polynomialring. The degree of a polynomial is denoted ∂f. We denote by sign f the leading coefficient of f. The absolute value of a polynomial f is defined by $|f| = q^{\partial f}$. We can assume that the polynomials in $\mathbf{F}_q[x]$ are arranged in lexicographical order $(=<)$ based on an arbitrary ordering of $\mathbf{F}_q$.

Let $A \subset \mathbf{F}_q[x]$ denote a sequence of polynomials and $A(n)$ denote Card $\{f \in A | \partial f \leqq n\}$. Further let P denote the sequence of irreducible polynomials in $\mathbf{F}_q[x]$.

We denote by $r_f(A)$ the number of representations of f in the form:

$$f = f' + f'', \quad f', f'' \in A, \quad \partial f' = \partial f, \quad \partial f'' < \partial f. \tag{1.1}$$

Also let $R_f(A)$ denote the number of representations of f in the form:

$$f = p + f', \quad p \in P, \quad f' \in A, \quad \partial p = \partial f, \quad \text{sign } p = \text{sign } f. \tag{1.2}$$

Definition 1.1.
$A \subset \mathbf{F}_q[x]$ is said to be an asymptotic basis of order 2 if all polynomials of sufficiently high degree lie in $A + A = 2A$.

Definition 1.2.
For a given sequence $A \subset \mathbf{F}_q[x]$ the sequence B is said to be "complementary" to A if the sequence $A + B$ contains all polynomials of sufficiently high degree.

The subject of this paper is to translate two principal results of a chapter of the book of H. Halbertstam and K. F. Roth to the case of a polynomialring over a finite field.

Discussion and introduction of the first result.
The following question is a direct translation to the polynomialring $\mathbf{F}_q[x]$ of the same question raised by S. Sidon (see [1]) concerning the existence and nature of certain integer sequences A whose representation functions $r_n(A)$ are bounded or in some sense exceptionally small.

Does there exist an asymptotic basis $A \subset \mathbf{F}_q[x]$ of order 2 which is economical in the sense that, for every $\varepsilon > 0$

$$\lim_{\partial f \to \infty} \frac{r_f(A)}{|f|^{\varepsilon}} = 0$$

By elementary methods we have proved the existence of a subset A of $\mathbf{F}_q[x]$ which is a basis of order two and have zero-density (see [2]).

By probability methods we shall obtain theorem 1.1 below which is much sharper than is required for an answer to the question above.

Theorem 1.1.
There exists an asymptotic basis of order 2 such that

$$\partial f \ll r_f(A) \ll \partial f \text{ for large } \partial f. \tag{1.3}$$

It should be remarked that the proof of theorem 1.1 is based on Bernstein's improvement of Chebychev's inequality (see the book of A. Renyi: Probability theory [3]).

Discussion and introduction of the second result.

By elementary methods we have proved the existence of a complementary sequence B to P such that

$$B(n) \ll n^3 \qquad \text{(see [2])} \tag{1.4}$$

By probability methods we shall prove that we can reduce the factor n^3 of the right hand side of (1.4) to n^2.

The proof of this result is rather complicated and requires beside the probabilistic machinery also some deep results concerning the distribution of irreducibles in the ring over a finite field. (See the paper of D.R. Hayes and the work of Georges Rhin [4], [5]).

Further is should be remarked that the definition of $R_f(A)$ is essential and will affect the result. If for instance we let $R_f(A)$ be the number of representations of f in the form $f = p + f'$, $p \in P$, $f' \in A$, $\partial p < \partial f$ we would not by this method obtain the estimate n^2 but only n^3 in (1.4). We state the theorem as follows.

Theorem 1.2.
Let P denote the sequence of irreducible polynomials in $\mathbf{F}_q[x]$. There exists a "complementary" sequence such that the counting number

$$B(n) \ll n^2. \tag{1.5}$$

Finally we remark that these theorems correspond to results obtained by Erdös-Renyi for integer sequences (see [1]) and can be considered as their directly translations to the polynomialring $\mathbf{F}_q[x]$.

I am very grateful to professor Georges Rhin (Metz, France) to have communicated his work
"Repartition modulo 1 dans un corps de series formelles sur un corps fini".

Also I would like to thank professor Asmus L. Schmidt, Copenhagen for his comments and very helpful instruction.

§2. Probability methods on the space of sequences of polynomials in $\mathbf{F}_q[x]$

We shal use an idea of Erdös to impose a probability measure on the space of polynomial sequences such that (in the resulting probability space) almost all polynomial sequences have some prescribed rate of growth.

From now on we use w to denote an (infinite) subsequence of $\mathbf{F}_q[x]$. Let Ω denote the space of all such sequences w. We shall need the following variant of a theorem from Halberstam and Roth's book [1] chapter III.

Theorem 2.1.
Let

$$\{p_g | g \in \mathbf{F}_q[x]\} \tag{2.1}$$

be real numbers satisfying

$$0 \leqq p_g \leqq 1 \quad (g \in \mathbf{F}_q[x]) \tag{2.2}$$

Then there exists a probability space (Ω, S, P) with the following two properties:

$$\begin{gathered}\text{For every polynomial } g \in \mathbf{F}_q[x] \text{ the event} \\ B^{(g)} = \{w : g \in w\} \text{ is measureable and } P(B^{(g)}) = p_g.\end{gathered} \tag{2.3}$$

$$\text{The events } B^{(g)},\ g \in \mathbf{F}_q[x] \text{ are independent.} \tag{2.4}$$

Further we assume that the sequence $\{p_g\}$ of probabilities (introduced in theorem 2.1) satisfies the following conditions:

$$0 < p_g < 1, \quad g \in \mathbf{F}_q[x]. \tag{2.5}$$

$$\text{If } \partial g = \partial f \text{ then } p_g = p_f. \tag{2.6}$$

$$p_g \downarrow 0 \text{ as } \partial g \to \infty. \tag{2.7}$$

We denote $\chi_g(w)$ the characteristic function of the event $B^{(g)}$. Then (2.4) is equivalent to saying that $\chi_g, g \in \mathbf{F}_q[x]$ are independent (simple) random variables. Further we shall need the following definitions.

Definition 2.1.
Let w be a constituent sequence of the space Ω, and let f be a polynomial. We denote by $w(f)$ the counting number of the sequence w, so that $w(f)$ is the number of polynomials of w which do not exceed f. We denote by $w(n)$ the number of polynomials of w which degree do not exceed n. Furthermore let $r_f(w)$ and $R_f(w)$ be as in the introduction.

Definition 2.2.
Let $x: \Omega \to R$ denote a random variable. We denote by $E(x(w))$ the mean of $x(w)$ and by $V(x(w))$ the variance of $x(w)$.

Definition 2.3.

$$\sum_{\partial\varphi < \partial f} p_\varphi^i p_{f-\varphi}^i = \lambda_f^{(i)}, \; i = 1,2,3,4, \; \lambda_f^{(1)} = \lambda_f \tag{2.8}$$

Obviously we have:

$$w(f) = \text{Card}\{g \in w \mid g = < f\} = \sum_{g = < f} \chi_g(w) \tag{2.9}$$

$$w(n) = \text{Card}\{g \in w \mid \partial g \leqq n\} = \sum_{\partial g \leqq n} \chi_g(w) \tag{2.10}$$

$$r_f(w) = \sum_{\partial\varphi < \partial f} \chi_\varphi \chi_{f-\varphi}(w) \tag{2.11}$$

$$R_f(w) = \sum_{\substack{p \in P \\ \partial p = \partial f \\ \text{sign } p = \text{sign } f}} \chi_{f-p}(w) \tag{2.12}$$

§3. A limit distribution for $r_f(w)$

Theorem 3.1.
Let us choose a sequence $\{p_f\}$ of probabilities such that

$$V(r_f) \to \infty \quad \text{as} \quad \partial f \to \infty \tag{3.1}$$

Then we have for $-\infty < x < \infty$:

$$\lim_{\partial f \to \infty} P\left(\frac{r_f - \lambda_f}{\sqrt{V(r_f)}} < x\right) = \Phi(x) \tag{3.2}$$

where $\Phi(x)$ denote the standard form of the normal distribution function.

Proof.
By the central limit theorem (see [3]) we need only to prove that the Lyapunov condition is satisfied.

That is:

$$\forall \varepsilon > 0 : \frac{1}{\varepsilon} \sum_{\partial g < \partial f} E \left| \frac{\chi_g \chi_{f-g} - p_g p_{f-g}}{\sqrt{\lambda_f - \lambda_f^{(2)}}} \right|^3 \to 0 \tag{3.3}$$

$$\text{as } \partial f \to \infty$$

We obtain:

$$E \left| \frac{\chi_g \chi_{f-g} - p_g p_{f-g}}{\sqrt{\lambda_f - \lambda_f^{(2)}}} \right|^3$$

$$= \frac{1}{(\lambda_f - \lambda_f^{(2)})^{\frac{3}{2}}} ((1 - p_g p_{f-g})^3 P(B^{(g)} \cap B^{(f-g)}) + p_g^3 p_{f-g}^3 P(C(B^{(g)} \cap B^{(f-g)})))$$

$$= \frac{1}{(\lambda_f - \lambda_f^{(2)})^{\frac{3}{2}}} (p_g p_{f-g} - 3p_g^2 p_{f-g}^2 + 4p_g^3 p_{f-g}^3 - 2p_g^4 p_{f-g}^4)$$

Hence we have:

$$\sum_{\partial g < \partial f} E \left| \frac{\chi_g \chi_{f-g} - p_g p_{f-g}}{\sqrt{\lambda_f - \lambda_f^{(2)}}} \right|^3 = \frac{\lambda_f - 3\lambda_f^{(2)} + 4\lambda_f^{(3)} - 2\lambda_f^{(4)}}{(\lambda_f - \lambda_f^{(2)})^{\frac{3}{2}}} \tag{3.4}$$

By (3.1) and (3.4) we have (3.3) and this proves the theorem.

Application of theorem 3.1.
We will prove that $V(r_f) \to \infty$ as $\partial f \to \infty$ in the case:

$$p_g = \begin{cases} \frac{1}{2} & \partial g < 11 \\ k_1 \sqrt{\frac{\partial g}{|g|}} & \partial g \geqq 11,\ k_1^2 = \frac{65}{4} \frac{\log q}{\sqrt{q}} \end{cases} \tag{3.5}$$

Let Y denote a random variable such that

$$P(Y = k) = \frac{\sqrt{q} - 1}{(\sqrt{q})^k} \text{ for } k = 1, 2, \ldots$$

We need the following lemmas:

Lemma 3.1.

$$\lim_{n \to \infty} \frac{1}{\sqrt{n}\sqrt{q^n}} \sum_{k=1}^{n-1} \sqrt{k}\sqrt{q^k} = \frac{1}{\sqrt{q} - 1}$$

Proof.
First we note $\sum_{k=1}^{n-1} \sqrt{k}\ \sqrt{q^k} = \sum_{k=1}^{n-1} \sqrt{n-k}\sqrt{q^{n-k}}$

Then we have:

$$\frac{1}{\sqrt{n}\sqrt{q^n}} \sum_{k=1}^{n-1} \sqrt{k}\sqrt{q^k} = \sum_{k=1}^{n-1} \frac{1}{\sqrt{q} - 1} \frac{\sqrt{n-k}}{\sqrt{n}} P(Y = k) =$$

$$\frac{1}{\sqrt{q}-1}\ \mathrm{E}\left(\frac{\sqrt{\max(0,n-Y)}}{\sqrt{n}}\right) \to \frac{1}{\sqrt{q}-1}\cdot \mathrm{E}(1) = \frac{1}{\sqrt{q}-1}$$

since $\dfrac{\sqrt{\max(0,n-Y)}}{\sqrt{n}} \to 1$ and

$$\forall n: \frac{\sqrt{\max(0,n-Y)}}{\sqrt{n}} \leq 1 .$$

Lemma 3.2.

$$\lambda_f \sim k_1^2(\sqrt{q}+1)\partial f \text{ as } \partial f \to \infty . \tag{3.6}$$

Proof.
We put $\partial f = n$
Hence we obtain:

$$\frac{\lambda_f}{n} = k_1^2(q-1)\ \frac{1}{\sqrt{n}\sqrt{q^n}}\left(\sum_{k=1}^{n-1}\sqrt{k}\sqrt{q^k} + 0(1)\right)$$

Then by lemma 3.1:

$$\frac{\lambda_f}{n} \to k_1^2(q-1)\cdot\frac{1}{\sqrt{q}-1} \text{ as } n \to \infty$$

and the lemma is proved.

Lemma 3.3.

$$\lambda_f^{(2)} \to 0 \text{ as } \partial f \to \infty \tag{3.7}$$

Proof.
Obvious.
Then by lemma 3.2 and lemma 3.3

$$V(r_f) = \lambda_f - \lambda_f^{(2)} \to \infty \text{ as } \partial f \to \infty$$

§4. The law of large numbers for w(f)

By a variant of the strong law of large numbers (see [1]) we obtain the following theorem.

Theorem 4.1.
If

$$\sum_{g \in \mathbf{F}_q[x]} E(\chi_g) = \sum_{g \in \mathbf{F}_q[x]} p_g = +\infty \tag{4.1}$$

and

$$\sum_{f \in \mathbf{F}_q[x]} \frac{V(\chi_f)}{E^2(w(f))} < +\infty \tag{4.2}$$

Then with probability 1

$$\lim_{\partial f \to \infty} \frac{w(f)}{E(w(f))} = 1 \tag{4.3}$$

Applications of theorem 4.1.
We define:

$$p_g = \begin{cases} \dfrac{1}{2} & \partial g \leqq 4 \\ k_2 \dfrac{\partial g}{|g|} & \partial g \geqq 5,\ k_2 = \dfrac{20}{3} \dfrac{\log q}{q-1} \end{cases} \tag{4.4}$$

From this definition follows

Lemma 4.1.

$$E(w(n)) = \sum_{\partial g \leqq n} p_g \sim \frac{10}{3} (\log q)\, n^2 \text{ as } n \to \infty$$

Lemma 4.2.
We have with probability 1

$$w(n) \sim \frac{10}{3} \log q\, n^2 \text{ as } n \to \infty \tag{4.5}$$

where $\{p_g\}$ is defined by (4.4).

Proof.
By lemma 4.1 the conditions (4.1), (4.2) are satisfied since

$$\sum_f \frac{V(\chi_f)}{E^2(w(f))} \ll \sum_{k=1}^{\infty} \frac{\frac{k}{q^k}}{k^4} q^k = \sum_{k=1}^{\infty} k^{-3} < \infty$$

Then by (4.3) we have (4.5).

§5. Some results concerning the distribution of irreducibles in the ring over a finite field

Let M denote the multiplicative semigroup consisting of the polynomials f with sign f = 1 in the ring $\mathbf{F}_q[x]$.

Let $B = x^n + b_{n-1}x^{n-1} + \ldots + b_{n-k}x^{n-k} + \ldots + b_0$ be a polynomial in M. The field elements $b_{n-1}, b_{n-2}, \ldots, b_{n-k}$ are called the first k coefficients of B, it being understood that $b_i = 0$ if $i < 0$.

Let k be a non-negative integer, and let a sequence of k field elements be given. Let H be a polynomial in $\mathbf{F}_q[x]$ and let K be a polynomial prime to H. We denote by h the degree of H, and $\Phi(H)$ denotes the number of polynomials in M of degree h and prime to H.

Let $\pi(n, H, k, K)$ denote the number of irreducibles in M of degree n which (1) are congruent to K modulo H and (2) have as first k coefficients the given field elements, then by comparing results in [4] and [5] we obtain the following explicit estimate.

$$\left| \pi(n, H, k, K) - \frac{q^n}{nq^k \Phi(H)} \right| \leqq (k + h + 1) q^{\frac{n}{2}} \tag{5.1}$$

In the estimate (5.1) we put

$$H = x, K = \beta_0 \neq 0 \ (\in \mathbf{F}_q), \text{ then } \partial H = 1, (x, \beta_0) = 1 \text{ and } \Phi(x) = q - 1.$$

Then we have the following estimate

$$\left| \pi(n,x,k,\beta_0) - \frac{q^n}{nq^k(q-1)} \right| \leqq (k+1+1)q^{\frac{n}{2}} \tag{5.2}$$

(5.2) implies the following lower bound estimate

$$\pi(n,x,k,\beta_0) \geq \frac{q^n}{n} \frac{1}{q^k(q-1)} - (k+2)q^{\frac{n}{2}} \tag{5.3}$$

We denote by $\pi(n,k)$ the number of irreducibles in M of degree n and with the k first coefficients being fixed. Then by (5.3) we obtain the lower bound estimate we need for the proof of theorem 1.2.

$$\pi(n,k) = \sum_{\beta_0 \in \mathbf{F}_q^*} \pi(n,x,k,\beta_0) \geq \frac{q^{n-k}}{n} - (q-1)(k+2)q^{\frac{n}{2}} \tag{5.4}$$

§6. Proof of theorem 1.1 §1

We prove theorem 1.1 by establishing theorem 6.1 below.

Theorem 6.1.
Suppose that Ω is the probability space generated in accordance with theorem 2.1 §2 by the choice (3.5) of the probabilities p_g. Then with probability 1:

$$\partial f \ll r_f(w) \ll \partial f \text{ for large } \partial f. \tag{6.1}$$

Proof.
We have $\{\chi_\varphi \chi_{f-\varphi} | \partial\varphi < \partial f\}$ are independent random variables such that:

$$E\left(\sum_{\partial\varphi < \partial f} \chi_\varphi \chi_{f-\varphi} \right) = E(r_f) = \lambda_f$$

$$V(r_f) = \lambda_f - \lambda_f^{(2)}$$

$$\forall \varphi : \partial\varphi < \partial f \quad |\chi_\varphi \chi_{f-\varphi} - E(\chi_\varphi \chi_{f-\varphi})| \leqq 1$$

We put $\mu = \frac{\frac{1}{2}\lambda_f}{\sqrt{\lambda_f - \lambda_f^{(2)}}}$. Then by lemma 3.2 and lemma 3.3 §3: $\mu \leqq \sqrt{V(r_f)}$ for large ∂f. Hence by Bernstein's improvement of Chebychev's inequality (see [3] p. 387) we obtain the following result:

$$P\left(\left|r_f - \lambda_f\right| \geq \frac{1}{2}\lambda_f\right) \leqq 2\exp\left\{-\frac{\mu^2}{2\left(1+\frac{\mu}{2\sqrt{V(r_f)}}\right)^2}\right\} \tag{6.2}$$

for large ∂f.

By (3.6) and (3.7) we have for large ∂f:

$$\frac{\mu^2}{2\left(1+\frac{\mu}{2\sqrt{V(r_f)}}\right)^2} = \frac{\frac{1}{4}\lambda_f^2}{2\left(1+\frac{\frac{1}{2}\lambda_f}{2(\lambda_f-\lambda_f^{(2)})}\right)^2\left(\lambda_f-\lambda_f^{(2)}\right)} \geq \frac{\lambda_f^2}{8\left(\lambda_f+\frac{\lambda_f}{8}+\frac{\lambda_f}{2}\right)} = \frac{\lambda_f}{13} \tag{6.3}$$

Hence by (6.2), (6.3) and (3.6) we have for large ∂f:

$$P\left(\left|r_f - \lambda_f\right| \geq \frac{1}{2}\lambda_f\right) \leqq 2e^{-\frac{\lambda_f}{13}} \leqq 2q^{-\left\{\frac{1}{\log q}\cdot\frac{k_1^2\sqrt{q}\,\partial f}{13}\right\}} = 2q^{-\frac{5}{4}\cdot\partial f} = 2|f|^{-1-\frac{1}{4}} \tag{6.4}$$

We put $E_f = \{w : |r_f - \lambda_f| \geq \frac{1}{2}\lambda_f\}$

Then by (6.4):

$$\sum_{f\in\mathbf{F}_q[x]} P(E_f) < \infty \tag{6.5}$$

Hence by the Borel-Cantelli lemma, with probability 1, at most a finite number of the events E_f can occur or equivalently:

$$P(\{w : |r_f - \lambda_f| < \frac{1}{2}\lambda_f \text{ for } \partial f > n_0(w)\}) = 1 \tag{6.6}$$

(6.6) implies since $\lambda_f \sim k_1^2(\sqrt{q}+1)\partial f$ that:

$$P(\{w : \partial f \ll r_f(w) \ll \partial f \text{ for large } \partial f\}) = 1 \tag{6.7}$$

This completes the proof of theorem 6.1.

§7. Proof of theorem 1.2 §1

We prove theorem 1.2 by establishing theorem 7.1 below.

Theorem 7.1.
Suppose that Ω is the probability space generated, in accordance with theorem 2.1 §2 by the choice (4.4) §4 of the probabilities p_g. Then with probability 1:

$$w(n) \ll n^2 \tag{7.1}$$

$$R_f(w) > 0 \text{ for } \partial f > n_0(w) \tag{7.2}$$

Proof.
By lemma 4.2 §4 we obtain (7.1). To establish the theorem, we must prove that, with probability 1, $R_f(w) > 0$ for large ∂f. By the Borel-Cantelli lemma we need only show that

$$\sum_{f \in \mathbf{F}_q[x]} P(\{w : R_f = 0\}) < \infty , \tag{7.3}$$

and in view of (7.3) it suffices to establish the existence of a number $\delta > 0$ such that

$$P(\{w : R_f = 0\}) \ll q^{-\partial f(1+\delta)} . \tag{7.4}$$

Let f be a fixed polynomial of degree n and sign $f = a (\neq 0)$. We have the following estimate

$$P(\{w : R_f(w) = 0\}) = \prod_{\substack{p \in P \\ \partial p = \partial f \\ \text{sign } p = \text{sign } f}} P(\{w : \chi_{f-p} = 0\}) \tag{7.5}$$

$$= \prod_{\substack{p \in P \\ \partial p = \partial f \\ \text{sign } p = \text{sign } f}} P(CB^{(f-p)}) = \prod_{\substack{p \in P \\ \partial p = \partial f \\ \text{sign } p = \text{sign } f}} (1 - p_{f-p})$$

$$\leqq \prod_{k=1}^{\left[\frac{n}{2}(1-\varepsilon)\right]} \left(\prod_{\substack{p \in P \\ \partial(f-p) = n-k}} (1 - p_{f-p}) \right)$$

$$\leqq \prod_{k=1}^{\left[\frac{n}{2}(1-\varepsilon)\right]} e^{-P_{f-p}} \sum_{\partial(f-p)=n-k} 1 , \quad 0 < \varepsilon < 1$$

To obtain the estimate (7.4) we need first to establish a lower bound estimate for $\sum_{\partial(f-p)=n-k} 1$ and secondly an upper bound estimate for

$$e^{-P_{f-p}} \sum_{\partial(f-p)=n-k} 1 .$$

Let

$$f = ax^n + a_{n-1}x^{n-1} + \ldots + a_{n-k}x^{n-k} + \ldots + a_0$$

$$p = ax^n + \beta_{n-1}x^{n-1} + \ldots + \beta_{n-k}x^{n-k} + \ldots + \beta_0$$

$$\partial(f-p) = n-k \Rightarrow$$

$$\beta_{n-1} = a_{n-1}$$

$$\vdots$$

$$\beta_{n-k+1} = a_{n-k+1}$$

$$\beta_{n-k} \neq a_{n-k}$$

By (5.4) we obtain

$$\sum_{\partial(f-p)=n-k} 1 \tag{7.6}$$

$$= \mathrm{Card}\{p \in P \mid \partial p = n;\ \mathrm{sign}\, p = a;\ \beta_{n-i} = a_{n-i},\ i = 1,2,\ldots k-1;\ \beta_{n-k} \neq a_{n-k}\}$$

$$= \mathrm{Card}\{p \in P \mid \partial p = n;\ \mathrm{sign}\, p = 1;\ \gamma_{n-i} = \frac{a_{n-i}}{a},\ i = 1,2,\ldots k-1;\ \gamma_{n-k} \neq \frac{a_{n-k}}{a}\}$$

$$\geq (q-1)\left(\frac{q^{n-k}}{n} - (q-1)(k+2)q^{\frac{n}{2}}\right)$$

(7.6) implies

$$e^{-P_{f-p}} \sum_{\partial(f-p)=n-k} 1 \leqq e^{-k_2(q-1)\frac{n-k}{n}\left[1-n(q-1)(k+2)q^{k-\frac{n}{2}}\right]}. \tag{7.7}$$

Now take any $\varepsilon_1 : 0 < \varepsilon_1 < 1$. Then for every $k : k = 1,2,\ldots \left[\frac{n}{2}(1-\varepsilon)\right]$ we have

$$n(q-1)(k+2)q^{k-\frac{n}{2}} \leqq \varepsilon_1 \text{ if } n > N_0(\varepsilon, \varepsilon_1, q). \tag{7.8}$$

Then by (7.7) and (7.8)

$$e^{-P_{f-p}} \sum_{\partial(f-p)=n-k} 1 \leqq e^{-k_2(q-1)(1-\frac{k}{n})(1-\varepsilon_1)} \quad \text{if } n > N_0(\varepsilon, \varepsilon_1, q). \tag{7.9}$$

By (7.5) and (7.9)

$$P(\{w : R_f = 0\}) \leqq e^{-k_2(q-1)(1-\varepsilon_1)} \sum_{k=1}^{[\frac{n}{2}(1-\varepsilon)]} (1-\tfrac{k}{n}) \tag{7.10}$$

Take $\varepsilon = \sqrt{2}-1\,(<1)$, then we obtain

$$\sum_{k=1}^{[\frac{n}{2}(1-\varepsilon)]} \left(1-\frac{k}{n}\right) \geq \frac{n}{4}-\frac{5}{4}. \tag{7.11}$$

(7.10) and (7.11) implies

$$P(\{w: R_f = 0\}) \ll q^{-n\left(\frac{k_2(q-1)(1-\varepsilon_1)}{4\log q}\right)} \tag{7.12}$$

To obtain (7.4) with $\delta = \frac{1}{4}$ we need only choose in (7.12)

$$\varepsilon_1 = \frac{1}{4}, \quad _2 = \frac{(1+\delta)4\log q}{(q-1)(1-\varepsilon_1)} = \frac{20}{3}\frac{\log q}{q-1}$$

and this proves the theorem.

References

[1] H. HALBERSTAM and K. F. ROTH: "Sequences". Oxford University Press 1966.

[2] J. CHERLY: "On complementary sets of group elements". Archiv der matematik vol. 35, 1980 p. 313-318.

[3] A. RENYI: "Probability theory". North-Holland Publishing Company, Amsterdam-London, 1970.

[4] D. R. HAYES: "The distribution of irreducibles in GF[q,x]". Trans. Amer. Math. Soc 117 (1965), p. 101-127.

[5] GEORGES RHIN: "Repartition modulo 1 dans un corps de series formelles sur un corps fini". Dissertationes mathematicae XCV. Warszawa 1972.

Indleveret til Selskabet august 1982.
Færdig fra trykkeriet oktober 1983.

East Greenland and the Faeroe Islands: A Fission Track Study

By SOHAN L. KOUL, LEWIS T. CHADDERTON,
and C. KENT BROOKS

Det Kongelige Danske Videnskabernes Selskab
Matematisk-fysiske Meddelelser **40**: 13

Kommissionær: Munksgaard
København 1983

Synopsis

A study has been made of the etching characteristics of fission fragment tracks in certain zeolites, including chabazite, stilbite and heulandite, collected from the Upper, Middle and Lower Series basalt in the Faeroe Islands. Etching conditions with respect to annealing temperature have been standardized and optimized, with special attention being given to chabazite, and annealing experiments have been carried out on this mineral in order to derive the appropriate correction curve for application to igneous activity over geological time. It is shown that chabazite, employed as a solid state detector, registers fission fragment tracks anisotropically. Studies of the influence of both annealing the sample and varying the etchant temperature reveal no improvement in the degree of isotropy. Nevertheless the fission track method is applicable to the dating of chabazite in particular, and almost certainly for the dating of zeolites in general. Fission track dating of the Faeroe Islands yields a spread of corrected ages from $41.6 \pm 1.1 \times 10^6$ y. to $55.4 \pm 2.6 \times 10^6$ y., which are substantially less than ages obtained previously using radiometric methods.

Fission track ages are also reported for the minerals zircon, sphene and apatite, and for a few micaceous minerals – particurlarly phlogopite – collected from alkaline igneous intrusions in East Greenland (the Kangerdlugssuaq and Gardiner intrusions, and the island of Aliuarssik). The correction curve for phlogopite has been determined in laboratory annealing experiments. Extrapolation of the experimentally determined temperatures for annealing suggests that a temperature of 195°C will erase all tracks in $\sim 10^6$ y. The annealing data is therefore interpreted in terms of the paleoisotherm of the fission track clock in the mineral.

The results obtained for the Faeroe Islands indicate a relatively short time span for the volcanic activity, a general conclusion which is not at variance with earlier radiometric studies, and which is consistent with the results for contemporaneous East Greenland lavas. The geological histories of the three selected areas of East Greenland, and differences between them, are discussed in the light of the fission track ages uncovered. For the Kangerdlugssuaq intrusion in particular it is proposed that there is clear evidence for strong doming and regional uplift, and that this was parallelled by a similar behaviour at the same time, although on a less grand scale, in an extensive area west of the Faeroe islands. The linkage in time of similar activity in the two geographical zones has implications in the dating of plate motions and for continental break-up of the North Atlantic province.

SOHAN L. KOUL LEWIS T. CHADDERTON
Division of Chemical Physics, CSIRO,
P.O. Box 160, Clayton, Victoria, Australia 3168

C. KENT BROOKS
Institute of Petrology, University of Copenhagen,
Øster Voldgade 5, 1350 Copenhagen K, Denmark
(from 1. February 1983: University of Papua, New Guinea)

Printed in Denmark by Bianco Lunos Bogtrykkeri A/S. ISSN 0023-3323. ISBN 87-7304-139-4

List of Contents

I. Introduction

The ways in which fission track (FT) procedures are normally applied in geology to determine times of mineral crystallization and ages of rock strata are now well understood. The general method itself has seen wide acceptance; there have been applications in such diverse disciplines as archaeology,[1–3] cosmology[4–12] and biology[13–16]. Since its introduction by FLEISCHER et al.[17] a growing number of laboratories have employed the FT technique in a variety of interdisciplinary studies.

This rapid growth in the importance of the FT technique is due in part to the maturity which certain of the experimental procedures have reached, not only in straightforward dating of igneous and metamorphic events,[18–23] but also in stratigraphic studies by the dating of ash layers,[24, 25] the elucidation of rock uplift history,[26–28] and in the measurement of uranium, thorium and plutonium concentrations in various materials of both terrestrial and extraterrestrial origin. There have also been surprising applications in such unexpected fields as paleozoology[29] and botany.[30, 31] Moreover, there are hopes that FT methods may hold the key to a solution of some of the most urgent problems confronting geochronology and cosmochronology today.

In this paper we describe in particular reconnaissance studies of the fission track dating of zeolites, a complex group of tectosilicates which is, for example, widely developed in basaltic rocks subsequent to their emplacement by later stage processes. Zeolites have assumed increasing importance in recent years due to a rapidly expanding interest in hydrothermal systems and in detailed studies of oceanic floors, as a consequence of the demonstration that typical volcanic areas have been permeated by huge quantities of hot water of meteoric origin,[32] and because of the need to understand hydrothermal processes in connection with the exploration and utilization of geothermal energy. The chemical etching conditions have been standardized by investigations of the temperature dependence of the etching behaviour for certain zeolites (in particular the minerals chabazite, stilbite and heulandite) and, for chabazite, have been used to study the track recording and retention characteristics in some detail, with particular reference to fossil hydrothermal systems in the Faeroe Islands. In order to check the general reliability of the method on zeolites, samples from the Faeroe Islands were selected in such a way that for some of them comparison could be made with age estimates established on geological grounds. Further experiments have been made to determine the calibration curve relating track length shrinkage with track density reduction – an important element in all fission track geochronology

Fission track ages are also reported for minerals in alkaline igneous rocks from the Tertiary deposits of East Greenland, since this zone has held a key position during formation of the Noth Atlantic, and since both volcanic and epeirogenic events are better displayed here than in any other geographic area around that sea.

II. The Geology of the Faeroe Islands

The Faeroe Islands lie at the extreme northwestern edge of the European continental margin which consists here of a series of banks extending from the Rockall Plateau northwards to the Faeroe Plateau, a distance of about 1000 km. These banks are separated from the European Shelf by the Rockall trough and The Faeroe-Shetland Channel, a deep water area of partially unknown structure. The banks themselves are underlain with continental material and are therefore believed to be microcontinents detached from the European shelf by ocean-floor spreading. Indeed, inclusion of the Rockall and Faeroe Plateaus in pre-drift reconstructions[33] considerably improves the fit of continental models from which they have been omitted.[34]

The Faeroe Islands themselves cover about 1,400 km^2 and are the erosional remnants of a Lower Tertiary basaltic plateau which may once have been as extensive as 24,000 km^2, the area of the insular shelf. The basalts are similar in structure, composition and age to those of East Greenland and have an exposed thickness of about 3,500 m, although the top and bottom of the sequence are not seen. Our knowledge of the geology of the islands stems mainly from the work of RASMUSSEN and NOE-NYGAARD,[35,36] and from that of WAAGSTEIN,[37] who also studied the insular shelf and the neighbouring banks. The exposed sequence is divided into three series; the Lower, Middle and Upper Basalts. The Lower Basalts (Fig. II.1), consist almost exclusively of aphyric and slightly plagioclase-phyric, olivine-poor, lava flows with a thickness averaging about 20 m. They are separated from the Middle Basalts by a distinctive horizon of volcanogenic sediments and coal, while the Middle Basalts begin explosively with the deposition of up to about 100 m of pyroclastics (a tuff-agglomerate zone). Typical Middle Basalts differ from the Lower Basalts in being thin pahoehoe units averaging about 2 m in thickness. Most are plagioclase-phyric, but olivene-phyric and aphyric flows, and a single orthopyroxene-phyric flow, also occur. The base of the Upper Basalts (Fig. II.2) is marked by a prominent group of olivine-phyric and aphyric flows which have been shown to form very flat shield volcanoes of great areal extent. The Upper Basalts are a comparatively variable group but are typically characterized by olivine-phyric, LIL-element depleted flows which are best developed in the northeastern and northern parts of the islands. There is still evidence for unconformities in the Faeroe lava sequence and it is believed that jointing, faulting and gentle warping are subsequent to the extensive phase. Many dikes and sills cut the lavas and these intrusives also seem largely to postdate major Basaltic flows.

Fig. II.1. The western side of Kunoy seen from Kalsoy in The Faeroe Islands. The lavas have a very shallow dip and the base of the Upper Basalts is at the first thick horizon going up to the top. Mountains are up to about 800 m (A. Noe-Nygaard).

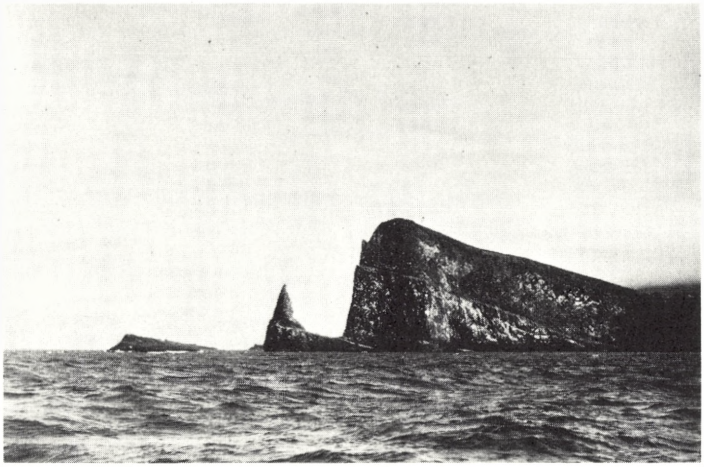

Fig. II.2. Lower Basalts on Mykinesholmur in the Faeroe Islands showing a relatively steep easterly dip. The cliff is just over 100 m (A. Noe-Nygaard).

III. The Geology of East Greenland

The Tertiary rocks of the east of Greenland (Fig. III.1) originally covered an area of some 100,000–200,000 km^2. They were deposited in the Lower Tertiary in connection with continental break-up in the North Atlantic and, as such, are part of the North Atlantic igneous province whose continuing activity still is evident in Iceland. Rock types in East Greenland include volcanics which are largely voluminious plateau basalts of tholeiitic composition, and a wide spectrum of intrusives, including layered

gabbros (e.g., the famous Skaergaard intrusion), granites, syenites and nepheline syenites (e.g., the Kangerdlugssuaq intrusion) with minor amounts of others. Recent reviews of the province have been published by one of us,[38] and by other workers.[39–41]

Briefly, the evolution of the province was as follows. After a long period continental conditions emerged, and subsidence with accompanying sedimentation began towards the end of the Cretaceous in the Kangerdlugssuaq area. In more northerly areas continental rifting had been active throughout most of the Mesozoic. Outpouring of basaltic lavas, mostly of tholeiitic character but some picritic, subsequently commenced and filled up the basin rapidly so that, although the first lavas are submarine, the bulk of the plateau is subaerial. There is, however, evidence that subsidence still continued but not at a rate rapid enough to keep pace with the volcanic accumulation. The total thickness of basaltic products is thought to have locally attained some 7 km.[42] The basalts themselves were erupted via a fissure swarm parallel to the present coast line, where dike swarms occur which are sometimes so intense as to make up 100% of the total outcrop. Associated with this extensive activity the newly forming continental margin became attenuated and flexured in the direction of the embryonic ocean floor. Numerous gabbroic bodies were emplaced in and close to the dike zone. Radiometric dating results allied with biostratigraphic evidence[43,44] indicate that these events took place around the Palaeocene-Eocene boundary (53–54 m.y ago).

While the magmatic activity along the coast was almost exclusively tholeiitic, areas inland experienced minor alkaline activity characterized by nephelinites similar to those of the African continent. After a few million years of relative quiescence syenitic bodies were largely emplaced in the Kangerdlugssuaq area. Brooks[45] has suggested that this phase here was accompanied by a major crustal doming event (fig. III.2) which he delineated. At the present erosional level, syenites and related rocks are the most voluminous Tertiary bodies exposed and, apart from minor dike swarms, represent the final stages of local magmatism. Conversely, in the Kialineq (67°N) area, a number of felsic plutons were emplaced at about 35 m.y[60–62] and, to the north, the Werner Bjerge pluton (72°N) was active at around 30 m.y.[46–49]

IV. The Etching Behaviour of Damage in Zeolites with Particular Reference to Chabazite as a Track Detector

The fact that solid state track detectors (SSTD's) can tolerate large neutron doses without detectable deterioration makes them uniquely suitable for measuring the concentrations of certain heavy elements in specific samples. Presently glasses, plastics and a limited number of single crystalline materials are being used in applications of FT methods,[50–52] and in addition there is ample evidence that SSTD's are not only the

Fig. III.1. East Greenland basalts inland from the northern part of the Blosseville Kyst. They remain relatively undisturbed and have only been subjected to regional uplift. Tops of the mountains in this area are very close to the original top of the basalt pile (Geodetic Institute, Copenhagen).

Fig. III.2. Inner part of the Kangerdlugssuaq-Nordfjord (Greenland) extending into the left, with the Kangerdlugssuaq Gletscher Snout at the bottom. The plateau to the distant left is an exhumed Pre-Tertiary peneplain which was covered by basalts. To the right is the Kangerdlugssuaq dome carved in uplifted Precambrian gneisses.

best integrating type of detector for swift heavy charged particles, but can be used for fast neutron detection.[53–56] Studies are also being made of the effects of high fast neutron doses on track registration generally and on the thermal stability of tracks. Crystalline detectors have been used less frequently than glasses and plastics in part, at least, because they are more temperature-resistant. Moreover, the bulk etch rate velocity V_g examined by various investigators in crystalline detectors such as bronzite,[57] feldspar,[58,59] sphene,[60] and labradorite,[57] has been shown to be anisotropic.

Experiments were first carried out to determine the effect of etching at various temperatures, the effect of heat on the anisotropic properties of chabazite used as a track detector, and a systematic search made for a suitable etchant to reveal tracks in the zeolites chabazite, stilbite and heulandite. Track recording and retention characteristics for chabazite, however, will be described in detail. The FT etching efficiency of a mineral is defined as that fraction of the total number of fission fragments to have crossed a given surface which is visible in the optical microscope. If the rate of chemical etching is very much greater than the general rate of etch, then due to the fact that the etchant penetrates along the full length of the damage trajectory, the majority of tracks are revealed as hollow cylinders, and the efficiency is high, as is the case with chabazite.

Our investigations have concentrated upon the suitability of the solvents NaOH and KOH for chabazites in particular. Homogeneous, inclusion-free chabazite crystals from Vágar were selected for this study. Samples were prepared by first using normal grinding methods to the finer stage, and then polishing with diamond abrasives ranging from the 8 μ to the 0.5 μ grades, after which the samples were divided into two groups. To determine the appropriate etchant for chabazite, samples from the first group were etched in boiling NaOH for times varying from a few minutes to several hours, the density of spontaneous tracks due to natural fission being measured at discrete intervals. We found neither the track geometry nor the variation of track density with time to be satisfactory. After trying a number of other solvents, a satisfactory etching of the chabazite specimens was finally accomplished using KOH (3g in 4g H_2O). Again the samples were etched for from a few minutes to several hours and the track density measured after each time step. It is a clear characteristic of KOH that, compared with NaOH, this etchant gives an almost uniform distribution of tracks, with better defined contours. The results (Figure IV.1) indicate that with NaOH a maximum in track density is reached, followed by a slow decrease due to progressive chemical removal of surface layers of the crystal. For KOH, a plateau, which is reached rather quickly, remains invariant with time (Figure IV.2).

The second group of samples was annealed for 2 hour at 540°C (further details are given in section V) in order to erase all spontaneous tracks. Artificial tracks were then created using a ^{252}Cf source in a 2π geometry and chemical etching experiments carried out on two sets for different times, using NaOH and KOH. Again, in the case of KOH, a constant track density plateau was reached after a short time (Figure IV.2). These different relationships for various etchants are due to fundamental differences in the velocity of etching along the tracks (V_t) relative to that for the bulk solid (V_g). The ratio V_t/V_g is high for KOH in the case of chabazite. It is much lower for NaOH.

A few samples of chabazite were annealed at 540°C for two hours, mounted in epoxy resin along the cleavage plane, and mechanically polished in order to investigate both possible effects of track orientation and of heating on the registration efficiency of

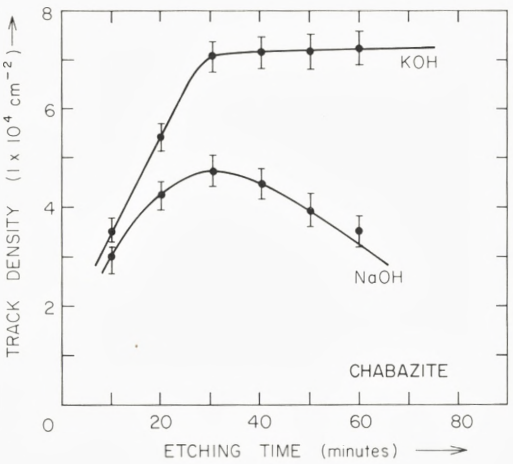

Fig. IV.1. Etching rates of chabazite for NaOH and KOH (spontaneous fission tracks).

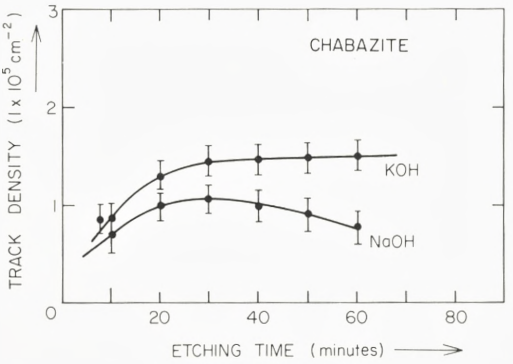

Fig. IV.2. Etching rates of chabazite for NaOH and for KOH (induced (artificial) fission tracks).

chabazite. The polished samples were irradiated from a ^{252}Cf source in a 2π geometry for equal times in order to implant the same number of fission fragments. The angular track distribution was then obtained by measuring the inclination of the ends of tracks relative to a fixed, but arbitrary direction, the analysis being carried out using both optical and scanning (SEM) microscopes. The distribution of etched tracks in the $\{10\bar{1}1\}$ plane for different etching times is shown in Figure IV.3. It is quite clear that, beyond a certain minimum etching time, the track density remains constant. Similar results have been reported by NISHIDA and TAKSHIMA[61] and KOUL et al.[62] However, it may be shown that for certain materials the track density or an internal surface continues to increase with prolonged etching. With glass, for example, there is a further exposure of new tracks as the surface is progressively attacked by the etchant. These are then added to the previous tracks which remain visible with continued

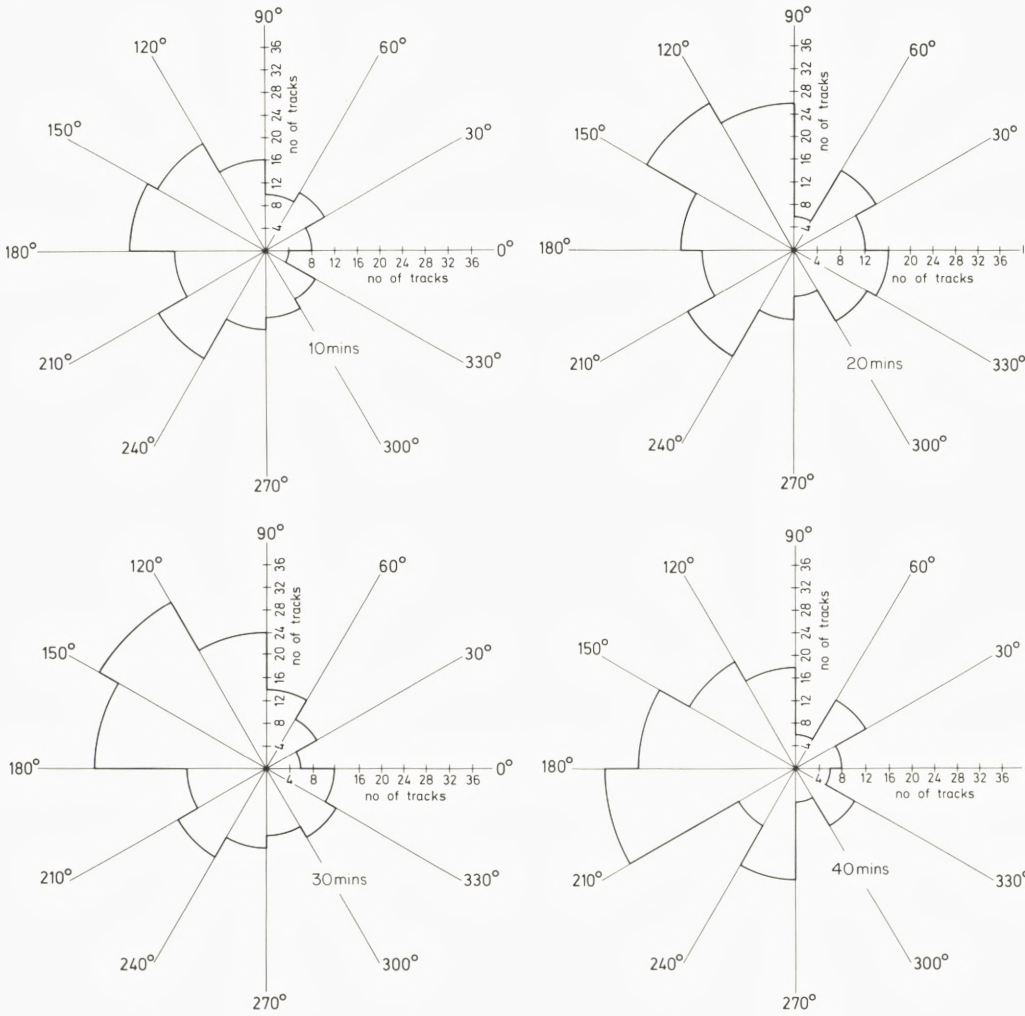

Fig. IV.3. Sets of contour lines showing the angular distributions of etched tracks in the $\{10\bar{1}1\}$ plane obtained by etching the same chabazite sample for 10, 20, 30 and 40 minutes in KOH. The efficiency and the degree of isotropy with increasing etching are not improved.

etching. In the case of chabazite etched in KOH this effect does not occur. The present experiment demonstrates in addition that the etching of $\{10\bar{1}1\}$ chabazite at different temperatures, however prolonged, does not improve the degree of isotropy of the etched tracks. Other crystal planes ($\{\bar{1}101\}$ and $\{01\bar{1}2\}$) gave identical results.

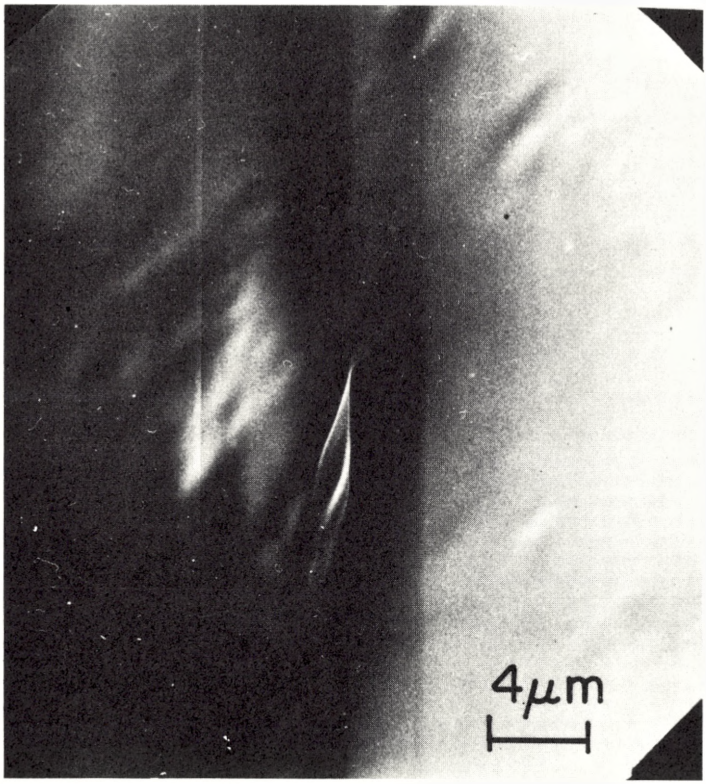

Fig. IV.4. Scanning electron micrograph of a fission fragment track in chabazite, etched in KOH (3 g in 4 g H_2O). The micograph was taken at a dip angle of 45°.

Experiments were also carried out to determine the *relative* effect of heating on the degree of isotropy of the etched tracks in the $\{10\bar{1}1\}$, $\{\bar{1}101\}$ and $\{01\bar{1}2\}$ planes. Samples of chabazite were heated at different temperatures and afterwards etched in KOH for the appropriate length of time. No amount of prior annealing improved the isotropy of the tracks in a sample. We conclude that the anisotropic etching behaviour of fission fragment damage trails is accordingly a natural and inherent property, unaffected either by etching or heating.

The brief scanning electron microscope (SEM) study of fission fragment damaged chabazite was made in order to examine etched tracks at a higher magnification. Samples of chabazite of about 1–2 cm^2 in area were irradiated in the thermal column of the reactor to a total thermal neutron dose of 10^{15} nvt in order to induce fission of uranium impurity atoms. These samples were then polished down to a thickness of ~ 3 microns, and etched in the appropriate chemical reagent (see earlier sections) for the appropriate length of time. After evaporation of a thin layer of gold the samples were examined in the JEOL instrument. Figure IV.4 shows a single fission track in a

Fig. IV.5. Scanning electron micrograph of a fission fragment track in chabazite, etched in KOH (3 g in 4 g H_2O) after heating at 400°C for 1 hour. No substantial change is observed although the track is reduced in size due to annealing.

chabazite specimen tilted to an angle of 45°. Annealing was carried out at successively higher temperatures (ranging from 100–500°) in an attempt to observe any change with temperature in the morphology of a typical etched fission track. No substantial change was observed in the 100–300°C temperature range, though at 400°C tracks were reduced in size due to annealing (Figure IV.5). From the present study we therefore conclude that the shape of the etch pits does not change in different planes of the crystal when using the same chemical reagent, and there is no temperature dependence in the degree of track anisotropy in chabazite. The shape of the etch pits was different when the samples were etched in different chemical reagents. Different etchants, however, gave no improvement in the degree of anisotropy of chabazite when used as a track detector. The general etching velocity, V_g, apparently does not vary from plane to plane in the same crystal. It is more than likely that the anisotropy has its origin in the spatial variation of electronic stopping power Se for natural fission fragments moving in chabazite.[63]

V. The Annealing Correction to Fission Track (FT) Ages

Due to the effect of thermal (igneous) annealing over geological time the ages of minerals determined by the fission track technique have on occasion been observed to be lower[64–66] than corresponding ages determined by the far more conventional radiometric methods.[67,68] No theory exists which can completely explain the annealing of radiation damage and rejuvenation of minerals on heating, though models have been proposed on the basis of limited experimental observations.[69] It is rather clear, however, that when a mineral is heated at high enough temperatures there is a return of some atoms to lattice sites and, although dislocations and other extended defects are formed, most of the strain present due to radiation damage disappears. The degree of the annealing in general depends both upon the temperature and the time of heating. For each mineral, however, there is a characteristic 'annealing temperature' at which measurable strain is totally removed; virtually complete restoration can be considered to have taken place.

Some possibility of the annealing of radiation damage and therefore of track fading in minerals always exists. The track fading can be caused by a short time, higher temperature event or by a lengthy anneal at only a slightly elevated temperature during the geothermal history of the earth's crust. The importance of thermal excursions which take place during the geological history of a sample and of the consequent effect upon the final fission track age must not be minimized. Experiments were accordingly carried out both to determine the extent of this effect and to provide a calibration curve for making the appropriate correction.*

The specific mineral samples selected for this work included chabazite from Vágar (Faeroe Islands), and phlogopite from Gardiner, East Greenland. Both minerals were separated from crushed rock using common laboratory techniques, and samples polished by the usual procedures. After annealing chabazite at 520°C for 3 hours,** and phlogopite at 570° for 3 hours, induced fission tracks were created at a thermal neutron dose of 10^{15} (nvt). The fission fragment track density was then determined by etching aliquots, which had undergone heat treatments varying from 100 to 500° (± 5°C) for a period of one hour in each case, and the reduction of track density and track length was observed. A procedure for etching through different planes was adopted for the revealing of full length tracks. Length measurement itself was per-

* STROZER and WAGNER[70] first proposed an appropriate method for correction of a thermally lowered track density, using calibration curves of residual track density as a function of average length of etch pit, both quantities being expressed as fractions of their unannealed values. The method has frequently been used in the correction of thermally lowered fission track ages;[12,66,70–74] it is applicable both to glasses[12,73] and minerals.[66,75–78]

** It is important to note that the chabazite crystal structure only begins to break down at approximately 840°C.[79]

formed by measuring both track dip and projected length, and optical phase contrast methods used to enhance precision. An average of 'major' and 'minor' axes for each etch pit was recorded as the corresponding 'etch pit length'. For almost 9000–11000 etch pits scanned a total of between 800 and 900 track lengths were measured – an extremely lengthy and laborious process but one absolutely necessary for proper statistics. Figure V.1 shows how the reduction in track density and track length in chabazite depends upon temperature. This kind of information makes possible an immediate estimate of the degree of fading of the spontaneous tracks, and hence the reduction in age. At 100°C, a slight decrease of ~ 2.0% in track density and ~ 3,5% in the mean track length of etch pits was observed in the case of chabazite. At higher temperatures, the track length decreased more rapidly than the track density. At a constant temperature of 500°C a period of 1 hour reduced the track density by 57.3% and the track length by 78.3%. Following 1 hour at 600°C all tracks were completely annealed. In the case of phlogopite, changes in track length and track density at 100°C were almost negligible. At 100°C, a decrease of 3.5% in track length and *no* change in track density was observed. At higher temperatures, however, the track length decreased more rapidly than the track density as was precisely the case for chabazite. At 700°C, the track density was reduced by 60% and the track length by 69%. At 800°C all the tracks were annealed out, due to a phase change in the solid.

The observation that the reduction in track density with temperature lags behind the track length (Figure V.1) is important. Measurement of ^{235}U induced fission fragment tracks in unannealed samples, and in samples which had been subjected to various annealing treatments, were therefore carried out. It is the shrinkage in track length, plotted as a function of track density reduction, which gives the proper calibration relationship. The ratio of mean etch pit legth of uannealed and annealed fission tracks is shown as a function of the percentage of fission track density reduction in Figure V.2. The resulting calibration curve has been used to correct thermally lowered fission track ages of chabazite, and we find the correction to fission track ages to be ~ 3% for chabazite, and ~ 6% for phlogopite.

The stability of fission tracks varies from substance to substance. Indeed it is this very variation which gives rise to optimism as to the reconstruction of rock cooling histories, provided that the temperatures or temperature ranges below which the tracks are retained can correctly be estimated. Therefore, in some cases it is possible to learn about the igneous (annealing) activity which the mineral has endured over geological time. For example, in the case of phlogopite from the Gardiner complex of East Greenland, annealing studies confirm that fossil fission fragment tracks (radiation damage) in the mineral can be erased during intense metamorphic episodes, thus resetting the geological clock.

The fission track method has, of course, already proved to be a valuable technique for the dating of the mica group.[27, 80–83] Furthermore, the fact that these minerals have the

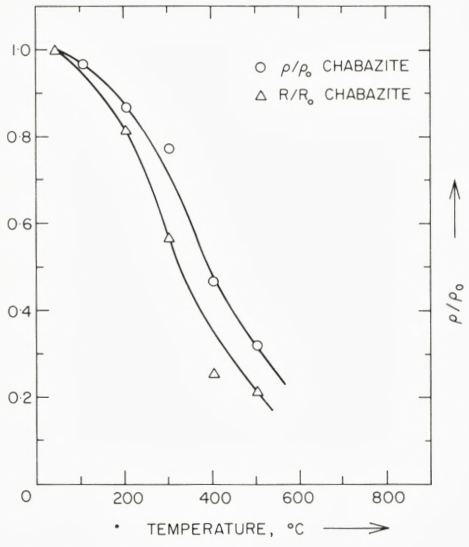

Fig. V.1. Normalized track densities $\varrho/\varrho_0(0)$ and track lengths $R/R_0(\Delta)$ displayed as a function of annealing temperature T for chabazite.

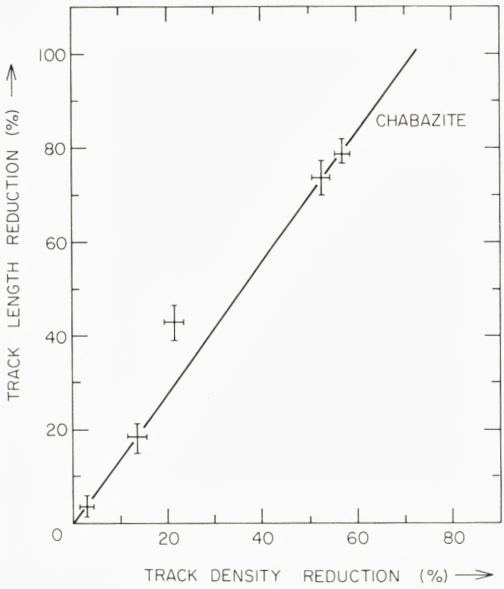

Fig. V.2. Percentage reduction of fission track lengths in chabazite shown as a function of the percentage reduction in fission track density.

potential for an unravelling of the geothermal history of the area of origin is well documented.[20, 21, 84–86] In what now follows we are primarily concerned with the thermal annealing behaviour of phlogopite in particular. The annealing data obtained is interpreted in terms of a palaeoisotherm of the fission track clock in the mineral. Measurement are also presented of the etchable "ranges" of spontaneous and induced fission tracks in the phlogopite samples.

In general the method most commonly used to study the annealing behaviour of minerals involves attention to the following:

(1) The selected sample should have a uniform and large induced track density. It should be irradiated to a suitable thermal neutron dose in the reactor.
(2) The sample should have a well defined and well polished plane and as uniform a distribution of uranium as possible.

After preparation of good phlogopite samples according to these criteria etching was accomplished by immersing the specimens in 40% HF at 23°C. The tracks, randomly distributed, could easily be distinguished from surface dislocations. Following deter-

mination of the *spontaneous* track density, samples were heated in a furnace in air (for 3 hours at 600°C) to anneal all fossil tracks, and then irradiated to a thermal neutron dose of 10^{15} nvt in the thermal column of the reactor. They were then scanned in the optical microscope and the density of *induced* tracks was determined at a total magnification of $\times 600$ using a 5×5 ocular graticule. Studies were also made of the variation of track density as a function of temperature and time. The irradiated samples were recleaved in order to remove upper layers and any possible uranium contaminant of non-crystalline origin. These cleaved samples were then heated in a furnace at temperatures between 500°C at intervals of 30°C, and for times varying from a few minutes to several hours. They were then etched and scanned for any change of track density. The annealing data for phlogopite, shown in Figure V.3 represent 0%, 25%, 50%, 75%, and 100% track reductions, determined at various temperatures and corresponding to different times. The data have been extrapolated to geologically meaningful times and temperatures.

Annealing of fission tracks[87] has been reported for tektites,[12,88–90] for epidote,[91,92] for micas,[66,93] for zircons[94] and for apatite. As Table 1 shows, each mineral has different annealing characteristics, and fission tracks in phlogopite anneal out at lower temperatures than those in muscovite and zircon. In almost every instance, however, the annealing rate is represented by a simple Arrhenius relationship:

$$\log_e t = \log_e a + \left(\frac{\varepsilon}{kT}\right), \qquad (1$$

where t and T are the annealing time and temperature respectively, ε is the activation energy, a is a material specific constant dependent on the degree of annealing, and k is Boltzmann's constant. Figure V.3 shows that phlogopite is no exception.

Phlogopite loses some fission tracks at ~ 45°C in 10^6 years, and all tracks are erased at 195°C in 10^6 years.***

From Figure V.3 it is also possible to make some assessment of the thermal history of a typical phlogopite of this type. Thus, if the fission track (FT) age agrees with an absolute age or ages determined by some other method, then the rock temperature must have remained to the right of the 0% track loss curve throughout. Conversely, if the FT age is less than those recorded by other methods, then the FT age implies that a geological cooling period has taken place. A "mixed" FT age results if the rock has been heated to such a temperature and for such a length of time that the corresponding point falls in the field between the 0% and 100% reduction in track density curves. Our

*** It has also been found that heating under pressure shows no detectable effect on the annealing properties of phlogopite. The annealing characteristics of zircon, on the other hand, are slightly affected by a hydrostatic pressure.[94]

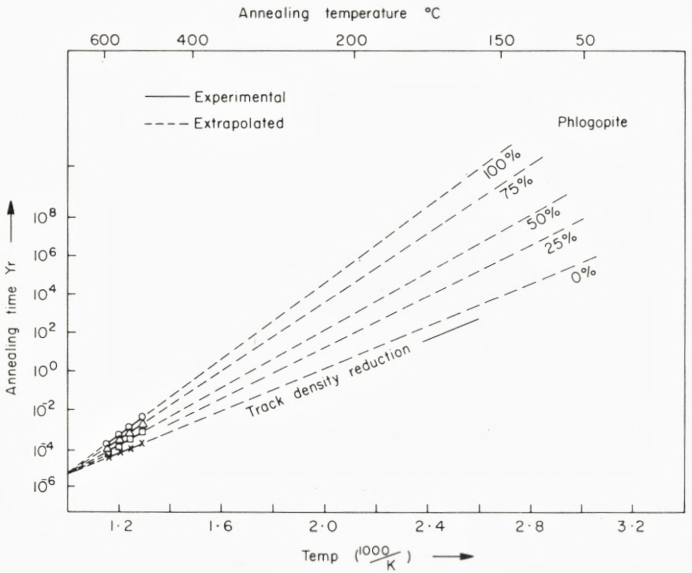

Fig. V.3. Annealing time as a function of annealing temperature for track density reductions in phlogopite of between 0% and 100%. Experimental results (———) are extrapolated to geologically meaningful times and temperatures (-----).

annealing experiments with phlogopite both confirm that fossil fission tracks are unstable and that the degree of instability varies from mineral to mineral. Furthermore, as with other radiometric methods, the FT age of phlogopite determines neither the age of mineralization nor the deposition age of the rock. It is the cooling age of the mineral which is established.

The demonstrable value of the fission track method has also stimulated specific laboratory experiments by a number of investigators on the track retention properties of minerals and glasses. The annealing data for certain minerals have been interpreted in terms of what might be called a "blocking temperature", which is a sharp transition of the palaeoisotherm at some time during the process of cooling. Different materials of course display different track retention properties, and the retention temperature depends upon the etching parameters, chemical variations in the material composition and on the track orientation.[95] All these factors have to be considered when annealing experiments directed at determining the thermal history of a sample (and its blocking temperature) are carried out. According to Haack[96] when a rock cools steadily to lower temperatures, the growth of track density increases linearly with time. For a specific cooling rate it is therefore possible to extrapolate back to a palaeotime of $\sim 10^5$ to $\sim 10^8$ years and hence to the temperature at which the track density was zero. Fission track blocking temperatures of various micaceous and accessory minerals, and some selected zeolites are compiled in Table VI.1. Temperatures are given both for full and half track fading, and for different annealing times.

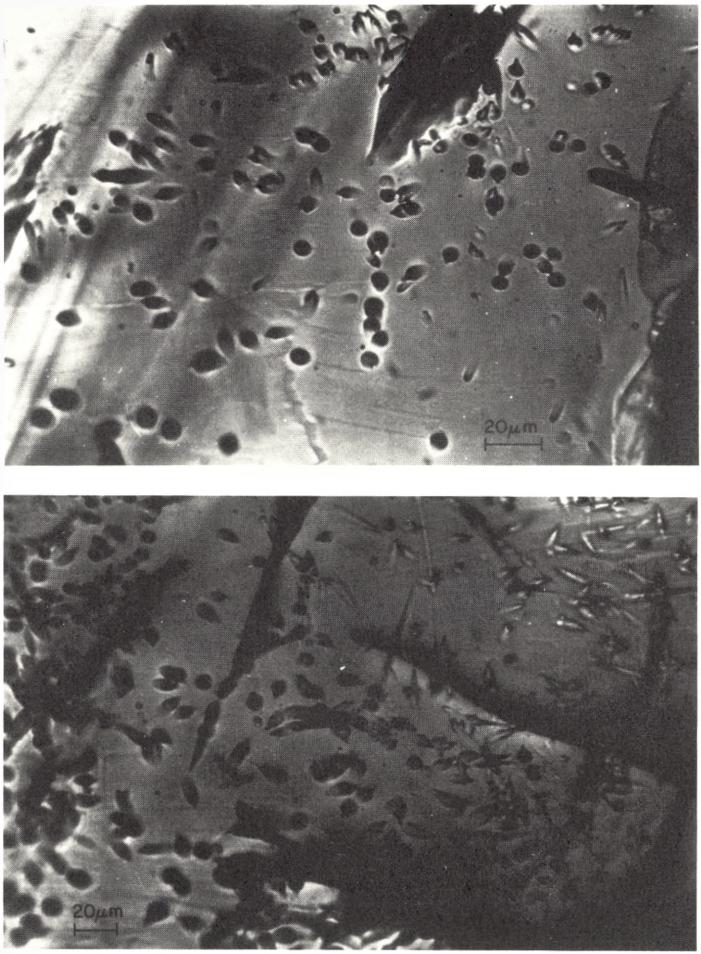

Fig. VI.1. Photomicrographs showing spontaneous fission tracks in chabazite etched in KOH (3 g in 4 g H_2O) (a), and induced fission tracks in chabazite irradiated with 1.42×10^{15} nvt thermal neutrons, and etched similarly (b).

VI. Fundamentals of Fission Track (FT) Dating

The experimental FT technique used was similar to that of both NAESER and co-workers,[91] and KOUL and VIRK,[20] though with minor modifications which are briefly described. Thin transparent specimen sections approximately 0.5 mm across were separated from the host rock and mounted in epoxy resin, the upper surface of each sample being ground successively with 400, 600 and 800 mesh emery, polished with cerium oxide, and then followed by a final polishing with 6, 3, 1 and ¼ μm diamond paste. Samples of chabazite, stilbite, heulandite, apatite, sphene and zircon were

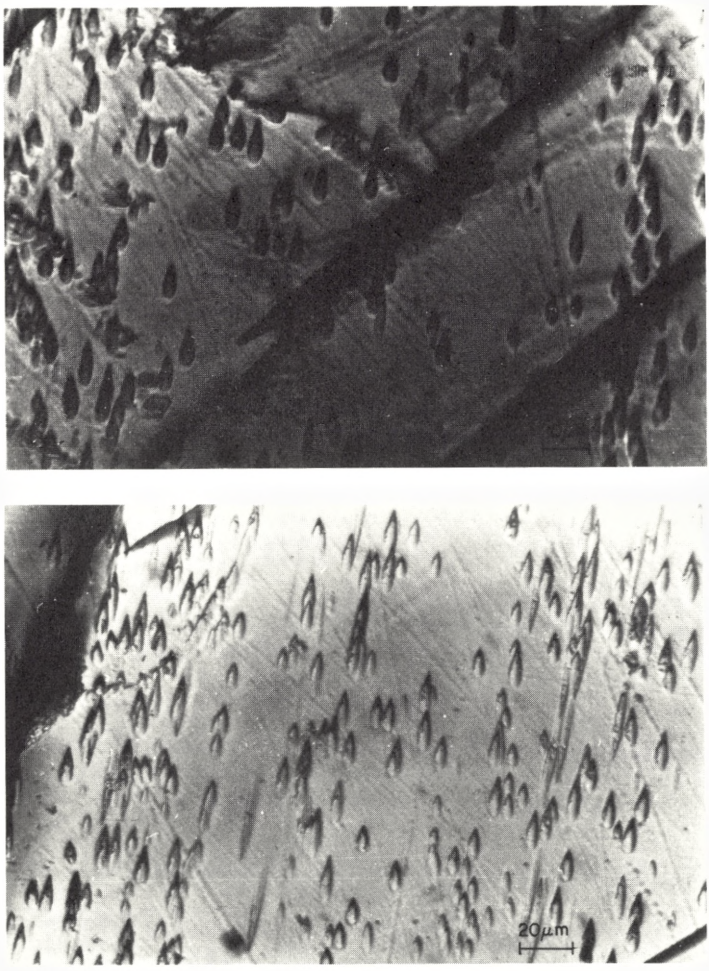

Fig. VI.2. Photomicrographs showing spontaneous fission tracks in stilbite etched in 2% HF at 23°C (a), and induced fission tracks in stilbite irradiated with 7.12×10^{15} nvt thermal neutrons, and etched similarly (typical anisotropic behaviour) (b).

treated identically, although the preliminary grinding was somewhat longer for crystals of zircon and sphene. Etching of the polished samples was by simple immersion in the appropriate chemical solvent.

The zeolites (chabazite, stilbite and heulandite) and the accessory minerals from igneous rocks (zircon, apatite and sphene) were all dated using the EDM (external detector) method;[61, 97] samples were sandwiched between muscovite mica detectors for the registration and counting of induced tracks. Chabazite itself was etched in KOH (3 g in 4 g H_2O) (see, e.g., Figure VI.1), while studies of various etchants for stilbite resulted in the use of 2% HF at 23°C for 20–30 secs (Figure VI.2), and 10 ml aqua regia

Table VI.1

Fission track retention and blocking temperatures of minerals

Material	Degree of Loss	Annealing Temperature 1 hour °C	Blocking Temperature °C	Reference
Apatite	Half	336	108	(26)
	full	370	165	(21)
	full	400	170	(23)
	half	–	130	(110)
Australite	full	520	250	(111)
Biotite	full	500	–	(66)
	half	–	100	(110)
Basaltic glass	full	230	–	(112)
Chabazite	full	510	149	(62, 109)
Epidote	full	620	390	(113)
Garnet	full	545	–	(93)
	full	610	–	(109)
Heulandite	full	545	–	(109)
Moldavite	full	495	–	(12)
Muscovite	full	700	–	(66)
Phlogopite	full	625	195	Present work
Stilbite	full	495	–	(109)
Sphene	half	610	350	(21)
Zircon	full	750	–	(23)
	full	870	–	(61)
		–	380	(114)

with 1 ml 2% HF at 23°C for 30–50 secs for heulandite. Zircon and sphene were etched in KOH: NaOH (the eutectic contains 50.6 mol % KOH and 49.4 mol % NaOH) at 200° for 8–20 hours and 50N.NaOH at 140° for 1–6 hours respectively. Apatite was etched in 5% HNO_3 for 20–30 secs, and phlogopite in 48% HF.

After determinations of spontaneous track density samples of all minerals were sandwiched between mica detectors and irradiated in the thermal column of the nuclear reactor. The integrated thermal neutron dose to which the samples were exposed was itself determined by counting tracks in a muscovite detector irradiated in contact with the standard NBS glasses SRM-962 and SRM-963 (calibrated against copper). The muscovite dosimeters were etched with freshly prepared 48% HF for 40–50 minutes at 23°C in order to obtain well defined induced tracks, approximately 800–1000 pits again being scanned for each consignment. An investigation of the general relationship between track counting on internal mineral surfaces and that on external

detectors was also made in order to determine the geometric factor for use of external detectors with zeolites. For the zeolites studied the geometric factor varied between 0.51 ± 0.02 and 0.57 ± 0.03, assuming the etching rate and the counting effiency for external detectors to be the same for each zeolite, and the track shape also to be the same. The track etching rate was always found to be greater than the general etching rate of the mineral surface. However, etching of tracks lying in different orientations was highly anisotropic giving rise to etch pits of varying topographic appearance. The constants used in the age calculations were λ_f (spontaneous decay of ^{238}U) $= 6.8 \times 10^{-17}$ yr^{-1}, λ_d (total decay constant of uranium) $= 1.551 \times 10^{-10}$ yr^{-1}, I (isotopic abundance of ^{235}U with respect to ^{238}U) $= 7.253 \times 10^{-3}$, and σ_f (cross-section for thermal neutron induced fission of ^{235}U) $= 5.802 \times 10^{-22}$ cm^2. Errors were calculated throughout according to the methods af McGEE and JOHNSON[98] and NAESER et al.[99], and expressed as one standard deviation.

VII. Results

VII.1. The Faeroe Islands

Our knowledge of the geology of the Faeroe Islands (section II and Figure VII.1) described by RASMUSSEN and NOE-NYGAARD[100] and WAAGSTEIN[37] may be considered to have been supplemented by SCHRØDER[101] who, on the basis of a limited magnetic survey, was able to demonstrate the presence of two domes centred to the west of the Islands. One of these lies just off Mykines where, on the most westerly point of the Islands (Mykines Holmur) the lavas attain an eastward dip of up to 15°. The other is to the southwest of Suduroy where a similar increase in dip occurs. This doming apparently affected the plateau subsequent to the volcanic activity, but may have overlapped and given rise to the tensional stress field which determined the emplacement of many of the minor intrusions.

WAAGSTEIN[37] reports the recovery of abundant reworked pyroclastic material from the sedimentary basins adjacent to the Islands, suggesting that the latest volcanic activity was submarine and due to submergence of the plateau. Thus volcanism and subsidence apparently kept approximate pace with each other as in the case of East Greenland. Uplift of the entire area took place later and the present mountain tops roughly define a gipfelflur ranging from about 800 m in the north to around half this in the central islands, and rising again to around 500 m on Suduroy. It is of considerable interest to determine the mechanisms ot these vertical movements. The subsidence, doming and regional uplift strongly resemble those of East Greenland (although on a less grand scale). To this end it is important to establish the timing of these events.

It is clear from the field relationships that significant time gaps separated the three series, though this has not shown up in radiometric dating, from which variable ages

lying between $49.2 \pm 1.5 \times 10^6$ up to $60.4 \pm 1.4 \times 10^6$ y have been obtained.[102] Indeed, subseqent refinement of the data[103] suggests that the entire Faeroese lava pile from the bottom of the Lower to the top of the Middle Series was erupted in the interval $55.2 \times 1.0 = 10^6$ y and $54.6 \pm 1.2 \times 10^6$ y ago. Fission track results for chabazite, stilbite and heulandite shown in Table VII.1, for samples taken as shown in Figure VII.1, yield a spread of FT ages from $41.6 \pm 1.1 \times 10^6$ y up to $55.4 \pm 2.5 \times 10^6$ y, and the distribution of ages is such that the oldest value is from the Lower Series. However, we have no other evidence to contradict the general K-Ar results which indicate a relatively short time span for the volcanic activity, consistent with results from contemporaneous East Greenland and Faeroese lavas.[104] Our interpretation of the observed distribution is that it is most reasonably explained as being regional, the youngest ages in the north-eastern part of the Islands reflecting a more prolonged cooling there. This conclusion clearly requires an investigation of many more samples. It is consistent, however, with the belief of WAAGSTEIN[37] that volcanic activity had continued much longer than may be seen today, with the formation of overlying tuffs, since stripped away and deposited as clastic sediments on the insular shelf. If this activity had been confined to the north-eastern part of the islands, it would have provided an insulating cover which could have allowed hydrothermal circulation (with associated zeolite depositions) over a long period. Ages from the Lower Series on Suduroy and Mykines which are close to the accepted age of volcanism indicate that in the south and west of the islands the lavas underwent rapid cooling either as a result of lack of burial by significant amounts of overlying material, or as a result of very rapid uplift. Such a rapid uplift is likely to be a consequence of the dome-shaped structures believed to be present offshore to the north-west of Mykines and under Suduroy.[100] These domes, although on much smaller scale, invite comparison with East Greenland where a large domal uplift described by one of us[45] was raised shortly after the basaltic volcanism and rapidly dissected by erosion.

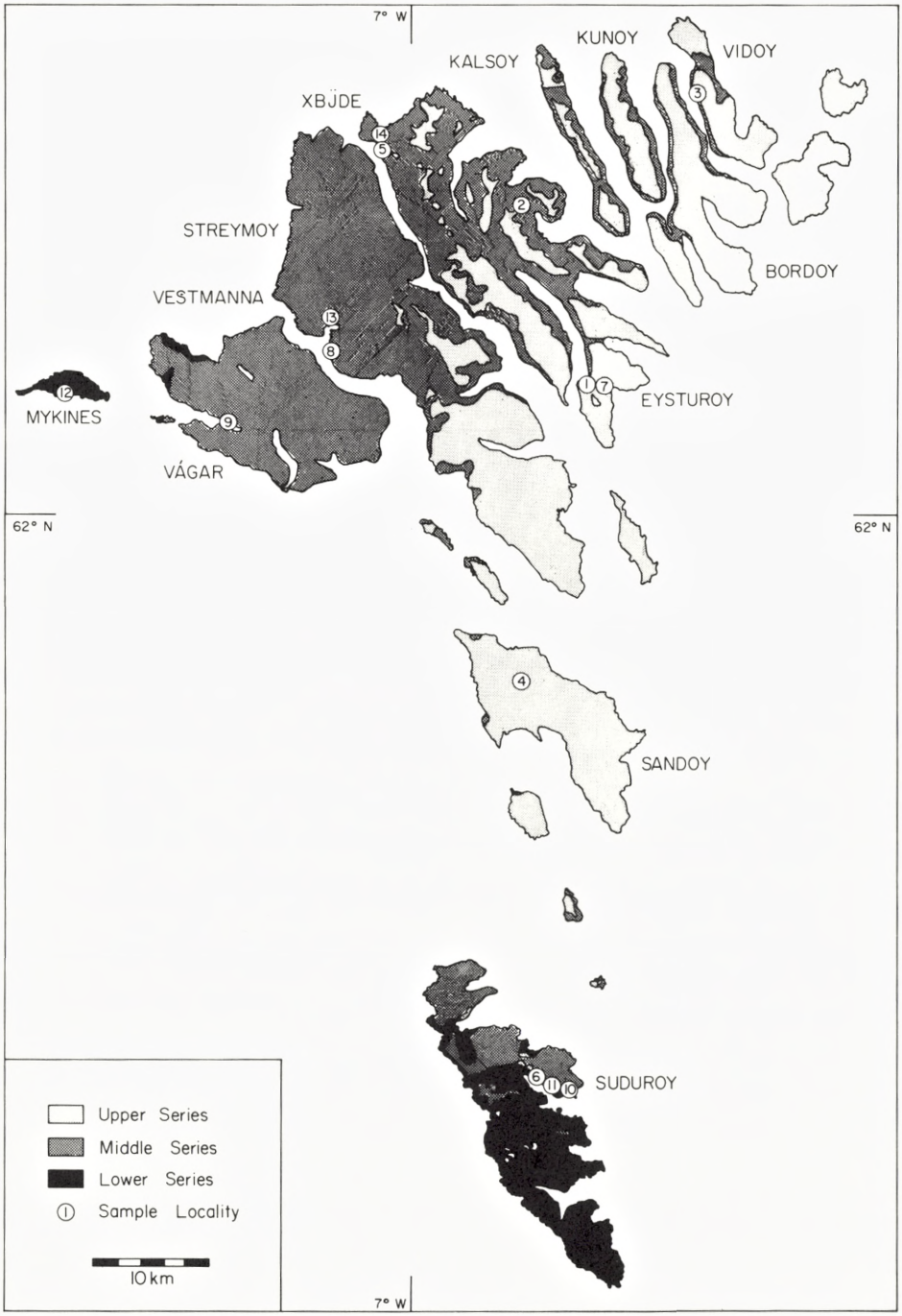

Fig. VII.1. Geological map of the Faeroe Islands (see reference 113).

Table VII.1

Fission track results for minerals from the Faeroe Islands

Sample location*	Lab. symbols	ϱ_s (cm^{-2})	ϱ_i (cm^{-2})	Φ (nvt)	R	N	F.T. age (m.y.)
1. Chabazite.	CR105	1.54×10^4	1.73×10^5	7.52×10^{15}	0.98	5	41.2 ± 1.8
Runvik, Eysturoy.	CR109	1.75×10^4	1.73×10^5	–	0.965	5	41.0 ± 1.6
(U.S.)	CR115	1.68×10^4	1.74×10^5	–	0.882	6	44.7 ± 2.0
	CR116	1.35×10^4	1.48×10^5	–	0.865	8	42.3 ± 2.0
	CR118	1.92×10^4	2.06×10^5	–	0.786	6	43.2 ± 2.1
	CR120	1.39×10^4	1.41×10^5	–	0.744	7	45.7 ± 2.1
	CR125	1.42×10^4	1.65×10^5	–	0.971	10	40.0 ± 1.8
2. Chabazite.	79-500/A1	1.64×10^4	3.50×10^4	1.51×10^{15}	0.974	6	43.5 ± 1.6
Slaettafjall,	79-500/A2	1.82×10^4	3.81×10^4	–	0.945	6	44.4 ± 1.6
Eysturoy.	79-500/A5	1.35×10^4	2.74×10^4	–	0.895	9	45.7 ± 2.0
U.S.	79-500/A6	1.95×10^4	4.54×10^4	–	0.893	5	39.9 ± 1.9
	79-500/A7	1.74×10^4	3.31×10^4	–	0.873	5	48.8 ± 2.1
3. Chabazite.	79-2/C2	1.48×10^3	2.34×10^4	9.80×10^{15}	0.745	6	38.2 ± 1.7
Malinsfjall,	79-2/C5	1.65×10^3	2.41×10^4	–	0.894	8	41.3 ± 2.0
Vidoy.	79-2/C6	1.54×10^3	2.23×10^4	–	0.981	6	41.7 ± 1.9
(U.S.	79-2/C8	1.37×10^3	1.95×10^4	–	0.984	4	42.4 ± 2.1
	79-2/C9	1.52×10^3	2.20×10^4	–	0.989	7	41.7 ± 1.8
4. Chabazite.	79-95/A	1.54×10^4	3.52×10^4	1.51×10^{15}	0.996	7	40.7 ± 1.7
Nordara, Sandoy.	79-95/7A	1.73×10^4	4.12×10^4	–	0.832	6	39.1 ± 1.9
(U.S.)	79-95/8A	1.64×10^4	3.54×10^4	–	0.919	8	43.1 ± 2.0
	79-95/11A	1.94×10^4	4.15×10^4	–	0.895	7	43.3 ± 2.1
	79-95/1B	2.34×10^4	4.81×10^4	–	0.983	6	45.2 ± 1.9
	79-95/5B	1.34×10^4	2.63×10^4	–	0.865	8	47.3 ± 2.2
5. Chabazite.	CHVF1	7.85×10^4	1.42×10^5	1.42×10^{15}	0.853	13	48.3 ± 1.1
Eidi, Eysturoy,	CHVF2	7.22×10^4	1.34×10^5	–	0.764	8	47.1 ± 1.8
(M.S.)	CHVF3	6.84×10^4	1.21×10^5	–	0.985	9	49.4 ± 1.6
	CHVF5	6.42×10^4	1.15×10^5	–	0.982	9	48.8 ± 1.9
	CHVF5	7.35×10^4	1.36×10^5	–	0.891	7	47.3 ± 1.9
6. Chabazite.	CH205	6.42×10^4	3.22×10^5	4.23×10^{15}	0.891	5	51.9 ± 3.1
Suduroy, Tvöroyri.	CH207	6.13×10^4	3.12×10^5	–	0.980	8	51.2 ± 3.0
(L.S.)	CH208	5.84×10^4	2.85×10^5	–	0.912	11	53.4 ± 3.1
	CH231	5.73×10^4	2.91×10^5	–	0.943	7	51.3 ± 3.0
	CH232	6.02×10^4	3.0×10^5	–	0.650	9	52.3 ± 3.2
	CH239	6.35×10^4	3.21×10^5	–	0.960	5	51.5 ± 3.0
7. Stilbite.	SRF1	6.5×10^4	1.38×10^5	1.51×10^{15}	0.934	7	43.8 ± 1.2
Runavik, Eysturoy,	SRF2	7.2×10^4	1.41×10^5	–	0.782	7	47.5 ± 1.8
(U.S.)	SRF3	6.3×10^4	1.35×10^5	–	0.835	6	43.4 ± 2.0
	SRF4	4.5×10^4	0.85×10^5	–	0.992	10	49.2 ± 2.1
	SRF5	7.2×10^4	1.4×10^5	–	0.982	7	47.8 ± 1.9

8. Stilbite.	43865/B	1.34×10^4	4.51×10^4	2.48×10^{15}	0.984	8	45.4 ± 1.9
Gassá-Breidá,	43865/B5	1.47×10^4	4.23×10^4	–	0.987	6	53.1 ± 2.3
Streymoy	43865/B6	1.68×10^4	5.65×10^4	–	0.973	10	45.4 ± 1.9
(U.S.)	43865/B7	2.13×10^4	7.54×10^4	–	0.931	9	43.2 ± 1.9
	43865/BB	1.54×10^4	5.23×10^4	–	0.843	5	45.1 ± 2.0
9. Stilbite.**	SK737	3.25×10^4	2.71×10^5	6.24×10^{15}	0.862	5	46.1 ± 2.0
Sörvágur,	SK835	3.02×10^4	2.7×10^5	–	0.938	4	43.0 ± 1.9
Vágar.	SK1071	2.72×10^4	2.34×10^5	–	0.895	9	44.7 ± 2.0
(M.S.)	SK1072	2.85×10^4	2.5×10^5	–	0.795	9	43.8 ± 2.1
	SK1079	3.12×10^4	2.35×10^5	–	0.692	8	51.0 ± 2.2
	SK1080	2.24×10^4	1.95×10^5	–	0.935	10	44.2 ± 2.1
	SK1081	2.90×10^4	2.52×10^5	–	0.892	7	44.2 ± 2.0
10. Stilbite.	18304/X3	4.35×10^4	1.26×10^5	2.49×10^{15}	0.943	8	52.9 ± 2.8
Hamar, Suduroy.	18304/X5	5.24×10^4	1.57×10^5	–	0.912	8	51.2 ± 3.0
(L.S.)	18304/X6	4.14×10^4	1.21×10^5	–	0.981	7	52.5 ± 2.9
	18304/X9	3.27×10^4	0.90×10^5	–	0.894	6	55.7 ± 3.2
	18304/X10	3.84×10^4	1.14×10^5	–	0.895	5	50.9 ± 3.0
	18304/X10A	4.44×10^4	1.32×10^5	–	0.794	5	50.9 ± 3.1
11. Stilbite.	18301/FS	4.32×10^5	7.63×10^5	1.51×10^{15}	0.878	5	52.6 ± 3.2
Frodböur Kirke,	18301/FS2	4.14×10^5	7.25×10^5	–	0.985	10	53.1 ± 2.8
Suduroy.	18301/FS7	7.25×10^4	1.23×10^5	–	0.913	6	54.8 ± 3.2
(L.S.)	18301/FS9	3.75×10^5	7.13×10^5	–	0.986	7	48.9 ± 2.6
	18301/FS10	5.64×10^5	9.87×10^5	–	0.895	6	53.1 ± 3.0
	18301/FS13	4.56×10^5	7.65×10^5	–	0.764	5	56.5 ± 3.1
12. Heulandite.	HL1	4.72×10^4	4.50×10^5	8.04×10^{15}	0.970	5	51.9 ± 2.9
Smörbúshellisgjógv,	HL2	5.12×10^4	4.62×10^5	–	0.890	4	54.8 ± 3.1
Mykines.	HL3	4.81×10^4	4.55×10^5	–	0.981	7	52.3 ± 3.0
(L.S.)	HL5	5.24×10^4	4.64×10^5	–	0.973	8	55.9 ± 2.9
	HL9	4.65×10^4	4.30×10^5	–	0.952	5	53.5 ± 3.0
	HL10	5.23×10^4	4.75×10^5	–	0.895	6	54.5 ± 2.9
	HL13	4.90×10^4	4.62×10^5	–	0.965	6	52.5 ± 2.8
	HL8	5.04×10^4	4.21×10^5	–	0.891	8	59.2 ± 3.1
13. Heulandite,	HG22	3.45×10^4	5.55×10^5	9.64×10^{15}	0.772	6	36.9 ± 1.9
Gassá-Breidá.	HG25	4.51×10^4	6.03×10^5	–	0.894	7	43.7 ± 1.8
Vestmanna	HG28	2.2×10^4	3.04×10^5	–	0.983	8	43.4 ± 1.8
Streymoy. (U.S.)	HG33	5.34×10^4	7.76×10^5	–	0.712	6	40.9 ± 1.9
14. Heulandite,	HIE50	8.04×10^4	5.67×10^5	5.64×10^{15}	0.882	5	49.2 ± 2.0
Eidi, Eystoroy.	HIE55	7.23×10^4	5.24×10^5	–	0.813	5	47.9 ± 2.0
(M.S.)	HIE57	4.73×10^4	3.65×10^5	–	0.954	9	45.0 ± 1.9

ϱ_s is the spontaneous track density, ϱ_i the induced track density, n the thermal neutron dose (nvt), N the number of grains counted, and R the correlation coefficient.

* US, Upper Series; MS, Middle Series; LS, Lower Series.

** Fissure-filling, all others are from amygdales.

VII.2. Greenland

The East Greenland sector of the North Atlantic province is an exceptionally well exposed and well developed example of continental break-up which has been subject to a number of expeditions from Copenhagen with the specific object of documenting the magmatic and tectonic activity associated with this important phase of plate motions. In the present work material from the following localities (Figure VII.2) has been studied.

(i) The Kangerdlugssuaq Intrusion

This exceptionally large syenite pluton is roughly circular with a diameter of more than 30 km. It contains both oversaturated and undersaturated rocks and was emplaced centrally in the Kangerdlugssuaq domal structure. Several workers have dated the area using various methods. BECKINSALE et al., using the K-Ar method,[46] and PANKHURST et al.,[105] using the Rb/Sr method, obtain a mean age of 49.2 ± 0.6 m.y. BECKINSALE et al.[46] have also dated amphibole from the Kap Boswell syenite, which is in good agreement with results for Kangerdlugssuaq. Fission track dating of zircons from Skaergaard, made by BROOKS and GLEADOW,[43] yields an age of 54.6 ± 1.7 m.y, showing the emplacement to be close to 50 m.y. However, our FT ages (Table VII.2) and the ages reported more recently by GLEADOW and BROOKS[48] are in close agreement, and we also conclude that there must have been a slow cooling at former deep levels, which now lie at the surface due to erosion of as much as 6 km of the overlying dome. The apatite cooling age (which records cooling through the approximate 100°c isotherm (see section V) is somewhat in agreement with that reported earlier.[26]

Our new fission track ages for zircon from the Kangerdlugssuaq intrusion (Table VII.2) have a weighted mean of 49.6 ± 2.9 m.y. These figures are in good agreement with the ages reported previously.[43] The apatite ages from the above intrusion give a mean age of 38.2 ± 2.2 m.y, significantly lower than the ages obtained for zircons, suggesting prolonged cooling in this area followed later by uplift and erosion. It is suggested,[45] for the area south of Scoresbysund centred on the fjord of Kangerdlugssuaq, that an analysis of the physiographic elements of landscape indicates the major uplift to have occurred in two phases. A project using both K/Ar and fission track dating is presently underway in order to clarify this. Further studies show that on approaching the Kangerdlugssuaq district the pre-syenitic basalt become increasingly tilted upwards and are finally completely dissected to expose a core of Precambrian gneisses centred on Kangerdlugssuaq. These gneisses form jagged alpine peaks rising to around 2.5 km and it is clear that erosion has been active for a much longer time than in outlying basaltic areas. By making certin simple and reasonable assumptions it is

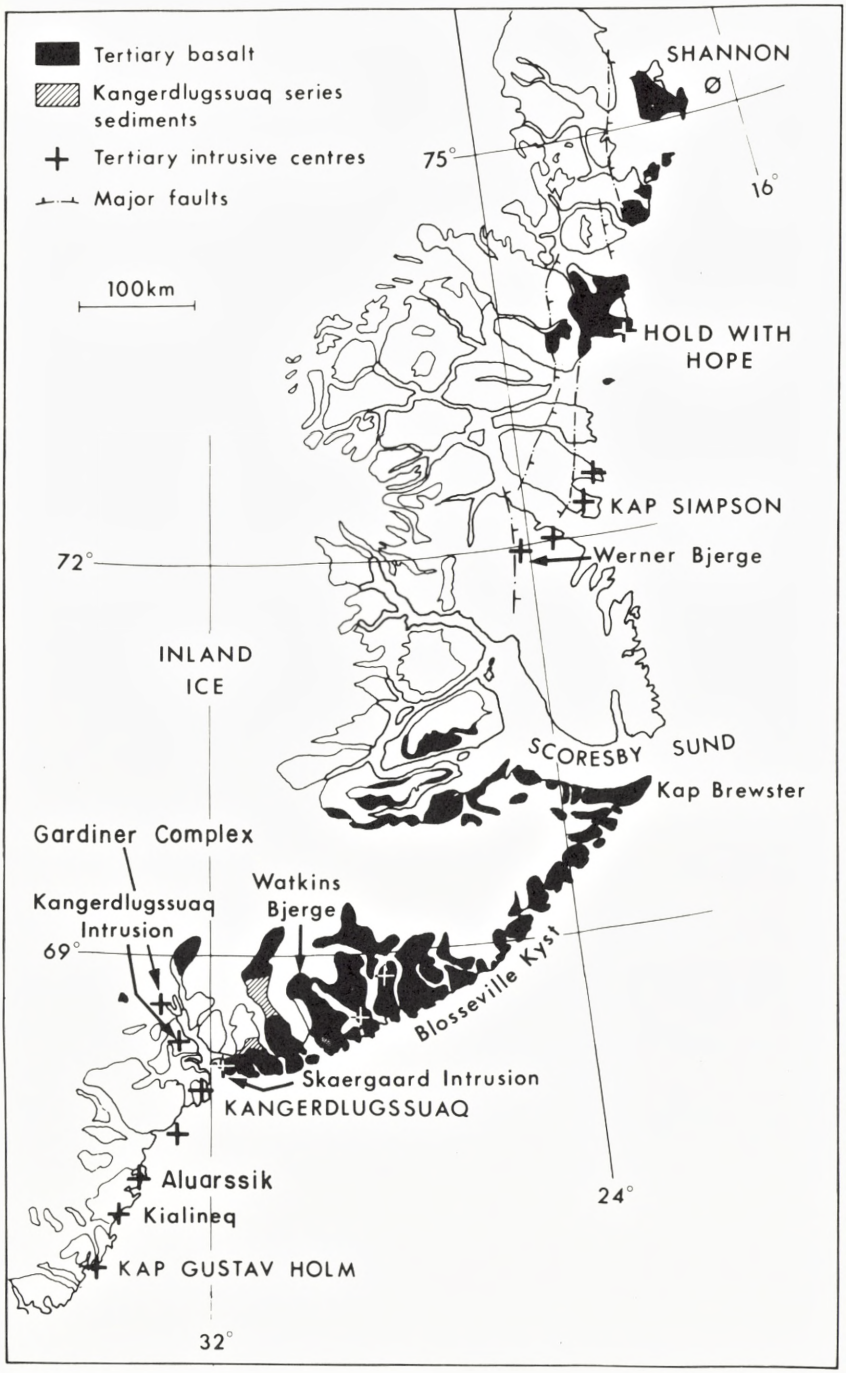

Fig. VII.2. Geological map of East Greenland.

Table VII.2

Fission track results for minerals from Greenland

Sample location	Lab. symbols	ϱ_s (cm^{-2})	ϱ_i (cm^{-2})	Φ (nvt)	R	N	F.T. age (m.y.)
1. Apatite.	ZR10	3.90×10^4	1.8×10^5	3.8×10^{15}	0.948	9	50.7 ± 2.8
Gardiner,	ZR02	8.40×10^4	3.9×10^5	–	0.858	9	50.4 ± 3.1
East Greenland.	ZR03	7.32×10^4	3.3×10^5	–	0.991	11	51.9 ± 3.2
	ZR09	6.72×10^4	3.2×10^5	–	0.981	10	48.8 ± 2.9
2. Apatite.	AA101	1.75×10^5	2.73×10^6	8.83×10^{15}	0.953	7	34.9 ± 1.8
Aliurssik,	AA102	2.45×10^5	4.12×10^6	–	0.967	6	32.4 ± 1.7
East Greenland.	AA104	1.64×10^5	$2,57 \times 10^6$	–	0.880	6	34.7 ± 2.0
	AA105	1.42×10^5	2.12×10^6	–	0.995	9	36.5 ± 1.6
	AA106	1.52×10^5	2.31×10^6	–	0.987	8	35.8 ± 1.9
3. Apatite	KT15	4.7×10^4	2.8×10^5	3.84×10^{15}	0.754	5	38.8 ± 2.3
Kangerdlugssuaq,	KT16	4.3×10^4	2.8×10^5	–	0.895	6	36.3 ± 2.0
East Greenland.	KT17	4.2×10^4	2.4×10^5	–	0.982	5	41.4 ± 2.1
	KT18	3.9×10^4	2.5×10^5	–	0.923	7	36.9 ± 2.4
	KT19	8.4×10^4	5.0×10^5	–	0.897	6	39.7 ± 2.3
	KT19A	5.4×10^4	3.4×10^5	–	0.985	8	37.6 ± 2.1
	KT20	5.6×10^4	3.5×10^5	–	0.727	5	37.9 ± 2.6
	KT22	4.8×10^4	3.1×10^5	–	0.895	7	36.6 ± 2.0
4. Sphenes.	BK1	5.3×10^5	1.70×10^6	2.69×10^{15}	0.895	6	51.6 ± 2.6
Gardiner,	BK2	4.5×10^5	1.50×10^6	–	0.974	8	49.7 ± 2.2
East Greenland.	BK3	4.9×10^5	1.62×10^6	–	0.747	6	50.1 ± 2.4
	BK4	6.1×10^5	2.10×10^6	–	0.985	5	48.1 ± 1.9
	BK5	$5,31 \times 10^5$	1.79×10^6	–	0.991	7	47.5 ± 2.1
	BK7	5.62×10^5	1.64×10^6	–	0.985	8	55.3 ± 1.9
	BK8	7.25×10^5	2.38×10^6	–	0.874	7	50.5 ± 2.4
	BK9	6.41×10^5	2.14×10^6	–	0.768	13	49.6 ± 2.6
	BK10	4.25×10^5	1.33×10^6	–	0.845	8	52.9 ± 2.8
5. Zircon.	AG21	5.23×10^5	1.45×10^6	2.40×10^{15}	0.994	7	53.3 ± 1.9
Gardiner,	AG28	4.84×10^5	1.32×10^6	–	0.932	5	54.2 ± 2.1
East Greenland.	AG29	4.75×10^5	1.30×10^6	–	0.897	5	53.9 ± 2.3
	AG32	5.41×10^5	1.53×10^6	–	0.983	6	52.2 ± 1.8
	AG39	6.22×10^5	1.75×10^6	–	0.763	8	52.5 ± 2.4
6. Zircon.	AZ91	3.24×10^5	2.12×10^6	3.84×10^{15}	0.973	6	36.2 ± 1.1
Aliuarssik,	AZ95	3.51×10^5	2.24×10^6	–	0.895	7	37.1 ± 1.2
East Greenland.	AZ98	2.84×10^5	1.92×10^6	–	0.932	6	35.0 ± 1.1
	AZ99	3.12×10^5	2.11×10^6	–	0.981	8	35.0 ± 1.0
	AZ103	4.03×10^5	2.70×10^6	–	0.871	6	35.4 ± 1.2

7. Zircon.	KZ49	9.34×10^5	2.75×10^6	2.39×10^{15}	0.892	6	49.9 ± 3.0
Kangerdlugssuaq,	KZ53	8.62×10^5	2.63×10^6	–	0.954	6	48.2 ± 2.8
East Greenland.	KZ57	8.50×10^5	2.45×10^6	–	0.983	8	51.5 ± 3.1
	KZ59	4.73×10^5	1.52×10^6	–	0.980	11	45.8 ± 3.0
	KZ60	4.70×10^5	1.34×10^6	–	0.894	8	51.6 ± 3.1
	KZ65	8.32×10^5	2.40×10^6	–	0.943	7	50.5 ± 2.9
8. Phlogopite.	PL107	5.15×10^5	3.31×10^6	5.28×10^{15}	0.975	8	50.6 ± 2.1
Gardiner,	PL109	5.45×10^5	3.43×10^6	–	0.891	7	51.4 ± 2.0
East Greenland.	PL110	3.72×10^5	2.25×10^6	–	0.774	5	53.7 ± 2.5
	PL111	4.66×10^5	3.03×10^6	–	0.981	7	50.0 ± 2.0
	PL112	$4{,}35 \times 10^5$	$2{,}85 \times 10^6$	–	0.672	9	$49{,}8 \pm 2.3$
	PL113	5.04×10^5	3.11×10^6	–	0.743	5	52.7 ± 2.2

ϱ_s is the spontaneous track density, ϱ_i the induced track density, n the thermal neutron dose (nvt), N the number of grains counted, and R the correlation coefficient.

possible to construct an original land surface which shows that the area was domed up over some 300 km and to a height of around 6.5 km above the present sea level, or 4 km relative to the surrounding terrain. The Watkins Bjerge, which reaches a height of nearly 4 km, is part of the eroded remnants of this dome. In accordance with the ideas of GASS,[106] this suggests that the dome developed in association with the intrusion of the Kangerdlugssuaq syenites about 50 m.y ago. Our fission track ages (Table VII.2) show distinct cooling in this area.

(ii) The Gardiner Intrusion

According to NIELSEN and BROOKS[107] and FRISCH and KEUSEN,[108] this intrusion is a ring complex composed of ultramafic and melelite bearing rocks of a rather unusual type situated at the head of the Kangerdlugssuaq Fjord on the continental side of the province where the plateau basalts are strongly thinned. It is believed to be derived from a nephelinitic parent magma and its age is similar to that of the Kangerdlugssuaq intrusion. The concordance of apatite, sphene, phlogopite and zircon fission track ages (Table VII.2) as well as agreement with K/Ar ages[45] for mica indicates that it was emplaced at shallow levels and cooled rapidly. This conclusion is also in accord with field evidence. Small variations in the fission track ages depend on the rates of annealing of spontaneous tracks in the minerals; each mineral anneals over its own specific temperature range. The annealing behaviour of zircon, sphene and apatite has been described previously.[21, 23, 94] The mineral phlogopite was also selected for study, especially with respect to track retention and annealing characteristics; hence the detailed experiments described in section V on the "ranges" of both spontaneous and induced fission fragments. Phlogopite records cooling through a 195°C isotherm which is somewhat higher than reported earlier for apatite. The closing temperature for this mineral is lower than that for muscovite.

The zircon FT ages (Table VII.2) agree closely with previous K/Ar results for this complex. The suggestion is that there was a virtually simultaneous intrusion of different bodies, followed by rapid cooling to a temperature below 195°C. Samples of sphene, phlogopite and apatite yielded FT ages between 47 ± 2 and 54 ± 2 m.y. There is therefore no evidence in the present work for ages older than about 55 m.y indicating that up to that time at least the region was so thermally unstable that even tracks in zircon were completely annealed. However, the Gardiner complex is believed to be of a similar emplacement age to that of the Kangerdlugssuaq intrusion, confirming that rapid cooling took place in the area. All of this, and the petrological and field evidence,[108] suggests the Gardiner intrusion to be a very high level one indeed.

(iii) Aliuarssik

This island in the Kialineq district is partially occupied by a circular granitic intrusion. Several studies indicate that magmatic activity in this area was substantially later than that in the Kangerdlugssuaq area, and possibly occurred in response to major readjustments of plate motions which are known to have taken place at this time. The apatite and zircon results reported here (Table VII.2) confirm the dating of this activity and also that cooling again took place rapidly. This is in agreement both with the previous results and with the field evidence, since the granite is strongly miarolitic, a texture characteristic of shallow level or sub-volcanic intrusions. BECKINSALE et al.[46] give K/Ar dates for biotite and amphibole of 37.5 ± 1.6 and 49.0 ± 3.1 m.y respectively, whilst a Rb/Sr age of 35 ± 2 m.y for various rocks has been reported by BROWN et al.[47] The same authors have made K/Ar measurements on the minerals biotite and hornblende yielding figures of 35.9 m.y and 35.4 m.y respectively. The fission track age we report (35 ± 1.1 m.y) once more indicates a rather rapid cooling at about this time, in support of earlier work by GLEADOW and BROOKS,[48] who find for this granite a weighted mean of zircon and apatite FT ages of 36.8 ± 0.9 m.y. They also find similar ages for the Qajarsak granite and Bjørn syenite using zircon samples. The measured ages confirm that the last thermal event at about 35 m.y did not affect the fossil tracks stored in zircon and sphene, as they show no significant shrinkage. However, the event has had an effect on the measured ages of apatites.

VIII. Conclusion

It is a basic assumption of fission track dating methods that the ratio of track to bulk chemical etch rate is unity, which is to say that the revelation of both spontaneous and induced tracks is the same under identical etching and counting conditions. In addition as the experiments with chabazite and other minerals clearly show, because of a fundamental anisotropic etching behaviour it is necessary that only surfaces with identical etching characteristics be used for dating purposes. For zeolites both population† (internal) and external†† detection procedures can be followed providing that certain intrinsic limitations are appreciated. For example, due to varying registration geometry, surface etching efficiency and angular track anisotropy, the use of external detectors should be avoided if the sample consists of tiny mineral grains mounted in epoxy resin. Violation of the assumption of identical registration and etching conditions makes the final fission track ages quite unreliable.

Annealing experiments show that the thermal stablilty of tracks in chabazite is lower than in sphene, garnet, epidote, allanite and hornblende. Data from these and corresponding experiments on track shrinkage suggest that ages determined by applying the fission track method to zeolites will be slightly affected by annealing. Nevertheless the basic FT method is considered to be generally applicable to the dating of zeolites.

Similar annealing experiments on phlogopite indicate that fission fragment tracks are unstable, and confirm that the degree of instability varies from mineral to mineral. Fossil tracks can be erased in minerals during intense metamorphic episodes, thus resetting the geological clock. For the case of phlogopite in particular, extrapolation of the experimentally determined temperatures for annealing suggests that a temperature of 195°c will erase all tracks in 10^6 years.

The fission track ages obtained for samples from the Faeroe Islands lead us to the conclusion that onshore volcanism was limited to a span of time between $41.6 \pm 1.1 \times 10^6$ and $55.4 \pm 2.6 \times 10^6$ years ago. It is likely that this volcanic activity coincided, at least in part, with either global or more regional movements of both a plate-tectonic and epeirogenic character in East Greenland. Volcanism and epeirogenesis are supposed to reflect major processes taking place in the upper mantle and are, therefore, intimately associated with plate tectonic events.

The observed distribution of ages in the Faeroe Islands is probably regional, with the youngest ages in the north-eastern part of the islands reflecting more prolonged cooling in that area. Ages from the Lower Series on Suduroy and Mykines, which are close to the currently accepted age for volcanism, indicate that in the south and west of the

† The average spontaneous track density is here measured in one sample, and the induced track density in a separate sample which is annealed prior to irradiation.

†† Spontaneous tracks are etched in the mineral grains and induced tracks in an adjacent track detector of either muscovite or lexan polycarbonate.

islands the lavas underwent rapid cooling either as a result of lack of burial by significant amounts of overlying material, or as a result of rapid uplift. Such a rapid uplift is most likely due to dome-shaped structures believed to be present offshore to the north-west of Mykines, and under Suduroy. These domes, although occurring on much smaller scale, invite comparison with East Greenland, where a large uplift was raised after the basaltic volcanism, and rapidly dissected by erosion. For the Kangerdlugssuaq area in particular it is proposed that there is clear evidence for strong doming and regional uplift about 50 m.y ago, giving rise to the Kangerdlugssuaq intrusion at a high level in the crust, close to the unconformity between Precambrian gneisses and the overlying tertiary basalts. With respect to identification of the 40–55 m.y event as that occurring during continental breakup it should be noted that this is by far the most widespread and voluminous event in the North Atlantic. There is separate evidence for a volume of basalts in East Greenland of the order of 2×10^5 km^3, and a similar volume of magma in dikes. In addition, considerable volumes of basalts, believed to be contemporaneous, are found in the Faeroe Islands.

The north Atlantic area is of particular interest, not only because of its position between the Eurasian and American land masses, but also with respect to faunal and floral migration.

Acknowledgements

The authors are grateful to Mr. Ole Jørgensen for donation of the zeolite samples, to Dr. R. L. Fleischer for supplying the glass dosimeters, and to Dr. R. McCorkell for plastic detectors. The support of the Danish Natural Science Research Council and the DANIDA office of the Danish Foreign Ministry is gratefully acknowledged.

Indleveret til Selskabet august 1982.
Færdig fra trykkeriet december 1983.

The Wider Himalaya, a Model for Scientific Research

By AUGUSTO GANSSER

A J. C. Jacobsen Memorial Lecture

Det Kongelige Danske Videnskabernes Selskab
Matematisk-fysiske Meddelelser **40** : 14

Kommissionær: Munksgaard
København 1983

Det Kongelige Danske Videnskabernes Selskab
udgiver følgende publikationer:

The Royal Danish Academy of Sciences and Letters
issues the following series of publications:

	Bibliographical Abbreviation
Oversigt over Selskabets Virksomhed (8°) *(Annual in Danish with an English summary)*	Overs. Dan. Vid. Selsk.
Historisk-filosofiske Meddelelser (8°)	Hist. Filos. Medd. Dan. Vid. Selsk.
Historisk-filosofiske Skrifter (4°) *(History, Philology, Philosophy, Archaeology, Art History)*	Hist. Filos. Skr. Dan. Vid. Selsk.
Matematisk-fysiske Meddelelser (8°) *(Mathematics, Physics, Chemistry, Astronomy, Geology)*	Mat. Fys. Medd. Dan. Vid. Selsk.
Biologiske Skrifter (4°) *(Botany, Zoology, General Biology)*	Biol. Skr. Dan. Vid. Selsk.

Selskabets sekretariat og postadresse
The address of the Academy is:

Det Kongelige Danske Videnskabernes Selskab/
The Royal Danish Academy of Sciences and Letters
H. C. Andersens Boulevard 35
DK-1553 Copenhagen V
Denmark.

Selskabets kommissionær
The publications are sold by the agent of the Academy:

Munksgaard Eksport- og Tidsskriftservice/
Munksgaard Export and Subscription Service
35, Nørre Søgade
DK-1470 Copenhagen K
Denmark.

The Wider Himalaya, a Model for Scientific Research

By AUGUSTO GANSSER

A J. C. Jacobsen Memorial Lecture

Det Kongelige Danske Videnskabernes Selskab
Matematisk-fysiske Meddelelser **40** : 14

Kommissionær: Munksgaard
København 1983

A grant from The Carlsberg Bequest to the Memory of Brewer J. C. Jacobsen has made it possible to arrange and print a series of public J. C. Jacobsen Memorial Lectures, for which the Academy expresses its sincere gratitude

Synopsis

The Himalaya and part of Tibet were formed by the collision of India with Eurasia. Following a complicated pre-collision history, the post-collision phases, after the formation of the Suture Zone with its ophiolites, were characterised by the Transhimalayan plutons – their uplifts and erosion producing a molasse which forms the famous Kailas mountain – the subsequent intracrustal thrusting, and the Himalayan metamorphism with the final leucogranite intrusions. These initiated the morphogenic phase, with the uplift of the Himalaya and Tibet, en area of 2 500 000 km^2, in Pleistocene time. The related inland glaciation produced, on melting, numerous lakes, and was followed by the early immigration of a population which adapted to the difficult conditions, assisted by their religious belief and their cultural heritage.

AUGUSTO GANSSER
Institute for Geology
Eidgenössische Technische Hochschule
and the University of Zürich
CH-8092 Zürich
Switzerland

Printed in Denmark by Bianco Lunos Bogtrykkeri A/S. ISSN 0023–3323. ISBN 87-7304–141–6

Introduction

Since ancient times, the Himalaya, the highest and youngest of the world's mountain ranges, has had a special attraction to mankind. As a mysterious, impassable barrier it was the abode of good and bad spirits, of gods and many more goddesses. Its numerous cave were a retreat for meditating hermits, such as the world-famous Milaräpa with unforgetable legends and the "hundred thousand" songs which have spread all over the Himalaya and Tibet.

Scientific investigations in the Himalaya began relatively early, considering its relative remoteness, and compared to other mountain ranges. With the foundation of the Geological Survey of India in 1851 started a golden age of Himalayan exploration. It was in particular the efforts of famous European geologists which provided a cover of the Himalaya except its eastern part but including some regions of southern Tibet and Afghanistan. Though modern travel faclities did not exist in those early days, there was plenty of time, and contact with the field was much more intimate compared to our hectic exploration with rapid but superficial coverage by jeeps and helicopters. Political boundaries already existed, and work in Tibet had to be done by trained natives – the famous "pundits" – or in disguise. Nepal and Bhutan were hermetically sealed countries.

The results of these early explorations were mostly stratigraphical. The recognition of complicated structures was handicapped by failure to recognize the conspicuous allochtonous masses in many regions, in spite of the fact that the nappe theory was understood in the Himalaya before it was published in the Alps. It was the Hungarian geologist Louis von Loczy who visited Sikkim in 1878 and, on the basis of previous work and his own field observations, recognized for the first time huge recumbent folds or nappes. These had a crystalline core over 10 km thick and were thrust southwards for over 100 km on top of the Permocarboniferous Damudas, which again were thrust over the Tertiary molasse, the Siwaliks (Fig. 1). At the same time Alpine geologists were still struggling with the famous "Glarner Doppelfalte", until Marcel Bertrand in 1887 published his sweeping interpretation of the Glarus thrust without ever having been on the spot. Unfortunately, regarding scientific priorities, von Loczy did not publish his findings until 1907, nearly 30 years after his discovery. Much later E. Argand, in his masterly synthesis "Tectonie de l'Asie" (1924), expressed some surprisingly modern views, suggesting crustal collision between Gondwana and Eurasia. Ten years earlier, however, Colonel Burrard of the Indian Survey had on the basis of geodetic evidence already suggested underthrusting of India as the reason for the origin of the Himalayan mountains. But more than 20 years elapsed before Auden, Heim and Gansser convinced Himalayan geologists of the existence of large crystalline thrust sheets (Auden 1937, Heim and Gansser 1939).

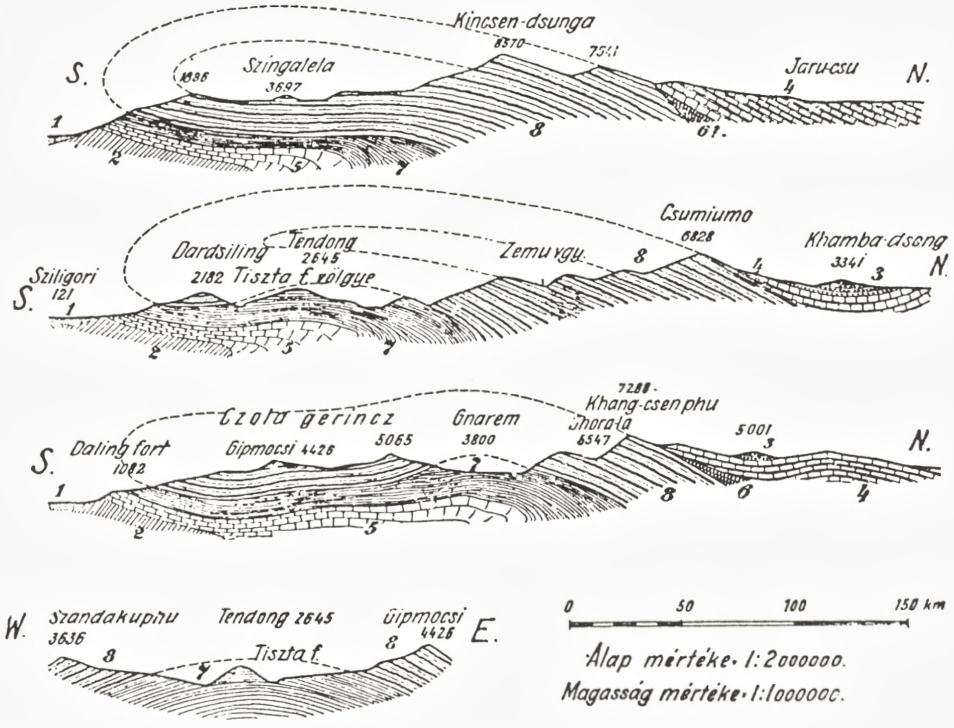

Fig. 1. The recumbant folds in the Sikkim Himalaya by L. v. Lóczy 1907 (observed 1878).

Geological History

The present fascinating picture of the Himalaya and adjoining Tibet, the largest positive land mass on earth, is based on a most complex geological history (Fig. 2). There is hardly any doubt that the Himalayan orogen is the product of a collision between the greater Indian block and a complicated Eurasian mass, and we may subdivide the process of Himalayan mountain building into a pre- and post-collision phase. In pre-collision time, from the Precambrian to the end of the Palaeozoic, northern India was bordered by a shallow marine belt, which was called Paleotethys by some authors without, however, their having a precise idea of the size of this shallow shelf sea. It seems likely that this shelf, with no oceanic crust, was never bordered by a wide ocean, and that India was never far away from an Eurasian continent. An excellent account of this situation was recently given by J. B. Auden in his inspiring paper, "India's former crustal neighbours", published on the occasion of the Wadia commemoration (Auden 1981).

Palaeogeographic reconstruction clearly shows the thick late Precambrian to Cambrian sediments of northern India following the pronounced Aravalli orogeny, and the younger Gondwana cover. These latter sediments gradually become more marine and the stratigraphic section more complete the further one goes to the north. This leads to the large sedimentary section of the northern Himalaya (Tethys or Tibetan Himalaya of some authors) which represents a conformable sequence from Cambrian to Eocene, without any orogenic break but with some marked epeirogenic uplifts near the end of the Palaeozonic. This event coincided with a basaltic alkaline volcanism, the Panjal trap, localised in the western Himalaya only. The interfingering of a Gondwana and a Tethyan facies is well known in the Kashmir region and has been observed on the north side of Mt. Everest (Mu An Tse et al. 1973). These facts clearly show that one cannot support the idea, often ventured by various authors, of two sedimentary basins, one Gondwana in the south and one Tethyan to the north, separated by a crystalline divide which has formed the High Himalaya. This divide did not yet exist during the time of deposition, but was formed much later (Main Central Thrusts), after the collision of India and Eurasia.

Fig. 2. Geological block-diagram of the Himalaya and Tibet. (Photoreduction colored map by A. Gansser, 1979.)

AT	Astin Tagh	Ks	Mt. Kailas
B	Brahmaputra river	L	Lhasa
CL	Chomo Lungma (Everest)	NB	Namche Barwa
D	Delhi	Ng	Naga range
G	Ganges river	NP	Nanga Parbat
HK	Hindu Kush	PA	Pamir
Hu	Hundes basin	PI	Peninsular India
I	Indus river	S	Sutledj river
Is	Islamabad	SH	Shillong plateau
K	Kathmandu	TB	Isaidam basin
KA	Karakorum	TS	Tien-Shan (southern part)
Kb	Kabul		
KL	Kun Lun		

Cr	Crust: base 30 km below India, 70–75 km below Himalaya and Tibet, 30 km below Tarim basin.
MTL	Mantle, "obducted" along SZ and older sutures in central and northern Tibet (Kun Lun).
SZ	Suture Zone, Indus Tsangpo Line, doubled in western Himalaya.
MCT	Main Central Thrust, major intra-crustal fracture. (Miocene).
MBT	Main Boundary Thrust, on southern molasse (Siwaliks). (Pleistocene).
MFT	Main Frontal Thrust, recent events, Siwaliks thrust on Quaternary.
1	Tertiary to Quaternary acide to interm. volcanics in Tibet.
2	Transhimalayan Pluton, 110–40 my, located N of Suture Zone.
3	Siwalik Molasse in S and southern Tarim Molasse in N.
0	Ophiolites along Suture Zone.

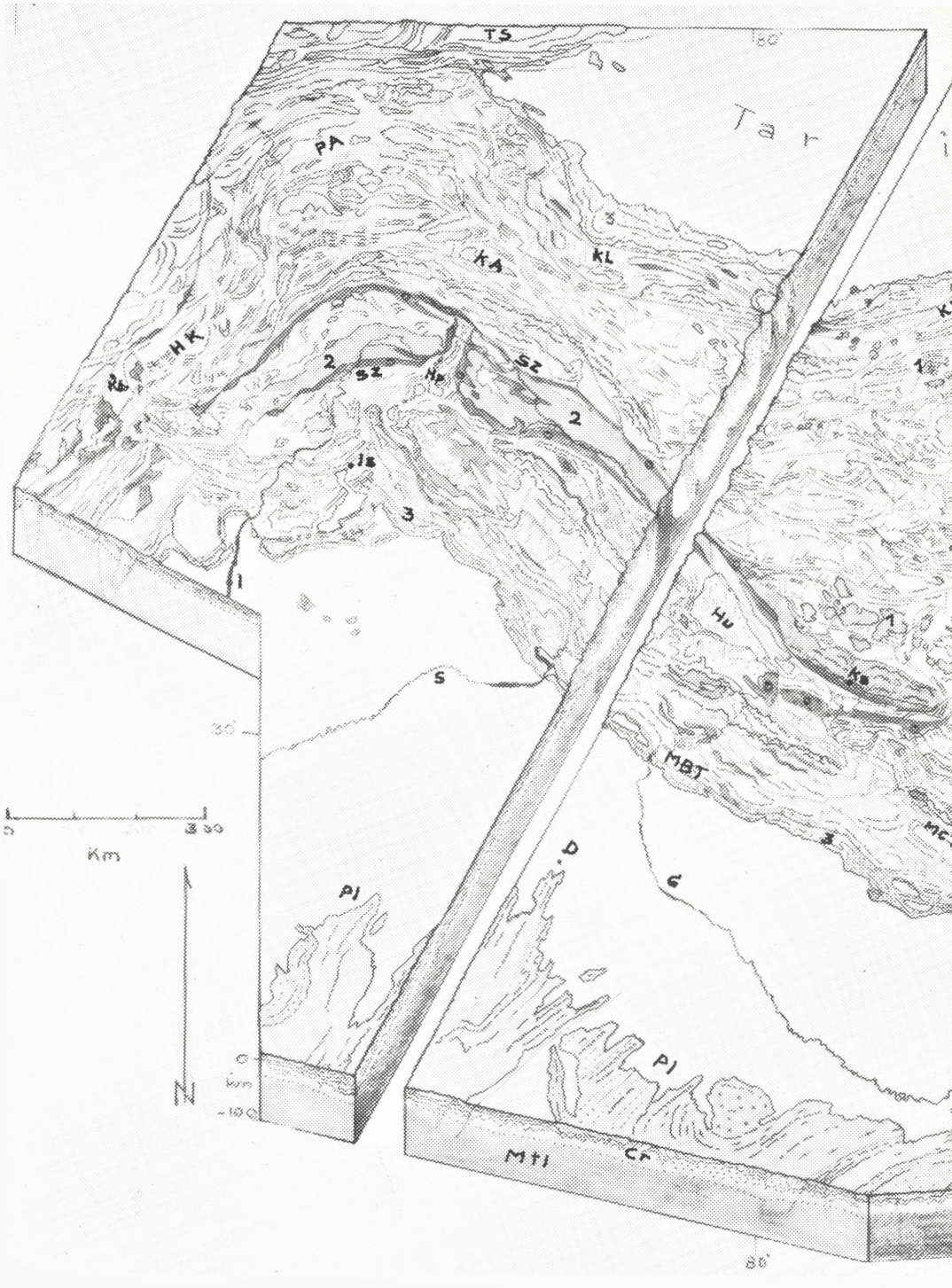
TS
PA
KA
KL
HK
SZ
MBT
MCT
Hu
Ka
Pl
Mtl
Cr
Tar
km
N

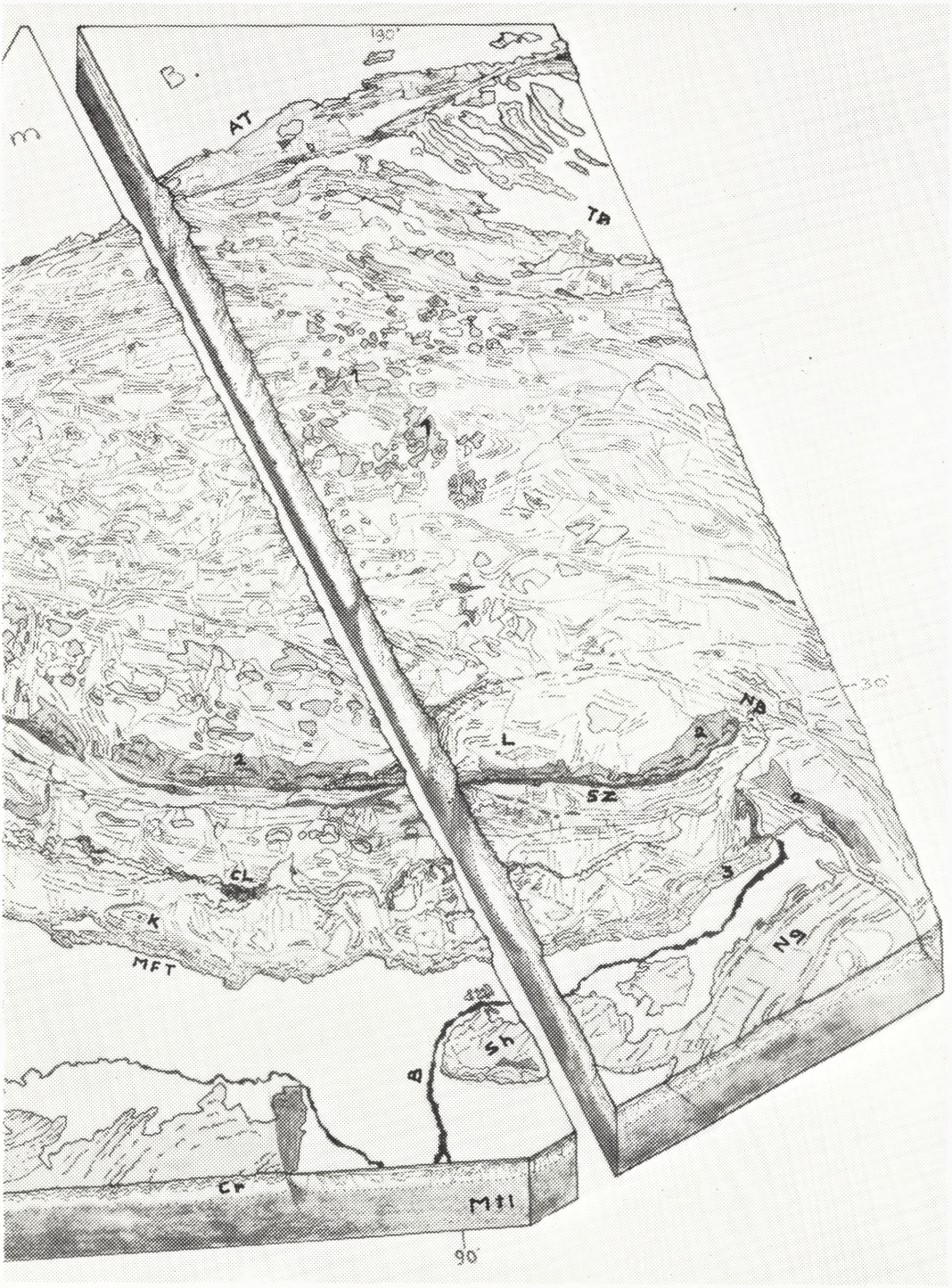
B.
AT
TB
NP
L
SZ
CL
K
MFT
B
Sh
CP
M11
90

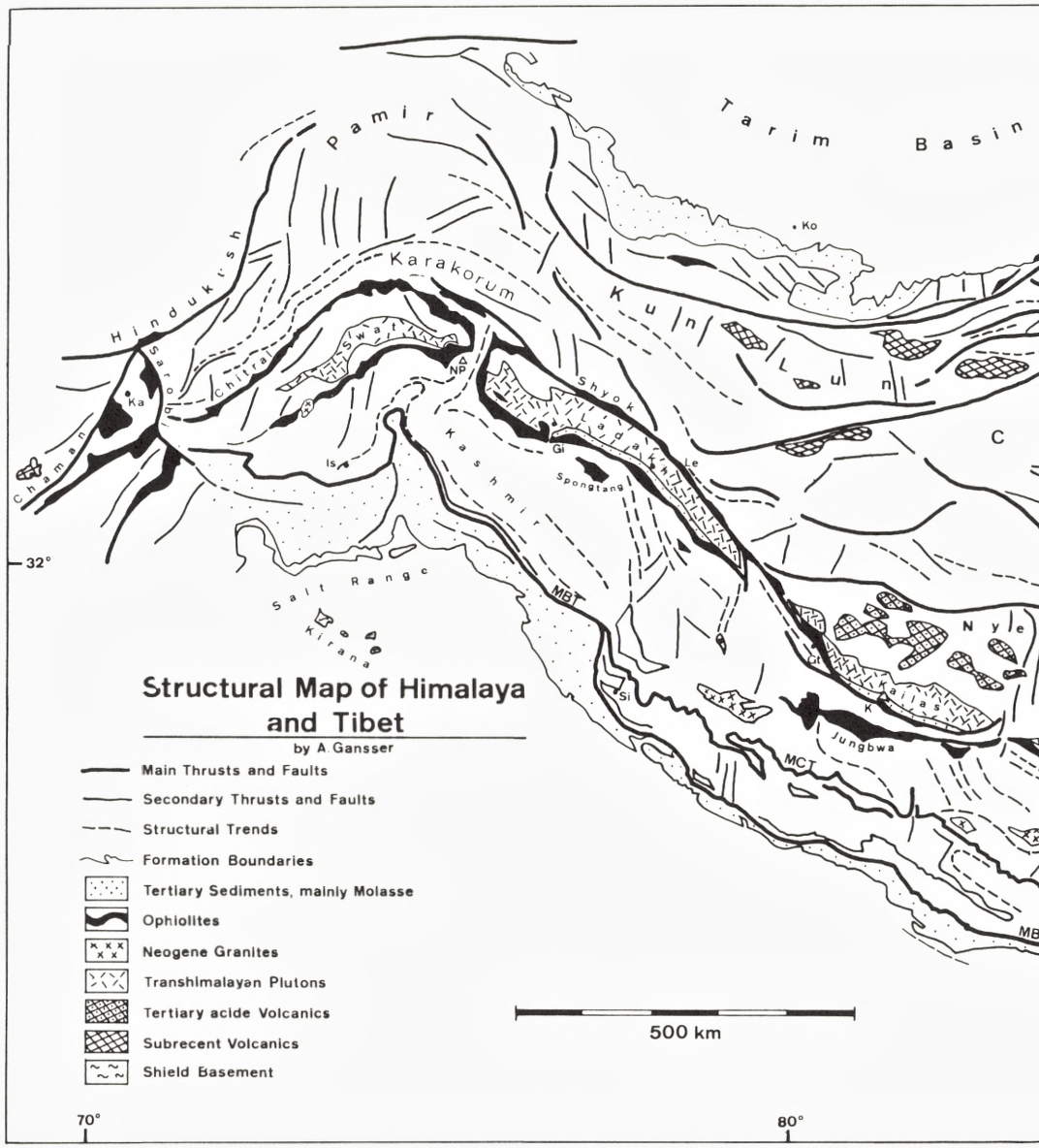

Fig. 3. Structural map of the Himalaya and Tibet. (After Gansser 1980).

CL	Chomo Lungma (Everest)	Ka	Kabul	Le	Leh
Gt	Gartok	K	Kailas Mt.	NB	Namche Barwa
Gi	Gilgit	Kt	Kathmandu	NP	Nanga Parbat

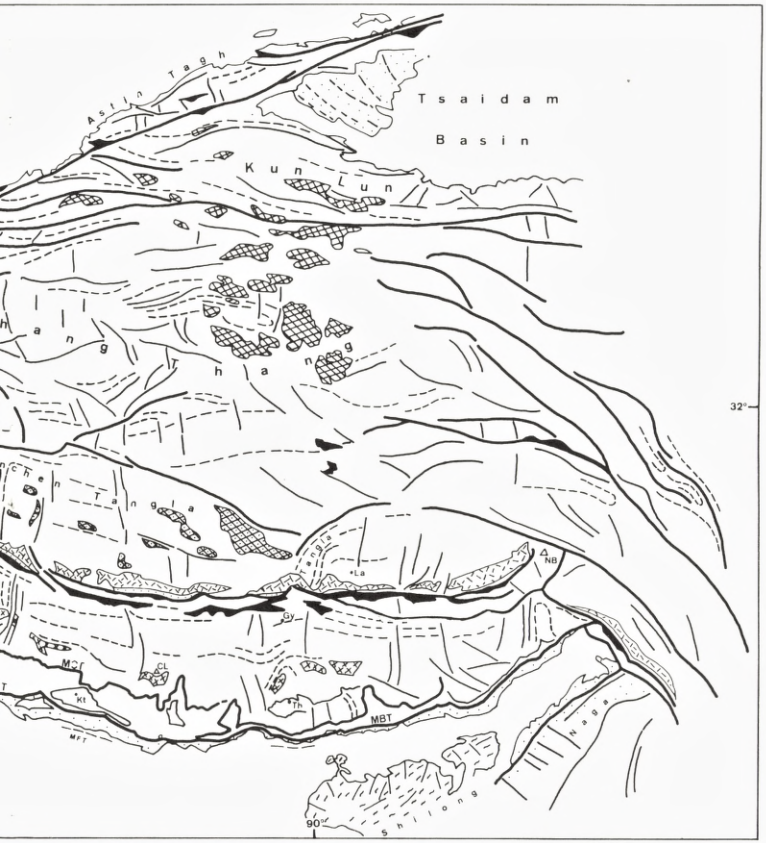

Gy	Gyantse	Ko	Khotan	Si	Simla
Is	Islamabad	La	Lhasa	Th	Thimphu

SZ Suture Zone, MCT Main Central Thrust, MBT Main Boundary Thrust, MFT Main Frontal Thrust.

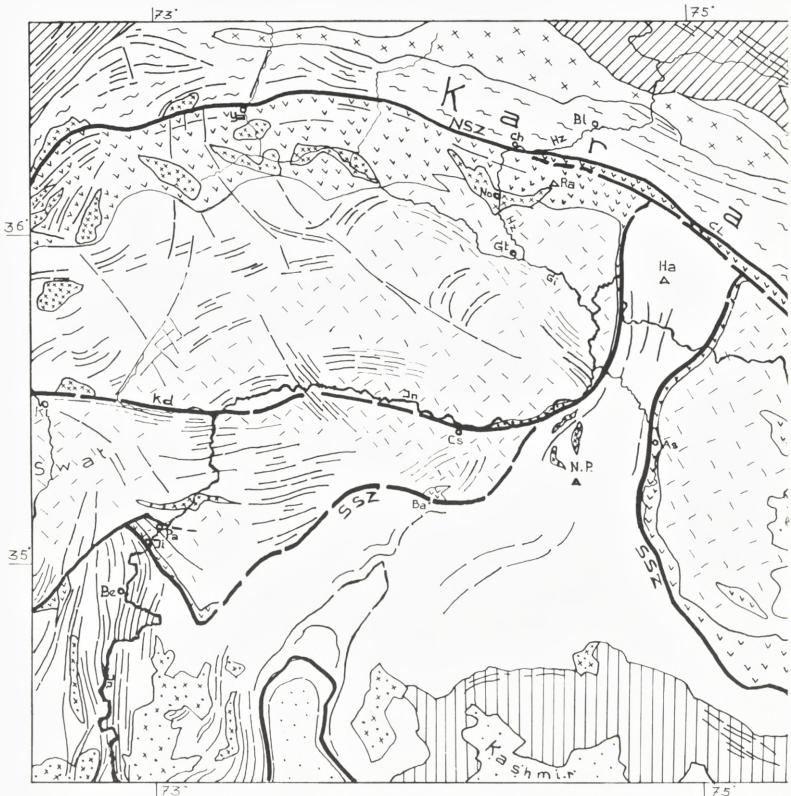

Fig. 4. Geological sketch map of the NW Himalaya and Karakorum. (After Gansser 1980).

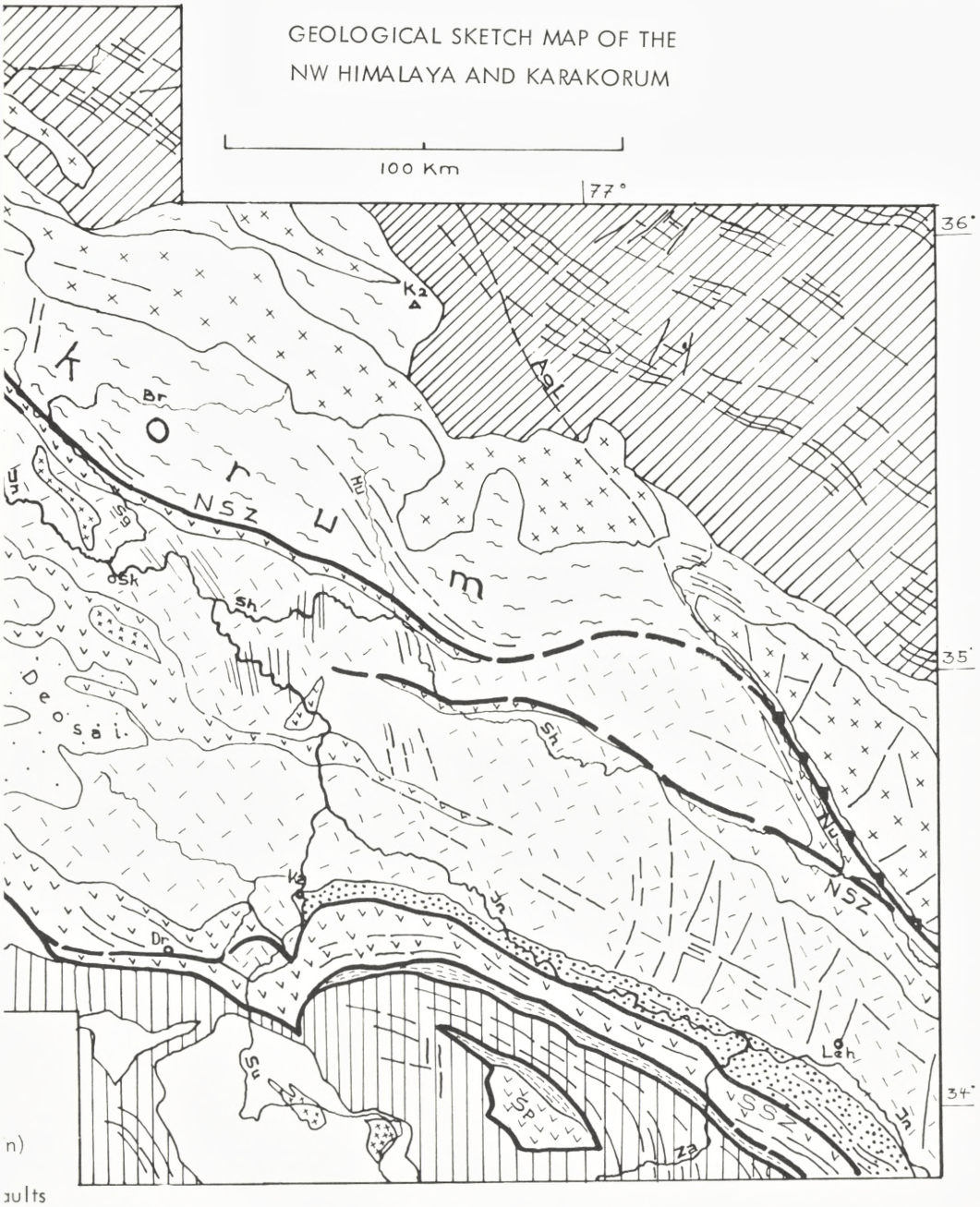

n)

aults

ru

ınskar

Ha Haramosh
NP NangaParbat
Ra Rakaposhi
CL Chogo Lungma Gl.

NSZ Northern Suture Zone
SSZ Southern Suture Zone
Agl Aghil Line
Spa Spongtang Nappe

The collision of India with the complex southern margin of Eurasia, which included some micro-continents of doubtful origin (today called "displaced continents"), is well outlined by the Peri-Indian Suture Zone. This exposes ophiolitic rocks which range from volcanics with pillow lavas to ultramafics with associated ophiolitic melanges and oceanic sediments, predominantly in the form of radiolarites. This association, in particular the melanges, suggests originally steep and narrow oceanic basins and not large oceans as frequently suggested on the basis of palaeomagnetic results. The suture zone can be followed over a length of 5000 km from Karachi in the SW over the Quetta belt (western section) to the High Himalaya (northern section) and the Arakan Yoma branch to the Andaman islands in the SE (eastern belt), still with well exposed ophiolitic melanges. In all these sections the overall composition of the ophiolites is, in spite of most complicated tectonics, surprisingly similar. Actually the ophiolitic belt is the only constant feature all along the Alpine-Himalayan orogeny in spite of the greatly varying fore- and backlands (Gansser 1974, 1980a).

The collision took place during the very latest Cretaceous and early Eocene, with the final emplacement of the oceanic rocks (ophiolites) pre-middle Eocene in the Himalaya, while in the Middle East this process was mainly pre-Maestrichtian and in the Alps proper pre-Upper Jurassic and Upper Cretaceous. This phase and the subsequent formation of conspicuous ophiolite nappes not only characterises the Himalayan section but in precisely the same way occur along the Quetta belt which was never along the front of northwards drifting India. In all the ophiolitic nappes we note the curious facts that the ultramafic masses, representing mantle sections, form the highest structural element, underlain by the ophiolitic melanges and the oceanic volcanics.

After this major collision we note a certain calm with no orogenic activity. During this period the intrusion of the Transhimalayan batholiths ended all along and to the north of the Himalayan suture zone with pronounced volcanic activity 40 my ago (Fig. 3). Convincing geochemical evidence shows that the Transhimalayan batholiths were derived by melting of a downwarped oceanic crust. This melt was intruded along the continental rocks of the southern Asian plate border with more or less pronounced contamination. The intrusions started about 110 my ago with basic, mostly noritic gabbros, grading over diorites to the widespread tonalites (60 my) and ending with granites and vulcanics of 40 my (Honegger et al. 1982). The intrusive activity was not continuous but occurred in various phases, well displayed in the Ladakh area with granites along the southern border, while south of Lhasa to the east the older, more basic rocks outcrop in the south and become more acid and younger in a northward direction. The famous granite of Lhasa is highly contaminated by Jurassic limestones of the northern continental crust (Academia Sinica 1980).

In the western Himalaya the suture zone consists of two sutures. The Transhimalayan intrusions occur between a southern (Indus) and a northern (Shyok)

suture, the latter forming a sharp structural contact between the Himalaya and the Karakorum. The two sutures merge westwards towards the Kabul region where they are sharply cut by the N-S-trending Sarobi fault which limits the northwards directed Kabul spur (a possible continuation of the Indian shield) to the east. Both suture zones, particularly the southern one, are affected by the late N-trending Nanga Parbat/Haramosh crystalline antiform, which runs perpendicular to the E-W-trending Karakorum (Fig. 4). This remarkable structure also cuts the Transhimalayan batholith into an eastern Ladakh and a western Swat batholith. Both batholiths contain large inclusions of pre-batholithic basement, some not unlike the crystalline of the Nanga Parbat/Haramosh, which however is different from the Indian shield crystalline to the south of the suture. Most of these large inclusions still show a N-S-structural grain, contrasting with the E-W regional trend, and are parallel to the Nanga Parbat spur (Gansser 1980b). "Displaced" microcontinents of as yet unknown origin may have influenced the tectonic trends of this part of the Himalaya. This highly complicated area can hardly be explained as one large island arc (Coward et al. 1982). We have here one of the most fascinating and problematic sections of the whole Himalayan range.

The possible existence of microcontinents along the southern front of Tibet is another most important but still unsolved problem. We know that a large slice of southern Tibetan crust, the Nyenchen Tangla belt (Fig. 3), is separated by fault zones and sporadic ophiolite outcroups – some shown on the new 1:1 500000 map of Tibet (1980) – from the northern part of Tibet, suggesting a northern suture zone which however does not reach the importance of the Tsangpo/Indus Suture to the south. From the latter suture, the northern suture branches off NW of Gartok were the Indus river turns east towards its sources north of Kailas mountain. It has recently been investigated by French-Chinese teams to the north of Lhasa (E.U.G. abstracts 1983). The eastern continuation of the Nyenchen Tangla belt is the Lhasa block of the French teams, separated from the Nyenchen Tangla belt by the abnormally NE-striking Precambrian Tangla range.

Returning to the Transhimalayan batholith we note that the intrusions and volcanism were followed by a very rapid uplift, so that the Transhimalaya dominated the Himalaya, forming an important watershed. The remarkable uplift and consequent erosion was responsible for the formation of a molasse, deposited along the south side of the range and transgressing with a large basal conglomerate directly onto the plutonic rocks. Volcanic pebbles increase in abundance upwards and dominate together with some Lower Eocene limestones which give a lower age limit for this upper part of the molasse. The average age is most likely Oligocene. This molasse is particularly well developed in the central part of the over 2000 km long Transhimalaya and dominates in the Kailas mountain, a most striking relic of 4000 m of near-horizontal conglomerates and subordinate sandstones sitting on the tonalite and granites. This Kailas molasse is surprisingly thickly bedded in contrast to similar molasse in the Ladakh region (Fig. 5).

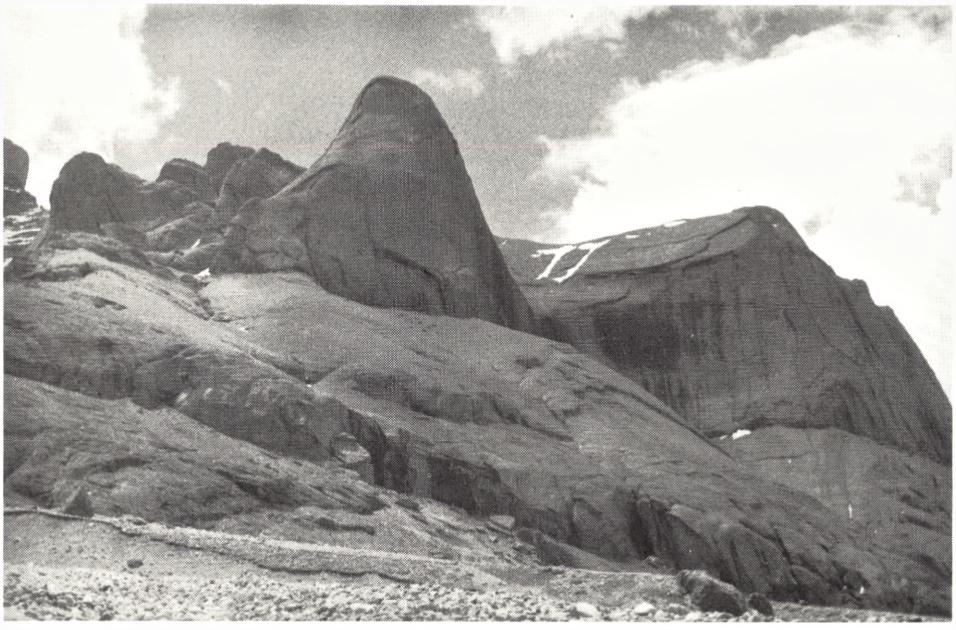

Fig. 5. The very thickbedded lower conglomerates of the Kailas Molasse, view eastwards, summit of Kailas to the left. (Fot. A. Gansser).

With its 6800 m the Kailas is most likely the highest molasse mountain known and because of its extraordinary shape (Fig. 6) it has become the most holy mountain of Asian religions (Allen 1982). It has been widely illustrated in old wall paintings together with its surrounding monasteries and the holy lakes of Manasarovar and Raksas, also important places of worship (Fig. 7). Not only the form of Kailas but also its geographical position is striking: all the largest rivers of the Himalaya and Transhimalaya have their sources near this mountain, the Indus in the north, the Sutledj in the west, the Tsangpo (Brahmaputra) in the east and the Ganges in the south (Fig. 8). The fact that in the old scripts Kailas was regarded as the centre of the known world has its geographical meaning.

After the deposition of the Kailas molasse and a period of relative orogenic calm, India reassumed its northward drift, but since the suture zone was welded and fixed, this movement was compensated by intracrustal adjustments. In the Miocene we recognize the Main Central Thrust along which a crystalline slab more than 15 km thick and its Tethyan sedimentary cover moved more than 100 km over the metasediments of the Lower Himalaya. At the base of the MCT we note a highly complicated zone of imbrications, particularly well exposed in Nepal, from which larger secondary thrust

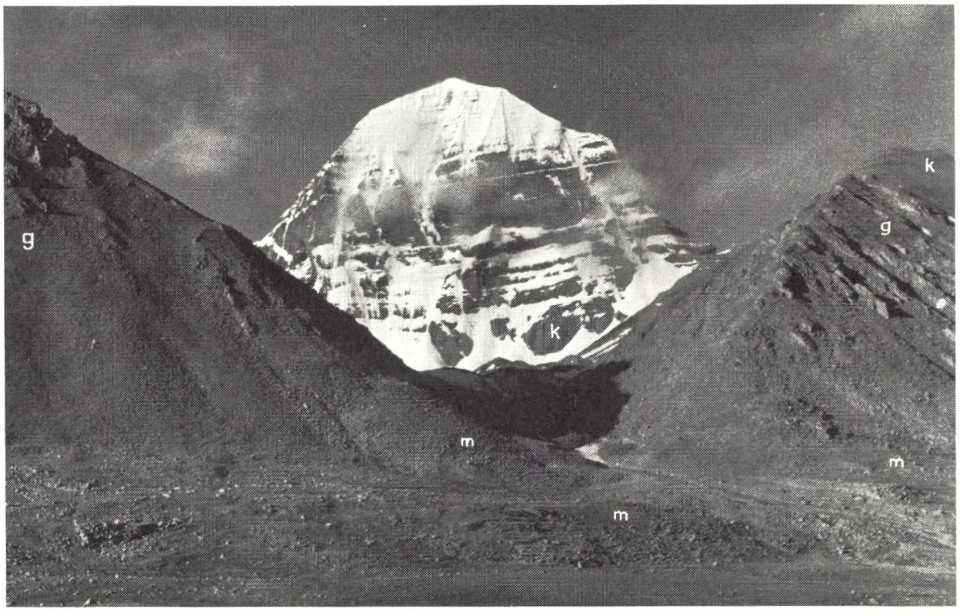

Fig. 6. The Mt. Kailas, seen from the N. The most holy mountain in the world. k = Kailas Molasse, g = Transhimalayan granite to tonalite, m = local moraines. (Fot. A. Gansser).

sheets developed, such as the crystalline thrust of Almora in the Kumaon Himalaya. A further pulse from India was taken up by the Lower Pleistocene Main Boundary Thrust further to the south, bringing the Lower Himalayan rocks over the frontal molasse, the Plio-Pleistocene Siwaliks. At present the Siwalik belt is steeply thrust along the Main Frontal Thrust over the Quaternary, tilting and warping the foothill deposits, in an area outlined by recent seismicity. These facts clearly reveal the intracrustal activity becoming younger and shallower from north to south (Fig. 3).

The regional Himalayan metamorphism coincides with the renewed Miocene orogeny. It is interesting to note that this metamorphism affected mostly the already metamorphosed rocks dating from late Precambrian events. Rarely it involves younger sediments, such as the lower Mesozoic of the western Himalaya (Nun Kun region in Ladakh – Honegger et al. 1982). In the adjoining Spiti basin the transgressive Ordovician sediments are non-metamorphic and enclose Precambrian metamorphic rocks in their basal conglomerates, proving without any doubt the presence on an old pre-Himalayan metamorphism (Fuchs 1982). The Himalayan metamorphism, which in the Lower Himalaya overprints the late-Precambrian sediments, is of anchi to high greenschist facies. The metamorphic grade increases towards the inner and higher

Fig. 7. Old wall painting of Mt. Kailas (upper left) and lake Manasarowar (bottom center) with monasteries which belonged to Bhutan, 1000 km away! Fotographed in a small village temple in Tinkar, NW Nepal, by A. Gansser.

units, displaying a remarkable reversed metamorphism. Within the crystalline thrust sheets of the Higher Himalaya only the lowest sections expose a reversed metamorphism (kyanite/staurolite to sillimanite); the metamorphic grade decreases again gradually towards the overlying Tethyan sediments. In the high-grade crystalline units it is most difficult to distinguish the Himalayan metamorphic overprint from Precambrian metamorphic events. The existence of the latter is furthermore documented in a few places by radiometric ages of 1800 and 1400 my (Bhanot et al. 1977). As a final and closing phase of the Himalayan metamorphism we note the intrusions of leucogranites in the High Himalaya which outdate the metamorphism and cut all visible structures. They usually intrude the highest part of the range from Nanga Parbat in the west over Badrinath, Manaslu, Shisha Pangma, Makalu to the Bhutan peaks in the east. Over a distance of nearly 2000 km their composition, age and mode of intrusion is surprisingly constant (Le Fort 1973). They usually intrude high-grade metamorphic rocks but can reach locally into the Mesozoic sediments of the Tethyan cover, where

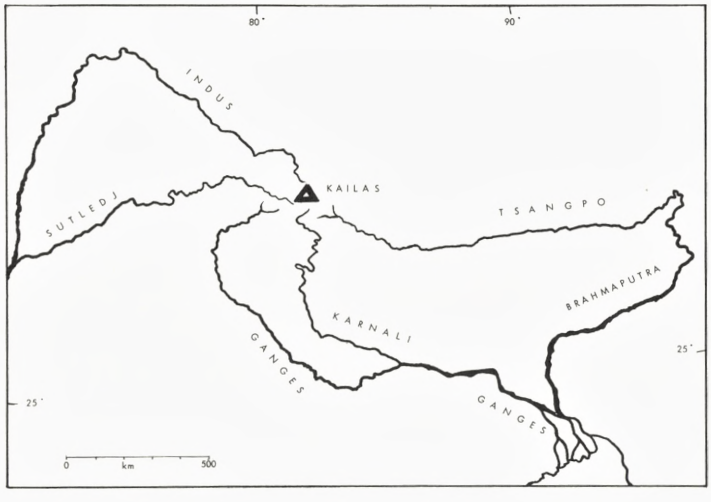

Fig. 8. The unique position of Mt. Kailas, the source of all the major Himalayan rivers. The "center of the world".

they produce a marked contact metamorphism. The extremely high ($^{87}SR/^{86}Sr$) ratio suggests melting of old sialic crust which distinguishes the leucogranites clearly from the Transhimalayan intrusions (Dietrich and Gansser 1982). The leucogranites close the Himalayan orogenic and metamorphic events and initiate the regional uplift of the range, the morphogenic phase.

Morphogenic phase

This regional uplift involves not only the Himalaya and Transhimalaya but also the large adjoining mass of Tibet to the north as well, an enormous area of over 2 500 000 km^2. New investigations of flora and fauna from terraces now between 5000 and 6000 m a.s.l. on the northern slopes of the Himalaya in the Sisha Pangma region revealed subtropical and tropical species, suggesting uplifts since the early Pleistocene of 4–5000 m (Hsu et al. 1978). Well known are the famous Karewa lake beds of Kashmir, which also suggest subrecent to recent upplifts in the western Himalaya (De Terra and Paterson 1939). Already over 100 years ago, in the gravel terraces of Hundes, nearly 5000 m up in the Tibetan part of the northern Central Himalaya, Lydekker found rhinoceros bones in beds which, in spite of having been uplifted several thousand metres, are still perfectly horizontal (Lydekker 1881). These gravel horizons are cut by steep gullies, and in the rock walls as well as on steep cliffs there are remnants of monasteries from the time of the kings of Guge. They contain the oldest and finest buddhist wall paintings known (Fig. 9), which, unfortunately, are slowly deteriorating (Tucci 1937).

Fig. 9. The eastern end of the large Hundes basin with Quaternary terraces rich in old remnants of cave monasteries. In the central basin the horizontal gravels contain tropical mammal bones, now at 4–5000 m elevation. (Fot. A. Gansser).

New results on precise levelling and triangulations which may provide quantitative data on recent uplifts are not yet available. Fault zones along the foothills show movements more of a horizontal than a vertical nature. The recent measurements of Everest (Chomolungma) suggest increasing height, but previous data were not too reliable. In his last publication of 1982, Eric Norin, who died at an age of 87 years, discussed the triangulation work of the 1932 Swedish expedition into western Tibet. Between 1857 and 1861 the Survey of India under excellent British surveyors carried out

triangulation work over Leh into SW Tibet. The subsequent, careful Swedish triangulation work of 1932 found a general increase of about 37 m and this over a span of only 71 years. This would give the incredible uplift rate of about 0.5 m per year for this particular area. This is far in excess of a reasonable morphogenic uplift rate for the whole Himalaya and Tibet, covering 2 500 000 km^2, which is assumed to be about 1–1½ cm year. Accepting such a figure one has to realize that the morphogenic uplift was never uniform in time nor in place. The present rates, at least for the Himalaya, are probably slowly increasing.

The effect of this young, regional uplift in connection with the later glaciations is of particular interest. According to Li and Cheng (1980) and recently Kuhle (1982), the Pleistocene snow line was at about 3800 m in northern Tibet and was lower along its southern border. This old snow line level is lower than the average height of the plateau (4200–5200 m) which rises in its central part as well as at its border into mountains between 6000–8000 m, all highly glaciated and with some perfectly preserved plateau glaciers (Landsat photos). These facts suggest that during the largest ice age (the third or second last period) a great part of the Tibetan plateau was covered by a widespread inland ice type glaciation (Kuhle 1982). An extended ice cover was already suggested for the eastern Karakorum and NW Tibet by Norin on the basis of results from his expeditions from 1927 to 1935 (Norin 1982). After the skrinkage of the inland ice cover, great depressions must have been preserved for some time by dead ice bodies which began melting along their border, giving rise to marginal lakes, the sediments of which can still be observed high on the flanks of such basins. This is even the case in large valleys such as the upper Indus. Most of the numerous present Tibetan lakes resulted from melting of such an ice cap and were originally fresh water bodies. Judging from the present lake sediments some must have had a very large extension. During their rather short existence of 10 000–20 000 years they gradually became brackish and finally salty. The eventual drying up of those water bodies can be seen on the Landsat photos which show many strand terraces surrounding the lakes concentrically.

This partly ice covered highest and largest land mass on our globe, situated in the northern desert girdle, must have influenced the Pleistocene climate to a great extent. The strong irradiation effect may have changed the higher atmospheric circulation and even been responsible for the drying up of the Sahara (discussions during Tibet conference 1980). The main change to present conditions began about 12 000 years ago at the end of the last ice age. This last stage was however not very pronounced and many of the Tibetan lakes originated already during the last interglacial period. Lake sediments show sometimes the effects of an overburden of lateral glaciers of the last stage (Bürgisser et al. 1982).

The foundation of famous monasteries is sometimes related to mysterious, now vanished lakes. The old history of the well known Lamayuru monastery in the Ladakh region is based on a mystic lake, which was the abode of the bad Naga spirits. Once a

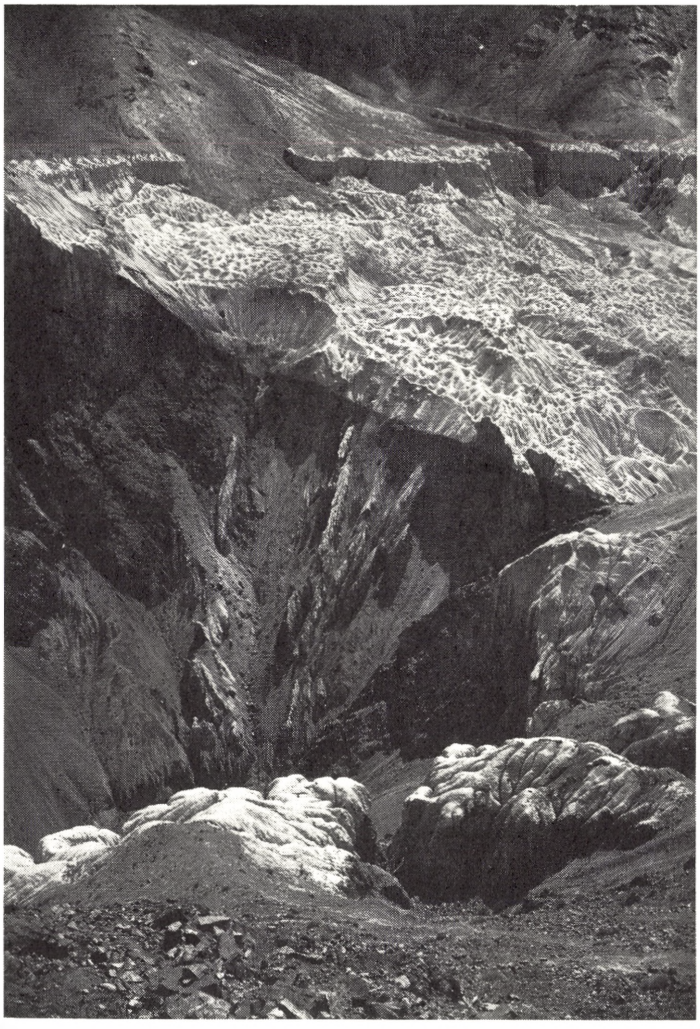

Fig. 10. Lake sediments which indicate the existence of a former Lamayuru lake. They have been strongly eroded with a 600 m deep gorge draining towards the Indus river. (Ladakh) (Fot. A. Gansser).

famous lama landed on a small island in this lake. He made offerings to appease the bad spirits and drained the lake thus preparing the site for this famous monastery. Old lake sediments are still present in this area, preserved 600 m above the level of the Indus river (Fig. 10). Unique is the rare depiction of boats surrounded by bodhisattvas in the Alchi monastery, the most famous and oldest temple of the Ladakh region (Fig. 11).

Human history

Uplift, glaciation and subsequent deglaciation in the Himalaya and Tibet must have caused special conditions as far as the flora and fauna were concerned. Survivals from the central ice plateau are most unlikely and the post ice age immigration must have come from the peripheral and more favorable regions. Unfortunately practically nothing is known of this early beginning. One realizes today how flora and fauna have adapted to the height, insolation and temperatures. The Himalayan traveller is struck by the adapted form of rubarb or the fury aspect of a *Saussurea,* living above 4500 m, to give just two examples. Even less is known of the human migrations and populations of the High Himalaya and Tibetan plateau. Archeological work has hardly begun. Of interest are the human artifacts in the Karewa lake beds of Kashmir, believed to be older than the last glaciation and the latest uplift of the Himalaya (De Terra and Paterson 1939). During the time of Peking man, travelling over the Himalaya must have been easier and the subtropical hipparion grazed happily on both sides of the range.

Fig. 11. The presentation of boats in the middle of Bodhisattwas in the hall of the Alchi monastery, the oldest buddhistic temple in Ladakh. (Fot. K. Riklin).

Between these meagre paleolithical data and 600 AD exists a large historical gap. It is the time when the animistic Bön religion, rich in sagas, was widespread in the northern Himalaya and Tibet. Many of the sagas were orally delivered, often in the form of songs, still popular to the present day. Most famous of all are the songs of the Geza Epos, well known today in the Bhutan Himalaya, which are a treasure of old religious history (Olschak 1979). The old sagas also tell us of the famous flood, the great event known all over the world, even in such remote regions as in the South American jungles. They tell us that Tibet (and the northern Himalaya) was covered by a big lake and that a "Buddha of that period" had mercy upon the land and with his sword cut a gap into the mountains of SE Tibet, draining the lake (Bell 1928). This gap is preserved today in the unique gorge of the Tsangpo river, where it cuts the 7800 m high Namche Barwa mountains in one of the wildest canyons in the world, and even today only partly explored. The flood story of Tibet refers to the lakes formed after the melting of the ice cap. It is certainly not related to the so-called Tethyan sea which once covered the Himalaya and Tibet, often referred to in interpretations of old texts. It is well known that most of the Himalaya and practically all of Tibet became land after the Tethyan sea vanished in the Middle Eocene, 40 my ago, and that since that time the whole area, not yet uplifted to its present height, was a large continent.

According to the old sagas, the Tibetans originated in the Yarlung valley. This drains the mountains to the E of the Bhutan Himalaya and its river flows northwards into the Tsangpo, southeast of Lhasa. The first Tibetans were believed to have lived in caves in this valley, which are still venerated today. They resembled large langoor monkeys more than human beings, but they cut their tails and began to populate the area. The first Tibetan Kings are reported from the Yarlung valley and there they built the first towered castle, the prototype for the dzongs, the famous fortress monasteries of the Bhutan Himalaya. This outstanding building, the oldest in Tibet, still existed and was photographed by Ernst Krause of the Schäfter expedition in 1938, but after the Chinese invasion of Tibet it has been completely destroyed. In the Lower Yarlung valley the grave hills of the ancient kings are still preserved, similar to the "tepes" in the Middle East. They seem hardly touched by archeological investigations. The famous 5th Dalai Lama, the founder of the Potala in Lhasa and the most outstanding figure in Tibetan history, was born in 1617 in the Yarlung valley. According to old legends even the eastern Himalaya was populated from the Yarlung region.

The northern Bhutan Himalaya is dominated by a famous peak, the Masang Kang (Fig. 12). Its name relates to the Masang tribes, the mythological forefathers of the Tibetans, whose descendents, coming from SE Tibet, settled in NE Bhutan. Gesar, the hero of the epic songs, is said to be a son of the Masangs, as recorded in precious old block prints (Olschak 1979). It may not be a mere coincidence that just at the foot of the Masang Kang we find the small village of Laya at 3900 m elevation. Here the inhabitants are strikingly different from the rest of the Bhutanese mountain people.

Fig. 12. The holy Masang Kang seen from the Toma La at the Tibetan border in the northern Bhutan Himalaya. The highly glaciated 7200 m high peak is the abode of the mythological Masang tribes which are reported to have populated the Bhutan Himalaya. (Fot. A. Gansser).

The women wear long dresses of sheep and yak wool, with a peculiar colour design. Contrasting with other Bhutanese they have long hair and speak a special dialect (Fig. 13). Their buddhist religion seems highly mixed with animistic Bön elements. Could these little known Laya people be some remnants of the famous Masang tribes?

In the western Himalaya and adjoining western Tibet we may find some even earlier migrations. Since ancient times western Tibet was known for its gold digging. The legends of gold-digging ants were already mentioned by Herodot (Lindegger 1982). They tell of huge ants "smaller than dogs but larger than foxes" which dug gold nuggets from deep narrow holes. Giuseppe Tucci discovered near Jiu monastery at the Manasarowar lake old gold-digging sites, exposing many deep narrow holes which reminded him of giant ant holes, "tanti formicai" (Tucci 1937). The Buddhist authorities in Lhasa later forbade mining in Tibet. Along the middle Indus river and in the Hunza region there exist old rock carvings and paintings. The black rocks, covered by desert varnish along the rivers, present an ideal surface to carve and scratch drawings and inscriptions. These petroglyphs have been recently investigated by Karl Jettmar, who

Fig. 13. The women of Laya, a small village at 3900 m in northern Bhutan. It lies at the foot of the holy Masang Kang. These unique people may be the remnants of the mythological Masang tribes? (Fot. A. Gansser).

discovered over 1000 pictures and inscriptions spanning a time interval of over 3000 years, not unlike visiting cards of the passing caravans (Jettmar 1981) (Fig. 14). Surprising are old inscriptions dating from the time of the Persian kings during the reign of Alexander. The results of these current investigations will eventually shed new light on the migration and population of the western Himalaya and Tibet, and tell of the caravans which travelled from NW India through the Baltistan mountains along the Indus and Hunza rivers towards Tibet. An interesting relic may be the Hunza people which kept their own special language. One may even venture the suggestion that this old trail, which joins the »silk road« in the north, may actually be a revival of much older, possibly even paleolithic migration routes from Kashmir (Karewa lake beds) through the western Himalaya at a time when the mountains had not yet reached their forbidding height.

In historical time, the great elevation of Tibet and the wild mountain ranges of the Himalaya were no longer an impassable barrier for the inhabitants which populated

these areas. With the taming of the wild yak they found an incredible domestic animal which carries heavy loads, climbs like a goat over the highest passes ploughing through deep snow, but also capable of ploughing the fields. Its wool is used for blankets, ropes and tents, it has a particularly rich milk for butter and cheese, and its yak dung is a precious fuel in regions above the tree line. It feeds very frugally, but can also be eaten itself when necessary. Along steep rock slopes ingenious trails were built with dry stone clinging to inclined rock faces. Most important of all was the construction of hanging bridges which cross the wildest rivers in the Himalayan mountains. Originally "invented" in China, they were known already over 2000 years ago from the eastern Himalaya, built of bamboo and liana (Fig. 15). After the 6th century iron-chain hanging bridges

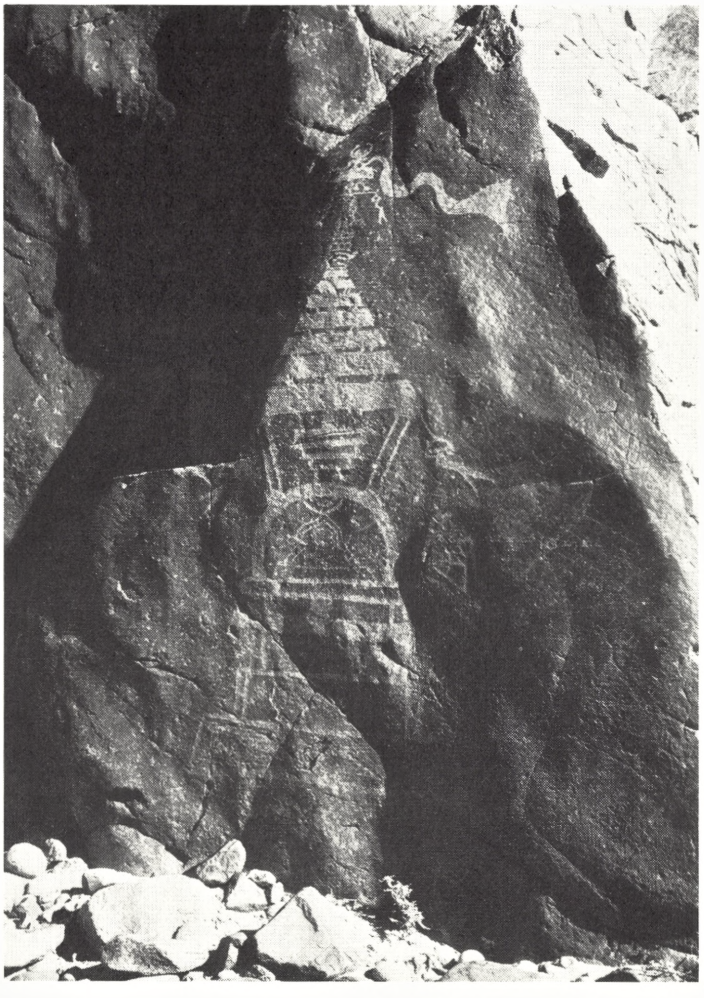

Fig. 14. A buddhistic stupa drawn on gabbroidic rocks at the Indus river near Chilas (Baltistan). Here and in the Hunza region Karl Jettmar has studied over 1000 drawings and inscriptions, spanning a time of 3000 years. They suggest a very old migration route to western Tibet. (Fot. A. Gansser).

Fig. 15. A primitive hanging bridge in the north-eastern Bhutan Himalaya. This bridge is built in a primitive way, only by liana and bamboo, a systhem over 2000 years old. (Fot. A. Gansser).

began to appear. They were propagated by the Bhutanese lama Thang-stong Gyalpo who used an ingenious method of welding the various chain links. The locally mined iron was melted into rods. These were forged to chain links and the links where welded together, probably on the spot. The analysis of such a welding seam (at the ETH in Zürich) showed an arsenic content of 2.6%. Arsenic lowers the melting temperature but produces a very hard welding junction. It is most surprising that this completely forgotten method was used in these remote areas (Epprecht 1979). Hanging bridges are up to now still the best system, considering the irregular floods of the wild Himalayan rivers.

Today we note a new type of migration. It has already invaded the western and central part of the Himalaya and now infiltrates also the eastern part and even to some extent southern Tibet. Is is international tourism with trekking and mountaineering, mostly in groups littering their paths with modern sediments. A certain contamination of the local population seems unavoidable, and it may be to the detriment of its important heritage, still documented in the numerous religious centres. It is a heritage of outstanding importance, considering the ill-fated development of our civilisation. Modern science may be able to preserve and to better understand those valuable

documents, many still hidden in block prints of remote monasteries but many more destroyed.

The visitor who enters the inner courtyard of the famous Paro Dzong, the monastery fortress in the western Bhutan Himalaya, is struck by a large wall painting. It represents a mandala of outstanding interest. Within a frame of red flames it shows the cosmic rings suggesting the planetary system or the modern picture of an atom. This Buddhist iconograph is the more astonishing since its conception is over 1000 years old (Fig. 16).

Acknowledgement: T.C.R. Pulvertaft kindly improved the original English manuscript.

Fig. 16. The "Cosmic Mandala" in the Paro Dzong, western Bhutan Himalaya. It represents a strikingly modern picture of a forgotten wisdom from ancient times. (Fot. U. Markus-Gansser).

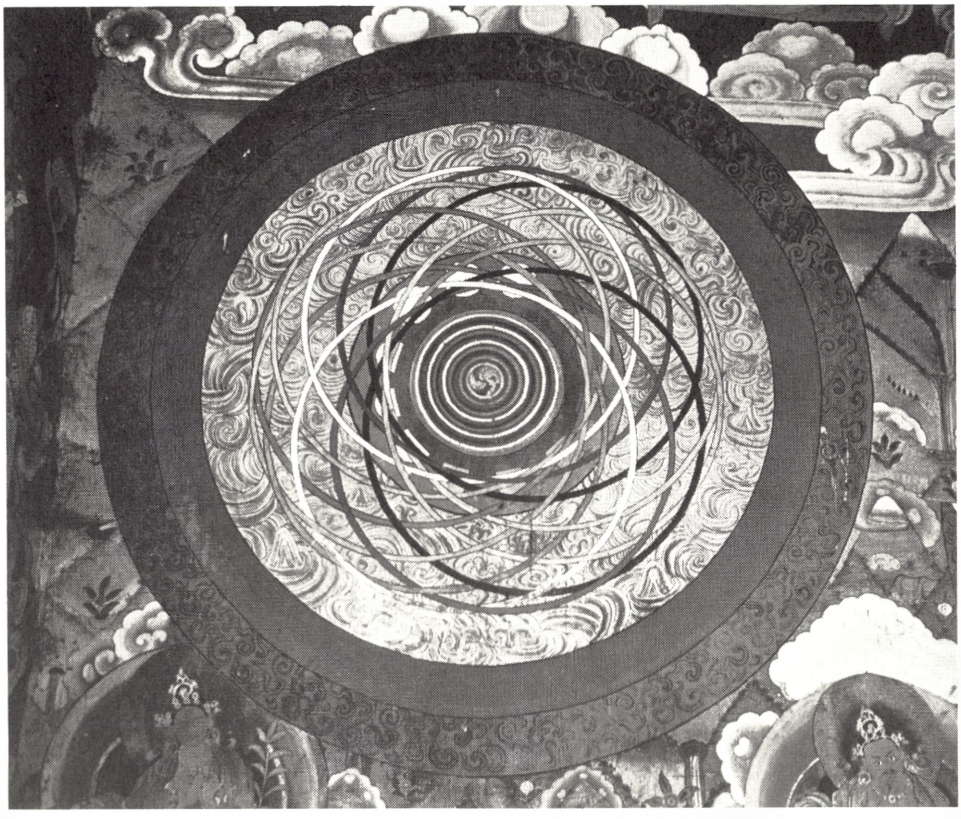

References

Academia Sinica, (1980): Scientific Guidebook to South Xizang (Tibet). Symposium on Oinghai-Xizang Plateau. Peking, 104 pp.

Allen, C. (1982): A Mountain in Tibet. André Deutsch Ltd. London. 255 pp.

Argand, E. (1924): La tectonique de l'Asie. C. R. 13 Congr. géol. Intern., 1922, 171–372.

Auden, B. J. (1935): Traverses in the Himalaya. Rec. geol. Surv. India, 69, 123–167.

Auden, J. B. (1937): The Structure of the Himalaya in Garhwal. Rec.geol.Surv.India, 71, 407–433.

Auden, J. B. (1981): India's former crustal neighbours. Proc. Indian Nat. Sc.Acad., New Delhi, 6, 47, 588–630.

Bell, Ch. (1928): The People of Tibet. Clarendon Press, Oxford. 319 pp.

Bhanot, V. B., Singh, V. P., Kansal, A. K. and Thakur, V. C. (1977): Early Proterozoic Rb-Sr Whole-rock Age for Central Crystalline Gneiss of Higher Himalaya, Kumaon. Jour. Geol. Soc. India, 18, 2, 90–91.

Buergisser, H. M., Gansser, A. and PICA, J. (1982): Late Glacial lake sediments of the Indus valley area, northwestern Himalayas. Ecolog. geol. Helv. 75/1, 51–63.

Burrard, S. G. (1912): On the Origin of the Himalaya Mountains. Survey of India, Prof. Paper Nr. 12, 8 pp.

Coward, M. P., Jan, M. Q., Rex, D., Tarney, J., Thirwall, M. and Windley, B. F. (1982): Geo-tectonic framework of the Himalaya of N. Pakistan. J. geol. Soc. London, 139, 299–308.

De Terra, H. and Paterson, T. T. (1939): Studies on the Ice Age in India and associated human cultures. Carnegie Inst. Washington, 354 pp.

Dietrich, V. and Gansser, A. (1981): The Leucogranites of the Bhutan Himalaya. Schweiz. mineral. petrogr. Mitt. 61, 177–202.

Epprecht, W. (1979): Schweisseisen-Kettenbrücken aus dem 14. Jahrhundert in Bhutan (Himalaya) mit arsenreicher Feuerschweissung. Arch. Eisenhüttenwes. 11, 473–477.

E. U. G. Meeting (1983): Abstracts, Terra Cognita, Strasbourg.

Fuchs, G. (1982): The Geology of the Pin Valley in Spiti, H. P. India. Jahrb. Geol. B.-A. 124/2, 325–359.

Gansser, A. (1974): The ophiolitic melange, a worldwide problem on Tethyan examples. Eclog.geol.Helv. 67, 497–507.

Gansser, A. (1980a): The Peri-Indian suture zone. Mémoire du B.R.G.M., 115, 140–148.

Gansser, A. (1980b): The Division between Himalaya and Karakorum. Geol.Bull.Univ.Peshawar, 13, 9–22.

Gansser, A. (1981): The Geodynamic History of the Himalaya. Geodynamic Series Vol. 3, Amer. Geoph. Union. 111–121.

Honegger, K., Dietrich, W., Frank, W. Gansser, A., Thöni, M. and Trommsdorff, V. (1982): Magmatism and metamorphism in the Ladakh Himalayas. Earth planet. Sci. Lett. 60, 253–292.

HSU, J. (1978): On the Paleobotanical Evidence for Continental Drift and the Himalayan Uplift. The Paleobotanist, Vol. 25, 131–142.

Jettmar, K. (1981): Felsbilder und Inschriften am Karakorum Highway. Indo-Asia 23, 1, Burg Verlag, 34–39.

Kuhle, M. (1982): Was spricht für eine pleistozäne Inlandvereisung Hochtibets? In Sonderheft 6, 1. Chinesisch-deutsche Tibet Expedition 1981. Braunschw. Wiss. Ges. 68–77.

Le Fort, P. (1973): Les leucogranites de l'Himalaya, sur l'example du granite du Manaslu (Népal central). Soc. Geol. France Bull. 7, 555–561.

Li Chi-chun and Cheng Pen-hsing (1980): Recent research on glaciers on the Chinghai-Tibet Plateau. Iahs-Aish Publ. Nr. 126, 121–127.

Lindegger, P. (1982): Griechische und Römische Quellen zum peripheren Tibet. Opuscula Tibetana, Fasc. 14, Tibet Institut, Rikon. 192 pp.

Loczy, L. von (1907): Beobachtungen im östlichen Himalaya (1878). Földr. Közlem. 35/9, 1–24.
Lydekker, R. (1881): Observations on the ossiferous beds of Hundes in Tibet. Rec. geol. Surv. India 14, 178–184.
Mu An-tze, Wen Shih-Hsuan, Wang Yi-Kang, Chang Ping-Kao and Yin Chi-Hsiang (1973): Stratigraphy of the Mount Jolmo Lungma region in southern Tibet, China. Scientia Sinica 16, (1), 96–111.
Norin, E. (1982): The Pamirs, K'unlun, Karakoram and Chang T'ang regions. Sino-Swedish Expedition, Publication 54. I. Geography, Vol. III/1. Stockholm. 61 pp.
Olschak, B. C. (1979): Ancient Bhutan, a study on Early Buddhism in the Himalayas. Swiss Foundation of Alp. Res. Zürich, 222 pp.
Schaefer, E. (1943): Geheimnis Tibet. München.
Tucci, G. (1937): Santi e Briganti nel Tibet ignoto. U. Hoepli, Milano. 190 pp.

Indsendt til Selskabet maj 1983
Færdig fra trykkeriet december 1983

Det Kongelige Danske Videnskabernes Selskab

Matematisk-fysiske Meddelelser

Mat. Fys. Medd. Dan. Vid. Selsk.

Priser excl. moms

Vol. 39 (Dkr. 590.–)

1. LINDHARD, J.: On the Theory of Measurement and its Consequences in Statistical Dynamics. 1974 ..... 50.–
2. KLEIN, OSKAR: Le principe d'équivalence d'Einstein utilisé pour une alternative de la cosmologie relativiste en regardant le système des galaxies comme limité et non comme l'univers. 1974 ..... 40.–
3. ANDERSEN, NILS, and SIGMUND, PETER: Energy Dissipation by Heavy Ions in Compound Targets. 1974 ..... 50.–
4. SIDENIUS, G.: Systematic Stopping Cross Section Measurement with Low Energy Ions in Gases. 1974 ..... 40.–
5. PEDERSEN, GERT KJÆRGÅRD: Borel Structure in Operator Algebras. 1974 40.–
6. KALCKAR, JØRGEN, and ULFBECK, OLE: On the Problem of Gravitational Radiation. 1974 ..... 40.–
7. MØLLER, C.: A Study in Gravitational Collapse. 1975 ..... 40.–
8. HYNNE, F.: A Class of Molecular Correlation Functions Related to Ursell Functions. 1975 ..... 40.–
9. KALCKAR, JØRGEN, and ULFBECK, OLE: Studies in Classical Electron Theory. I. 1976. ..... 50.–
10. ANDERSEN, J. U., ANDERSEN, S. KJÆR, and AUGUSTYNIAK, W. M.: Channeling of Electrons and Positrons, Correspondence between Classical and Quantal Descriptions. 1977 ..... 70.–
11. SIGMUND, PETER: Classical Scattering of Charged Particles by Molecules: Single and Multiple Collisions at Small Angles. 1977 ..... 40.–
12. DAHL, JENS PEDER: The Spinning Electron. 1977 ..... 50.–
13. MØLLER, C.: On the Crisis in the Theory of Gravitation and a Possible Solution. 1978 ..... 40.–

Vol. 40 (Dkr. 700.–)

1.–2. Investigations of Formaldehyde Oxime, its Polymers and Coordination Compounds.

1. Jensen, K. A., and Holm, Arne: On the Nature of the So-Called "Triformoxime" and Isolation of the Authentic Trimer, 1,3,5-Trihydroxyhexahydro–1,3,5-triazine. 1978 ..... 40.–
2. Andersen, Flemming A., and Jensen, K. A.: The Infrared Spectrum of Poly(formaldehyde oxime). 1978 ..... 40.–
3. Besenbacher, F., Andersen, H. H., Hvelplund, P., and Knudsen, H.: Stopping Power of Swift Hydrogen and Helium Ions in Gases. 1979 .. 50.–
4. Rasmusen, Hans Qvade: Three Revolutions of the Comets Halley and Olbers 1759–2024. 1979 ..... 60.–
5. Sigmund, Peter: Statistics of Particle Penetration. 1978 ..... 50.–
6. Aaboe, Asger, and Hamilton, N.T.: Contributions to the Study of Babylonian Lunar Theory. 1979 ..... 50.–
7. Andersen, J. U., Jensen, A. S., Jørgensen, K., Lægsgaard, E., Nielsen, K. O., Forster, J. S., Mitchell, I.V., Ward, D., Gibson, W. M., and Cuomo, J. J.: Lifetime Measurements for Heavy-Ion-Induced Fission by the Crystal-Blocking Technique. 1980 ..... 60.–
8. Brice, David K., and Sigmund, Peter: Secondary Electron Spectra from Dielectric Theory. 1980 ..... 50.–
9. Besenbacher, F., Andersen, H. H., Hvelplund, P., and Knudsen, H.: Straggling in Energy Loss of Swift Hydrogen and Helium Ions in Gases. 1981 ..... 50.–
10. Neugebauer, Otto: The 'Astronomical' Chapters of the Ethiopic Book of Enoch (72–82). Translation and Commentary. With Additional Notes on the Aramaic Fragments by Matthew Black. 1981 ..... 50.–
11. Kalckar, J., Lindhard, J., and Ulfbeck, O.: Self-Mass and Equivalence in Special Relativity. 1982 ..... 60.–
12. Cherly, Jørgen: Additive Theory for $\mathbf{F}_q$ [x] by Probability Methods. 1983 ..... 40.–
13. Koul, L., Chadderton, Lewis T., and Brooks, C. Kent: East Greenland and the Faeroe Islands: A Fission Track Study. 1983 ..... 50.–
14. Gansser, Augusto: The Wider Himalaya, a Model for Scientific Research. 1983 ..... 50.–

Printed in Denmark by Bianco Lunos Bogtrykkeri A/S. ISBN 0023-3323. ISBN 87-7304-141-6